

ELECTROSPINNING OF TISSUE ENGINEERED BLOOD VESSEL SCAFFOLDS UTILISING MULTIMODAL FIBRE DISTRIBUTIONS AND DYNAMIC LIQUID COLLECTED YARNS

A dissertation submitted for the degree of Ph.D.

Richard A.O'Connor B.Eng (Hons)

School of Mechanical and Manufacturing Engineering

Dublin City University

Under the supervision of

Dr. Garrett B. McGuinness

Prof. Paul A. Cahill

September 2018

Declaration

I hereby certify that this material, which I now submit for assessment on the programme of study leading to the award of Ph.D. is entirely my own work, that I have exercised reasonable care to ensure that the work is original, and does not to the best of my knowledge breach any law of copyright, and has not been taken from the work of others save and to the extent that such work has been cited and acknowledged within the text of my work.

Signed: _____ ID No.: 58526303 Date: _____

Publications and Presentations

Peer Reviewed Papers

R.A. O'Connor & G.B. McGuinness, Electrospun Nanofibre Bundles and Yarns for Tissue Engineering Applications: A Review, Proc. Inst. Mech. Eng. H 230 (11) (2016) 987–998.

Book Chapter Contribution

G.B. McGuinness, I. Pascu, C. Lally, R. O'Connor, Scaffold Processing Technologies for Tailored Cell Interactions. *Cell and material Interface: Advances in Tissue Engineering, Biosensor, Implant and Imaging Technologies*.

Peer Reviewed Conference Abstracts

R.A O'Connor & G.B. McGuinness, Electrospun yarns – offering the strength and porosity required for tissue engineering applications, CAPE, Edinburgh, 2015 (Oral presentation)

R.A O'Connor & G.B. McGuinness, Bi-layered Vascular Graft Incorporating Novel Electrospun Yarns, UK Society for Biomaterials, Belfast, 2015 (Oral presentation)

R.A O'Connor & G.B. McGuinness, Generation of Electrospun Yarns for Tissue Engineered Blood Vessels, 21st Bioengineering in Ireland Conference, Kildare, 2015 (Poster and rapid fire presentation)

R.A O'Connor & G.B. McGuinness, Generation of Electrospun Nanoyarns Scaffolds for use as Tissue Engineered Blood Vessels, European Society for Biomaterials, Liverpool, 2014 (Poster)

Internal Presentations

R.A. O'Connor, G.B. McGuinness, Electrospinning of Porous PCL Tissue Engineered Blood Vessel Scaffolds utilising Multimodel Fibre Distributions and Dynamic Liquid Collected Yarns. *Faculty of Engineering and Computing Research Day*, Dublin, Ireland, 2017 (Poster & rapid fire presentation)

R.A. O'Connor, G.B. McGuinness, Growing Blood Vessels in the Lab: It's Not Just a Yarn. *DCU 'Tell It Straight' Competition*, Dublin, Ireland, 2016 (Oral presentation-Category Winner)

Acknowledgments

Firstly, I would like to sincerely thank my project supervisor Dr. Garrett McGuinness, for providing me the opportunity to complete my research under his excellent stewardship. I am very grateful for the support and advice you offered me throughout the completion of my work and most importantly the continued patience you extended to me. Thank you also to Professor Paul Cahill for your guidance and advice.

I would like to thank all the staff who helped me during my times in DCU, especially the technical staff within the School of Mechanical and Manufacturing Engineering. To Liam, Chris, Michael M., Jim, Alan, Cian, Eoin, Dean, Keith & Michael T. I can only imagine the levels of frustration my continued pestering caused you, but I sincerely appreciate the pleasant manner and humour that you always afforded me.

To all my friends within the School of Mechanical and Manufacturing Engineering and the Vascular Biology & Therapeutics Group. Your friendship was the continued constant in a field of so many variables. A special thanks also to Renata Nunes Oliveira, who I like to think came all the way from Brazil to give me a crash course in bee wax and how to drink coffee. I hope to visit the sunny beaches of Rio de Janeiro soon.

To my best friends Niall, Paddy, Chris, Shane, Ben and Anto. I thank you for keeping me sane/embracing the madness, and for putting up with my long hibernations periods in DCU. Also, to all my friends and colleagues in STHOEE lifeguards, thank you for always putting a smile on my face, keep up the excellent work.

A very special thanks is owed to my girlfriend Mariana, who not only showed me unwavering support even on my grumpiest days but provided her excellent knowledge and counsel on all things cell culture related. I hope to show you the same love & support throughout the final months of your Ph.D.

Last, and most importantly, I would like to thank my Mam and Dad who over the last five years have shown me immense patience, love and support, throughout the trials

and tribulations of my studies. There are no words to describe my gratitude to you and I only hope you know this would not have been possible without you.

Contents

Declaration	i
Publications and Presentations	iii
Acknowledgments	v
List of Figures	xii
List of Tables	xxvii
Nomenclature	xxxii
Abstract	xxxiii
Chapter 1 Introduction	1
1.1 Cardiovascular Disease	1
1.2 Bypass Surgery	2
1.3 Vascular Grafts.....	2
1.4 Objectives.....	3
Chapter 2 Literature Review	7
2.1 Coronary Arteries	7
2.1.1 Architecture and Function.....	7
2.1.2 Mechanical Properties.....	9
2.1.3 Coronary Artery Disease.....	11
2.2 Coronary Artery Bypass Grafting	12
2.2.1 Vascular Grafts	14
2.2.2 Compliance Mismatch	15
2.3 Tissue Engineering and Tissue Engineered Blood Vessels.....	18
2.3.1 Tissue Engineered Approaches	18
2.3.2 Tissue Engineered Blood Vessels	20
2.3.3 Biomaterials for TEBVs.....	22
2.3.4 Poly(ϵ -caprolactone)	24
2.3.5 The Use of Stem Cells for Tissue Engineering Applications.....	25
2.4 Electrospinning.....	26
2.4.1 Fundamentals of Electrospinning.....	26
2.4.2 Electrospinning Parameters.....	28
2.4.3 Limitations of Electrospun Scaffolds.....	37
2.5 Methods to Improve Cell Infiltration on Electrospun Constructs	39
2.5.1 Multi-Modal Electrospinning.....	41
2.5.2 Nanofibre Bundles & Yarns.....	44
2.6 Rationale of Project and Research Approach.....	58

Chapter 3	Multi-scale Electrospinning of PCL Fibres.....	61
3.1	Introduction	61
3.2	Materials & Equipment	62
3.2.1	Materials.....	62
3.2.2	Equipment	63
3.3	Methods.....	64
3.3.1	Solutions Preparation and Characterisation	64
3.3.2	Electrospinning	66
3.3.3	Morphological and Fibre Diameter Assessment of Scaffolds.....	67
3.3.4	Characterisation of Electrospun Membranes	69
3.4	Design of Studies.....	73
3.4.1	Solution Screening Trial	73
3.4.2	Polymer Concentration Trial for Multimodal Fibres	75
3.4.3	Electrospinning of Nanofibre Membranes as Controls.....	75
3.5	Results	77
3.5.1	Solution Screening Trial	77
3.5.2	Polymer Concentration Trial for Multimodal Fibres	89
3.5.3	Electrospinning of Nanofibre Membranes as Controls	92
3.6	Discussion	99
3.6.1	Solution Screening Trial	99
Chapter 4	Development of Multimodal Hybrid Fibre Diameter Vessels by Rotating Mandrel Electrospinning Process	111
4.1	Introduction	111
4.2	Materials & Equipment	113
4.2.1	Materials.....	113
4.2.2	Equipment	113
4.3	Methods.....	114
4.3.1	Solution Preparation and Characterisation.....	114
4.3.2	Electrospinning of Small Diameter Tubular Scaffolds	115
4.3.3	Characterisation of Electrospun Membranes	116
4.4	Design of Studies.....	125
4.4.1	Regression Analysis of Multi-modal Electrospinning Process	125
4.4.2	Control of Molecular Weight Variation between PCL Batches through the Matching of Solution Viscosities	129
4.5	Results	132
4.5.1	Regression Analysis of Multimodal Rotating Mandrel Electrospinning	

	Process	132
4.5.2	Control of Molecular Weight Variation between PCL Batches through the Matching of Solution Viscosities	158
4.6	Discussion	172
4.6.1	Regression Analysis of Multimodal Rotating Mandrel Electrospinning Process	172
4.6.2	Control of Molecular Weight Variation between PCL Batches through the Matching of Solution Viscosities	180
Chapter 5	Development of Dynamic Liquid Collection Apparatus for the Production of Nanofibre Bundles.....	185
5.1	Introduction	185
5.2	Materials & Equipment	187
5.2.1	Materials.....	187
5.2.2	Equipment	187
5.3	Methods.....	188
5.3.1	Solution Preparation and Characterisation.....	188
5.3.2	Characterisation of Electrospun Membranes	190
5.4	Design of Studies.....	192
5.4.1	Process Development of Dynamic Liquid Electrospinning	192
5.5	Results	194
5.5.1	Process Development of Dynamic Liquid Electrospinning Process	194
5.6	Discussion	204
5.6.1	Process Development of Dynamic Liquid Collection.....	204
Chapter 6	Assessment of mMVSC Viability and Infiltration Capabilities on Electrospun Bi-Layer Vessels.....	207
6.1	Introduction	207
6.2	Materials and Equipment.....	209
6.2.1	Materials.....	209
6.2.2	Equipment	210
6.3	Methods.....	210
6.3.1	Preparation of Cell Culture Medium.....	210
6.3.2	General Cell Culture of mMVSCs	211
6.3.3	Preparation of Control Specimens and Scaffold Constructs	211
6.3.4	Seeding of mMVSCs on Control and Scaffold Constructs	212
6.3.5	Metabolic Activity by Resazurin Sodium Salt (AlamarBlue®).....	213
6.3.6	Quant-iT™ PicoGreen® dsDNA Assay	214

6.3.7	4',6-diamidino-2-phenylindole (DAPI) Staining	216
6.3.8	Cryofixation Fixation and Sample Sectioning	218
6.3.9	SEM of Cell Scaffold Constructs.....	220
6.4	Design of Cell Studies.....	220
6.4.1	alamarBlue® Analysis of mMVSCs Seeded on Electrospun Bi-layer Vessels	220
6.4.2	PicoGreen® Analysis of mMVSCs Seeded on Electrospun Bi-layer Vessels	220
6.4.3	Cell Nuclei Staining of mMVSCs Seeded on Electrospun Bi-layer Vessels by DAPI.....	221
6.4.4	Assessment of mMVSC Infiltration of Electrospun Bi-Layer Vessels by Cryosectioning Techniques.....	221
6.4.5	SEM of Cell Scaffold Constructs.....	221
6.5	Results	222
6.5.1	alamarBlue® Analysis of mMVSCs Seeded on Electrospun Bi-layer Vessels	222
6.5.2	PicoGreen® Analysis of mMVSCs Seeded on Electrospun Bi-layer Vessels	223
6.5.3	Cell Nuclei Staining of mMVSCs Seeded on Electrospun Bi-layer Vessels by DAPI.....	225
6.5.4	Assessment of mMVSC Infiltration of Electrospun Bi-Layer Vessels by Cryosectioning Techniques.....	226
6.5.5	SEM of Cell Scaffold Constructs.....	227
6.6	Discussion	230
6.6.1	Viability of mMVSCs Seeded upon Electrospun Materials.....	230
6.6.2	Comparison of Cell Infiltration Properties.....	231
6.6.3	Assessment of Cell morphology	232
Chapter 7	Conclusions & Recommendations.....	233
7.1	Main Findings.....	233
7.2	Recommendations	234
	Bibliography.....	236
	Appendices	263
	Appendix A: Complete Results of Solution Screening Trial.....	264
	Appendix B: Complete Results of Multimodal Fibre Spinning - Solution Concentration Study	282
	Appendix C: Development of Uniaxial Ringlet Test Method.....	295

Appendix D: Mechanical Assessment of Tubular Latex Membranes for Compliance	
Testing	300
Appendix E: Regression Analysis of Multi-modal Electrospinning Process	304
Appendix F: Residual Plots for Regression Analysis of Multi-modal Electrospinning	
Process	323
Appendix G: SEM Images of PCL Comparison Trial.....	329
Appendix H: SEM Images of Dynamic Liquid Electrospinning Screening Trial	336

List of Figures

Figure 1.1: Coronary Artery Bypass Grafting (A) Schematic of coronary artery bypass surgery showing bypassing of left anterior descending coronary (LAD) (Image obtained from www.medmovie.com); (B) Compliance characteristics of current bypass grafts correlated with long term patency characteristics [11] 3

Figure 2.1: Schematic cross section of an artery showing the three primary layers of arteries- the intima, media and adventitia and their constituents [30] 8

Figure 2.2: Uniaxial tensile response of vascular tissue (A) Typical Stress-Strain or ‘J-shaped’ curve of soft tissue [35] (B) Preconditioning curve showing hysteresis during five preconditioning cycles [32]..... 10

Figure 2.3: Atherosclerotic plaque formation and onset of MI (A) Adhesion of molecules result in monocytes and LDLs adhering to endothelium (B) Monocytes mature to macrophages absorbing LDLs to become Foam cells, T-cell activation and further macrophages recruited to lesion site (C) SMCs migrate from medial layer to lesion forming fibrous cap (D) Plaque ruptures resulting in thrombosis formation (adapted from [44]) 12

Figure 2.4: Percutaneous transluminal coronary angioplasty (PTCA) with stent [52] 13

Figure 2.5: Schematic of Coronary Artery Bypass Grafting (CABG) using the Autologous vessels ‘Saphenous vein (SVG)’ and the ‘Internal Mammary Artery (IMA)’ [55] 14

Figure 2.6: Intimal hyperplasia formation at the distal end of the vessel at anastomosis site[41]..... 16

Figure 2.7: Compliance-mean pressure curves for vessels and grafts used in CABG [42] 17

Figure 2.8: Schematic of the tissue engineering process [66]..... 19

Figure 2.9: Timeline showing the ideal development of arterial matrix in response to degradation of a biodegradable scaffold [67] 20

Figure 2.10: Ring opening Polymerisation of monomer ϵ -caprolactone to Poly(ϵ -caprolactone) and subsequent polymer chemical structure [119]..... 24

Figure 2.11: The electrospinning Process (A) Schematic of the basic electrospinning set-up with a flat metallic plate collector. Electrostatic forces result in Taylor's cone formation and subsequent jet initiation. An SEM image of a typical 2D random fibre mesh is also shown [147] (B) Trajectory of fluid jet with instabilities regions shown [150]..... 28

Figure 2.12: Image showing solvent molecules and molecular chains of polymers with the electrospinning jet (A) A high viscosity solution with solvent molecules evenly distributed amongst the polymeric molecular chains leading to a smooth fibre formation (B) Low viscosity solution show solvent congregation within the jet resulting in beaded solutions [161].....	31
Figure 2.13: Formation of polymer skin and subsequent removal in PEO/Chloroform solutions result in defects forming on the electrospun membrane surface [166]	32
Figure 2.14: H&E staining of SDRAECS seeded scaffolds after 7 days culture (A) PCL/Gelatin/pNSR32 with no cells (B) PCL (C) PCL/pNSR32 (D) PCL/Gelatin/pNSR32 [116]	38
Figure 2.15: (A) Viability (MTT assay) (B) Proliferation of MC3T3-E1 osteoblasts on the control PLGA and PLGA/5HAp nanofibrous scaffolds as a function of culture time (adapted from Lao et al. [194])	39
Figure 2.16: Dual Nozzle setup with simultaneous electrospinning of nanofibres and microfibrils (Adapted from [184])	42
Figure 2.17: SEM micrograph showing the PCL nonwovens with bimodal fibre size distribution (a1) 15 w/v% PCL/Chloroform solution at a rate of 0.2 ml/hr and ~50% humidity. Thick and thin fibres caused by different stretch rates can be observed. At ~30% humidity, unimodal fibres (rate: 0.2 ml/hr) were processed (b1). High speed images of the spin jet leading to the bimodal fibre meshes (a2: 1–3) and as comparison, the corresponding straight jet that leads to unimodal, microsized fibre meshes are shown (b2) (a2/b2: spin direction from right to left, pictures are taken at 1 995 fps close to the syringe tip, 50 ms exposure time). (Taken from [199]).....	43
Figure 2.18: Electrospun yarns created through disc edge collection (a) Aligned P(LLA-CL) yarns created by Xu et al. [173] (b) Electrospun PCL yarns in dynamic loading system as reported by Bosworth et al. [234]	54
Figure 2.19: SEM Images of L929 cells on the nanoyarn scaffold (A) and nanofiber scaffold (B). H&E staining images reveal cell infiltration in nanoyarn (C) scaffold and nanofiber scaffold (D). Cell proliferation on the scaffolds was determined by MTT assay (E) (Reproduced from Wu et al. [25])	55
Figure 2.20: Images of H&E-stained sections of P(LLA-CL)/collagen random nanofibre and aligned nanofibre scaffolds and yarn scaffold. (A, D, G) H&E staining of random nanofibre mesh at 4, 7 and 14 days post seeding, cellular infiltration limited to top layer of scaffold (B, E, H) H&E staining	

of aligned nanofibre mesh at 4, 7 and 14 days post seeding showing monolayer of cells on scaffold surface (C, F, I) H&E staining of yarn scaffold at 4, 7 and 14 days post seeding. Progressive infiltration of cells into nanoyarn scaffold body can be seen from day 4 to day 14 (Reproduced from Xu et al. [26]).....57

Figure 2.21: Schematic representation of proposed bi-layer vessel geometry with an inner layer of multimodal diameter fibres coated with a porous outer layer of electrospun nanofibre bundles..... 60

Figure 3.1: Brookfield DV-II+ Pro viscometer with temperature controlled recirculation unit used to maintain solution temperature at 25°C during testing..... 65

Figure 3.2: HD 8706 Conductivity meter with custom built PTFE probe guard and custom built PTFE sample cup..... 66

Figure 3.3: 2D random fibre membrane system (A) Components of electrospinning rig: high voltage power supply, syringe pump, capillary and metallic spinneret (B) Close up view showing 2D collector plate apparatus 67

Figure 3.4: Rotating drum system for the creation of aligned fibre membranes (A) Components of rig: Capillary and spinneret on optional traversing platform (B) Close up view showing large diameter rotating drum with deposited PCL fibre membrane. 68

Figure 3.5: Orientation J Analysis of electrospun fibre membrane (A) Colour map indicator of electrospun fibre edges (B) Representative colour map indicator (C) Orientation distribution of electrospun fibre membrane..... 69

Figure 3.6: Uniaxial tensile testing sample preparation (A) Custom designed ‘dogbone’ punch with gauge length of 10mm and width of 3mm (B) Custom designed punch system with sample holder and punch guide (C) Sample dogbone specimen cut from electrospun membrane 71

Figure 3.7: Uniaxial tensile testing of dogbone samples (A) Sample in no loaded state (B) Sample during testing shown significant elongation (C) Sample after failure showing fracture along centre of specimen..... 72

Figure 3.8: Fibre diameter analysis of micron and multimodal spinning solutions produced over the parameter range of 6-12 ml/hr flow rate, 15-20kV applied voltage and 15-20cm collector distance (A) Diameter results for Chloroform, Chloroform/Ethanol (9:1) and Chloroform/Ethanol (7:3) solutions (B) Diameter results for Chloroform, Chloroform/Methanol (9:1) and Chloroform/Methanol (7:3) solutions..... 80

Figure 3.9: Fibre diameter analysis of nanofibre spinning solutions produced over the

parameter range of 0.25-1ml/hr flow rate, 10-20kV applied voltage and 10-15cm collector distance (A) Diameter results for 8wt% Chloroform/DMF (7:3) (B) Diameter results for 11wt% Chloroform/DMF (7:3) and 11wt% Chloroform/DMF (5:5) solutions 85

Figure 3.10: Viscosity and conductivity results of Chloroform/DMF solutions studied for nanofiber generation (A) Viscosity and conductivity profile of 6, 8 and 11wt% PCL Chloroform/DMF (7:3; v:v) solutions, showing linear increase in viscosity with increasing polymer content ($R^2 = 0.9899$) and consistent conductivity value of $0.9\mu\text{S}/\text{cm}$ at all polymer concentrations. (B) Viscosity and conductivity profile of 6, 8 and 11wt% PCL Chloroform/DMF (5:5; v:v) solutions showing linear increase in viscosity with increasing polymer content ($R^2 = 0.9948$) and consistent conductivity value of $1\mu\text{S}/\text{cm}$ at all polymer concentrations. N=3 per test group. 88

Figure 3.11: Sample set of SEM images for multimodal polymer concentration trial showing the changes in fiber morphology with increasing polymer concentration from 10-18wt% in 2wt% increments. Samples were produced at the processing parameter combination of 6ml/hr flow rate, 20kV applied voltage and 20cm collector distance. Corresponding fiber diameter comparison (n=150 per group) is presented, with a statistical difference observed between 10 and 16wt% solutions ($p < 0.001$) and 18wt% ($p < 0.0001$). A statistical difference was also detected between 12wt% and 18wt% solution ($p < 0.001$). No statistical difference observed between all other polymer concentration levels. Kruskal-Wallis with Dunn correction was used for multiple comparisons due to unequal variances between groups..... 90

Figure 3.12: Viscosity and conductivity profile of solutions studied for multimodal spinning applications. Polymer concentration increased from 10 to 18wt%, in 2wt% increments. N=3 per test group. 91

Figure 3.13: Fiber diameter comparison of randomly orientated nanofiber membranes collected over 1hr (n=5) and 4hr (n=5) time periods. No statistical difference in fiber diameters observed between any of the membranes collected ($p = 0.0938$)..... 92

Figure 3.14: Fiber diameter comparison of aligned nanofiber membranes collected over 4hr (n=5) and 12hr (n=5) time periods. No statistical difference in fiber diameters observed between any of the membranes collected ($p = 0.1099$) 93

Figure 3.15: Fiber diameter and orientation analysis of electrospun nanofiber

membranes (A) Comparison of fibre diameters within aligned and random fibre membranes (n=150) showing statistical decrease in aligned fibre diameters ($p < 0.0001$) (B) Coherency assessment of nanofibre membranes (n=5) showing statistical increase in fibre alignment within aligned nanofibre membranes ($p < 0.0001$) (C) Random fibre membrane showing no dominant direction of alignment (D) Aligned membrane showing preferential alignment of fibres	95
Figure 3.16: Thickness comparison of Aligned nanofibre membranes (Deposition period 12hrs) and Random nanofibre membranes (Deposition period 4hrs) showing no statistical difference in sample thickness ($p = 0.0533$). N=5 for each test group.....	96
Figure 3.17: Stress vs Strain profiles obtained for uniaxial dogbone testing of random and aligned nanofibre membranes. Aligned fibre membranes were tested in both a parallel and perpendicular to preferential fibre orientation. N=5 for each test group.....	97
Figure 3.18: Focused view showing the initial loading and strain region for random and aligned nanofibre dogbone specimens. N=5 for each test group.....	97
Figure 3.19: Summarised results of uniaxial tensile tests of random and aligned nanofibre membrane dog-bone specimens (A) Ultimate tensile strength (UTS) of nanofibres membranes showing statistically higher UTS between aligned fibre membrane tested parallel to the preferential axis of fibre alignment (PFA) and perpendicular to the PFA (n=5 per test group) (B) Young's modulus of nanofibres membranes showing statistically higher modulus between aligned fibre membrane tested parallel and perpendicular to PFA (n=5 per test group) (C) Strain at break of nanofibres membranes showing statistical decrease in strain at break in aligned fibre membranes tested parallel to PFA and those tested perpendicularly. No statistical difference was detected between the random nanofibre membranes and the aligned membranes for any of the response characteristics observed with random membranes exhibiting properties between those of the two aligned fibre test cases (n=5 per test group) (D) Porosity results of aligned and random membranes showing no detectable statistical difference (n=10 for each test group).	98
Figure 4.1: Electrospinning of 3D tubular scaffolds (A) Rotating mandrel rig indicating traversing motion and direction of mandrel rotation (B) PCL tubular scaffold removed from copper mandrel after methanol soaking step.....	115

Figure 4.2: Schematic diagrams of ringlet dimensions (A) Internal and external diameters measured at two orthogonal orientations (B) Length of ringlet specimens ‘L’ (C) Configuration of vessel when true gauge length (L_0) of specimen is reached.....	118
Figure 4.3: Uniaxial ringlet test (A) Sample before testing mounted on extension pins (B) Schematic of gauge length (L_0) used in post processing of tensile data (C) Sample of image after testing.....	118
Figure 4.4: Stress vs strain profile of electrospun ringlet specimen showing distinct loading stages with corresponding specimen configurations as verified by video extensometer. Region (1) shows sample after pre-load with walls of ringlet in a non-parallel configuration resulting in a large strain for a small applied load. Region (2) shows an increased stress response with the video extensometer confirming the specimen has reached its theoretical gauge length point. Region (3) shows yielding of sample. Region (4) showing specimen failure. It is noted that enhanced outlines have been added to the samples to aid in image clarity	120
Figure 4.5: Stress vs strain response of electrospun ringlet specimen with initial toe region removed and strain normalised to theoretical gauge length point. It is observed that the strain response is significantly altered, compared to that of the non-normalised response as seen in Figure 4.4 indicating the importance of this method for the calculation of Young’s modulus and strain at break.	121
Figure 4.6: Static compliance test (A) Test rig showing sample chamber attached to inflater device used to control the pressurisation of samples. An attached extension device control by a micrometer allows for the controlled strain of samples (B) Latex membrane used to prevent fluid leakage through wall of electrospun scaffolds (C) Electrospun sample mounted over latex balloon.....	122
Figure 4.7: Static compliance test of electrospun tubular vessel showing a sample specimen pressurised at predetermined intervals ranging from 0 to 750mmHg. Image J analysis used to determine average sample diameter based upon three diameters taken along length of sample	123
Figure 4.8: Stress strain profiles obtained from uniaxial ringlet testing of tubular specimens created at a flow rate of 4ml/hr, applied voltage of 15kV and collection distance of 15cm prepared as part of the linear regression analysis study (A) Replicate specimens created at the lower mandrel	

rotational speed of 1600 RPM (B) Replicate specimens created at the higher mandrel rotational speed of 3200 RPM. N=3 per scaffold.....	135
Figure 4.9: Main effects and interaction plot for the regression variable ‘UTS (Y_1)’ showing the effects of changing input variable levels to the response variable of interest. Greyed backgrounds represent a term or interaction not included within the reduced model used to predict the output response.	138
Figure 4.10: Main effects and interaction plot for the regression variable ‘YM (Y_2)’ showing the effects of changing input variable levels to the response variable of interest. Greyed backgrounds represent a term or interaction not included within the reduced model used to predict the output response.	140
Figure 4.11: Main effects and interaction plot for the regression variable ‘Max Force (Y_3)’ showing the effects of changing input variable levels to the response variable of interest. Greyed backgrounds represent a term or interaction not included within the reduced model used to predict the output response.	142
Figure 4.12: Main effects and interaction plot for the regression variable ‘Ring modulus (Y_4)’ showing the effects of changing input variable levels to the response variable of interest. Greyed backgrounds represent a term or interaction not included within the reduced model used to predict the output response.	144
Figure 4.13: Main effects and interaction plot for the regression variable ‘Porosity (Y_5)’ showing the effects of changing input variable levels to the response variable of interest. Greyed backgrounds represent a term or interaction not included within the reduced model used to predict the output response.	146
Figure 4.14: Main effects and interaction plot for the regression variable ‘Mean Inner Fibre Diameter (Y_6)’ showing the effects of changing input variable levels to the response variable of interest. Greyed backgrounds represent a term or interaction not included within the reduced model used to predict the output response.....	148
Figure 4.15: Main effects and interaction plot for the regression variable ‘Mean Outer Fibre Diameter (Y_7)’ showing the effects of changing input variable levels to the response variable of interest. Greyed backgrounds represent a term or interaction not included within the reduced model used to predict the output response.....	150
Figure 4.16: Main effects and interaction plot for the regression variable ‘Inner Fibre Coherency (Y_8)’ showing the effects of changing input variable levels to the response variable of interest. Greyed backgrounds represent a term or interaction not included within the reduced model used to predict the output	

response.....	152
Figure 4.17: Main effects and interaction plot for the regression variable ‘Outer Fibre Coherency (Y ₉)’ showing the effects of changing input variable levels to the response variable of interest. Greyed backgrounds represent a term or interaction not included within the reduced model used to predict the output response.....	154
Figure 4.18: Interval plot of UTS responses for sample studies as part of the multi-modal electrospinning regression analysis, with lower and upper boundary ranges of common blood vessels indicated. Data for Human Coronary Arteries (HCA’s) is adapted from Karimi et al. [173], and the Great Saphenous Vein (GSV) from Donovan et al. [279].....	155
Figure 4.19: Interval plot of Young’s modulus responses for specimens studied as part of the multi-modal electrospinning regression analysis, with lower and upper boundary ranges of common blood vessels indicated. Data for Human Coronary Arteries (HCA’s) is adapted from Karimi et al. [173], and the Great Saphenous Vein (GSV) from Donovan et al. [279].....	156
Figure 4.20: Comparison of ring modulus, cross sectional area and max force properties of parameters Sets 1 and 2 identified from multi-modal regression analysis (n=9 per set). The ring modulus (p=0.0297), cross sectional area (p=0.0042) and maximum force at failure (p=0.0049) were found to be statistically higher for Set 1 compared to those of Set 2.	158
Figure 4.21: GPC results of ‘00807DJ-Original’ and ‘MKBV3325V-New’ PCL batches showing a significant difference in retention time indicating a clear difference between the molecular weight of the two PCL batches. ‘00807DJ-Original’ PCL was found to have ~M _w of 80,000 g/mol while ‘MKBV3325V-New’ was found to have a ~M _w of 100,000 g/mol.....	159
Figure 4.22: Solution standard curves prepared using the Original and New PCL batches used to select the concentration of a solution prepared using 100,000 g/mol PCL (100kDa) that possessed a comparative viscosity to that of a 16wt% solution prepared using 80,000 g/mol PCL (80kDa). A weight percentage concentration of 7.8wt% for the 100kDa PCL was found to provide a solution with equivalent viscosity characteristics. N=3 per solution.	160
Figure 4.23: Viscosity and conductivity comparison of 16wt% solutions (n=3) prepared using the PCL batch ‘00807DJ-Original’ and 7.8wt% solutions (n=3) prepared using the PCL batch ‘MKBV3325V-New’. No statistical difference was observed between either viscosity (p=0.106) or	

conductivity..... 160

Figure 4.24: UTS results for PCL batch comparison showing statistically larger UTS properties for 100kDa specimens to 80kDa specimens for all time points and test configurations studied (A) UTS response for Set 1 ringlet samples showing higher UTS for 100kDa PCL to 80kDa PCL. UTS for 40min ringlets prepared using 100kDa PCL are seen to be statistically higher than those collected over 10 and 20 mins. All time points for 80kDa PCL were however equivalent (B) UTS response for Set 2 ringlet samples showing statistically higher UTS for 100kDa PCL to 80kDa PCL. UTS for 20min ringlets prepared using 100kDa PCL was found to be statistically lower than those collected over 40 (***) and 60 min (****). All time points for 80kDa PCL were again equivalent (C) UTS response for Set 1 dogbone samples showing statistically higher UTS for 100kDa PCL to 80kDa PCL. UTS for 10min ringlets prepared using 100kDa PCL was found to be statistically lower than those collected over 40min (*). All time points for 80kDa PCL were equivalent (D) UTS response for Set 2 dogbone samples showing statistically higher UTS for 100kDa PCL to 80kDa PCL. UTS for 10min ringlets prepared using 100kDa PCL was found to be statistically lower than those collected over 40min (*). All time points for 80kDa PCL were equivalent. (* $P \leq 0.05$)(** $P \leq 0.01$)(*** $P \leq 0.001$)(**** $P \leq 0.0001$). N=3 per test group..... 162

Figure 4.25: Young's modulus (YM) results for PCL batch comparison (A) YM response for Set 1 ringlet samples showing increased YM for 80kDa PCL compared to 100kDa PCL for 10 and 20 minute collection times (B) YM response for Set 2 ringlet samples showing statistically higher YM for 80kDa PCL to 100kDa PCL for all collection periods (C) YM response for Set 1 dogbone samples showing statistically higher YM for 100kDa PCL to 80kDa PCL over 40min (****). PCL 100kDa and 80kDa were statistically equivalent for all other time points (D) YM response for Set 2 dogbone samples showing statistically higher YM for 80kDa PCL to 100kDa PCL over 20min collection period. PCL 100kDa and 80kDa were statistically equivalent for all other time points (* $P \leq 0.05$)(** $P \leq 0.01$)(*** $P \leq 0.001$)(**** $P \leq 0.0001$). N=3 per test group. 163

Figure 4.26: Ring and Force modulus results for PCL batch comparison study (A) Ring modulus (RM) response for Set 1 ringlet specimens showing increased RM responses with increasing deposition time (B) RM responses for Set 2

ringlet samples showing statistically higher RM for 80kDa PCL to 100kDa PCL for all collection periods. RM responses also seen to increase with increasing deposition time (C) Force modulus (FM) response for Set 1 dogbone samples showing statistically higher FM for 100kDa PCL at 40min to 10min specimens (**). No other statistical differences observed (D) FM response for Set 2 dogbone samples showing statistically higher FM for 80kDa PCL and 100kDa PCL at 60min collection period to those collected for 20min. All other comparisons were statistically equivalent (* $P \leq 0.05$)(** $P \leq 0.01$)(*** $P \leq 0.001$)(**** $P \leq 0.0001$). N=3 per test group. 165

Figure 4.27: Strain at break results for PCL batch comparison (A) Set 1 ringlet samples showing increased strain at break properties for 100kDa PCL specimens compared to those made using 80kDa PCL (B) Strain at break for Set 2 ringlet samples showing statistically higher strains for 100kDa PCL to 80kDa PCL for all collection periods (C) Strain at break for Set 1 dogbone samples showing statistically higher strains for 100kDa PCL to 80kDa PCL for all collection periods (D) Strain at break for Set 2 dogbone samples showing statistically higher strains for 100kDa PCL to 80kDa PCL for all collection periods (* $P \leq 0.05$)(** $P \leq 0.01$)(*** $P \leq 0.001$)(**** $P \leq 0.0001$). N=3 per test group. 166

Figure 4.28: Morphological attributes of scaffolds examined in PCL batch comparison trial (A) Diameter of fibres at outer surface of scaffold prepared using parameter Set 1 showing no difference in fibre diameters between PCL batches or collection times (B) Diameter of fibres at outer surface of scaffold prepared using parameter Set 2 showing no difference in fibre diameters between PCL batches or collection times (C) Diameter of fibres at inner surface of scaffold prepared using parameter Set 1 showing no difference in fibre diameters between PCL batches or collection times (D) Diameter of fibres at inner surface of scaffold prepared using parameter Set 2 showing no difference in fibre diameters between PCL batches or collection times (E) Coherency of outer surface fibres for parameter Set 1. Statistical difference observed between 100kDa and 80kDa specimens produced for 10 min with decreased coherency for 100kDa specimens (F) Coherency of outer surface fibres for parameter Set 2. Statistical difference observed between all 100kDa and 80kDa specimens produced. 100kDa specimens significantly lower coherency compared to 80kDa specimens indicating decreased fibre alignment (G) Coherency of inner surface fibres

for parameter Set 1. Statistical difference observed between 100kDa and 80kDa specimens produced for 10 & 20 mins with decreased coherency observed for 100kDa specimens (F) Coherency of inner surface fibres for parameter Set 2. Statistical difference observed between all 100kDa and 80kDa specimens produced. 100kDa specimens significantly lower coherency compared to 80kDa specimens. N=3 per test group. 167

Figure 4.29: Porosity results for PCL batch comparison study (A) Set 1 specimens showing increased porosity properties for 80kDa PCL specimens compared to those made using 100kDa PCL for all collection periods (B) Porosity results for Set 2 specimens showing statistically higher porosity values for 80kDa PCL to 100kDa PCL for all collection periods (* $P \leq 0.05$)(** $P \leq 0.01$)(*** $P \leq 0.001$)(**** $P \leq 0.0001$). N=3 per test group. 168

Figure 4.30: XRD profiles of PCL tubular scaffolds prepared using 80,000 (80kDa) and 100,000 g/mol (100kDa) PCL at the same spinning parameters. No shift in peak positions are seen indicating equivalent crystallinity properties. A baseline of cellulose tape is shown..... 169

Figure 4.31: Compliance properties of tubular scaffolds fabrication from 7.8wt% PCL ($M_w=100,000$ g/mol) in Chloroform/Ethanol (7:3) solutions spun according to parameter combinations for Set 1 & 2 (n=3 per group). ‘Set 1 - 10 min’ vessels showed visually equivalent compliance properties to that of native arteries and higher than that of veins and ePTFE grafts (n=6 per group). ‘Set 2 – 20min’ specimens showed increased compliance properties compared to those of the biological vessels at 100 mmHg. Data for biological vessels was adapted from Tia et al. [42]..... 170

Figure 5.1: Images of custom built dynamic liquid electrospinning rig (A) Broad view of spinning apparatus showing two tier water bath system, syringe pump, along with rotating and traversing collector mandrel (B) Zoomed view showing vortex formation in top tier water bath used to induce nanofibre bundle formation (C) Sample image of nanofibre bundle materials deposited on collector mandrel..... 189

Figure 5.2: Removal of nanofibre assemblies from collection mandrels (A) Pure nanofibre bundles collected on mandrel before and after removal (B) Bi-layer vessel collected on mandrel before and after removal 190

Figure 5.3: Process development map for 8wt% PCL in Chloroform/DMF (7:3) solutions spun using dynamic liquid collection rig, showing stability and quality characteristics for specimens collected at the flow rates of 0.25, 0.5,

1 and 2ml/hr.....	195
Figure 5.4: Process development map for 8wt% PCL in Chloroform/DMF (7:3) solutions spun using dynamic liquid collection rig, showing combined ranking characteristics for specimens collected at the flow rates of 0.25, 0.5, 1 and 2ml/hr.....	196
Figure 5.5: Process development map for 11wt% PCL in Chloroform/DMF (7:3) solutions spun using dynamic liquid collection rig, showing stability and quality characteristics for specimens collected at the flow rates of 0.25, 0.5, 1 and 2ml/hr.....	197
Figure 5.6: Material aggregation during dynamic liquid collection process (A) Material collecting of face of water bath/surface of water (B) Fibre forming between collection frame and water surface (C) Subsequent breakdown of water vortices due to material aggregation within the water baths	198
Figure 5.7: Process development map for 11wt% PCL in Chloroform/DMF (7:3) solutions spun using dynamic liquid collection rig, showing combined ranking characteristics for specimens collected at the flow rates of 0.25, 0.5, 1 and 2ml/hr.....	198
Figure 5.8: Mechanical assessment of bi-layer vessels and their constituents (A) UTS characteristics of ‘set 1’ cores, nanofibre bundle layers and subsequent bi-layer vessels (B) UTS characteristics of ‘set 2’ cores, nanofibre bundle layers and subsequent bi-layer vessels (C) Young’s modulus characteristics of ‘set 1’ cores, nanofibre bundle layers and subsequent bi-layer vessels (D) Young’s modulus characteristics of ‘set 2’ cores, nanofibre bundle layers and subsequent bi-layer vessels (E) Force modulus characteristics of ‘set 1’ cores, nanofibre bundle layers and subsequent bi-layer vessels (F) Force modulus characteristics of ‘set 2’ cores, nanofibre bundle layers and subsequent bi-layer vessels (G) Strain at break characteristics of ‘set 1’ cores, nanofibre bundle layers and subsequent bi-layer vessels (H) Strain at break characteristics of ‘set 2’ cores, nanofibre bundle layers and subsequent bi-layer vessels. N=6 per group.....	201
Figure 5.9: Mechanical and morphological assessment of bi-layer vessels and their constituents (A) Maximum force characteristics of ‘set 1’ cores, nanofibre bundle layers and subsequent bi-layer vessels (B) Maximum force characteristics of ‘set 2’ cores, nanofibre bundle layers and subsequent bi-layer vessels (C) Porosity characteristics of ‘set 1’ cores, nanofibre bundle layers and subsequent bi-layer vessels (D) Porosity characteristics of ‘set	

2' cores, nanofibre bundle layers and subsequent bi-layer vessels (E)	
Density measurements of 'set 1' cores, nanofibre bundle layers and	
subsequent bi-layer vessels (F) Density measurements of 'set 2' cores,	
nanofibre bundle layers and subsequent bi-layer vessels. N=6 per group.....	202
Figure 5.10: Compliance properties of multimodal PCL cores and bi-layer vessels (A)	
Compliance results for core layers and bi-layer vessels produced by 'set 1'	
processing parameters (B) Compliance results for core layers and bi-layer	
vessels produced by 'set 2' processing parameters. N=6 per data set.	203
Figure 6.1: Preparation of controls and scaffold constructs for cell culture (A) Cell	
crown assembly method showing the process used to mount electrospun	
specimens and control glass slides in CELLCROWN™ inserts (B) Random	
and aligned fibre discs punched from electrospun membranes (C)	
Composite vessel specimens cut from larger tubular scaffold (D) Sample	
image showing scaffolds mounted in insert system	212
Figure 6.2: Schematic of cell counting method used on glass slides and scaffold	
constructs.....	217
Figure 6.3: Schematic of protocol utilised for cryofixation and sectioning of electrospun	
specimens used to determine cell infiltration rates.....	219
Figure 6.4: alamarBlue® of mMVSCs seeded upon control and electrospun specimens	
(A) %Metabolic activity of mMVSCs seeded on random, aligned and bi-	
layer electrospun structures with metabolic activity expressed relative to	
day 1 control specimens (B) Cell standard curve generated for	
alamarBlue® assay. (*P≤0.05)(**P≤0.01)(*** P≤0.001)(**** P≤0.0001).	
N=3 for each group (three replicates taken per sample).....	222
Figure 6.5: PicoGreen® of mMVSCs seeded upon control and electrospun specimens	
(A) %DNA concentration of mMVSCs seeded on random, aligned and bi-	
layer electrospun structures expressed relative to day 1 control specimens	
(B) Cell standard curve generated for PicoGreen® assay (C) DNA standard	
curve used to relate RFI to DNA concentration. N=3 for each group (three	
replicates taken per sample).	224
Figure 6.6: DAPI nuclei staining of mMVSCs seeded upon electrospun scaffolds and	
control specimens (A) Percentage cell count results showing count of	
aligned, nanofibre and bi-layer electrospun structures expressed with	
respect to day 1 control specimens. N=3 for each group (three replicates	
taken per sample). (B) Sample image of DAPI stained cells showing blue	
cell nuclei (taken at 20X magnification)	225

Figure 6.7: Assessment of mMVSC infiltration of electrospun specimens (A) ‘%Relative Cell Infiltration’ showing statistically higher infiltration of cells on bi-layer vessels at day 14 compared to both aligned and random fibre constructs (B) Actual depth measurements of infiltrating cells showing statistically higher infiltration on bi-layer vessels for both day 7 and 14 specimens compared to the random and aligned fibre constructs. N=5 per group.....	227
Figure 6.8: Cross sectional images of electrospun scaffolds seeded with mMVSCs after 7 and 14 days in culture (A) Cross sectional views of aligned, random and bi-layer electrospun structures showing DAPI stained cell nuclei and corresponding light microscope images of scaffold after 7 days in culture (B) Cross sectional views of aligned, random and bi-layer electrospun structures showing DAPI stained cell nuclei and corresponding light microscope images of scaffold after 14 days in culture.	228
Figure 6.9: SEM images of cell laden electrospun scaffolds viewed at low level magnification.....	229
Figure 6.10: SEM images of cell laden electrospun scaffolds viewed at high level magnification.....	229
Figure C.0.1: Uniaxial ringlet testing of electrospun vessels using video extensometer tracking (A) Calibration of extensometer using tracking gauge (B) Ringlet specimen prior to loading with black tracking beads attached to surface of specimen (C) Ringlet specimen after testing with black track beads intact	297
Figure C.0.2: Stress vs strain profiles obtained from one test specimen showing the three methods used to determine the point at which test commencement began	298
Figure C.0.3: Stress vs strain profile of electrospun ringlet specimen showing distinct loading stages with corresponding specimen configurations as verified by video extensometer. Region (1) shows sample after pre-load with walls of ringlet in a non-parallel configuration, resulting in a large strain for a small applied load. Region (2) shows an increased stress response with the video extensometer confirming the specimen has reached its theoretical gauge length point. Region (3) shows yielding of sample. Region (4) showing specimen failure. It is noted that enhanced outlines have been added to the samples to aid in image clarity	298
Figure D.0.1: Stress-Strain response of latex membranes (n=3) and electrospun tubular scaffolds (n=6) showing a distinct difference in sample stiffness. It is noted that the full profile of the latex balloon is not displayed due to excessively	

high strain at break witnessed.....	302
Figure D.0.2: Compliance comparison of pure latex membranes (n=10) compared to electrospun tubular specimens (n=6) mounted upon latex membranes. Latex membranes showed significantly higher compliance (p=0.004).	302
Figure F.0.1: Residual Plots for Response Variable UTS ‘Y ₁ ’	324
Figure F.0.2: Residual Plots for Response Variable Young’s modulus ‘Y ₂ ’	324
Figure F.0.3: Residual Plots for Response Variable Max Force ‘Y ₃ ’	325
Figure F.0.4: Residual Plots for Response Variable Ring modulus ‘Y ₄ ’	325
Figure F.0.5: Residual Plots for Response Variable Porosity ‘Y ₅ ’	326
Figure F.0.6: Residual Plots for Response Variable Mean Inner Fibre Diameter ‘Y ₆ ’	326
Figure F.0.7: Residual Plots for Response Variable Mean Outer Fibre Diameter ‘Y ₇ ’	327
Figure F.0.8: Residual Plots for Response Variable Inner Fibre Coherency ‘Y ₈ ’	327
Figure F.0.9: Residual Plots for Response Variable Outer Fibre Coherency ‘Y ₉ ’	328

List of Tables

Table 2.1: Compliance and patency rates for arterial and venal grafts [10]	17
Table 2.2: Properties of the ideal TEBV for use in vascular bypassing as set out by Walpoth & Bowlin (adapted from [9])	21
Table 2.3: Parameters known to affect fibre formation during electrospinning and typical working ranges (adapted from [152][152])	29
Table 2.4: Typical jet characteristics and corresponding effect on fibre formation [171]	34
Table 2.5: Short nanofibre bundles and yarns.....	47
Table 2.6. Continuous bundles and yarn.....	51
Table 3.1: Solvent Screening Combinations	73
Table 3.2: Design Matrix for Micron and Multimodal Diameter Fibre Spinning.....	74
Table 3.3: Design Matrix for Nano Diameter Fibre Spinning	74
Table 3.4: Design Matrix for Solution Concentration Optimisation Experiment (Multimodal Fibres)	76
Table 3.5: Optimum parameters identified for the electrospinning of nanofibre membranes.....	76
Table 3.6: SEM images of scaffolds produced using Chloroform and the surfactants Ethanol and Methanol. Images show scaffolds produced at a sample processing parameters range of a 6ml/hr flow rate, applied Voltage of 20kV over a range of 15-20cm collector distance.....	79
Table 3.7: SEM images of scaffolds produced using Chloroform and the surfactant N,N- Dimethylformamide (DMF). Images show scaffolds produced at a sample processing parameters range of a 0.25ml/hr flow rate, applied voltage of 15kV over a collector distance range of 10-15cm using Chloroform/DMF (7:3;v:v) and Chloroform/DMF (5:5;v:v) solutions	82
Table 3.8: Conductivity of pure electrospinning chemicals and solvent/surfactant combinations measured at 25°C	86
Table 3.9: Conductivity of complete electrospinning solutions studied within solution screening trial, multimodal study and nanofibre spinning measured at 25°C (n=3 per solution).....	87
Table 3.10: Ambient spinning conditions and airflow measurements recorded during nanofibre spinning of control membrane	94
Table 4.1: Processing parameters under investigation as part of the multi-modal spinning DOE with corresponding levels for each working parameter.....	126

Table 4.2: Design matrix for the regression analysis of multimodal electrospinning process utilising 16wt% Chloroform/Ethanol (7:3) solutions	127
Table 4.3: Response properties of scaffolds (Ys) assessed as part of multi-modal electrospinning regression analysis	128
Table 4.4: Polymer concentration levels used to generate viscosity profile for comparison to original PCL batch	131
Table 4.5: Parameter combinations identified for comparison of 16wt% solutions prepared with original PCL batch to 7.8wt% solutions prepared using new PCL batch.....	131
Table 4.6: Sample images of specimens obtained from the regression analysis of the multimodal electrospinning process. Specimens were produced over the flow rate range of 4-12ml/hr, applied voltage range of 10-20kV and a collection distance of 17.5cm	133
Table 4.7: Adjusted parameter range for multi-modal spinning trial to account for loss of samples ensuring orthogonality of study.....	136
Table 4.8: Full Model vs. Reduced Model in Coded Variables for Output Variable Y ₁ ‘UTS’ Obtained by dropping All Terms with p>0.05	137
Table 4.9: Full Model vs. Reduced Model in Coded Variables for Output Variable Y ₂ ‘YM’ Obtained by dropping All Terms With p>0.05	139
Table 4.10: Full Model vs. Reduced Model in Coded Variables for Output Variable Y ₃ ‘Max Force’ Obtained by dropping All Terms With p>0.05	141
Table 4.11: Full Model vs. Reduced Model in Coded Variables for Output Variable Y ₄ ‘Ring modulus’ Obtained by dropping All Terms With p>0.05	143
Table 4.12: Full Model vs. Reduced Model in Coded Variables for Output Variable Y ₅ ‘Porosity’ Obtained by dropping All Terms With p>0.05.....	145
Table 4.13: Full Model vs. Reduced Model in Coded Variables for Output Variable Y ₆ ‘Mean Inner Fibre Diameter’ Obtained by dropping All Terms With p>0.05	147
Table 4.14: Full Model vs. Reduced Model in Coded Variables for Output Variable Y ₇ ‘Mean Outer Fibre Diameter’ Obtained by dropping All Terms With p>0.05.....	149
Table 4.15: Full Model vs. Reduced Model in Coded Variables for Output Variable Y ₈ ‘Inner Fibre Coherency Obtained by dropping All Terms With p>0.05	151
Table 4.16: Full Model vs. Reduced Model in Coded Variables for Output Variable Y ₉ ‘Outer Fibre Coherency’ Obtained by dropping All Terms With p>0.05	153
Table 4.17: Parameter Combinations Identified for Preparation of Multi-modal Core	

Layer by Rotating Mandrel Electrospinning	157
Table 4.18: Parameter combinations identified for comparison of 16wt% solutions prepared with original PCL batch to 7.8wt% solutions prepared using new PCL batch.....	170
Table 5.1: Process parameters utilised to fabricate PCL multi-modal core scaffolds.....	190
Table 5.2: Stability & Collection Criteria.....	192
Table 5.3: Quality Criteria	193
Table 5.4: Design Matrix used for the process development of dynamic liquid electrospinning process	193
Table 6.1: Cell Standard Curve used for Alamar Blue and PicoGreen Experiments.....	214
Table 6.2: DNA standard curve solution quantities and final DNA concentrations	216
Table A.0.1: SEM results of micron and multimodal solution screening trial.....	264
Table A.0.2: Fibre diameter results for micron and multimodal solution screening trial. Results presented as average \pm standard deviation.....	269
Table A.0.3: Ambient spinning conditions and airflow measurements recorded during solution screening trial	269
Table A.0.4: SEM results of solution screening trial for nanofibre solution screening	270
Table A.0.5: Fibre diameter results for nanofibre spinning solution screening trial. Results presented as average \pm standard deviation.....	279
Table B.0.1: SEM results of multimodal polymer concentration trial showing sample created over a polymer concentration range of 10-18wt%, flow rate range of 6 and 12ml/hr, applied voltage of 15 and 20kV, and collector distance of 15 to 20cm.....	282
Table B.0.2: Fibre diameter results for multimodal fibre spinning – polymer concentration study. Results.....	293
Table B.0.3: Ambient spinning conditions and airflow measurements recorded during multimodal polymer concentration trial	294
Table E.0.1: SEM images of samples prepared using 16wt% PCL dissolved in Chloroform/Ethanol (7:3; v:v) spun onto rotating mandrel spinning at 1600 RPM	305
Table E.0.2: SEM images of samples prepared using 16wt% PCL dissolved in Chloroform/Ethanol (7:3; v:v) spun onto rotating mandrel spinning at 3200 RPM	308
Table E.0.3: Mechanical and Porosity Results for Regression Analysis Specimens created at 1600 RPM.....	311
Table E.0.4: Morphological Results for Regression Analysis Specimens created at 1600	

RPM	314
Table E.0.5: Mechanical and Porosity Results for Regression Analysis Specimens created at 3200 RPM	317
Table E.0.6: Morphological Results for Regression Analysis Specimens created at 3200 RPM	320
Table G.0.1: SEM images of PCL Comparison Trial	330
Table H.0.1: SEM images of PCL nanofibre bundles created through dynamic liquid electrospinning approaches	337

Nomenclature

ANOVA – Analysis of Variance	Coronary artery
BET – Brunauer–Emmett–Teller	LCX – Left Circumflex Coronary artery
CABG – Coronary Artery Bypass Grafting	M – Molar
CAD – Coronary Artery Disease	MCF-7 – Mammary Carcinoma Cells
cm – Centimetres	mm – Millimetre
CPU – Poly(carbonate)polyurethane	mM – milli-Molar
CVD – Cardiovascular Disease	mMVSCs – Mouse Multipotent Vascular Stem Cells
DAPI – 4',6-diamidino-2-phenylindole	mg/ml – Milligram/millilitre
DMF – Dimethylformamide	ml/hr – Millimetres Per Hour
dH ₂ O – Distilled Water	mPa – Millipascal
EC – Endothelial Cells	MPA – Megapascal
ESC – Embryonic Stem Cells	mPa.s – Millipascal seconds
ECM – Extracellular Matrix	mS/cm – millisiemens/centimeter
ePTFE – Expanded Polytetrafluoroethylene	Mw – Molecular Weight
FM – Force Modulus	OD – Outer Diameter
g – Grams	P4HB – Poly-4-hydroxybutyrate
g/mol – gram/mole	PAN – Poly(acrylonitrile)
GSV – Great Saphenous Vein	PBS – Phosphate Buffered Saline
h – Hours	PCL – Poly(ε-caprolactone)
HDMS – Hexamethyldisilazane	PDI – Polydispersity index
hMSCs – Human Mesenchymal Stem Cells	PET – Polyethylene Terephthalate
H&E – Hematoxylin and Eosin	PGA – Poly(glycolic acid)
ID – Internal Diameter	PIECs – Pig Iliac Endothelial Cells
IM – Internal Mammary Artery	PLA – Poly(lactic acid)
ISO – International Organization for Standardisation	PLGA – Poly(lactide-co-glycolide)
kDa – Kilodalton	P(LLA-CL) – Poly(L-lactide-co-caprolactone)
kV – Kilovolts	PMMA – Poly(methyl methacrylate)
LAD – Left Anterior Descending	PTCA – Percutaneous Transluminal Coronary Angioplasty
	PTFE – Polytetrafluoroethylene

PU – Polyurethane	vessel
PVA – Poly(vinyl alcohol)	TFM – Tissue Freezing Medium
PVAc – Poly(vinyl acetate)	THF – Tetrahydrofuran
PVDF – Poly(vinylidene difluoride)	tpm – Twists per Minute
PVDF-co-HFP – Poly(vinylidene difluoride-co-hexafluoropropylene)	UTS – Ultimate Tensile Stress
PVP – Poly(vinyl pyrrolidone)	v – Volume
RFI – Relative Fluorescence Intensity	vSMC – Vascular Smooth Muscle Cells
ROI – Region of Interest	WAXD – Wide Angle X-Ray Diffraction
RM – Ring Modulus	wt% – Weight Percent
RPM – Revolutions Per Minute	YM – Young’s Modulus
s – Seconds	XRD – X-Ray Diffraction
S.D – Standard Deviation	μm – Micrometre
SEM – Scanning Electron Microscope	μL – Microlitre
SDRAECs – Sprague Dawley Aorta Endothelial Cells	$\mu\text{S/cm}$ – Microsiemens/centimeter
TEBV – Tissue Engineered Blood	

Abstract

Electrospinning of Tissue Engineered Blood Vessel Scaffolds Utilising Multimodal Fibre Distributions and Dynamic Liquid Collected Yarns

Richard A. O'Connor

The successful replacement of small-diameter blood vessels, affected by cardiovascular disease, with natural and synthetic bypass grafts remains limited due to long-term patency issues. The development of a tissue engineered blood vessel (TEBV), with properties mimicking that of the native vessel to be replaced, may provide a potential solution. Electrospinning, a polymer processing technique capable of producing nano to micron-scale in diameter fibres has been studied extensively in the last decade as a potential technique for the fabrication of tissue scaffolds. Insufficient cell infiltration into electrospun constructs, and thus incomplete remodelling of the scaffolds, has however hindered their use in clinical applications to date. Electrospinning variations, including the production of multi-modal fibre diameter scaffolds and nanofibre bundles that offer increased porosities compared to traditional electrospun materials may allow these limitations to be overcome. This study looks at the development of a bi-layer scaffold consisting of a small diameter multi-modal core layer paired with highly porous nanofibre bundles.

Electrospun tubular core layers possessing multi-modal fibre diameter populations were created using poly(ϵ -caprolactone) solutions prepared in chloroform and ethanol. Dynamically liquid collected nanofibre bundles were subsequently deposited on the core layers using a bespoke collector system and optimised spinning solutions. The final bi-layer vessels fabricated possessed UTS properties of 2.584 ± 0.453 MPa and compliance rates of 2.366 ± 0.732 % per mmHg $\times 10^{-2}$. These properties were highly comparable to that of native vascular tissue indicating the potential long-term success of these scaffolds. In addition, the use of nanofibre bundles was shown to provide increased cell infiltration rates compared to traditional electrospun nanofibre membranes, with cells shown to penetrate to depths of $\sim 30\mu\text{m}$ after 14 days in culture. These combined findings are highly promising for the development of next generation tissue engineered blood vessels.

Chapter 1 Introduction

1.1 Cardiovascular Disease

Cardiovascular disease (CVD) accounts for an estimated 17.5 million global deaths each year and is currently the leading cause of mortality and morbidity in the world [1]. It is estimated that approximately 92.1 million US adults suffer from at least 1 type of CVD, with the mortality rate standing at 219.9 persons per 100,000 translating to 30.8% of all US deaths annually [2]. Increased public health awareness paired with early patient access and continuing advancements in medical device technology have resulted in declining CVD related deaths across Europe and the United States in recent years [2][3]. Despite this it remains a major source of economic concern with treatment estimated to have cost the US economy \$316.1 billion in the year 2013 alone. Of this \$189.7 billion can be attributed to direct costs including hospital care and medication, and a further \$126.4 billion attributed to the indirect loss of productivity due to patient absence from the workplace [2]. By 2030 an estimated \$1 trillion will be spent on the direct medical costs of CVDs in the US alone [2].

Coronary artery disease (CAD) is one of the most prevalent forms of cardiovascular disease and can be attributed to ~1 of every 7 deaths in the United States [1]. CAD is associated with the build-up of atheroma, also referred to as atherosclerotic plaques, within the coronary arteries of the heart. The coronary arteries supply the myocardium of the heart with oxygen and nutrient rich blood, which is essential for its efficacious functionality. Plaque formation results in both the stiffening of the arteries and the stenosis (narrowing) of the lumen preventing adequate blood flow reaching tissues downstream of blockage sites, ultimately resulting in medical conditions such as myocardial infarctions, known commonly as a heart attack.

1.2 Bypass Surgery

The development of non-invasive surgical techniques such as angioplasty and stenting along with pharmaceutical drug treatments have allowed for many cardiovascular diseases including stenosis of the coronary arteries to be relieved without the need for invasive surgeries [4][5]. In severe cases, coronary artery bypass grafting (CABG) may be required to fully re-vascularise the cardiac tissue. Bypass surgery is a highly invasive vessel reconstruction procedure whereby a blocked coronary artery segment is bypassed with an alternative vessel referred to as a vascular graft. Figure 1.1 (A) shows a diagrammatic representation of a vascular graft used to bypass a blockage in the left coronary artery. Here a graft is used to connect the aortic root to the left anterior descending coronary (LAD) below the point of blockage, restoring an adequate supply of blood to the heart and the surrounding tissues.

1.3 Vascular Grafts

Autologous vascular grafts, or grafts taken from an alternative site within the patient, are currently considered the gold standard vessels for use in arterial bypassing with the Great Saphenous Vein (GSV) traditionally being the vessel of choice for small diameter applications [6]. Increased patient risk due to infection at the site of harvest and the declining supply of suitable host vessels in aging populations have, however, driven a search for an alternative source of suitable vascular grafts [7]. A number of synthetic grafts have been developed including Polyethylene Terephthalate (PET, Dacron®) and expanded Polytetrafluoroethylene (ePTFE) based vessels. Although proven successful in the bypassing of medium to large diameter blood vessels (>6mm internal diameter) they have shown poor patency rates when used in small diameter (<6mm) applications [8][9].

Failure of these synthetic grafts is often linked with the term ‘compliance mismatch’ wherein the elastic properties of the bypass graft do not match those of the native arteries. This mismatch is suggested to generate flow instabilities that damage the endothelial lining of arteries leading to thrombus formation and intimal hyperplasia, ultimately resulting in long-term graft failure [10].

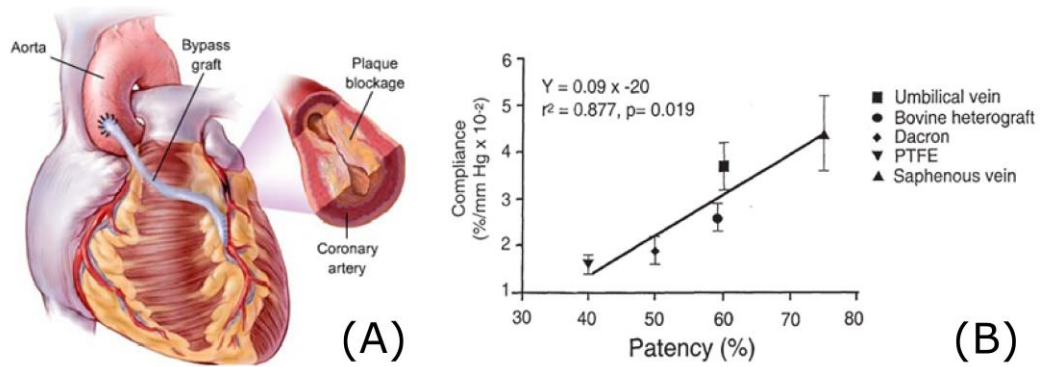


Figure 1.1: Coronary Artery Bypass Grafting (A) Schematic of coronary artery bypass surgery showing bypassing of left anterior descending coronary (LAD) (Image obtained from www.medmovie.com); (B) Compliance characteristics of current bypass grafts correlated with long term patency characteristics [11]

Figure 1.1 (B) shows the relationship between vessel compliance and patency rates for a range of vascular grafts used in femoral-popliteal bypassing. It is observed that with decreasing vessel compliance comes a reduction in vessel patency. The development of a small-diameter graft with biomechanical properties matching those of native coronary arteries is a pressing clinical need.

1.4 Objectives

Continuous advancements in engineering and the life sciences have driven researchers towards the interdisciplinary field of tissue engineering as a possible solution to the shortage of suitable vessels for use in coronary artery bypass grafting (CABG) [9][12][13][14]. Tissue engineering combines the principles of engineering and the life sciences in order to develop biological substitutes that can be used to restore or replace tissue and organ function [15]. By combining cells with highly porous 3D biodegradable structures referred to as scaffolds, replacement tissue structures can be created either *in vitro* or *in vivo* [16]. These scaffolds act as templates for newly populating cells, offering stability and guidance during the early stages of tissue formation. The seeded cells are anticipated to secrete supporting molecules allowing for the formation of an extracellular matrix (ECM) as the polymer degrades away [17]. The final envisaged product is a stand-alone biological construct that aims to match the properties of the native tissue to be replaced.

Electrospinning is a scaffold fabrication technique capable of producing nano to micron-scale diameter fibres that has been studied extensively in the last decade for the creation of tissue engineered vascular grafts (TEVG) [17][18]. Its ability to create fibrous structures that resemble the body's natural ECM in both scale and architecture, along with high surface area to volume ratios and tuneable mechanical characteristics has made it a versatile scaffold production technology to study [19].

A significant challenge in the development of electrospun TEVGs is a lack of cell penetration and the insufficient transport of nutrients throughout the scaffold body, due to the small size, complex distribution and lack of connectivity of pores within electrospun structures [19][20]. Inadequate penetration of cells into the scaffold depths prevents complete remodelling of the tissue occurring throughout, often leading to graft failure as the fibres begin to degrade. A number of techniques have been proposed within the literature for the development of electrospun materials that demonstrate enhanced porosity characteristics such as porogen leaching [21][22], and sacrificial fibre spinning [23]. These techniques do however typically suffer from a number of limitations including a loss of mechanical integrity which has prevented them from being successfully employed [24].

Two variations of the electrospinning process that may provide a potential route for the creation of electrospun scaffolds that demonstrate increased cell penetration properties are multi-modal fibre spinning and dynamic liquid electrospinning. Multi-modal electrospinning allows for the simultaneous creation of nano and micron-scale diameter fibres from a single spinning solution. This method offers increased pore sizes due to the crossing of large micron scale fibres within deposition planes, while intermixed nanoscale diameter fibres offer anchorage sites for cell attachment. The second approach considered is the production of linear bundles of electrospun fibres through dynamic liquid electrospinning. Membranes formed from these fibrous bundles have been shown to exhibit increased porosity and pore volumes compared to traditional electrospun structures while also offering increased post-processing potential due to their ability to be incorporated in to techniques such as knitting and weaving [25][26].

A scaffold assembled from multi-modal fibres paired with electrospun fibre bundles is

anticipated to provide increased cell penetration rates and ultimately lead to the increased success of electrospun materials in tissue engineering applications. The objectives of this project are as follows:

- To explore the multi-modal electrospinning of poly(ϵ -caprolactone) (PCL) solutions using a single step spinning process and to further develop a small diameter tubular construct with properties mimicking that of native vascular tissue
- To implement and characterise a dynamic liquid electrospinning process for the creation of PCL fibrous bundles, studying the effect of solution and processing parameters on overall process stability and fibre bundle morphology
- To develop a composite electrospun vessel fabricated from multi-modal PCL fibres paired with dynamically collected fibrous bundles characterising mechanical attributes including vessel compliance
- To compare the cellular infiltration properties of the composite electrospun vessel to traditional electrospun nanofibre membranes

Specific objectives and research methodologies will be further outlined within the research rational following a review of the current literature.

Chapter 2 Literature Review

2.1 Coronary Arteries

The cardiovascular system of the body consists of three essential components; the heart, the blood vessels and the fluid they contain, blood. Within this, blood vessels can be designated to be part of the systemic circulatory or pulmonary circulatory system [27]. The systemic system consists of the blood vessels that carry oxygenated blood away from the heart to the body and the vessels that return the deoxygenated blood back to the heart. The pulmonary circulatory system consists of the blood vessel loop that transports blood between the heart and the lungs. The right and left main coronary arteries, members of the systemic circulatory system, are small diameter blood vessels that branch from the ascending aorta at the right and left aortic sinuses respectively. The right coronary artery encircles the right atrium and ventricle supplying them with oxygenated blood and has an internal diameter (ID) of 1.5 - 5.5mm [28]. The left coronary artery supplies the left atrium and ventricle with oxygenated blood, and is the larger of the two coronaries. It bifurcates into the left anterior descending coronary artery (LAD) with an ID range of 2.0-5.5 mm and the left circumflex coronary artery (LCX) with ID 1.5-5.5mm [27][28].

2.1.1 Architecture and Function

Arteries are complex vessels whose architecture depends highly on their location within the vasculature system. Arteries can be categorised into two main groups' namely elastic and muscular arteries. Elastic arteries are the largest arteries of the body including the aorta and the common carotid and are often located close to the heart. Muscular arteries are generally small to medium diameter vessels including the coronary arteries and the radial artery. All arteries contain three distinct layers referred to as the tunics; the tunica intima, tunica media and the tunica adventitia as shown in Figure 2.1 [29].

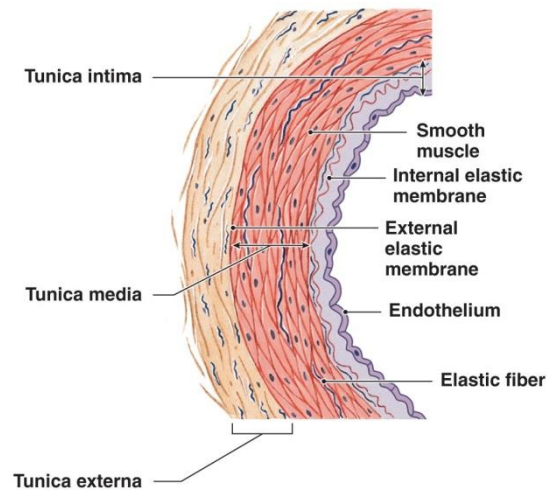


Figure 2.1: Schematic cross section of an artery showing the three primary layers of arteries- the intima, media and adventitia and their constituents [30]

The tunica intima is the inner layer of the artery and is comprised of the endothelium and the basal lamina. It contributes little to the mechanical resistance of a vessel but is important for stable blood flow. The endothelium is a monolayer of endothelial cells that are orientated in the direction of blood flow whose function is to provide a smooth non-thrombogenic lining allowing for smooth blood flow and selective diffusion [28]. A cushioning layer known as the basal lamina (~80nm in thickness) surrounds the endothelium allowing for the vessel to bend and change diameter under pulsatile flow conditions and provides a surface on which the endothelial cells grow [8]. The basal lamina is comprised of collagen type IV, proteoglycans and the adhesion molecules laminin and fibronectin.

The tunica media is the mid layer of an artery and offers the main structural resistance of a vessel. The categorisation of arteries as elastic or muscular depends on the composition of this layer. In elastic arteries the media layer is composed of 5 to 15 μm concentric rings of vascular smooth muscle cells (vSMCs) separated by sheets of elastic fibres. Thick elastic arteries may be composed of 40 to 70 of these layers. Muscular arteries contain a single thick layer of helically orientated vSMCs embedded in a loose extracellular matrix of elastin and collagen fibres.

The adventitial layer or the outer most layer of an artery is composed of fibroblasts, large-diameter type I collagen fibres, proteoglycans, nerves and in large to medium

diameter vessels the vasa vasorum [29]. Again, this layer does not contribute extensively to the mechanical resistance and response of the vessel but rather acts as a binding and anchorage layer to surrounding tissues.

2.1.2 Mechanical Properties

In order to develop a suitable vascular graft for CABG it is important to understand the biomechanical properties of the native tissues to be replicated. The unique architecture of soft tissues including vascular tissue gives rise to an equally unique set of biomechanical properties including non-linearity, anisotropy and viscoelasticity.

Uniaxial tensile testing of vascular tissue has been performed by a number of researchers with non-linear responses observed [31]–[33]. This nonlinear behaviour arises due to the multi-component composition of the arterial wall and is often referred to as the J-shaped profile of soft tissues, Figure 2.2 (A). As reviewed previously the layers of the arteries, most notably the tunica media, contain collagen and elastin fibres. Collagen is the primary load-bearing element of arteries and offers resistance during the systolic phase of the cardiac cycle. Collagen has a natural undulated morphology under normal physiological conditions. The elastin fibres of an artery provide a recoil effect that smooths the flow of blood during the transition from the systole to diastole phase of the cardiac cycle. During initial loading of vascular tissue elastin fibres provide the principal mechanical resistance. These fibres strain significantly under small applied loads giving a large initial strain region known as the ‘toe’. As loading increases the undulated collagen fibres begin to straighten and align in the direction of loading. Collagen, the dominant load-bearing fibre does not strain significantly, so a stress-stiffening effect is witnessed.

Fibrous and cellular content within the arterial walls are highly orientated aiding in resisting specific stresses experienced during pulsatile blood flow. As a result arterial tissue is highly anisotropic with different stress-strain responses seen when loading occurs in the axial, circumferential and radial directions. Circumferentially orientated intima and adventitia samples have been shown to stiffen at higher strains compared to longitudinal samples. In contrast the medial layers has been shown to stiffen at lower strains in the circumferential orientation compared to the longitudinal [33][34].

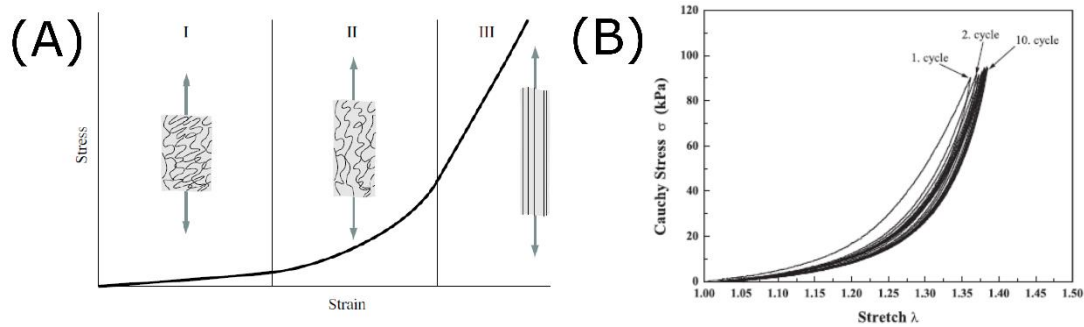


Figure 2.2: Uniaxial tensile response of vascular tissue (A) Typical Stress-Strain or ‘J-shaped’ curve of soft tissue [35] (B) Preconditioning curve showing hysteresis during five preconditioning cycles [32]

Pure elastic solids strain instantaneously when loaded and regain their original dimensions when the stress is removed. Newtonian fluids on the other hand exhibit a constant rate of strain when a constant viscous stress is applied, and do not retract when the stress is removed. Arterial tissue contains both solid material and fluid constituents so exhibits a combination of these properties, a behaviour known as viscoelasticity. Viscoelastic materials demonstrate creep, stress relaxation and hysteresis characteristics. Creep is the time-dependent change in strain due to a constant stress while stress relaxation is characterised by a decrease in stress under a constant strain [36].

In vivo arteries are subjected to both longitudinal stretching and internal pressurisation. When the material is excised from the body the corresponding stresses are released [37]. This stress release results in the samples visibly shrinking in the longitudinal and circumferential directions indicating the sample has entered a no-load state [36]. If a sample is then loaded, unloaded and reloaded the stress-strain response can be seen to change between the first and second loading cycles. This non-coincidental loading path occurs due to the reorientation of fibres and cells within the tissue. If cyclic loading and unloading is performed a sufficient number of times a stable stress vs strain loop is achieved, the sample is now said to be in a preconditioned state [36][38]. It can also be observed (Figure 2.2 (B)) that the loading and unloading cycles do not follow an identical path, a characteristic known as hysteresis. This hysteresis occurs due to the internal changes of the tissue structure coupled with energy dissipation caused by friction forces generated between fibres during loading [37].

Another important property of vascular tissue is compliance. Compliance is a measure of vessel distensibility and is defined as the ratio between the change in volume (ΔV) or diameter ($\Delta\phi$) of a vessel for a given internal pressure change (ΔP) [39]. Compliance is a significant characteristic to be considered when designing a vascular graft as numerous studies have shown the significance of reducing “compliance mismatch” for maintaining long term graft patency [40]–[42]. A number of formulas exist for calculating the compliance of a vessel with each formula dependent on the experimental methodology used. The general formula for the compliance of a vessel is given by [42];

$$Compliance = \frac{D_s - D_d}{D_d \times (P_s - P_d)} \times 10^4 \text{ (\% per mmHg} \times 10^{-2}) \quad (\text{Equation 2.1})$$

Where ‘D’ and ‘P’ are vessel diameter and blood pressure respectively. Subscript ‘d’ and ‘s’ refer to diastole and systole measurements.

2.1.3 Coronary Artery Disease

Coronary artery disease (CAD) is the most prevalent form of cardiovascular disease and is the leading cause of death amongst men and women throughout the world [43]. CAD is associated with the accumulation of atherosclerotic plaques within the coronary arteries resulting in ischemia of the myocardium.

Arteriosclerosis is the general classification of diseases that result in the thickening of artery walls and a loss of elasticity. Atherosclerosis is one form of arteriosclerosis and is a progressive disease associated with a chronic inflammatory response within arteries. A cascade of immune cell signalling and factor secretion induce vSMC proliferation from the medial layer of the artery into the atherosclerotic lesion. The vSMCs form a fibrous cap over the plaque protecting it from blood flow. A schematic of the lesion formation process can be seen in Figure 2.3. Atherosclerotic plaques typically do not fully occlude the vessel with myocardial infarctions predominantly occurring when the fibrous cap breaks open in response to chemical factors secreted by foam cells within the lesion. These factors in turn lead to thrombosis formation which rapidly decreases the flow of blood to the myocardium [27][44][45].

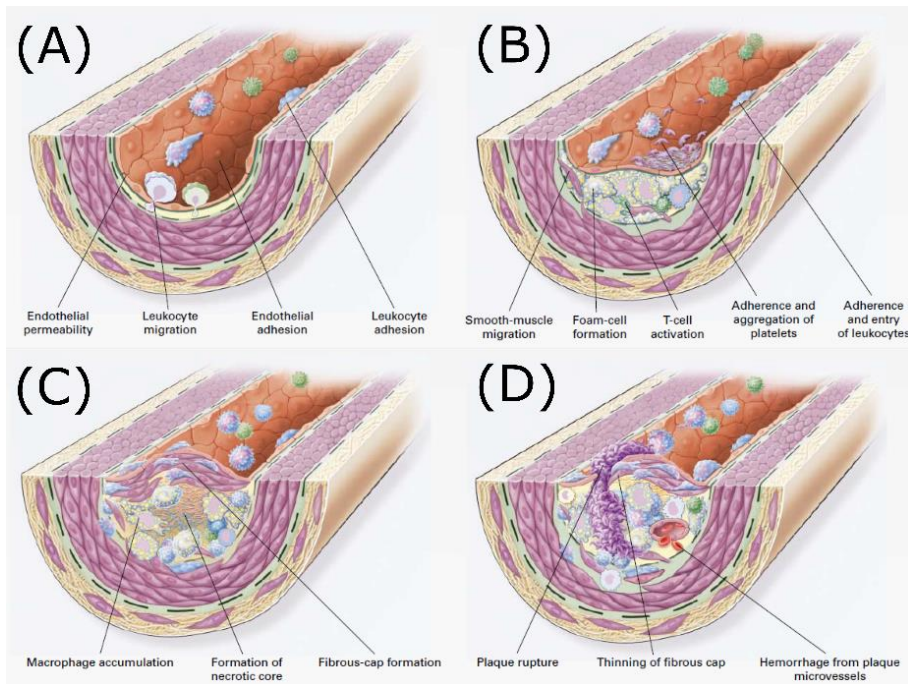


Figure 2.3: Atherosclerotic plaque formation and onset of MI (A) Adhesion of molecules result in monocytes and LDLs adhering to endothelium (B) Monocytes mature to macrophages absorbing LDLs to become Foam cells, T-cell activation and further macrophages recruited to lesion site (C) SMCs migrate from medial layer to lesion forming fibrous cap (D) Plaque ruptures resulting in thrombosis formation (adapted from [44])

Specific regions within the vasculature are highly prone to endothelium dysfunction and in turn atherosclerosis such as branches, bifurcations and curvatures in arteries. This is hypothesised to occur due to increased turbulence and reduced shear stress at these sites [44].

2.2 Coronary Artery Bypass Grafting

A number of non or minimally-invasive techniques have been developed for the treatment of atherosclerotic lesion formation and the resulting medical complications. Drugs such as anti-hypertensives, beta blockers and clot-dissolving agents have been designed to increase the blood supply to the heart and prevent thrombosis formation [4][46]. Percutaneous transluminal coronary angioplasty (PTCA) is a minimally invasive technique used to reopen narrowed coronary arteries whereby an uninflated balloon is threaded through the vasculature system to the obstructed area and subsequently inflated stretching the arterial wall and compacting the atherosclerotic plaque [27]. PTCA is however a poor long-term management solution for atherosclerosis with approximately 42% of arteries experiencing restenosis within a

six month period [47]. A variation of PTCA utilises a fine wire tube known as a stent to aid in the maintenance of vessel patency, as seen in Figure 2.4 [5]. Despite improved patency rates, in-stent restenosis rates remain high with approximately 22.2% of patients arteries becoming re-occluded within six months of the procedure [48].

Coronary artery bypass grafting (CABG) is a highly invasive surgical procedure for the treatment of coronary stenosis with approximately 600,000 procedures performed each year in the USA [49]. In CABG, blockages within the coronary arteries are bypassed using small diameter vessels (<6mm) referred to as bypass or vascular grafts. Oxygen and nutrient rich blood is channelled directly from the aorta through these vessels and into the coronaries below the point of blockage as demonstrated in Figure 2.5. Continuous improvements in surgical techniques have led to an expected 30-day mortality rate of less than 1% and survival rates of 92% and 81% at 5 and 10 years post-surgery respectively [6][50]. CABG has also demonstrated improved survival rates compared to Percutaneous Coronary Intervention (PCI) techniques particularly noticeable in multiple vessel disease treatment suggesting it is a superior long term treatment strategy for coronary stenosis [51].

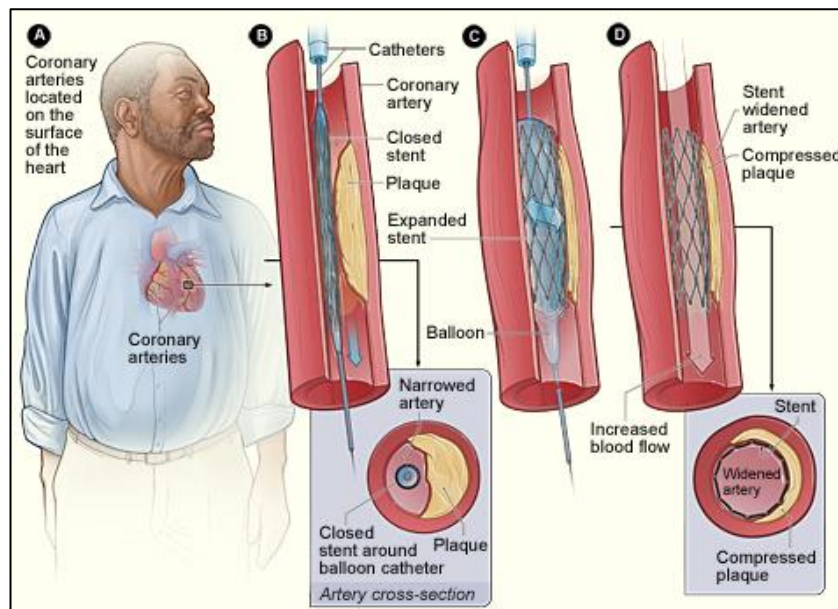


Figure 2.4: Percutaneous transluminal coronary angioplasty (PTCA) with stent [52]

2.2.1 Vascular Grafts

Due to the small diameter (<6mm) nature of the coronary arteries, autologous vessels, which are vessels taken from an alternative site within the patient are considered the grafts of choice for use in CABG [17]. Their resemblance in size and mechanical properties to native tissues along with the removed risk of immune rejection makes them the optimum graft choice. The current gold standard vessel for CABG is the great saphenous vein (GSV) [6]. Its long, bilateral nature and easy of accessibility has made it the favourable choice for surgeons [53]. Despite this it does not fully match the biomechanical properties, namely compliance, of the coronary arteries and has shown only a 66% patency rate at 10 years post-surgery [6]. Grafts derived from the Internal Mammary Artery (IMA) have demonstrated increased patency rates of up to 90% at 10 years, however, the difficulty in harvesting them has prevent their widespread use by surgeons [6][54]. With ever aging demographics, the use of autologous vessels as a conceivable treatment strategy for coronary stenosis diminishes. Complications such as the degradation of host tissues along with previous myocardial or peripheral arterial reconstructions greatly limit the source of suitable vessels in ageing populations [9].

Allografts (grafts taken from a donor) have been studied as a possible solution to overcome this shortage. Fresh allograft tissues have been seen to experience rapid immune rejection and subsequent dissolution on implantation resulting in high short term failure rates. Preserved and slightly degraded grafts offer increased clinical life due to decreased cellular content, however they too experience immune rejection after some time.

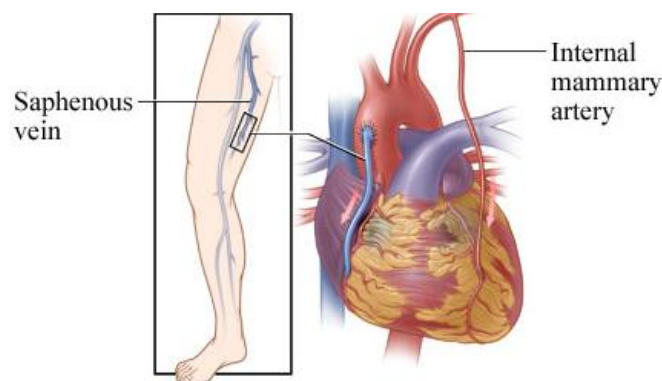


Figure 2.5: Schematic of Coronary Artery Bypass Grafting (CABG) using the Autologous vessels 'Saphenous vein (SVG)' and the 'Internal Mammary Artery (IMA)' [55]

In order to successfully introduce allografts immune suppression must be utilised which is not ideal for patients undergoing severely invasive surgeries [56]. A number of synthetic polymers have been employed in the development of vascular grafts for use in CABG. Synthetic approaches allow for the production of shelf ready grafts that offer convenience to surgeons along with reduced risk of secondary infection and immune rejection [53]. Polyethylene terephthalate (PET or Dacron®) and expanded Polytetrafluoroethylene (ePTFE, GORE-TEX®) have been used extensively in large internal diameter (ID) (12-38mm) and medium ID (6-10mm) bypassing applications with significant clinical success respectively [8]. These synthetic grafts however suffer from a mismatch in their compliance properties compared to the adjoining native vasculature. ePTFE demonstrates high occlusion rates with 64% patency at 1 year and 32% at 2 years post implantation [9]. A lack of an endothelial cell (EC) lining also contributes to their failure due to turbulent hemodynamics resulting in thrombosis formation [57][58]. ePTFE grafts seeded with an endothelial lining have shown improved patency of 85% at 3 years and 65% at 9 years [59]. Due to the non-adherent nature of PTFE the EC lining typically delaminates resulting in scaffold failure so has not been successfully adopted as a treatment strategy for small diameter bypassing [7][57].

2.2.2 Compliance Mismatch

The long-term success rates of CABG procedures are limited due to atherosclerosis and occlusion of the bypass vessel. The failures of these grafts are attributed to compliance mismatch between the bypass grafts and the native vessels [10][40][42]. Compliance mismatch arises due to a change in the rigidity or elasticity of a blood vessel along its length such as a native artery meeting a synthetic graft [40]. Physical variation of the artery diameter along with the pulsatile nature of blood flow result in altered wall shear rates [39]. Increased shearing may damage the endothelial cell lining giving rise to the onset of atherosclerosis and intimal hyperplasia while decreased shearing leads to blood stagnation and in turn thrombosis formation [11][60]. Compliance mismatch between stenotic and distal segments of arteries has also been linked with the development of unstable atherosclerotic lesions leading to the onset of myocardial infarctions [61], or cerebrovascular attacks [62].

Intimal hyperplasia is the thickening of the tunica intima of an artery and is a biological response to the injury of a blood vessel. An increased growth of the intima due to vSMC proliferation and differentiation can lead to the graft becoming stenosed or occluded similar to atherosclerosis. Vascular smooth muscle cell (vSMC) remodelling occurs in response to the damage of the endothelial lining and is a healing response [41]. Intimal hyperplasia prominently occurs at the anastomosis (junctions) of two vessels of different compliances and is hypothesised to occur due to increased flow instabilities at these sites [61]. A schematic of intimal hyperplasia development at the distal anastomosis of a bypass vessel can be seen in Figure 2.6 [11][39].

The compliance properties of a number of synthetic and biological grafts used in CABG for a range of mean pressures can be observed in Figure 2.7. Synthetic vessels such as Dacron, ePTFE and compliant poly(carbonate)polyurethane (CPU) do not experience significant volume changes with increased pressurisation. In comparison, biological tissues exhibit large volume changes at low-pressure levels and small volume rate changes at high pressures. It is noted that veins such as the great saphenous vein (GSV) rapidly stiffen with increasing pressure compared to arteries, which show a smoother transitional stiffening effect as pressurisation increases indicating compliance mismatch issues amongst autologous vessels.

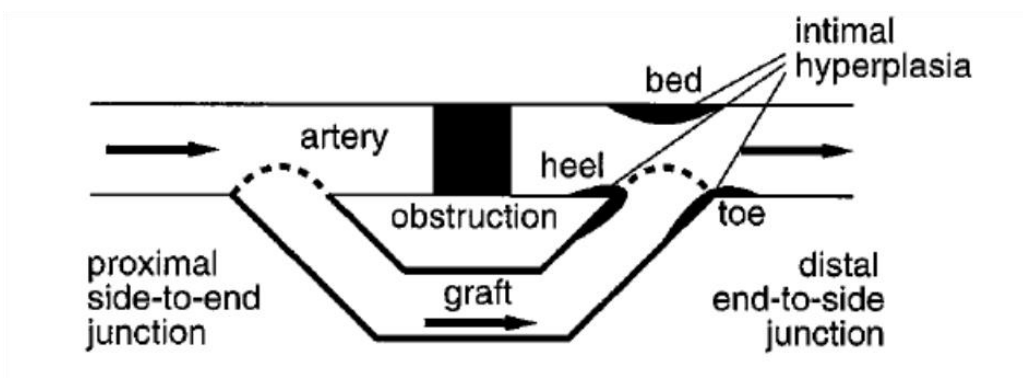


Figure 2.6: Intimal hyperplasia formation at the distal end of the vessel at anastomosis site[41]

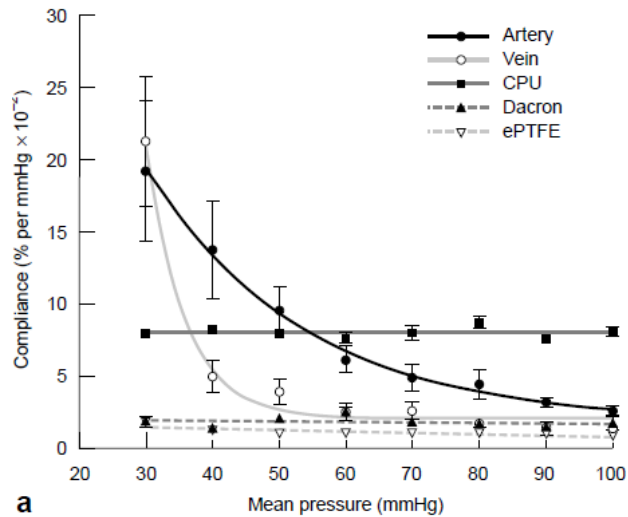


Figure 2.7: Compliance-mean pressure curves for vessels and grafts used in CABG [42]

The mean compliance values for arterial, venous and synthetic bypass grafts along with their patency at 1 and 2 years post implantation are shown in Table 2.1. Increased compliance directly correlates with long-term patency and ultimately the success of the grafts.

Limitations of current synthetic vascular grafts and the declining supplies of autologous vessels with ageing demographics highlights an imperative clinical need for a readily available bypass graft with improved biomechanical and compatibility properties. Tissue engineering approaches may provide a solution to this problem through the development of biological replacement vessels. These vessels should better mimic the structure and biomechanics of native coronary arteries and in turn out perform current vascular grafts.

Table 2.1: Compliance and patency rates for arterial and venal grafts [10]

	Compliance	1-year % patency	2-year % patency
Host artery	5.9	-	-
Saphenous Vein	4.4	88	84
Umbilical vein	3.7	83	80
Bovine hetrograft	2.6	65	59
Dacron	1.9	65	42
EPTFE	1.6	60	42

* % radial change per mmHg X 10⁻²

2.3 Tissue Engineering and Tissue Engineered Blood Vessels

2.3.1 Tissue Engineered Approaches

Every year millions of patients suffer from tissue loss or end stage organ failure due to trauma, disease or congenital anomalies. Current treatments for organ and tissue loss include transplantation, surgical reconstruction or the use of medical devices to replace lost tissue functionality [15]. Despite saving countless lives these treatments suffer from a number of inherent limitations including a lack of donor tissue for use in transplantation [63], long-term secondary complications resulting from reconstructive surgeries [64], and the incomplete restoration of tissue functionality through mechanical approaches [15]. These limitations have motivated researchers to explore alternative treatment strategies for the replacement and repair of tissues and organs.

Tissue engineering is one research strategy that may provide an answer to this call. It can be defined as an interdisciplinary field that applies the scientific principles of engineering and the life sciences towards the design, construction, modification, growth and maintenance of living tissues [15][65]. Three main tissue engineering approaches have been identified for the generation of new tissues. The first approach looks towards the isolation of cells from donor tissue in order to replace the non-functioning cells within a patient [15]. This method reduces the need for complicated and invasive surgeries and replaces only the damaged components of a tissue structure. Immune rejection of these infused cells is however a limiting issue. The second approach requires inducing local tissues to aid in self-repair through the infusion of signalling molecules and growth factors [15]. This approach is limited by the difficulty in delivering a sustained dose of factors to a specific site and in cases where there is a poor supply of resident cells to aid in repair. The third and most commonly investigated approach looks to create whole tissue structures by combining cells with 3D matrices known as scaffolds [17][65]. A schematic of the tissue engineering process can be seen in Figure 2.8.

In this process, cells are first isolated from the body or another source and cultured to sufficient levels *in vitro*. These cells are then seeded onto the scaffold and further

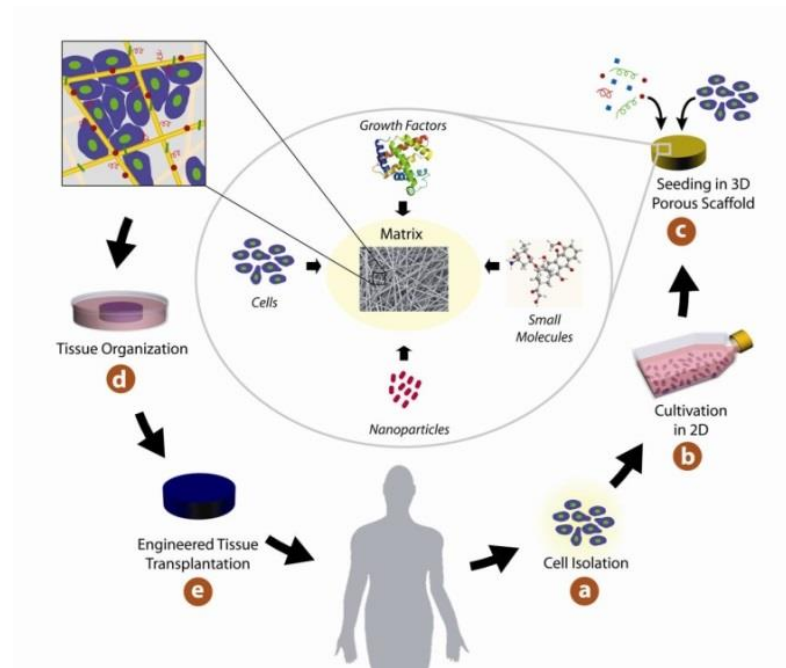


Figure 2.8: Schematic of the tissue engineering process [66]

culturing of the cell-scaffold combination takes place [65]. Finally, the scaffold and cell hybrid are implanted into the patient at the desired site. As the cells continue to grow they excrete natural ECM proteins including collagen allowing for tissue formation and structural remodelling to occur. The scaffolds should degrade at sufficient rates to match this natural remodelling process as in Figure 2.9 [67]. The desired end construct is a completely biological tissue that matches the structural and functional properties of the native tissue it is replacing. Immunological rejection of these cell seeded scaffolds is avoided through the use of autologous cells or more recently demonstrated through the use of stem cells [68]. Researchers have attempted to create a number of tissues and organs through this approach including skin [69], heart valves [70], bone [71], cartilage [72], the liver [73]–[75], and blood vessels [12], [76]–[81].

The scaffolds used in this approach should provide a number of functions and features. Their architecture should provide sufficient void volume to allow for revascularisation where applicable and to facilitate host tissue regeneration [10]. In addition, the biomaterials used within the scaffold should be cyto and tissue compatible allowing for cells to attach, grow and differentiate during *in vitro* and *in vivo* culturing [8]. Bioactivity of the scaffold is also desirable in order to facilitate and regulate cellular

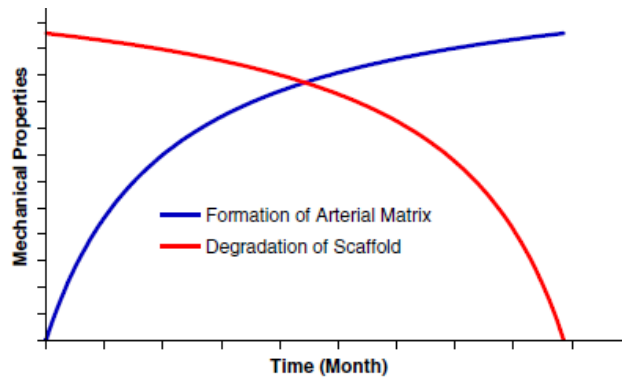


Figure 2.9: Timeline showing the ideal development of arterial matrix in response to degradation of a biodegradable scaffold [67]

activity. This can include the addition of adhesion molecules to the scaffold surface to aid in cell attachment and appropriate surface topography to induce correct cell morphology and alignment as would be seen in the host tissue [82]. The incorporation of growth factors within the matrix to stimulate tissue regeneration is also of great interest [83]. The mechanical properties of the scaffold are also key attributes and highly depend on the shape and size of the defect or tissue to be regenerated [84]. The intrinsic mechanical attributes of the material should match that of the native host tissue to be replicated.

2.3.2 Tissue Engineered Blood Vessels

Considerable research has focussed on the development of small diameter tissue engineered blood vessels (TEBVs) for use in CABG. This approach provides a potentially sustainable, inexpensive and effective solution to the current shortage of suitable bypass vessels. By designing these TEBVs to have equivalent structural, mechanical and chemical properties as the native arterial structures they are replacing, vessels with appropriate long-term patency rates may be achieved [7][9][12][13][79]. Walpoth & Bowlin, outlined the key properties they believed an ideal TEBV should possess, as summarised in Table 2.2.

These criterion included ease of surgical handling, leak resistance to prevent critical blood loss, sufficient porosity to allow for tissue regeneration and compliance characteristics matching native vasculature [9]. Tissue engineers should strive to develop scaffolds that achieve as many of these characteristics as possible while maintaining a feasible design strategy.

Table 2.2: Properties of the ideal TEBV for use in vascular bypassing as set out by Walpoth & Bowlin (adapted from [9])

Properties of the Ideal Vascular Graft
➤ Biocompatible (non-toxic & non thrombogenic)
➤ Leak resistant, but adequate porosity for healing/tissue regeneration
➤ Compliance matching that of native artery
➤ Resistant to Aneurysm formation
➤ Post implantation durability after tissue ingrowth
➤ Easily manufactured, stored and sterilised
➤ Suture retention
➤ Flexibility with kink resistance

In 1986, Weinberg and Bell, produced the first completely biological TEBV [14]. In this effort, a collagen gel combined with bovine aortic cells was studied. The mechanical properties of the resulting scaffold were insufficient for *in vivo* implantation and despite the addition of a Dacron® mesh for reinforcement the vessel lacked the required burst strength characteristics. Koing *et al.* utilised a complete biological approach that removed the need for an exogenous scaffold. In this approach, human fibroblast cells were cultured until cell sheets were formed [76]. Subsequently these cell sheets were wrapped around a mandrel to produce a tubular scaffold and further cultured until layer fusion was achieved. The tissue was later dehydrated in air for several hours in order to form an acellular construct. This approach yielded a scaffold with good mechanical properties but required 3 months in culture before a graft that was sufficiently stable for implantation was produced. L'Heureux *et al.* similarly produced a completely biological tissue engineered construct by culturing human vSMCs with ascorbic acid until cellular sheets formed. These cellular sheets were wrapped around a tubular mandrel to form the medial layer of the vessel. Sheets of human fibroblasts were subsequently cultured and wrapped around the vSMC layer to form an adventitia like layer that was comprised of dense collagenous material. Following maturation the tubes were removed and the lumen seeded with endothelial cells. The TEBVs formed possessed burst pressures of 2000 mmHg but lacked the dense SMC stricture typically witnessed in native arterial tissue. When implanted the vessels were prone to thrombosis formation resulting in overall patency rates of only

50% [85].

Hoerstrup and collaborators, combined non-woven meshes of PGA with thin layers of poly-4-hydroxybutyrate (P4HB), endothelial cells and myofibroblasts to produce their vessel [12]. Their research demonstrated advanced tissue formation through the use of 'biomimetic' pulsatile culturing compared to commonly used static culture techniques. Burst strengths of approximately 3000 mmHg were achieved after 28 days of culture. These burst strengths are well above the hypertensive blood pressure threshold of 140 mmHg [49], and comparable with the burst strength values recorded for coronary arteries and the saphenous vein at 3000 ± 500 mmHg [86], and 1599 ± 877 mmHg respectively [76]. Similar studies utilising PGA meshes have again demonstrated that the addition of cyclic strain during culturing periods increased vessel burst strengths to approx. 2000 mmHg after 8 weeks in culture [13].

While these studies have made important steps towards the development of suitable TEBVs they also highlight deficiencies in the selection of suitable biomaterials. In order to reduce the need for prolonged culturing times, biomaterials with mechanical properties suitable for direct implantation should be considered. This will allow for *in vivo* stability while vessel remodelling occurs within the patient.

2.3.3 Biomaterials for TEBVs

The identification and selection of appropriate biomaterials and fabrication techniques for the creation of 3D scaffolds is an ongoing source of interest for tissue engineers. Biomaterials used in these applications should offer mechanical stability while maintaining a suitable microenvironment for the growth and proliferation of the seeded cells [17]. In addition, these materials should be biocompatible, blood compatible, fatigue resistant and ideally biodegradable [8]. Biodegradable materials should degrade *in vitro* and *in vivo* into either products that are normal metabolites of the body or products that can be eliminated with or without further metabolic transformations [17]. Two main classes of materials have been studied extensively for the development of TEBVs, namely natural biomaterials and synthetic polymers.

Natural biomaterials used in TEBV applications generally consist of protein

components found within the natural ECM of arteries. The ECM is the structure left within a tissue once all cells are removed [37]. Scaffolds based on vascular ECM proteins include those derived from collagen [14][87][88], elastin [89], fibronectin [90], and combinations of these proteins [91][92]. Other natural biomaterials commonly explored include fibrin, a protein involved in the clotting of blood [93][94], and polymers derived from biological sources such as those of the polyhydroxyalkanoate (PHA) family [95]. Biological scaffolds derived from natural biomaterials offer increased biocompatibility, non-toxicity and increased cell adherence [96]. Despite these favourable characteristics, they suffer from poor mechanical properties, a lack of reproducibility when processed, rapid degradation and can induce immune rejection and pose disease transmission risks if taken from a non-autologous source [96].

Synthetic polymers have been investigated due to their ability to create reproducible, inexpensive and easily manufactured scaffolds. A number of non-biodegradable synthetic polymers including ePTFE and Dacron® have been studied as potential candidate materials. These materials have shown poor cellular interaction and mechanical characteristics ultimately leading to their poor success in small diameter applications [9][57]. Numerous biodegradable synthetic polymers have also been utilised including poly(glycolic acid) (PGA) [12][13][97], poly(lactide-co-glycolide) (PLGA) [98][99], and poly(ϵ -caprolactone) (PCL) [79][100]–[104]. The disadvantages of using synthetic polymers is the potential to induce an inflammatory response upon implantation, a problem commonly seen with such materials [105]. This inflammatory response includes platelet and leukocyte activation which are known triggers for the initiation of thrombogenesis and intimal hyperplasia formation [60].

Despite this, the synthetic flexibility these polymers offer make them highly desirable for use as tissue scaffolds as they can be manipulated to offer the desired properties. By altering their chemical structure the physical, bioactive and mechanical properties of various tissues can be replicated [17]. Studies have also shown the ability to blend these polymers with additional biomolecules that aid in increased cell adherence and proliferation [82], [106], [107]. Furthermore surface and chemical modification of the synthetic polymers can be used to help reduce the inflammatory response they typically initiate upon implantation [108].

2.3.4 Poly(ϵ -caprolactone)

Poly(ϵ -caprolactone) (PCL) is a biocompatible and biodegradable aliphatic polyester synthesised through ring opening polymerisation of ϵ -caprolactone [109]. It has a semi crystalline structure with a melt temperature (T_m) above that of the core body temperature (37°C) at $58\text{-}64^\circ\text{C}$ [110]. Its glass transition temperature (T_g) of -60°C results in the material possessing a rubber like consistency at room temperature [110]. This soft pliable nature along with suitable implantation properties makes it a desirable material for use in a wide range of soft tissue engineering applications [111][112].

PCLs low cost, suitable mechanical properties and high solubility in organic solvents has made it widely popular for use in the development of TEBV scaffolds. To date PCL has been successfully processed using a number of common scaffold fabrication techniques including solvent casting [113][114], and electrospinning [79][100]–[102][104].

Electrospun membrane's prepared using PCL demonstrated Young's modulus values of $2\text{-}4\text{ MPa}$ [111] which is comparable to the stiffness of native blood vessels ranging from $2\text{-}6\text{ MPa}$ [115]. The use of a material with stiffness values comparable to native vasculature should aid in reducing compliance mismatch issues within vascular grafts. Drawbacks of the polymer however are its inherent hydrophobic nature, lack of cell-binding signals [116], and long degradation times of over 2 years [109]. The ability to chemically modify the polymer by attaching RGD groups has however been shown to improve cell attachment [117], and the addition of biomolecules such as gelatin have been used to make the polymer more hydrophilic [118]. The chemical composition of the monomer ϵ -caprolactone and the polymer PCL can be seen in Figure 2.10

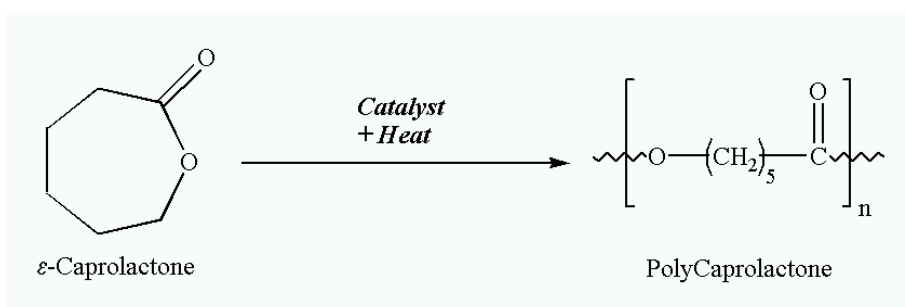


Figure 2.10: Ring opening Polymerisation of monomer ϵ -caprolactone to Poly(ϵ -caprolactone) and subsequent polymer chemical structure [119]

2.3.5 The Use of Stem Cells for Tissue Engineering Applications

In order to develop an *in vitro* based tissue engineered construct a source of cells is often required in order to initiate population of the scaffold body prior to implantation. These cells are expected to proliferate and produce ECM as the scaffold degrades, allowing for standalone tissue structures to be achieved. The main successes in this field have come from the use of primary cells, taken from the patient, and used in conjunction with scaffolds to produce tissue constructs for re-implantation [120]. This method however suffers from a number of limitations including the invasive nature of cell collection and the potential for cells to be in a diseased state upon harvest [121]. An appreciation of the inherent diversities of organ systems paired with the difficulty of harvesting primary cells has therefore led researchers to focus upon the use of stem cells, including embryonic stem (ESC) cells, mesenchymal stem cells (MSCs) and Induced pluripotent stem cells (iPSCs) for tissue engineering applications [122][123]. Stem cells provide a readily available source of cells that have the potential to be differentiated into a number of cell lineages [124], provide better proliferation rates compared to primary cell lines [125], while also retaining the ability to induce a reduced immune response upon implantation [68]. One of the critical steps of stem cell usage for regenerative medicine is the ability to control the differentiation of the cells into the desired tissue lineages. This is achieved through the control of their micro and nano environment [126], along with appropriately activating differentiation pathways through biochemical stimuli [127]. It is therefore desirable to use a stem cell niche that naturally aids in the creation and self-repair of a particular tissue of interest in order to better mimic the natural tissue formation process.

2.3.5.1 Multi-Potent Vascular Stem Cells (MVSCs)

As discussed previously the unique biomechanical and architecture properties of blood vessels require the careful consideration and selection of a cell-scaffold construct to ensure successful functionality upon implantation. A stem cell lineage that aids in vascular tissue repair has the potential to increase the long-term success of such scaffolds through the appropriate natural differentiation of cells and subsequent remodelling of the vessel. Recently, there has been evidence demonstrating the presence of resident vascular stem cells in the tunica media of arteries, which have been coined as multipotent vascular stem cells (MVSCs) [128]. These cells have been

shown to proliferate and differentiate into vascular SMCs whilst also be shown to possess the potential to be differentiated into neural cells, and mesenchymal stem like cells giving rise to their multipotent classification [129]. Lineage-tracing experiments have also importantly shown that these MVSCs are not derived from mature SMCs but rather a distinct cell group residing within the vascular walls. The unique nature of this stem cell group makes them an attractive potential for future TEBV studies.

2.4 Electrospinning

Along with the selection of suitable biomaterials and cell groups for seeding, the morphology of a scaffold is of critical importance for the efficient remodelling of tissue [8]. Scaffolds should offer suitable surfaces for the adherence and support of applied cells, should appropriately relay physiological cues to induce guided proliferation and differentiation of the cells while also providing mechanical stability to the tissue defect during regeneration [82][130]. These scaffolds should also contain sufficient porosity and pore volumes to allow for adequate vascularisation, tissue formation, metabolite diffusion and the removal of degradation waste to occur [10]. The ultimate goal is to fabricate a scaffold that possesses a morphology mimicking that of the natural extracellular matrix (ECM) [84][130]. A scaffold morphology that mimics the collagen and elastin fibre network found within the arterial tissue is highly anticipated to provide increased graft success within TEBV applications. Electrospinning is one such fabrication technique capable of reproducing the fibrous architecture of the natural ECM both in morphology and in scale.

2.4.1 Fundamentals of Electrospinning

Electrospinning is a polymer process technique capable of producing continuous fibres with diameters ranging from microns to nanometres in size [132][133]. The first use of electrostatic forces to manipulate polymer solutions was demonstrated in 1902 when Cooley developed a system for the dispersion of polymer fluids under electrical potentials [134]. Later in 1934 the process was developed further into the now recognisable electrospinning process for the production of polymeric fibres using electrostatic forces [135]. Despite being patented over a century ago the potential of electrospinning for biomedical applications was not realised until the 1990s [136]. The simple and versatile nature of the process paired with its capability to produce highly

porous membranes with high surface area to volume ratios has generated enormous interest in the process amongst the research community. Electrospun materials have been utilised in a broad range of applications including wound dressings [137], [138] tissue scaffolds [18][139], nano-electronics [140][141], textiles [142][143], filtration devices [144][145] and composite materials for aerospace design [133][146].

At the laboratory scale the basic electrospinning set-up consists of a high voltage DC power supply (1 to 30kV), a capillary with attached spinneret (syringe with a flat tip needle), a syringe pump and a grounded metallic collector system. A schematic of the electrospinning set-up can be seen in Figure 2.11(A) [19], [147]. The electrospinning process produces fine diameter fibres through the simple principle of applying a uniaxial stretching force to a viscoelastic solution [19]. The process begins by drawing a polymer solution usually derived from a raw polymer dissolved within a mono or poly-solvent system into a syringe. A flat tip metallic needle is connected to the syringe and the solution is extruded at a constant and controlled rate using a syringe pump.

A high voltage potential is applied to the solution by connecting the DC power supply to the metallic needle. This high voltage electrifies the solution and the surface of the polymer droplet dispensing from the needle tip begins to charge. Electrostatic forces including repulsive forces between the surface charges and the coulombic force exerted by the collector potential begin to act on the polymer droplet [148]. These forces elongate the droplet forming a conical shape referred to as the Taylors' cone [149]. When the voltage is increased sufficiently the electrostatic forces overcome the surface tension of the polymer solution and a jet of fluid erupts from the cone. The jet initially travels in a stable motion near the tip but then enters an instability region as it travels towards the collector system as seen in Figure 2.11(B) [19].

The fine diameter fibres are formed by the stretching, whipping and acceleration of the fluid jet within this instability region. The solvent used to dissolve the polymer evaporates leaving a solid material to deposit on the collector surface. 2D randomly orientated fibrous meshes can be produced using a flat metallic plate as the collector.

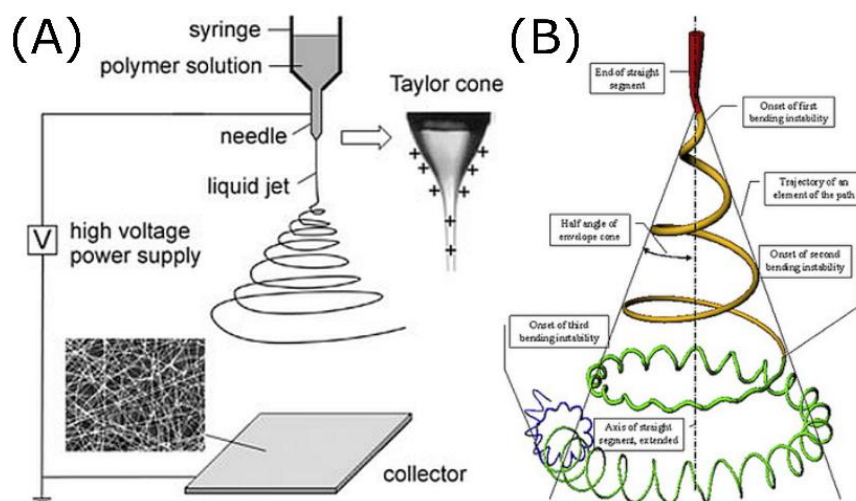


Figure 2.11: The electrospinning Process (A) Schematic of the basic electrospinning set-up with a flat metallic plate collector. Electrostatic forces result in Taylor's cone formation and subsequent jet initiation. An SEM image of a typical 2D random fibre mesh is also shown [147] (B) Trajectory of fluid jet with instabilities regions shown [150]

A number of researchers have modified the basic electrospinning process to alter both fibre morphology and the general structure and geometry of the electrospun construct. Matthews and collaborators utilised a grounded rotating drum spinning at high RPMs to produce aligned collagen fibres. These aligned collagen constructs were produced to mimic the fibre morphology seen within native arterial tissue [87]. Along with the spinning of polymeric materials electrospinning has been adopted to spin ceramics, metals, proteins and cellular growth factors [151].

2.4.2 Electrospinning Parameters

The electrospinning process and the morphology of fibres produced through it are highly dependent on a number of parameters. These parameters include solution properties, processing parameters and ambient conditions. A summarised list of these parameters and their typical working ranges can be seen in Table 2.3 [152][153].

2.4.2.1 Solution Parameters

Molecular Weight, Polymer Concentration and Viscosity

The molecular weight and molecular weight distribution, polymer concentration and viscosity of a solution are highly interlinked parameters and must be considered in unison. Electrospinning solutions should contain polymers with sufficiently long

Table 2.3: Parameters known to affect fibre formation during electrospinning and typical working ranges (adapted from [152][152])

Solution Parameters	Equipment Parameters	Ambient Cond.
Molecular weight (10^4 - 10^7 g/mol)	Applied Voltage (5-100kV)	Humidity
Polymer conc. (1-40 wt%)	Flow rate (0.01-1ml/min)	Temperature
Surface Tension (20-75 mN/m)	Collector characteristics	Pressure
Conductivity (0.05-30 mS/m)	Needle Size	
Solution Volatility	Distance from tip to collector (1-100cm)	

molecular chain lengths for stable jet initiation to take place [154]. The entanglement of the molecular chains within the spinning solution gives rise to fibre formation and prevents the polymer jet from breaking apart during the elongation and whipping process. If a solution contains a polymer of insufficient chain length, a process known as electrospraying takes place [155]. Here chain entanglements cannot form and subsequently droplets of polymer deposit. Despite the importance of chain entanglement in polymer solutions, ceramic precursors have been electrospun that contained very low molecular weights [156]. This indicates that molecular weight characteristics are not solely sufficient to assess the spin-ability of a solution.

Molecular weight has also been shown to be an important parameter in determining the resultant morphological, mechanical and degradation characteristics of electrospun structures. Zhang *et al.* demonstrated that by varying the molecular weight of the PCL polymer dissolved in a chloroform/methanol solvent system, structures with tuneable fibre characteristics and mechanical properties could be obtained [157]. PCL with a molecular weight of $40,000 \text{ g mol}^{-1}$ resulted in highly beaded fibres while an increased molecular weight of $80,000 \text{ g mol}^{-1}$ provided fibres with well defined diameters and a narrow fibre diameter distribution. A further increase in molecular weight to $120,000 \text{ g mol}^{-1}$ resulted in fibres with an uneven fibre diameter distribution. Increasing the molecular weight of PCL was also shown to decrease the crystallinity of the collected fibres. Crystallinity was observed to be 60.2% and 47.6% for fibres created with $40,000$ and $120,000 \text{ g mol}^{-1}$ PCL respectively [157]. This is attributed to more chain

entanglements and weaker mobility in the high molecular weight solutions, which may hinder crystalline growth within the fibres. The rate of crystallinity within PCL nanofibers in turn alters fibre ductility with increased crystallinity yielding stiffer PCL fibres [158].

The variation of polymer concentration within a solution has been seen to have a pronounced effect on fibre diameters produced [152]–[154]. Low concentration solutions generally yield ultra-thin or beaded fibres while high concentration solutions lead to large uniform diameter fibres [153]. This effect is attributed to a change in the solutions viscosity with low concentration solutions generally yielding less inter and intramolecular entanglements which in turn reduce viscosity. The opposite is seen with high concentration solutions. Solution viscosity has been identified as the critical electrospinning parameter and the ability to spin a solution is highly dependent on this characteristic [154]. Beaded fibres form in low viscosity solutions due to the excessive ratio of solvent molecules compared to polymer chains within the jet [153]. As the polymer content increases a greater interaction between the solvent molecules and polymer chains occur leading to a homogenous distribution of solvent within the jet and consequently smooth fibre formation [159]. At increased viscosities, thicker fibres are formed due to the fluid jet resisting bending instabilities during its travel to the collector. If the viscosity is increased excessively a jet cannot form at the tip leading to the solidification of material at the needle. Both polymer molecular weight and polymer concentration can be used to tune the solutions viscosity [154].

Surface Tension, Solution Volatility and Conductivity

The surface tension of a solution is a property that is vital for the formation of bead free fibres. The surface tension forces within a solution try to pull the liquid droplets at the tip into spheres in order to reduce the surface area per unit mass of the liquid [160]. The electrostatic forces on the other hand try to increase the surface area by elongating the droplet [159]. If the surface tension is too high, the jet breaks into droplets or forms beaded areas along the fibres length. Beading occurs due to the solvent molecules congregating within particular regions of the jet as seen in Figure 2.12.

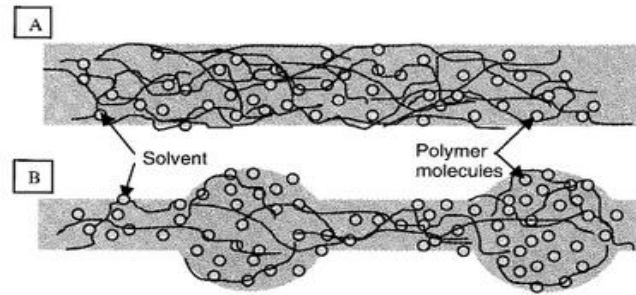


Figure 2.12: Image showing solvent molecules and molecular chains of polymers with the electrospinning jet (A) A high viscosity solution with solvent molecules evenly distributed amongst the polymeric molecular chains leading to a smooth fibre formation (B) Low viscosity solution show solvent congregation within the jet resulting in beaded solutions [161]

As stated previously a high viscosity solution exhibits greater interactions between solvent molecules and the polymer chains. This interaction reduces the tendency for the solvent molecules to congregate due to the influence of surface tension. Viscosity and surface tension attributes of the solution must be finely balanced for the spinning of smooth defect free fibres. The selection of solvents used generally determines the surface tension properties of the solution. In addition, surfactants, materials that reduce the surface tension of a liquid may be added to aid in bead free fibre formation. Jia & Qin demonstrated the use of such surfactants including Gemini quaternary and Rosin acid sodium for the spinning of poly(vinyl alcohol) (PVA) nanofibres. The addition of these materials reduced the surface tension of the spinning solutions while also increasing viscosity and conductivity. A marked decrease in fibre diameter from 405nm to 100nm was demonstrated using these additives [162].

Solution conductivity is determined by the choice of polymer, solvents and the addition of surfactants and salts. Increased solution conductivity has been shown to improve fibre quality with reduced bead formation demonstrated. This occurs as the increased conductivity allows the solution to carry more charge that in turn leads to greater stretching forces within the beaded regions [163]. Salts have been used extensively to increase the conductivity of solutions but introduce impurities to the final fibre network [164][165]. Surfactants such as ethanol which possess high dielectric potentials have been shown to increase solution conductivity while also decreasing surface tension, resulting in thin uniform fibres being assembled [160]. These liquid surfactants evaporate away so do not contaminate the final electrospun construct.

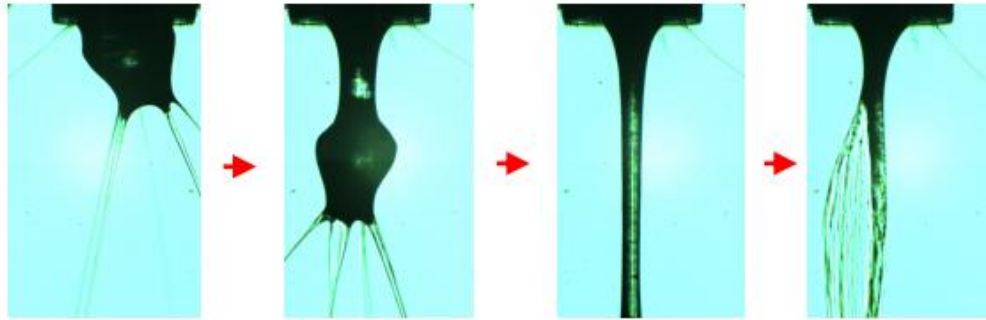


Figure 2.13: Formation of polymer skin and subsequent removal in PEO/Chloroform solutions result in defects forming on the electrospun membrane surface [166]

The final solution property to consider is volatility. Solution volatility refers to the tendency of a solution to vaporise. Electrospinning solutions made from low volatility solvents may result in wet fibres or fused fibre depositing on the collector [159]. Such fibre morphologies occur due to a lack of solvent evaporation during jet flight. This incomplete evaporation results in residual solvents depositing on the plate which may in turn fully or partially dissolve the fibres deposited. On the other hand, solutions made with highly volatile solvents and surfactants experience rapid vaporisation which may result in a polymer skin developing at the needle tip [166]. This skin can block the flow of polymer resulting in the jet breaking down. The skin may then be expelled from the needle tip forming a defect on the surface of the sample as seen in Figure 2.13.

2.4.2.2 Equipment Settings

Flow Rate

The rate at which the polymer solution is extruded from the tip is referred to as the flow or feed rate parameter. Adjusting the flow rate of a solution has been associated with both changes in fibre diameter and their corresponding quality [153]. At low flow rates, an imbalance may exist between the supply of polymer to the tip and the rate of material removal to the collector. This mismatch results in beaded fibre formation [154]. Excessively high flow rates produce wet, beaded and interconnected fibre structures. These occur due to insufficient evaporation of solvent before the material reaches the collector [167].

Applied Voltage

The voltage applied during electrospinning has been shown to control the rate at which material is drawn away from the tip. With increasing voltage, greater volumes of the solution are removed from the tip. This effect occurs due to an increase in repulsive forces within the jet [164]. The voltage and flow rate used to electrospin are highly dependent on each other. Higher flow rates generally require a higher applied voltage to maintain stable jet formation.

The effect of voltage variation on fibre diameter is a source of contention amongst many electrospinning groups. Reneker and Chun demonstrated that a change in voltage had no effect on the diameters of electrospun polyethylene oxide (PEO) fibres [132]. Other research groups have shown increasing fibre diameters with increasing voltage, with this hypothesised to occur due to a decrease in travel time between the tip and collector resulting in reduced whipping effects [168]. Contrary to this, higher voltages have been associated with thinner fibre production with this attributed to greater stretching of the solution during its flight [169]. Subsequent studies by Wu *et al.* further demonstrated that fibre diameters were found to reduce with increasing voltage to a minimum before increasing with a further increase in voltage [170].

Extremely high voltages may also result in the formation of multiple jets from the cone. While providing smaller diameter fibres, they produce fibres with non-uniform morphologies [152]. Higher working voltages also have a greater tendency to induce bead formation [164][166]. Deitzel *et al.* demonstrated that at a fixed flow rate an increase in voltage results in the Taylor cone receding into the needle orifice which may affect the stability of the cone formation leading to beading [167]. Table 2.4 shows a general relationship between jet formation and the corresponding fibre characteristics. These jet formations are highly related to both the feed rate and voltage used to spin a solution.

Collector Distance

The distance between the tip of the needle and the collector surface determines both the path and travel time of the liquid jet. Increasing the distance between the tip and collector generally reduces the fibre diameters due to the increased stretching of the

Table 2.4: Typical jet characteristics and corresponding effect on fibre formation [171]

Electrospinning behaviour	Fibre physical characteristics
Multiple jets from spinneret tip	No change in fibre diameter Wide distribution of fibre diameter
Increased jet diameter	Increased fibre diameter which leads to ribbon/flat fibres forming Wet or fused fibres
Increased jet diameter with secondary jets	No change in fibre diameter Bimodal distribution of fibre diameter
Gathering of semi-solidified solution at the tip	Beads on fibres Defects on surface of samples
Insufficient viscoelastic force to suppress surface tension	Bead on fibres

jet [154]. The distance should be sufficiently high as to allow the solvents sufficient time to evaporate, to achieve dry fibre formation. If a sufficient distance is not utilised wet fibres and liquid polymer will deposit on the plate or highly interconnected fibre structures will be produced.

Collector Characteristics

Another important aspect of electrospinning is the type of collector system employed. Standard flat meshes with randomly orientated fibres are created by spinning onto aluminium foil or flat metallic plates [172]. In order to achieve constructs with increased fibre alignment and complex geometries a number of researchers have fashioned novel collector systems. The simplest method to achieve aligned fibres is through the use of rotating metallic drums. Matthews and collaborators utilised a grounded rotating drum spinning between 500-4500 RPM to collect collagen nanofibres [87]. Samples made at 500 RPM demonstrated random fibre orientation while those created at 4500 RPM showed highly aligned substructures with fibres orientating themselves along the circumferential axis of the drum. Xu *et al.* again formed highly aligned structures but this time in the form of thin poly(l-lactic acid-co-caprolactone) [P(LLA-CL)] filaments [173]. In this system a large diameter disc with a sharpened edge was used to collect thin linear bundles of fibres.

2.4.2.3 Electrospun PCL Vascular Grafts

As introduced previously the polymer Poly(ϵ -caprolactone) (PCL) has been studied extensively for the development of scaffolds for soft tissue engineering applications. In particular, electrospun PCL has been studied in a number of configurations and blends for the creation of TEBV scaffolds for arterial bypass applications. One of the first studies investigating the potential of PCL for small diameter graft fabrication was detailed by Vaz *et al* [80]. In this work a bi-layer electrospun tubular construct consisting of an inner layer of randomly orientated pliable PCL fibres combined with a stiff outer layer of poly(lactic acid) (PLA) fibres was presented. Vessels of inner diameter 6 mm with tensile strengths and Young's modulus values of 4.3 ± 0.2 MPa and 30.9 ± 6.6 MPa respectively, were created. The modulus of the end constructs were significantly higher those reported for native blood vessels, including human coronary arteries at 1.55 ± 0.26 MPa [174], and cerebrovascular vessels at 2-6 MPa [115]. This excessive Young's modulus characteristic, paired with a lack of compliance data, brings into question whether these bi-layer vessels possessed the required distensibility required for smaller diameter bypass applications.

McClure *et al.* developed composite PCL/Silk and PDO/Silk vessels with tuneable compliance characteristics through the manipulation of fibre alignment within the scaffold body [175]. This was achieved by altering the rotational speed of the collection mandrel from 500 RPM to 8000 RPM. Samples collected at 500 RPM were seen to be more compliant than those collected at 8000 RPM, with a marked increase in fibre alignment witnessed at the higher collection speeds. This demonstrated that fibre anisotropy was crucial for determining the resulting compliance characteristics of the grafts [175]. Further studies by McClure looked at developing a tri-layer electrospun scaffold consisting of PCL combined with silk fibroin, collagen and elastin [176]. By adjusting the ratio and combination of PCL and the natural polymers, three distinct layers of electrospun fibres were consecutively spun onto a rotating mandrel in order to mimic the intimal, medial and adventitial layers of natural arteries. Dynamic compliance testing showed that electrospun grafts with compliance ranging from 0.4–2.5% per 100 mmHg and comparable to that of the saphenous vein at 1.5% per 100 mmHg, could be achieved. The ability to tune the compliance of PCL based scaffolds may aid in limiting potential compliance mismatch issues upon implantation.

Drilling *et al.* developed a pure PCL electrospun tubular scaffold with burst pressures of up to 4000 mmHg recorded [177]. These pressures were determined to be significantly higher than the typical maximum burst pressure of 2000 mmHg that native arteries have been shown to withstand [77]. This suggests that despite its pliable nature PCL can be successfully incorporated into a scaffold that can comfortably resist physiological loading conditions. An interesting note of Drilling's study was the lack of fibre orientation within the scaffold body, suggesting that the traditional quest for highly aligned fibre structure may not be necessary for achieving the required tensile properties and burst strength required for graft success [177].

Perhaps the most limiting factor of electrospun PCL fibres is the known inflammatory response and calcification of the material experienced after implantation [100][178]. This is often attributed to the products of fibre degradation triggering pathways for a local immune response and stimulating the growth factors such as transforming growth factor- β 1 which results in chondroid metaplastic degradation [178]. In spite of this, blended PCL scaffolds with superior cell binding, proliferation and infiltration characteristics have been created in order to minimise the negative response to the implanted structures. Fukunishi *et al.* developed a PCL/Chitosan scaffold with the aim of increasing the degradation rates of electrospun PCL fibres in order to improve cell infiltration properties of the scaffold and ultimately reduce calcification rates [179]. The unseeded scaffolds were implanted into murine and ovine animal models with histological results showing that the blend fibres experienced no classification or aneurysm formation after 6 months implantation.

The significant volume of work and continued interest in PCL for tissue engineering applications clearly demonstrates the promise researchers have placed in this material [179]–[183]. Its versatile ability to be electrospun into a number of configurations with equivalent or superior mechanical properties to that of native vascular tissue through the use of bespoke collector systems and the variation of spinning conditions has allowed for tuneable fibre structures to be readily fabricated. The potential to blend PCL with a wide array of natural polymers also offers the ability to create scaffolds that minimise the negative attributes of synthetic based materials while still maintaining the reliability and reproducibility that they offer.

2.4.3 Limitations of Electrospun Scaffolds

While the selection of appropriate biomaterials for use in the development of electrospun TEBV's is paramount to their success, perhaps, the most limiting factor facing this fabrication technique is the morphological attributes of the fibre constructs themselves. Researchers have demonstrated the increased adherence and proliferation properties that electrospun nanofibre based materials offer compared to those of the micron scale [184]–[186], however, a clear limiting factor in their success to date is the inadequate cell infiltration rates currently observed [20][187][188]. This lack of cell penetration has been attributed to the small size, complex distribution and lack of connectivity of pores within nanofibre based electrospun scaffolds [182].

The porous nature of electrospun structures arise due to the crossing of fibres within 2D deposition planes [153]. As fibre diameters decrease towards the nanoscale their packing density greatly increases resulting in a severe reduction in the pore volume between fibres [189]. Without sufficient pore volumes and interconnectivity, cells cannot fully penetrate electrospun scaffolds and become trapped within the scaffold peripheries, often termed the 'fishnet effect' [190]. This lack of complete infiltration prevents appropriate tissue remodelling occurring throughout the full thickness of the scaffold [191], along with cell necrosis due to inadequate nutrient and waste diffusion [182]. Deficiencies in new tissue generation can ultimately lead to the long-term failure of the grafts as the scaffold material degrades [188].

In early studies by Vaz *et al.* it was observed that cells seeded onto bi-layer PCL/PLA electrospun tubular constructs tended to congregate on and within the outer layer of the scaffold [80]. Histological examination revealed the cells became confluent upon the surface of the scaffold after 4 weeks in culture but few cells penetrated past the outer PLA layer, with this attributed to insufficient pore sizes within the scaffold body. Similarly, histological examination of electrospun PCL, PCL/Gelatin, and PCL/Gelatin/pNSR32 (RGD peptides (Arg-Gly-Asp)) tubular scaffolds seeded with endothelial cells isolated from Sprague Dawley Aortas (SDRAECs) showed accumulation of cells upon the surface of the scaffolds without noticeable penetration into the scaffold depths [116]. Cross sectional views of PCL and composite PCL scaffolds stained with Hematoxylin and Eosin (H&E) demonstrated poor penetration

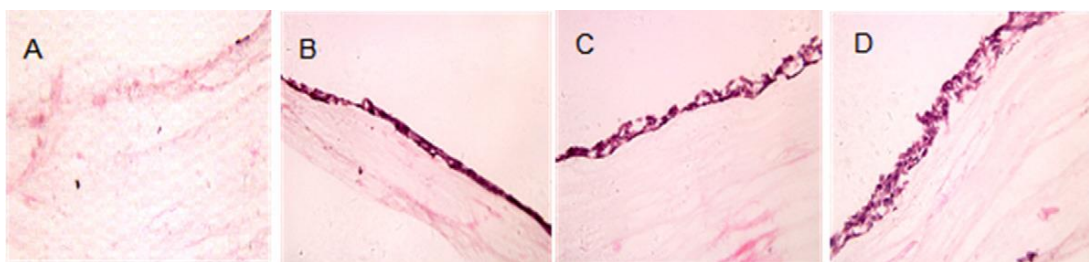


Figure 2.14: H&E staining of SDRAECS seeded scaffolds after 7 days culture (A) PCL/Gelatin/pNSR32 with no cells (B) PCL (C) PCL/pNSR32 (D) PCL/Gelatin/pNSR32 [116]

of cells into the scaffold body's after 7 days in culture despite the use of biomolecules and peptides to increase cell proliferation rates (Figure 2.14).

Further studies examining the effect of extended culturing periods on cell infiltration rates have again showed that electrospun materials experience incomplete cell infiltration despite culturing periods of up to several weeks. Baker *et al.* examined Meniscal fibrochondrocytes (MFCs) and Mesenchymal stem cells (MSCs) cultured on PCL nanofibre meshes for up to 70 days post seeding [192]. After 14 days a complete monolayer of cells formed on the scaffolds surface with cells penetrating between 100-200 μm into the scaffold body. Full colonization of the ~ 1 mm thick construct was achieved between six to ten weeks post seeding. It is noted that despite cells colonising the entire scaffold thickness, they remained less dense at the centre of the scaffolds compared to the edge.

The congregation of cells at the peripheries of scaffolds may not only result in the incomplete remodelling of tissue within the inner regions of the construct, but may also result in the reduced viability of cells at the surface. A cell motility effect known as 'contact inhibition' arises when a cell makes contact with an adjoining cell. This contact modulates cell proliferation rates at the site in order to prevent an uncontrolled overgrowth of cells as seen in cancerous tumours [193]. Similarly, contact inhibition has been observed to occur within cells seeded on the surface of electrospun constructs. Lao *et al.* noted that MC3T3-E1 osteoblast cells cultured on poly(lactide-co-glycolide)/hydroxyapatite (PLGA/HAp) nanofibrous scaffolds showed increased viability rates up to 7 days in culture, however, a marked decrease in viability between day 7 and 14 was subsequently observed as shown in Figure 2.15 [194].

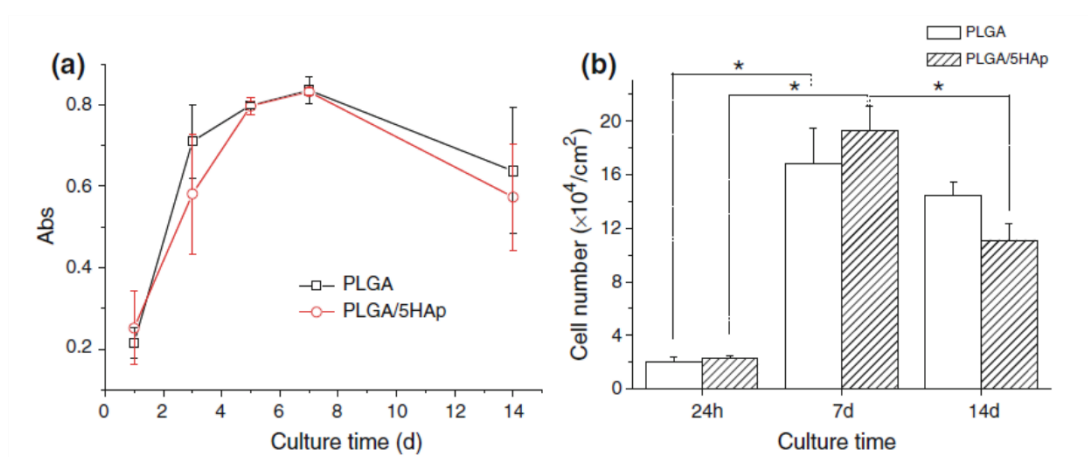


Figure 2.15: (A) Viability (MTT assay) (B) Proliferation of MC3T3-E1 osteoblasts on the control PLGA and PLGA/5HAp nanofibrous scaffolds as a function of culture time (adapted from Lao *et al.* [194])

This increase in viability up to day 7 and subsequent decrease suggests that the surface of the scaffold allowed for sufficient proliferation, such that the surface became confluent at day 7. A subsequent lack of void space may have prevented a sufficient ingress of cells into the scaffold ultimately resulting in contact inhibition effects within the surface cell population accounting for the reduced metabolic activity observed.

2.5 Methods to Improve Cell Infiltration on Electrospun Constructs

A number of techniques have been proposed within the literature for the development of electrospun materials that demonstrate enhanced porosity characteristics such as cryogenic electrospinning [22], [195], porogen leaching [21], and sacrificial fibre spinning [23]. Methods such as cryogenic electrospinning and porogen leaching utilise additives that are interspersed within the fibre networks during the spinning process. These additives are then subsequently removed to leave large void spaces in their place. In cryogenic electrospinning a chilled electrospinning target is used to collect depositing electrospun fibres whilst simultaneously forming ice crystals amongst the fibres due to a humid spinning environment [22]. These ice particles are later removed through a freeze drying process allowing for scaffolds with tuneable porosity and pore volume characteristics to be fabricated. Leong *et al.* developed a bi-layer Poly(D,L-lactide) (PLA) scaffold through the combination of a conventionally electrospun membrane combined with a cryogenically formed layer [195]. Porcine esophageal epithelial cells (PEECs) and smooth muscle cells (SMCs) cultured upon the bilayer

scaffold penetrated 100 μm into the cryogenically spun layer of the scaffold after 2 months in culture. No infiltration was observed in the conventional spun layer and similarly, no cell infiltration was observed in pure conventionally spun PLA membranes. Cryogenically electrospun materials do however typically suffer from a loss of mechanical integrity which has prevented the technique from being successfully exploited. Cryogenic spun membranes of PLA have been shown to possess tensile strengths of 0.04 ± 0.01 MPa which is significantly lower than that of conventional PLA nanofibre membranes with tensile strengths of 1.5 ± 0.1 MPa [22].

Alternative porogen leaching processes typically employ salt particles to increase the pore sizes within electrospun materials. PCL/Gelatin solutions have been successfully co-spun with sodium bicarbonate particles in order to form ‘crater-like’ structures within the surface of the membranes [21]. Subsequent immersion of the membranes in citric acid and deionised water leached the sodium bicarbonate from the membranes leaving voids within the surface of the scaffold. Scaffolds without crater-like voids prevented seeded human mesenchymal stem cells (hMSC) from infiltrating in, with cells only found on the surface of the scaffold. Scaffolds possessing the crater voids on the other hand showed adequate spreading of the hMSCs throughout the entire thickness of the scaffold after only 7 days in culture.

Sacrificial fibre spinning is a technique that employs two polymers that are soluble in dissimilar solvents, concurrently electrospun to create an interspersed fibre network consisting of the dual fibre populations. By immersing the scaffold in one of the appropriate solvent systems, typically water, one population of fibres is removed from the scaffold leaving void spaces in their place. PCL has been successfully co-spun alongside the water soluble polymer poly(ethyleneoxide) (PEO) [23][24]. The PCL/PEO scaffolds were immersed in water post spinning to remove the PEO fibres. By adjusting the ratio of PEO to PCL fibres, the resultant sacrificial fibre content could be tuned to 20%, 40%, or 60% of the initial scaffold mass. Biological evaluation of the scaffolds showed that the increased pore size and the overall morphology of the PCL/PEO after PEO dissolution allowed for increased cell penetration of MSCs when compared to pure PCL fibre scaffolds. Again a significant drop in modulus was seen in the PCL/PEO scaffolds compared to that of pure PCL.

2.5.1 Multi-Modal Electrospinning

While a number of promising techniques have been proposed to increase the porosity and pore volumes of electrospun materials, they often require complex spinning apparatus or a number of additional post processing steps which increase the risk of contaminants entering the final scaffold prior to cell culture. It is desirable to achieve a porous electrospun network directly through the electrospinning process that offers both nanoscale architecture for cell binding and multiscale porosity for cell infiltration purposes. An attractive solution to this problem is the use of hybrid fibre diameter populations. Simultaneous or sequential electrospinning of nanoscale and micron scale fibres allows for desirable properties of each fibre scale to be incorporated into a single electrospun scaffold. These scaffolds should in principle possess increased pore volumes due to the crossing of the micron size fibres within deposition planes, while the intermixed nanoscale diameter fibres support cell binding.

Electrospun nano and micro fibre hybrid scaffolds can be prepared by two methods. The first technique utilises two-nozzle electrospinning, where one nozzle creates the nanofibre population and the other generates the microfibre population [102][196][197]. One of the first studies to investigate hybrid PCL scaffolds by dual nozzle spinning was reported by Pham *et al.* [196]. In this work layered scaffolds were created by the sequential spinning of nanofibre and microfibre layers. By altering the diameter of the depositing fibres materials through the adjustment of spinning solution concentrations and solvents, scaffolds with pore sizes ranging from 20 to 45 μm and a constant porosity of $\sim 84\%$ could be created. Interestingly cell attachment after 24 hrs did not appear to increase with increasing percentage of nanofibres, however enhanced cell spreading was seen by stronger F-actin staining suggesting the nanofibres allowed for superior anchorage of the cells. It is also noted that the MSC infiltration was reduced with increasing nanofibre percentage indicating that this layered technique still suffers from cell infiltration issues in the nanofibre portion of the scaffold.

Rather than using a sequential spinning process, Soliman *et al.* created hybrid PCL scaffolds by simultaneously spinning nano and microfibrils onto a rotating disc collector as seen in Figure 2.16, to provide an interspersed fibre network [184].

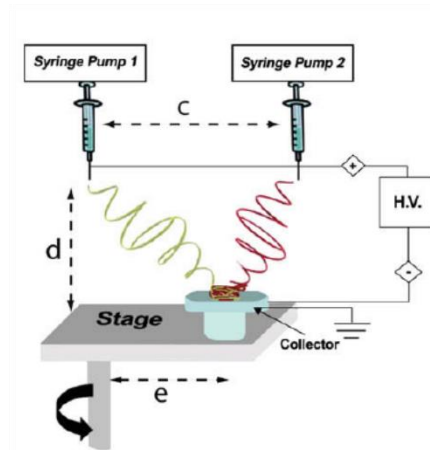


Figure 2.16: Dual Nozzle setup with simultaneous electrospinning of nanofibres and microfibrs (Adapted from [184])

This hybrid fibre diameter matrix referred to as a ‘MIX’ scaffold within the study was found to yield better cell performance rates compared to pure nanofibre and microfibre based materials. MSCs cultured on nanofibre scaffolds were found to have lower adhesion and viability rates compared to the microfibre and MIX scaffolds. The nanofibre element of the MIX scaffold was however found to have a synergistic effect with enhanced cell survival compared to the pure microfibre scaffolds. These results indicate that the MIX scaffold had the best overall biological performance, confirming that cell attachment and survival within the scaffolds are strongly influenced by the microfibre diameter porosity and that nanoscale fibres can substantially add to the performance.

The second method by which hybrid fibre diameter populations can be achieved is through multimodal electrospinning [100][102][198][199]. Multimodal electrospinning refers to the process of simultaneously electrospinning interspersed nano and micron diameter fibres from a single spinning solution rather than dual nozzles. This is achieved through the manipulation of solution properties and processing parameters such as polymer concentration, dielectric potential, flow rate and voltage. By inducing splaying effects within the electrospinning jet, streams that generate nanofibres and streams that generate microfibrs can be concurrently achieved [200]. The interspersed distribution of micro and nano fibres reduces infiltration difficulties compared to layered constructs whilst also removing the need for a second spinning solution reducing the complexity of the spinning apparatus.

Gentsch and colleagues, investigated the bi-modal spinning of PCL fibres in order to increase the cell infiltration properties of such meshes [199]. In this study, solutions of PCL dissolved in chloroform were used to produce micron and hybrid fibre diameter scaffolds through the alteration of solution concentration, spin rates and humidity. Using a 15w/v% solution it was observed that bi-modal scaffolds were achieved when the solution flow rate was reduced to 0.2 ml/hr (Figure 2.17 (A1)), with micron scale meshes produced at higher flow rates (B1). This was attributed to the occurrence of axial-symmetric instability within the spin jet that resulted in different stretching rates along the length of the jet resulting in thick and thin jet regions as seen in Figure 2.17 (A2). The jet subsequently deposited to form micron and nano fibres respectively. It should be noted that the fibres created through this process appeared to be highly elongated beads rather than true micron and nanofibres. Initial cell penetration studies did however show superior ingrowth of epithelial cells into the mixed fibre meshes compared to the unimodal micron fibre meshes (~1.5 μm fibres).

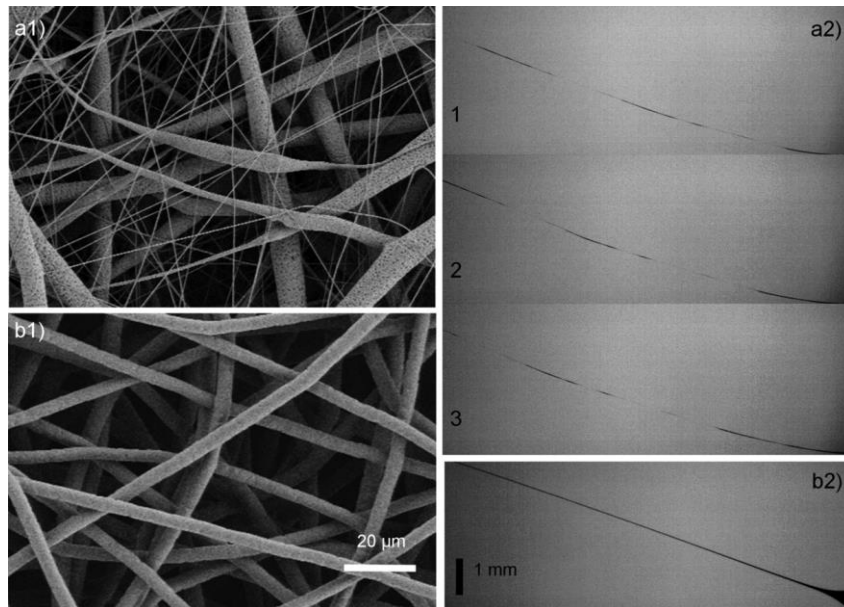


Figure 2.17: SEM micrograph showing the PCL nonwovens with bimodal fibre size distribution (a1) 15 w/v% PCL/Chloroform solution at a rate of 0.2 ml/hr and ~50% humidity. Thick and thin fibres caused by different stretch rates can be observed. At ~30% humidity, unimodal fibres (rate: 0.2 ml/hr) were processed (b1). High speed images of the spin jet leading to the bimodal fibre meshes (a2: 1–3) and as comparison, the corresponding straight jet that leads to unimodal, micro-sized fibre meshes are shown (b2) (a2/b2: spin direction from right to left, pictures are taken at 1 995 fps close to the syringe tip, 50 ms exposure time). (Taken from [199])

Valence *et al.* developed a PCL vascular graft consisting of multimodal fibres, although this did not appear to be an objective of the research but rather a result of the solvent/surfactant combination chosen, of Chloroform and Ethanol [100]. The implanted scaffolds containing average fibre diameters of $2.2 \pm 0.6 \mu\text{m}$ maintained patency and were free of aneurysm formation after 18 months implantation. In addition, *in vivo* compliance was maintained at $7.8 \pm 0.9\%/mm\text{Hg}$ for the duration of study. After 6 weeks implantation, the entire thickness of the graft was sparsely infiltrated by macrophages and fibroblasts. The cellular population further increased up to 12 months, at which point a regression was observed. The extent of cell invasion at 18 months was comparable to that at 6 weeks, at about 25%, leaving areas of sparse cellularity in the centre of the graft wall. Rapid neovascularization was also observed at 6 weeks, but this was followed by a progressive regression over time with only a few capillaries remaining within the graft wall at 18 months. This regression was attributed to a disappearance of macrophages which in turn reduced the angiogenic factors stimulating neovascularisation resulting in an inadequate supply of nutrients and oxygen to the cells within the centre of the scaffold. The researchers concluded that although the PCL multimodal scaffold had excellent mechanical properties and patency rates additional cues were required in order to ensure continuous infiltration of the scaffold over long implantation periods. This indicates it may be necessary to perform pre-culture steps rather than direct implantation to ensure an inflammatory response as seen by the macrophage ingress does not occur and to provide suitable time for stable neovascularization to occur.

2.5.2 Nanofibre Bundles & Yarns

An alternative solution to tackling the problem of inadequate cell infiltration in electrospun materials may lie in the development of electrospun nanofibre bundles and yarns. The origins of this electrospinning variation began with the goal of incorporating nanofibre technology into standard fibre assembly techniques for use within the textile industry. Nanofibre based textiles offer the potential to fabricate super-structures that possess the characteristic benefits of electrospun materials while providing enhanced properties that include ultra-high specific surfaces, increased pore volumes and increased mechanical strength [201]. Individual electrospun nanofibres are too in nature fragile to withstand the manipulations required for industrial

processing [202], while nonwoven membranes suffer from a lack of processing versatility and poor cost efficiency [203][204]. These reasons have so far led to electrospinning being impractical for large scale fibre production.

To overcome this issue, it has been proposed to form linear bundles of nanofibres containing a high degree of order and alignment comparable to traditional textile yarn filaments. By doing this, filaments robust enough to be assembled into fibrous structures through weaving, knitting and embroidery techniques can be created [205]. The concept of nanofibre based textiles was first proposed in a sequence of patents by Formhals, which included the first electrospinning patent itself [135][206]–[208]. Here methods to produce continuous non-twisted filaments comprised of materials such as cellulose acetate nanofibres were presented.

Assembly Techniques

The following terminologies are used within the literature for the classification of electrospun filaments types' dependant on their morphology. The terms 'nanofibre bundles' or 'tows' are commonly used when referring to untwisted groups of uniaxial aligned electrospun fibres, while 'nanofibre yarns', 'nanoyarns' or 'yarns' are used to describe fibre bundles containing an imparted twist [204][209]–[211].

Short Nanofibre Bundles and Yarns

Theron and co-workers, studied one of the first techniques for the fabrication of electrospun nanofibre bundles [212]. In this work, a large diameter spinning disc with a tapered edge of half angle 26.6° was utilised as the collector mechanism (Table 2.5 (A)). Solutions of polyethylene oxide (PEO) dissolved in water and ethanol were electrospun onto the edge of the disc. The high linear velocity of the collector surface aligned the depositing fibres with respect to the circumferential axis of the disc. The diameter of the collected fibres were found to range between 100-300 nm but no details on the length, thickness or mechanical properties of the samples was presented. Further studies on this technique have shown that depositing fibres are often prone to necking due to the high rotational velocities of the collection surface. This necking effect severely reduces the strength of the collected materials [213].

The first use of the term ‘electrospun yarn’ appeared in work by Fong *et al.* [214]. Here solutions of nylon and nylon 6-montmorillonite (NLS) were electrospun onto a rapidly oscillating grounded frame to form short, aligned fibre structures referred to as yarns. Despite the term yarn being used to describe the fibres collected they were not strictly yarns but rather bundles as they did not contain an imparted twist. Fibres with diameters between 100 to 500 nm were collected but few details on the collector system or fibre mechanics were however provided.

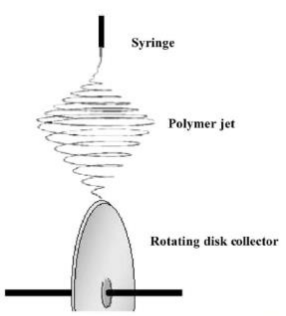
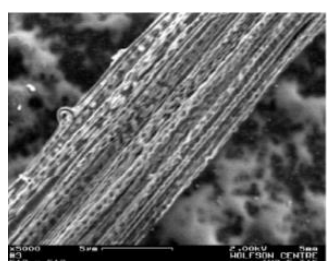
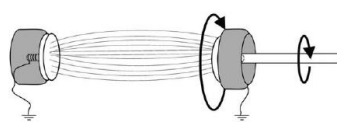
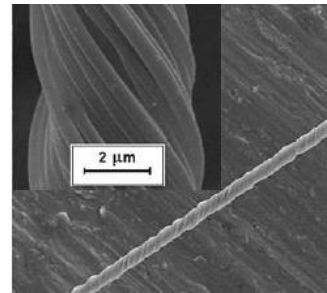
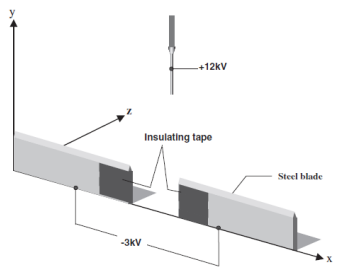
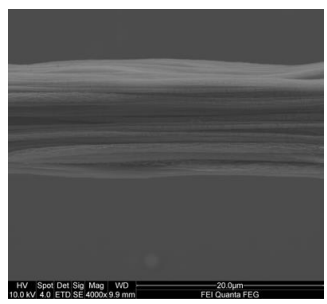
Dalton *et al.* employed grounded parallel disc electrodes to collect aligned fibrous yarns of poly(ϵ -caprolactone) (PCL) [215]. In this process, short yarn segments of about 50 mm were produced by positioning two annular collectors within the path of the electrospinning jet. Depositing fibres with diameters of $1.26 \pm 0.19 \mu\text{m}$ were found to bridge between the two disc electrodes and the individual fibres were combined to form a yarn by rotating one of the electrodes (Table 2.5 (B)). The gap distance between the electrodes was found to be critical for appropriate fibre formation as a gap of less than 40 mm or greater than 100 mm produced poor quality fibre arrays.

In a study by Teo and Ramakrishna, two negatively charged steel blade electrodes positioned at a set distance apart were used as the collector mechanism as shown in Table 2.5 (C) [216]. Fibres spun from a solution of PCL dissolved in chloroform and methanol were found to deposit between the blades. The collected fibres were bundled together using a post dipping treatment where the surface tension of a fluid bath was used to pack the fibres. Stray fibre formation was, however, observed in this technique due to the accumulation of surface charges within the bundle that subsequently repelled further depositing fibres. Bundles of a limited length could be produced through this system as a gap between the collector blades of 8 cm or greater resulted in limited fibre deposition.

A number of studies have also looked at methods to produce nanofibre bundle and yarns from conventional 2D nonwoven membranes. Briefly, Deitzel *et al.* used a series of charged rings containing the same polarity as the electrospinning jet to deposit a thin strip of PEO fibres (0.6 cm wide) on a rotating drum collector [167][217]. For the purposes of wide angle X-ray diffraction (WAXD) the fibres were bundled and twisted

together forming a yarn. Fennessey and Farris, used a similar approach whereby solutions of polyacrylonitrile (PAN) dissolved in dimethylformamide (DMF) were electrospun onto a rotating drum collector [218]. The spun membranes were removed forming unidirectional tows of nanofibres. The tows were subsequently linked and twisted together using an electric spinner system. By increasing the twist angle within the yarns the ultimate tensile strength and modulus were found to increase.

Table 2.5: Short nanofibre bundles and yarns

Set-up	Morphology	Comments
<p>A. 2001 <i>Theron et al.</i> [212]</p>  <p>Fig. 1. Schematic setup to fabricate aligned nanofibrous scaffold by electrospinning with a disk collector.</p>		<p>Advantages:</p> <ul style="list-style-type: none"> Simple process Aligned substructure <p>Disadvantages:</p> <ul style="list-style-type: none"> Limited sample length Fibres often experience necking
<p>B. 2005 <i>Dalton et al.</i> [215]</p> 		<p>Advantages:</p> <ul style="list-style-type: none"> Simple process Ability to control twist rate and direction Highly aligned fibres <p>Disadvantages:</p> <ul style="list-style-type: none"> Limited sample length
<p>C. 2005 <i>Teo et al.</i> [216]</p> 	<p>*After dipping treatment</p> 	<p>Advantages:</p> <ul style="list-style-type: none"> Simple process Highly aligned fibres <p>Disadvantages:</p> <ul style="list-style-type: none"> Limited sample lengths Stray fibres Additional step to bundle fibres

Continuous Nanofibre Bundles and Yarns

In order to develop a process for the continuous production of undamaged bundles and yarns, Khil *et al.* utilised a process known as ‘electro-wet spinning’ [219]. In this set-up PCL was electrospun onto a coagulation bath of distilled water as shown in Table 2.6 (A). A filament guide and take up winder were used to direct and collect the bundles containing fibres ranging from 500 nm to 12 μm in diameter. The liquid media prevented the fibres breaking apart, while the take up roller aided in aligning the fibres. Smit *et al.* similarly demonstrated that this technique could be used to produce poly(vinyl acetate) (PVAc), poly(vinylidene difluoride) (PVDF) and polyacrylonitrile (PAN) based bundles. Production rates of only 3 metres min^{-1} were attained through this method [220].

To improve the production capabilities of electro-wet spinning and provide increased control over the fibre assemblies, Teo *et al.* designed a system that utilised dynamic liquid collection techniques [221]. In this approach, the collector apparatus consisted of a two tier water bath system as shown in Table 2.6 (B). A water vortex is generated in the top tier bath by the motion of fluid draining through an outlet located in the base of the bath. A reservoir and pump positioned below the outlet re-circulated the water and a ground wire was inserted to remove residual charges. Solutions of poly(vinylidene fluoride-co-hexafluoropropylene) (PVDF-HFP) were electrospun onto the fluid surface creating a nanofibre mat. The vortex in turn bundled and aligned the fibres forming a continuous nanofibre bundle. A rotating mandrel positioned below the outlet collected the emerging material with production rates of up to 60 metres min^{-1} achieved. The effect of solution concentration and flow rate on the yarn diameters was also investigated. An increase in diameters from 463 nm to 1224 nm was witnessed when the solution concentration was raised from 0.08 g/mol to 0.12 g/mol. Similarly, the flow rate was seen to alter the bundle diameter with a flow rate of 1 ml/hr yielding a diameter of 740 nm and 15 ml/hr giving 1300 nm.

By twisting aligned nanofibre bundles around their axis to form yarns the mechanical properties of the collected materials have been demonstrated to increase compared to the non-twisted versions [218]. Yousefzadeh *et al.* adapted the dynamic liquid collection technique to induce self-twisting during the collection process [222]. In this

work, a guide mechanism was used to lift material directly off the vortex surface and through a guide mechanism resembling an insulated spring. By manoeuvring the fibre bundle around the spring coils a twist was imparted. A stress at break of 13.91 ± 3.70 MPa for a 15° twist angle compared to 3.07 ± 0.35 MPa for a non-twisted bundle again demonstrated the advantages of imparted twists on fibre assemblies. Teo *et al.* and Yousefzadeh *et al.* also demonstrated that the dynamic liquid system could be used to directly produce 3D constructs comprised of randomly deposited layers of nanofibre bundles [223][224]. By allowing the fibre mat to freely fall from the top tier bath into the reservoir tank positioned below, highly porous 3D meshes were self-assembled. By freeze drying the collected meshes in custom moulds, cylindrical and hemispheric structures could be produced [223]. Additionally by collecting the fibre mat directly from the top tier water bath surface without inducing bundling a ring shaped structure could be produced containing nanofibre bundles [224].

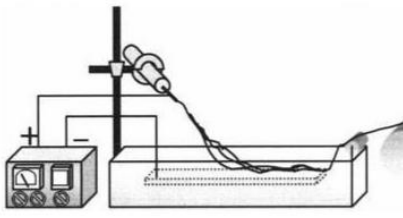
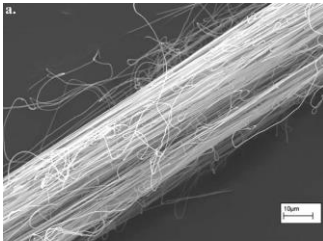
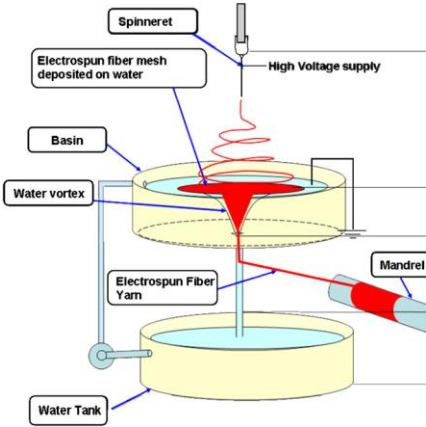
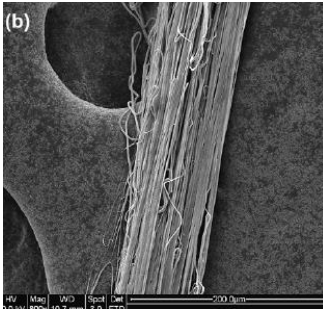
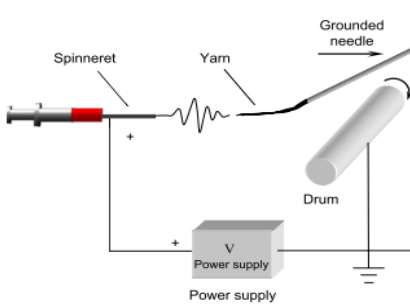
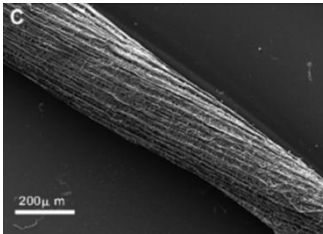
Wang *et al.* reported a method to produce nanofibre bundles using a self-assembly technique (Table 2.6 (C)) [225]. In this process a grounded needle tip was used as the collection surface, whereby, the electrospinning jet collected on the needle tip due to a large electrostatic convergence effect. A continuous self-bundling process could be initiated by gently manoeuvring the collection needle away and winding the deposited fibres onto a grounded rotating collector. In this method it is vital that the surface velocity of the rotating collector matches that of the bundle formation speed to ensure a stable and continuous bundle formation process occurs. It was also outlined that by increasing the conductivity of the electrospinning solution, self-bundling could be initiated without requiring the intermediate needle collector.

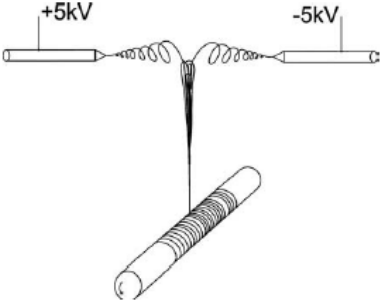
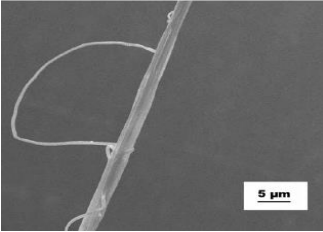
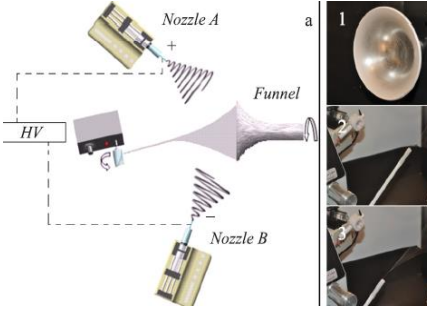
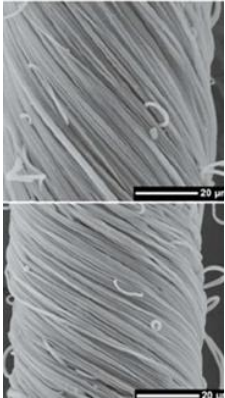
In work by Pan *et al.* a process known as conjugate electrospinning was used to produce nanofibre yarns [226]. In this conjugate approach, two oppositely charged spinnerets were directed towards each other and fibres spun forming a mid-air fibre bundle. The bundle was subsequently manually drawn away onto a winding mandrel, initiating yarn formation (Table 2.6 (D)). Poly(vinyl alcohol) (PVA) and poly(vinyl pyrrolidone) (PVP) solutions were successfully spun into yarn structures. 13wt% PVA solutions produced yarns with average fibre diameters of about 346 nm and 12wt% PVP solutions produced average fibre diameters of 670 nm.

Ali *et al.* developed a variation of the conjugate spinning technique whereby dual oppositely charged nozzles were directed towards a stainless steel rotary funnel, see Table 2.6 (E) [227]. PVDF–HFP fibres were electrospun onto the edge of the rotating funnel forming a nanofibre ‘web’. The web was drawn away forming a hollow fibre cone that was collected on a rotating mandrel. It was observed that by increasing the rotational speed of the funnel both fibre and yarn diameters could be decreased. Yarns with diameters of 200 μm and containing fibres with average diameters of 1100 nm were created at a funnel speed of 200 rpm whereas fibre diameters of approximately 500 nm and corresponding yarn diameter of 60 μm were seen when the funnel speed was increased to 2000 rpm. Additionally, increasing the rotational speed resulted in higher twist angles within the yarns. Yarns with increased twist angles demonstrated increased tensile strength and elongation to break. However, at too high of a rotational speed a decrease in tensile strength was observed while elongation to break continued to increase.

A similar method was patented by He *et al.*, whereby, a metal funnel was positioned between two sets of dual oppositely charged jets [228]. 15wt% PAN solutions were spun onto an unearthened funnel and the hollow fibre web drawn away to a collection mandrel. The effect of increasing the spinning voltage was seen to decrease fibre diameters within the yarn but resulted in an overall yarn diameter increase. At a spinning voltage of 14kV average fibre diameters of 75 nm and yarn diameters of approximately 490 μm were observed. When the voltage was increased to 22kV fibre diameters decreased to approximately 54 nm while yarn diameters increased to 650 μm . Twist levels within the yarns were also seen to alter the strength and elongation at break of the samples. Strengths increased from 1.81 to 55.70 MPa and strains from 24.47% to 41.31% when the twist level was raised from 0 twist per metre (tpm) to 375 tpm. Numerous variations on the conjugate process have been presented within the literature including those that use neutral collection plates [229], and cylinders [230], rotating disc electrodes [231][232], and water baths [233], as intermediate collection surfaces for the fibre webs.

Table 2.6. Continuous bundles and yarn

Set-up	Morphology	Comments
<p>A. 2005 <i>Khil et al.</i> [219]</p>		
		<p>Advantages:</p> <ul style="list-style-type: none"> Continuous production Simple process <p>Disadvantages:</p> <ul style="list-style-type: none"> Low production rate Stray fibres, difficult to control assembly of nanofibres
<p>B. 2007 <i>Teo et al.</i> [221]</p>		
		<p>Advantages:</p> <ul style="list-style-type: none"> Continuous bundles High production rate Production of yarns possible <p>Disadvantages:</p> <ul style="list-style-type: none"> Difficult to transfer yarn to mandrel Complex system Additional mechanism to induce twist
<p>C. 2008 <i>Wang et al.</i> [225]</p>		
		<p>Advantages:</p> <ul style="list-style-type: none"> Continuous bundles Self-assembling once process is initiated <p>Disadvantages:</p> <ul style="list-style-type: none"> Difficult to initiate bundling Speed of collection and production must be finely matched

Set-up	Morphology	Comments
<p>D. 2006 <i>Pan et al.</i> [226]</p> 		<p>Advantages:</p> <ul style="list-style-type: none"> Simple set up <p>Disadvantages:</p> <ul style="list-style-type: none"> Difficult to initiate yarn collect Non-twisted bundles
<p>E. 2007 <i>Ali et al.</i> [227]</p> 		<p>Advantages:</p> <ul style="list-style-type: none"> Continuous production of yarns Ability to adjust the twist angle within yarns <p>Disadvantages:</p> <ul style="list-style-type: none"> Complex system Limited production rate

Applications In Tissue Engineering

Whilst initially envisaged as materials for use within the textile industry the potential of electrospun nanofibre bundles and yarns for the development of advanced tissue engineered scaffolds was quickly identified. The highly aligned substructure of these nanofibre filaments is thought to offer increased controlled of cell guidance and proliferation, while the void space created between adjacent filaments and pore volumes within the filaments themselves offers multi-scale porosity and permeability to the tissue scaffolds. This increased porosity should aid cellular penetration overcoming a critical issue in the development of current electrospun tissue scaffolds [20][189].

One of the first studies on the use of electrospun nanofibre bundles and yarns for tissue engineering applications was presented by Khil *et al.* in the development of the electro wet-spinning process [219]. PCL fibre bundles were processed into a plain weave

fabric and cell compatibility studies performed. Mammary carcinoma cells (MCF-7) were seeded on the woven PCL fabrics and a 6-well tissue culture plate used as a control. The results of cell proliferation studies showed that there was a sharp increase in the number of cells on the PCL woven structure from 1 to 3 days compared with those grown on the control. The hydrophobic nature of PCL did however result in cells forming large aggregates rather than forming a confluent layer along the entire woven fabric.

Xu *et al.* studied the effect of cell adhesion and proliferation on highly aligned electrospun fibre bundles made from the block copolymer P(L-Lactic acid-co-caprolactone) [P(LLA-CL)] [173]. Bundles containing nanofibres with an average diameter of 550 ± 120 nm were produced by electrospinning onto a large diameter disc (200mm) with a tapered edge similar to that presented by Theron *et al.* as shown in Table 2.5 (A) [212]. This study aimed to investigate the effect of an aligned scaffold morphology resembling that of the medial layer of an artery on *in vitro* cell signalling and proliferation rates. A cell suspension of human coronary artery smooth muscle cells (SMCs) was seeded onto the aligned nanofibre bundles. The seeded SMCs were seen to adhere and elongate themselves along the length of aligned scaffold after 1 hr with almost all cells adhering to the structure with a spindle-like contractile phenotype after 5 hrs. Cells seeded on a control substrate of tissue culture polystyrene (TCPS) exhibited a flat fibroblast appearance with no expression of contractile markers such as α -actin and myosin filaments. Increased cell adherence was also witnessed on the nanofibre bundle scaffolds (63.78%) compared to solvent cast P(LLA-CL) films (44%) at 8 hrs post seeding. After 3 days of culture, cells were seen to proliferate along the longitudinal direction of the nanofibres. At 7 days post seeding cells began to increase in number forming a monolayer around the scaffold.

Bosworth and co-workers similarly demonstrated the importance of aligned substructures on mesenchymal stem cell development [234]. Here electrospun PCL yarn scaffolds (diameters of $\sim 200\mu\text{m}$) were studied for the purpose of developing a tissue engineered tendon. Human mesenchymal stem cells (hMSCs) were seeded onto the PCL yarn scaffolds and were exposed to either static or cyclic loading conditions during the culture period. Cyclically loaded scaffolds were subjected to a loading regime of 5% strain at 1 Hz for 1 hr per day through a custom built system as shown

in Figure 2.18 (B). Cellular infiltration into the yarn cores was assessed via microXCT at 21 days post seeding. Initial porosity measurements of acellular yarn scaffolds indicated porosity levels of 56%, however, no details of internal pore diameters were provided. No cellular penetration into the yarn depth was observed on either of the yarn groups but rather cells formed layers on their peripheries. This lack of infiltration was attributed to the diameters of the hMSCs (20 μm) which were considerably larger than the pores between fibres. Cells were however shown to grow on the outer surfaces of the yarn constructs with those under dynamic loading forming a 30 μm thick layer of cells. Only a thin layer of cells was seen on the statically culture samples. Tensile testing of the yarn scaffolds showed increased tensile strengths and stiffness properties for cell-cultured yarns irrespective of loading conditions compared to the acellular control group. The ultimate tensile strength (UTS) of loaded samples after 21 days of culture was approximately 55 MPa with a corresponding Young's modulus of approximately 100 MPa. The statically cultured samples showed a UTS of approximately 20 MPa after 21 days of culture and an average Young's modulus of 80 MPa. While these studies demonstrate the benefits that nanoyarns offer for cell culturing, they only study individual yarn filaments rather than complex 3D multi-filament scaffolds.

A number of studies have sought to develop 3D nanofibre bundle and yarn based scaffolds through the use of dynamic liquid collection techniques as first reported by Teo *et al.* [221]. Wu and colleagues, produced fibre bundle scaffolds spun from P(LLA-CL)/silk fibroin composite solutions [25]. In this method, the composite

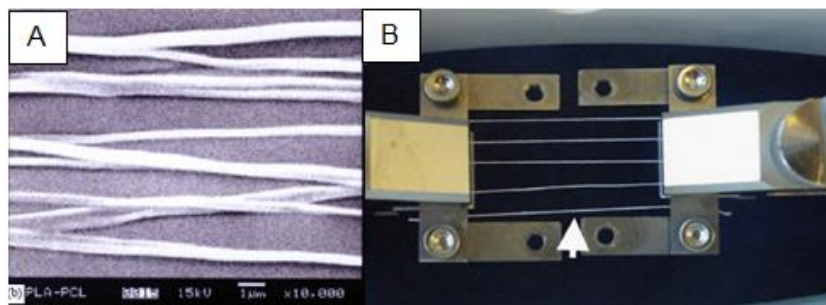


Figure 2.18: *Electrospun yarns created through disc edge collection (a) Aligned P(LLA-CL) yarns created by Xu et al. [173] (b) Electrospun PCL yarns in dynamic loading system as reported by Bosworth et al. [234]*

solutions were spun onto the moving water surface, bundled, aligned, and collected on a rotating and traversing drum as they emerged from the basin outlet. The fibre bundles were allowed to deposit freely on the drum forming a tube. The tube was subsequently cut along its longitudinal length forming a 2D fibrous membrane that exhibited fibre bundle diameters of $\sim 20\ \mu\text{m}$ and pore sizes of 20 to $50\ \mu\text{m}$ between bundle segments. Randomly orientated nanofibre meshes were spun as a comparison scaffold. L929 murine fibroblast cells were seeded onto the nanofibre bundle scaffolds and nanofibre membranes. Infiltration and proliferation rates were studied for both scaffolds. Cellular infiltration was assessed 4 days post seeding using H&E staining techniques. Cross sectional slices of the membranes measuring $10\ \mu\text{m}$ showed advanced cellular infiltration into the yarn (Figure 2.19 (C)) scaffold compared to the nanofibre meshes that displayed a monolayer formation on the surface (Figure 2.19 (D)). Cells within the nanofibre bundle scaffold showed elongated morphologies, grew along the bundle lengths and were also seen to bridge gaps between adjacent fibre segments. Uni-axial mechanical characterisation of the scaffold was also performed. A difference in tensile strengths was observed when testing was conducted parallel ($3.55 \pm 0.21\ \text{MPa}$) and perpendicular ($0.23 \pm 0.04\ \text{MPa}$) to the nanofibre bundle axis. These results indicate that fibre bundle based scaffolds can only resist loading along the axis of the yarn and may not be suitable for bi-axial loading applications.

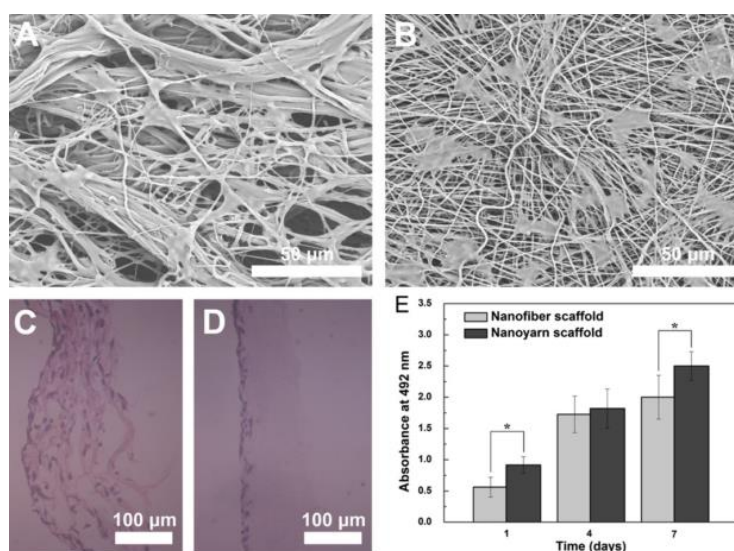


Figure 2.19: SEM Images of L929 cells on the nanoyarn scaffold (A) and nanofiber scaffold (B). H&E staining images reveal cell infiltration in nanoyarn (C) scaffold and nanofiber scaffold (D). Cell proliferation on the scaffolds was determined by MTT assay (E) (Reproduced from Wu et al. [25])

Xu *et al.* demonstrated that solutions of P(LLA-CL)/collagen could be used to create electrospun fibre bundles containing fibre diameters of 641 ± 68 nm through dynamic liquid collection techniques [26]. A comparative study to random orientated nanofibre meshes (fibre dia. 632 ± 81 nm) and aligned nanofibre meshes (643 ± 97 nm) show that an increased infiltration of human tendon cells into the nanofibre bundle scaffolds was observed when compared to the random and aligned fibre meshes. The histology images can be seen in Figure 2.20.

Further studies by Wu *et al.* again showed with pig iliac endothelial cells (PIECs) and MC3T3-E1 pre-osteoblastic cells that P(LLA-CL)/collagen fibre bundles (diameters of $\sim 24\mu\text{m}$) containing nanofibres of diameter 612 nm demonstrated accelerated proliferation rates compared to those cultured on 2D nanofibre membranes (fibre dia. 455 nm) [235]. After 7 days of culturing both PIECs and MC3T3-E1 penetrated the full depth of the nanoyarn scaffolds while no apparent infiltration was observed on the conventional 2D scaffolds. This was attributed to the small average pore sizes of $5\mu\text{m}$ within the nanofibre membranes compared to the yarns which contained grooves and pores between yarns of approximately $28\mu\text{m}$. These studies indicate huge potentials for nanofibre bundle and nanoyarn based scaffolds due to the excellent cell adherence, proliferation and infiltration rates that they offer compared to conventional electrospun meshes. A method to increase the stability of the produced constructs for multi axial loading applications is, however, an ongoing pursuit. The concept of using nanofibre bundles and yarns within composite scaffolds is also a promising idea.

Liu *et al.* integrated P(LLA-CL) fibre bundles into type I collagen hydrogels for bone regeneration applications [236]. The P(LLA-CL) nanofibrous bundles were produced using a dynamic liquid system as previously described. The bundles were allowed to freely deposit in the lower reservoir bath and were subsequently removed and freeze dried. The resulting mesh bundle was chopped into lengths of approximately 1 mm and added to type I collagen solutions. The composite mixture and pure collagen solutions were refrigerated overnight until fully the solutions gelled. Human mesenchymal stem cells (hMSCs) were seeded onto the scaffolds and proliferation monitored at 7, 14 and 21 days post seeding.

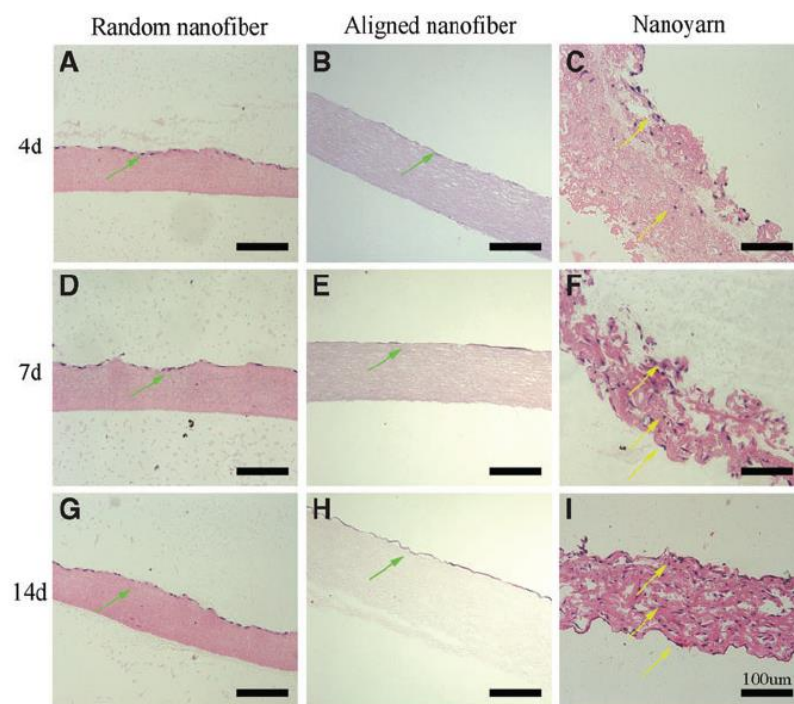


Figure 2.20: Images of H&E-stained sections of P(LLA-CL)/collagen random nanofibre and aligned nanofibre scaffolds and yarn scaffold. (A, D, G) H&E staining of random nanofibre mesh at 4, 7 and 14 days post seeding, cellular infiltration limited to top layer of scaffold (B, E, H) H&E staining of aligned nanofibre mesh at 4, 7 and 14 days post seeding showing monolayer of cells on scaffold surface (C, F, I) H&E staining of yarn scaffold at 4, 7 and 14 days post seeding. Progressive infiltration of cells into nanoyarn scaffold body can be seen from day 4 to day 14 (Reproduced from Xu et al. [26])

Cells were observed to grow well on both scaffolds with a clustered formation of cells observed on the pure collagen gels at 21 days while those on the composite gel showed a well spread morphology. Alkaline phosphatase activity and osteocalcin expression of hMSCs was higher on the gel/bundle scaffolds compared to the pure collagen gels indicating the importance of the fibre bundle additives to stem cell differentiation. In addition, the incorporation of the nanofibrous bundles increased the mechanical properties of the gels preventing shrinkage of gels under cell contractile forces.

Despite being in its infancy, research into the use of nanofibre bundles and yarns for the development of new generation medical textiles and tissues scaffolds have already demonstrated the unique potential and versatility of such structures. The ability to promote cell attachment, guidance and controlled proliferation as well as superior infiltration qualities makes the resultant structures particularly suitable for tissue

engineering applications. In particular, the development of continuous nanofibre bundles and yarns through dynamic liquid electrospinning offers a versatile production technology to study. The development of 3D tissue scaffolds through these bundles and yarns is, however, a step that still needs to be studied in great depth and detail in order for their potential to be truly realised. To the best of the authors knowledge, no studies have yet shown a tubular graft constructed using nanofibre bundles or yarns for tissue engineered blood vessel applications. This may be attributed to the highly aligned substructure of the fibre bundles and yarns which may only provide sufficient resistance in one axis of loading making them unsuitable for biaxial loading conditions. Their incorporation into composite materials does however appear to be a promising strategy to merge the increased porosity and pore volumes they offer while maintaining an structure with sufficient mechanical stability for implantation.

2.6 Rationale of Project and Research Approach

Despite past and current research efforts to develop a suitable small diameter vascular graft (<6mm) for use in coronary artery bypass surgery, it is clear there is still a pressing clinical need for a vessel that can maintain long-term patency. Tissue engineered blood vessel (TEBV) approaches offer a promising pathway to accomplish this task due to the ability to create vessels with biomechanical properties matching that of the native vasculature system. Nanofibre constructs generated through electrospinning techniques possess both the morphology and scale of the natural ECM found within arteries. This unique architecture can facilitate endothelialisation of the lumen with a confluent monolayer of cells, but restricts the infiltration of vSMCs through the thickness of the vessel. This clear and defining limitation prevents cells fully populating the scaffold and in turn results in the incomplete remodelling of the graft often leading to their failure. This ‘fishnet’ effect must be overcome if a electrospun scaffold suitable for small diameter vascular tissue engineering applications is to be achieved.

The electrospinning of multimodal diameter fibres through a single step process appears to be a hugely promising technique to incorporate the inherent benefits of nanofibre diameter materials whilst also maintaining the increased porosity than micro diameter fibres offer. Although the enhanced cellular infiltration qualities of this

technique have been demonstrated within the literature, the limited content and scope of current studies has prevented the true potential of this technique from being realised compared to alternative electrospinning processes and porogen techniques. Further study of this process is required in order to develop scaffolds with tuneable and controllable properties to better mimic the biomechanical properties of native vascular tissue including vessel compliance.

The development of scaffolds from dynamic liquid electrospinning techniques again appears to be a promising step towards developing electrospun materials with enhanced cell infiltration properties. The challenge however, is to combine these uniaxial oriented fibre bundles into a vessel capable of performing under bi-axial loading applications. It is envisaged that a composite vessel combining the mechanical strength of a multimodal fibre membrane paired with the increased porosity of nanofibre bundles may allow for the improved success of electrospun materials for TEBV applications.

The proposed approach of this work is to develop a bi-layered vessel combining the strength and relative leak resistance of a multimodal fibre tube with an outer sheath of aligned nanofibre bundles for enhanced cellular infiltration. A schematic of the proposed vessel can be seen in Figure 2.21. Specific aims of the study will be:

***Aim 1:** To explore the electrospinning of Poly(ϵ -caprolactone) (PCL) to develop micro, nano and multimodal diameter fibre membranes through the controlled alteration of solution and processing parameters.*

***Aim 2:** To develop a single-step multimodal spinning process, whereby regression analysis tools will be used to identify key input variables for the development of defect free fibre membranes. Based on these results a small diameter tubular construct known as the 'core' comprised of multimodal fibres with properties closely mimicking that of native bypass graft materials will be developed.*

***Aim 3:** To design and develop a dynamic liquid electrospinning process for the creation of PCL fibre bundles, studying the effect of solution and processing parameters on overall process stability, fibre bundle morphology and mechanical*

properties.

Aim 4: To develop a composite bi-layered electrospun vessel fabricated from the selected PCL core paired with the optimal dynamically collected fibrous bundles, characterising mechanical attributes including vessel compliance.

Aim 5: To study the effect of Multi Potent Vascular Stem Cells (MVSCs) seeded upon the composite bi-layer vessel assessing proliferation and infiltration properties compared to traditional electrospun nanofibre membranes.

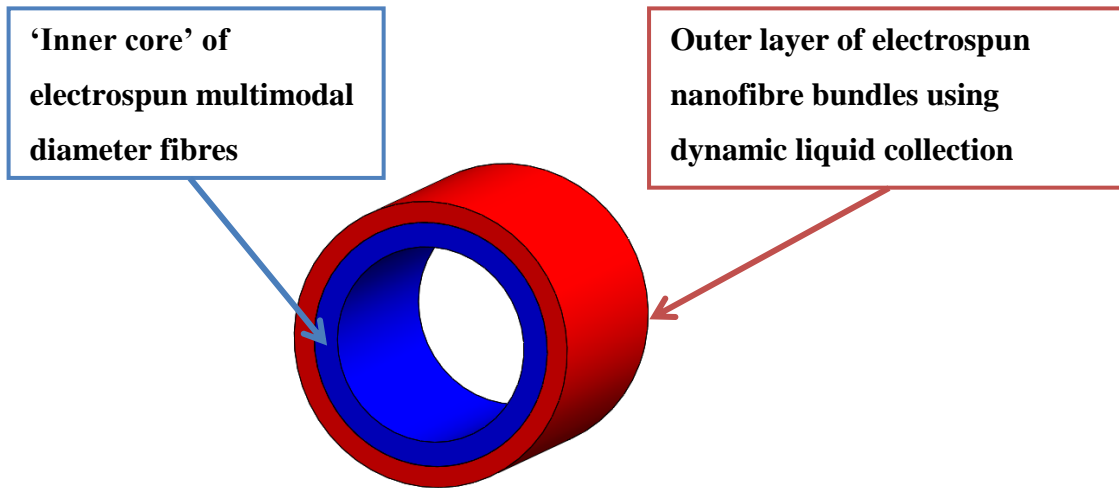


Figure 2.21: Schematic representation of proposed bi-layer vessel geometry with an inner layer of multimodal diameter fibres coated with a porous outer layer of electrospun nanofibre bundles

Chapter 3 Multi-scale Electrospinning of PCL Fibres

3.1 Introduction

Electrospinning is a versatile technique for the development of materials assembled from continuous fibres whose diameters can range from a few microns to several nanometres in scale. The creation of tissue-engineered scaffolds by electrospinning approaches has been widely examined as a method to achieve a structurally and biomechanically compatible scaffold for vascular bypass applications. In order to successfully electrospin a chosen polymer, a number of solution and processing variables, along with their corresponding interactions must be considered. These typically include the choice of solvents used to dissolve the polymer, the addition of surfactants to tailor electrostatic properties, the concentration of polymer within the final solution, along with processing parameters and the collection system used to fabricate the fibre constructs. Through the careful tailoring of such factors, defect free membranes with controllable fibre diameters, orientations, porosities, tensile strengths and stiffness properties can be fabricated.

Studies within the literature focusing on the development of electrospun materials for tissue engineering applications typically present select working solutions and processing parameters when detailing scaffold production methods. While important for the development of the scaffold in question, this provides limited information on the broader electrospinning process itself, and the rationale behind the selection of solution and processing parameters is generally absent. This chapter will consequently investigate methods to produce Poly(ϵ -caprolactone) (PCL) membranes with fibre diameters at several different magnitudes of scale as a basis for the development of novel scaffold structures within subsequent chapters. This will include the spinning of pure micron and nano based constructs, along with those containing hybrid fibre diameter distributions created through a single step multimodal spinning process. In

this assessment, the following criteria will be studied:

- **Effect of Solvent and Surfactant Combination**

The appropriate selection of a solvent and surfactant combination for the electrospinning of PCL micron, nano and multimodal diameter fibres will be investigated. In this, specific combinations of the solvent chloroform and the addition of the surfactants ethanol, methanol and N,N-Dimethylformamide will be examined, in order to determine their effect on overall fibre morphology and process stability.

- **Effect of Polymer Concentration**

The concentration of the raw polymer PCL within the select spinning solutions will be examined in order to produce defect free constructs with tuneable fibre diameters and morphology. Solutions properties including viscosity and conductivity will be observed to provide a comprehensive understanding of the contribution of solution attributes to the spinning of PCL at different fibre diameter scales.

- **Effect of Processing Parameters**

In order to establish optimal processing parameters for the spinning of various solutions, an array of processing parameters will be investigated. In this, their contribution to process stability and overall fibre morphology will again be determined. These will include Solution Flow Rate, Applied Voltage, Collector Distance and Collection Method.

The resultant solutions and processing parameter windows obtained from this chapter will be later utilised in the production of multimodal tubular membranes, dynamically liquid collected fibre bundles and nanofibre control membranes used for cell culture assessment.

3.2 Materials & Equipment

3.2.1 Materials

- Poly(ϵ -caprolactone) with an average molecular weight (M_w) of 80,000 g/mol (Sigma Aldrich, USA)

- Poly(ϵ -caprolactone) with a measured average molecular weight (M_w) of 100,000 g/mol (Sigma Aldrich, USA)**
- Chloroform ($\geq 99\%$) with amylenes as a stabiliser (Sigma Aldrich)
- Ethanol (≥ 99.5 , 200 proof) (Sigma Aldrich)
- Methanol (≥ 99.8) (Fluka)
- N,N-Dimethylformamide (99.8%) (Sigma Aldrich)
- Acetone (Sigma Aldrich)
- Poly(dimethylsiloxane), viscosity 100 cSt (Sigma Aldrich)
- Poly(dimethylsiloxane), viscosity 500 cSt (Sigma Aldrich)
- Potassium Chloride Standard Solutions (A-C) (Fluka)
- Phosphate Buffered Solution (PBS) (Sigma Aldrich)

**Purchased as equivalent 80,000 g/mol from Sigma Aldrich but verified by Gel Permeation Chromatography (GPC) to be 100,000 g/mol

3.2.2 Equipment

- KDS200P Syringe Pump (KD Scientific, USA)
- ES30P-20W/DAM Power Supply (Gamma High Voltage Research, USA)
- 20G x 1.5” Hypodermic Needle (Tip Blunted) (Terumo, USA)
- 20ml Gas Tight Glass Syringe (SGE Analytical Science, Australia)
- 100 mm x 100 mm x 0.25 mm Aluminium Collector plates (Goodfellow, UK)
- High Speed Drum Collector System (Custom, DCU)
- Testo 615 Digital Humidity Meter (Testo Inc., Germany)
- AVM-8880 Hot Wire Anemometer (ATP Instrumentation Ltd, UK)
- High Voltage Probe (Radionics, Ireland)
- AT-6 Tachometer (Farnell, UK)
- Magnetic Stir Plate (Bibby, HB502, Sterlin UK)
- Mettler AE50 balance (Mettler Toledo, Switzerland)
- DVII+ PRO Viscometer (Brookfield Engineering, USA)
- HD 8706 Conductivity Meter (DeltaOHM, Italy)
- EVO LS15 Scanning Electron Microscopy (Zeiss, Germany)
- Edwards Pirani 501 Scancoat Sputtering Coater (Edwards Laboratories, USA)
- Dogbone Specimen Cutting Die (Custom, DCU)
- Zwick Z005 Tensile Test Machine with 500N Load cell (Zwick-Roell,

Germany)

- External Micrometer (Draper Tools, UK)

3.3 Methods

3.3.1 Solutions Preparation and Characterisation

3.3.1.1 Solution Preparation

All solutions used within this study were prepared according to wt% methods. In this method the polymer content of a solution is expressed with respect to the total solution weight after all contents have been added i.e. a 14wt% solution contains a polymer content that weighs 14% of the total solution (solvents + surfactants + polymer) weight. Solutions prepared using only the solvent chloroform were prepared as follows. Raw PCL pellets were first weighed (AE50 balance) and then added to a 100ml media bottle with a magnetic stirring bar. The appropriate quantity of chloroform was weighed and then added to the bottle. The media bottles were sealed and the solutions mixed on a stirring plate at room temperature ($21^{\circ}\text{C}\pm 1^{\circ}\text{C}$) for 24hrs to achieve a homogenous solution. Solutions were used within 4 days post preparation and remixed for 1hr before use.

To prepare chloroform/surfactant solutions the polymer was similarly weighed and added to a glass media bottle with stir bar. The appropriate quantity of chloroform was then added and the solutions mixed for 2hrs at room temperature. After 2hrs the surfactant was introduced and the solution mixed for a further 22hrs. Solutions were kept sealed until required, due to the volatility of the surfactants in air. Solutions were used within 4 days post preparation and remixed for 1hr before use.

3.3.1.2 Solution Characterisation

Viscosity

Viscosities of selected solutions were assessed using a Brookfield DV-II+ Pro viscometer. Before measuring, the solutions were heated and maintained at a temperature of 25°C using a temperature controlled water bath and circulation pump (Figure 3.1). Following this, the test solutions were injected into the base sample cup and cone height adjusted accordingly to ensure a correct gap distance was achieved.



Figure 3.1: Brookfield DV-II+ Pro viscometer with temperature controlled recirculation unit used to maintain solution temperature at 25°C during testing

Solution viscosity was measured immediately using a CPA-40Z testing cone. Three batches of the selected solution combinations were prepared and tested to ensure the uniformity of the preparation protocol. The cone and sample cup were cleaned thoroughly with acetone between each run to ensure no cross contamination between testing. Calibration of the viscometer was verified prior to testing using two Poly(dimethylsiloxane) standards with viscosities of 100cSt and 500cSt at 25°C (Sigma Aldrich).

Conductivity

Reagent and selected solution conductivities were assessed using a modified HD 8706 conductivity meter with a custom-made PTFE probe guard (Figure 3.2). Before measuring the reagents and solutions were heated and maintained at a temperature of 25°C. After this, the test sample was poured into a custom built PTFE measurement cup. Conductivity was measured immediately and probe temperature noted. Three batches of each reagent and solution combination were prepared and tested to ensure the uniformity of the preparation protocol. The machine probes and sample cups were cleaned thoroughly with acetone between each run to ensure no cross contamination. Calibration of the conductivity meter was verified prior to testing using three potassium chloride standard solutions (A-C, Fluka) with conductivities of 12.90 mS/cm, 1.41 mS/cm and 0.147 mS/cm.



Figure 3.2: HD 8706 Conductivity meter with custom built PTFE probe guard and custom built PTFE sample cup

3.3.2 Electrospinning

3.3.2.1 2D Random Fibre Membranes

For the electrospinning of 2D random fibre membranes a flat metallic plate electrospinning system was employed. In this set-up, a 20ml glass syringe with 20G attached stainless steel blunted needle was used as the capillary and spinneret respectively. 100mm square aluminium foil plates with thickness of 0.25mm (Goodfellow) were used as the collector targets. A positive bias was applied to solution via a voltage source and an electrical ground connection was attached to the rear surface of the plate. A high voltage probe (Radionics, Ireland) was used to ensure a correct voltage bias was achieved. A syringe pump (KDS, US) was used to dispense the polymer solution at a controlled feed rate from the capillary. All electrospinning experiments were conducted within a fume hood cabinet to extract evaporating chemicals. Humidity within the fume hood was assessed using a Testo 615 digital meter and spinning performed between 40-60% RH. Air speed was assessed at several points with the fume hood using a Hot Wire Anemometer to observe air speed variations, which may affect the trajectory of the electrospinning jet. An image of the 2D random electrospinning set-up used can be seen in Figure 3.3. Following spinning samples were removed from the plates and allowed to air dry at room temperature within the fume hood for 72hrs, following this samples were stored in a desiccator prior to use.

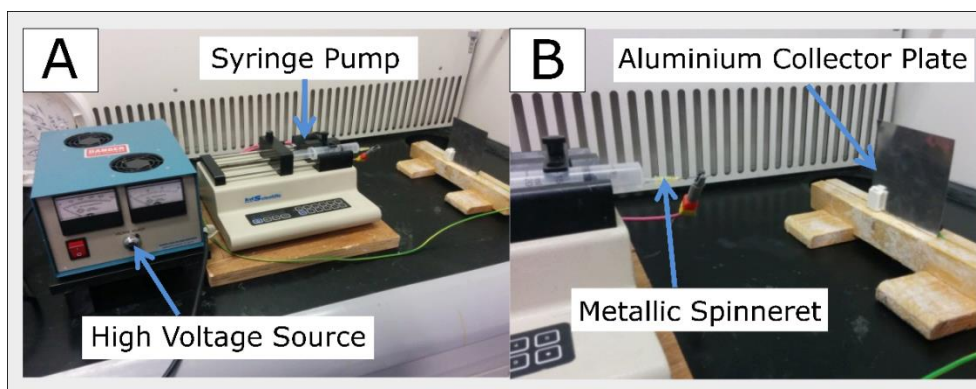


Figure 3.3: 2D random fibre membrane system (A) Components of electrospinning rig: high voltage power supply, syringe pump, capillary and metallic spinneret (B) Close up view showing 2D collector plate apparatus

3.3.2.2 2D Aligned Fibre Membranes

For the electrospinning of 2D aligned fibre membranes a custom built large diameter rotating drum ($\varnothing 80$ mm) collection system was employed (Figure 3.4). Similarly, in this set-up a 20ml syringe with 20G attached stainless steel blunted needle was used as the capillary and spinneret respectively. The drums rotational speed was maintained at 3000 RPM as verified using an AT-6 tachometer (Farnell, UK). A positive bias was applied to the solution via a gamma voltage source and a syringe pump used to dispense the polymer solution via a small diameter PTFE tubing connected to the capillary tip. Air speed was again assessed at different points with the fume hood along with humidity. Once collected the deposited fibre membrane was cut along the axial length of the drum, and removed from the drum as 2D fibre membrane segments.

3.3.3 Morphological and Fibre Diameter Assessment of Scaffolds

Sample morphology was assessed using a EVO LS15 Scanning Electron Microscope (SEM). Prior to viewing, samples were dried at room temperature for a minimum of 3 days and stored in a desiccator prior to use. Samples were mounted onto adhesive carbon tabs and coated with a thin layer of gold (Scancoat, US), at a deposition current of 30mA for 60s. This gold layer prevents the accumulation of electrostatic charge during sample scanning. Samples were typically viewed with an acceleration voltage ranging from 10 to 15kV. Image J image processing software was utilised to measure the sample fibre diameters ($n=30$) from the recorded images.

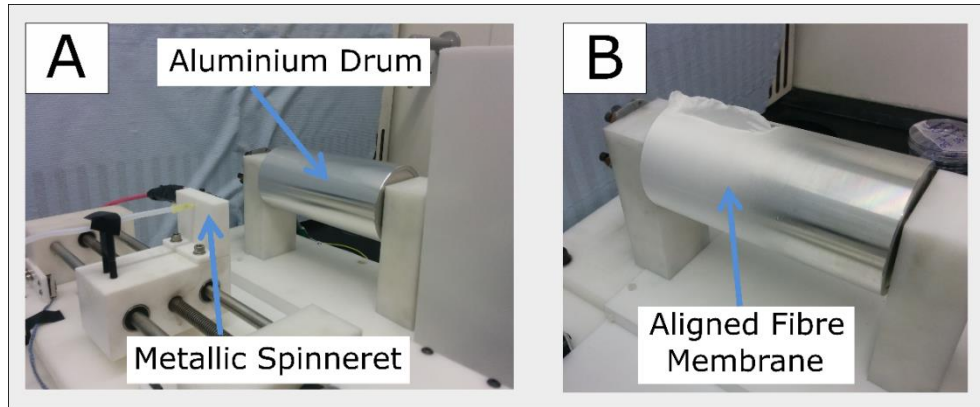


Figure 3.4: Rotating drum system for the creation of aligned fibre membranes (A) Components of rig: Capillary and spinneret on optional traversing platform (B) Close up view showing large diameter rotating drum with deposited PCL fibre membrane.

The Image J plugin ‘Orientation J’ as developed by the Biomedical Imaging Group (École Polytechnique Fédérale De Lausanne, Switzerland) was used to assess the orientation of electrospun fibres [237]. In this method, the image under investigation is broken into regions of interest (ROI) which are comprised of a square group of pixels. The size of the ROI squares can be specified by the user. For each ROI the direction in which the maximum directional derivative is calculated and using this the measured pixels are allocated to direction bins ranging between $+90^\circ$ to -90° . Based on the individual orientations of the ROI groups an overall orientation distribution for the image is constructed. To ensure that larger diameter fibres with increased surface area did no bias the distribution, only the edges of fibres were considered (Figure 3.5 (A)). This was achieved by ignoring areas where pixel grey values were found to be uniform (centre portions of fibres). This was achieved by setting a minimum coherency value of 5%, and a minimum energy value of 5%, which was found to result in block areas comprised of a single pixel grey value being omitted from the orientation distribution. Based upon these an overall coherency value for an image is generated. This coherency term is calculated through the ratio of the first and second eigenvector terms calculated for each ROI. Coherency indicates if the local image features are oriented or not. A ‘C’ value of 1 indicates the local structure has one dominant orientation, and a C of 0 obtained for an image represents an isotropic local neighbourhood.

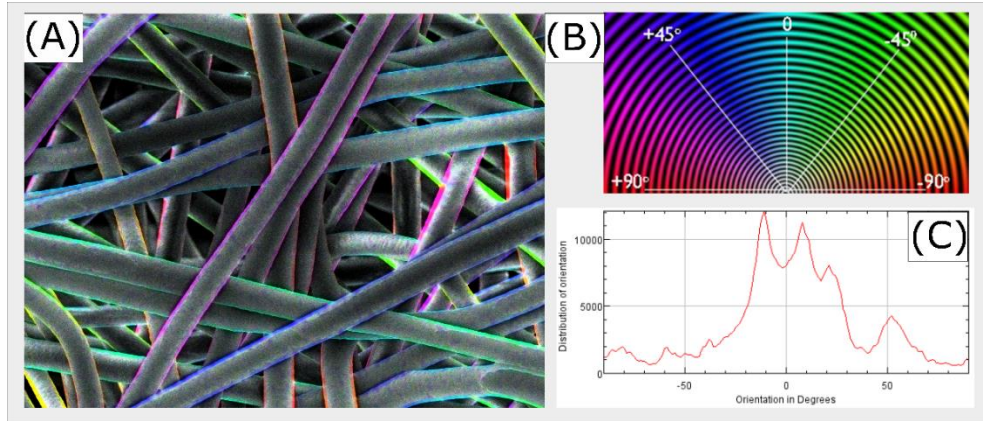


Figure 3.5: Orientation J Analysis of electrospun fibre membrane (A) Colour map indicator of electrospun fibre edges (B) Representative colour map indicator (C) Orientation distribution of electrospun fibre membrane

3.3.4 Characterisation of Electrospun Membranes

3.3.4.1 Porosity

Porosity of electrospun 2D membranes were quantified using the liquid intrusion technique. In this method the dry weight of 10mm diameter disc samples punched from the membranes were first measured at room temperature. Samples were subsequently immersed in 100% ethanol for 24hrs under agitation to ensure complete wetting. The samples were then removed and the surfaces blotted dry to remove excess fluids. The wet weight was then measured and the porosity (ξ) calculated using the following formulas:

$$V_{PCL} = \frac{m_{dry}}{\rho_{PCL}} \quad (3.1)$$

$$V_{EtOH} = \frac{m_{wet} - m_{dry}}{\rho_{EtOH}} \quad (3.2)$$

$$Porosity (\xi) = \frac{V_{EtOH}}{V_{PCL} + V_{EtOH}} \times 100\% \quad (3.3)$$

Where V_{PCL} is the volume of PCL within the sample and V_{EtOH} is the volume of ethanol entrapped in the scaffold pores. m_{dry} and m_{wet} refer to the dry and wet weights of the samples respectively while ρ_{EtOH} is the density of ethanol (0.789 g cm^{-3}) and ρ_{PCL} is the density of PCL (1.145 g cm^{-3}). It is noted that this method may suffer from inaccuracies such as residual ethanol remaining on the surface of samples prior to

weighing which could alter the overall porosity measured. This technique has however been shown to be effective for assessing overall scaffold porosity in electrospun materials when compared to other pore assessment techniques such as mercury porosimetry and BET surface area testing [196][238]. The high pressures required to assess the pore structure of electrospun scaffolds comprised of fibres containing diameters less than 3 μ m has been shown to result in the collapsing and compression of the scaffolds when mercury porosimetry methods are employed [196], while BET theory results in the measurement of specific surface area only so often excludes the complex internal pore structure that electrospun materials possess [238].

3.3.4.2 Uniaxial Tensile Testing – Dogbone Specimens

Uniaxial tensile testing of ‘dogbone’ specimens was performed on select 2D fibre membranes. Samples were prepared using a custom designed and manufactured stainless steel cutting die. Briefly, the die consisted of a sample gauge length of 10mm and test width of 3mm (Figure 3.6 (A)). Samples were punched from the spun membranes using the cutting die and a custom-built sample holder and guide as shown in Figure 3.6 (B). The desired dogbone samples (Figure 3.6 (C)) were subsequently immersed in phosphate buffered saline (PBS) at 37°C for 24hrs prior to testing. It is noted that the geometry of the dogbone specimens could not be prepared according to an ISO specific standard due to the limited membrane length available for testing.

Tensile testing was conducted using a Zwick Z005 tensile test machine with a 500N load cell attached. The thickness of the test sample (t) was measured using a micrometer (Draper Tools, UK) before being secured within the test grips. A small piece of sand paper was placed either side of the grip areas to ensure no slipping of the specimen occurred during testing. The testing cycle consisted of an initial preload of 0.05N to remove any slack from the sample, with the grip separation at this point used as the gauge length (L₀) within the following calculations. Following this, the sample was elongated at a strain rate of 10 mm/min with failure determined to occur when the force dropped to 80% of the max force value recorded.

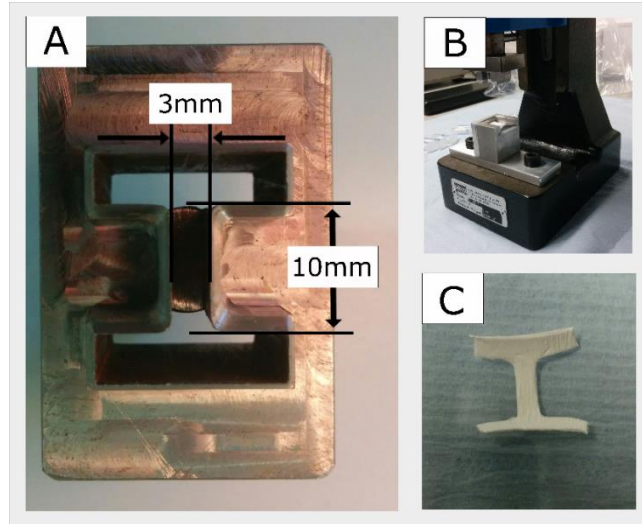


Figure 3.6: Uniaxial tensile testing sample preparation (A) Custom designed ‘dogbone’ punch with gauge length of 10mm and width of 3mm (B) Custom designed punch system with sample holder and punch guide (C) Sample dogbone specimen cut from electrospun membrane

The cross sectional area of the sample was calculated using Equation 3.4, with ‘w’ representing the width of the test area and ‘t’ representing sample thickness:

$$\text{Cross sectional area (A)} = w * t \quad (3.4)$$

Using this cross sectional area value, the engineering stress (σ) was calculated according to Equation 3.5 below, where F is the force within the sample and A is the cross sectional area resisting loading:

$$\sigma = \frac{F}{A} \quad (3.5)$$

Engineering strain (ϵ) was subsequently calculated according to Equation 3.6, where ΔL represents the change in sample length and L_0 corresponds to the gauge length of the sample measured at the preload point:

$$\epsilon = \frac{\Delta L}{L_0} \quad (3.6)$$

Figure 3.7 shows a dogbone specimen during the testing cycle. Figure 3.7 (A) shows a sample in a no load state before preload is applied. Figure 3.7 (B) showing the sample during loading and subsequently failure of the specimen within Figure 3.7 (C).

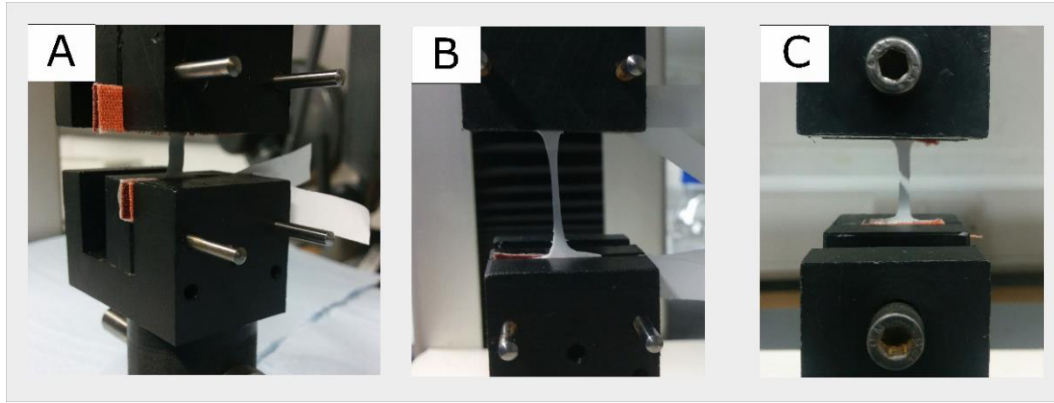


Figure 3.7: Uniaxial tensile testing of dogbone samples (A) Sample in no loaded state (B) Sample during testing shown significant elongation (C) Sample after failure showing fracture along centre of specimen

3.3.4.3 Statistical Analysis

Numerical data is presented as mean \pm standard deviation (S.D) with error bars indicating one standard deviation unless otherwise stated. Normality of data was verified according to the Shapiro-Wilk approach, and Bartlett's test conducted to assess equal variance amongst test groups (Minitab 17 Statistical Software, PA, USA). Where data was determined to comply with the relevant assumptions of a parametric analysis, including normality and equal variances, a 2-sample t-test was conducted for the comparison of pair wise samples. For the comparison of multiple samples one and two-way analysis of variance (ANOVA) were conducted where appropriate. Subsequent multiple comparisons were made using the Sidak correction test. The level of statistical significance was set to $p < 0.05$. Where data was found to violate the assumptions of an ANOVA analysis, most notably equal variance amongst groups (by Bartlett's statistic), non-parametric analysis was conducted. Mann-Whitney test was employed for 2-sample comparison, while Kruskal-Wallis analysis with subsequent Dunn Correction was utilised for multiple comparisons.

3.4 Design of Studies

3.4.1 Solution Screening Trial

In order to develop electrospun membranes with tailorable fibre diameters a number of solvent and surfactant solution combinations were initially screened (Table 3.1). These combinations were chosen in order to produce electrospun membranes containing micron, nano and multimodal fibre diameter populations. Chloroform was selected as the primary solvent due to its excellent ability to dissolve PCL compared to other common electrospinning solvents such as Tetrahydrofuran (THF) and Acetone [239]. In addition, the reduced dielectric properties of Chloroform ($\epsilon = 4.8-5.2$), allows for a more precise control of solution conductivity through the addition of surfactant materials [240][241].

The surfactants ethanol and methanol were initially selected due to their use in previously detailed multimodal fibre studies [102], [196], [199], [242], and for the creation of micron diameter fibres [243]. The ratio of the surfactants to solvent was explored, and pure chloroform solutions were spun for comparative purposes. The surfactant N,N-Dimethylformamide (DMF) was investigated as a means to induce nanofibre formation, as detailed in previous studies [196], [244]. Samples were electrospun according to the electrospinning protocol for the production of 2D random fibre membranes. To provide a preliminary observation of the change in scaffold architecture with changing processing variables, the solutions were spun over a sample array of parameters. Table 3.2 details the processing parameters explored for micron and multimodal fibres, while Table 3.3 is for nanofibre generation.

Table 3.1: Solvent Screening Combinations

Code	Solvent	Surfactant	Ratio (v:v)	M _w of PCL	Conc. (wt%)	Target Dia.
CH	Chloroform	-	100:0	80kDa	14	Micron
CE_9	Chloroform	Ethanol	90:10	80kDa	14	Micron
CE_7	Chloroform	Ethanol	70:30	80kDa	14	Multimodal
CM_9	Chloroform	Methanol	90:10	80kDa	14	Micron
CM_7	Chloroform	Methanol	70:30	80kDa	14	Multimodal
CD_7	Chloroform	DMF	70:30	100kDa	6,8,11	Nano
CD_5	Chloroform	DMF	50:50	100kDa	6,8,11	Nano

Table 3.2: Design Matrix for Micron and Multimodal Diameter Fibre Spinning

<i>Screening Solutions</i>										
Chloroform										
Chloroform/Ethanol (9:1)										
Chloroform/Ethanol (7:3)										
Chloroform/Methanol (9:1)										
Chloroform/Methanol (7:3)										
<i>Parameters</i>										
Spin Time (min)	10									
Flow Rate (ml/hr)	6			12				12		
Applied Voltage (kV)	15		20			15		20		
Tip-Collector Distance (cm)	15	20	15	20	15	20	15	20	20	

Table 3.3: Design Matrix for Nano Diameter Fibre Spinning

<i>Screening Solutions</i>										
Chloroform/DMF (7:3)										
Chloroform/DMF (5:5)										
<i>Parameters</i>										
Concentration (wt%)	6, 8, 11									
Spin Time (min)	10									
Flow Rate (ml/hr)	0.25, 0.5, 1									
Applied Voltage (kV)	10			15				20		
Tip-Collector Distance (cm)	10	12.5	15	10	12.5	15	10	12.5	15	

Sample morphology and fibre diameters were assessed by SEM analysis as previously described. Conductivity measurements of the pure solvents and surfactants, relative combinations and final electrospinning solutions were recorded. The viscosity of solutions for nanofibre production were assessed per the previously detailed methodology.

3.4.2 Polymer Concentration Trial for Multimodal Fibres

Based upon the results of the solution screening trial the solvent/surfactant combination of Chloroform/Ethanol at a volume ratio of 7:3 (v:v) was selected for further investigation due to its ability to electrospin membranes containing both micron and nano diameter fibres. In order to assess the effect of polymer concentration on fibre diameter and morphology attributes, five polymer concentration levels were identified for further study. Solutions concentrations ranging from 10 to 18wt% in step changes of 2wt% were prepared. 2D random fibre membranes were spun using an expanded range of processing parameters based on the observations noted from the previous screening trial. The experimental design matrix used for this study is presented in Table 3.4. Sample morphology and fibre diameters were assessed by SEM analysis, and viscosity and conductivity of the prepared solutions measured.

3.4.3 Electropinning of Nanofibre Membranes as Controls

In order to provide a comparison of cell growth and infiltration properties against the novel bi-layer vessel under investigation in this work, a number of nanofibre control membranes created through traditional electrospinning approaches were required. Solution and processing parameter combinations identified from the initial nanofibre screening trial that yielded desirable fibre diameters and morphological attributes were further examined for the creation of random and aligned 2D fibre membranes.

3.4.3.1 Randomly Orientated Fibre Membranes - Deposition Study

Table 3.5 shows the parameter combination chosen from the initial screening that yielded defect free nano diameter fibres and provided a stable spinning process. Samples were electrospun using a flat metallic collector for 1 and 4 hr time periods (n=5), in order to assess the ability to collect random membranes with suitable

Table 3.4: Design Matrix for Solution Concentration Optimisation Experiment (Multimodal Fibres)

<i>Spinning Solutions</i>																
10wt% Chloroform/Ethanol (7:3)																
12wt% Chloroform/Ethanol (7:3)																
14wt% Chloroform/Ethanol (7:3)																
16wt% Chloroform/Ethanol (7:3)																
18wt% Chloroform/Ethanol (7:3)																
<i>Parameters</i>																
Spin Time (min)	10															
Flow Rate (ml/hr)	6								12							
Applied Voltage (kV)	15				20				15				20			
Tip-Collector Distance (cm)	15	20	25	30	15	20	25	30	15	20	25	30	15	20	25	30

Table 3.5: Optimum parameters identified for the electrospinning of nanofibre membranes based upon initial solution screening trail

<i>Spinning Parameter</i>	<i>Value Set</i>
Polymer Concentration (wt%)	8
Chloroform/DMF volume ratio (v:v)	7:3
Flow Rate (ml/hr)	0.25
Applied Voltage (kV)	15
Tip-Collector Distance (cm)	15

thicknesses to withstand the physical manipulation required for further cell culture assessment, whilst also assessing the stability of the collection process over an extended deposition period. Fibre diameters, fibre orientations, and overall membrane morphology were again assessed by SEM and Orientation J plugin. Porosity of the fibre membranes was evaluated by liquid intrusion method (n=10). Thickness of the scaffolds were measured using a micrometre to determine collection uniformity. Uniaxial tensile testing of dogbone specimens were prepared by punching samples from the random fibre membranes collected (n=5). Specimens were tested according to the previously described methodology.

3.4.3.2 Aligned Fibre Membranes – Deposition Study

2D aligned fibre membranes were electrospun using a custom built rotating drum collection system previously detailed using the parameters detailed in Table 3.5. Due to the increased surface area of the drum compared to the flat metallic plate, the thickness of membranes is typically lower for the same spinning duration. In order to prepare membranes with suitable thickness for cell culture, increased deposition times were examined. Samples were collected for 4 and 12hr time periods (n=5). Fibre diameters, morphology and fibre orientations were assessed by SEM, porosity by liquid intrusion method (n=10), and thickness of the scaffolds by micrometer. Uniaxial dogbone specimens for tensile testing were prepared by punching samples from the aligned fibre membranes collected. In order to assess the anisotropic response of the aligned fibre membranes, samples were punched parallel to the circumferential direction (n=5) and perpendicular to the circumferential direction of the fibre drum (n=5).

3.5 Results

3.5.1 Solution Screening Trial

The full collection of SEM results and fibre diameter measurements for the solution screening trial can be found in Appendix A of this report. In this, Table A.1 presents the SEM results for the spinning solutions studied for micron and multimodal fibre creation, with Table A.0.2 reporting corresponding fibre diameters and Table A.3 reporting ambient conditions and airflow measurements recorded. Table A.4 presents

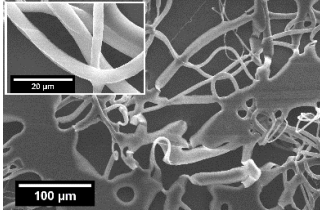
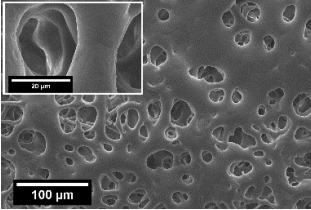
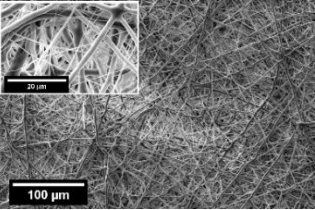
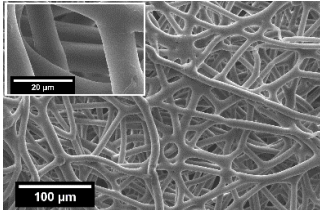
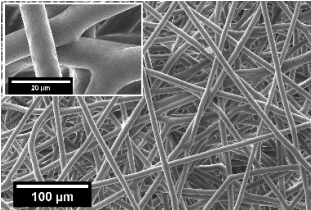
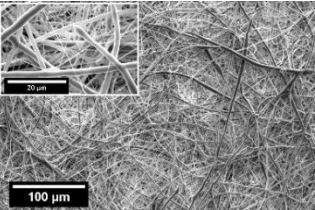
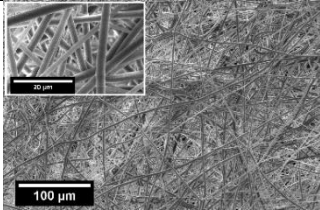
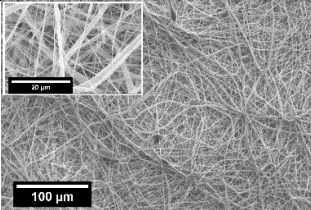
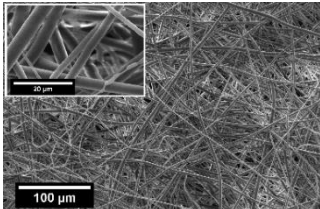
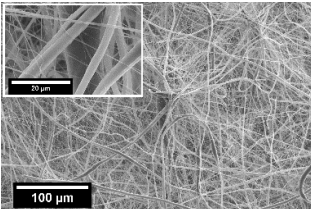
the SEM results for the solutions studied for nanofibre generation, while Table A.5 similarly presents corresponding fibre diameter measurements.

3.5.1.1 Micron and Multimodal Solution Screening

It was observed from the solution screening trial that PCL solutions prepared using the pure solvent chloroform (CH) typically resulted in poor electrospinning to the target collector. At a collector distance of 15cm, liquid polymer was found to deposit on the collection plate, irrespective of the flow rate and applied voltage used. Smooth bead free fibres could be collected by increasing the collector distance to 20cm and setting the applied voltage to 15kV. When the voltage was further increased to 20kV a combination of liquid polymer and fibrous material was found to deposit. At all other spinning conditions highly interconnected or webbed structures with non-distinct fibres were produced. Table 3.6 shows a sample selection of SEM images for membranes produced using the solvent chloroform and the surfactants ethanol and methanol, produced at a flow rate of 6ml/hr, applied voltage of 20kV and a collection range of 15-20cm.

Chloroform/Ethanol (9:1;v:v) (CE_9) solutions were found to produce large membranes on the collector plate. A single polymer jet was seen to emerge from the Taylors cone for all parameter combinations. Similar to the pure CH solutions a collector distance of 15cm typically led to liquid polymer deposition on the collector surface, albeit with a reduced liquid fraction. Figure 3.8 shows the fibre diameter results for the micron and multimodal spinning solutions produced over the process parameter range of 6-12ml/hr flow rate, 15-20kV applied voltage and 15-20cm collector distance. It is noted that in cases where liquid polymer or highly webbed structures were present, no fibre diameter measurements could be attained. With a collector distance of 15cm, applied voltage of 15kV and a flow rate of 6ml/hr, samples prepared using CE_9 contained distinct and uniform diameter fibres ranging from $5.22 \pm 1.57\mu\text{m}$. By increasing the collector distance to 20cm and keeping all other parameters constant, fibres with an increased diameters of $7.81 \pm 2.56\mu\text{m}$ were obtained. This increase in fibre diameter with increased collector distance is attributed to the presence of large beads forming along the fibre lengths at the expanded collection distance that skewed diameter measurements.

Table 3.6: SEM images of scaffolds produced using Chloroform and the surfactants Ethanol and Methanol. Images show scaffolds produced at a sample processing parameters range of a 6ml/hr flow rate, applied Voltage of 20kV over a range of 15-20cm collector distance

	Chloroform (100%)	Chloroform/Ethanol (9:1)	Chloroform/Ethanol (7:3)
15cm			
20cm			
	Chloroform/Methanol (9:1)	Chloroform/Methanol (7:3)	
15cm			
20cm			

14wt% Chloroform/Ethanol (7:3;v:v) (CE_7) solutions were found to produce fibrous meshes at all spinning conditions with no liquid polymer visible. A distinct difference in the jet formation from the Taylor's cone was observed with multiple jets branching from the cone. Upon cleaning of the spinneret tip, a single jet was found to form followed by subsequent re-branching. A considerable decrease in fibre diameter was observed with the formation of submicron to nano diameter fibres within the scaffold

structure compared to CH and CE₉ solutions. Membranes collected at a distance of 15cm, voltage of 15kV and flow rate of 6ml/hr contained fibres with a diameter range of $2.24 \pm 1.56\mu\text{m}$, with those collected at 20cm possessing a decreased fibre diameter range of $1.56 \pm 1.3\mu\text{m}$. 14wt% Chloroform/Methanol (9:1;v:v) (CM₉) solutions spun similarly to the CE₉ solutions, yielding large fibre membranes on the collector plate. Multiple branches were however observed to emerge from the Taylors cone similar to that of the CE₇ solutions. An increase in the applied voltage appeared to give rise to additional jet initiation from the cone with increased splaying effects observed. All spinning conditions led to the production of distinct fibre structures with no webbing or liquid polymer deposition on the plates. Small ridges/bumps were however seen to

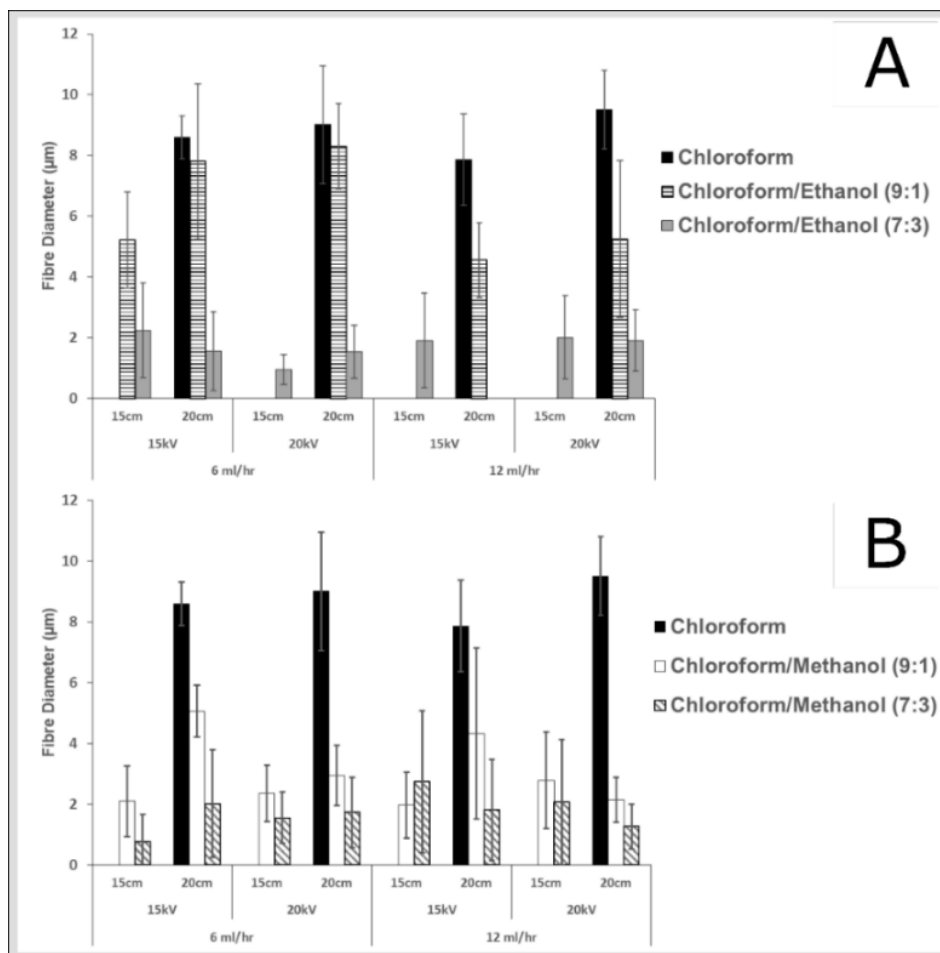


Figure 3.8: Fibre diameter analysis of micron and multimodal spinning solutions produced over the parameter range of 6-12 ml/hr flow rate, 15-20kV applied voltage and 15-20cm collector distance (A) Diameter results for Chloroform, Chloroform/Ethanol (9:1) and Chloroform/Ethanol (7:3) solutions (B) Diameter results for Chloroform, Chloroform/Methanol (9:1) and Chloroform/Methanol (7:3) solutions

be located on the surface of the collected meshes. SEM analysis and fibre measurements showed the presence of micron scale fibres and a very small population of nano scale fibres within the samples. Fibres collected at 15cm, 15kV and 6ml/hr possessed diameters of $2.10 \pm 1.17\mu\text{m}$ and those at 20cm having diameters of $5.06 \pm 0.86\mu\text{m}$. This increase in fibre diameters appeared to occur due to the decreased fraction of nanofibres present within samples collected at the higher collection distance.

Solutions with an increased methanol fraction, Chloroform/Methanol (7:3;v:v) (CM_7), led to poor fibre deposition on the collector plate. The electrospinning jet in this situation appeared to be drawn away from the collector surface by the airflow within the fume hood. Material that successfully deposited on the plate was prone to delaminating when being removed from the plate, with thin layers of residual material sticking to the collector surface. The Taylors cone also appeared to be highly unstable with the cone breaking off intermittently. Small ridges and defects were seen to form on the surface of the sample. SEM analysis again showed that nanofibre and micron scale fibres were present within the samples collected. Scaffolds produced at a distance of 15cm, 15kV and 6ml/hr yielded fibres with diameters of $0.76 \pm 0.9\mu\text{m}$ with those collected at 20cm having $2.02 \pm 1.77\mu\text{m}$. This increase in fibre diameters again appears to occur due to a decreased fraction of nanofibres within the membranes collected at the higher collector distance indicating a loss of nanofibre collection at increased collector distances. The small bumps seen on the surface of the sample appeared to be small pieces of PCL that were randomly deposited amongst the surface fibres.

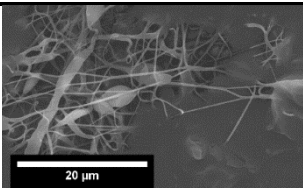
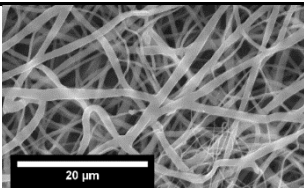
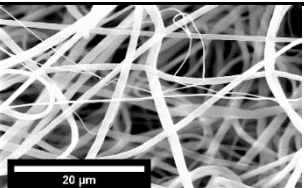
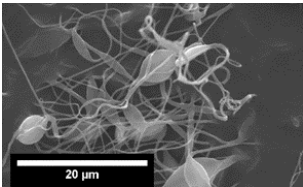
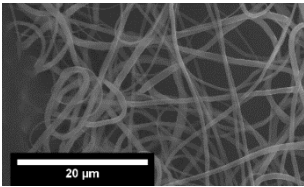
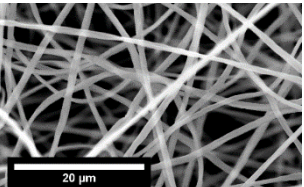
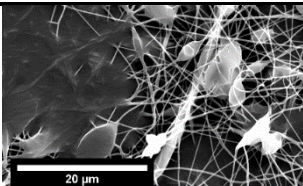
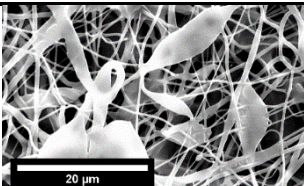
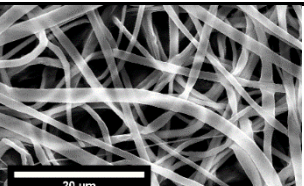
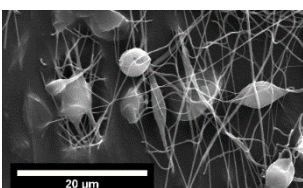
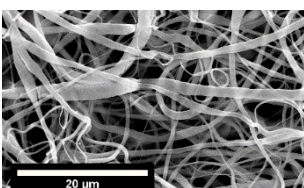
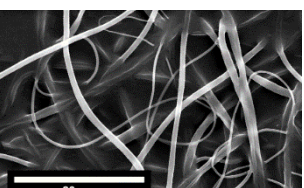
From this initial trial, it was determined that Chloroform/Ethanol (9:1) based solutions were the choice solvent/surfactant ratio combination for the production of micron diameter fibres. Chloroform/Methanol (9:1) solutions showed the presence of nanofibre formation amongst the micron diameter fibres so were multimodal in nature and the presence of small defects upon the surface on the sample was undesirable. Chloroform/Ethanol (7:3) solutions were found to be the choice solution for the production of multimodal fibre populations due to the distinct presence of micron and nanoscale diameter fibres along with the ease of scaffold production compared to those

produce using Chloroform/Methanol (7:3) which typically resulted in poor electrospinning to the target collector.

3.5.1.2 Nanofibre Solution Screening

A sample range of SEM images produced for the nanofibre screening trial can be seen in Table 3.7 while full results are presented in Table A.3 of Appendix A. Solutions prepared at a 6wt% polymer concentration resulted in the deposition of a powder like

Table 3.7: SEM images of scaffolds produced using Chloroform and the surfactant N,N-Dimethylformamide (DMF). Images show scaffolds produced at a sample processing parameters range of a 0.25ml/hr flow rate, applied voltage of 15kV over a collector distance range of 10-15cm using Chloroform/DMF (7:3;v:v) and Chloroform/DMF (5:5;v:v) solutions

Chloroform/DMF (7:3, v:v)			
	6wt%	8wt%	11wt%
10cm			
15cm			
Chloroform/DMF (5:5, v:v)			
	6wt%	8wt%	11wt%
10cm			
15cm			

material to the target and were extremely difficult to remove from the collector surface irrespective of the Chloroform/DMF ratio employed. SEM analysis showed the membranes contained highly beaded fibre structures, with nanoscale diameter fibres bridging between beads. Samples produced at the increased PCL concentration of 8wt% and the Chloroform/DMF ratio of (7:3) contained distinct fibres under most spinning permutations. Those produced at the higher flow rate of 1ml/hr experienced partial fibre fusing, particularly at the increased collection distance of 15cm while samples produced at the applied voltage of 20kV again appeared to show areas of fibre fusion. Membranes produced at the flow rates of 0.25ml/hr and 0.5ml/hr, with the applied voltage range of 10 to 15kV appeared to be defect free with uniform diameter fibres present. Fibre diameters within this parameter range were found to vary between the micron and nanofibre scale with samples produced at 0.25ml/hr, 10kV and 10cm contained fibre diameters of $1.21 \pm 0.58\mu\text{m}$ while increasing the collector distance to 15cm, reduced the fibre diameters to $0.50 \pm 0.18\mu\text{m}$. Despite an increased PCL concentration, 8wt% Chloroform/DMF (5:5) solutions again gave rise to the spinning of highly beaded fibre membranes. The beads did however appear to be more elongated in appearance to those produced at the 6wt% concentration with a combination of micron and nano diameter fibres bridging the beads.

11wt% Chloroform/DMF (7:3) solutions allowed for the spinning of smooth defect free fibres under the majority of spinning conditions investigated. Samples produced at the higher voltage of 20kV appeared to show partial fibre fusion particularly at the increased flow rate of 1ml/hr. Average fibre diameters typically ranged from a few microns to submicron diameters in scale. Membranes produced at 0.25ml/hr, 10kV and 10cm contained fibre diameters of $0.93 \pm 0.26\mu\text{m}$ and those at 15cm having $1.01 \pm 0.31\mu\text{m}$. Figure 3.9 shows the fibre diameter results for the nanofibre screening trial. It is noted that due to the highly beaded nature of samples produced from 6wt% solutions, no fibre diameter measurements are presented for this concentration level. Similarly, due to the beaded nature of 8wt% Chloroform/DMF (5:5) solutions no accurate fibre diameter measurements could be attained so are not presented. Finally, 11wt% Chloroform/DMF (5:5) solutions allowed for the spinning of defect free fibres under most spinning permutations. It was observed that a number of samples produced using this solution appeared to contain multimodal fibre distributions with large

micron and intermixed nanoscale fibres present. This includes samples produced at a flow rate of 0.5ml/hr, 20kV applied voltage and 12.5cm collector distance that possessed an average fibre diameter of $2.04 \pm 2.03\mu\text{m}$.

Overall it was determined that 8wt% Chloroform/DMF (7:3) solutions provided the most stable spinning process while producing fibres within the desired nanofibre scale. A number of processing parameter combinations provided defect free fibre spinning while also yielding nanoscale fibres. The parameter combination of 0.25ml/hr flow rate, 15kV applied voltage and 15cm collector distance was selected as the choice combination for further study due to its ability to produce defect free membranes with an average fibre diameter range of $0.78 \pm 0.31\mu\text{m}$. This parameter combination not only provided samples with desirable fibre diameters, but also proved to be highly stable requiring minimum user interaction such as spinneret cleaning and stray fibre removal. The produced membranes were also noted to be easily removed from the collector surface ensuring no damage to the fibres within.

3.5.1.3 Characterisation of Screening Solutions

Conductivity

The conductivity measurements of the pure electrospinning chemicals and solvent/surfactant combinations used within the solution screening trial are presented in Table 3.8. The conductivity of pure chloroform could not be characterised using the conductivity measurement system employed, as it is believed the low dielectric constant of chloroform results in the chemical acting as an insulator which in turn yields an immeasurable conductivity value [240], [241]. The conductivity measurements of the pure surfactants showed that ethanol possessed the lowest conductivity value at $1\mu\text{S/cm}$ followed by methanol at $1.2\mu\text{S/cm}$, and N,N-Dimethylformamide at $1.4\mu\text{S/cm}$. The combination of Chloroform/Ethanol (9:1) and Chloroform/Methanol (9:1) again were immeasurable using the conductivity meter. By increasing the ethanol fraction, Chloroform/Ethanol (7:3), solutions possessed a conductivity of $0.4\mu\text{S/cm}$. This value was lower than the pure ethanol component but increased the conductivity sufficiently to that of pure chloroform, so that a measurement was possible. Similarly, the increased methanol fraction within the Chloroform/Methanol (7:3) resulted in solutions yielding a conductivity of $0.7\mu\text{S/cm}$.

This value was lower than pure methanol but again increased conductivity to a measurable point compared to pure chloroform. Chloroform/DMF (7:3) solutions possessed a conductivity value of 1.2 $\mu\text{S}/\text{cm}$ slightly below that of pure DMF at 1.4 $\mu\text{S}/\text{cm}$, whereas Chloroform/DMF (5:5) solutions measured 1.4 $\mu\text{S}/\text{cm}$ matching that of pure DMF.

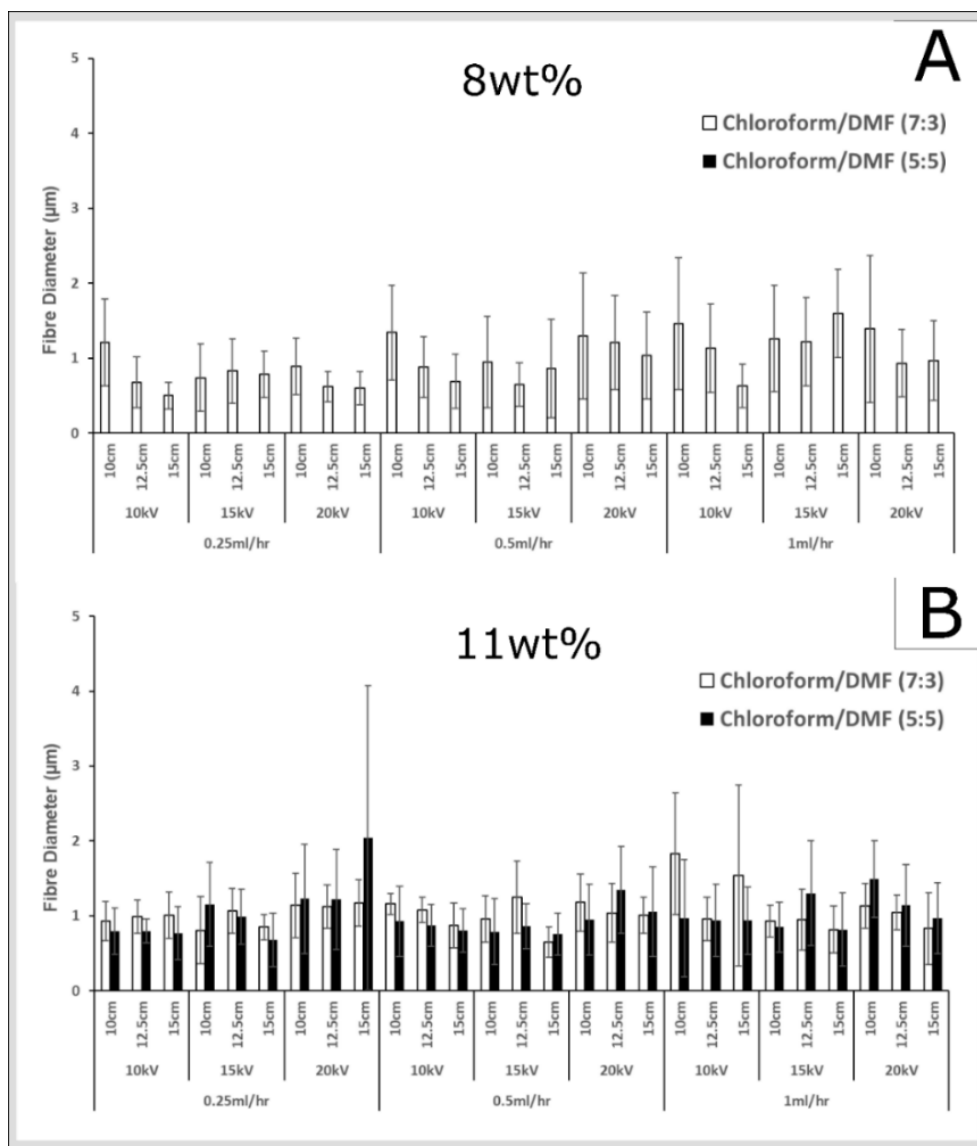


Figure 3.9: Fibre diameter analysis of nanofibre spinning solutions produced over the parameter range of 0.25-1ml/hr flow rate, 10-20kV applied voltage and 10-15cm collector distance (A) Diameter results for 8wt% Chloroform/DMF (7:3) (B) Diameter results for 11wt% Chloroform/DMF (7:3) and 11wt% Chloroform/DMF (5:5) solutions

Table 3.8: Conductivity of pure electrospinning chemicals and solvent/surfactant combinations measured at 25°C

Test Solution	μS/cm @25°C
Chloroform	-
Ethanol	1
Methanol	1.2
Chloroform/Ethanol (9:1)	-
Chloroform/Ethanol (7:3)	0.4
Chloroform/Methanol (9:1)	-
Chloroform/Methanol (7:3)	0.7
DMF	1.4
Chloroform/DMF (7:3)	1.2
Chloroform/DMF (5:5)	1.4

Table 3.9 shows the conductivity of the complete electrospinning solutions used within the solution screening trial. 14wt% Chloroform/Ethanol (9:1) and 14wt% Chloroform/Methanol (9:1) solutions again yielded immeasurable conductivity values when tested. 14wt% Chloroform/Ethanol (7:3) solutions possessed a conductivity of 0.3μS/cm, slightly lower than that of the pure chemical combinations only. No statistical comparison is presented as no deviation within triplicate measurement was observed which prevented a pair wise analysis from being performed. 14wt% Chloroform/Methanol (7:3) again possessed a slightly lower value than that of the chemical combinations only at 0.5μS/cm. Chloroform/DMF solutions at the concentrations of 6, 8 and 11wt% contained an average conductivity of 0.9μS/cm.

Chloroform/DMF solutions at the concentrations of 6, 8 and 11wt% contained an average conductivity of 1μS/cm. An interesting observation here was that Chloroform/DMF polymer solutions were the only combinations to report a deviation when tested in triplicate with all other chemical and solution variants yielding consistent measurements between replicates. No statistical difference was observed between the solutions prepared with different Chloroform/DMF ratios at each polymer concentration level, 6wt% (p =0.1161), 8wt% (p =0.1012) and 11wt% (p =0.4169). A two-way ANOVA analysis did however show a cumulative statistical difference in conductivity between Chloroform/DMF (7:3) and Chloroform/DMF (5:5) solutions.

Table 3.9: Conductivity of complete electrospinning solutions studied within solution screening trial, multimodal study and nanofibre spinning measured at 25°C (n=3 per solution)

Test Solution	$\mu\text{S}/\text{cm}$ @25°C
14wt% Chloroform	-
14wt% Chloroform/Ethanol (9:1)	-
14wt% Chloroform/Methanol (9:1)	-
14wt% Chloroform/Methanol (7:3)	0.5
10wt% Chloroform/Ethanol (7:3)	0.3
12wt% Chloroform/Ethanol (7:3)	0.3
14wt% Chloroform/Ethanol (7:3)	0.3
16wt% Chloroform/Ethanol (7:3)	0.3
18wt% Chloroform/Ethanol (7:3)	0.3
6wt% Chloroform/DMF (7:3)	0.9 ± 0.1
8wt% Chloroform/DMF (7:3)	0.9 ± 0.1
11wt% Chloroform/DMF (7:3)	0.9 ± 0.2
6wt% Chloroform/DMF (5:5)	1 ± 0.1
8wt% Chloroform/DMF (5:5)	1 ± 0.1
11wt% Chloroform/DMF (5:5)	1 ± 0.1

A statistical increase in solution conductivity with increasing DMF content ($p = 0.0320$) was found. Again the two-way ANOVA analysis showed that polymer concentration had no cumulative effect on solution conductivity ($p = 0.6021$).

Viscosity of Nanofibre Solutions

The combined results of viscosity and conductivity measurements for the solutions examined within the nanofibre screening trial are presented in Figure 3.10. Here, Figure 3.10 (A) shows the viscosity results of the 6, 8 and 11wt% PCL Chloroform/DMF (7:3) solutions. A linear increase in solution viscosity with increasing polymer content ($R^2 = 0.9899$) was observed. Figure 3.10 (B) shows the viscosity results of the 6, 8 and 11wt% PCL in Chloroform/DMF (5:5) solutions. Again, a linear increase in solution viscosity was observed ($R^2 = 0.9948$). A two-way ANOVA analysis indicated a statistical difference in solution viscosity at each polymer concentration. A statistical decrease in viscosity ($p < 0.0001$) from $213.5 \pm$

2.1 to 132.5 ± 3.6 mPa.s was observed for 6wt% solutions when the DMF percentage was increased from (7:3) to (5:5). Similarly, for 8wt% solutions a decrease ($p < 0.0001$) from 649.1 ± 14.3 to 411.4 ± 5.2 mPa.s was observed with increasing DMF percentage. 11wt% solutions again displayed a decrease in viscosity ($p < 0.0001$) from 1106.5 ± 9.3 to 963.2 ± 12.1 mPa.s with increasing DMF percentage. A statistical difference ($p < 0.0001$) was also found between each polymer concentration for the Chloroform/DMF ratios studied confirming a distinct increase in viscosity with increasing polymer concentration.

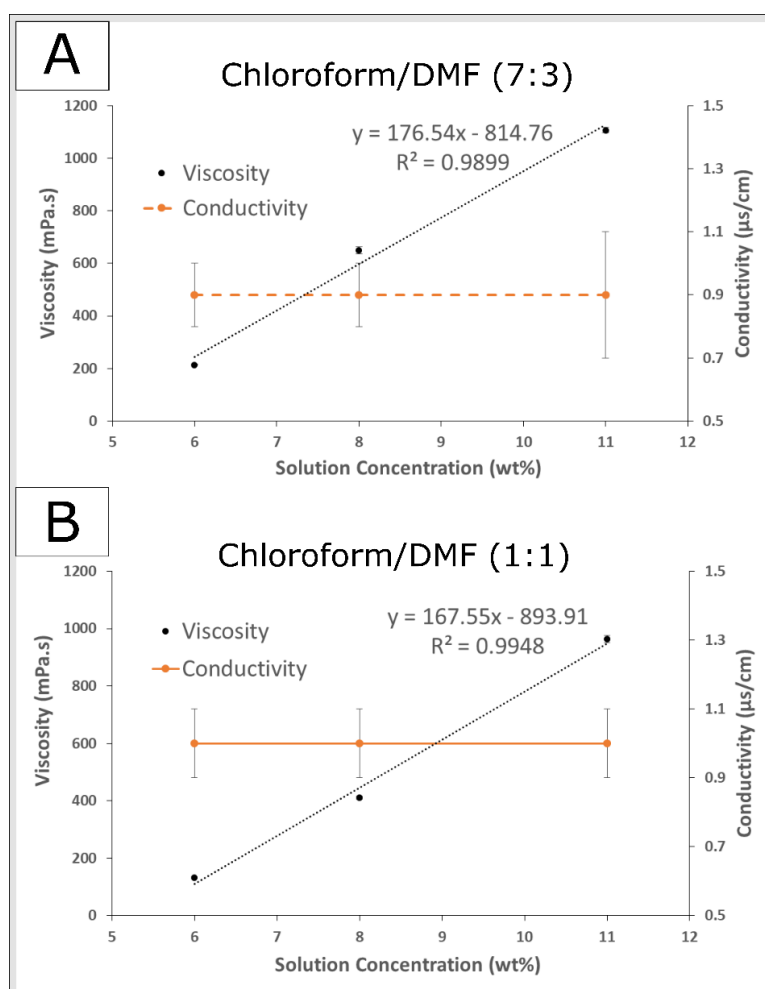


Figure 3.10: Viscosity and conductivity results of Chloroform/DMF solutions studied for nanofiber generation (A) Viscosity and conductivity profile of 6, 8 and 11wt% PCL Chloroform/DMF (7:3; v:v) solutions, showing linear increase in viscosity with increasing polymer content ($R^2 = 0.9899$) and consistent conductivity value of $0.9\mu\text{S/cm}$ at all polymer concentrations. (B) Viscosity and conductivity profile of 6, 8 and 11wt% PCL Chloroform/DMF (5:5; v:v) solutions showing linear increase in viscosity with increasing polymer content ($R^2 = 0.9948$) and consistent conductivity value of $1\mu\text{S/cm}$ at all polymer concentrations. $N=3$ per test group.

3.5.2 Polymer Concentration Trial for Multimodal Fibres

The complete set of SEM images obtained for the multimodal polymer concentration trial can be found in Table B.0.1 of Appendix B. In order to explore the effect of PCL concentration for multimodal spinning applications, five solutions with concentrations varying from 10 to 18wt% were prepared using the Chloroform/Ethanol (7:3) combination. 10wt% PCL in Chloroform/Ethanol (7:3) solutions (10CE_7) were found to electro spray rather than electro spin when a high voltage potential was applied. In this, droplets of the polymer solution were found to continuously breakaway from the Taylors' cone rather than forming a continuous polymer jet. No visible electrospinning was observed at any spinning parameter combination and poor material deposition onto the collector plates was also witnessed. The material collected on the plates exhibited a powder like consistency and could not be successfully removed in one piece. Small fragments of this material viewed under SEM showed highly beaded morphologies as shown in Figure 3.11. At increased flow rates and spinning voltages the production of nanoscale diameter fibres was observed, however, the nanofibre meshes contained large spherical beads throughout the structure.

12wt% Chloroform/Ethanol (7:3) solutions (12CE_7) similarly exhibited electro spraying like characteristics, with the Taylors cone breaking apart periodically during the spinning process. Samples viewed under SEM again showed the presence of polymer beads amongst submicron diameter fibres. These beads displayed an elongated, spindle like morphology rather than the highly spherical shape seen in 10CE_7 solutions. When the polymer concentration was increased further, successful fibre production was achieved. 14wt% Chloroform/Ethanol (7:3) membranes (14CE_7) exhibited multimodal fibre distributions with sparse beading observed at the higher flow rate condition of 12ml/hr. Increasing the polymer content further to 16 and 18wt% yielded smooth bead free fibres. 18CE_7 solutions did however cause difficulties during the spinning process due to the build-up of material at the tip. This excess polymer build-up resulted in the Taylors cone becoming extremely large and unstable, with subsequent collapse of the Taylors cone. It was also noted that at a collector distance of 25cm or greater, poor fibre deposition for 14CE_7, 16CE_7 and 18CE_7 solutions was observed. Fibres appeared to be blown away from the plate by the airflow within the fume hood.

The complete fibre diameter analysis of the multimodal polymer concentration trial can be found in Table B.2 of Appendix B. No diameters are presented for 10 and 12wt% solutions due to the presence of large beads within the membranes collected making fibre diameter analysis difficult. Figure 3.11 shows a sample comparison of fibre diameters at the five different concentration levels collected at a flow rate of 6ml/hr, applied voltage of 20kV and collection distance of 20cm. Fibre diameters are presented for 10 and 12wt% solutions purely for comparative purposes in this diagram. A Kruskal-Wallis test was employed to test for statistical differences in fibre diameters between the groups due to the unequal variances observed. A statistical difference in

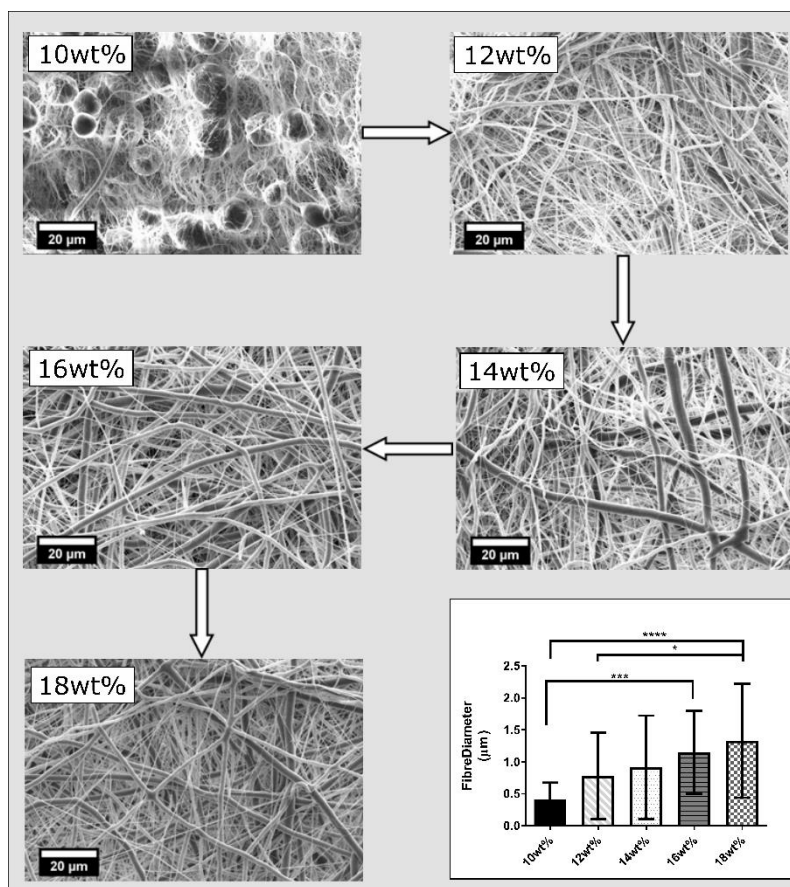


Figure 3.11: Sample set of SEM images for multimodal polymer concentration trial showing the changes in fibre morphology with increasing polymer concentration from 10-18wt% in 2wt% increments. Samples were produced at the processing parameter combination of 6ml/hr flow rate, 20kV applied voltage and 20cm collector distance. Corresponding fibre diameter comparison ($n=150$ per group) is presented, with a statistical difference observed between 10 and 16wt% solutions ($p<0.001$) and 18wt% ($p<0.0001$). A statistical difference was also detected between 12wt% and 18wt% solution ($p<0.001$). No statistical difference observed between all other polymer concentration levels. Kruskal-Wallis with Dunn correction was used for multiple comparisons due to unequal variances between groups.

fibre diameter was observed between 10 and 16wt% ($p < 0.001$) solutions, and 10 to 18wt% ($p < 0.0001$). A statistical difference was also detected between 12 and 18wt% solutions for the given process parameter combination. A slight increase in average fibre diameters could be seen with increasing polymer concentration, however, due to the presence of micron and nano scale diameter fibres with the membranes, large sample standard deviations were recorded. These deviations made detection at higher levels impossible to statistically observe.

Figure 3.12 shows the combined viscosity and conductivity profiles of the 10-18wt% solutions studied. It was observed that at all polymer concentration levels a consistent conductivity of $0.3\mu\text{S}/\text{cm}$ was recorded. Viscosity results again showed increasing viscosity with increasing polymer content with 10wt% solutions possessing viscosities of $49.2 \pm 4.5 \text{ mPa}\cdot\text{s}$ increasing to $818.6 \pm 10.5 \text{ mPa}\cdot\text{s}$ for 18wt% concentrations. The viscosities were found to best fit a power law relationship with a regression of $R^2 = 0.9953$ seen. Based on the combined qualitative and quantitative results of the multimodal polymer screening trial it was determined that 16wt% Chloroform/Ethanol (7:3) solutions appeared to be the most suitable choice for future multimodal investigations. This polymer concentration level not only provides a combination of bead free fibres with suitable multimodal fibre populations, it also provides a highly stable spinning process.

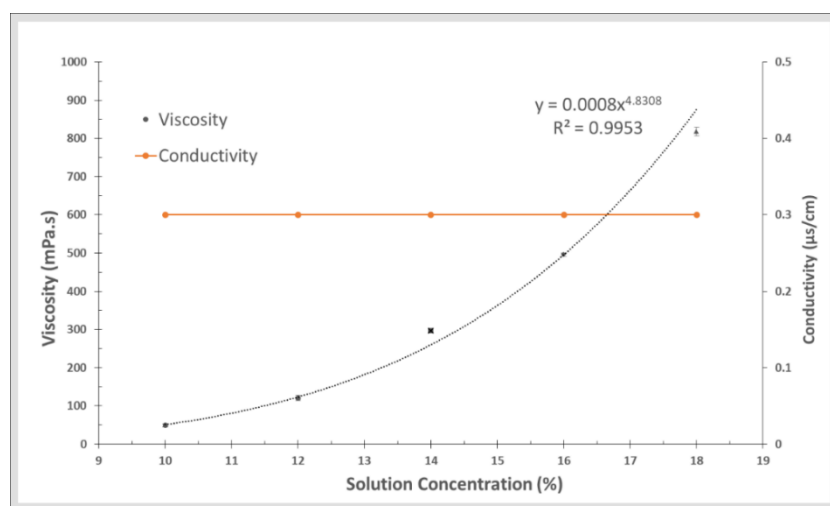


Figure 3.12: Viscosity and conductivity profile of solutions studied for multimodal spinning applications. Polymer concentration increased from 10 to 18wt%, in 2wt% increments. $N=3$ per test group.

3.5.3 Electrospinning of Nanofibre Membranes as Controls

Utilising the select working solution and processing parameter combination identified as part of the nanofibre screening trial a number of nanofibre membranes were spun for the development of control membranes for later use in cell culture studies. The electrospinning solution of Chloroform/DMF (7:3) was identified from the previous screening trial for the spinning of the control membranes due to its ability to produce defect free fibres of the desired diameter scale. The specific processing parameter combination of 0.25ml/hr flow rate, 15kV applied voltage and 15cm collector distance was further studied to investigate the repeatability of the spinning parameter combination and to determine the stability of the collection process over extended deposition periods. Figure 3.13 shows the fibre diameter measurements obtained for five membranes collected over a 1hr deposition period and five membranes collected over a 4hr deposition period for random 2D membrane spinning. No statistical difference in fibre diameters was detected ($p = 0.0938$) between any of the fibre membranes collected with a cumulative average fibre diameter and standard deviation of $0.704 \pm 0.351\mu\text{m}$. This indicates that the process was both repeatable within collection periods and stable over extended collection periods. It was still observed that the membranes produced over 1hr were delicate and prone to collapsing while being removing from the collector surface. The increased collection time of 4hrs

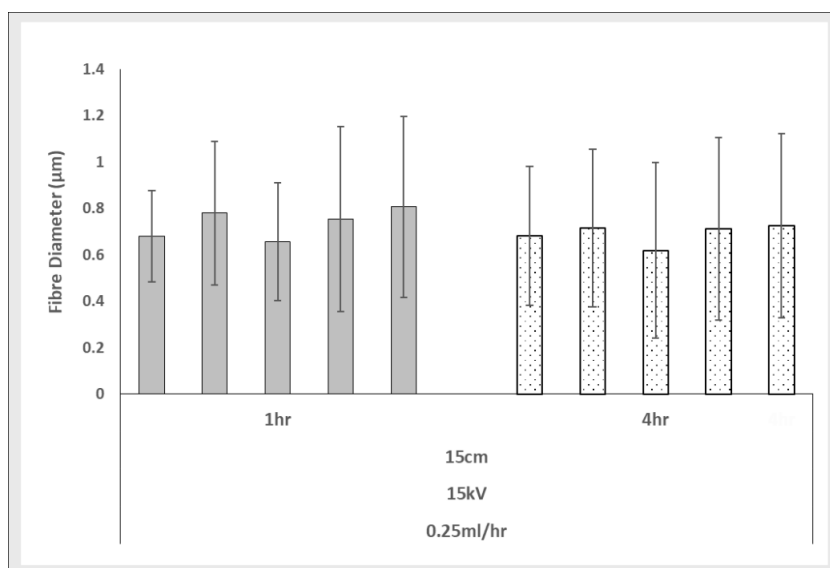


Figure 3.13: Fibre diameter comparison of randomly orientated nanofibre membranes collected over 1hr (n=5) and 4hr (n=5) time periods. No statistical difference in fibre diameters observed between any of the membranes collected ($p=0.0938$)

allowed for sufficiently thick samples to be obtained, that could be easily removed from the collector surface without any damage to the membrane. Due to the delicate nature of the 1hr samples only sections suitable for SEM analysis could be taken and no samples capable of being tested under uniaxial conditions could be attained. In addition, no thickness values for 1hr membranes could be recorded.

It was also desirable to prepare nanofibre membranes with aligned fibre orientations. The same spinning solution and processing parameters employed for the production of the 2D random control membranes was spun onto a high-speed large diameter drum collector for the production of aligned fibre membranes. Due to the increased surface area of the drum, extended deposition periods were required to produce a sample with sufficient thickness, capable of being removed from the drum without damage. Figure 3.14 shows the fibre diameter measurements recorded for five membranes produced over a 4hr collection period and five membranes produced over a 12hr collection period. No statistical difference in fibre diameters was detected ($p = 0.1099$) between any of the membranes collected, indicating that the process was both repeatable within collection periods and stable over extended collection periods also. A cumulative average fibre diameter and standard deviation for the aligned fibre membranes of $0.569 \pm 0.296\mu\text{m}$ was found.

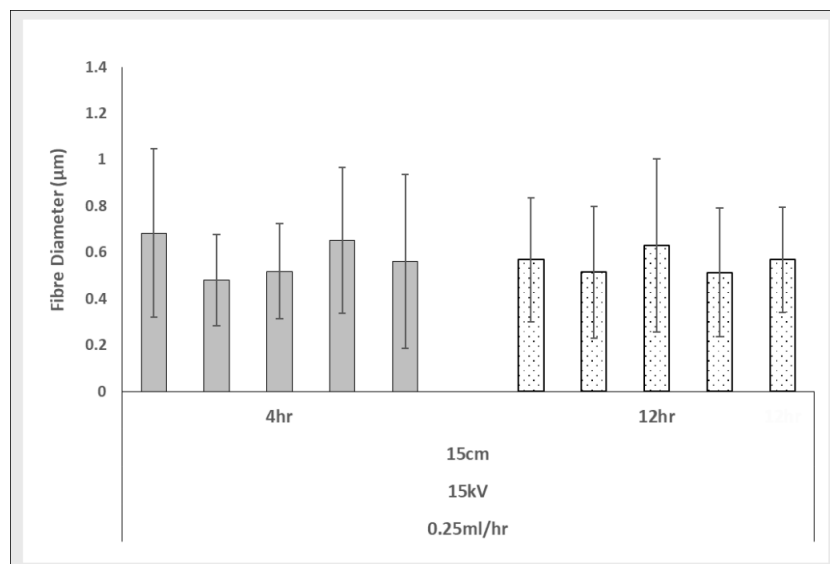


Figure 3.14: Fibre diameter comparison of aligned nanofibre membranes collected over 4hr (n=5) and 12hr (n=5) time periods. No statistical difference in fibre diameters observed between any of the membranes collected ($p = 0.1099$)

Table 3.10: Ambient spinning conditions and airflow measurements recorded during nanofibre spinning of control membrane

<i>Measured Parameter</i>	<i>Maximum</i>	<i>Minimum</i>	<i>Avg. ± S.D.</i>
Relative Humidity (RH%)	60.6	42.4	48.7 ± 5.6
Temperature (°C)	20.2	19.6	20 ± 0.2
<i>2D plate system</i>			
Air Speed at Spinneret Tip (m/s)	0.67	0.41	0.51 ± 0.11
Air Speed at Collector Surface at 15cm (m/s)	0.14	0.08	0.12 ± 0.02
Air Speed at Collector Surface at 25cm (m/s)	0.13	0.0	0.08 ± 0.03
<i>Aligned Drum System</i>			
Air Speed at Spinneret Tip (m/s)	0.58	0.40	0.55 ± 0.2
Air Speed at Drum at 25cm - OFF (m/s)	0.25	0	0.22 ± 0.13
Air Speed at Drum at 25cm - ON (m/s)	3.26	2.97	3.11 ± 0.1

Similar to that observed in 2D random spinning, the reduced collector time of 4hrs prevented samples of sufficient thickness for tensile testing from being produced. Samples collected over 12hrs were however found to be of sufficient thickness and quality required for tensile testing and thickness measurement. An interesting point to note in relation to production of the aligned fibre membranes was the significantly altered travel path of the electrospinning jet towards the drum system compared to that commonly seen when using the flat metallic plate collector system. The spinning jet was observed to whip and appeared to be pushed upwards past the drum before being rapidly pulled back towards the drums surface, whereas, the jet whipped and travelled directly to the flat metallic plate. Table 3.10 above shows the ambient conditions and airspeed measurements recorded during the spinning of the nanofibre control membranes. It was seen that airspeed around the drum system was radically altered by the rotation of the drum itself with an increase in max airspeed from 0.25 to 3.26m/s when the drum was powered on.

A comparison of fibre diameters for random and aligned membranes showed a statistical decrease ($p < 0.0001$) in fibre diameters between those created using the aligned drum collection system and the random 2D plate system as shown in Figure

3.15 (A). The results of the analysis for fibre orientation confirmed that the membranes created using the aligned drum collection system exhibited a significantly higher coherency ($p < 0.0001$) at 0.702 ± 0.07 compared to 0.089 ± 0.029 for random fibre membranes (Figure 3.15(B)). Figure 3.15 (C) showing the colour orientation map of a sample random nanofibre membrane exhibiting several distinct colour groups, representing multiple distinct orientation categories. Figure 3.15 (D) similarly shows the colour orientation map of the aligned fibre membranes. Here a decreased range of colours is exhibited representing a reduced set of fibre orientations within the image and therefore indicating a more aligned structure. The comparison of membrane thickness between the random membranes collected over 4hrs and the aligned membranes collected over 12hrs showed that the aligned membranes had a slightly larger average thickness at $12 \pm 4\mu\text{m}$ compared to $8 \pm 2\mu\text{m}$ for random fibre membranes as shown in Figure 3.16. Statistical analysis did however show that this

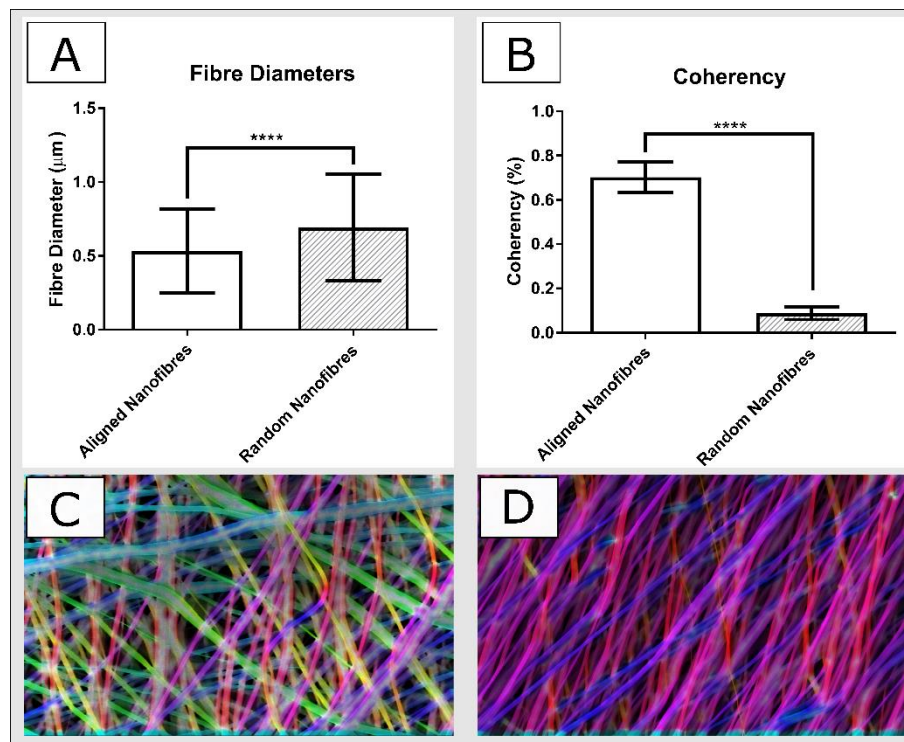


Figure 3.15: Fibre diameter and orientation analysis of electrospun nanofibre membranes (A) Comparison of fibre diameters within aligned and random fibre membranes ($n=150$) showing statistical decrease in aligned fibre diameters ($p < 0.0001$) (B) Coherency assessment of nanofibre membranes ($n=5$) showing statistical increase in fibre alignment within aligned nanofibre membranes ($p < 0.0001$) (C) Random fibre membrane showing no dominant direction of alignment (D) Aligned membrane showing preferential alignment of fibres

this increase was non-significant ($p = 0.0533$).

The mechanical response of the uniaxial dogbone specimens punched from the 4hr random membranes and 12hr aligned nanofibre membranes can be seen in Figure 3.17. Figure 3.18 subsequently shows the summarised ultimate tensile strength (UTS) (A), Young's modulus (B) and strain at break (C) characteristics for the specimens examined. It is observed that the aligned nanofibre membranes exhibited different stress versus strain responses when tested parallel (APL) and perpendicular (APR) to the preferential axis of fibre alignment. The aligned fibre membranes showed a statistically higher UTS and Young's modulus ($3.24 \pm 0.94\text{MPa}$, $10.76 \pm 3.05\text{MPa}$) when loaded parallel to the preferential fibre axis, compared to those tested perpendicular to it ($0.96 \pm 0.36\text{MPa}$, $3.24 \pm 1.22\text{MPa}$) ($p < 0.001$).

No statistical difference was observed between the UTS and Young's modulus for the aligned membranes and the random membranes ($1.71 \pm 0.26\text{MPa}$, $0.80 \pm 0.31\text{MPa}$). The random membrane exhibited a characteristic response between that of the parallel and perpendicular aligned conditions. Strain at break was statistically lower for the APL membranes ($98.17 \pm 26.6\%$) compared to APRs ($238.4 \pm 33.3\%$) (< 0.001). Again no statistical difference was observed between the strain at break for the aligned membrane conditions and random membranes, with the random membranes again

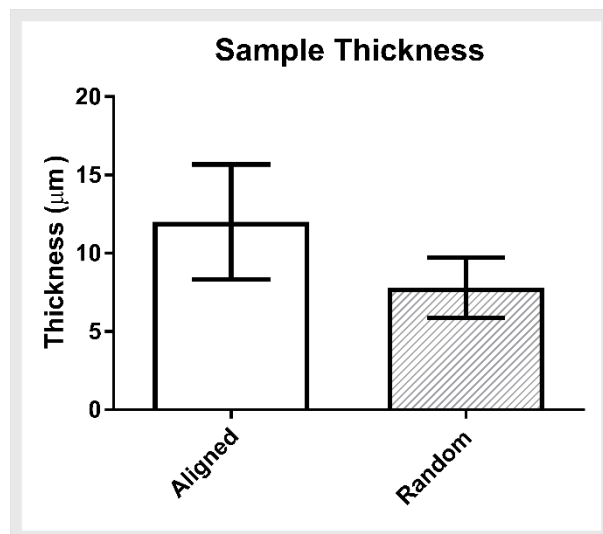


Figure 3.16: Thickness comparison of Aligned nanofibre membranes (Deposition period 12hrs) and Random nanofibre membranes (Deposition period 4hrs) showing no statistical difference in sample thickness ($p = 0.0533$). $N=5$ for each test group.

exhibiting a characteristic response between that of the APL and APR samples at $160.5 \pm 39.9\%$. Lastly Figure 3.18 (D) shows a comparison of porosity results between the aligned ($89.4 \pm 1.3\%$) and random fibre membranes ($89.5 \pm 0.8\%$) with no statistical difference observed ($p = 0.8979$).

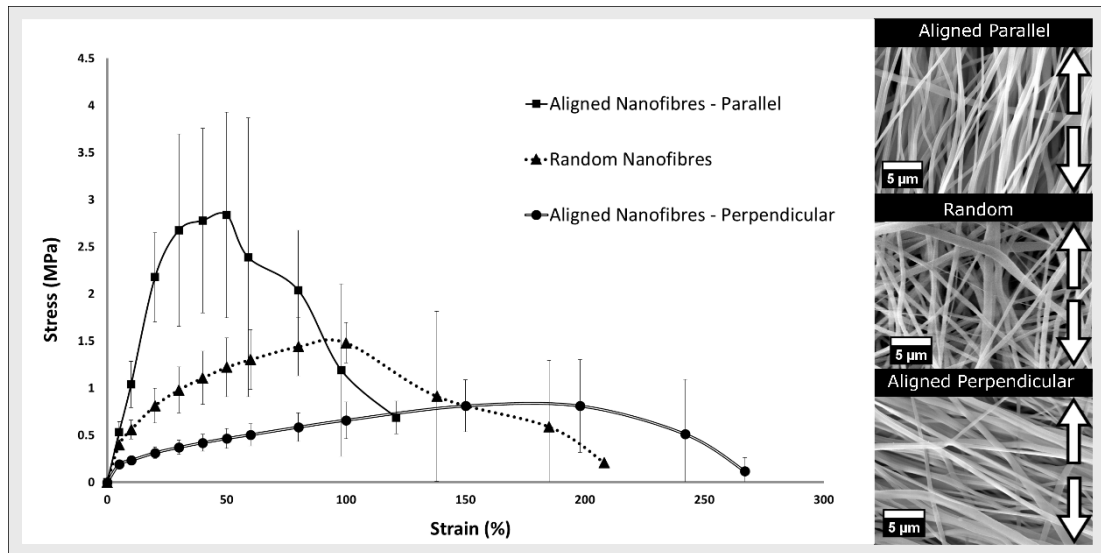


Figure 3.17: Stress vs Strain profiles obtained for uniaxial dogbone testing of random and aligned nanofibre membranes. Aligned fibre membranes were tested in both a parallel and perpendicular to preferential fibre orientation. $N=5$ for each test group.

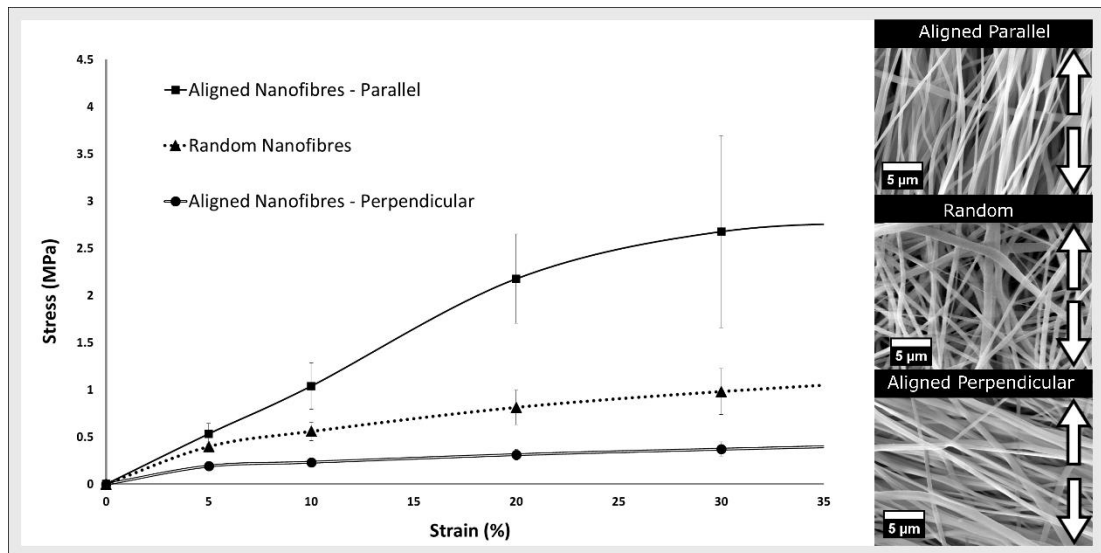


Figure 3.18: Focused view showing the initial loading and strain region for random and aligned nanofibre dogbone specimens. $N=5$ for each test group.

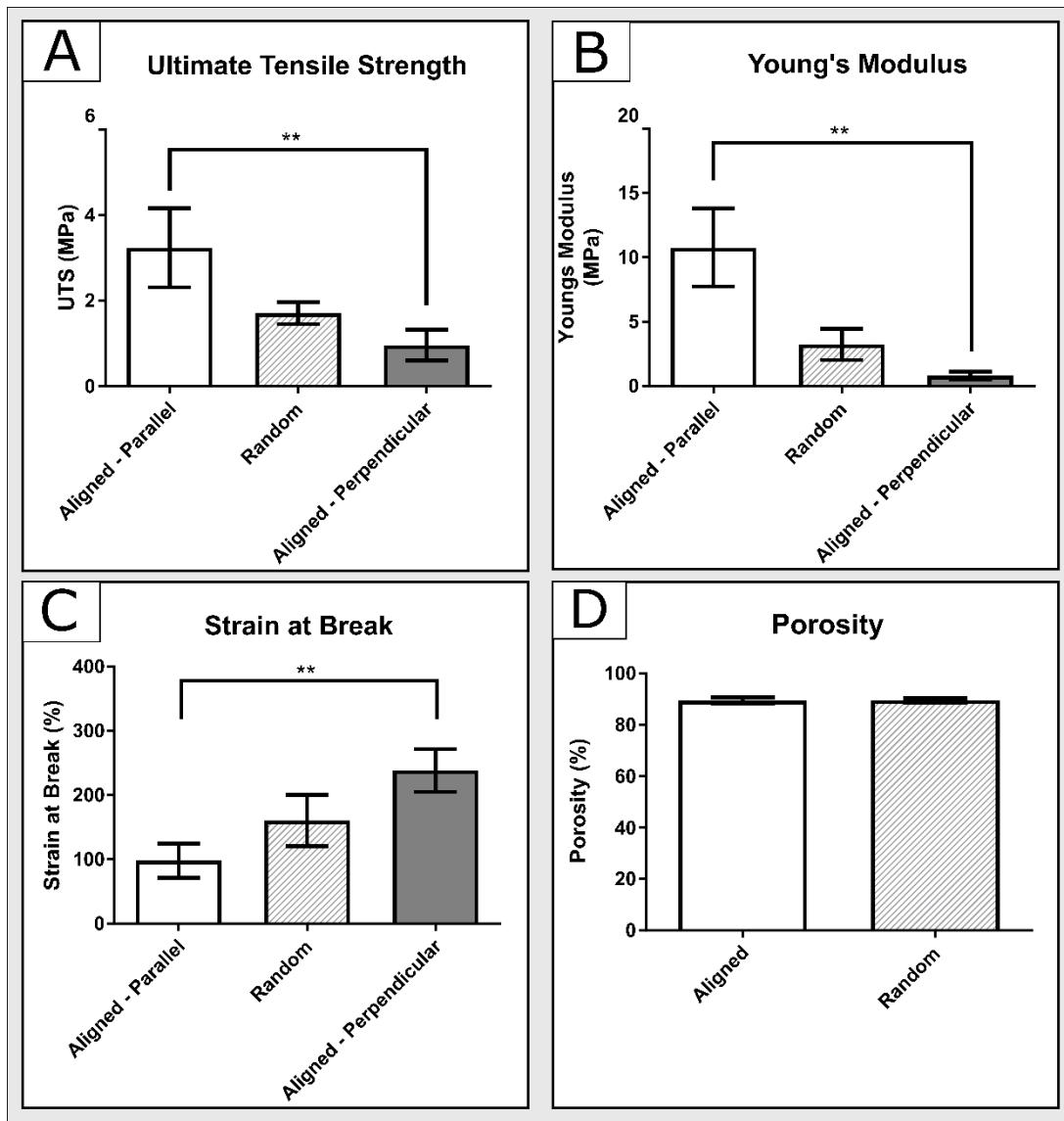


Figure 3.19: Summarised results of uniaxial tensile tests of random and aligned nanofibre membrane dog-bone specimens (A) Ultimate tensile strength (UTS) of nanofibres membranes showing statistically higher UTS between aligned fibre membrane tested parallel to the preferential axis of fibre alignment (PFA) and perpendicular to the PFA ($n=5$ per test group) (B) Young's modulus of nanofibres membranes showing statistically higher modulus between aligned fibre membrane tested parallel and perpendicular to PFA ($n=5$ per test group) (C) Strain at break of nanofibres membranes showing statistical decrease in strain at break in aligned fibre membraned tested parallel to PFA and those tested perpendicularly. No statistical difference was detected between the random nanofibre membranes and the aligned membranes for any of the response characteristics observed with random membranes exhibiting properties between those of the two aligned fibre test cases ($n=5$ per test group) (D) Porosity results of aligned and random membranes showing no detectable statistical difference ($n=10$ for each test group).

3.6 Discussion

3.6.1 Solution Screening Trial

3.6.1.1 Micron and Multimodal Solution Screening

From the results obtained for the solution screening trial it is clear that the addition of the surfactants ethanol and methanol to the chloroform based spinning solutions greatly affected the fibre architecture and deposition process of the corresponding electrospun membranes produced. This fact can be attributed to changes in solution properties such as conductivity (Table 3.8 and 3.9), surface tension and viscosity (Figure 3.12), which are known to significantly affect the mechanics of the electrospinning process. One particularly important characteristic of the surfactants is their dielectric constants. The dielectric constant of a material refers to the ratio of its permittivity to that of free space. Materials with high dielectric properties experience greater charging effects under the presence of an applied electric field compared to those with low dielectric constants. This occurs due to the increased availability of free charges within the solutions of higher dielectric potentials [245]. This change in dielectric potential in turn relates to a change in the solution permittivity and conductivity.

The organic solvent chloroform possess a low dielectric constant (ϵ) of 5.62 while the surfactants ethanol and methanol have increased dielectrics of 24.5 and 32.7 respectively [246]. Solutions prepared with the polymer PCL and the pure solvent chloroform are not expected to experience high charging effects when a voltage is applied. This is due to the low dielectric constant of chloroform and the natural insulating properties of the raw polymer PCL. This lack of charging potential is believed to have resulted in the immeasurable conductivity of the PCL chloroform (CH) solutions witnessed in this study. Fibre structures within the membranes produced using the CH solutions exhibited highly interconnected and fused architectures with the presence of liquid polymer deposition on the collector surface under certain spinning permutations. A lack of charge flow within the CH solutions resulted in reduced bending instabilities within the jet as it travelled through the air towards the collector surface due to decreased charge repulsion within the jet [247]. Reduced jet repulsion results in reduced elongation forces, which in turn contribute to

the insufficient thinning of the electrospinning jet. This lack of thinning results in large diameter fibres [240]. These large diameter fibres in turn experience reduced solvent evaporation due to solvent particles becoming trapped within the central core of the fibres. A collector distance of 15cm was shown to be insufficient for complete chloroform evaporation to occur. By increasing the collector distance to 20cm and maintaining a voltage of 15kV the polymer jet experienced an increased travel time allowing for greater solvent evaporation to take place. When however, the flow rate and applied voltage was increased a greater mass transfer of material away from the tip was experienced. This increased mass of material results in higher quantities of solvent within the emerging jet which could not sufficiently evaporate over a 20cm path leading to the webbed structures observed at the higher flow rates of 12ml/hr, and applied voltages of 20kV.

The addition of the surfactant ethanol to the electrospinning solutions is expected to decrease the solution viscosity while also increasing its conductivity and volatility [160]. An increased conductivity allows for a greater charge transfer within the solution that subsequently leads to increased forces within the jet due to increased surface charge repulsion and coulombic collector potentials. The increased volatility of the ethanol compared to the solvent chloroform also aids in greater evaporation rates during travel to the collector. A decreased viscosity may have also contributed to a more stable jet formation process due to the decreased stretching forces required to initiate jet repulsion compared to the pure CH solutions [136]. Chloroform/Ethanol (9:1) (CE_9) solutions were however shown to still possess an immeasurable conductivity value but a decrease in solution viscosity was however observed. This was reflected by the insufficient solvent evaporation that still occurred at a collection distance of 15cm, where liquid polymer deposition or highly interconnected fibre structures were seen to occur. Increasing the collector distance to 20cm allowed for greater evaporation and thinning of the jet to occur, yielding better fibre quality at the expanded collector distances. Some fibre fusion was still however present at the higher flow rate and applied voltage ranges, again suggesting an imbalance in mass transfer away from the tip resulting in insufficient solvent evaporation occurring before deposition.

Chloroform/Ethanol (7:3) (CE_7) solutions could be successfully spun at the lower collector distance of 15cm, with this being attributed to the increased elongation forces and volatility within the emerging electrospinning jet due to the increased ethanol fraction within the solutions. This was reflected in the increased conductivity of CE_7 solutions to a measurable limit of 0.3 μ S/cm although the reduced dielectrics of chloroform and the insulating nature of PCL resulted in reduced conductivity values compared to the pure ethanol component of 1 μ S/cm, and the polymer free combination of chloroform/ethanol (7:3) at 0.4 μ S/cm. The increased bending instabilities experienced by the solution aids in elongating the jet allowing sufficient evaporation to occur at the collector distances of 15 and 20cm. It was also observed that the spinning of CE_7 solutions resulted in the splitting of the Taylors cone into multiple sub-jets in a process known as splaying or branching [248]. This effect occurs when a change in the charge per unit area of the jet takes place due to its elongation and the evaporation of the solvents and surfactants. This change in unit charge per area shifts the balance between the surface tension and the electrostatic forces, and the jet becomes highly unstable [248]. In order to reduce its local charge per unit surface area, the unstable cone or jet ejects a smaller stream from its surface in order to dissipate the collecting charge. These smaller streams or jets may explain the formation of the thinner nanofibres seen within the electrospun membranes giving rise to their multimodal nature [167]. Additionally the thinner fibres may be explained by the greater bending and whipping forces experienced by the primary jet due to increased elongation forces experienced due to increased solution conductivity [199]. This increased thinning effect was reflected in the reduced average fibre diameters within the electrospun membranes compared to the pure CH and CE_9 membranes. The large deviations in average fibre diameter measurements again reflect the multimodal nature of the membranes as the mixed populations of micro and nano diameter fibres resulted in large fibre diameter distributions.

The solvent methanol similarly decreases the surface tension and viscosity of the spinning solutions while also increasing volatility within the electrospinning jet [184]. The increased dielectric constant of methanol compared to ethanol may define how mixed fibre diameter populations were observed to collect for CM_9 solutions at the collector distances of 15cm. The increased conductivity of the solution again resulted

in greater bending instabilities within the jet allowing for a greater travel distance over which solvent evaporation and fibre thinning can occur, allowing for regions of the jet to elongate such that nano diameter fibres deposited. The high volatility of methanol may also explain the observation of the defects found to form on the surface of samples. As previous studies have shown, solutions made with highly volatile components may result in the formation of polymer skins at the needle tip if the flow rate is too large for sufficient material removal to occur. This polymer skin is later jettisoned from the needle tip as new polymer is delivered and in turn lands on the surface of the sample [166]. These polymer skins give rise to the small bumps/ridges observed on the surface of the sample. Despite the regular morphology of fibres produced using methanol, their nano to submicron scale size is believed to have resulted in their poor deposition to the collector as the fibres were drawn away by the airflow extraction within the fume hood. This was particularly noted at the greater spinning distance of 20cm where the small nanoscale fibres present within 15cm samples were not found to deposit. Similarly, Chloroform/Methanol (7:3) solutions may have resulted in the spinning of nanofibres which were subsequently drawn away by the airflow with the fume hood preventing their deposition to the collector surface, again explaining the poor deposition rates observed for this spinning solution.

From these results it was concluded that chloroform and ethanol based spinning solutions, and in particular solutions prepared with a chloroform to ethanol ratio of 7:3 (v:v) were the solution of choice for future studies surrounding multimodal fibre spinning. The ability to create multimodal diameter structures while also achieving superior deposition compared to the methanol based solutions makes it highly desirable for the creation of the multimodal fibre layer that will become the core layer of the composite tubular scaffold under investigation in this work. Ethanol is also typically used for the sterilisation of scaffolds before cell seeding experiments so the potential presence of residual ethanol within the scaffolds after electrospinning is not expected to adversely affect future cell culture experiments [249][250].

3.6.1.2 Nanofibre Solution Screening

The surfactant DMF was chosen for the nanofibre generation trial as it has both a higher dielectric constant ($\epsilon = 36.7$) and volatility compared to that of both ethanol and

methanol [247][251]. By using the increased charging effects that the surfactant offers, and in turn the increased axial forces within the emerging jet, it is possible to induce sufficient bending instabilities within the jet so that sufficient thinning towards the nanoscale occurs [251]. The conductivity of PCL Chloroform/DMF (7:3) (CD_7) and PCL Chloroform/DMF (5:5) (CD_5) solutions were significantly higher than those of Chloroform/Ethanol (7:3) ($0.3\mu\text{S}/\text{cm}$) and Chloroform/Methanol (7:3) ($0.5\mu\text{S}/\text{cm}$) solutions with near double the conductivities at 0.9 and $1\mu\text{S}/\text{cm}$, for CD_7 and CD_5 respectively. It was also observed that the conductivity of the Chloroform/DMF electrospinning solutions did not appear to change with polymer concentration level. A number of studies have shown that increasing PCL content does not greatly affect the conductivity of electrospinning solutions. Du *et al.* showed that for PCL Dichloromethane/DMF (7:3;v:v) solutions a change of approximately $0.2\mu\text{S}/\text{cm}$ was observed between 3 and 13wt% solutions, and less than $0.1\mu\text{S}/\text{cm}$ between a 5 and 10wt% solution [252]. A lack of sensitivity in the measurement system used within this work may have prevented a discernible difference from being detected over the 6 to 11wt% range studied.

Along with increasing the conductivities of the nanofibre solutions, a larger molecular weight PCL of 100,000 g/mol was employed for nanofibre generation compared to 80,000g/mol for the multimodal and micron screening. By employing a large molecular weight PCL a reduced polymer concentration was required for sufficient chain entanglement and subsequent stable jet initiation to occur [152][154]. By doing this reduced flow rates could be employed to provide a stable Taylor cone at flow rates as low as 0.25ml/hr. Using these reduced flow rates a smaller Taylor cone forms and subsequent smaller emerging jets could be produced without breaking down [253]. Membranes produced using 6wt% solutions were found to be highly beaded irrespective of the DMF ratio used. This is believed to occur due to the average solution viscosity range of 132.5 and 213.5mPa.s, for the CD_5 and CD_7 solutions respectively. When the solution viscosity is below a critical point, solvent congregation occurs due to the insufficient dispersion caused by a lack of polymer chain interactions. This congregation of solvent in turn leads to beads forming along the length of the fibres [161]. If the concentration is too low it can also result in the entangled polymer chains fragmenting before reaching the collector surface resulting

in electrospaying to the collector plate [254]. This gave rise to the powder like consistency of samples observed to collect on the target plate.

8wt% Chloroform/DMF (7:3) solutions appeared to have a sufficient average viscosity at 649mPa.s for appropriate uniform thinning of the jet to occur. This resulted in the deposition of uniform fibres to the collector surface at the majority of spinning permutations. The higher flow rates of 1m/hr displayed some fibre fusion attributed to the increased flux of material to the spinneret tip. The increased spinning voltage of 20kV also resulted in fibre fusion again attributed to insufficient solvent evaporation. This may occur due to the increased ejection of material from the spinning jet typically seen at higher voltage levels which results in an excessive mass within the jet for complete solvent evaporation to occur within [253]. Using the 8wt% Chloroform/DMF (7:3) solutions with a 0.25ml/hr flow rate and 15kV applied voltage average fibres could be tuned from the micron to nano scale by adjusting the collector distance appropriately from 10cm to 15cm. This thinning of the fibres over the increased collector distance again occurs to the increased travel time and in turn increased axial elongation forces experienced by the fibre jet before deposition [133][151][253][254].

8wt% Chloroform/DMF (5:5) solutions again gave rise to the electrospinning of highly beaded fibre membranes. This was attributed to the decreased viscosity of 411mPa.s observed compared to 649mPa.s for 8wt% Chloroform/DMF (7:3) solutions. Du *et al.* again demonstrated that with the increasing percentage of DMF in PCL/Dichloromethane based solutions, both an increase in surface tension and a decrease in viscosity was observed [252]. This increasing surface tension paired with insufficient viscosity results in solvent congregation giving rise to the presence of highly beaded fibre structures despite having an equal polymer concentration level. By further increasing, the polymer concentration sufficient viscosity was achieved for both 11wt% Chloroform/DMF (7:3) and Chloroform/DMF (5:5) solutions. It is however thought that this increased viscosity prevented uniform thinning due to the high content of polymer within the spinning jet. This resulted in areas of the fibre membranes exhibiting both micron and nanoscale diameter fibre populations. As it was desired to have pure nanoscale diameter fibres for the subsequent comparative

cell culture trials the higher polymer concentration level of 11wt% was not suitable for future study. Based upon the results of the initial nanofibre screening trial it was determined that the 8wt% polymer concentration in Chloroform/DMF at a ratio of 7:3 (v:v) was the solution of choice for future studies surrounding nanofibre membrane spinning. The particular processing parameter combination of a 0.25ml/hr flow rate, 15KV applied voltage and 15cm collector distance was again selected for further studies due to the ability to create membranes with desirable average fibre diameters and a tight standard deviation.

3.6.1.3 Polymer Concentration Trial for Multimodal Fibres

Solutions prepared using the solvent surfactant combination of Chloroform/Ethanol (7:3) were chosen for the further exploration of multimodal electrospinning due to the preliminary ability to create hybrid fibre diameter populations as seen within the solution screening trial. In order to better assess the contribution of polymer concentration to the fabrication of multimodal fibre populations, solutions ranging from 10 to 18wt% polymer concentrations were spun over an initial range of processing parameters. Scaffolds prepared using solution concentrations of 10 and 12wt% demonstrated highly beaded sub-structures when viewed under SEM. Insufficient polymer concentration resulted in solution viscosities below 150mPa.s which is thought to have led to inadequate formation of chain entanglements within the electrospinning jet. Insufficient chain entanglements and interactions with solvent molecules led to severe solvent aggregation within the spinning jet giving rise to the beaded structures observed. Membranes produced from the 12wt% solutions exhibited beads with spindle like morphologies compared to the spherical beads viewed within 10wt% membranes [247]. These spindle like beads demonstrated the increased chain interactions amongst the solvent molecules due to the increasing polymer content. The increased concentration of polymer chains reduced the congregation of the solvents due to surface tension forces but lacked sufficient viscosity to counteract them fully leading to elongated beads forming. By increasing the polymer concentration to 14wt% the majority of scaffolds produced were shown to be bead free and contained distinct multimodal fibre populations. Some beading was observed at the increased collector distances with this being attributed to increased bending instabilities and a

reduced electrostatic potential which resulted in the non-uniform stretching of the polymer jet during flight [150]. Increasing the polymer concentration further to 16wt% resulted in increased chain entanglements within the solution, which in turn enhanced jet formation resulting in the reduced presence of beads within the membranes. Increased polymer content was also seen to increase the diameters of fibres within the membranes, a typical observation seen in the electrospinning of polymer samples [167]. Despite having an increased polymer content the multimodal fibre distributions were maintained within the fibre membranes with distinct micron and nanoscale fibres present. A further increase to 18wt% concentration again allowed for the spinning of bead free multimodal fibres. It was however observed that the electrospinning jet was prone to excess build-up of material at the spinneret tip that required operator interaction to prevent clogging. This was attributed to the high viscosity level of the solution at approximately 819mPa.s which was believed to be too high for sufficient withdrawal of the material under the electrostatic repulsive forces. This lack of repulsion resulted in an imbalance of material being removed and supplied to the spinneret tip. This led to an excess of material at the tip that began to dry in the presence of air, leading to blockage formation over time. Further to this, fused fibres were seen to form within the membranes suggesting that insufficient evaporation was occurring at the higher concentration solution. This again is believed to occur due to an excess of material within the spinning jet that results in solvent molecules becoming trapped within the centre of jets preventing their appropriate evaporation before depositing. The residual solvent melts the depositing fibres forming the fused sections seen under SEM.

Based on the results of the multimodal polymer concentration trial, 16wt% Chloroform/Ethanol (7:3) solutions appeared to be a desirable solution for the production of multimodal tubular scaffolds that will become part of the composite scaffold under investigation in this study. The increased diameters of the micron fibres seen in the 16wt% solutions may produce a more mechanically stable scaffold while the intermixed nanoscale diameter fibres may still offer suitable binding profiles for cell attachment and infiltration.

3.6.1.4 Electrospinning of Nanofibre Membranes as Controls

In order to assess the viability and infiltration of cells grown on the composite bi-layer vessel under study in this work, a number of comparative electrospun membranes were required in order to provide a baseline comparison to traditional electrospinning approaches. Numerous studies have shown that cells grow and proliferate differently dependent on the size and orientation of the electrospun fibres they are seeded upon [184][186][255], with nanofibre membranes shown to offer appropriate support, guidance and differentiation cues to seeded cells [256]–[259]. It was therefore desirable to produce nanofibre membranes in order to provide a comparison against the ideal attachment and guidance characteristics that electrospinning can offer. Using the select solution and processing parameter conditions identified as part of the nanofibre screening trial, a number of fibre membranes were studied. In this, the effect of the collector system on depositing fibre orientations and diameters was studied, along with the stability of the electrospinning processes over extended collection periods.

2D random membranes collected on flat metallic collector plates showed no significant changes in fibre diameters irrespective of the collection time employed. This is important as residual charging within depositing fibre membranes has been previously shown to interact with further depositing fibres altering the collection process [19]. This may result in deposited fibres repelling further depositing fibres resulting in morphological changes to the collected membranes [260]–[262]. No apparent changes to the deposited membranes were observed over any of the extended collection periods suggesting that any residual charges were dissipated sufficiently upon deposition. It was however observed that over 1hr collection periods the nanofibre membranes could not be removed with sufficient ease from the collector surface and were prone to tearing upon removal. The membranes lacked the integrity required for manipulations such as loading into cell culture inserts, and general handling during sterilisation processes that will be discussed further in subsequent chapters. Membranes collected over 4hrs were of sufficient thickness to be removed as complete membranes, again demonstrating the stability of the collection process over longer deposition periods.

Membranes prepared using the rotating drum collector allowed for the preparation of highly aligned fibre membranes, as confirmed by their significantly higher fibre coherency compared to those created using the flat metallic plate. In addition, the collected fibres displayed decreased diameters to those collected on the metallic plates. It is suspected that the increased rotational velocity of the collector surface may have resulted in two additional thinning effects being imparted on the depositing fibres. Firstly, it was observed that the path of the electrospinning jet was highly influenced by the rotation of the drum. It was observed that the rotation increased the local airspeed surrounding the drum from less than 1ms^{-1} to several ms^{-1} . This in turn is believed to have resulted in an air current that repelled and pushed fibres away from the drum as they approached the collector. The electrospinning jet was found to arc over the drum before being rapidly pulled back to the drum surface upon passing. This may have allowed for greater bending instabilities and in turn increased axial loading giving rise to further thinning during travel. Kim *et al.* similarly observed that PET fibres were shown to ‘fly’ into the air instead of being deposited to a rotating drum collector once the rotational velocity of the drums surface reached a critical point of 45mmmin^{-1} [263]. In turn, the rapid linear velocity of the collector surface has been demonstrated to induce tensile forces within the depositing fibres [153]. These forces pull the fibres into alignment with the direction of rotation, giving rise to the aligned nature of the collected fibres. These tensile forces may not only given rise to the increased fibre alignment seen, but in addition may have resulted in further elongation of the fibres resulting in the decreased diameters observed [264].

The mechanical analysis of the 2D fibre membranes showed the importance of fibre alignment on a number of mechanical responses. The UTS, Young’s modulus and strain at break were found to be highly dependent of the fibre orientation and the corresponding axis of alignment in which the membranes were tested. The UTS of the aligned fibre membranes was shown to be statistically higher when the membranes were tested parallel to the preferential fibre axis (PFA) compared to the perpendicular PFA. This occurs due to the altered support levels that the fibres offer upon being loaded [265]. When loaded parallel to the PFA, the fibres significantly resist the loading allowing for significantly higher forces to be imparted before failure. When tested perpendicularly to the PFA, the fibre membranes were free to separate upon the

application of an applied load due to limited number of fibres orientated in the direction of loading and the decreased fibre entanglements. No statistical difference was detected in UTS for either of the aligned fibre test orientations and the random membranes. This is thought to occur due to the significant variation in UTS seen within the aligned fibre membranes. This may have occurred due to necking of the fibres due to the high linear velocity of the collector surface, which may have resulted in weakened areas of the fibre membranes which lead to the large variations seen [213]. No necking of fibres was however visible within the layer of fibres observed under SEM. Aligned fibre membranes also typically experience decreased point bonds between fibre when compared to random membranes [111]. These point bonds significantly increase the resistance of the membranes to deformation that may account for the non-statistical difference between the random and aligned membranes observed.

Similarly, the Young's modulus was found to be statistically higher for the parallel PFA test case. Again, this is attributed to the increased resistance that the orientated fibres offer upon loading. The fibres are expected to resist straining before succumbing to fracturing. Again, when tested perpendicular to the PFA poor fibre entanglements allowed the fibre membranes to be freely pulled apart rather than a true fracturing effect amongst the fibres. This ability to be freely pulled apart was again reflected by the increased strain at break observed for the perpendicular PFA test case. The random membranes again appeared to possess a characteristic Young's modulus and strain at break between that of two aligned fibre test cases. This may occur due to the ability of the random fibre membranes to reorient upon loading. This reorientation allows the fibres to resist loading with increased strain while also allowing increased strain of the sample before the fibres begin to fracture accounting for the increased strain at break compared to the parallel PFA samples. This reorientation of fibre networks has been demonstrated by Koh *et al.* [266]. In this work electrospun PCL fibre membranes displayed reorientation of fibres under an applied load, with fibres aligning parallel to the axis of loading and perpendicular to the direction of crack propagation.

The porosity of the nanofibre membranes tested was shown be unaltered with fibre orientation. It is typically expected that aligned fibre networks should possess a

decreased porosity to random membranes due to the increase packing density of fibres [242]. This lack of change in porosity may have occurred as porosity refers to overall void space rather than the size distribution of the pores themselves. Membranes have been shown to exhibit similar porosities while containing different pore size distributions [196].

It was concluded from the nanofibre control membrane studied that two distinct fibrous structures, with unique fibre architectures and mechanical responses could be freely spun through the use of bespoke collection systems. Using these fibre membranes a comparative assessment of the bi-layer vessel being investigated can be performed allowing for a definitive comparison to traditional electrospinning approaches.

Chapter 4 Development of Multimodal Hybrid Fibre Diameter Vessels by Rotating Mandrel Electrospinning Process

4.1 Introduction

The electrospinning of three-dimensional structures comprised of hybrid fibre diameter populations offers the unique potential to create a scaffold that possesses both the large pores required for cell infiltration while also providing appropriate sites for cell adhesion in the form of nano diameter fibres. Single step multimodal electrospinning has been demonstrated to be a hugely promising technique to incorporate the inherent benefits of multiscale diameter fibres while maintaining a simple fabrication process. Although the enhanced cellular infiltration qualities of this technique have been presented within the literature, the limited range of current studies has prevented a true understanding of the process from being achieved. While the effect of solution and processing parameters on the morphological and mechanical attributes of traditional electrospun materials is well known, little work has explored their effect on scaffolds created by multimodal approaches. As introduced in Chapter 3, solutions prepared using the polymer PCL and the solvent surfactant combination of chloroform and ethanol can be employed to create membranes comprised of distinct micron and nanofibre populations. This chapter will further employ regression analysis principles to assess the mechanical and morphological responses of small diameter electrospun tubular scaffolds prepared through a multimodal spinning process in connection with a rotating mandrel collector. In this, the systematic variation of processing parameters will be examined in order to develop an increased understanding of the variation of scaffold attributes with changing parameters. Using these findings, a tubular scaffold with mechanical properties comparable to that of native vascular tissue, including vessel compliance will be fabricated. This tubular

scaffold will subsequently be used as the basis for the bi-layer vessel under investigation in this work.

In order to create the tubular scaffold that suitably mimics the mechanical and morphological attributes of native vasculature a number of activities were undertaken within this chapter, they include:

- **Regression Analysis of Multi-Modal Rotating Mandrel Electrospinning Process**

Using regression analysis principles, the effects of a number of processing parameters on the morphological and mechanical attributes of small diameter tubular scaffolds created through multimodal approaches were evaluated. Processing parameters under investigation included solution flow rate, applied voltage, tip to collector distance and rotational speed of collection mandrel. Characterisation of the tubular scaffolds includes fibre morphology by SEM, mechanical properties by modified uniaxial test methods and porosity by liquid intrusion.

- **Control of Molecular Weight Variation Between PCL Batches by Matching Solution Viscosities**

Due to a variability of molecular weights observed between batches of the purchased polymer PCL, a method to provide consistent multimodal electrospinning was explored. In this, the ability to control the electrospinning process through the appropriate matching of solution viscosities is assessed. To determine the effect of such variations on the mechanical attributes a comparison of scaffolds created using different PCL batches was performed.

- **Fabrication of Tubular Scaffolds Containing Hybrid Fibre Diameter Populations**

Using the established multimodal spinning process, the ability to develop a small diameter tubular scaffold with properties mimicking that of native vascular tissue was evaluated. In this, properties including vessel compliance were assessed and compared to traditional arterial bypass constructs.

4.2 Materials & Equipment

4.2.1 Materials

- Poly(ϵ -caprolactone) with an average molecular weight (M_w) of 80,000 g/mol (Sigma Aldrich, USA)
- Poly(ϵ -caprolactone) with a measured average molecular weight (M_w) of 100,000 g/mol (Sigma Aldrich, USA)**
- Chloroform ($\geq 99\%$) with amylenes as a stabiliser (Sigma Aldrich)
- Ethanol (≥ 99.5 , 200 proof) (Sigma Aldrich)
- Methanol (≥ 99.8) (Fluka)
- Acetone (Sigma Aldrich)
- Tetrahydrofuran, HPLC grade ($\geq 99.9\%$) (Sigma Aldrich)
- Poly(dimethylsiloxane), viscosity 100 cSt and 500cst (Sigma Aldrich)
- Potassium Chloride Standard Solutions (A-C) (Fluka)
- Phosphate Buffered Solution (PBS) (Sigma Aldrich)
- Liquid Latex (Kryolan, UK)

**Purchased as equivalent 80,000 g/mol from Sigma Aldrich but verified by Gel Permeation Chromatography (GPC) to be 100,000 g/mol

4.2.2 Equipment

- KDS200P Syringe Pump (KD Scientific, USA)
- ES30P-20W/DAM Power Supply (Gamma High Voltage Research, USA)
- 20G x 1.5” Hypodermic Needle (Tip Blunted) (Terumo, USA)
- 20ml Gas Tight Glass Syringe (SGE Analytical Science, Australia)
- Rotating Copper Mandrel Collector System (Custom, DCU)
- Testo 615 Digital Humidity Meter (Testo Inc., Germany)
- AVM-8880 Hot Wire Anemometer (ATP Instrumentation Ltd, UK)
- High Voltage Probe (Radionics, Ireland)
- AT-6 Tachometer (Farnell, UK)
- Magnetic Stir Plate (Bibby, HB502, Sterlin UK)
- Mettler AE50 balance (Mettler Toledo, Switzerland)
- EVO LS15 Scanning Electron Microscopy (Zeiss, Germany)
- Edwards Pirani 501 Scancoat Sputtering Coater (Edwards Laboratories, USA)

- Dogbone Specimen Cutting Die (Custom, DCU)
- Zwick Z005 Tensile Test Machine with 500N Load cell (Zwick-Roell, Germany)
- Mintron Video Extensometer (Mintron, Taiwan)
- ‘Parallel Pin Grips’ for Uniaxial Ringlet Tensile Testing (Custom, DCU)
- Dual Parallel Blade Cutter – 10mm Spacer (Custom, DCU)
- Static Compliance Test Rig (Custom, DCU)
- Ø5mm Stainless Steel Mandrels
- External Micrometer (Draper Tools, UK)
- Mitutoyo Toolmakers Microscope (Mitutoyo, Japan)
- Dogbone Specimen Cutting Die (Custom, DCU)
- Agilent 1200 series GPC, equipped with two PSS GRAM analytical columns (8x300 mm, 100Å and 3000Å, 10µm) (Agilent, US)
- Ready Cal-Kit (PMMA, 800-1,820,000 Da) (PSS Polymer, Germany)
- Brüker D8 Advance X-ray Diffractometer (Bruker, US)
- Nicolet IR Spectrometer with ATR Cell (Thermo Scientific, US)

4.3 Methods

4.3.1 Solution Preparation and Characterisation

4.3.1.1 Solutions Preparation

PCL in Chloroform/Ethanol (7:3;v:v) solutions were prepared according to the previously described solution preparation protocol as detailed in Chapter 3 (p.65).

4.3.1.2 Viscosity and Conductivity Characterisation

Viscosities and conductivities of selected solutions were assessed according to the previously described methods detailed in Chapter 3 (pp.65-66).

4.3.1.3 Gel Permeation Chromatography (GPC) of Poly(ε-caprolactone)

GPC measurements of PCL polymer pellets was performed using an Agilent 1200 series GPC. The GPC was equipped with two PSS gram analytical columns with a molecular weight range of 300-60,000Da (100Å) and 5,000-5,000,000Da (3000Å).

The PCL pellets under investigation were first dissolved in tetrahydrofuran (THF) at a concentration of 1mg/ml. 50 μ l samples of the PCL test solutions were injected at a flow rate of 1 ml/min in columns heated to 40°C with THF used as the eluent. Ready Cal-Kit PMMA standards (800-1,820,000Da) were used to generate a standard curve from which the molecular weight to retention time relationship could be calculated.

4.3.2 Electrospinning of Small Diameter Tubular Scaffolds

In order to prepare small diameter tubular scaffolds, a custom designed and built rotating mandrel system (DCU) was utilised as shown in Figure 4.1 (A). Interchangeable solid copper mandrels with diameters of 6mm were used as the target collectors. The mandrels were rotated at 1600-3200 RPM using a variable speed motor with a custom-built speed controlled unit. The RPM of the collection system was verified prior to testing using a digital tachometer (Farnell, UK). To aid in the uniform deposition of fibres along the length of the mandrel, the collector system was capable of traversing horizontally with respect to the needle tip at a velocity of 0.6m/s and 14cm amplitude. A slip disc mechanism attached to one end of the copper mandrel ensured continuous grounding with respect to the high voltage power supply during rotation. All other components of the system were identical to those used for the spinning of 2D random membranes on flat metallic plates.

In order to remove the electrospun tubular scaffolds from the mandrels without

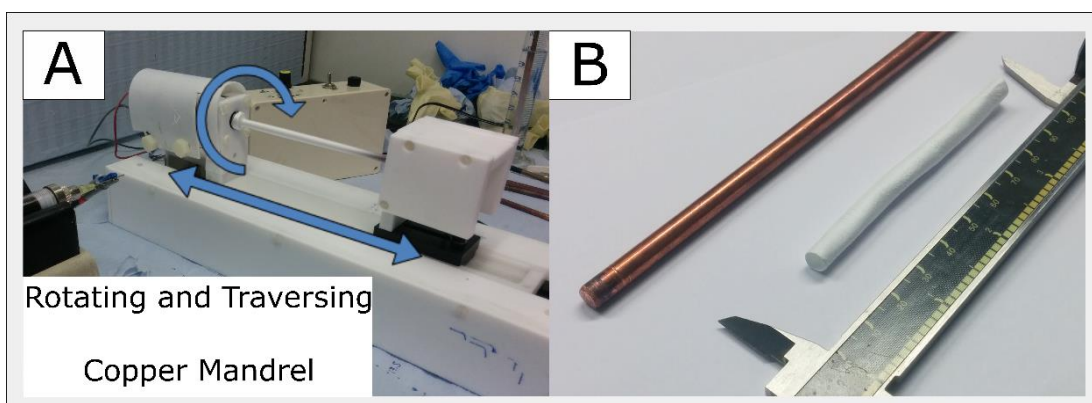


Figure 4.1: Electrospinning of 3D tubular scaffolds (A) Rotating mandrel rig indicating traversing motion and direction of mandrel rotation (B) PCL tubular scaffold removed from copper mandrel after methanol soaking step

damaging the fibre structures, samples were immersed in 100% methanol for 1h post spinning. After this soaking step, samples could be easily detached from the mandrel as shown in Figure 4.1 (B) without any change to sample morphology [267]. The tubular scaffolds were allowed to air dry at room temperature within the fume hood for 72hrs post spinning. Following this, samples were stored in a desiccator prior to further use.

4.3.3 Characterisation of Electrospun Membranes

4.3.3.1 Morphological and Fibre Diameter Analysis

In order to view the inner and outer surfaces on the tubular scaffolds 10mm long ringlet specimens were cut from the tubular scaffolds using a dual blade cutter (Custom, DCU). The ringlets were subsequently cut open along their longitudinal axis to form a flat membrane. Samples of the inner and outer surface were prepared for SEM using the previously described methodology (p.67), and viewed using an EVO LS15 SEM.

4.3.3.2 Uniaxial Tensile Testing – Dogbone Specimens

Uniaxial tensile testing of ‘dogbone’ specimens was performed on the tubular vessels by first cutting and opening the vessels along their longitudinal axis. Samples were subsequently punched from the membrane and tested as previously described in Chapter 3 (p.71).

4.3.3.3 Uniaxial Tensile Testing – Ringlet Specimens

Uniaxial tensile testing is a commonly employed method for evaluating the mechanical properties of materials. Typically, flat dog bone shaped specimens are subjected to a programmed force or a specified strain rate by a tensile test machine. This results in the gradual elongation and eventual failure of the specimen. The force-extension data is monitored and can be used to quantify a number of mechanical properties, such as Young’s modulus and ultimate tensile stress.

Vessels of the vasculature system are, however, known to contain residual stresses within their walls when in a no-load state [36]. When cut open to produce flat dog-bone specimens these stresses are released from the vessel which may in turn alter the

load-extension profiles of the vessel. An adapted uniaxial test method is proposed within ISO 7198 for the testing of tubular vessels such as cardiovascular grafts that represents a loading configuration more typical to that seen *in vivo* [268]. This test method examines the circumferential strength of a vessel as this characteristic can be correlated to a vessels burst strength [269][270]. In this standard tubular specimens, commonly referred to as ‘ringlets’, are placed over two round pins that are subsequently separated by a unidirectional load. This uniaxial ringlet test or hoop test has been used in the characterisation of a number of biological vessels including human coronary arteries [271], the great saphenous vein [272], along with a number of TEBV constructs [273][274].

To prepare samples for testing, ringlet specimens with approximate lengths of 10mm were cut from electrospun tubular scaffolds and hydrated in phosphate buffer solution for 24h at 37°C before testing. The internal and external diameters of the ringlets were then measured on a Mitutoyo light microscope with a toolmakers micrometer. Internal (D_i) and external diameters (D_o) were measured at two orientations orthogonal to each other as indicated in Figure 4.2 (A). An average specimen diameter was then calculated from this and used to calculate the wall thickness (t) of the vessel. The length of the samples (L) as shown in Figure 4.2 (B) are measured using a Vernier callipers and used to calculate the cross sectional area of the sample that resists loading using equation (4.1) [272]. Subsequently the stress within the sample is calculated from equation (4.2).

$$\text{Cross sectional area (A)} = 2 * t * L \quad (4.1)$$

Where, t is the wall thickness of vessel and L = length of sample. To account for two wall segments resisting loading this value is multiplied by two.

$$\sigma = \frac{F}{A} \quad (4.2)$$

Where σ is stress in vessel wall, F is the force within the sample and A is the cross sectional area resisting loading as found from equation (4.1).

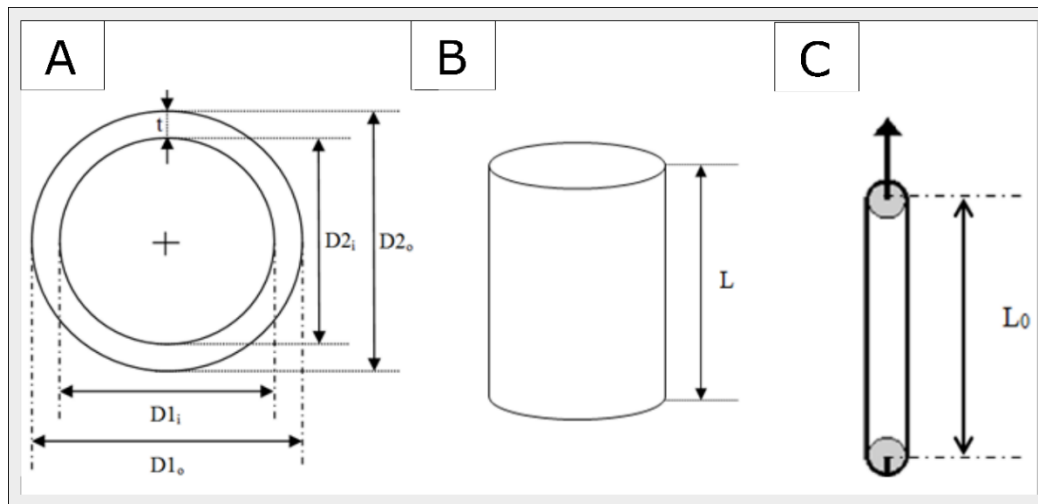


Figure 4.2: Schematic diagrams of ringlet dimensions (A) Internal and external diameters measured at two orthogonal orientations (B) Length of ringlet specimens ‘L’ (C) Configuration of vessel when true gauge length (L_0) of specimen is reached

For this study, uniaxial ringlet testing was conducted on a Zwick Z005 displacement controlled tensile testing machine with a 500N load cell attached. Custom built pin grip fixtures designed according to ISO 7198 specifications were used as shown in Figure 4.3 (A). These grips consisted of 1.5mm \varnothing mounting pins with a centre to centre spacing of 2.5mm before commencement of the test. An adapted testing program based on ISO 7198 and previously described protocols for the testing of vascular vessels was used [275]. Briefly, a pre-load of 0.1N was applied to the specimens in order to remove any slack from the sample. Following this specimens were test to failure at a rate of 10 mm min⁻¹.

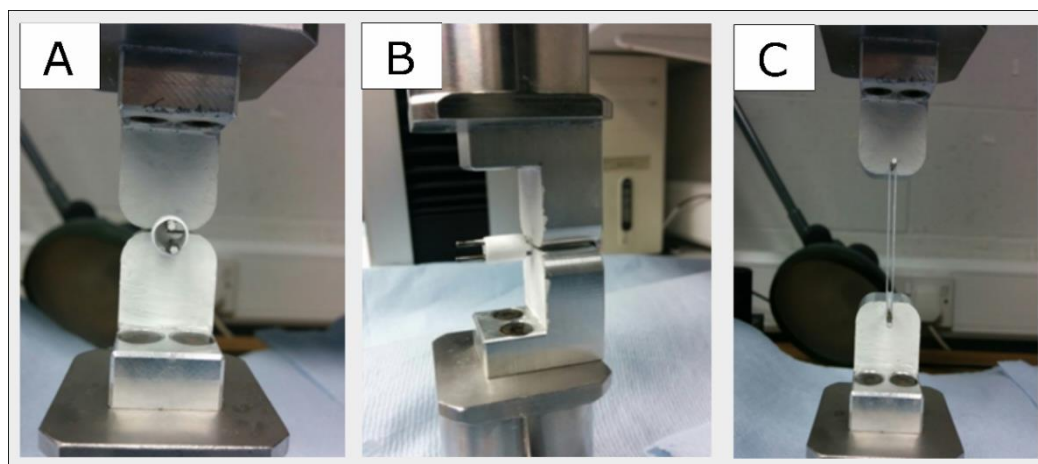


Figure 4.3: Uniaxial ringlet test (A) Sample before testing mounted on extension pins (B) Schematic of gauge length (L_0) used in post processing of tensile data (C) Sample of image after testing

The gauge length (L_0) of the sample was determined to be the distance between the centre to centre of the loading pins when the vessel walls aligned to the configuration shown in Figure 4.2 (C). In this configuration, the vessel walls are aligned parallel to the direction of loading without any change to the overall perimeter length of the vessel compared to its non-loaded state. This ensured that no strain due to the alignment of the vessel walls was included within the tensile responses but rather solely the strain due to the deformation of the specimen. Typically the application of the pre-load accounts for this unwanted strain region but due to the complex and wide array of vessel structures under investigation, no single pre-load value could be applied that ensured all specimens were in the proper configuration before testing. To counteract this, the theoretical L_0 for each specimen was manually calculated following testing based upon the measured dimensions recorded. Using this information the initial strain region experienced before the theoretical gauge length was removed from the loading cycle and the remainder of the strain cycle normalised to a starting point of 0% strain. The measured force at this point remained unchanged.

This method of normalising the strain to the initial theoretical gauge length was verified as part of an initial test method development study. In this study, a video extensometer attached to the tensile test machine was used to correlate the loading profile of the sample to the corresponding specimen configuration via time series analysis. The full details of this development study can be found in Appendix C. The summarised finding of this study is represented in Figure 4.4. Here it can be observed that an initial toe region is observed within the stress-strain response curve. This toe occurred not due to a true deformation of the test specimen, but rather due to a reconfiguration of the specimen geometry upon loading. This reconfiguration element of the stress-strain response curve is represented in region 1 of the profile. A stress stiffening effect was found to occur within the vessel with this being correlated to the point at which the theoretical gauge length was achieved, represented by the transition at region 2. After this, the specimen was elongated until yielding (region 3) and finally failure of the specimen occurred (region 4). Failure to remove this initial toe region results in an inaccurate representation of the stress-strain profile and subsequently inaccurate Young's modulus and strain at break measurements.

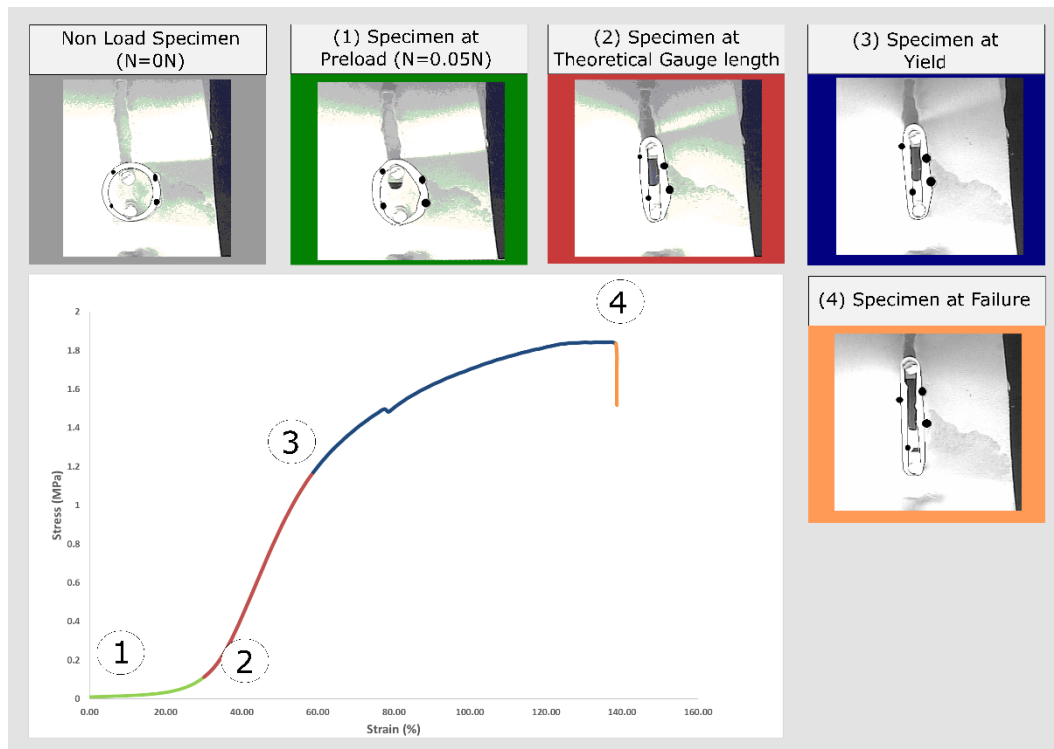


Figure 4.4: Stress vs strain profile of electrospun ringlet specimen showing distinct loading stages with corresponding specimen configurations as verified by video extensometer. Region (1) shows sample after pre-load with walls of ringlet in a non-parallel configuration resulting in a large strain for a small applied load. Region (2) shows an increased stress response with the video extensometer confirming the specimen has reached its theoretical gauge length point. Region (3) shows yielding of sample. Region (4) showing specimen failure. It is noted that enhanced outlines have been added to the samples to aid in image clarity

Figure 4.5 shows a typical stress-strain profile of electrospun ringlet specimen with the initial toe region removed and strain normalised to the point at which the theoretical gauge length is achieved. It was also desired to assess the stiffening response of vessels without considering the cross sectional area of the test specimens due to the highly complex and porous nature of the fibrous scaffolds. The ‘ring modulus’ response of the vessels was calculated based upon the pure force vs strain data obtained from the test cycle, with the modulus calculated from the gradient of the linear response section of the force vs strain curve. This can be viewed as a property of the structure rather than an intrinsic material property.

4.3.3.4 Static Compliance Testing

Static compliance testing of electrospun tubular specimens was conducted in accordance with ISO 7198 using a custom-built fixture as shown in Figure 4.6 (A).

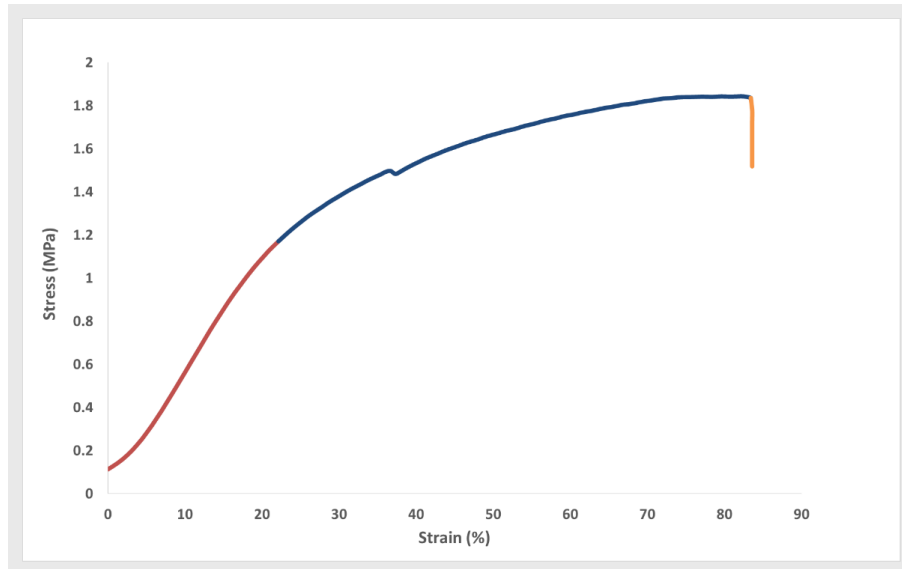


Figure 4.5: Stress vs strain response of electrospun ringlet specimen with initial toe region removed and strain normalised to theoretical gauge length point. It is observed that the strain response is significantly altered, compared to that of the non-normalised response as seen in Figure 4.4 indicating the importance of this method for the calculation of Young's modulus and strain at break.

The test fixture consisted of a test chamber for the mounting of vessels, where one luer connection was attached to an extension device controlled by a micrometre stage system. An inflater device was used to pressurise the closed system after flushing with deionised water. Due to the porous nature of electrospun specimens they often required a method to seal their pores in order to prevent fluid leakage under pressurisation. Based upon the indications of ISO 7198, tubular latex membranes (Figure 4.6 (B)) of significantly higher compliance were used as an intermediate barrier layer between the fluid and the electrospun specimen wall (Figure 4.6 (C)). Using these latex membranes appropriate pressurisation of the vessel can be achieved without fluid loss. The latex membranes were made using a latex dipping method in which 5mm diameter stainless mandrels were twice dipped into a liquid latex solution and allowed to air dry (Kryolan,UK). The latex membranes could be subsequently removed from the mandrel by covering in talcum powder and inverting the membrane.

In order to ensure the latex balloons were of an appropriately higher compliance than the test specimen, uniaxial ringlet tensile testing (n=10) and static compliance testing (n=5) was performed and compared to a sample electrospun tubular vessel. The results of this experiment can be found in Appendix D. In brief, it was found that the latex

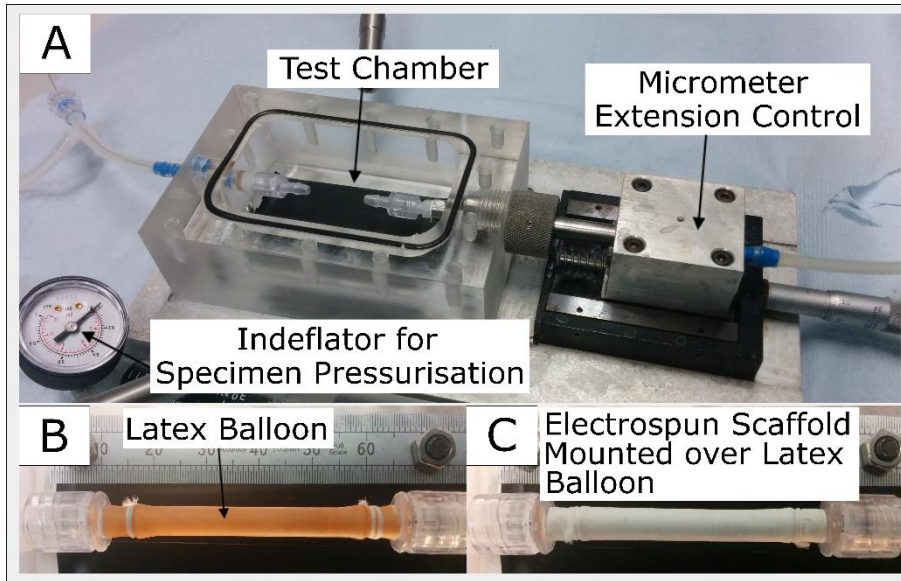


Figure 4.6: Static compliance test (A) Test rig showing sample chamber attached to inflator device used to control the pressurisation of samples. An attached extension device controlled by a micrometer allows for the controlled strain of samples (B) Latex membrane used to prevent fluid leakage through wall of electrospun scaffolds (C) Electrospun sample mounted over latex balloon

membranes exhibited considerably lower Young's modulus characteristics compared to the electrospun tubular specimen and also was found to demonstrate a significantly higher compliance rate when pressurised, compared to that of the combined electrospun specimen and latex membrane test method. This ensures that the tubular electrospun specimen experiences the complete pressurisation effect and resists the loading forces exhibited.

Compliance of the scaffolds was assessed by increasing the pressure with the vessels from 0 to 750mmHg in controlled increments as shown in Figure 4.7. Image J analysis was used to measure the diameter of the vessel at 3 points providing an average diameter measurement for each pressurisation level. Using this information compliance of the vessel was calculated from the Equation 4.3 below:

$$\text{Compliance} = \frac{D_s - D_d}{D_d(P_s - P_d)} \times 10^4 \quad \%mmHg^{-1} \times 10^{-2} \quad (4.3)$$

Where, D_s and D_d are systolic and diastolic external diameters, and P_s and P_d are the systolic and diastolic pressures. In this test, P_s and P_d is maintained at 105 and

30mmHg respectively. This pressure range was selected as to provide an appropriate comparison to the work detailed by Tai *et al.* that explored the compliance properties of typical conduits used within in vascular reconstruction surgeries over a pressure range of 30mmHg to 100mmHg [42].

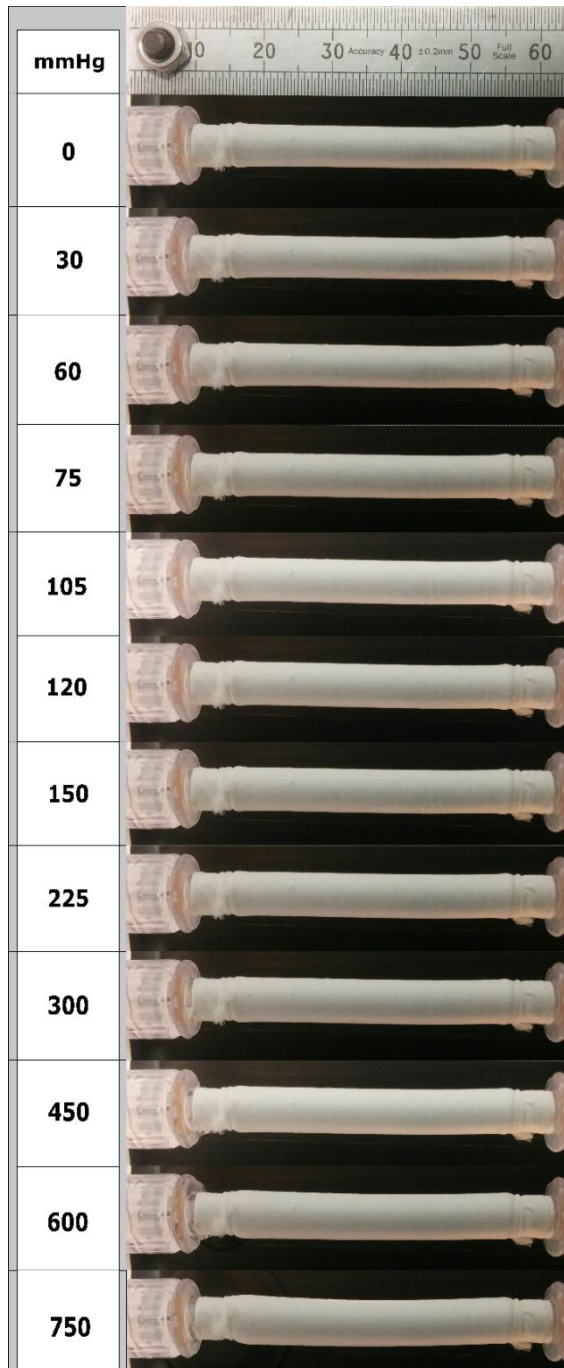


Figure 4.7: Static compliance test of electrospun tubular vessel showing a sample specimen pressurised at predetermined intervals ranging from 0 to 750mmHg. Image J analysis used to determine average sample diameter based upon three diameters taken along length of sample

4.3.3.5 XRD of Electrospun Membranes

X-ray diffraction was performed on select electrospun vessels using a Brüker D8 Advance X-ray Diffractometer to determine crystallinity of the fibrous structures. Vessels were prepared by first cutting them open along their longitudinal axis and flattening to form a membrane. A blank scan of the glass slides and double-sided adhesive tape was made prior to measurement to provide a baseline scan. Scanning was performed over a 2θ range of 10 to 60° , in 0.05° increments at a scan rate of 1° per minute. It is noted that the baseline scans were not removed from the scan profiles but rather used in conjunction with the measured profile.

4.3.3.6 Porosity

Sample porosity was quantified using the previously described liquid intrusion technique as detailed in Chapter 3 (pp.70-71). A slight variation of this method was the geometry of the test specimens used. For this test, ringlet specimens of 10mm in length were cut from the tubular scaffold of interest using a dual blade cutter. The ringlets were dimensioned with a light microscope and Vernier callipers as previously described within the uniaxial tensile testing of ringlet specimens.

4.3.3.7 Statistical Analysis

Numerical data is presented as mean \pm standard deviation (S.D). Where data was determined to comply with the relevant assumptions of a parametric analysis, 2 sample t-test was conducted for the comparison of pair wise samples. For the comparison of multiple samples one and two-way analysis of variance (ANOVA) were conducted where appropriate. Subsequent multiple comparisons were made using the Sidak correction test. The level of statistical significance was set to $p < 0.05$. Where data was found to violate the assumptions of an ANOVA analysis, most notably equal variance amongst groups (by Bartlett's statistic), non-parametric analysis was conducted. Mann-Whitney test was employed for 2-sample comparison, while Kruskal-Wallis analysis with subsequent Dunn Correction was utilised for multiple comparisons. Regression analysis was conducted using the statistical software package Minitab 17.

4.4 Design of Studies

4.4.1 Regression Analysis of Multi-modal Electrospinning Process

Based upon the results of the initial solution screening trial performed in Chapter 3, 16wt% PCL in Chloroform/Ethanol (7:3;v:v) was identified as the choice solution combination for the development of the inner ‘core’ layer of the bi-layer scaffold. This solution combination offers the potential to create scaffolds with hybrid fibre diameter populations that offer increased pore volumes for cell infiltration while providing nano diameter fibres for cell attachment and guidance [196]. In order to establish the effects of a number of processing parameters on the mechanical and morphological attributes of scaffolds created by multi-modal spinning approaches, a factorial regression analysis was conducted. Regression analysis provides a method to obtain a first order approximation for the dependence of output responses on corresponding input parameters, through the systematic and randomised variation of factor combinations referred to as ‘treatments’ [276]. The parameter ranges selected for this study were based upon previously identified boundary conditions, and chosen to provide the minimum and maximum limits for each parameter identified. It is however noted that due to the complex interactions of parameters in electrospinning, it could not be said with certainty that scaffolds could be successfully produced at all treatment levels studied. Due to this, it was decided that an orthogonal design was to be maintained throughout the analysis, which may require the loss of particular parameter levels if they do not yield suitable samples for all treatments studied.

The tubular scaffolds were prepared according to the previously described electrospinning protocol for the preparation of small diameter tubular scaffolds using a poly(ϵ -caprolactone) with an average molecular weight (M_w) of 80,000 g/mol (Sigma Aldrich, USA). Table 4.1 details the parameters and their associated levels selected for study in this investigation. Briefly, four main processing variables were identified for analysis; solution flow rate, applied voltage, tip to collector distance and the rotational speed of the collection mandrel. Three scaffolds were prepared for each of the parameter combinations identified, to provide appropriate replicate measurements to assess process variation. Uniaxial ringlet tensile testing and liquid intrusion porosity were conducted on specimens harvested from the tubular scaffolds.

Table 4.1: Processing parameters under investigation as part of the multi-modal spinning DOE with corresponding levels for each working parameter

	Parameter	Unit	Level	Level	Level	Level 4
			1	2	3	4
X ₁	Flow rate (Q)	mL/hr	4	8	12	-
X ₂	Applied Voltage (V)	kV	10	15	20	-
X ₃	Distance (D)	cm	15	17.5	20	22.5
X ₄	Collection Speed (S)	RPM	1600	3200	-	-

Three ringlet specimens (n=3) were taken from each of the tubular scaffolds in order to determine vessel homogeneity along its length for each of the characterisation tests method investigated. An average representative value for the scaffold was in turn calculated based on the corresponding results. SEM analysis was also performed according to the previously described protocol with a sample of the inner and outer surface of the tubular scaffolds viewed, with corresponding fibre diameters (n=30) and orientations assessed. In total 72 unique factor combinations ‘treatments’ were investigated as part of this regression analysis with three replicates per combination, giving 216 observations as outlined in Table 4.2. Table 4.3 details the subsequent responses variables (Ys) assessed as part of the analysis which includes the ultimate tensile strength, Young’s modulus, porosity, average fibre diameters, and fibre orientation (coherency) for each treatment level.

Linear regression analysis of the multi-modal electrospinning process was performed using the statistical software Minitab. In the modelling approach employed, the role of each input parameter and corresponding interactions was normalized to a standardised ranking system. Normalising parameters in this manner allows for the immediate relative importance of each parameter to be compared through the determination and comparison of the corresponding t-value [276]. In order to reduce the complexity of the regression model a stepwise elimination method was utilised to remove non-significant terms. Stepwise elimination works upon the principle of removing a non-significant term from the model based upon a statistical significance threshold level. The significance threshold level was selected to be p=0.05 for all the models under investigation in this work. If a parameter was found to have a p-value

Table 4.2: Design matrix for the regression analysis of multimodal electrospinning process utilising 16wt% Chloroform/Ethanol (7:3) solutions

<i>Parameters</i>													
Mandrel Speed (RPM)	1600RPM						3200RPM						
Spin time (min)	20												
Flow rate (ml/hr)	4												
Voltage (kV)	10						15						20
Distance (cm)	15	17.5	20	22.5	15	17.5	20	22.5	15	17.5	20	22.5	
Spin time (min)	20												
Flow rate (ml/hr)	8												
Voltage (kV)	10						15						20
Distance (cm)	15	17.5	20	22.5	15	17.5	20	22.5	15	17.5	20	22.5	
Spin time (min)	20												
Flow rate (ml/hr)	12												
Voltage (kV)	10						15						20
Distance (cm)	15	17.5	20	22.5	15	17.5	20	22.5	15	17.5	20	22.5	

higher than this threshold level it was removed from the model. This corresponds to the parameter having a non-significant effect on the regression model. After the removal of the term, the model was subsequently reevaluated and the next parameter/interaction examined for significance. This method continued until all non-significant terms were eliminated. It is noted that a non-hierarchical model was deemed acceptable for this work in order to reduce unnecessary terms to prevent over fitting of the model from occurring. For each of the terms found to be significant a coefficient value was assigned to the term that was used to calculate its effect on the output response variable.

The coefficient of determination or ‘R²’ was also calculated for the corresponding models in order to assess the quality of the fitted model to the data [277]. In addition the R² (adj) was calculated in order to determine the fit of the model independent of the number of predictor terms included within it. This is again important when assessing if a model has become over fitted. Similarly the R² (pred) term was calculated to determine the capability of the model to accurately predict new observations not currently included in the model. Using these values a true estimation of the model power could be determined. Main effects and interaction plots were generated to allow for the visual assessment of output responses to the corresponding input parameters and their interactions.

Table 4.3: Response properties of scaffolds (Ys) assessed as part of multi-modal electrospinning regression analysis

	Response	Unit	Abbreviation
Y ₁	Ultimate Tensile Strength	MPa	UTS
Y ₂	Young’s Modulus	MPa	YM
Y ₃	Max Force	N	MF
Y ₄	Ring Modulus	N/%	RM
Y ₅	Porosity	%	PO
Y ₆	Mean Inner Fibre Diameter	µm	IFD
Y ₇	Mean Outer Fibre Diameter	µm	OFD
Y ₈	Inner Fibre Coherency (0-1)	-	IC
Y ₉	Outer Fibre Coherency (0-1)	-	OC

4.4.2 Control of Molecular Weight Variation between PCL Batches through the Matching of Solution Viscosities

Polymers prepared by synthetic means including poly(ϵ -caprolactone) are often prone to experiencing variations in molecular chain characteristics depending on the synthesis pathway used and the precision of the reaction process itself [278]. While raw polymer materials are typically supplied with an average molecular weight characteristic, they often have varying chain lengths reflected by their poly dispersity index (PDI), and may also present different molecular weight distribution patterns [279]. These variations in molecular weight characteristics can result in significant changes to the polymers electrospinning potential, due to the processes high dependence on the viscoelastic properties of the prepared solutions. This can result in polymers forming different electrospun structures despite possessing equivalent average molecular weight characteristics [280].

Two batches of the polymer PCL were purchased as part of this work from Sigma Aldrich, both having a molecular weight of $M_w = 80,000$ g/mol. The first batch of PCL (#00807DJ), referred to as the ‘original’ PCL batch for future reference, was heavily utilised in initial experiments including the solution screening trial, the multimodal polymer concentration study and the regression analysis of the multimodal spinning process. During the course of the final experiments surrounding the preparation of the core layer of the bi-layer scaffold, the second PCL batch (#MKBV3325V), referred to as the ‘new’ batch, was utilised due to constraints surrounding the continued availability of the original PCL material. Solutions prepared using the new PCL batch at a concentration level of 16wt%, were observed to have significantly different viscosity attributes compared to those prepared using the original PCL for the same wt% level. This in turn resulted in a radically altered electrospinning process, with no spinning possible due to the highly viscous nature of the prepared solutions. Due to this observation it was suspected that the supplied PCL batches may have possessed dissimilar molecular weight properties despite being supplied as an equivalent material. In order to establish the molecular weight characteristics of the two PCL batches, GPC was performed according to previously described method (pp.116-117).

Due to the significant variation of viscosity between the two PCL batches for a set wt% concentration level, an alternative method was required in order to establish equivalent solutions for electrospinning. One technique considered for the control of molecular weight variation between PCL batches, was to directly match solution viscosity rather than using equivalent concentrations [263]. In order to achieve this, a series of solutions with varying concentrations were prepared using the new PCL batch. The solutions were prepared as per Table 4.4, to provide an appropriate comparison range to the previously obtained viscosity data for the original PCL batch. The viscosity and conductivity properties of each concentration level were measured and the corresponding curve generate was compared to the previously obtained viscosity curve for the original PCL batch (as found in Chapter 3 (p.92)). Based on these results an interpolation was used to identify a polymer concentration level that yielded a comparative viscosity to that of an original 16wt% solution at 495.8 ± 4.3 mPa.s. To confirm the suitability of the selected concentration, 3 solutions were prepared and corresponding viscosity and conductivity was statistically compared to the original 16wt% solution.

4.4.2.1 Assessment of Mechanical Response Variation between PCL Batches and Fabrication of Vessels with Optimal Compliance Characteristics

Based upon the results of the viscosity comparison study, a 7.8wt% PCL solution was found to provide an appropriate viscosity value comparable to that of the original 16wt% solutions. In order to assess any resulting variation in the mechanical responses of electrospun vessels prepared using these alternative PCL batches, a comparison study was performed. As part of this two parameter combinations were identified from the multimodal regression study and specimens prepared using the original and new PCL batches. These parameter combinations were chosen based on yielding UTS and YM properties comparable to that of common conduits used in arterial bypass applications (Table 4.5). Mechanical assessment was performed through both uniaxial ringlet and dogbone test methods as previously described. This dual mechanical comparison was performed in order to identify any variation that may be imparted due to the test method selected and to provide further assessment of the uniaxial ringlet test method. Five tubular specimens were prepared at each of the parameter combinations for both the original and new PCL batches.

Table 4.4: Polymer concentration levels used to generate viscosity profile for comparison to original PCL batch

PCL Batch	Polymer Concentration (wt%)
#MKBV3325V “new batch”	5
	6
	6.5
	7.5
	8.5
	9
	10
	14

Porosity of the specimens was assessed according to the previously described liquid intrusion method (p.126), and morphology and fibre diameters assessed by SEM analysis. X-ray diffraction (XRD) analysis was performed on the specimens created at the maximum collection time for Set 1 & 2 using both the original and new PCL batches in order to examine any potential changes in crystallinity due to the molecular weight variation. In addition to assessing the variation of mechanical responses within changing PCL batches, the ability to further tune compliance characteristics of the tubular scaffolds prepared using the new PCL batch was assessed. As part of this, static compliance testing was conducted according to the previously described protocol for each of the parameter sets and their corresponding collection time variations (n=6). Subsequent comparisons of compliance properties were made to common vessels used in arterial bypass procedures as adapted from Tai *et al.* [42].

Table 4.5: Parameter combinations identified for comparison of 16wt% solutions prepared with original PCL batch to 7.8wt% solutions prepared using new PCL batch

Parameter	Flow Rate	Applied	Tip-Collector	Mandrel	Collection Time		
Set No.	(ml/hr)	Voltage (kV)	Distance (cm)	Speed (RPM)	(min)		
<u>Set 1</u>	12	20	17.5	3200	10	20	40
<u>Set 2</u>	4	15	17.5	3200	20	40	60

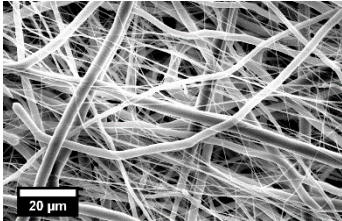
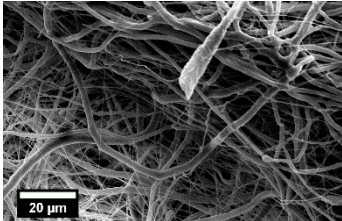
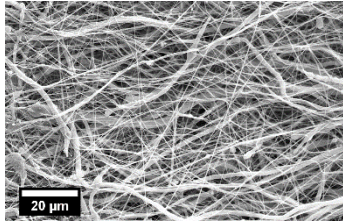
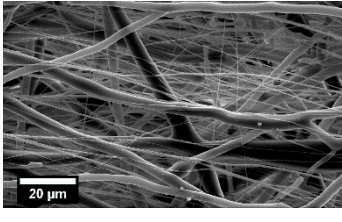
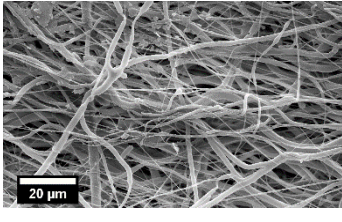
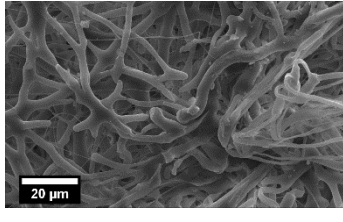
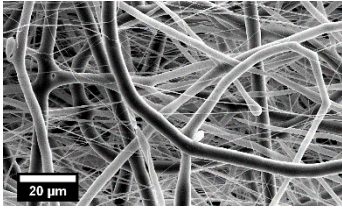
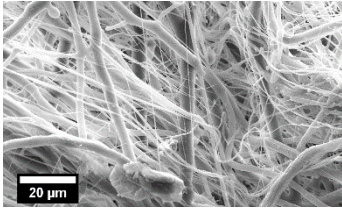
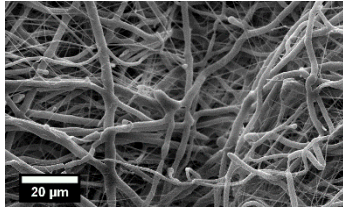
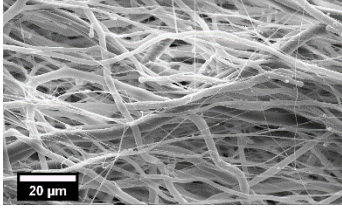
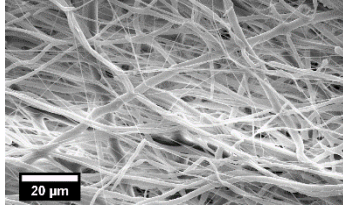
4.5 Results

4.5.1 Regression Analysis of Multimodal Rotating Mandrel Electrospinning Process

While completing the regression analysis of the multimodal electrospinning process, it was observed that specimens could not be prepared at all of the parameter combinations under investigation. Particular parameter interactions including that of the lower boundary voltage of 10kV's, combined with the increased flow rates of 8 and 12ml/hr, resulted in excessive 'electrospitting' (uncontrolled repulsion of liquid polymer droplets) and material aggregation at the spinneret tip. This electrospitting and material aggregation prevented successful sample collection, with wet polymer deposition observed to occur directly on the collection mandrel or limited deposition of fibrous material due to the blockage of the spinneret tip respectively. Specimens created at the collector distances of 20cm or greater were often difficult to remove from the mandrel following the methanol-soaking step. The increased collector distance of 22.5cm paired with a flow rate of 4ml/hr resulted in such poor spinning that no samples could be removed from the mandrel intact.

It was also noted that when spinning at the increased voltages of 15 and 20kV, increased splaying effects occurred at the spinneret tip with an increased number of visible jets emerging from the Taylor's cone. A portion of specimens created at these voltages were also found to possess irregular surface topographies, with small ridges present on the surface of the tubular scaffolds. It was observed that increasing the applied voltage typically resulted in more distinct ridges upon the surfaces of the specimens. Some areas of fibre merging were also visible at the decreased collection distance of 10cm, again particularly prevalent at increased flow rates. SEM results of specimens successfully spun during the regression analysis can be found in Tables E.1 and E.2 of Appendix E, with E.1 showing samples produced at the lower mandrel speed of 1600 RPM and Table E.2 at a mandrel speed of 3200 RPM. A sample selection of specimens obtained at a collector distance of 17.5cm over the flow rate of 4-12ml/hr and applied voltage range of 10-20kV can be seen in Table 4.6. The complete SEM results for one experimental replicate can be found in Table E.1 (1600 RPM specimens) and Table E.2 (3200 RPM specimens) of Appendix E.

Table 4.6: Sample images of specimens obtained from the regression analysis of the multimodal electrospinning process. Specimens were produced over the flow rate range of 4-12ml/hr, applied voltage range of 10-20kV and a collection distance of 17.5cm

Flow Rate: 4ml/hr			
Applied Voltage			
10kV	15kV	20kV	
1600 RPM			
			
3200 RPM			
			
<hr/>			
Flow Rate: 8ml/hr			
Applied Voltage			
10kV	15kV	20kV	
1600 RPM			
			
3200 RPM			
No Specimen Collected			

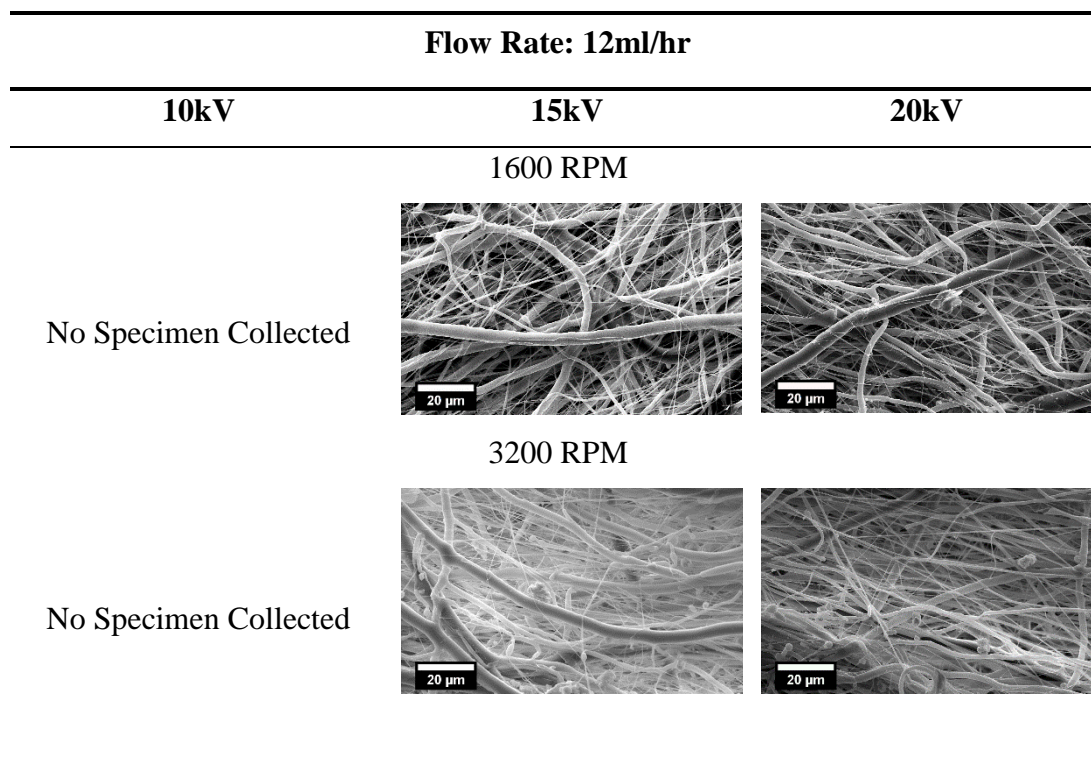


Figure 4.8 shows a typical stress-strain profile obtained for the uniaxial ringlet tensile testing of the PCL tubular scaffolds. Figure 4.8 (A) shows the response of three scaffolds created at a flow rate of 4ml/hr, applied voltage of 15kV, collector distance of 17.5cm and a rotational mandrel speed of 1600RPM. Figure 4.8 (B) similarly shows three scaffolds created at an identical flow rate, applied voltage and collector distance but with the increased rotational mandrel speed of 3200 RPM. Again, it is noted that each of the scaffold profiles is comprised of the average tensile data and subsequent deviations of three ringlet specimens taken from various positions along the length of the scaffold. From these profiles, it can be seen that specimens created at the increased mandrel speed of 3200RPM displayed greater deviation in their mechanical properties both within the sample itself and between specimens. This was a common observation for all the tubular scaffolds assessed within the study. Specimens were also found to fail at varying strain levels. This was attributed to the complex and varying ways in which the samples failed. This included the rapid fracturing of the specimens, the gradual failure of the sample wall and delamination of layers in certain instances. Typically this delamination effect was observed to occur in samples with larger wall thicknesses.

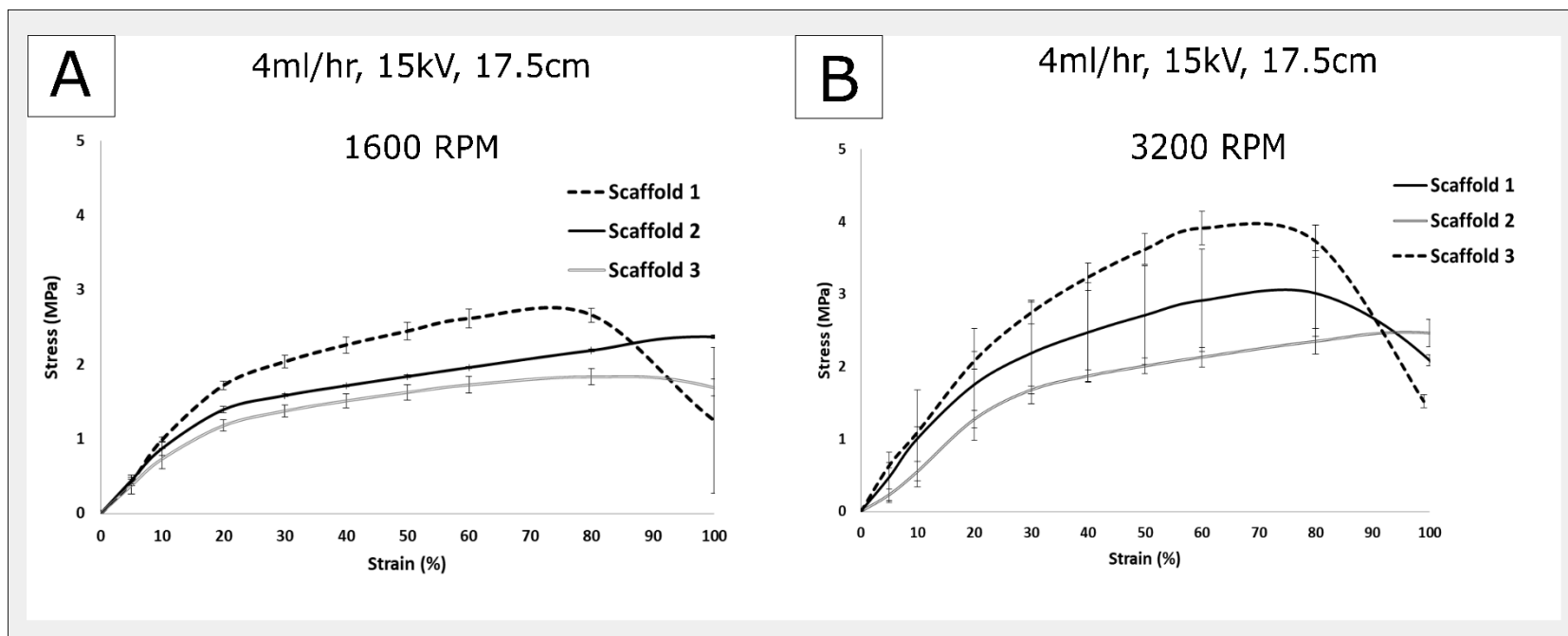


Figure 4.8: Stress strain profiles obtained from uniaxial ringlet testing of tubular specimens created at a flow rate of 4ml/hr, applied voltage of 15kV and collection distance of 15cm prepared as part of the linear regression analysis study (A) Replicate specimens created at the lower mandrel rotational speed of 1600 RPM (B) Replicate specimens created at the higher mandrel rotational speed of 3200 RPM. N=3 per scaffold.

4.5.1.1 Analysis of Response Variables (Ys) to Input Parameters (Xs)

Mechanical Response Variables

Due to the loss of samples at particular parameter interactions, the original regression design matrix was adjusted to account for the specimen loss. This required the removal of the 10kV voltage level and the collector distance of 22.5cm across the entire matrix. These level removals were required in order to ensure an orthogonal design with equal sample sizes was maintained throughout the study. The adjusted design matrix levels are subsequently detailed in Table 4.7, yielding a total number of treatments at 36, with 108 observations made. The full results of the regression trial can be found in Appendix E, where Table E.3 and Table E.4 shows the mechanical and morphological results for specimens produced at the collection speed of 1600RPM. Table E.5 and Table E.6 subsequently show the mechanical and morphological results of specimens produced at the collection speed of 3200 RPM.

Table 4.8 shows the tabulated results of the modelling analysis performed for the vessel ‘UTS’ or regression variable Y_1 . Here the modelling coefficients for the full model can be viewed, along with the reduced model terms identified based on a significance value threshold of $p < 0.05$. A number of parameters were found to have a significant effect in predicting the UTS properties of the vessels. Based upon the calculated t-values, the most significant parameter for determining the UTS property of the vessel was the rotational speed of the collection mandrel. An increase in rotational speed was found to result in higher UTS properties, with vessels possessing an average of ~1.9 MPa at 1600 RPM and ~2.4 MPa at 3200 RPM as shown in the corresponding main effects and interactions plot (Figure 4.9). The collector distance

Table 4.7: Adjusted parameter range for multi-modal spinning trial to account for loss of samples ensuring orthogonality of study

	Parameter	Unit	Level	Level	Level
			1	2	3
X ₁	Flow rate (Q)	mL/hr	4	8	12
X ₂	Applied Voltage (V)	kV	15	20	-
X ₃	Distance (D)	cm	15	17.5	20
X ₄	Collection Speed (S)	RPM	1600	3200	-

was also found to be a significant variable for determining UTS with an increase in collector distance found to result in falling UTS properties with ~2.3 MPa at 15cm and ~2 MPa at 20cm. A number of interactions were also found to effect the UTS including the gross interaction of the four input variables ($X_1 * X_2 * X_3 * X_4$) along with the interaction of the flow rate and collection distance ($X_1 * X_4$). The effect of flow rate and applied voltage were found to be non-significant in the model although a slight

Table 4.8: Full Model vs. Reduced Model in Coded Variables for Output Variable Y_1 ‘UTS’ Obtained by dropping All Terms with $p > 0.05$

	Main Effect/ Interaction	p	Coefficients Full Model	t-Value	Keep/ Drop	Coefficients in Reduced Model	Significance Rank
1	Constant	0.000	2.1861	91.51	Keep	2.1861	(0)
2	X_1	0.016	-0.0720	-2.46	Keep	-0.0720	6,7
3	X_2	0.652	-0.0108	-0.45	Drop	-	
4	X_3	0.000	-0.1426	-4.87	Keep	-0.1426	2
5	X_4	0.000	0.2190	9.17	Keep	0.2190	1
6	$X_1 * X_2$	0.043	0.0600	2.05	Keep	0.0600	9
7	$X_1 * X_3$	0.000	-0.1341	-3.74	Keep	-0.1341	4
8	$X_1 * X_4$	0.034	-0.0630	-2.15	Keep	-0.0630	8
9	$X_2 * X_3$	0.051	-0.0578	-1.97	Drop	-	
10	$X_2 * X_4$	0.009	-0.0635	-2.66	Keep	-0.0635	5
11	$X_3 * X_4$	0.339	-0.281	-0.96	Drop	-	
12	$X_1 * X_2 * X_3$	0.016	0.0882	2.46	Keep	0.0882	6,7
13	$X_1 * X_2 * X_4$	0.483	0.0206	0.70	Drop	-	
14	$X_1 * X_3 * X_4$	0.220	-0.0442	-1.23	Drop	-	
15	$X_2 * X_3 * X_4$	0.081	-0.0517	-1.77	Drop	-	
16	$X_1 * X_2 * X_3 * X_4$	0.000	0.1578	4.40	Keep	0.1578	3
17	Block	0.859	N/A	-	Drop	-	
	S		R-Sq		R-Sq (adj)		R-Sq (pred)
Full	0.248262		66.10%		60.57%		53.02%
Reduced	0.253481		62.36%		58.90%		53.79%

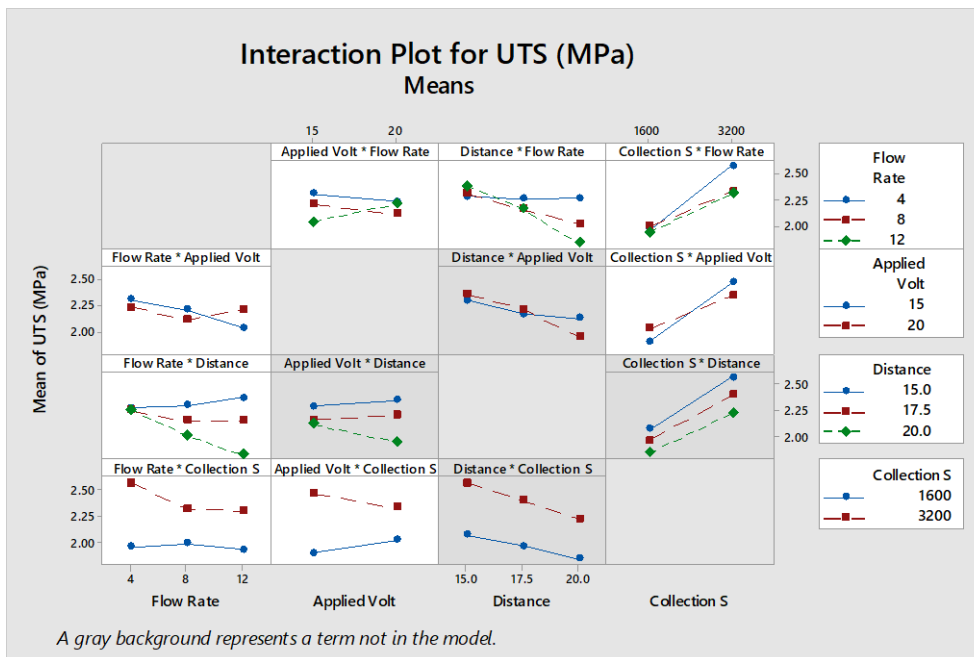
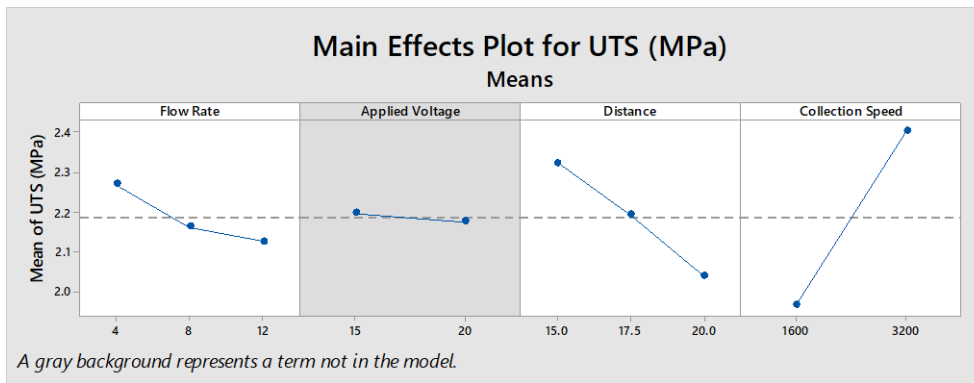


Figure 4.9: Main effects and interaction plot for the regression variable ‘UTS (Y_1)’ showing the effects of changing input variable levels to the response variable of interest. Greyed backgrounds represent a term or interaction not included within the reduced model used to predict the output response.

decrease in UTS was observed with decreasing flow rate. The R-sq and R-sq (pred) values of the reduced model were found to be 62.36% and 53.79% respectively. An S value of 0.25 MPa was calculated for the model accounting for ~11% variation based upon the UTS coefficient at 2.1861 MPa. Appendix F shows the complete collection of residual plots for the regression analysis.

Overall the UTS is predicted through the equation, where the variables Q=Flow Rate, V=Applied Voltage, D=Collector Distance and S=Collection Speed. These variables represent the levels of the corresponding variable under investigation expressed in

$$UTS = 2.1861 - (0.720 * Q) - (0.1426 * D) + (0.2190 * S) + (0.0600 * Q * V) - (0.1341 * Q * D) - (0.0630 * Q * S) - (0.0635 * V * S) + (0.0882 * Q * V * D) + (0.1578 * Q * V * D * S) \quad (4.4)$$

terms of coded units.

Table 4.9: Full Model vs. Reduced Model in Coded Variables for Output Variable Y_2 'YM' Obtained by dropping All Terms With $p > 0.05$

	Main Effect/ Interaction	p	Coefficients Full Model	t-Value	Keep/ Drop	Coefficients in Reduced Model	Significance Rank
1	Constant	0.000	6.5767	97.02	Keep	6.5767	(0)
2	X ₁	0.000	-0.6246	-7.52	Keep	-0.6246	3
3	X ₂	0.294	0.0716	1.06	Drop	-	
4	X ₃	0.000	0.7961	9.59	Keep	0.7961	1
5	X ₄	0.000	0.5187	7.65	Keep	0.5187	2
6	X ₁ * X ₂	0.017	0.2018	2.43	Keep	0.2018	7
7	X ₁ * X ₃	0.490	-0.071	-0.69	Drop	-	
8	X ₁ * X ₄	0.779	-0.0234	-0.28	Drop	-	
9	X ₂ * X ₃	0.495	-0.0569	-0.69	Drop	-	
10	X ₂ * X ₄	0.400	0.0574	0.85	Drop	-	
11	X ₃ * X ₄	0.000	0.3266	3.93	Keep	0.3266	4
12	X ₁ * X ₂ * X ₃	0.005	0.294	2.90	Keep	0.294	6
13	X ₁ * X ₂ * X ₄	0.407	0.0692	0.83	Drop	-	
14	X ₁ * X ₃ * X ₄	0.063	-0.191	-1.88	Drop	-	
15	X ₂ * X ₃ * X ₄	0.252	-0.0957	-1.15	Keep	-0.0957	8
16	X ₁ * X ₂ * X ₃ *X ₄	0.003	0.312	3.07	Keep	0.312	5
17	Block	0.679	N/A	-	Drop	-	
	S		R-Sq		R-Sq (adj)		R-Sq (pred)
Full	0.704448		73.47%		69.14%		62.36%
Reduced	0.705949		71.04%		69.01%		65.71%

Table 4.9 shows the tabulated results of the modelling analysis performed for the Young's modulus of the vessels or the regression variable 'Y₂'. For this term, collector distance was found to be the most significant input variable for determining YM with an increase from ~5.7 MPa to ~7.4 MPa with an increase in collection distance over 15 to 20 cm. Following this, the rotational speed of the mandrel was also found to be the next significant with an increase in YM observed as the speed increased from 1600 (~6.0 MPa) to 3200 RPM (~7.1 MPa) (Figure 4.10). The reduced model had an overall R-sq of 71.04% and a predictive R-sq of 65.71%. An S value at ~0.705 MPa again accounted for ~11% variation based upon the YM coefficient at 6.5767 MPa.

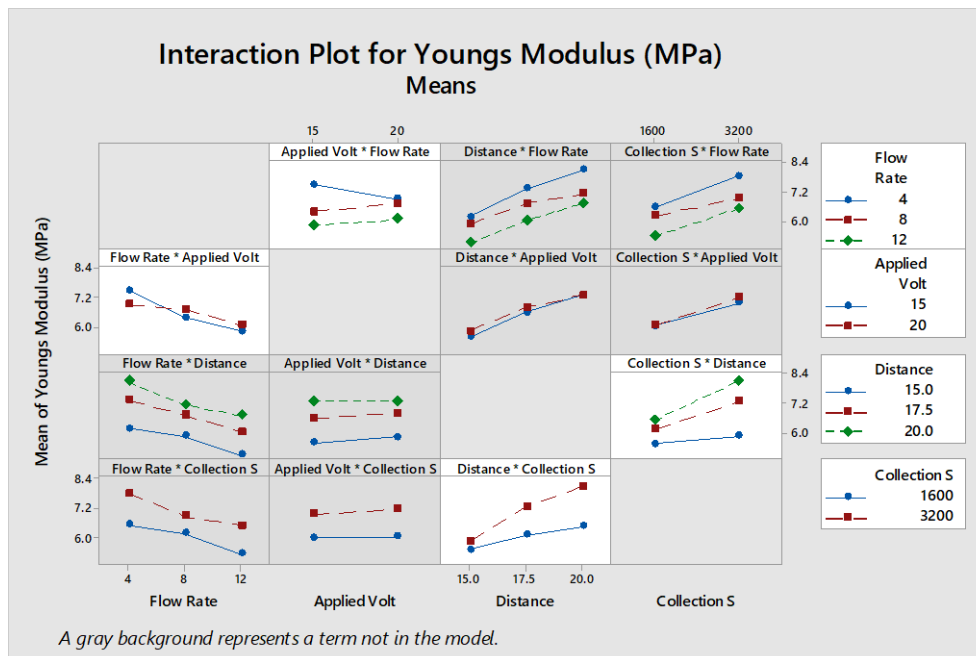
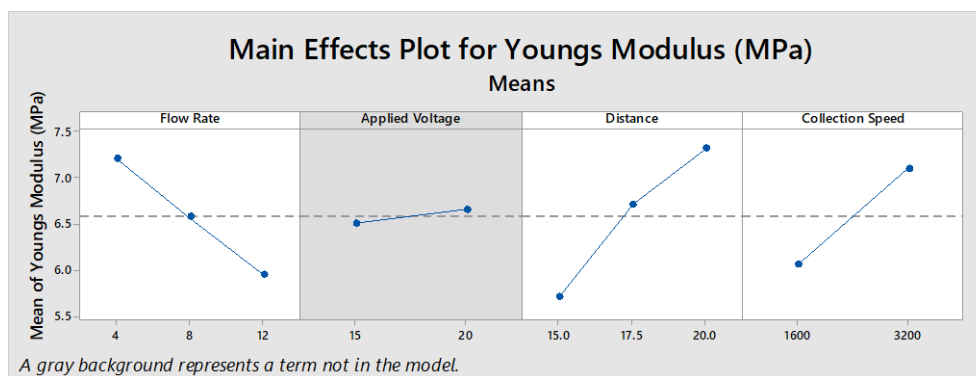


Figure 4.10: Main effects and interaction plot for the regression variable 'YM (Y₂)' showing the effects of changing input variable levels to the response variable of interest. Greyed backgrounds represent a term or interaction not included within the reduced model used to predict the output response.

Table 4.10 shows the tabulated results of the modelling analysis performed for maximum force (MF) response of the vessels or response variable ‘Y₃’. Collector distance was again found to be the most significant input variable for determining the MF, with a decrease from ~30 N at 15cm to ~10 N at 20cm. Following this, the solution flow rate was found to be next significant term with an increase from 15 N at 4ml/hr to ~27 N at 12ml/hr. This increase was however not linearly proportional with

Table 4.10: Full Model vs. Reduced Model in Coded Variables for Output Variable Y₃ ‘Max Force’ Obtained by dropping All Terms With p>0.05

	Main Effect/ Interaction	p	Coefficients Full Model	t-Value	Keep/ Drop	Coefficients in Reduced Model	Significance Rank
1	Constant	0.000	19.780	34.10	Keep	19.718	(0)
2	X ₁	0.000	5.696	7.91	Keep	5.696	2
3	X ₂	0.757	0.180	0.31	Drop	-	
4	X ₃	0.000	-9.292	-13.25	Keep	-9.292	1
5	X ₄	0.000	2.263	3.81	Keep	2.263	5
6	X ₁ * X ₂	0.937	0.056	0.08	Drop	-	
7	X ₁ * X ₃	0.000	-3.545	-4.25	Keep	-3.545	3
8	X ₁ * X ₄	0.462	-0.523	-0.74	Drop	-	
9	X ₂ * X ₃	0.542	0.434	0.61	Drop	-	
10	X ₂ * X ₄	0.106	0.934	1.63	Drop	-	
11	X ₃ * X ₄	0.002	-2.207	-3.25	Keep	-2.207	4
12	X ₁ * X ₂ * X ₃	0.328	-0.853	-0.98	Drop	-	
13	X ₁ * X ₂ * X ₄	0.923	0.068	0.10	Drop	-	
14	X ₁ * X ₃ * X ₄	0.786	-0.236	-0.27	Drop	-	
15	X ₂ * X ₃ * X ₄	0.011	1.938	2.61	Keep	1.938	6
16	X ₁ * X ₂ * X ₃ *X ₄	0.621	0.430	0.50	Drop	-	
17	Block	0.172	N/A	-	Drop	-	
	S		R-Sq	R-Sq (adj)		R-Sq (pred)	
Full	6.00874		76.42%	72.28%		66.73%	
Reduced	5.91500		74.64%	73.14%		71.20%	

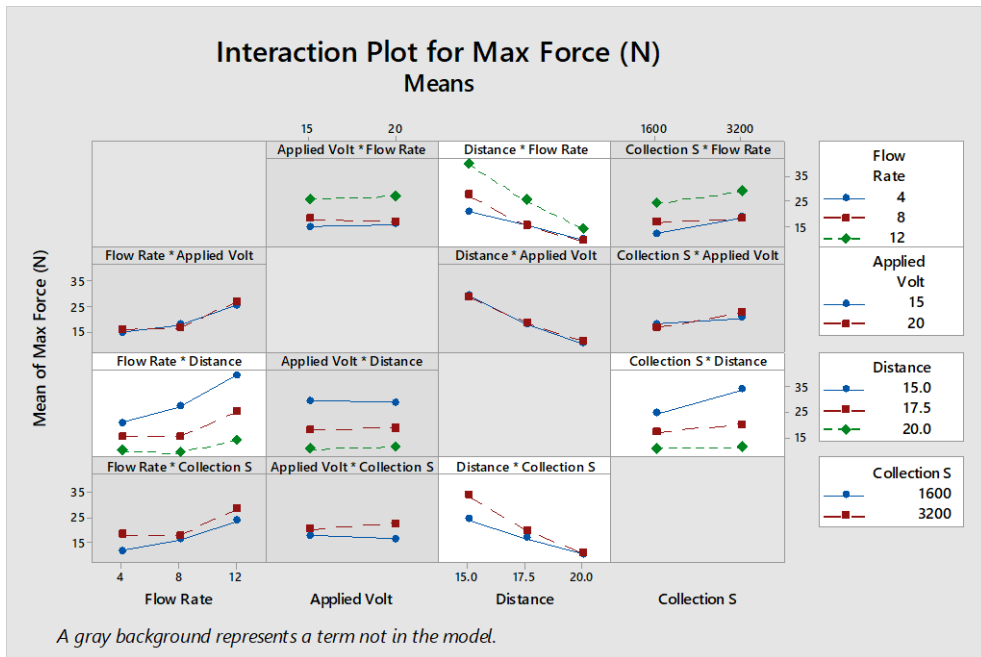
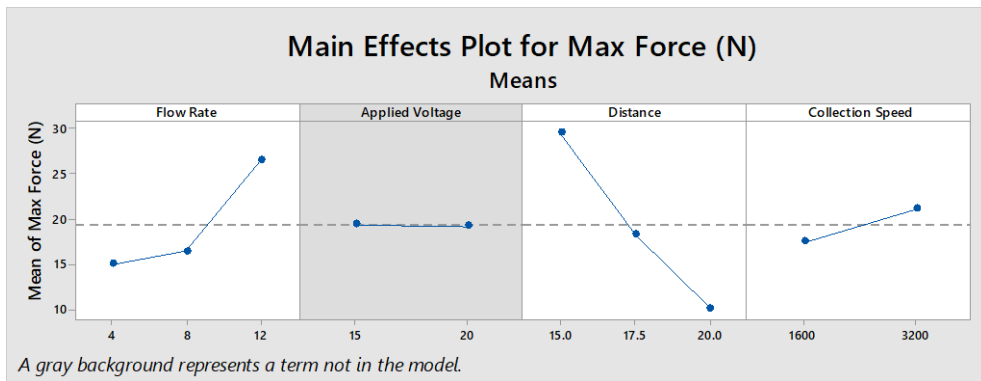


Figure 4.11: Main effects and interaction plot for the regression variable ‘Max Force (Y_3)’ showing the effects of changing input variable levels to the response variable of interest. Greyed backgrounds represent a term or interaction not included within the reduced model used to predict the output response.

only a small increase from 4 ml/hr to 8 ml/hr at ~17N. The interactions of the flow rate and collection distance ($X_1 * X_3$) was again found to be significant with an increase in max force with increasing flow rate as shown in the main effects and interactions plot, Figure 4.11. This increase with flow rate was however, less prominent at the increased collector distance of 20cm compared to that of 15cm. The reduced model had an overall R-sq of 74.64% and a predictive R-sq of 71.20%. An S value at ~5.915 N suggested the model was prone to variation with this accounting for ~30% of the MF coefficient at 19.780 N.

Table 4.11 shows the tabulated results of the modelling analysis performed for the ring modulus (RM) response of the vessels or response variable 'Y₄'. The most significant input variable for determining the RM was again found to be the collector distance, with a decrease from 0.7 N/% at 15cm to 0.37 N/% at 20cm. Following this, the solution flow rate was again found to be the next significant term with an increase of ~0.48 N/% at 4ml/hr to 0.66 N/% at 12ml/hr.

Table 4.11: Full Model vs. Reduced Model in Coded Variables for Output Variable Y₄ 'Ring modulus' Obtained by dropping All Terms With p>0.05

	Main Effect/ Interaction	p	Coefficients Full Model	t-Value	Keep/ Drop	Coefficients in Reduced Model	Significance Rank
1	Constant	0.000	0.5488	44.22	Keep	0.5488	(0)
2	X ₁	0.000	0.0956	6.29	Keep	0.0956	2
3	X ₂	0.294	0.0131	1.06	Drop	-	
4	X ₃	0.000	-0.1627	-10.70	Keep	-0.1627	1
5	X ₄	0.001	0.0430	3.46	Keep	0.0430	3
6	X ₁ * X ₂	0.658	-0.0067	-0.44	Drop	-	
7	X ₁ * X ₃	0.074	-0.0337	-1.81	Drop	-	
8	X ₁ * X ₄	0.334	-0.0148	-0.97	Drop	-	
9	X ₂ * X ₃	0.292	0.0161	1.06	Drop	-	
10	X ₂ * X ₄	0.001	0.0422	3.40	Keep	0.0422	4
11	X ₃ * X ₄	0.066	-0.0283	-1.86	Drop	-	
12	X ₁ * X ₂ * X ₃	0.210	-0.0235	-1.26	Drop	-	
13	X ₁ * X ₂ * X ₄	0.755	-0.0048	-0.31	Drop	-	
14	X ₁ * X ₃ * X ₄	0.726	-0.0065	-0.35	Drop	-	
15	X ₂ * X ₃ * X ₄	0.001	0.0514	3.38	Keep	0.0514	5
16	X ₁ * X ₂ * X ₃ *X ₄	0.600	-0.0098	-0.53	Drop	-	
17	Block	0.089	N/A	-	Drop	-	
		S	R-Sq	R-Sq (adj)	R-Sq (pred)		
Full	0.128990	69.18%	63.76%	56.69%			
Reduced	0.131594	64.04%	62.28%	59.84%			

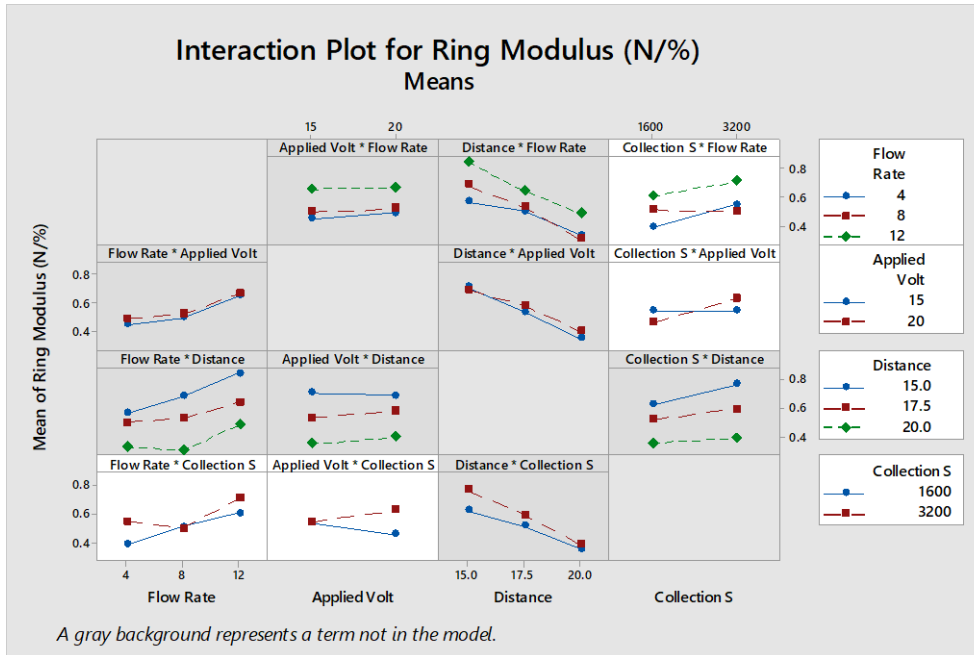
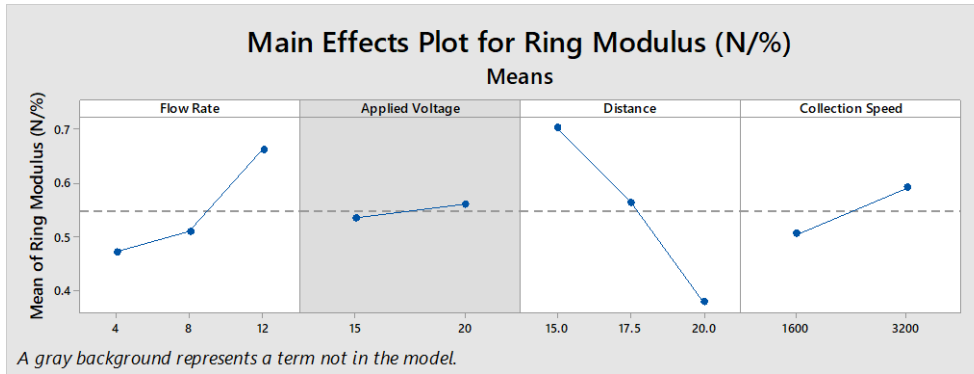


Figure 4.12: Main effects and interaction plot for the regression variable ‘Ring modulus (Y_4)’ showing the effects of changing input variable levels to the response variable of interest. Greyed backgrounds represent a term or interaction not included within the reduced model used to predict the output response.

This increase was again not linearly proportional with a small increase seen between samples at 4ml/hr and 8ml/hr (0.5 N/%). Collection Speed was also found to have a significant effect with an increase in the ring modulus from ~0.5 N/% at 1600 RPM to ~0.6 N/% at 3200RPM. The interactions between the applied voltage and collection distance ($X_3 * X_4$) was found to be significant despite the applied voltage term being found to be insignificant on its own as shown in Figure 4.12. The reduced model had an overall R-sq of 64.04% and a predictive R-sq of 59.84%. An S value of ~0.131 N/% represents an overall model variation of ~24% when compared to the RM coefficient at 0.5488 N/%.

4.5.1.2 Porosity and Morphological Analysis

The results of the porosity assessment indicated consistent specimen porosities across all scaffolds irrespective of the process parameters used, with porosities typically ranging from of 80 to 85%. Collection speed was found to be the most significant parameter (Table 4.12) to effect porosity, with a small average decrease from ~84%

Table 4.12: Full Model vs. Reduced Model in Coded Variables for Output Variable Y_5 'Porosity' Obtained by dropping All Terms With $p > 0.05$

	Main Effect/ Interaction	p	Coefficients Full Model	t-Value	Keep/ Drop	Coefficients in Reduced Model	Significance Rank
1	Constant	0.000	83.605	561	Keep	83.605	(0)
2	X_1	0.352	0.171	0.94	Drop	-	
3	X_2	0.001	-0.515	-3.45	Keep	-0.515	2
4	X_3	0.011	-0.472	-2.59	Keep	-0.472	3
5	X_4	0.000	-0.587	-3.94	Keep	-0.587	1
6	$X_1 * X_2$	0.669	0.078	0.43	Drop	-	
7	$X_1 * X_3$	0.090	-0.384	-1.72	Drop	-	
8	$X_1 * X_4$	0.232	-0.220	-1.20	Drop	-	
9	$X_2 * X_3$	0.174	0.250	1.37	Drop	-	
10	$X_2 * X_4$	0.092	0.254	1.71	Drop	-	
11	$X_3 * X_4$	0.195	-0.238	-1.31	Drop	-	
12	$X_1 * X_2 * X_3$	0.324	-0.221	-0.99	Drop	-	
13	$X_1 * X_2 * X_4$	0.844	0.036	0.20	Drop	-	
14	$X_1 * X_3 * X_4$	0.875	-0.035	-0.16	Drop	-	
15	$X_2 * X_3 * X_4$	0.627	0.089	0.49	Drop	-	
16	$X_1 * X_2 * X_3 * X_4$	0.039	0.469	2.10	Keep	0.469	4
17	Block	0.609	N/A	-	Drop	-	
		S	R-Sq	R-Sq (adj)	R-Sq (pred)		
Full	1.54876	36.37%	25.19%	9.37%			
Reduced	1.55988	26.95%	24.11%	19.77%			

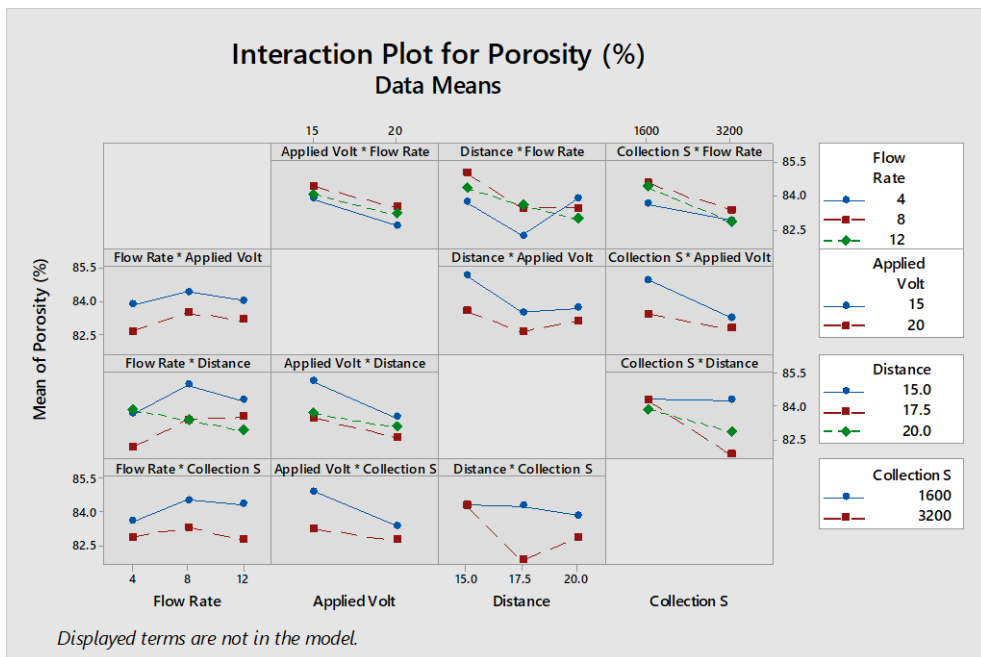
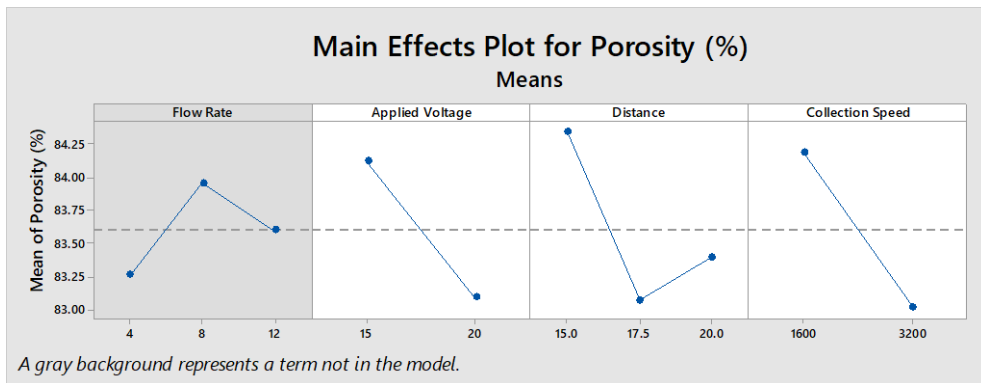


Figure 4.13: Main effects and interaction plot for the regression variable ‘Porosity (Y_5)’ showing the effects of changing input variable levels to the response variable of interest. Greyed backgrounds represent a term or interaction not included within the reduced model used to predict the output response.

to 83% observed when the speed was increased from 1600 to 3200 RPM. Applied voltage and collector distance were also found to be statistically significant although the R-sq and R-sq predicted were extremely low at 29.95% and 19.77% respectively. This paired with an S value of ~1.55% showed the model was extremely poor at predicting the porosity of specimens. This is attributed to the limited variation between specimens which makes it extremely difficult to detect a clear signal. Figure 4.13 again shows the main effects and interaction plot for the porosity analysis. No interactions were included within the model accounting for the greyed out model terms.

Table 4.13 shows the tabulated results of the modelling analysis performed for the Mean Inner Fibre Diameter (IFD) or response variable ‘ Y_6 ’. The only significant input variable for determining the IFD was the rotational speed of the collection mandrel. A small decrease in the average IFD from $\sim 1.23 \mu\text{m}$ at 1600 RPM to $1.11 \mu\text{m}$ at 3200 RPM was observed as shown in Figure 4.14. The reduced model had an overall R-sq

Table 4.13: Full Model vs. Reduced Model in Coded Variables for Output Variable Y_6 ‘Mean Inner Fibre Diameter’ Obtained by dropping All Terms With $p > 0.05$

	Main Effect/ Interaction	p	Coefficients Full Model	t-Value	Keep/ Drop	Coefficients in Reduced Model	Significance Rank
1	Constant	0.000	1.1731	56.23	Keep	1.1731	(0)
2	X_1	0.478	0.0182	0.71	Drop	-	
3	X_2	0.289	-0.0223	-1.07	Drop	-	
4	X_3	0.160	-0.0362	-1.42	Drop	-	
5	X_4	0.003	-0.0639	-3.06	Keep	-0.0639	1
6	$X_1 * X_2$	0.599	-0.0135	-0.53	Drop	-	
7	$X_1 * X_3$	0.472	-0.0226	-0.72	Drop	-	
8	$X_1 * X_4$	0.639	-0.0120	-0.47	Drop	-	
9	$X_2 * X_3$	0.278	0.0279	1.09	Drop	-	
10	$X_2 * X_4$	0.136	0.0314	1.51	Drop	-	
11	$X_3 * X_4$	0.105	0.0419	1.64	Drop	-	
12	$X_1 * X_2 * X_3$	0.416	0.0256	0.82	Drop	-	
13	$X_1 * X_2 * X_4$	0.456	-0.0191	-0.75	Drop	-	
14	$X_1 * X_3 * X_4$	0.700	0.0121	0.39	Drop	-	
15	$X_2 * X_3 * X_4$	0.253	-0.0294	-1.15	Drop	-	
16	$X_1 * X_2 * X_3 * X_4$	0.631	-0.0151	-0.48	Drop	-	
17	Block	0.222	N/A	-	Drop	-	
	S		R-Sq	R-Sq (adj)		R-Sq (pred)	
Full	0.216818		21.30%	7.47%		0.00%	
Reduced	0.217085		8.10%	7.24%		4.60%	

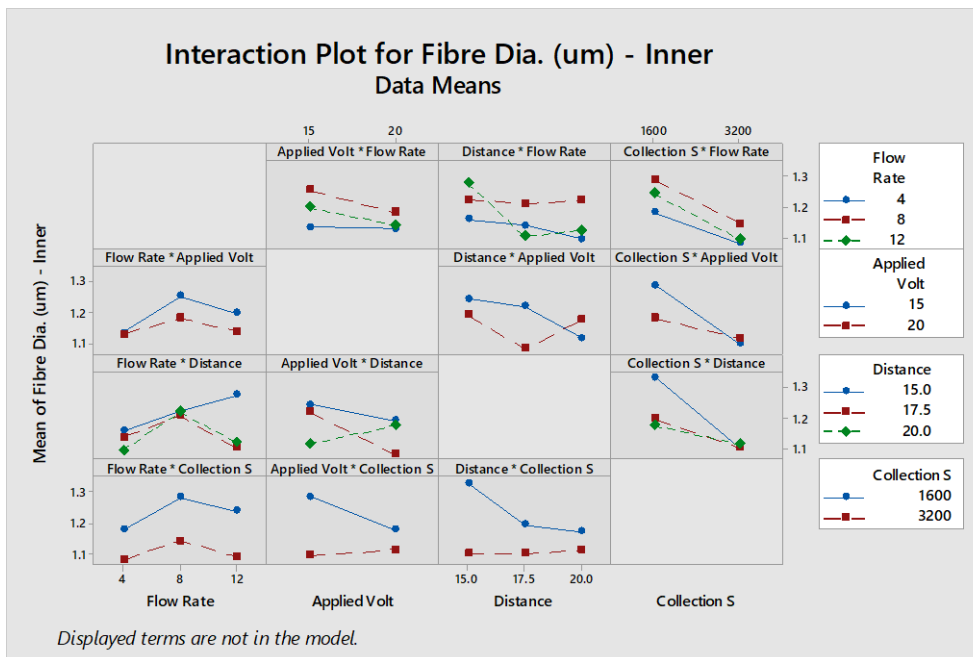
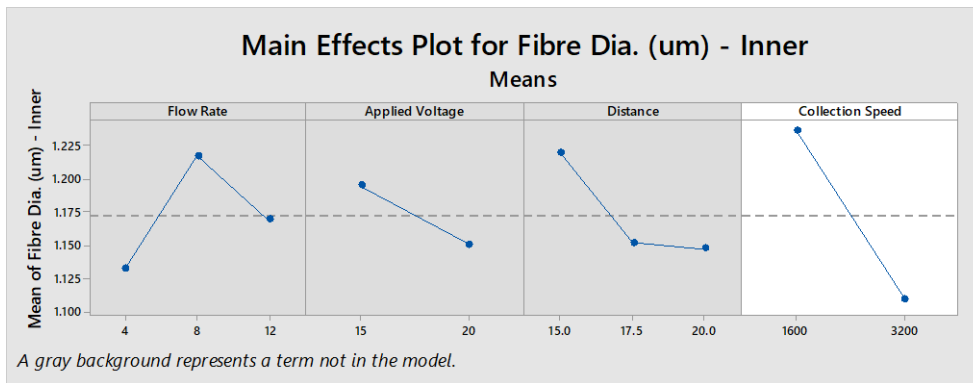


Figure 4.14: Main effects and interaction plot for the regression variable ‘Mean Inner Fibre Diameter (Y_6)’ showing the effects of changing input variable levels to the response variable of interest. Greyed backgrounds represent a term or interaction not included within the reduced model used to predict the output response.

And R-sq predicted of 8.10% and 4.6% respectively. These significantly low values suggest that the use of linear regression analysis tools may not be suitable for the prediction of fibre diameters created through multi-modal spinning techniques.

Table 4.14 shows the tabulated results of the modelling analysis performed for the Mean Outer Fibre Diameter (OFD) or response variable ‘ Y_7 ’. Similar to the IFD response, the rotational speed of the collection mandrel was the most significant predictor for determining the diameter of the produced outer surface fibres. A decrease in the average OFD from $\sim 1.17 \mu\text{m}$ at 1600 RPM to $\sim 1.03 \mu\text{m}$ at 3200 RPM was

observed as shown in the main effects plots in Figure 4.15. The 3-way interaction of flow rate, applied voltage and collection speed ($X_1 * X_2 * X_4$) was also found to be significant. In addition, the individual main effects of flow rate and applied voltage were also seen to have a significant effect on the diameter of fibres produced. Fibre diameters were seen to increase from an average of $\sim 1.02 \mu\text{m}$ to $1.14 \mu\text{m}$ at 4ml/hr and 8ml/hr respectively. No significant increase was however seen when the flow rate

Table 4.14: Full Model vs. Reduced Model in Coded Variables for Output Variable Y_7 ‘Mean Outer Fibre Diameter’ Obtained by dropping All Terms With $p > 0.05$

	Main Effect/ Interaction	p	Coefficients Full Model	t-Value	Keep/ Drop	Coefficients in Reduced Model	Significance Rank
1	Constant	0.000	1.1016	65.19	Keep	1.1016	(0)
2	X_1	0.008	0.0565	2.73	Keep	0.0565	3
3	X_2	0.012	-0.0432	-2.55	Keep	-0.0432	4
4	X_3	0.429	-0.0164	-0.79	Drop	-	
5	X_4	0.000	-0.0820	-4.85	Keep	-0.0820	1
6	$X_1 * X_2$	0.628	-0.0101	-0.49	Drop	-	
7	$X_1 * X_3$	0.698	-0.0099	-0.39	Drop	-	
8	$X_1 * X_4$	0.925	0.0019	0.09	Drop	-	
9	$X_2 * X_3$	0.677	-0.0086	-0.42	Drop	-	
10	$X_2 * X_4$	0.374	0.0151	0.89	Drop	-	
11	$X_3 * X_4$	0.901	0.0026	0.12	Drop	-	
12	$X_1 * X_2 * X_3$	0.336	0.0245	0.97	Drop	-	
13	$X_1 * X_2 * X_4$	0.003	-0.0625	-3.02	Keep	-0.0625	2
14	$X_1 * X_3 * X_4$	0.389	-0.0220	-0.87	Drop	-	
15	$X_2 * X_3 * X_4$	0.947	-0.0014	-0.07	Drop	-	
16	$X_1 * X_2 * X_3 * X_4$	0.095	-0.0428	-1.69	Drop	-	
17	Block	0.573	N/A	-	Drop	-	
	S		R-Sq		R-Sq (adj)		R-Sq (pred)
Full	0.175627		37.02%		25.95%		9.96%
Reduced	0.171206		32.26%		29.63%		25.13%

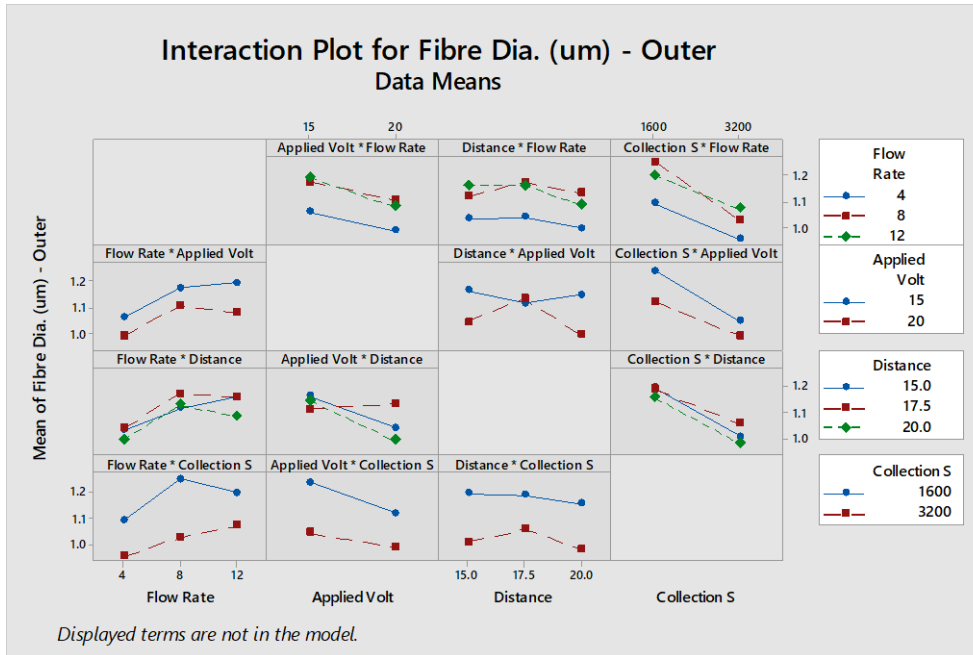
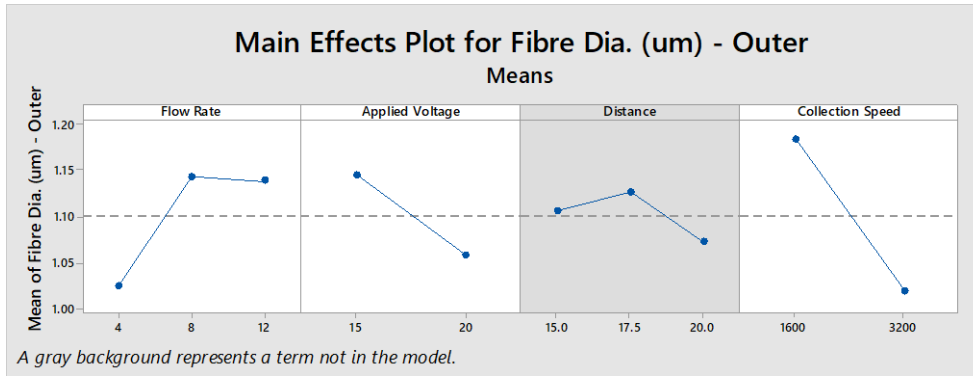


Figure 4.15: Main effects and interaction plot for the regression variable ‘Mean Outer Fibre Diameter (Y_7)’ showing the effects of changing input variable levels to the response variable of interest. Greyed backgrounds represent a term or interaction not included within the reduced model used to predict the output response.

was increased further to 12ml/hr with average fibre diameters holding at $\sim 1.14 \mu\text{m}$. Increasing the collector voltage from 15 to 20 kV was seen to result in a decrease in fibre diameters, with the diameters reducing from an average of $\sim 1.14 \mu\text{m}$ to $1.05 \mu\text{m}$ in size. The reduced model had an overall R-sq of 32.26% and a predictive R-sq of 25.13%. An S value of $\sim 0.171 \mu\text{m}$ represents an overall model variation of $\sim 15.4\%$ when compared to the OFD coefficient at $1.1016 \mu\text{m}$.

Table 4.15 shows the tabulated results of the modelling analysis performed for the Inner Fibre Coherency (IC) or response variable ‘ Y_8 ’. The rotational speed of the

collection mandrel was found to be the most significant predictor for determining the coherency of the fibres. Coherency was found to increase on average from ~0.205 to 0.255 when the speed was increased from 1600 to 3200 RPM. The interaction of Flow rate, applied voltage and collection speed ($X_1 * X_2 * X_4$) was found to be the next strongest predictor of fibre alignment. Increasing the applied voltage was found to result in a reduction of the IC, with the coherency of fibres falling from ~0.245 to 0.21

Table 4.15: Full Model vs. Reduced Model in Coded Variables for Output Variable Y_8 'Inner Fibre Coherency Obtained by dropping All Terms With $p > 0.05$

	Main Effect/ Interaction	p	Coefficients Full Model	t-Value	Keep/ Drop	Coefficients in Reduced Model	Significance Rank
1	Constant	0.000	0.23012	32.83	Keep	0.23012	(0)
2	X_1	0.409	0.00712	0.83	Drop	-	-
3	X_2	0.018	-0.01693	-2.42	Keep	-0.0432	3
4	X_3	0.286	0.00921	1.07	Drop	-	
5	X_4	0.001	0.02474	3.53	Keep	-0.0820	1
6	$X_1 * X_2$	0.292	-0.00910	-1.06	Drop	-	
7	$X_1 * X_3$	0.665	0.0046	0.43	Drop	-	
8	$X_1 * X_4$	0.338	-0.00828	-0.96	Drop	-	
9	$X_2 * X_3$	0.027	-0.01925	-2.24	Keep	-0.01925	4
10	$X_2 * X_4$	0.557	0.00413	0.59	Drop	-	
11	$X_3 * X_4$	0.823	-0.00193	-0.22	Drop	-	
12	$X_1 * X_2 * X_3$	0.827	-0.0023	-0.22	Drop	-	
13	$X_1 * X_2 * X_4$	0.006	0.02420	2.82	Keep	-0.0625	2
14	$X_1 * X_3 * X_4$	0.876	0.0016	0.16	Drop	-	
15	$X_2 * X_3 * X_4$	0.471	-0.00622	-0.72	Drop	-	
16	$X_1 * X_2 * X_3 * X_4$	0.688	-0.0042	0.40	Drop	-	
17	Block	0.270	N/A	-	Drop	-	
	S		R-Sq	R-Sq (adj)		R-Sq (pred)	
Full	0.0728538		29.31%	16.88%		0.00%	
Reduced	0.0708704		24.28%	21.34%		16.72%	

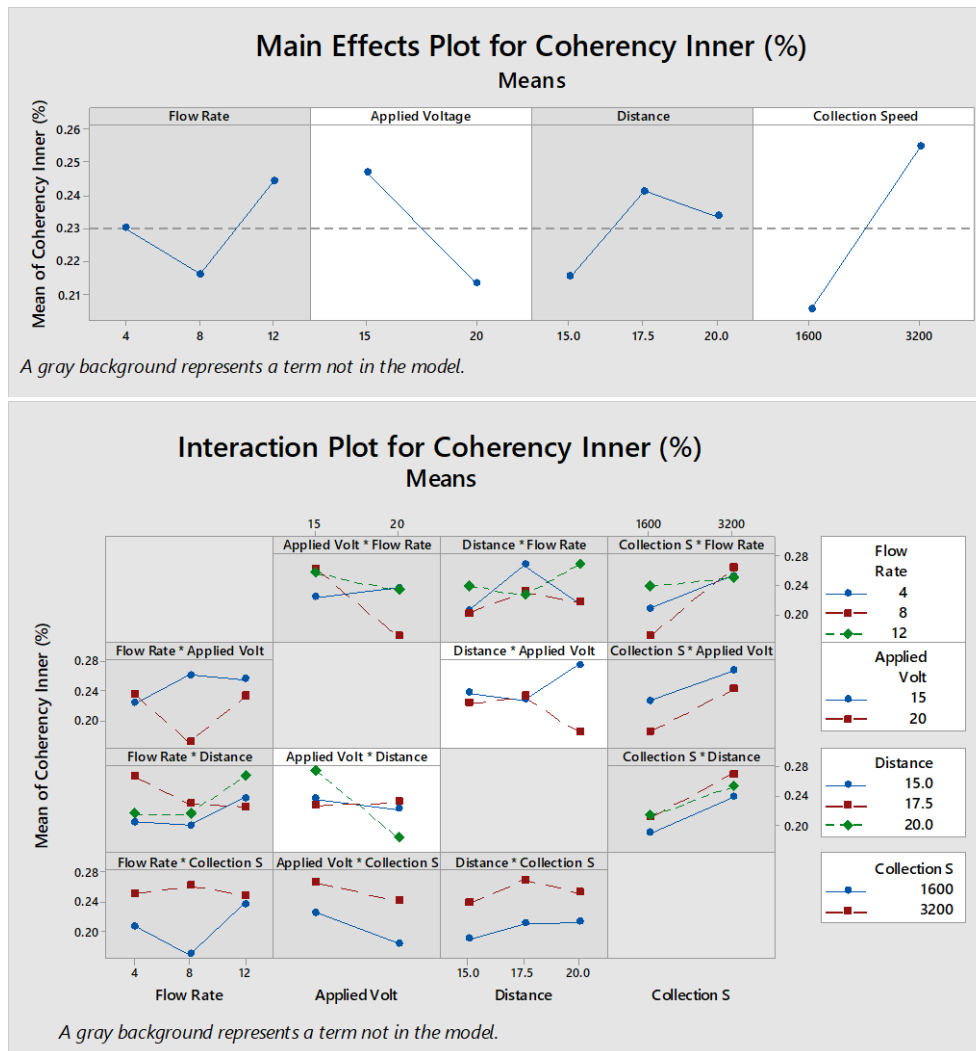


Figure 4.16: Main effects and interaction plot for the regression variable ‘Inner Fibre Coherency (Y_8)’ showing the effects of changing input variable levels to the response variable of interest. Greyed backgrounds represent a term or interaction not included within the reduced model used to predict the output response.

when the voltage was increased from 15 to 20kV. The reduced model had an overall R-sq of 24.28% and a predictive R-sq of 16.72%. An S value of ~0.0708704 represents an overall model variation of ~30.8% when compared to the IC coefficient at 0.30322.

Table 4.16 shows the tabulated results of the modelling analysis performed for the Outer Fibre Coherency (OC) or response variable ‘ Y_9 ’. The most significant factor for determining the coherency of the outer surface fibres was the voltage applied. An increase in applied voltage from 15 to 20 kV resulted in a reduction in coherency from ~0.34 to 0.21, representing a decrease in fibre alignment. Solution flow rate was also found to be a significant factor for influencing fibre coherency with an increase from

~0.27 to 0.34 when the flow rate was increased from 4 to 12 ml/hr respectively. Collector speed was again found to be an influencing factor in determining coherency with an increase in coherency again resulting in the increased fibre alignment as shown in Figure 4.17

Table 4.16: Full Model vs. Reduced Model in Coded Variables for Output Variable Y9 ‘Outer Fibre Coherency’ Obtained by dropping All Terms With $p > 0.05$

	Main Effect/ Interaction	p	Coefficients Full Model	t-Value	Keep/ Drop	Coefficients in Reduced Model	Significance Rank
1	Constant	0.000	0.30322	36.89	Keep	0.30322	(0)
2	X ₁	0.001	0.0351	3.49	Keep	0.0351	2
3	X ₂	0.000	-0.03573	-4.35	Keep	-0.03573	1
4	X ₃	0.130	0.0154	1.53	Drop	-	
5	X ₄	0.001	0.02800	3.41	Keep	0.02800	3
6	X ₁ * X ₂	0.123	0.0157	1.56	Drop	-	
7	X ₁ * X ₃	0.191	0.0162	1.32	Drop	-	
8	X ₁ * X ₄	0.572	-0.0057	-0.057	Drop	-	
9	X ₂ * X ₃	0.115	-0.0160	-1.59	Drop	-	
10	X ₂ * X ₄	0.858	-0.00147	-0.018	Drop	-	
11	X ₃ * X ₄	0.132	-0.0153	-1.52	Drop	-	
12	X ₁ * X ₂ * X ₃	0.587	-0.0067	-0.55	Drop	-	
13	X ₁ * X ₂ * X ₄	0.017	0.0246	2.44	Keep	-0.0625	5
14	X ₁ * X ₃ * X ₄	0.005	0.0358	2.90	Keep	0.0358	4
15	X ₂ * X ₃ * X ₄	0.173	0.0138	1.37	Drop	-	
16	X ₁ * X ₂ * X ₃ *X ₄	0.402	-0.0104	0.84	Drop	-	
17	Block	0.103	N/A	-	Drop	-	
		S	R-Sq	R-Sq (adj)	R-Sq (pred)		
Full	0.0854220	44.97%	35.29%	22.48%			
Reduced	0.0880148	34.51%	31.30%	26.65%			

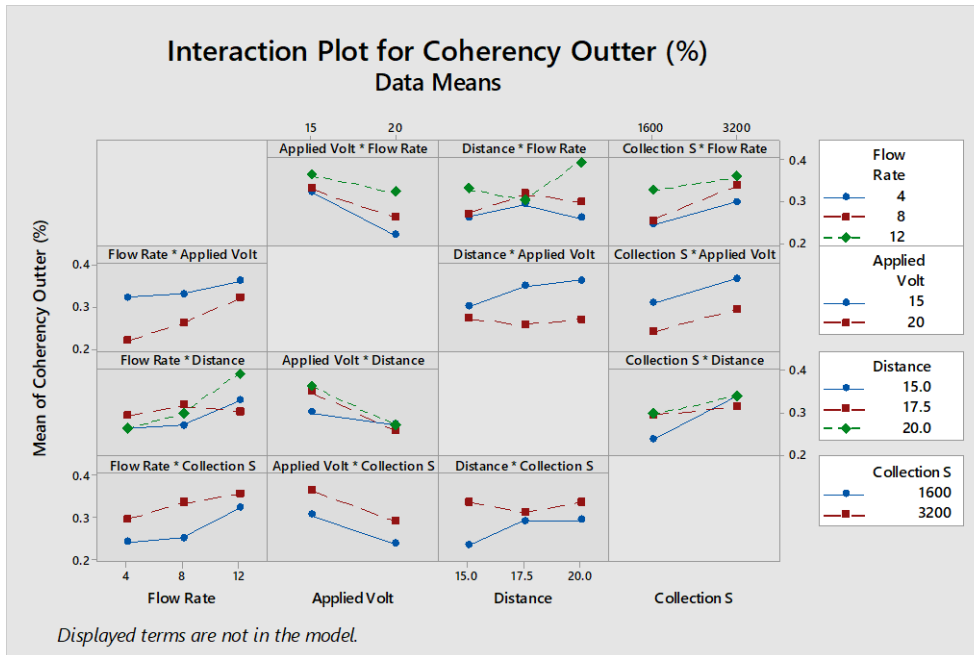
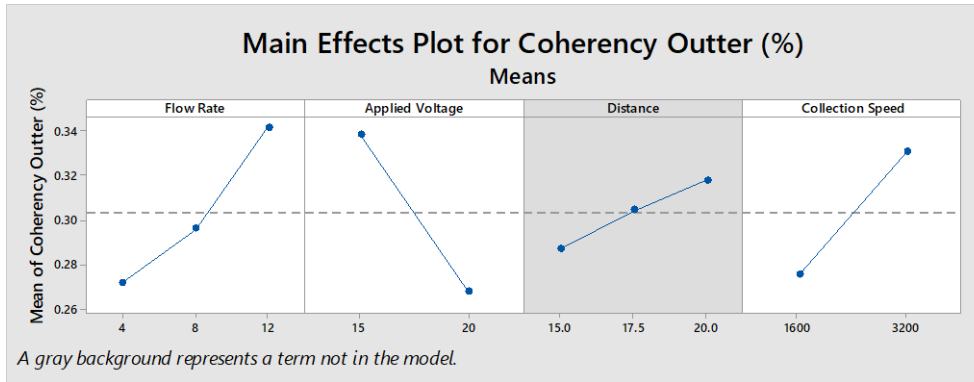


Figure 4.17: Main effects and interaction plot for the regression variable ‘Outer Fibre Coherency (Y_9)’ showing the effects of changing input variable levels to the response variable of interest. Greyed backgrounds represent a term or interaction not included within the reduced model used to predict the output response.

A number of 3-way interactions were also found to be significant including that of flow rate, applied voltage and speed of collector ($X_1 * X_2 * X_4$) along with the interaction of flow rate, collector distance and speed of collector ($X_1 * X_3 * X_4$).

4.5.1.3 Identification of Choice Parameter Combinations for Preparation of Multi-modal Core Layer

In order to develop an electrospun tubular scaffold with properties suited for use in arterial bypass applications, a number of mechanical criteria are assessed with respect to both Human Coronary Arteries (HCAs), and the current gold standard vessel for

use in bypass surgery, the Great Saphenous Vein (GSV). Figure 4.18 shows the UTS characteristics of the electrospun vessels prepared during the multimodal regression trial, with reference lines indicating the typical UTS ranges of HCA's at 0.57-2.31 MPa [174], and the GSV's at 1.1-4.92 MPa [281]. It is noted that a number of parameter permutations yielded vessels with UTS matching that of HCA's, with all parameters yielding vessels below that of the upper GSV criteria of 4.92 MPa.

Figure 4.19 similarly shows the Young's modulus characteristics of the electrospun vessels compared to HCA's and GSV's. HCA's have been demonstrated to have moduli of 1.29-1.81 MPa [174], and GSV's at a wide range of 14.86-70.38 MPa [281]. Vessels were found to be stiffer than those of the HCA but significantly lower than that of the GSV. It can be observed and confirmed by the previous regression analysis, that vessels created at the increased mandrel speed of 3200 RPM displayed increased stiffness characteristics compared to those created at the lower mandrel

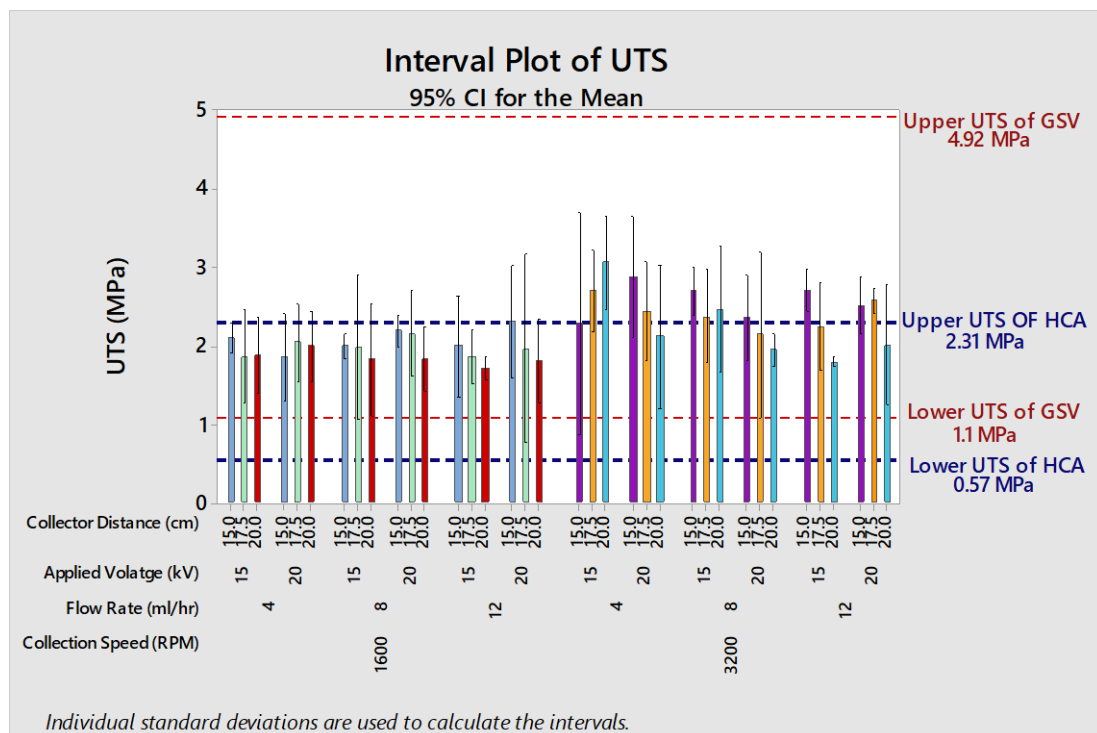


Figure 4.18: Interval plot of UTS responses for sample studies as part of the multi-modal electrospinning regression analysis, with lower and upper boundary ranges of common blood vessels indicated. Data for Human Coronary Arteries (HCA's) is adapted from Karimi et al. [173], and the Great Saphenous Vein (GSV) from Donovan et al. [279]

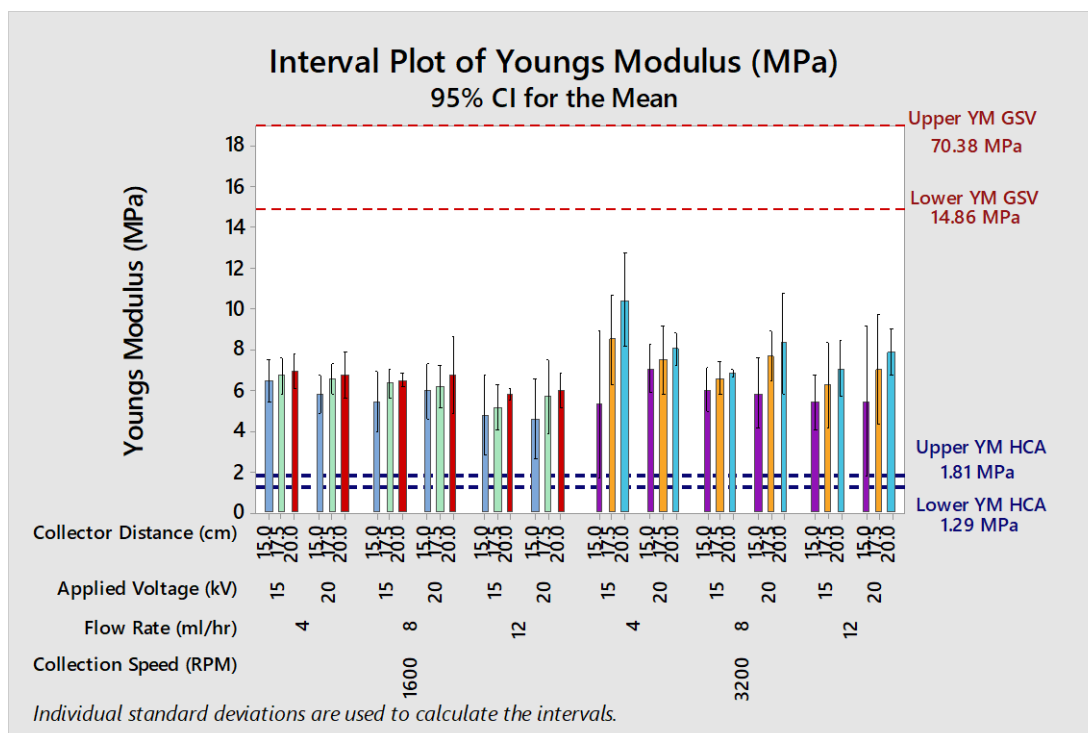


Figure 4.19: Interval plot of Young's modulus responses for specimens studied as part of the multi-modal electrospinning regression analysis, with lower and upper boundary ranges of common blood vessels indicated. Data for Human Coronary Arteries (HCA's) is adapted from Karimi et al. [173], and the Great Saphenous Vein (GSV) from Donovan et al. [279]

speed of 1600 RPM. Due to the similar spread of UTS and Young's modulus characteristics observed between the electrospun specimens, a number of additional criteria were employed to further eliminate possible parameter combinations.

One such criteria is the desire to have orientated fibres within the vessel walls in order to provide increased guidance to cells during growth. Due to this specimens created at the increased RPM speed of 3200 were selected for further analysis due to the statistically higher ($p=0.000$) coherency rates of 0.303 ± 0.106 , compared to 0.2301 ± 0.799 seen for 1600 RPM specimens. Samples produced at the collector distance of 20cm were typically difficult to handle and remove from the mandrels following the methanol soaking step. Similarly samples produced at the collection distance of 15cm were often prone to defects including fused fibres caused by incomplete solvent evaporation. Therefore the collection distance of 17.5cm was selected as the choice distance for sample collection. Samples produced at 15 and 20cm were removed from consideration.

The final criteria employed was findings regarding vessel specific properties such as the ring modulus, cross sectional area of the vessels walls and the overall maximum force to failure. These properties provide a more accurate assessment of the vessel specific response compared to the intrinsic material properties such as UTS and Young's modulus. In order to study these vessel properties further with regards to their effect on overall vessel compliance, two parameter sets as shown in Table 4.17. These parameter combinations identified, yielded considerably different ring modulus, cross sectional areas and maximum force characteristics despite having comparable UTS and Young's modulus properties.

Parameter Set 1 utilised a solution flow rate of 12ml/hr, applied voltage of 20kV paired with the collector distance of 17.5cm and mandrel speed of 3200 RPM. Parameter Set 2 utilised the lower flow rate level of 4ml/hr combined with an applied voltage of 15kV, collector distance of 17.5cm and mandrel speed of 3200 RPM. Figure 4.20 shows the comparison graphs for the ring modulus, cross sectional area and maximum force responses for the two parameter sets identified. The ring modulus for Set 1 was significantly higher ($p=0.297$) at 0.711 ± 0.049 N/% compared to that of Set 2 at 0.532 ± 0.057 N/%. The cross-sectional area for samples from Set 1 were again statistically higher ($p=0.0042$) than those of Set 2, at 10.37 ± 0.877 mm² and 5.92 ± 1.01 mm² respectively. The maximum force to failure of samples from Set 1 were again statistically higher ($p=0.0049$) than those of Set 2, at 30.64 ± 3.72 N compared to 16.82 ± 2.04 N. It is suspected that these differences in ring modulus, cross sectional area and max force results will provide vessels with altered compliance characteristics, ultimately allowing for the increased possibility to match the compliance characteristics of common conduits used in bypass surgery.

Table 4.17: Parameter Combinations Identified for Preparation of Multi-modal Core Layer by Rotating Mandrel Electrospinning

<i>Parameter Set</i>	<i>Flow Rate</i>	<i>Applied Voltage</i>	<i>Tip-Collector</i>	<i>Mandrel Speed</i>
<i>No.</i>	<i>(ml/hr)</i>	<i>(kV)</i>	<i>Distance (cm)</i>	<i>(RPM)</i>
<i>Set 1</i>	12	20	17.5	3200
<i>Set 2</i>	4	15	17.5	3200

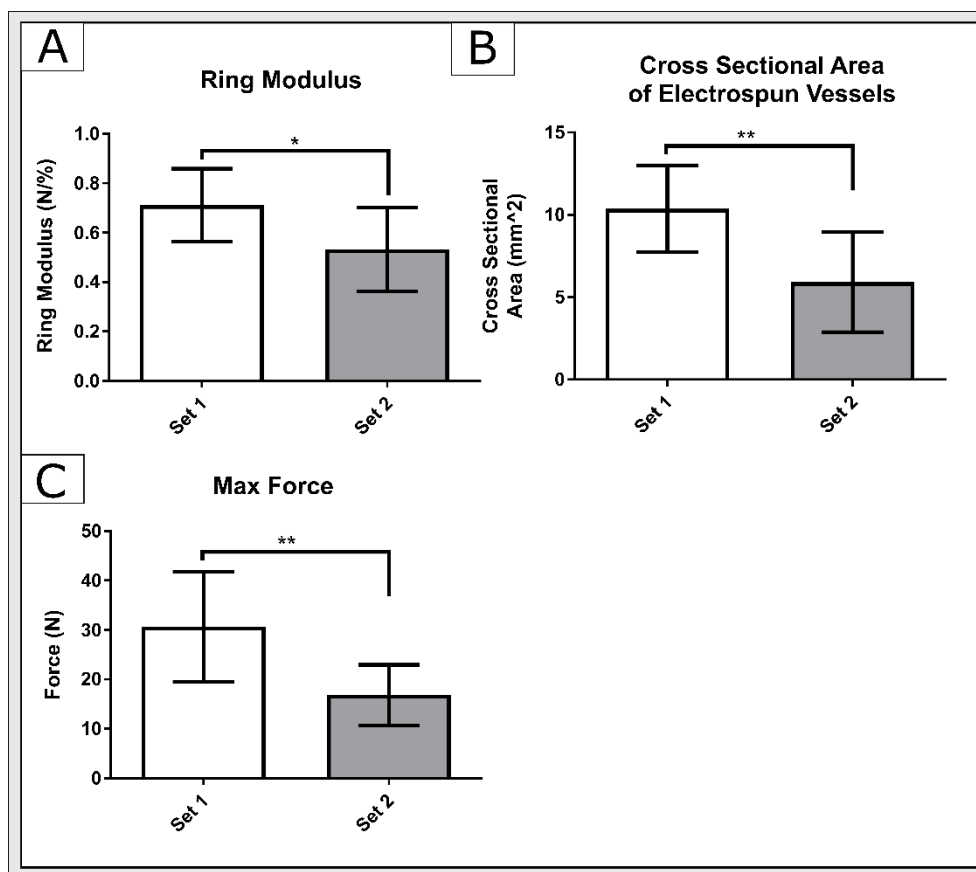


Figure 4.20: Comparison of ring modulus, cross sectional area and max force properties of parameters Sets 1 and 2 identified from multi-modal regression analysis ($n=9$ per set). The ring modulus ($p=0.0297$), cross sectional area ($p=0.0042$) and maximum force at failure ($p=0.0049$) were found to be statistically higher for Set 1 compared to those of Set 2.

4.5.2 Control of Molecular Weight Variation between PCL Batches through the Matching of Solution Viscosities

The results of Gel Permeation Chromatography (GPC) performed using the Agilent 1200 system previously discussed (pp.116-117) showed a distinct difference between the average molecular weight of the PCL batches ‘00807DJ-Original’ and ‘MKBV3325V-New’ despite being sold as equivalent materials (Figure 4.21). Based upon the retention time profiles observed and the use of calibration standards, the original PCL batch was found to have an estimated average molecular weight of $\sim 83,000$ g/mol with a polydispersity (PDI) of 2.10. This matched closely that of the listed molecular weight at 80,000 g/mol. PCL material tested from the new batch however showed a significantly higher molecular weight at $M_w \sim 100,000$ g/mol, with a slightly broader PDI than the previous batch at 2.21. Both batches showed a low molecular weight ‘tail’, which is an artefact of poor synthesis

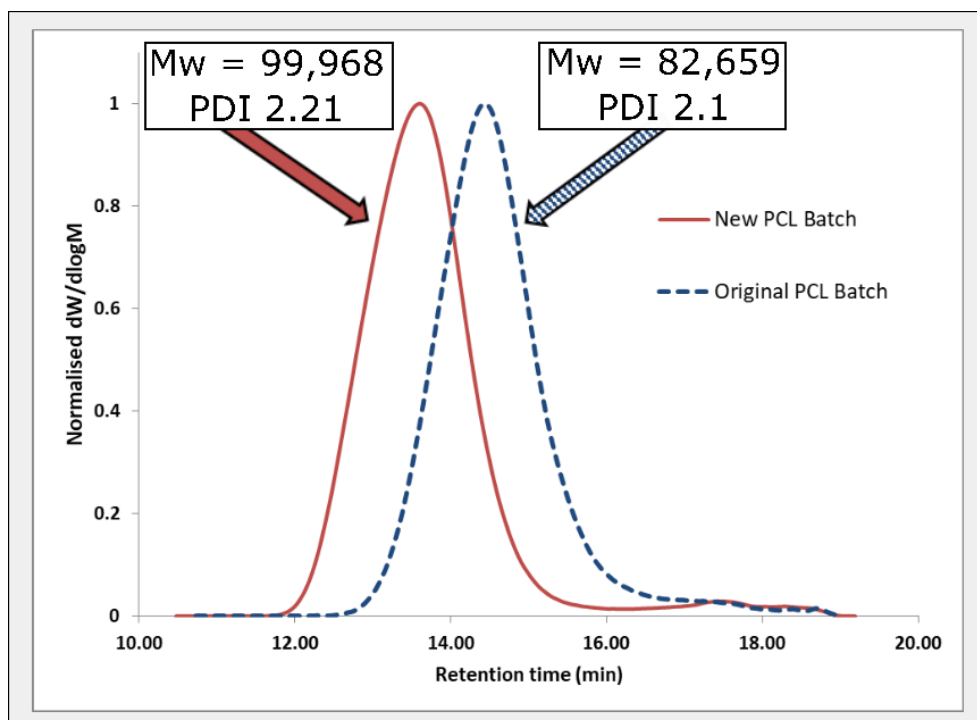


Figure 4.21: GPC results of ‘00807DJ-Original’ and ‘MKBV3325V-New’ PCL batches showing a significant difference in retention time indicating a clear difference between the molecular weight of the two PCL batches. ‘00807DJ-Original’ PCL was found to have $\sim M_w$ of 80,000 g/mol while ‘MKBV3325V-New’ was found to have a $\sim M_w$ of 100,000 g/mol

and possible degradation of the polymer chains. The PCL batches ‘00807DJ-Original’ will henceforth be referred to as 80kDa PCL ($\sim 80,000\text{g/mol}$), and ‘MKBV3325V-New’ as 100kDa PCL ($\sim 100,000\text{g/mol}$) in further analysis and discussion.

The standard solution concentration curves prepared using the two polymer batches can be seen in Figure 4.22. The resulting interpolation equations were used to identify a solution concentration for the 100kDa PCL material that yielded an equivalent viscosity characteristic to that of a 16wt% solution prepared using the 80kDa PCL at $495.8 \pm 4.3\text{ mPa}\cdot\text{s}$. A solution of concentration 7.8wt% prepared using 100kDa PCL was identified as having a potentially equivalent viscosity characteristic to that of the original 16wt% solutions. Subsequent viscosity and conductivity measurements performed on the new 7.8wt% solution showed a statistically comparative ($p=0.106$) viscosity at $503.97 \pm 5.19\text{ mPa}\cdot\text{s}$ and conductivity at $0.3\mu\text{S/cm}$ as shown in Figure 4.23. No statistical comparison could be made for conductivity due to no deviation being observed between the tested solutions.

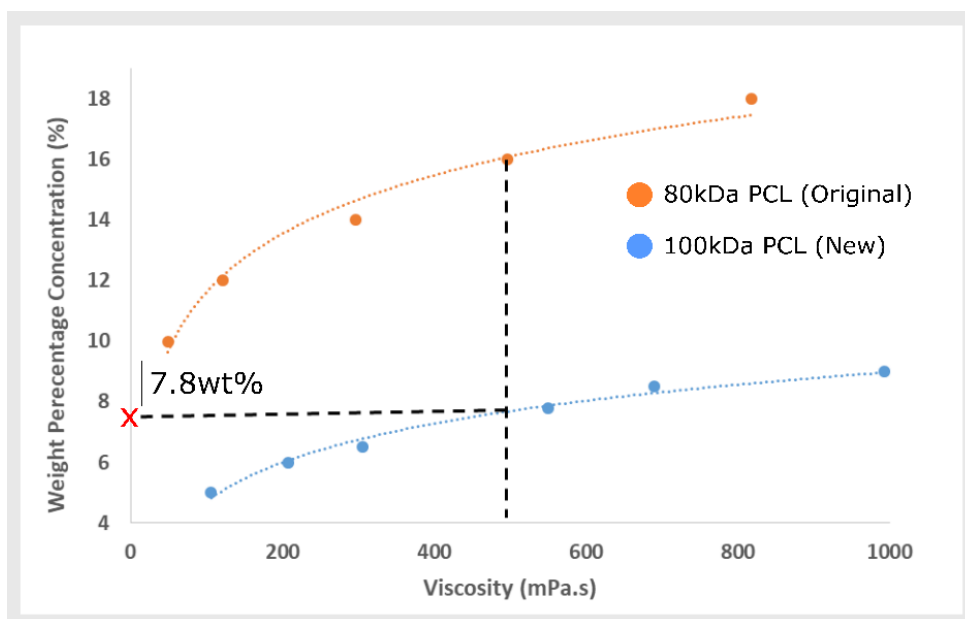


Figure 4.22: Solution standard curves prepared using the Original and New PCL batches used to select the concentration of a solution prepared using 100,000 g/mol PCL (100kDa) that possessed a comparative viscosity to that of a 16wt% solution prepared using 80,000 g/mol PCL (80kDa). A weight percentage concentration of 7.8wt% for the 100kDa PCL was found to provide a solution with equivalent viscosity characteristics. $N=3$ per solution.

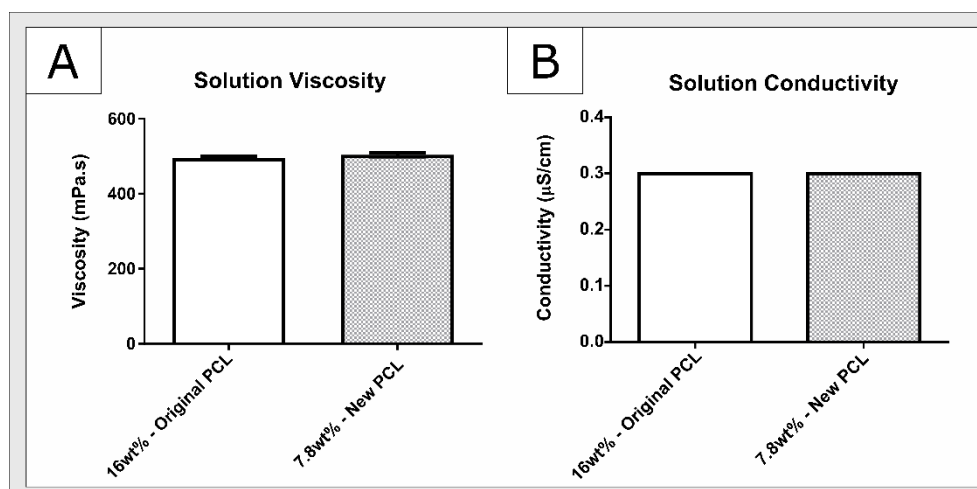


Figure 4.23: Viscosity and conductivity comparison of 16wt% solutions ($n=3$) prepared using the PCL batch '00807DJ-Original' and 7.8wt% solutions ($n=3$) prepared using the PCL batch 'MKBV3325V-New'. No statistical difference was observed between either viscosity ($p=0.106$) or conductivity.

4.5.2.1 Assessment of Mechanical Response Variation between PCL Batches

Based upon the results of the viscosity comparison study, a 7.8wt% concentration solution prepared using the 100kDa PCL was found to provide an appropriate viscosity

value comparable to that of the original 16wt% solutions (80kDa PCL). In order to assess any resulting variations in the mechanical responses of the electrospun vessels prepared using the alternative PCL batches, a comparative study was performed. Vessels were prepared according to the two selected parameter sets previously detailed in Table 4.5 (p.133), with ringlet and dogbone specimens examined. It was observed that the UTS of specimens prepared using 100kDa PCL were significantly higher than those prepared using the 80kDa material for both parameter sets and for all deposition times studied (Figure 4.24). This observation was comparable for both the ringlet and dogbone test methods examined. It is however noted that in certain instances the UTS values observed for dogbone specimens did not align to those of the ringlet specimens, particularly prominent for the 100kDa PCL batch specimens. One example of this can be seen within samples spun for 40 minutes using parameter Set 1. Vessels prepared using the 100kDa PCL had an average UTS of 4.974 MPa compared to 6.158 MPa for the corresponding dogbone specimens. Similarly specimens prepared for 20 minutes using parameter Set 2 showed a decreased ringlet UTS at 2.882 MPa compared to 4.233 MPa for dogbone specimens.

Figure 4.25 shows the Young's modulus properties recorded for the PCL batch comparison. Unlike the UTS response, Young's modulus properties were found to be highly irregular in terms of the variation between batches. Ringlet specimens tested for both Set 1 and Set 2 appeared to indicate a decrease in Young's modulus between 80kDa PCL compared to 100kDa PCL. This observation was not however seen to occur for all test cases as seen in Set 1 '40min' samples where there was no statistical difference between 100kDa and 80kDa PCL specimens. Dogbone specimens again showed inconsistent variation between PCL batches with the majority of the permutations showing equivalent properties. A decrease in Young's modulus was observed between 100kDa and 80kDa PCL in Set 1 for a deposition time of 40 minutes. Contrary to this an increase in Young's modulus was seen between 100kDa and 80kDa specimens for Set 2 over a 20minute collection period. These results may indicate a difficulty in assessing a material property that relies on a cross sectional area measurement for a fibrous material.

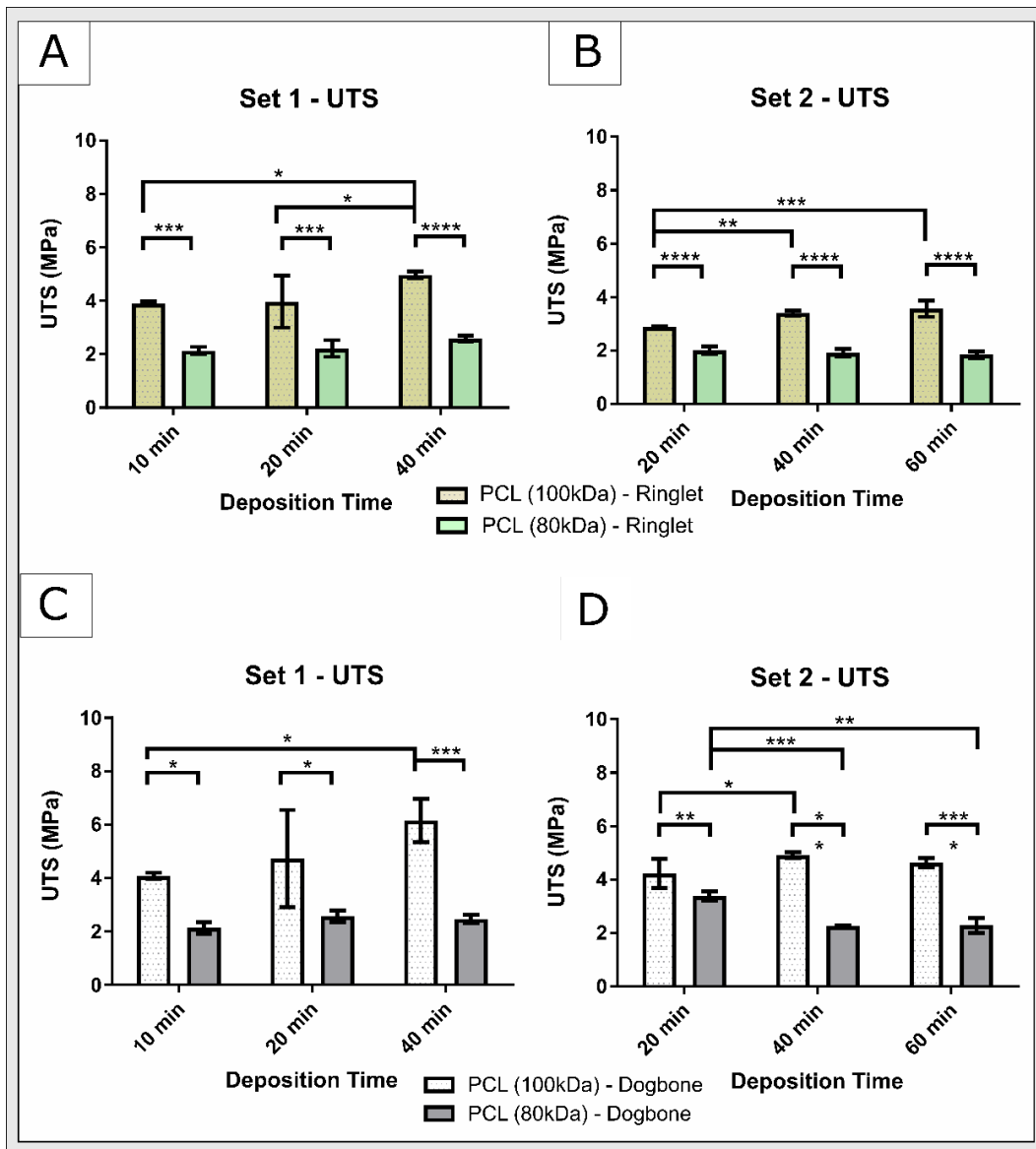


Figure 4.24: UTS results for PCL batch comparison showing statistically larger UTS properties for 100kDa specimens to 80kDa specimens for all time points and test configurations studied (A) UTS response for Set 1 ringlet samples showing higher UTS for 100kDa PCL to 80kDa PCL. UTS for 40min ringlets prepared using 100kDa PCL are seen to be statistically higher than those collected over 10 and 20 mins. All time points for 80kDa PCL were however equivalent (B) UTS response for Set 2 ringlet samples showing statistically higher UTS for 100kDa PCL to 80kDa PCL. UTS for 20min ringlets prepared using 100kDa PCL was found to be statistically lower than those collected over 40 (*) and 60 min (***). All time points for 80kDa PCL were again equivalent (C) UTS response for Set 1 dogbone samples showing statistically higher UTS for 100kDa PCL to 80kDa PCL. UTS for 10min ringlets prepared using 100kDa PCL was found to be statistically lower than those collected over 40min (*). All time points for 80kDa PCL were equivalent (D) UTS response for Set 2 dogbone samples showing statistically higher UTS for 100kDa PCL to 80kDa PCL. UTS for 10min ringlets prepared using 100kDa PCL was found to be statistically lower than those collected over 40min (*). All time points for 80kDa PCL were equivalent. (* $P \leq 0.05$)(** $P \leq 0.01$)(*** $P \leq 0.001$)(**** $P \leq 0.0001$). $N=3$ per test group.**

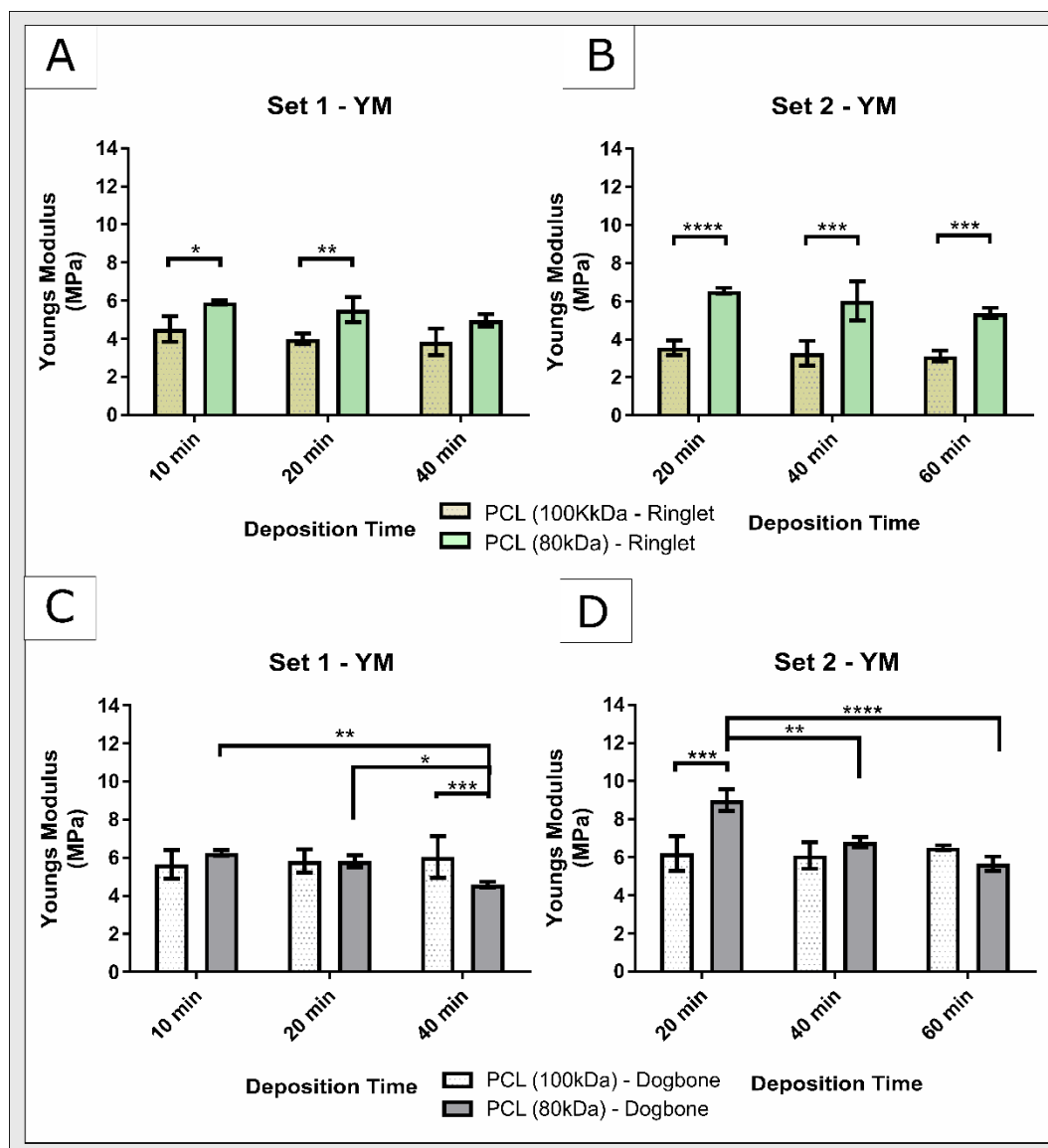


Figure 4.25: Young's modulus (YM) results for PCL batch comparison (A) YM response for Set 1 ringlet samples showing increased YM for 80kDa PCL compared to 100kDa PCL for 10 and 20 minute collection times (B) YM response for Set 2 ringlet samples showing statistically higher YM for 80kDa PCL to 100kDa PCL for all collection periods (C) YM response for Set 1 dogbone samples showing statistically higher YM for 100kDa PCL to 80kDa PCL over 40min (*). PCL 100kDa and 80kDa were statistically equivalent for all other time points (D) YM response for Set 2 dogbone samples showing statistically higher YM for 80kDa PCL to 100kDa PCL over 20min collection period. PCL 100kDa and 80kDa were statistically equivalent for all other time points (* $P \leq 0.05$)(** $P \leq 0.01$)(*** $P \leq 0.001$)(**** $P \leq 0.0001$). $N=3$ per test group.**

In order to assess the stiffness properties of the electrospun vessels while removing any potential artefacts that the cross sectional area calculations may impart on the resulting data, the force per unit strain of the vessels was evaluated as shown in Figure 4.26. The ring modulus was calculated for ringlet specimens, while the force modulus

was calculated for dogbone specimens. The resulting ring modulus measurements typically demonstrated increasing modulus characteristics with increasing deposition times, for both parameter sets examined. Only one deposition time showed a statistical difference between samples created with the alternative PCL batches for sample Set 1 with a decreased ring modulus for 100kDa specimens over a 10 min collection time compared to 80kDa specimens. All 100kDa specimens showed statistically decreased ring modulus characteristics compared to 80kDa ringlet specimens for sample Set 2. Examination of the dogbone specimens again appears to show increasing force modulus trends with increasing deposition time, however, only a limited number of comparisons were statistically different. For sample Set 1, 100kDa PCL specimens collected over 40 min had an increased modulus compared to those collected over 10 min. Similarly, samples collected at the extended collection time of 60 min for sample Set 2 were statistically higher than those of 20 min specimens for both PCL materials.

The strain at break of specimens was significantly higher for those prepared using the 100kDa PCL material compared to those fabricated from the 80kDa PCL, as shown in Figure 4.27. Specimens made with 100kDa PCL typically reached strain values double to triple that of those fabricated with the 80kDa PCL. Again this trend was seen to hold across both ringlet and dogbone specimens, although, the observed strains were slightly lower for the dogbone specimens compared to those of ringlets for both parameter sets.

The SEM results for the PCL batch comparison trial can be found in Table G.1 of Appendix G. No statistical difference was observed in the diameters of fibres at the inner and outer surface of specimens produced using Set 1 & 2 parameters (Figure 4.28 (A-D)). A decrease in fibre coherencies was observed for samples fabricated using 100kDa PCL compared to those manufactured from 80kDa PCL, indicating decreased fibre alignment within specimens spun using 100kDa PCL. The outer surface of specimens created using Set 1 parameters showed a statistical difference between samples collected for 10 minutes, however, no difference was observed over the extended collection periods of 20 and 40 minutes. It is noted that a larger coherency deviation was present in the 100kDa coherencies compared to that observed within 80kDa specimens, indicating greater variation in the spinning of these samples

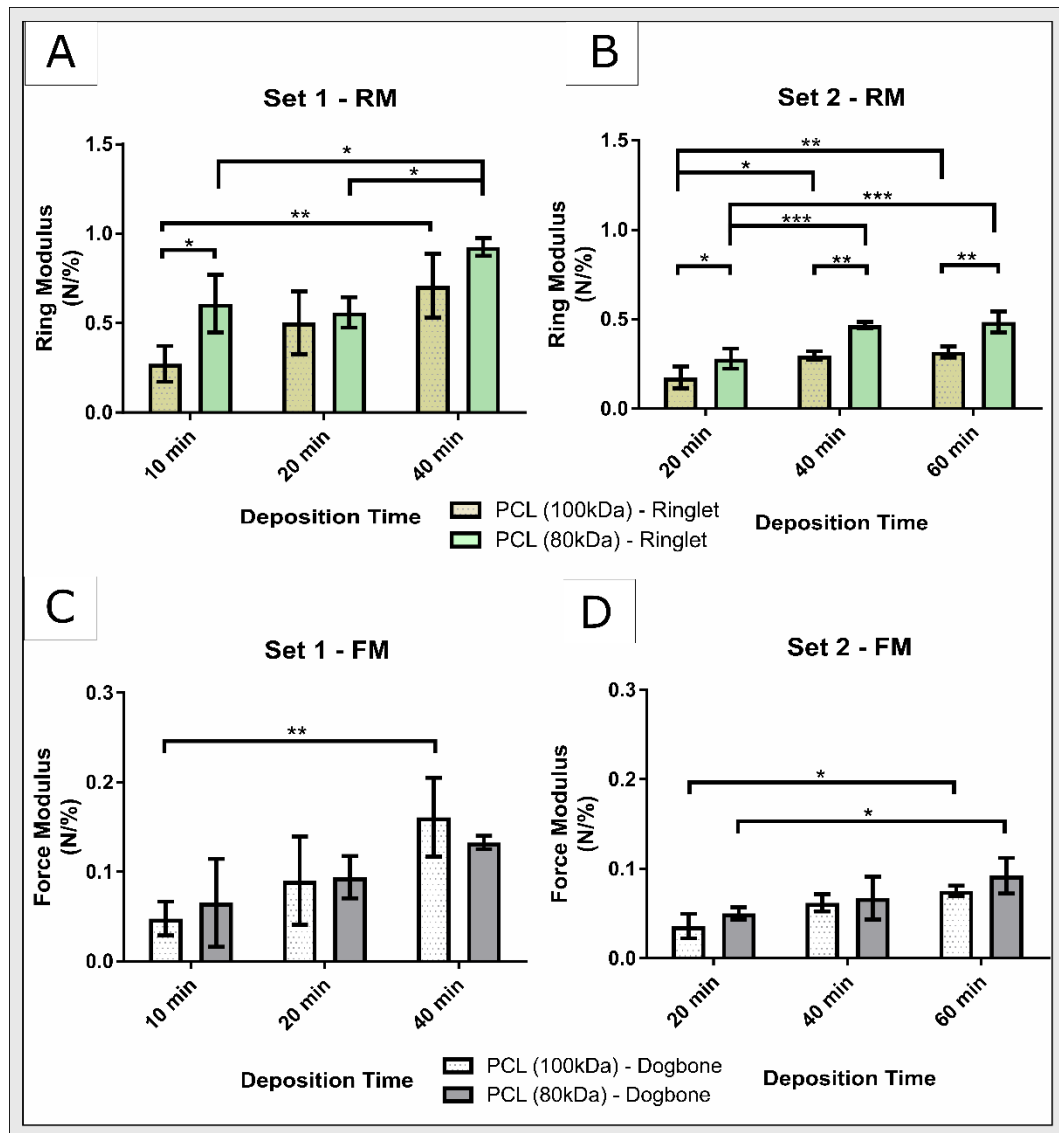


Figure 4.26: Ring and Force modulus results for PCL batch comparison study (A) Ring modulus (RM) response for Set 1 ringlet specimens showing increased RM responses with increasing deposition time (B) RM responses for Set 2 ringlet samples showing statistically higher RM for 80kDa PCL to 100kDa PCL for all collection periods. RM responses also seen to increase with increasing deposition time (C) Force modulus (FM) response for Set 1 dogbone samples showing statistically higher FM for 100kDa PCL at 40min to 10min specimens (). No other statistical differences observed (D) FM response for Set 2 dogbone samples showing statistically higher FM for 80kDa PCL and 100kDa PCL at 60min collection period to those collected for 20min. All other comparisons were statistically equivalent (* $P \leq 0.05$)(** $P \leq 0.01$)(*** $P \leq 0.001$)(**** $P \leq 0.0001$). $N=3$ per test group.**

(Figure 4.28 (E)). Significantly reduced fibre alignment was seen in the outer surfaces of specimens created using the 100kDa PCL For those prepared using parameter Set 2 for all time points (Figure 4.28 (F)). Similar to the outer surface fibres, the inner surface fibres of samples prepared using parameter Set 1 demonstrated decreased fibre alignment at certain time points. The 80kDa PCL fibres were found to possess

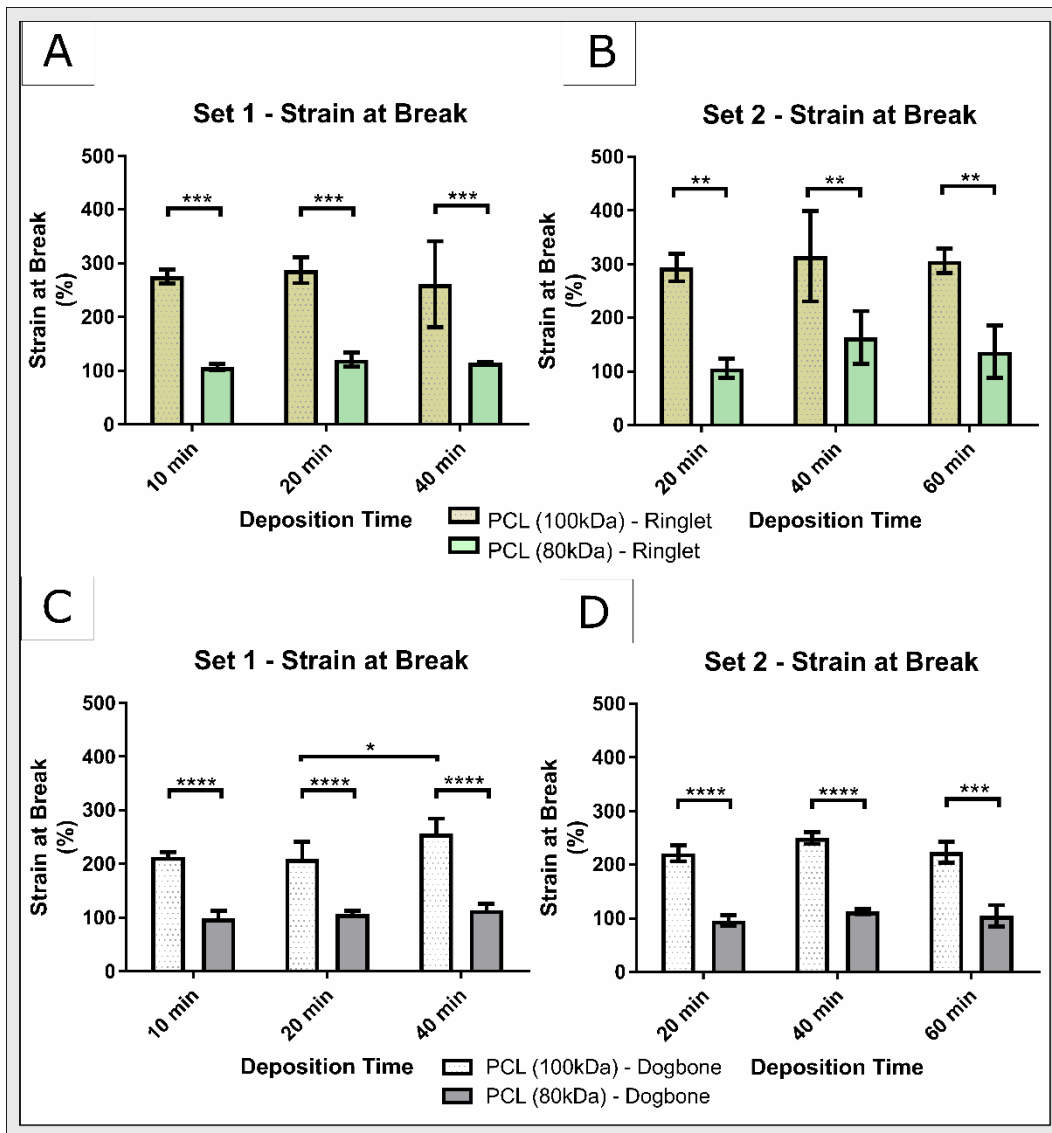


Figure 4.27: Strain at break results for PCL batch comparison (A) Set 1 ringlet samples showing increased strain at break properties for 100kDa PCL specimens compared to those made using 80kDa PCL (B) Strain at break for Set 2 ringlet samples showing statistically higher strains for 100kDa PCL to 80kDa PCL for all collection periods (C) Strain at break for Set 1 dogbone samples showing statistically higher strains for 100kDa PCL to 80kDa PCL for all collection periods (D) Strain at break for Set 2 dogbone samples showing statistically higher strains for 100kDa PCL to 80kDa PCL for all collection periods (* $P \leq 0.05$) ($P \leq 0.01$) (***) $P \leq 0.001$) (**** $P \leq 0.0001$). $N=3$ per test group.**

increased alignment compared to the 100kDa fibres for 10 and 20 minute collection periods. Those at the 40 min period appeared higher for the 80kDa specimens compared to the 100kDa PCL, although not statistically (Figure 4.28 (G)). The coherency of the inner surface fibres created by parameter Set 2 were again found to be statistically decreased for the 100kDa specimens compared to those of the 80kDa PCL. This again indicates a reduction in fibre alignment when the 100kDa PCL

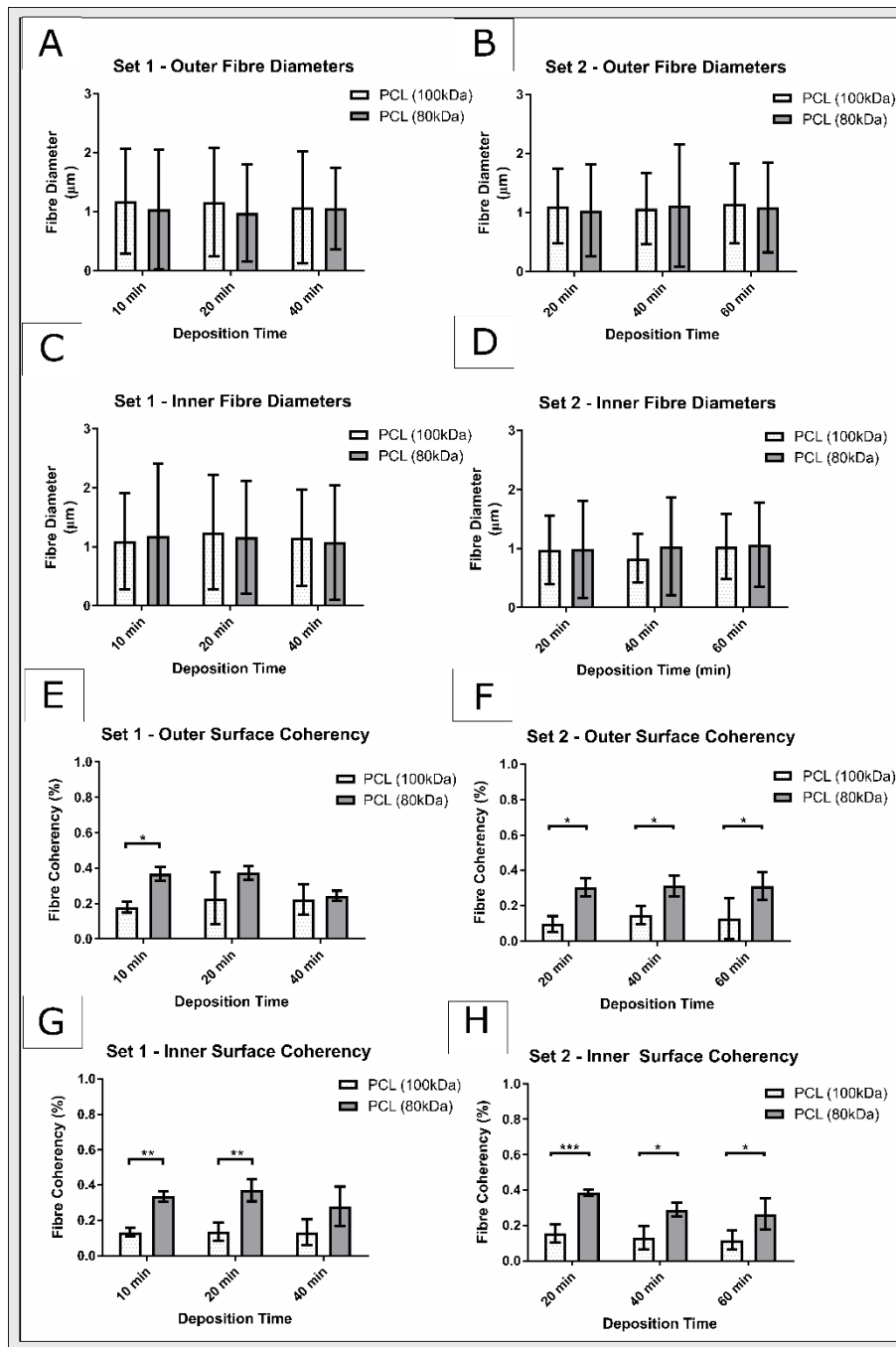


Figure 4.28: Morphological attributes of scaffolds examined in PCL batch comparison trial (A) Diameter of fibres at outer surface of scaffold prepared using parameter Set 1 showing no difference in fibre diameters between PCL batches or collection times (B) Diameter of fibres at outer surface of scaffold prepared using parameter Set 2 showing no difference in fibre diameters between PCL batches or collection times (C) Diameter of fibres at inner surface of scaffold prepared using parameter Set 1 showing no difference in fibre diameters between PCL batches or collection times (D) Diameter of fibres at inner surface of scaffold prepared using parameter Set 2 showing no difference in fibre diameters between PCL batches or collection times (E) Coherency of outer surface fibres for parameter Set 1. Statistical difference observed between 100kDa and 80kDa specimens produced for 10 min with decreased coherency for 100kDa specimens (F) Coherency of outer surface fibres for parameter Set 2. Statistical difference observed between all 100kDa and 80kDa specimens produced. 100kDa specimens significantly lower coherency compared to 80kDa specimens

indicating decreased fibre alignment (G) Coherency of inner surface fibres for parameter Set 1. Statistical difference observed between 100kDa and 80kDa specimens produced for 10 & 20 mins with decreased coherency observed for 100kDa specimens (F) Coherency of inner surface fibres for parameter Set 2. Statistical difference observed between all 100kDa and 80kDa specimens produced. 100kDa specimens significantly lower coherency compared to 80kDa specimens. N=3 per test group.

material was electrospun for the same processing conditions. Porosity analysis of Set 1 & 2 specimens indicated that vessels prepared using 100kDa PCL exhibited decreased porosity characteristics to those produced using 80kDa PCL. This finding was observed to occur for all time points studied, as shown in Figure 4.29.

XRD profiles of ‘Set 1 - 40min’ and ‘Set 2 - 60min’ specimens prepared using both 80kDa and 100kDa PCL can be seen in Figure 4.30 (A) and (B) respectively. The normalised intensity profiles demonstrated two distinct diffraction peaks at ~21 and ~23° for both parameter sets. These peaks are typically present for electrospun PCL materials [111]. The peaks are also noted to be sharp and distinct, indicating a high degree of crystallinity. Moreover the 80kDa and 100kDa specimens show showed similar profiles when overlaid, indicating similar crystallinity rates. The remaining peaks of the spectrum are attributed to those of the cellulose adhesive tape used to adhere the specimen to the mount. This is confirmed by the baseline scan of the pure cellulose tape used.

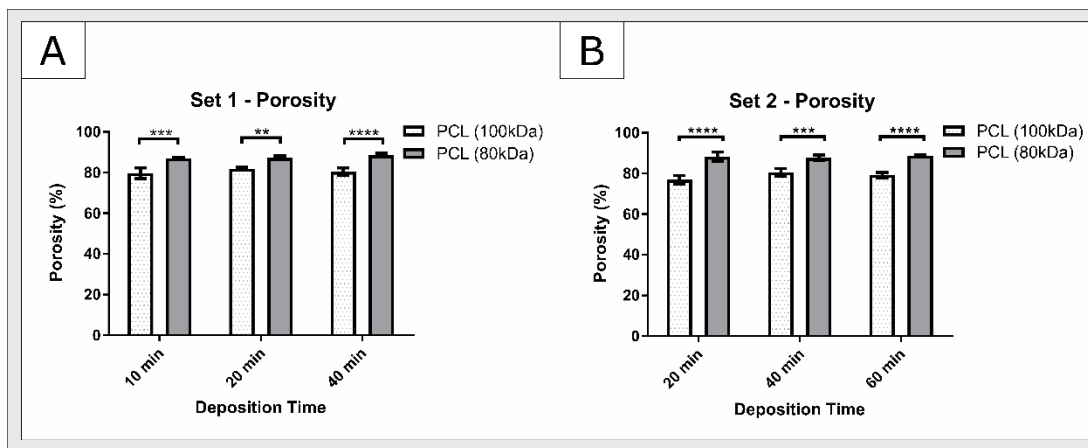


Figure 4.29: Porosity results for PCL batch comparison study (A) Set 1 specimens showing increased porosity properties for 80kDa PCL specimens compared to those made using 100kDa PCL for all collection periods (B) Porosity results for Set 2 specimens showing statistically higher porosity values for 80kDa PCL to 100kDa PCL for all collection periods (* $P \leq 0.05$)($P \leq 0.01$)(*** $P \leq 0.001$)(**** $P \leq 0.0001$). N=3 per test group.**

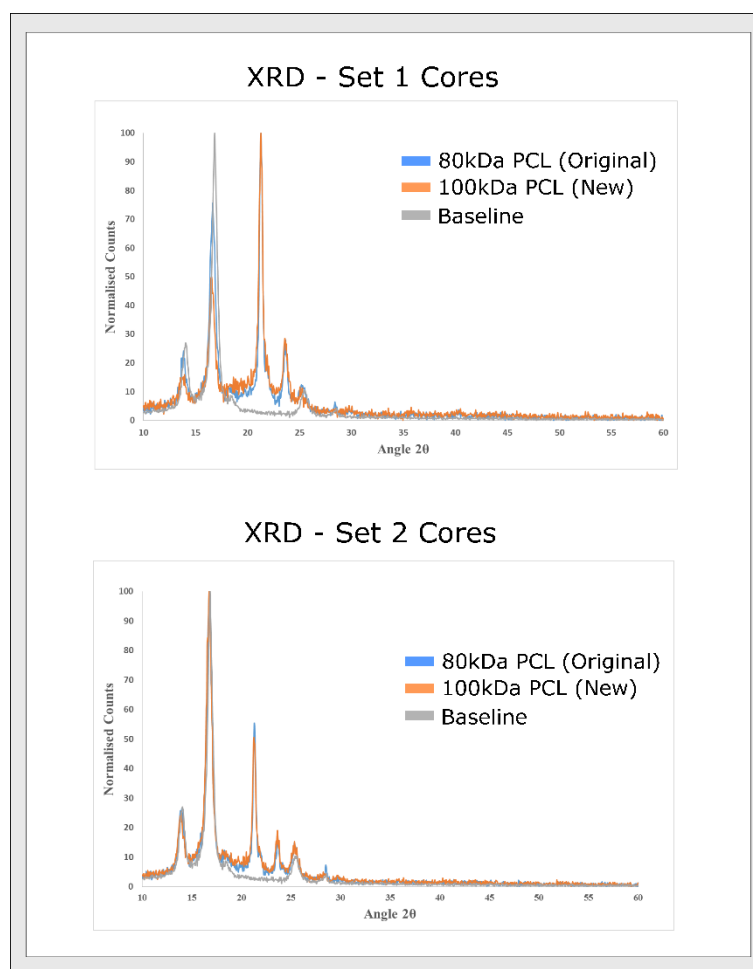


Figure 4.30: XRD profiles of PCL tubular scaffolds prepared using 80,000 (80kDa) and 100,000 g/mol (100kDa) PCL at the same spinning parameters. No shift in peak positions are seen indicating equivalent crystallinity properties. A baseline of cellulose tape is shown.

4.5.2.2 Compliance Properties of PCL cores prepared using New PCL batch ($M_w \sim 100,000$ g/mol)

The compliance properties of the tubular ‘core’ scaffolds prepared using PCL of $M_w = 100,000$ g/mol and electrospun according to set 1 & 2 processing parameters (Table 4.18) can be seen in Figure 4.31. Here it can be seen that with the increasing collection time of electrospun material on the rotating mandrels that the resultant tubular vessels possessed reduced compliance properties accordingly. The compliance of cores produced for set 1 processing conditions reduced from 2.548 ± 1.015 to 0.202 ± 0.349 %/mmHg $\times 10^{-2}$ when the collection time increased from 10 to 40 minutes. Cores for set 2 similarly reduced from 4.530 ± 0.773 to 0.995 ± 0.862 %/mmHg $\times 10^{-2}$ when the collection time was increased from 20 to 60 minutes. From these results it can also be

Table 4.18: Parameter combinations identified for comparison of 16wt% solutions prepared with original PCL batch to 7.8wt% solutions prepared using new PCL batch

Parameter	Flow Rate	Applied	Tip-Collector	Mandrel	Collection Time		
Set No.	(ml/hr)	Voltage (kV)	Distance (cm)	Speed (RPM)	(min)		
<u>Set 1</u>	12	20	17.5	3200	10	20	40
<u>Set 2</u>	4	15	17.5	3200	20	40	60

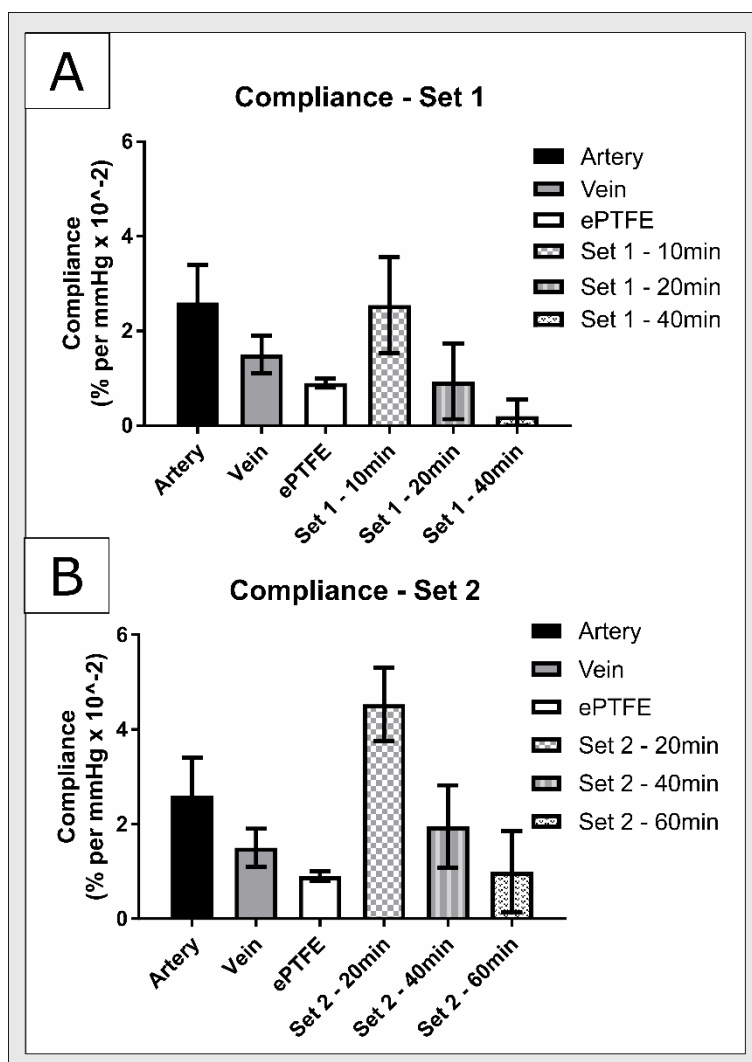


Figure 4.31: Compliance properties of tubular scaffolds fabrication from 7.8wt% PCL ($M_w=100,000\text{g/mol}$) in Chloroform/Ethanol (7:3) solutions spun according to parameter combinations for Set 1 & 2 ($n=3$ per group). ‘Set 1 - 10 min’ vessels showed visually equivalent compliance properties to that of native arteries and higher than that of veins and ePTFE grafts ($n=6$ per group). ‘Set 2 - 20min’ specimens showed increased compliance properties compared to those of the biological vessels at 100 mmHg. Data for biological vessels was adapted from Tia et al. [42]

seen that the compliance properties of vessels prepared by parameter set 2 are higher than those produced by parameter set 1 conditions, indicating greater distensibility properties within the tubular cores created at the lower solution flow rate of 4 ml/hr compared to 12 ml/hr. No statistical comparisons could be made to the biological vessels presented due to the non-parametric nature of the available data and the inability to obtain the medians from the source material (Tia *et al.* [42]). A visual comparison does however shown a good match between Set 1 cores collected for 10 minutes to that of arteries ($2.6 \pm 0.8 \text{ \%/mmHg} \times 10^{-2}$), with higher compliances compared to veins at 100 mmHg ($1.5 \pm 0.4 \text{ \%/mmHg} \times 10^{-2}$) and ePTFE vessels ($0.9 \pm 0.1 \text{ \%/mmHg} \times 10^{-2}$).

4.6 Discussion

4.6.1 Regression Analysis of Multimodal Rotating Mandrel Electrospinning Process

Although the fundamental principles governing the production of fibres by electrospinning are relatively simple in nature, the complexity of electrospinning arises due to the compounding interactions of processing parameters along with the distinctive chemical and physical properties of the solutions to be electrospun. A number of studies have examined the effects of solution and processing parameters on the spinning of electrospun fibrous materials in order to better predict and control the fibrous architectures produced. These studies often employ regression or factorial design principles in order to gain an improved understanding of the spinning process while removing the effects of possible extraneous inputs that may otherwise reduce the power of output signals [198][282]. While these studies have provided valuable insight into the spinning of electrospun fibres, including their applications as vascular grafts, they are often limited in their approach and focus upon individual processing parameters or limited parameter interactions [283]. Additionally few studies have examined the ability to produce hybrid fibre membranes through a single step multimodal spinning process, with the observation of multi-modal fibre generation a secondary observation during traditional spinning studies. Further to this, no study has dealt with the application of regression analysis principles for the production of multimodal PCL tubular scaffolds for arterial bypass applications.

From the outset of the multimodal regression analysis performed within this work, it was clear that the appropriate selection of processing parameter ranges were vital in order to ensure the production of defect free specimens. A number of processing parameter levels were removed from the study due to the inability to produce specimens at particular parameter permutations. This was a critical observation as the initial screening trials performed in Chapter 3 indicated the potential ability to produce specimens using these particular levels.

One such example of this included the lower spinning voltage range of 10 kV. While it was possible to create specimens at the reduced flow rate of 4 ml/hr with an applied

voltage of 10 kV, the interaction of the increased flow rate level of 12 ml/hr paired with the lower applied voltage resulted in what was termed as ‘electrospraying’. This uncontrolled repulsion of polymer droplets from the spinneret tip is suspected to have occurred due to an imbalance in the supply rate and removal of material at the spinneret. The increased flow rate of 12 ml/hr resulted in an excessive quantity of polymer material being supplied to the tip compared to that being removed to the collector. Once a critical mass of polymer solution gathered at the spinneret, the surface tension forces of the solution were no longer able to hold the droplet in place, resulting in its separation. Due to charging effects the droplets were repelled away from the spinneret upon separation resulting in droplets of wet polymer landing on the collection mandrel, similar to that of the electrospraying technique [284]. This wet polymer subsequently dissolved any fibrous material that had previously collected on the rotating mandrel. By increasing the applied voltage to between 15 and 20 kV, increased splaying effects were observed to occur within the Taylor’s cone. This is thought to have occurred due to a change in the charge per unit area of the electrospinning jet due to its elongation or increased evaporation of the solvent induced by the increased electric field strengths [150]. In order to reduce the charge per unit area, smaller jets erupted from the surface of the Taylor’s cone. These increased splaying effects resulted in an increased removal of polymer from the spinneret tip, allowing for a balance between material supply and removal. This effect is also believed to give rise to the multi-modal fibre distributions seen within the collected scaffolds [285][286].

In a similar fashion the collector distance level of 22.5 cm was found to be an excessively high distance when spinning at the reduced flow rate of 4 ml/hr. Although specimens could be successfully created at the flow rates of 8 and 12 ml/hr, it is thought that the fibres produced at 4 ml/hr underwent such thinning effects that their diameter reduced to a point at which the circulating airflow prevented their deposition to the rotating mandrel. This effect was also seen at the increased collector distances for all flow rates, where there was a reduction in the quantity of material collected per unit time. This practical limitation prevented the use of this collection level across the matrix to ensure orthogonality of the design was maintained. While the removal of these voltage and collector distance levels resulted in the overall reduction of the study

scope they were important for maintaining the power of the regression analysis.

4.6.1.1 Analysis of Response Variables (Ys) to Input Parameters (Xs)

The use of regression analysis principles allowed for the identification of a number of key factors during the assessment of mechanical and morphological responses of the multi-modal core scaffolds. The ultimate tensile strength (UTS) of specimens was found to be highly influenced by both the rotational speed of the collection mandrel and the tip to collector distance. UTS properties of vessels were found to increase as the rotational speed of the collection mandrel was varied from 1600 to 3200 RPM. This may in part be explained by the increased fibre coherencies observed within vessels collected at the increased mandrel speed. This increased fibre alignment provides additional resistance along the circumferential axis of vessels, allowing for greater loading before failure. In addition the augmented alignment of fibres allow for their increased packing densities, providing a greater number of fibres to resist loading per unit area. This belief is further reflected in the decreased porosities of the vessels collected at the higher rotational speed of 3200 RPM. Additionally the rotational speed of the mandrel was also found to reduce the diameters of fibres located on both the internal and external surfaces of the tubular vessels. This is anticipated to have occurred due to stretching effects imparted upon fibres as they landed on the rotating surface, similar to that witnessed with the rotating drum collector in Chapter 3. The UTS of specimens was also found to decrease as the collector distance increased from 15 to 20 cm. This may be attributed to the presence of fused fibres and increased fibre junctions at the lower collector distances, due to insufficient solvent evaporation before deposition [285]. By increasing the collector distance, greater solvent evaporation can occur, ensuring complete fibre separation upon deposition. While increased fibre connectivity typically results in increased UTS properties it may also reduce the ability of fibres to re-orientate upon the application of an applied load. This inability to align to the direction of loading may subsequently result in decreased Young's modulus characteristics at lower collector distances. This reduced Young's modulus result was seen to occur in specimens produced at the collector distance of 15 cm compared, with increasing Young's modulus values seen up to the collector distance of 20 cm.

An interesting observation for the UTS response was the reduction of UTS within vessels created at the increased flow rate range. This reduction was unexpected, particularly based upon the observation that the vessels produced at the higher flow rate ranges were typically easier to remove from the collection mandrels suggesting increased strength and rigidity characteristics. The results of the maximum force and force modulus analysis support this observation, with increased forces to failure found within vessels created at 8 and 12 ml/hr, and similarly increased force per unit strain characteristics suggesting stiffer vessel formation. It is suspected that although the vessels are stronger, the corresponding resistance per unit cross section of the vessels may not be equal. This unequal force resistance within the vessel walls result in the decreased UTS properties with increasing wall thicknesses. One possible explanation for this unequal loading scenario may be explained by the coherency characteristics observed for vessels. As previously shown fibres located on the external surface of the vessels exhibited increased coherencies compared to those at the internal surface of the vessels. This transitional change in fibre alignment between the internal and external surfaces of the vessel may in turn result in non-uniform fibre loading between those located at the inner and outer surfaces. Further analysis of this fact demonstrated that samples produced at 12 ml/hr showed a statistically greater transitional difference in the fibre coherencies ($p=0.024$) between their internal and external surfaces (0.098 ± 0.116) compared to those produced at 4ml/hr (0.0417 ± 0.0881). These results indicate the importance of understanding not only the material attributes but more importantly the structural attributes of the vessels themselves.

The regression analysis performed for the Young's modulus response similarly found that the collector distance and collection speed were strong predictors in the YM response of the produced vessels. It is suspected that the previously discussed increase in packing density may also explain the increase in Young's modulus found to occur in specimens created at the higher collection speed. Increased fibre alignment within the electrospun vessels will result in less deformation of fibres upon loading due to reduced reorientation effects under the application of the applied load [287]. Like that observed within the analysis of the UTS response, Young's modulus was similarly found to decrease with increasing flow rate. It is again suspected that this decrease occurred due to the non-uniform resistance of loading within the vessel walls. This

results in the apparent decrease in vessel stiffness although the force modulus results show that the vessels produced at the higher flow rates were in fact more rigid. The interaction between the collection speed and distance were also found to be significant, with Young's modulus characteristics found to be similar for both the 1600 and 3200 RPM specimens. As the collector distance was increased it can be seen that the increased collection speed of 3200 RPM resulted in a significantly higher increase in the Young's modulus response compared to the equivalent vessels at 1600 RPM. This suggests that the increased speed of rotation has a greater effect on vessel formation when the fibres were collected over a greater distance. This may be due to the decreased electric field strength felt by fibres with increasing collector distance, which allows for the greater re-orientation upon deposition.

The examination of the maximum forces to failure again shows that collector distance is a primary predictor in determining the vessel properties. A reduction in the maximum force can be seen with increasing collector distance, this is thought to occur due to the loss of material to the surrounding environment as the collector distance increases. As stated previously vessels created at the flow rate of 12 ml/hr possessed on average twice the maximum force to failure of samples prepared at 4 ml/hr despite an apparent decrease in UTS. Again this can occur due the reduced volume of polymer being spun per unit time reducing the overall quantity of material collected on the mandrel. The interaction between flow rate and collector distance was also found to be a significant predictor for the maximum force. As the collector distance increased the increase in flow rate resulted in a less significant effect. Again this may be attributed to the loss of fibres or due to the reduced number of fibre connections at the increased spinning distance. The higher solution flow rates would be expected to contain increased residual solvents upon deposition compared to that of the lower flow rate level. This increased quantity of solvent may have resulted in the greater fibre fusion and an overall more interconnected structure resulting in the higher maximum forces.

The analysis performed for the porosity characteristics of the produced vessels indicated a number of predictor variables. Collector distance and collection speed were again noted to be significant predictors for determining vessel porosity with this

suspected to be related to changes within the fibre packing density of the scaffolds [288]. An interesting observation was the apparent effect of the applied voltage, which was found to reduce porosity levels when increased from 15 to 20 kV. This may be related to the increased splaying effects observed when specimens were spun using the higher spinning voltage. Increased splaying effects should result in the increased production of nanofibres due to the increased jet formation at the spinneret tip. This is reflected within the outer fibre diameter measurements where a decrease in fibre diameters was observed with increasing applied voltage. The presence of these smaller fibres could potentially limit the size of pores between falling fibres, reducing the overall porosity of the specimen. It is however noted that the R-sq and R-sq predicted terms of the model were extremely low paired and paired with a large 'S' term suggest that the model is prone to variation. While it does not remove the significance of the predictor terms identified within this regression analysis, it does indicate the potential for the porosity variable to be prone to random effects, or effects not identified within this study.

Another interesting and unexpected result of the regression analysis was observed upon the examination of coherency rates for the external surface fibres. It was observed that fibre coherency was seen to be highly influenced by the applied voltage and flow rate of the electrospinning solutions. An increase in the applied voltage was found to result in an increase in random fibre deposition on the collector. This may be due to two influencing effects. Increased applied voltage typically results in increased whipping instabilities within the electrospinning jet [289]. This can in turn result in fibres possessing a more random orientation upon landing on the collector surface. In addition, the increased applied voltage may result in increased charge retention within depositing fibres. This charge retention in turn negatively impacts the alignment of subsequently deposited fibres [262]. A typical hallmark of charged retention is the formation of 'dimples' or 'ridge' like structures on the surface of the electrospun materials [167][290][291]. This observation was previously made for the specimens created at the applied voltage range of 15 and 20 kV within this work, with increased ridge presence seen for samples formed at 20 kV. Increasing the solution flow rate was also seen to result in increased fibre coherency in the outer surface of the vessels. This may be due to the increased resistance of polymer chains within the spinning jet

during flight, which resists whipping effects between the spinneret and collector [247], in turn preventing excessively random deposition.

The regression analysis performed for the diameter of inner surface fibres identified only a single predictor variable with that being the rotational speed of the collection mandrel. As previously noted the diameter of fibres were found to reduce with the increasing rotational speed of the collection mandrel, with this attributed to the increased tensile forces experienced by the fibres upon deposition, which subsequently result in increased stretching and thinning effects. An extremely low R-sq and R-sq predicted term were seen at 8.10 and 4.6% respectively suggesting that the model is poor at predicting fibre diameters. Equally the predictor analysis for the outer fibre diameters again demonstrated poor R-sq and R-sq predicted terms at 24.28% and 16.72% respectively. These poor coefficient of determination values are believed to be seen due to the multi-modal nature of the collected fibres. The ability to accurately assess the fibres based off a single response variable such as average fibre diameter presents a number of difficulties when investigating complex fibre distributions. Similarly the standard deviation or the coefficient of variation (CV) of the fibre diameters would not accurately predict the complex structures produced during multi-modal spinning. A way to accurately represent the multiple fibre populations found within the specimens, combined with their relative percentage contributions would be required in order to develop a tool capable of accurately predicting future fibre diameters. Similarly the use of linear regression principles may not be suitable for such a complex response variable and may require techniques such as response surface methodology to better account for model curvature.

4.6.1.2 Identification of Choice Parameter Combinations for Preparation of Multi-modal Core Layer

The tubular core scaffolds produced using the 16wt% Chloroform/Ethanol (7:3) solutions demonstrated average UTS values ranging from ~1.5 to 3 MPa. Previous studies have shown the circumferential tensile strength of native human coronary arteries (HCAs) to be 1.44 ± 0.87 MPa [174], and the gold standard vessel for arterial bypass grafting, the great saphenous vein (GSV) to be 3.01 ± 1.91 MPa [281]. The UTS values of the core scaffolds are comparable to these biological tissues and are

anticipated to have suitable resistance to loading when implanted. In addition, the scaffolds demonstrated Young's modulus properties ranging from ~4 to 10 MPa depending on the spinning conditions used. The previous studies noted have in turn demonstrated the Young's modulus of HCAs to be 1.55 ± 0.52 MPa, and GSVs to be 42.62 ± 27.76 . Other works have shown that porcine coronary arteries, a common conduit used in experimental studies for its mechanical resemblance to human tissue, exhibits Young's modulus values of $\sim 4 \pm 2$ MPa [292]. While these individual characteristics do not directly match those of the electrospun cores, the significant range of these biological vessels indicate that the core scaffolds may be suitable for arterial bypass applications. One significant point to be vigilant with, is the fact that successful matching of the Young's modulus properties will not necessarily provide vessels with the appropriate compliance properties required to avoid long term failure upon implantation. The successful matching of Young's modulus properties should however be used as a screening indicator to ultimately develop a vessel with matching compliance characteristics.

Although the regression analysis indicated significant predictors for UTS and Young's modulus responses, there was no clearly defined vessel that possessed out right superior qualities to another. Instead a number of secondary criteria were employed to further reduce the range of potential vessels for use in further studies. As introduced during the literature review, it is highly desirable to provide an orientated scaffold morphology on which cells can grow, in order to provide increased proliferation and guidance for tissue growth [235]. Specimens created at 1600 RPM were demonstrated to possess decreased fibre coherency compared to those vessels created at 3200 RPM. Again the fibre alignment was seen to align with the circumferential axis of the rotating mandrel, providing fibres that resemble the natural collagen and elastin structures found with in native blood vessels. For these reasons, specimens created at the lower rotational speed of 1600 RPM, were no longer considered. It is still however noted that these vessels possessed sufficient UTS and Young's modulus criteria, and may be suitable for future exploration studies.

A number of qualitative observations were subsequently employed to further refine the selection of parameters for the production of the final multi-modal core scaffolds.

These observations included the simplicity of the scaffold manufacturing process along with the quality of the final fibres produced. Specimens fabricated at the increased collection distance of 20 cm were often difficult to remove from the copper collection mandrels proceeding the methanol soaking release step. This was reflected in the force modulus and maximum force to failure of the specimens which was found to be considerably lower for vessels produced at 20 cm compared to those at 15 and 17.5 cm. It desirable to have a final manufacturing process that allows for the simple and repeatable production of the final scaffold designs. Due to this, the specimens collected at the distance of 20 cm were removed from further consideration. Finally, based on the observations of the UTS and Young's modulus properties, along with the visual screening of specimens, the collector distance of 15 cm was removed from consideration. This choice was taken based on the results of fused fibres within the specimens, particularly at the increased flow rate ranges. These fused fibres typically indicate the presence of residual solvents within the final scaffold which can be highly toxic to seeded cells. The fusing of fibres were also suspected of reducing the Young's modulus response of the vessels which may negatively affect compliance properties.

Instead of selecting a single choice core layer for use in further studies, two sets of parameter combinations were identified due to them possessing similar UTS and Young's modulus characteristics while equally presenting significantly different ring modulus, maximum forces to failure and cross sectional area characteristics. These differences highlighted the difficulty in using standard material properties to accurately assess the response of a complex fibrous construct. The selection of two parameter sets for further exploration was thought to allow for an increased understanding of material properties and their overall translation to structural properties including that of vessel compliance, while also improving the likelihood of developing a final vessel with suitable compliance characteristics.

4.6.2 Control of Molecular Weight Variation between PCL Batches through the Matching of Solution Viscosities

Gel Permeation Chromatography (GPC) performed on different batches of the raw polymer PCL indicated substantial discrepancies between the measured average

molecular weight of the material and that listed. These discrepancies were further seen in the preparation of solutions for electrospinning where viscosity characteristics for equal weight percentage solutions were seen to be unequal. The original PCL batch material (00807DJ-Original) used for the multi-modal concentration trial and regression analysis study was found to have an approximate average molecular weight of ~83,000 g/mol. This was in high agreement with the listed molecular weight of 80,000 g/mol. The second batch of PCL studied (MKBV3325V-New) was found to have an average molecular weight of ~100,000 g/mol compared to the listed M_w at 80,000 g/mol. It is noted that the M_w is very subjective when measured by GPC as the solvation of the polymer chains will affect its apparent weight against a universal calibration. This means there may be some error in the final recorded value of the M_w depending on the preparation and measurement of the GPC solutions. However, what the results clearly show is the existence of a significant difference between the molecular weights of the two PCL batches supplied.

As detailed during the literature review, viscosity is perhaps one of the most defining solution parameters for predicting the electrospinning potential of a polymer solution [154]. In turn the molecular weight and polymer concentration are key attributes for fine tuning solution viscosity characteristics [154]. The solution standard curves prepared demonstrated that an approximate difference of 20,000 g/mol between the two PCL batches resulted in significantly different viscosity solutions with changing polymer concentration. Solutions prepared using the new PCL batch (100kDa) required approximately 50% less polymer concentration to achieve an equivalent measured viscosity to that of the original PCL solutions (80kDa). Nezerati *et al.* similarly found for the spinning of PEG fibres that a difference in molecular weight between polymer batches of approximately 24 kDa or 24,000 g/mol resulted in a 20% difference in the measured viscosity of 17 wt% polymer solution between the two batches [280]. It is noted that in this case the average molecular weight of the polymer being used was approximately 220,000 g/mol, meaning the batch variation represented a smaller overall percentage at ~11% compared to that of ~25% seen in this work.

4.6.2.1 Assessment of Mechanical Response Variation between PCL Batches

A 7.8wt% PCL ($M_w = 100,000$ g/mol) in Chloroform/Ethanol (7:3) solution was found to possess equivalent viscosity and conductivity attributes to that of the 16wt% solutions prepared using the original PCL material ($M_w = 80,000$ g/mol). Kim *et al.* demonstrated that by maintaining equivalent viscosity characteristics for PET electrospinning solutions, regardless of molecular weight variations, nonwovens with equivalent fibre diameters could be successfully prepared [263]. It was anticipated that by maintaining the same viscosity and conductivity characteristics for the PCL solutions, scaffolds with equivalent fibre diameters to those seen in the regression analysis could be created. This in turn was anticipated to reduce any mechanical variations that may be imparted on the scaffolds due to the altered molecular weight of the polymer being spun.

Specimens were prepared using the two previously identified parameters sets employing both the original (80kDa) and new (100kDa) PCL materials in order to characterise any potential differences in their mechanical responses. In addition, the parameter sets were spun at altered spinning times in order to establish the effect of spinning time on their resultant mechanical attributes. Both ringlet and dogbone testing was performed based on the previous observation from the multimodal regression analysis, in which ringlet specimens of increased wall thickness typically displayed reduced UTS properties compared to thinner walled vessels. In order to study if this effect was an artefact of the test method or a broader structural property, the two specimen variations were considered.

Analysis of the scaffolds produced using the new PCL material confirmed that equivalent internal and external fibre diameters to those of the 80kDa PCL scaffolds could be achieved for both parameter sets tested. This observation reaffirms the concept that the matching of solution viscosities allows for the appropriate tailoring of solutions with varying molecular weight polymers.

An interesting and clear difference between the 80kDa and 100kDa scaffolds was the strain at break characteristics observed. The strain at break of specimens was considerably higher for vessels created using the 100kDa PCL, at nearly three times

larger than that seen within 80kDa specimens. This difference was clearly seen for both the ringlet and dogbone specimens. An examination of fibre coherencies may explain this observed difference, with both the inner and outer fibres of 80kDa PCL exhibiting increased coherency rates compared to the 100kDa specimens. This higher coherency in turn results in the specimens exhibiting decreased elongation before failure due to the pre-aligned nature of the fibres [293].

This difference in coherency was further reflected in the reduced Young's modulus responses for 100kDa PCL core scaffolds compared to those of the 80kDa PCL. It is noted that this difference in stiffness properties between PCL batches was not clearly detected through the testing of dogbone specimens. This suggested that the ringlet test method may be more sensitive to variations in fibre orientation compared to those of dogbones. This may be explained by the fact that the testing of ringlet specimens involves the testing of two larger wall cross sections compared to the small test area examined in dogbone specimens. This in turn may result in the fibre alignment having a more dominant effect within the structures throughout the test cycle.

The force modulus response of the vessels created using the new PCL was similarly found to indicate differences between the PCL batches when tested by the ringlet method, with no clear batch differences detected by the dogbone specimens. Again this effect may be amplified by the ringlet test method, with the larger wall sections potentially requiring larger forces to failure, allowing for clearer signals to be obtained. The force modulus was similarly seen to increase between time points for ringlet test specimens but not for dogbone specimens. This lack of a statistical increase was unexpected as the samples created at the increased collection time were expected to require significantly increased force to induce deformation, due to the increased wall thickness of the collected specimens. This again reiterates the concept that dogbone specimens do not fully capture the response characteristics of the fibre constructs.

Finally the UTS of the vessels created with the 100kDa PCL were significantly increased compared to those created with the 80kDa PCL. XRD results confirmed that the fibre constructs created from the two PCL batches possessed comparable

crystallinity rates, indicating that the altered mechanical results were not due to a change in molecular orientation within the fibres that as has been previously seen to occur when spinning higher molecular weight materials [157]. This suggests that the change may be due to a change in morphological properties. The 100kDa PCL specimens were show to possess statistically decreased porosities compared to the 80kDa specimens. This may suggest an increased in the packing density of fibres or an increase in fibre content, which provides increased resistance to loading and thus higher UTS properties.

Although the vessel properties of the newly formed core scaffolds were different to those previously studied it was ultimately considered that their properties were still comparable to those of the HCAs and GSV and therefore suitable for further examination. This involved the assessment of their compliance characteristic in order to assess the structural response of the core in its entirety.

4.6.2.2 Compliance Properties of PCL cores prepared using New PCL batch ($M_w \sim 100,000$ g/mol)

The resulting compliance properties measured for the core scaffolds fabricated using the 100kDa PCL further indicate the importance of not only assessing the intrinsic material properties of the material but also assessing the structural properties of the vessel. A reduction in vessel compliance with increasing material deposition was observed to occur, for both parameter sets studied. Previous testing by uniaxial ringlet and dogbone testing showed limited differences in specimen UTS and Young's modulus characteristics over the different collection periods. This makes it difficult to predict the overall vessel response when the vessel is subjected to physiological loading conditions.

Specimens prepared according to the set 1 spinning parameters and collected over a period of 10 minutes showed excellent equivalency to that of native arterial tissue. Similarly, specimens created using the parameters of set 2 and a deposition period of 20 minutes demonstrated superior compliance values to that of the arterial and venal tissue. These compliance results are highly encouraging and provide a promising basis for the development of the bi-layer composite vessel under investigation.

Chapter 5 Development of Dynamic Liquid Collection Apparatus for the Production of Nanofibre Bundles

5.1 Introduction

As detailed within the literature review, the use of nanofibre bundles and yarns has shown significant promise within the field of tissue-engineering due to the ability to produce scaffold constructs that possess increased pore volumes compared to traditional nanofibre membranes, while retaining the inherent benefits that nanofibre materials offer [26][236][294]. One particularly interesting method for the development of these fibre bundles is through dynamic liquid collection principles, as first detailed by Teo *et al.* [221]. Briefly, the dynamic liquid collection process consists of a two-tier water bath system wherein electrospun fibres are directly spun onto the surface of moving water located within the upper tier bath. The electrospun material subsequently bundles and aligns to form an electrospun filament as it is drawn through an outlet located in the base of the bath due to the effects of the draining fluid. A rotating collector is typically positioned below to the outlet to gather the falling material. This can be done by directly collecting it in the form of a tubular construct or by drawing the filament off to a winding bobbin.

In order to incorporate the benefits of these nanofibre bundles while maintaining a structure that is capable of withstanding physiological loading conditions, the nanofibre bundles were utilised as a secondary layer that were applied to the outer surface of the previously developed PCL multi-modal cores (Chapter 4). In order to fabricate the novel bi-layer scaffold, a custom built dynamic liquid collection electrospinning rig was first designed and commissioned, followed by the screening of a number of potential nanofibre spinning solutions. Based on these findings a final

bi-layer vessel was constructed and its mechanical properties assessed. The specific actions performed within this chapter are as follows:

- **Design and Implementation of Dynamic Liquid Collection System**

A custom built dynamic liquid collection system that allowed for the precise control and alteration of a number of key processing parameters was first designed and fabricated. These processing parameters were suspected of altering the morphologies of the nanofibre bundle constructs produced and so were vital to assess in later screening studies.

- **Process Development of Dynamic Liquid Electrospinning Process**

A number of PCL electrospinning solutions were prepared and then electrospun over an array of processing parameters in order to assess the resultant fibre morphologies and constructs produced. In this the relative manufacturability of the specimens along with their fibre quality attributes were assessed, in order to establish select processing conditions for the development of the final bi-layer constructs.

- **Production of Novel Bi-layer Vessels**

Using the choice electrospinning solution and process parameters identified, bi-layer vessels were fabricated by coating previously designed and manufactured multi-modal PCL cores with the nanofibre bundle assemblies.

- **Mechanical and Morphological Characterisation of Novel Bi-layer Scaffold**

The mechanical and morphological characteristics of the final bi-layer vessels were assessed through uniaxial ringlet testing, porosity analysis, scanning electron microscopy and static compliance testing.

5.2 Materials & Equipment

5.2.1 Materials

- Poly(ϵ -caprolactone) with a measured average molecular weight (M_w) of 100,000 g/mol (Sigma Aldrich, USA)**
- Chloroform ($\geq 99\%$) with amylenes as a stabiliser (Sigma Aldrich)
- N,N-Dimethylformamide (99.8%) (Sigma Aldrich)
- Ethanol (≥ 99.5 , 200 proof) (Sigma Aldrich)
- Acetone (Sigma Aldrich)

**Purchased as equivalent 80,000 g/mol from Sigma Aldrich but verified by Gel Permeation Chromatography (GPC) to be 100,000 g/mol

5.2.2 Equipment

- Custom Built Liquid Dynamic Collection Rig (DCU, Ireland)
- KDS200P Syringe Pump (KD Scientific, USA)
- ES30P-20W/DAM Power Supply (Gamma High Voltage Research, USA)
- 20G x 1.5” Hypodermic Needle (Tip Blunted) (Terumo, USA)
- 20ml Gas Tight Glass Syringe (SGE Analytical Science, Australia)
- Testo 615 Digital Humidity Meter (Testo Inc., Germany)
- AVM-8880 Hot Wire Anemometer (ATP Instrumentation Ltd, UK)
- High Voltage Probe (Radionics, Ireland)
- AT-6 Tachometer (Farnell, UK)
- Magnetic Stir Plate (Bibby, HB502, Sterlin UK)
- Mettler AE50 balance (Mettler Toledo, Switzerland)
- EVO LS15 Scanning Electron Microscopy (Zeiss, Germany)
- Edwards Pirani 501 Scancoat Sputtering Coater (Edwards Laboratories, USA)
- Zwick Z005 Tensile Test Machine with 500N Load cell (Zwick-Roell, Germany)
- External Micrometer (Draper Tools, UK)

5.3 Methods

5.3.1 Solution Preparation and Characterisation

5.3.1.1 Solution Preparation

Electrospinning solutions were prepared by dissolving PCL at the required concentration in Chloroform/DMF (7:3;v:v) according to the previously described solution preparation protocol detailed in Chapter 3 (p.65).

5.3.1.2 Dynamic Liquid Electrospinning

A custom built dynamic liquid collection system comprised of an electrically insulated light weight support frame, along with a two tier adjustable water bath system was designed and fabricated in DCU (Figure 5.1 (A)). The top tier water bath had a diameter of 300 mm and a depth of 95 mm. The outlet located in the base of the bath had a diameter of 5 mm. A syringe pump system suspended above the water bath was loaded with a glass syringe with attached spinneret (20G blunt tip needle). The axis of the spinneret tip was aligned directly to the centre of the top tier basin. A high voltage supply was attached to the spinneret and secured in a safety clamp to ensure no contact with the water could occur if the supply unexpectedly detached from the spinneret. A dual channel recirculating pump was used to maintain a constant fluid height within the top tier water basin (Figure 5.1 (B)). The distance between the surface of the water and spinneret tip could be easily and accurately adjusted by lifting the syringe pump assembly through a jack plate system. A custom built rotating and traversing mandrel system of $\varnothing 5$ mm with a rotational speed of 65 RPM, stroke length of 75 mm, and traversing speed of 0.2m/min was positioned directly below the outlet of the basin to collect the falling nanofibre bundles.

Following the collection of the nanofibre bundle assemblies, the collection mandrels containing the fibres (Figure 5.1 (C)) were frozen at -50°C for 4-6 hours. Following this the samples were lyophilised for a further 24 hrs in a vacuum freeze drier. For the production of the bi-layer vessels, the collection mandrels were loaded with a multimodal PCL core prior to spinning.

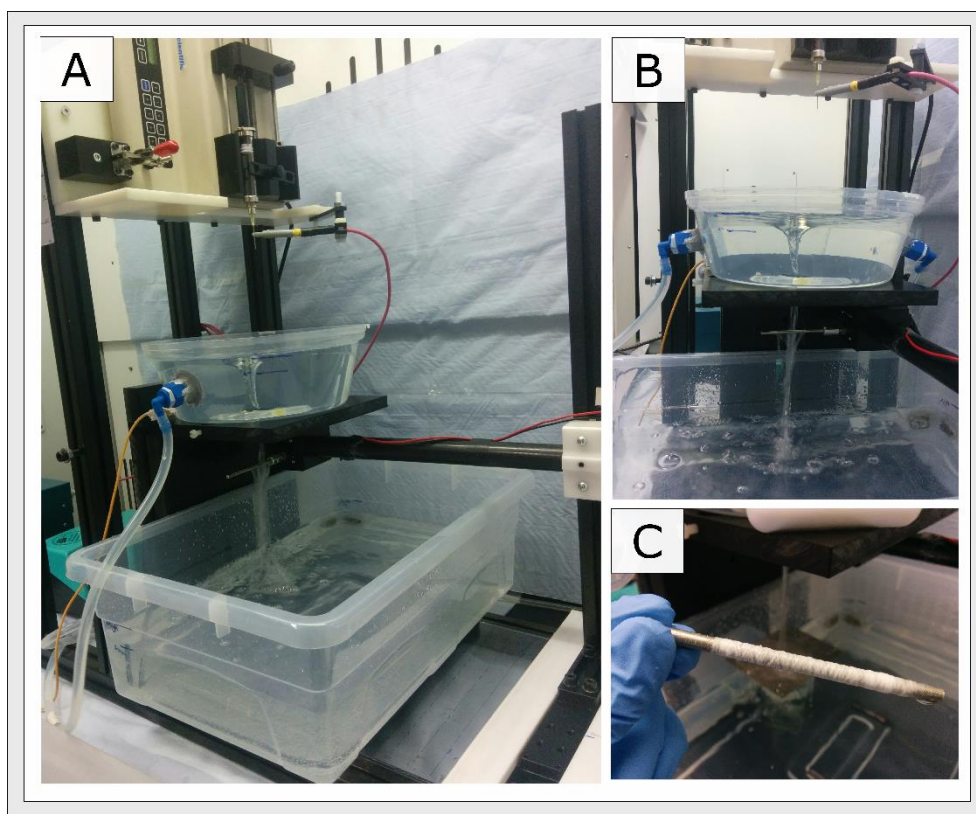


Figure 5.1: *Images of custom built dynamic liquid electrospinning rig (A) Broad view of spinning apparatus showing two tier water bath system, syringe pump, along with rotating and traversing collector mandrel (B) Zoomed view showing vortex formation in top tier water bath used to induce nanofibre bundle formation (C) Sample image of nanofibre bundle materials deposited on collector mandrel*

After freeze drying, the pure nanofibre bundles were slit open upon their longitudinal axis and removed as a flat membrane from the mandrel (Figure 5.2 (A)). For the case of the collected bi-layer vessels, they were first pre-trimmed to remove excessive nanofibres bundles, after which they could be easily removed from the mandrel (Figure 5.2 (B)).

5.3.1.3 Preparation of Multimodal PCL Core Scaffolds

The chosen PCL core scaffolds previously designed within Chapter 4 were fabricated according to the solution and processing parameters detailed in Table 5.1. Two parameter conditions were chosen for study in order to establish the resultant effects of nanofibre bundle deposition on the vessel compliance. Samples were electrospun according to the previously described protocol for rotating mandrel electrospinning.

Table 5.1: Process parameters utilised to fabricate PCL multi-modal core scaffolds

7.8wt% PICL in Chloroform/Ethanol (7:3; v:v)					
Parameter	Flow Rate	Applied	Tip-Collector	Mandrel	Collection
Set No.	(ml/hr)	Voltage (kV)	Distance (cm)	Speed (RPM)	Time (min)
<i>Set 1</i>	12	20	17.5	3200	10
<i>Set 2</i>	4	15	17.5	3200	20

5.3.2 Characterisation of Electrospun Membranes

5.3.2.1 Morphological and Fibre Diameter Analysis

Samples were prepared for SEM using the previously described methodology detailed in Chapter 3 (pp.68-69), and viewed using an EVO LS15 SEM.

5.3.2.2 Uniaxial Tensile Testing – Strip Specimens

Uniaxial tensile testing of ‘Strip’ specimens was performed on the pure nanofibre assemblies collected on the rotating mandrel by first cutting and opening the nanofibre bundle layer along its longitudinal axis. 10 mm wide samples were subsequently cut

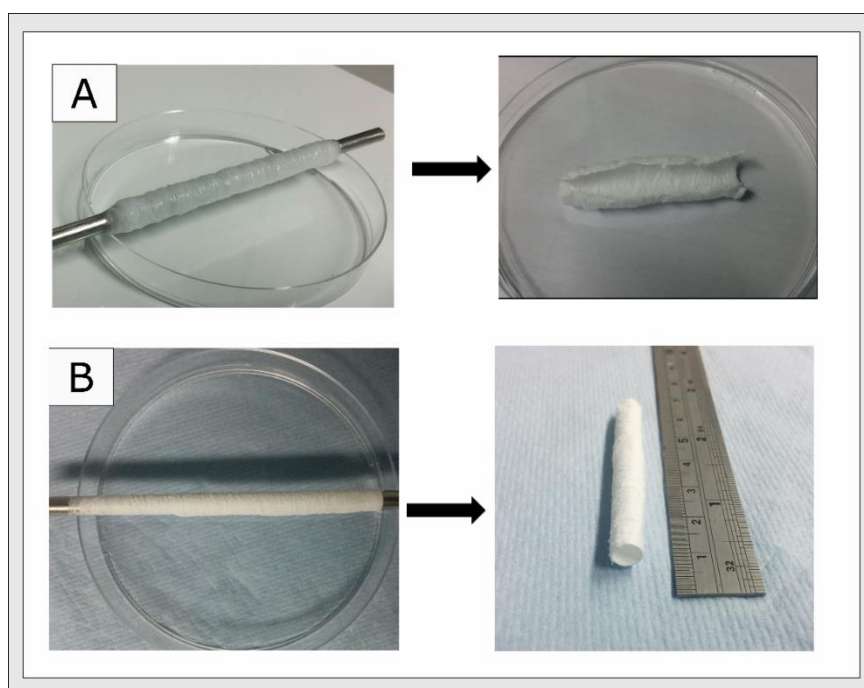


Figure 5.2: Removal of nanofibre assemblies from collection mandrels (A) Pure nanofibre bundles collected on mandrel before and after removal (B) Bi-layer vessel collected on mandrel before and after removal

from the fibre bundle membranes and tested according to the previously described uniaxial tensile test method of Chapter 3 (p.71).

5.3.2.3 Uniaxial Tensile Testing – Ringlet Specimens

Uniaxial ringlet tensile testing of the bi-layer constructs was conducted according to the previously described methodology detailed in Chapter 4 (pp.118-122).

5.3.2.4 Static Compliance Testing

Static compliance testing of the bi-layer vessels fabricated was conducted according to the previously described methodology outlined in Chapter 4 (pp.122-125).

5.3.2.5 Porosity

Sample porosity was quantified using the previously described liquid intrusion technique for ringlet specimens as detailed in Chapter 4 (p.122). For the assessment of the nanofibre bundle layer 10mm wide rectangular strips were harvested from the fibre bundles collected and subjected to the same protocol as ringlet specimens.

5.3.2.6 Statistical Analysis

Numerical data is presented as mean \pm standard deviation (S.D). Where data was determined to comply with the relevant assumptions of a parametric analysis, 2 sample t-test was conducted for the comparison of pair wise samples. For the comparison of multiple samples, one and two-way analysis of variance (ANOVA) were conducted where appropriate. Subsequent multiple comparisons were made using the Sidak correction test. The level of statistical significance was set to $p < 0.05$. Where data was found to violate the assumptions of an ANOVA analysis, most notably equal variance amongst groups (by Bartlett's statistic), non-parametric analysis was conducted. Mann-Whitney test was employed for 2-sample comparison, while Kruskal-Wallis analysis with subsequent Dunn Correction was utilised for multiple comparisons.

5.4 Design of Studies

5.4.1 Process Development of Dynamic Liquid Electrospinning

Based upon the results of nanofibre screening trials performed in Chapter 3 (pp.93-99) of this work, solutions of PCL dissolved in Chloroform/DMF (7:3) at concentrations of 8 and 11wt% were electrospun according to the design matrix shown in Table 5.4. These solutions were selected due to the appropriate size and morphology of fibres previously formed through their use. In this the flow rate of the solutions was assessed at 0.25, 0.5, 1 and 2 ml/hr, applied voltage varied from 10 to 20kV and the collector distance varied from 10 to 22.5, in 2.5cm increments. A number of PCL electrospinning solutions were prepared and then electrospun over an array of processing parameters in order to assess the resultant fibre morphologies and constructs produced through SEM analysis. In this the relative manufacturability of the specimens along with their fibre quality attributes were assessed through a qualitative screening process. The nanofibre bundle morphologies were ranked based upon stability and collection criteria according to that of Table 5.2, and fibre quality according to Table 5.3. Using the resultant values obtained, process maps were generated for each of the flow rates levels studied. An overall combined process rank map that incorporated the attributes of both the stability and quality characteristics was formed for each flow rate level by multiplying together the two individual rank values obtained from each table for each process point.

Table 5.2: Stability & Collection Criteria

Ranking	Category	Characteristics
1	Electrospinning not possible	No visible electrospinning to target basin Corona discharge from spinneret
2	Limited electrospinning	Limited material reaching target basin and subsequently poor deposition to mandrel
3	Unstable process	Electrospinning present Vortex unstable, fluid height fluctuating significantly Material accumulating in target basin
4	Minor instabilities	Minor changes in vortex height Some solidification at spinneret
5	Stable	Vortex stable, no fluctuations in height

Table 5.3: Quality Criteria

Ranking	Category	Characteristics
1	Non fibrous material	Electrospraying - Breakdown of Taylors' cone Liquid polymer deposition
2	Fibres with defects	No distinct fibre bundles Defects present (webbed fibres, beads, necking)
3	Fibre bundles with defects	Distinguishable fibre bundles Defects present (webbed fibres, beads, necking)
4	No distinct fibre bundles, defect free	No distinct fibre bundles Dry fibres free of defects (beads, necking)
5	Distinct fibre bundles, defect free	Distinguishable fibre bundles Dry fibres free of defects (beads, necking)

Table 5.4: Design Matrix used for the process development of dynamic liquid electrospinning process

8 and 11wt% Chloroform/DMF (7:3;v:v) solutions									
Parameters									
Spin Time (min)	20								
Flow Rate (ml/hr)	0.25, 0.5, 1, 2								
Applied Voltage (kV)	10		15				20		
Tip-Collector Distance (cm)	10	-	22.5	10	-	22.5	10	-	22.5

5.4.1.1 Mechanical and Morphological Assessment of final Bi-layer Vessels

Based on the process development results of the dynamic liquid collection process, a select solution and process parameter combination was identified. The chosen selection utilised an 11wt% PCL in Chloroform/DMF (7:3;v:v) solution spun using a flow rate of 1ml/hr, applied voltage of 20 kV, collection distance of 12.5 cm over a collection time of 20 minutes. Using these parameters fibre bundle layers were prepared along with bi-layer vessels specimens. Bi-layer specimens were fabricated for the two previously highlighted multi-modal core variations (Table 5.1).

Uniaxial tensile testing of strip specimens prepared from the pure nanofibre bundles layers (n=6) was conducted, along with uniaxial ringlet testing for the bi-layer vessels (n=6). The porosity was additionally assessed by the previously described liquid intrusion protocols (n=6).

5.5 Results

5.5.1 Process Development of Dynamic Liquid Electrospinning Process

The complete SEM results obtained for the process development of the dynamic liquid electrospinning process can be seen in Table H.1 of Appendix H. The subsequent quality and process stability of 8wt% PCL in Chloroform/DMF (7:3; v:v) spun using the dynamic liquid collection apparatus can be seen in Figure 5.3. These maps were generated based upon observational findings noted during the fabrication process, and through the analysis of the SEM images captured. It was observed that the 8wt% solutions were extremely difficult to spin at the lower solution flow rate of 0.25 ml/hr, with little to no deposition observed on the collection mandrels after 20 minutes. This effect was further exacerbated when spinning was performed over the increased collection distance of 15 cm, with no material observed to collect for any of the flow rates examined. Fibrous material could be seen to form on the collection mandrel when the collector distance was reduced between 10 to 12.5 cm and the increased flow rate ranges of 0.5 to 2 ml/hr were employed. The quality of the fibrous materials produced was however extremely poor, with no distinct fibre bundle formation observed. Large spindle-like beads were also seen to be present throughout the fibre structures. The combined ranking profiles for the 8wt% process are shown in Figure 5.4. These maps

similarly indicate the poor performance of the spinning process irrespective of the parameter permutations employed.

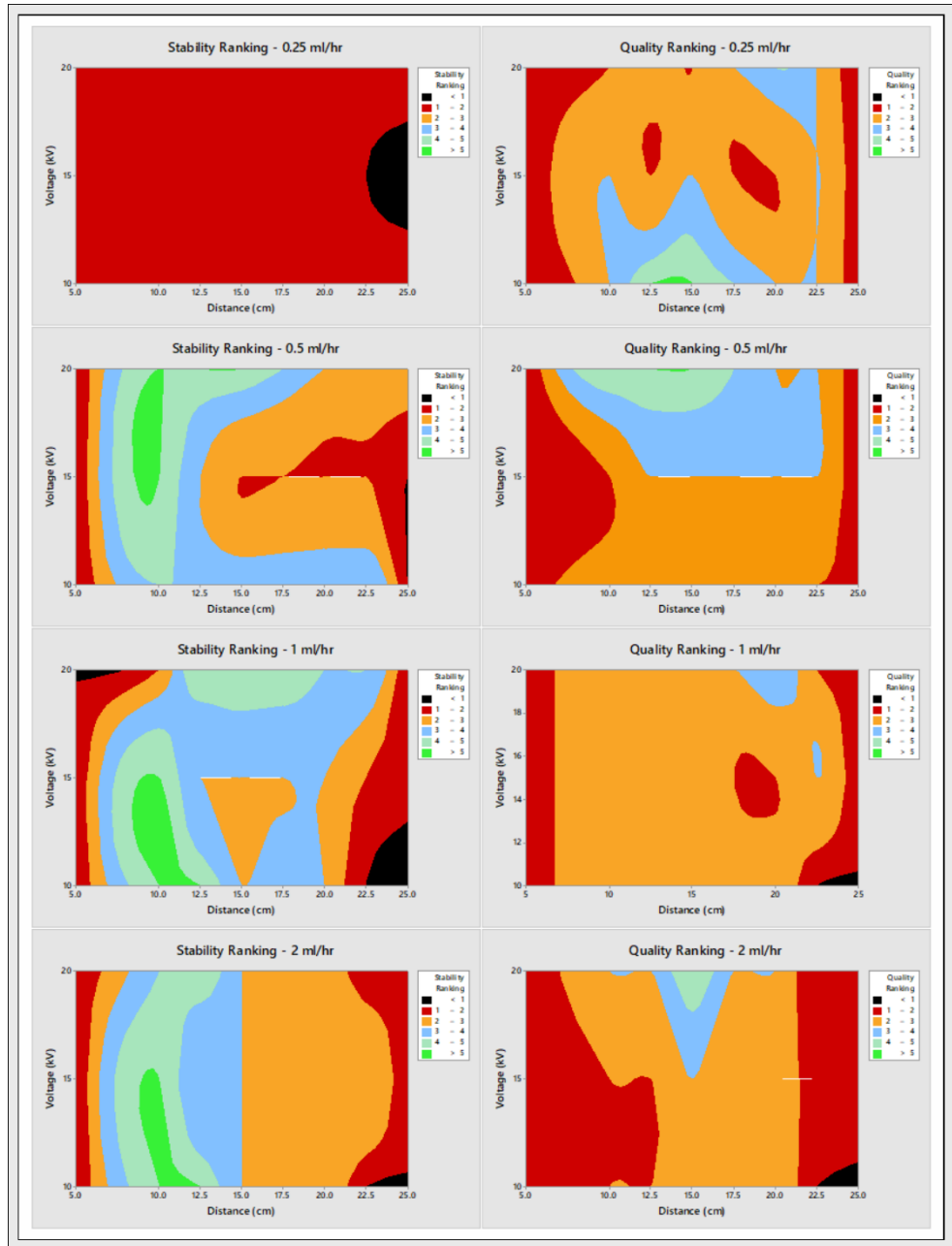


Figure 5.3: Process development map for 8wt% PCL in Chloroform/DMF (7:3) solutions spun using dynamic liquid collection rig, showing stability and quality characteristics for specimens collected at the flow rates of 0.25, 0.5, 1 and 2ml/hr

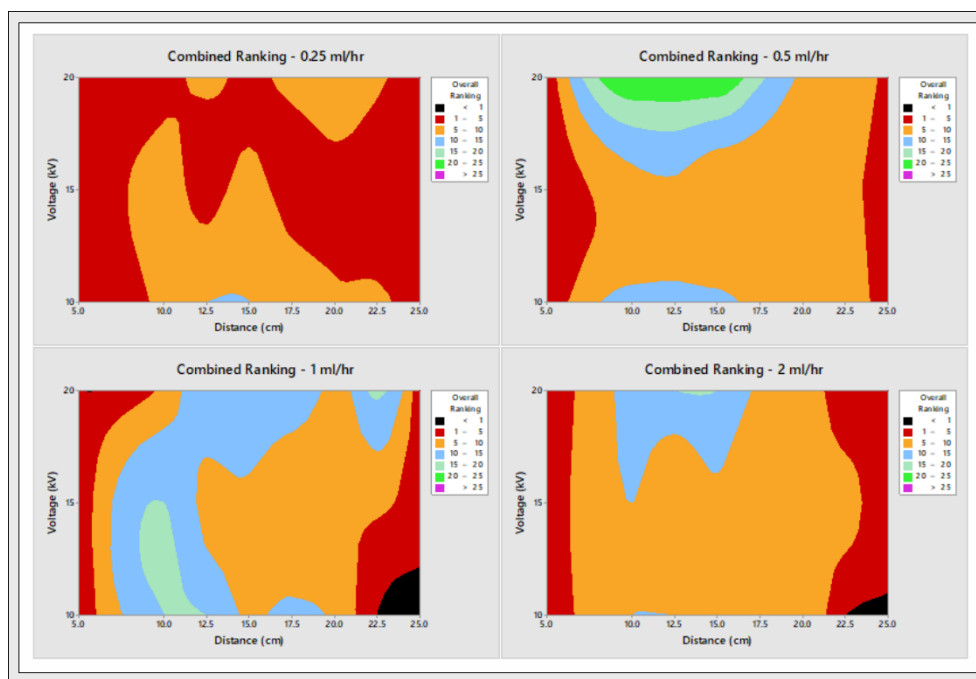


Figure 5.4: Process development map for 8wt% PCL in Chloroform/DMF (7:3) solutions spun using dynamic liquid collection rig, showing combined ranking characteristics for specimens collected at the flow rates of 0.25, 0.5, 1 and 2ml/hr

Figure 5.5 shows the quality and stability process maps for the 11wt% PCL in Chloroform/DMF (7:3; v:v) solutions spun using the dynamic liquid collection process. 11wt% solutions were found to result in a considerably more stable electrospinning process compared to that of the 8 wt% solutions with an increased ability to collect fibrous material observed. The stability maps generated again show the difficulty of forming specimens at collector distances greater than 15 cm. It was observed that electrospun fibrous material was found to deposit on the walls of the fume hood when spinning was performed above 15cm. This suggests that the electrospun fibre jets produced may be prone to airflow movements within the fume hood. The lower solution flow rate of 0.25 ml/hr again proved to be inadequate for the production of fibre bundles of significant quality. This time, however, material was observed to collect on the mandrels. This deposition was however irregular, with sparse and dense deposition areas observed. The formed membranes were extremely fragile and were prone to damage upon removal from the collection surface.

By increasing the solution flow rate to between 0.5 and 1 ml/hr, and spinning within a collector distance range of 10 to 15cm, a highly stable electrospinning process could

be achieved. The collected fibre materials also showed suitable morphological properties with distinct fibre bundle structures present. A further increase in flow rate to 2 ml/hr resulted in liquid polymer deposition to the water bath, or significant fibre collection upon the surface of the water bath (Figure 5.6 (A) and (B)). This aggregation of material within the top tier water bath ultimately led to the breakdown of the water vortex as shown in Figure 5.6 (C). This breakdown in the vortex resulted in significant

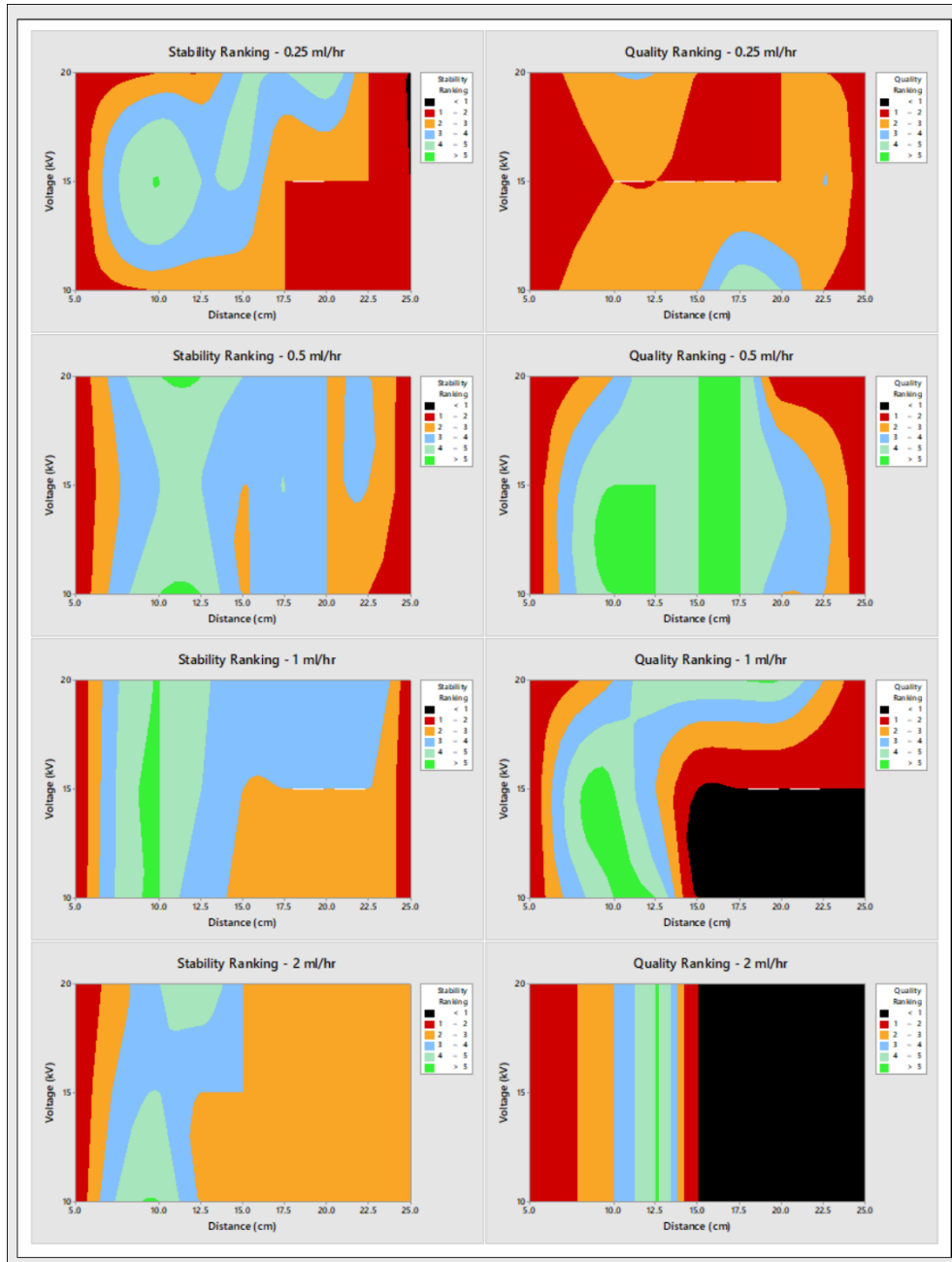


Figure 5.5: Process development map for 11wt% PCL in Chloroform/DMF (7:3) solutions spun using dynamic liquid collection rig, showing stability and quality characteristics for specimens collected at the flow rates of 0.25, 0.5, 1 and 2ml/hr

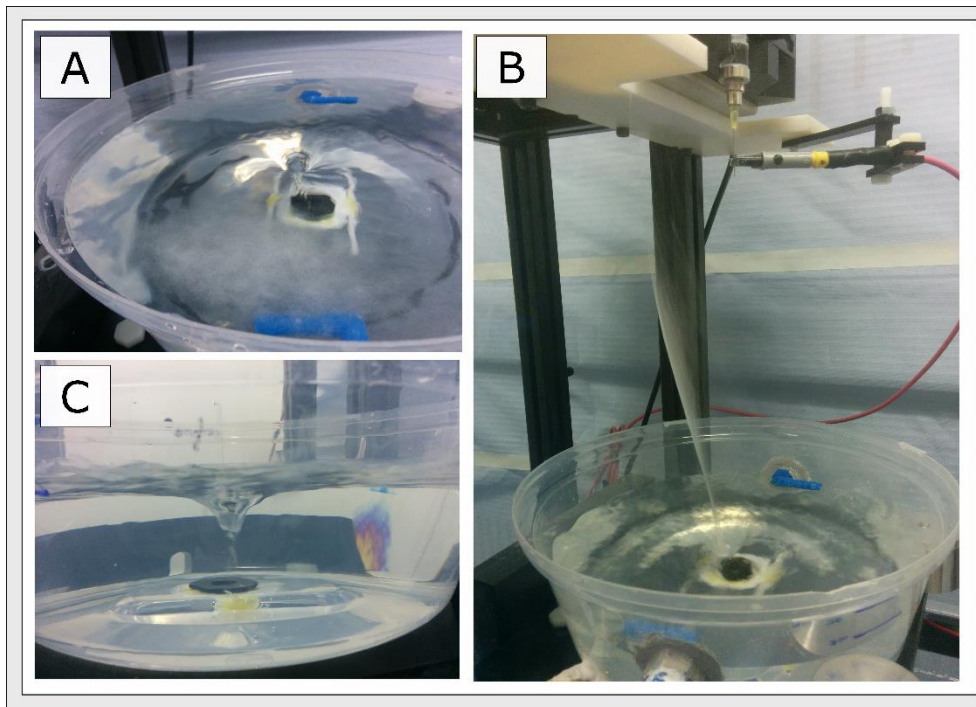


Figure 5.6: Material aggregation during dynamic liquid collection process (A) Material collecting of face of water bath/surface of water (B) Fibre forming between collection frame and water surface (C) Subsequent breakdown of water vortices due to material aggregation within the water baths

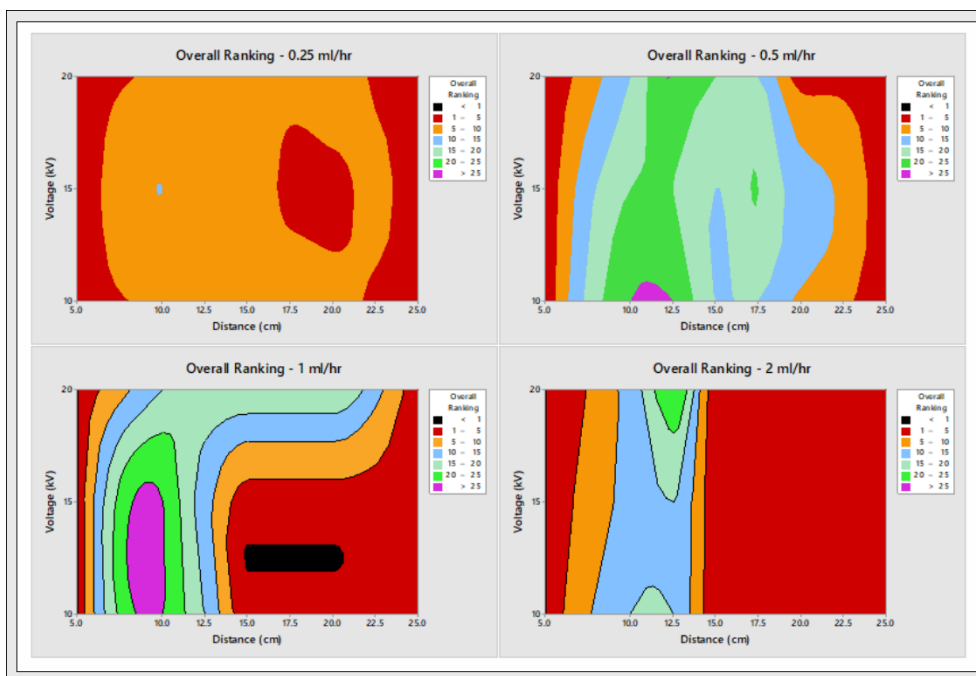


Figure 5.7: Process development map for 11wt% PCL in Chloroform/DMF (7:3) solutions spun using dynamic liquid collection rig, showing combined ranking characteristics for specimens collected at the flow rates of 0.25, 0.5, 1 and 2ml/hr

variation in the fluid height within the bath, preventing successful collection of the electrospun nanofibre bundles. Inspection of the overall ranking maps for the 11 wt% spinning solutions (Figure 5.7), again highlighted the superior processing potential of the 0.5 and 1 ml/hr flow rate levels. A number of potential processing parameters were found to provide suitable nanofibre bundle constructs that possessed statistically equivalent fibre diameter characteristics, whilst also providing a sufficiently stable electrospinning process. In order to further refine the selection of the final processing parameters, a secondary inspection criteria was employed. This criteria primarily focused upon the observed uniformity of the deposited fibre bundle materials upon the collection mandrel. While it was suspected that the uniformity of the nanofibre bundles would not critically alter the performance characteristics of the collected fibre bundle scaffolds, the observation allowed for the elimination of potential parameter permutations. The final selected processing parameter range of a 1 ml/hr flow rate, applied voltage of 20 kV, collector distance of 12.5 cm was seen to produce highly uniform bi-layer scaffolds. In addition this parameter combination was found to be located within a processing window, in which high quality fibre constructs could be produced repeatability and with high reproducibility. The average diameter of fibres present within the nanofibre bundle layers was measured to be $1.33 \pm 0.55 \mu\text{m}$.

5.5.1.1 Mechanical and Morphological Assessment of final Bi-layer Vessels

The mechanical characterisation of the nanofibre bundle layers and the final composite vessels can be seen in Figure 5.8 and Figure 5.9. An examination of the results showed extremely low UTS properties for the nanofibre bundle layers ($1.320 \pm 0.084 \text{ MPa}$) when compared to the core layers collected for set 1 ($3.523 \pm 0.572 \text{ MPa}$, $p=0.0004$) and those of set 2 ($2.675 \pm 0.0901 \text{ MPa}$, $p=0.0405$). The subsequent bi-layer vessel in turn exhibited statistically decreased UTS properties compared to that of the set 1 cores (2.584 ± 0.453 , $p=0.0103$). No statistical difference was detected between the bi-layer vessels made using set 2 cores and the core layers only. The nanofibre bundle layers also appeared to possess similar Young's modulus properties compared to the two core scaffolds at $3.601 \pm 0.635 \text{ MPa}$ compared to $3.861 \pm 0.835 \text{ MPa}$ for set 1 cores, and $3.270 \pm 0.5548 \text{ MPa}$ for set 2 cores. The subsequent bi-layer vessels for set 1 ($3.290 \pm 0.358 \text{ MPa}$) and set 2 ($2.835 \pm 0.362 \text{ MPa}$) displayed no statistical differences to either that of the core layers or nanofibre bundles.

The force modulus (FM) results of the measured vessels did however indicate an increase in vessel stiffness upon the deposition of the nanofibre bundle layer. Set 1 specimens showed an increase in FM between the core only specimens (0.237 ± 0.076 N/%) to those of the bi-layer vessel (0.398 ± 0.12 n/%, $p=0.0192$). A similar trend was exhibited within the set 2 specimens with the bi-layer vessel (0.363 ± 0.069 N/%) exhibiting statistically higher FM to both that of the core (0.164 ± 0.055 N/%, $p=0.0003$) and the nanofibre bundle layer (0.103 ± 0.001 N/%, $p=0.0004$). The strain at break of the specimens was found to be higher for the core layers compared to those of the nanofibre bundle layers. It appeared that the bi-layer vessels strain at break properties were dominated by the contribution of the core layers with no statistical difference observed for both sets assessed.

The maximum force to failure of the core layers were again seen to be significantly higher than those of the nanofibre bundle layer. Set 1 cores demonstrated maximum forces of 22.63 ± 9.35 N, while the nanofibre bundles exhibited significantly lower range at 3.863 ± 0.8 N ($p=0.0122$). The cores fabricated using set 2 spinning conditions yielded max forces slightly higher than that of the nanofibre bundle layer at 13.71 ± 6.9 N ($p=0.0496$). The bi-layer vessels again exhibited slightly higher maximum forces to that of the core only specimens but no statistical difference was detected. The results of the porosity testing showed that the nanofibre bundle layers were significantly more porous than that of the multi-modal cores, exhibiting porosities of 87.82 ± 2.041 %. The bi-layer vessel did however appear to have an equivalent porosity to that of the core only specimens at $83.59 \pm 2.024\%$ for set 1, and $83.70 \pm 1.90\%$ for those of set 2.

Figure 5.10 shows the subsequent compliance properties calculated for the PCL core layers and the final bi-layer scaffolds for the two core designs studied. Bi-layer vessels fabricated using set 1 cores appeared to show a small decrease in vessel compliance to that of the core only specimens, at 2.366 ± 0.732 % per mmHg $\times 10^{-2}$ and 2.542 ± 0.706 % per mmHg $\times 10^{-2}$ respectively. This decrease was however non statistical ($p=0.6806$). These compliance ranges were again highly comparable to that of the native arterial tissue at 2.6 ± 0.8 % per mmHg $\times 10^{-2}$ as seen in Figure 5.10 (A). The

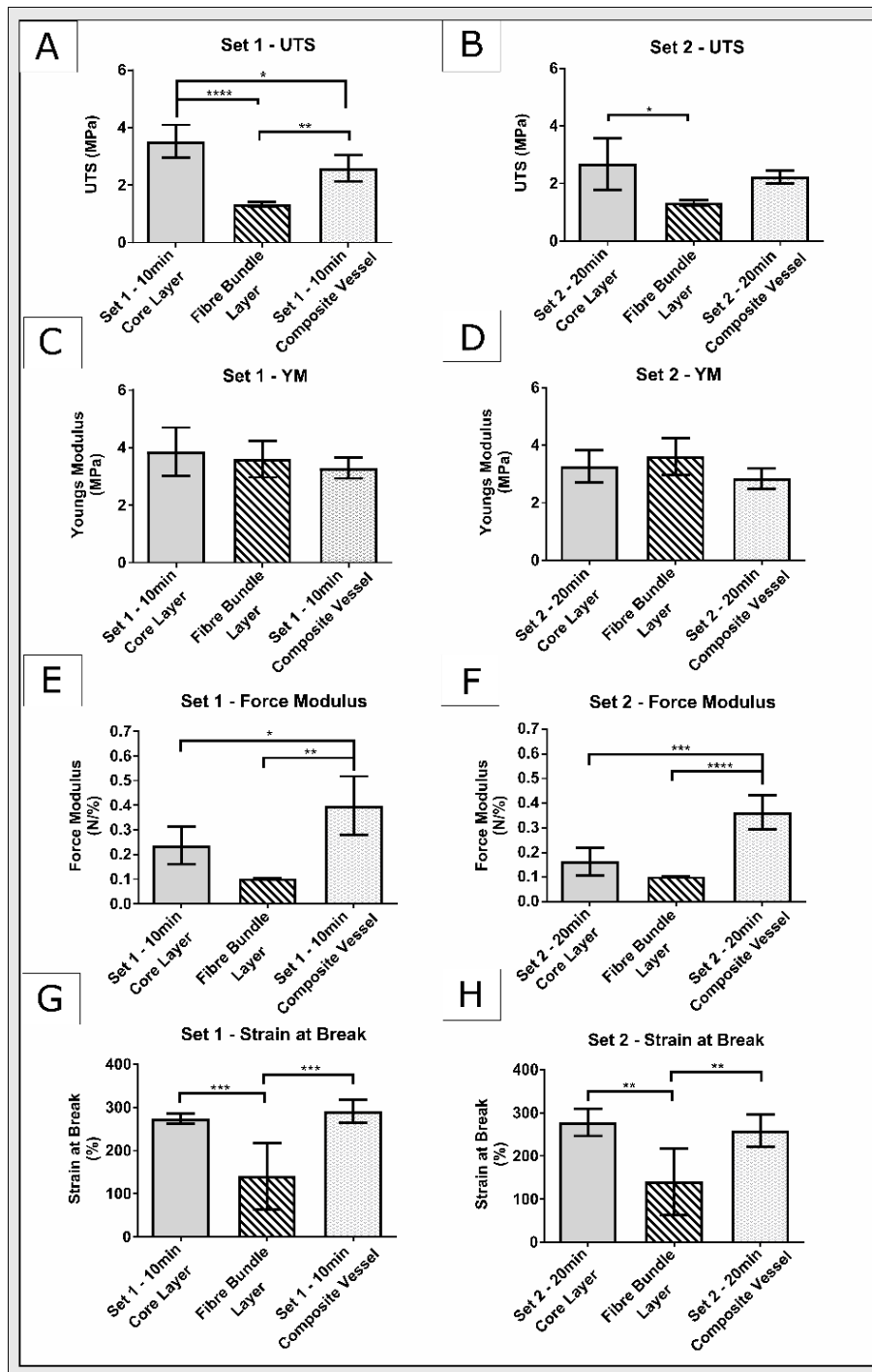


Figure 5.8: Mechanical assessment of bi-layer vessels and their constituents (A) UTS characteristics of ‘set 1’ cores, nanofibre bundle layers and subsequent bi-layer vessels (B) UTS characteristics of ‘set 2’ cores, nanofibre bundle layers and subsequent bi-layer vessels (C) Young’s modulus characteristics of ‘set 1’ cores, nanofibre bundle layers and subsequent bi-layer vessels (D) Young’s modulus characteristics of ‘set 2’ cores, nanofibre bundle layers and subsequent bi-layer vessels (E) Force modulus characteristics of ‘set 1’ cores, nanofibre bundle layers and subsequent bi-layer vessels (F) Force modulus characteristics of ‘set 2’ cores, nanofibre bundle layers and subsequent bi-layer vessels (G) Strain at break characteristics of ‘set 1’ cores, nanofibre bundle layers and subsequent bi-layer vessels (H) Strain at break characteristics of ‘set 2’ cores, nanofibre bundle layers and subsequent bi-layer vessels. N=6 per group.

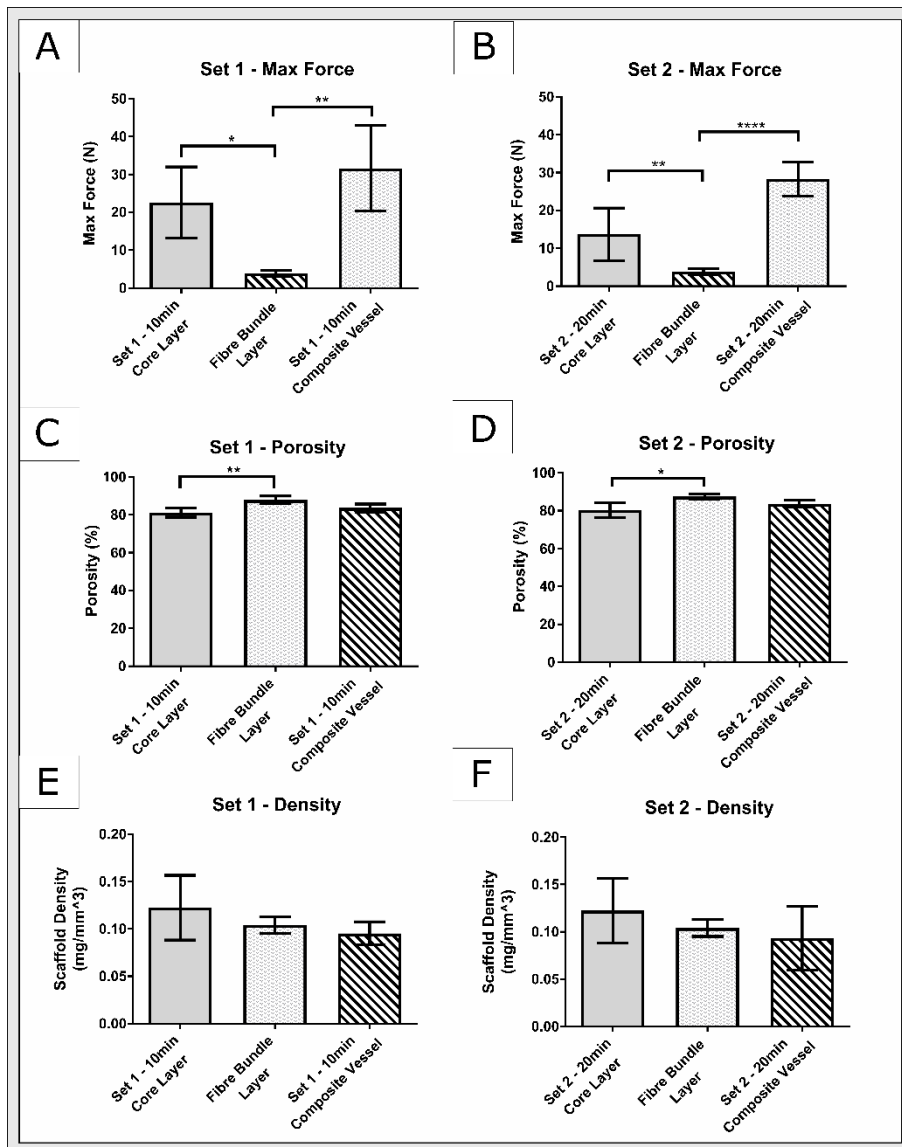


Figure 5.9: Mechanical and morphological assessment of bi-layer vessels and their constituents (A) Maximum force characteristics of ‘set 1’ cores, nanofibre bundle layers and subsequent bi-layer vessels (B) Maximum force characteristics of ‘set 2’ cores, nanofibre bundle layers and subsequent bi-layer vessels (C) Porosity characteristics of ‘set 1’ cores, nanofibre bundle layers and subsequent bi-layer vessels (D) Porosity characteristics of ‘set 2’ cores, nanofibre bundle layers and subsequent bi-layer vessels (E) Density measurements of ‘set 1’ cores, nanofibre bundle layers and subsequent bi-layer vessels (F) Density measurements of ‘set 2’ cores, nanofibre bundle layers and subsequent bi-layer vessels. N=6 per group.

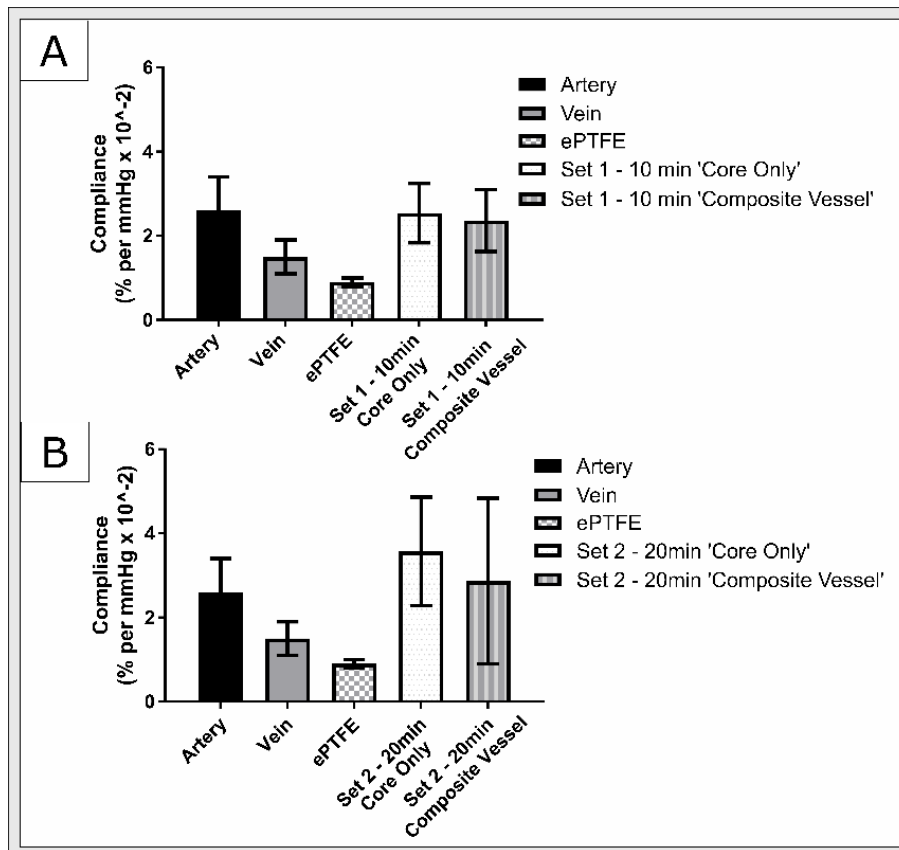


Figure 5.10: Compliance properties of multimodal PCL cores and bi-layer vessels (A) Compliance results for core layers and bi-layer vessels produced by 'set 1' processing parameters (B) Compliance results for core layers and bi-layer vessels produced by 'set 2' processing parameters. N=6 per data set.

compliance properties measured for the bi-layer vessel specimens prepared using set 2 cores can be seen in Figure 5.10 (B). The bi-layer vessel (2.866 ± 1.965 per mmHg $\times 10^{-2}$) again appeared to show equivalent properties to that of the core layer tested (3.576 ± 1.293 per mmHg $\times 10^{-2}$, $p=0.4767$). An interesting note at this point was the greater variation within the compliance data for specimens fabricated with set 2 cores compared to those fabricated using the set 1 core layers.

5.6 Discussion

5.6.1 Process Development of Dynamic Liquid Collection

In order to develop a suitable process for the production of the nanofibre bundle layers that will be used to form the outer layer of the bi-layer vessel under investigation, an extensive screening trial was employed in order to identify the key processing parameters and electrospinning solutions required. 8 and 11 wt% PCL in Chloroform/DMF (7:3; v:v) solutions were initially chosen for the development of the nanofibre bundle layers due to their ability to form defect free nanofibres previously observed within Chapter 3. These solutions were electrospun over an array of parameter permutations in order to identify combinations that yielded both a stable electrospinning process and high quality nanofibre materials. Contour plots or 'process maps' were assessed, in order to combine observational data surrounding the functionality of the dynamic liquid collection process with that of the resulting fibre morphology data assessed by SEM analysis. The process maps generated for the 8wt% PCL in Chloroform/DMF (7:3; v:v) solutions showed that they performed poorly across all the parameter permutations tested. This was typically due to the inability to efficiently collect material, with no visible spinning found to occur for a range of parameters examined. This was an interesting observation, as previous studies performed within this work have shown the ability to successfully collect fibres using this solution when standard metallic collector systems were employed. This reaffirms the importance of not only the electrospinning solutions and processing parameters but the fibre collection system itself.

11wt% PCL in Chloroform/DMF (7:3) solutions were found to successfully electrospin at a number of the parameter permutations examined. The flow rate range of 0.5 to 1 ml/hr was found to provide a highly stable electrospinning process, with good deposition to the water surface and subsequent material collection on the rotating mandrel. Examination of the SEM images showed consistent fibre morphologies and diameters across the flow rate range, making the choice of a single parameter combination difficult. Additional observational results were required in order to further refine the parameter selection with criteria including collection uniformity upon the mandrel used as a gating factor. Ultimately, the parameter combination of a

1 ml/hr flow rate, applied voltage of 20 kV, collector distance of 12.5 cm was chosen due to the excellent stability, quality and uniformity of the nanofibre bundles collected. The average diameter of the fibres present within the nanofibre bundle layers was measured to be $1.33 \pm 0.55 \mu\text{m}$. While the average fibre diameters did not technically fall within the nanoscale, it was observed that large diameter fibres were often found to deposit amongst the smaller fibres resulting in skewed the fibre diameter measurements. These fibre measurements were however still deemed to be acceptable for the required application.

An interesting observation seen within the testing of the 11wt% solutions was the ability of depositing fibrous material to significantly alter the flow properties of the water vortex. When the 11wt% solutions were electrospun at collector distances greater than 15 cm, fibrous material was found to adhere to the inner walls of the water bath. This material accumulation subsequently resulted in flow changes within the top tier water bath resulting in altered water vortex formation. The changing shape and stability of the water vortex subsequently resulted in fluctuating fluid height within the bath that led to poor fibre deposition on the collection mandrel. This finding was particularly pronounced at the increased flow rate levels along with the elevated applied voltages. This is suspected to have occurred due to increased whipping effects within the jet that led to the fibres spinning past the outer edge of the water bath and subsequently adhering to the bath and building up on the water surface.

5.6.1.1 Mechanical and Morphological Assessment of final Bi-layer Vessels

The mechanical assessment of the final composite bi-layer vessels was performed along with the constituent components, the core layer and nanofibre bundle layer, in order to assess the subsequent changes in mechanical properties. The UTS results showed that the PCL multi-modal core layers provided the main structural resistance of the vessel, with both core layer designs exhibiting significantly higher UTS properties compared to the nanofibre bundle layers. Similarly, to that observed within Chapter 4, the addition of the nanofibre bundle layer resulted in an apparent decrease in the mechanical strength of the bi-layer vessel compared to the core only specimens. This decrease is not a true reduction in mechanical strength but rather an apparent decrease caused by changes within the relative layer densities across the wall of the

ringlet specimens. This observation was reaffirmed by the maximum force to failure measurements, wherein the final bi-layer vessels displayed equivalent maximum forces to the core specimens despite the addition of the nanofibre bundle layer. This reiterates the importance of the core layers as the structural back bones of the scaffolds.

The Young's modulus properties of the constituent layers and final bi-layer vessels were statistically comparable. An increase in the force modulus for the bi-layer vessels was however observed, compared to that of core only specimens. This represents an increase in the vessel stiffness and again shows the importance of assessing not only intrinsic material properties but the structural properties of the vessels themselves.

The final compliance results for the bi-layer vessels produced using set 1 and set 2 cores both displayed minimal decreases within their compliance upon the addition of nanofibre layer. This suggests that the porous outer layer is not structurally significant to the final vessels produced. Bi-layer vessels produced using set 1 cores showed highly comparable compliance properties to arterial tissue. In addition, the compliance deviation was found to be considerably smaller than that of the vessels produced using set 2 cores. This indicates that set 1 cores are perhaps more reproducible in terms of their manufacturing process. Based on these findings a bi-layer vessel comprised of a PCL multi-modal core produced using the processing parameters defined by set 1 will be chosen for further study within the final cell culture chapter.

Chapter 6 Assessment of mMVSC Viability and Infiltration Capabilities on Electrospun Bi-Layer Vessels

6.1 Introduction

As discussed throughout this work, the unique biomechanical and architectural properties of native arterial tissue requires the careful consideration and selection of a cell-scaffold construct to ensure successful functionality upon implantation. Much of the work presented to this point has focused on the development of a scaffold that possesses the mechanical and morphological attributes required to successfully resist physiological conditions upon implantation. The ultimate goal of the scaffold is, however, to act as a suitable framework for the growth and guidance of seeded cells. One of the most limiting factors to date in the use of electrospun materials as tissue-engineered constructs is the previously discussed inability of cells to successfully infiltrate and populate the full volume of the fibrous materials. This could ultimately lead to the failure of the newly forming tissue structure upon the degradation of the polymer fibres. It is anticipated that the dynamic liquid collected fibre bundles, paired with the multi-modal tubular core layer investigated within this work, will allow for the successful creation of a bi-layer scaffold that not only possesses suitable mechanical properties but also allows for the adequate adhesion, proliferation and infiltration of seeded cells.

In order to assess the viability and infiltration capabilities of the bi-layer vessel fabricated throughout this work, mouse multipotent vascular stem cells (mMVSCs) will be seeded upon a number of electrospun scaffold variants and assessed with respect to standard cell culture control materials. The bi-layer vessel design will be compared to traditional electrospun material configurations including random and

aligned nanofibre membranes in order to provide a final assessment of the scaffolds ability relative to current scaffold designs. In this chapter the following activities will be performed:

- **Viability of mMVSCs Seeded upon Electrospun Materials**

The viability of mMVSCs seeded upon a range of electrospun constructs will be assessed in order to establish the capability of the newly designed bi-layer vessel to support cell attachment and growth at 1, 3 and 7 days post seeding compared to traditional electrospun scaffold structures. In this, a number of techniques will be employed to assess cell viability including alamarBlue® to measure cell metabolic activity, PicoGreen® to quantify dsDNA concentration and DAPI fluorescent staining to quantify the presence of cell nuclei. The combined results of these techniques will be used to provide an overall assessment of the scaffolds ability to support seeded cells compared to standard platforms used in cell culture.

- **Comparison of Cell Infiltration Properties**

The infiltration properties of mMVSCs on the bi-layer vessels will be assessed by seeding mMVSCs onto random and aligned nanofibre membranes along with the bi-layer vessels. Infiltration over 7 and 14 day time periods will be assessed through cryo-sectioning techniques combined with cell nuclei staining. Based on these finding the rate of cell infiltration for each of the scaffold variants will be established.

- **Assessment of Cell morphology**

Lastly the morphology of the seeded mMVSCs will be examined upon the bi-layer vessel and compared to the random and aligned nanofibre membranes. This will allow for the assessment of any potential morphological changes that the dynamic liquid collected fibre bundles may induce within the seeded cell population

6.2 Materials and Equipment

6.2.1 Materials

General Cell Culture

- Mouse Multi-Potent Vascular Stem Cells (DCU, Ireland)
- Sodium bicarbonate solution (S8761) (Sigma-Aldrich, Ireland)
- Sodium pyruvate solution (S8636) (Sigma-Aldrich, Ireland)
- Eagle's Minimum Essential Medium (EMEM) (56416C) (Sigma-Aldrich, Ireland)
- Penicillin-Streptomycin (P/S, P4333) (Sigma-Aldrich, Ireland)
- L-Glutamine Solution (G7513) (Sigma-Aldrich, Ireland)
- Fetal Bovine Serum, ES Cell Qualified (SCRR-30-2020™) (ATCC, US)
- 24 Well Culture Plate, Sterile, TS Treated (SPL Life Sciences, US)
- Trypan Blue (T8154) (Sigma-Aldrich, Ireland)
- Gibco TrypLE™ Select Enzyme (Thermo Fisher Scientific, US)
- Sterile DPBS Tablets (Fisher Scientific, US)
- 0.22µm Sartorius™ Minisart™ NML Syringe Filters, Sterile
- 0.22µm EMD Millipore™ Stericup™ Sterile Vacuum Filter Units (10440011)
- CELLCROWN™24, Cell Culture Inserts (Scaffdex, Finland)
- ø10mm Glass slides (#12658116, Thermo Fisher Scientific, US)
- Westran Clear Signal (CS) PVDF Membranes for Western Blotting (Z671010) (Sigma-Aldrich, Ireland)

Resazurin Blue

- Resazurin Sodium Salt (R7017) (Sigma-Aldrich, Ireland)
- De-Ionised Water (DCU, Ireland)

PicoGreen®

- Quant-iT™ PicoGreen® ds DNA Assay Kit (Invitrogen Corporation, USA)
- 96 well. Solid Bottom. Black PS plates (4Titude, UK)
- Sodium Carbonate (Na₂CO₃) (Sigma-Aldrich, Ireland)
- Triton X-100 (T8787) (Sigma-Aldrich, Ireland)

DAPI

- 4',6-diamidino-2-phenylindole (DAPI, D9542) (Sigma-Aldrich, Ireland)
- Formaldehyde (F-8775) (Sigma-Aldrich, Ireland)

- Triton X-100 (T8787) (Sigma-Aldrich, Ireland)
- Fluoromount™ Aqueous Mounting Medium (F4680) (Sigma-Aldrich, Ireland)

SEM Analysis

- Glutaraldehyde, Grade II, 25% Aqueous (Sigma Aldrich, Ireland)
- Ethanol (Sigma Aldrich, Ireland)
- Hexamethyldisilazane, ≥99% (HDMS) (Sigma Aldrich, Ireland)

Cryofixation

- Tissue Freezing Medium (OCT) (Leica Microsystems, Germany)
- Superfrost microscope slides (Z692255) (Sigma-Aldrich, Ireland)

6.2.2 Equipment

- Ø20mm Circular Specimen Cutting Die (Custom, DCU)
- Bio Air 2000 MAC laminar flow cabinet (Bio Air, Italy)
- Heracell CO₂ incubator (Thermo Scientific, US)
- Allegra 21 Centrifuge (Beckman Coulter, USA)
- Olympus CK30 Phase Contrast Microscope (Olympus Life Science, Japan)
- Olympus BX51 Fluorescence Microscope with Cell^F Image software (Olympus Life Science, Japan)
- Tecan Safire 2 Plate Reader (Tecan, Switzerland)
- CM3050s Research Cryostat (Leica, US)
- EVO LS15 Scanning Electron Microscopy (Zeiss, Germany)
- Edwards Pirani 501 Scancoat Sputtering Coater (Edwards Laboratories, USA)

6.3 Methods

6.3.1 Preparation of Cell Culture Medium

mMVSC Maintenance Media was prepared by combining Eagle's Minimum Essential Medium (EMEM) basal medium, 10% ATCC Fetal Bovine Serum (FBS), 1% L-Glutamine (4mM final concentration), and 1% Penicillin-Streptomycin (P/S). The EMEM basal medium was prepared in house in 1L stocks by combining 9.61g of EMEM Powder which contained an initial 2mM L-Glutamine, 20 ml of Sodium Bicarbonate, 10 ml of Sodium Pyruvate, and 970 mL of Ultra Pure Water (Merck

Millipore). The basal medium was ensured to be at pH 7, and filtered using a 0.22µm sterile 1L Vacuum Bottle-Top Filter (Merck Millipore) under sterile conditions.

6.3.2 General Cell Culture of mMVSCs

mMVSCs were cultured in 25 cm², 75 cm², and 175 cm² tissue culture flasks at 37 °C, 5% CO₂, and were routinely fed with the previously described maintenance media every 2 - 3 days. Cells were sub-cultured at 70-80% confluency, and split using Gibco TrypLE™ Select. Tryple was utilised to prevent damage to cell surface proteins/receptors, and differentiation of the stem cells compared to standard Trypsin [295].

6.3.3 Preparation of Control Specimens and Scaffold Constructs

Random and nanofibre control membranes were electrospun according to the previously described methods detailed in Chapter 3 (pp.66-67), using the finalised solution of 8wt% PCL (M_w=100,00g/mol) in Chloroform/DMF at a ratio of 7:3 (v:v). The membranes were fabricated at a flow rate of 0.25 ml/hr, applied voltage of 15 kV and a collector distance of 15 cm. The bi-layer vessel was fabricated using the final design detailed within Chapter 5 that utilised a multi-modal core layer prepared using a 7.8wt% PCL (M_w=100,00g/mol) in Chloroform/Ethanol (7:3; v:v), fabricated at a flow rate of 12 ml/hr, applied voltage of 20 kV, collector distance of 17.5cm and collection time of 10 min. The dynamic liquid collected fibre bundle layer was then spun over the core layer using a 11wt% PCL (M_w=100,00g/mol) in Chloroform/DMF (7:3; v:v) at a flow rate of 1 ml/hr, applied voltage of 20 kV, collector distance of 12.5 cm for a collection time of 20 minutes.

Prior to cell seeding the random and aligned nanofibre control scaffolds were prepared by punching ø20mm discs from the collected fibre membranes using a custom built punch (DCU), as shown in Figure 6.1 (B). For the preparation of the composite bi-layer vessels, the tubular scaffolds were first cut open along their longitudinal axis. Once opened into a flat membrane they were cut into 15 mm long rectangular segments using a scalpel (Figure 6.1 (C)). The electrospun samples were then mounted in previously autoclaved CELLCROWN™24 inserts as shown in Figure 6.1 (D)

according to the method detailed in Figure 6.1 (A).

Control specimens were prepared by first punching $\theta 20\text{mm}$ discs from Westran Clear Signal (CS) PVDF Membranes. The membranes were mounted in the CELLCROWN™24 inserts similar to that of the electrospun membranes. A UV sterilised $\theta 10\text{mm}$ glass slide was then placed into the centre of the cell crown on top of the PVDF membrane ensuring the glass slide was positioned flat on the PVDF material.

6.3.4 Seeding of mMVSCs on Control and Scaffold Constructs

Once mounted each control and electrospun construct was placed in the well of a sterile 24-well plate, and sterilised using 70% ethanol for 8 hours. Following

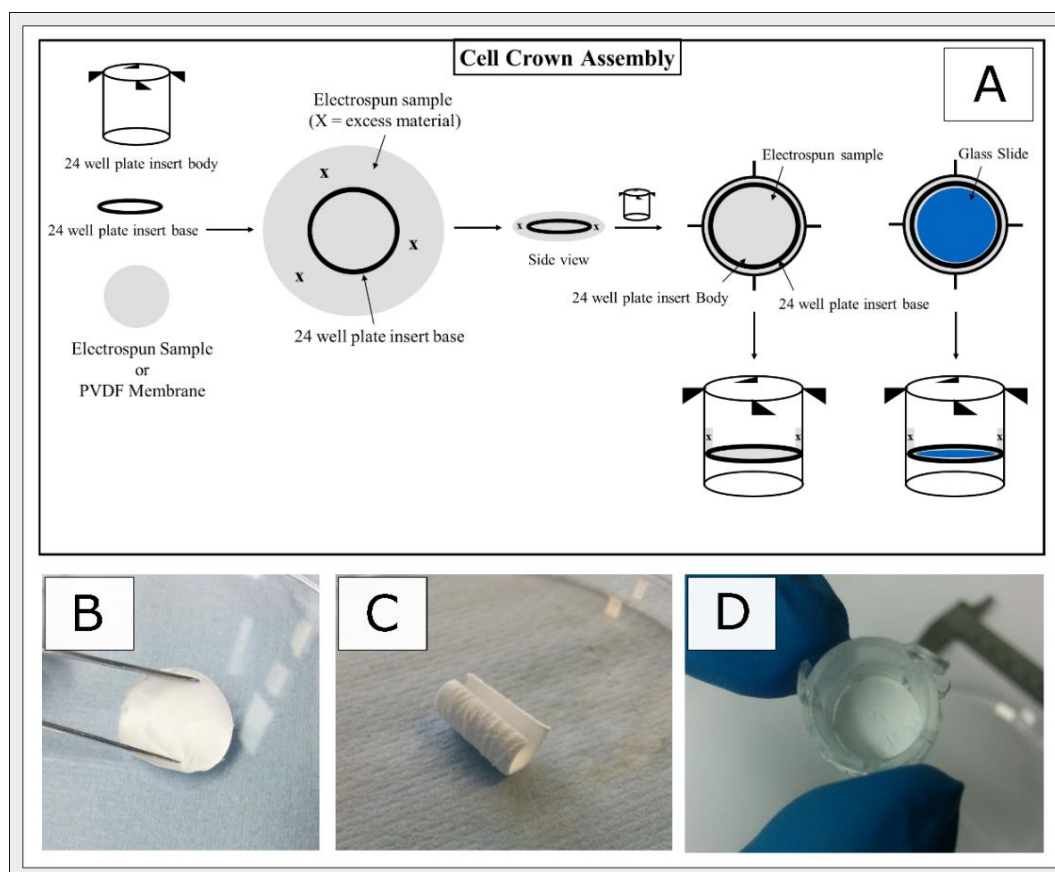


Figure 6.1: Preparation of controls and scaffold constructs for cell culture (A) Cell crown assembly method showing the process used to mount electrospun specimens and control glass slides in CELLCROWN™ inserts (B) Random and aligned fibre discs punched from electrospun membranes (C) Composite vessel specimens cut from larger tubular scaffold (D) Sample image showing scaffolds mounted in insert system

sterilisation the scaffolds were rinsed twice in sterile DPBS after which they were placed in fresh DPBS and left overnight. The scaffolds and controls were washed twice more the next day, and left to hydrate in sterile DPBS till use. mMVSCs, previously plated in a 75cm² flask, were harvested using 0.5X Gibco TrypLE™ Select, and counted using a cell counting chamber or hemocytometer by Trypan Blue. Cells were seeded at 25,000 cells per scaffold in 1 ml of maintenance medium per well, and incubated at 37°C, 5% CO₂ for 1, 3, 7 and 14 days depending on the desired experiment. Maintenance medium was changed every 2-3 days where required. All the steps were carried out under sterile conditions.

6.3.5 Metabolic Activity by Resazurin Sodium Salt (alamarBlue®)

Resazurin sodium salt/alamarBlue® cell metabolic assay is a commonly used method to determine cell proliferation by qualitatively assessing the reducing cytosolic environment of viable (live) cells. The active compound of alamarBlue® reagent is resazurin, a non-cytotoxic molecule capable of permeabilising the cell membrane. Resazurin is a blue compound, however in reducing environment such as the cell cytosol it is converted to a red and highly fluorescent molecule known as resorufin. Resorufin indicates the presence of metabolic activity within a cell and thus is an indirect indicator of cell viability. As long as viable cells and the substrate resazurin are contained in the same medium, resorufin is produced increasing the colour and thus the fluorescence of the medium.

alamarBlue® reagent stock solution was prepared by weighing resazurin sodium salt and adding to dH₂O at a final concentration of 0.1 mg/mL, and sterilised by filtration using a 0.22µm filter compatible for cell culture. Sterile 0.1 mg/mL alamarBlue® stock solution was stored in the dark at 4°C. A cell standard curve was generated to indirectly quantify the number of cells at each end point (Table 6.1), and to act as an internal control to assess the effectiveness of the assay. The alamarBlue® assay was performed on standards and experimental samples as follow: a) in a sterile 50mL tube, alamarBlue® reagent stock solution was added to warm fresh maintenance medium at a final concentration of 0.01 mg/mL (10% working solution, WS). The final volume of working solution was scaled up according the number of wells to be tested, for instance 1 ml of WS was added to a single well of a 24-well plate, b) maintenance

Table 6.1: Cell Standard Curve used for Alamar Blue and PicoGreen Experiments

Well Label	# Cells in Well
A	100,000
B	75,000
C	50,000
D	25,000
E	10,000
F	7,500
G	5,000
H	2,500
I	1,000
J	0

medium was aspirated off each sample (standards or experimental), and 1 ml of WS was added to each well, c) samples were incubated at 37°C, 5% CO₂ for 4 hours protected from light, d) Following incubation, the WS was removed from each sample to a pre-labelled 1.5 ml tube, e) samples were well-mixed by pipetting, and 100µL of the WS was transferred to a well of a 96-well plate with triplicates taken for each specimen, f) Florescence intensity was immediately measured using a Tecan Safire2™ plate reader with $\lambda_{\text{excitation}}$ 560 nm and $\lambda_{\text{emission}}$ 590 nm, Bandwidth 10 nm, Gain 50, measurements per sample 6, and integration time 40.

alamarBlue® Analysis

The fluorescent readouts of the standard samples were used to create a standard curve, and thus to obtain the equation of the line. The standard curve was assessed in order to verify the effectiveness of the assay by ensuring that a linearly proportional relationship existed between the seeded cell number and the relative fluorescence intensity (RFI) value observed. The cell viability for each experimental sample was calculated by expressing their average fluorescent intensity value as a percentage ratio to that of the control specimens.

6.3.6 Quant-iT™ PicoGreen® dsDNA Assay

Quant-iT™ PicoGreen® dsDNA reagent is a fluorescent dye used to quantify double-stranded DNA (dsDNA) concentration in the presence of ubiquitous contaminants

added within the DNA sample preparation such as phenols/chloroforms, proteins, ethanol, and detergents. The Quant-iT™ PicoGreen® dsDNA assay was developed to improve the Hoechst-based assays when carried out in 10 mM Tris-HCl, 1 mM in EDTA, pH 7.5 with no addition of NaCl (TE Buffer) in order to detect as little dsDNA concentration as 25 pg/mL with ssDNA and RNA minimal interference.

Quant-iT™ PicoGreen® dsDNA kit contained the following reagents, Quant-iT™ PicoGreen® dsDNA reagent (Compound A), a 20X TE Buffer (Compound B), and a Lambda DNA Standard (100 µg/mL in TE) (Compound C). The cell Lysis Buffer (LB) was prepared in-house by combining 0.2 M Sodium Carbonate (Na₂CO₃) and 1% Triton-X in dH₂O. The assay was performed on mMVSCs seeded on control and scaffold constructs to assess cell proliferation based on concentration of dsDNA. A dsDNA standard curve was generated using compound C to calculate dsDNA quantity at each end point. In addition, an mMVSC standard curve was generated in a 24-well cell culture plate according to Table 6.1 to ensure the efficiency of the cell lysis work step for each experimental run. mMVSCs were cultured, and lysed prior to PicoGreen Assay: a) mMVSCs were seeded on control and scaffold constructs (25,000 cells per sample) and cultured in maintenance medium at 37 °C, 5% CO₂ for the required number of days, b) on each end-point day, scaffolds washed three times in DPBS and subsequently removed from the cell crowns and placed in 1 mL of LB in a 1 mL tube, c) samples were subjected to three cycles of freeze-thaw, with freezing to -80 °C and thawed at 37 °C. Samples were stored at -80 °C until required. Once, all the samples were ready for analysis the PicoGreen analysis was performed.

PicoGreen® Assay was performed in a flat-bottom black 96-well plate as follow: a) in a sterile 50 mL tube, compound A was diluted in 1X compound B to a final concentration of 0.5% (PicoGreen® working solution, PGWS). The final volume of PGWS was scaled up according the number of DNA samples to be tested, for instance a single reaction consisted of 100 µL of sample/standard and 100 µL of PGWS, b) for the dsDNA standard curve: 1 mL of 2 µg/mL compound C in LB was prepared as the standard working stock (SWS), and a serial dilution was performed according to Table 6.2 with 2 µg/mL DNA being the most concentrated standard and 0 µg/mL DNA (LB

Table 6.2: DNA standard curve solution quantities and final DNA concentrations

Volume of 2µg/ml DNA working stock (µl)	Volume lysis buffer (µl)	Final conc. DNA (ng/ml)
400	0	2000
200	200	1000
100	300	500
40	360	200
20	380	100
10	390	50
4	396	20
0	400	0

only) acting as a blank standard, c) 100 µL of each standards and experimental samples were loaded in a well of a 96-well plate. Each standard/sample reaction was prepared in triplicate, d) 100 µl of PicoGreen® working solution was added to each standard/sample, e) samples were incubated at room temperature for 2-3 min while mixing by pipetting, f) Florescence intensity was immediately measured using the Tecan Safire2™ plate reader with excitation 485 nm and emission 538 nm, Bandwidth 20 nm, Gain 50, measurements per sample 6, and integration time 40.

Quant-iT™ PicoGreen® dsDNA analysis

The fluorescence readouts of the standard samples were used to create a standard curve, and thus to obtain the equation of the line. The standard curve was assessed in order to verify the effectiveness of the assay by ensuring that a linearly proportional relationship existed between dsDNA concentration and relative fluorescence intensity (RFI). The percentage DNA concentration for each experimental sample was calculated by expressing their average fluorescent intensity value as a percentage ratio to that of the control specimens.

6.3.7 4',6-diamidino-2-phenylindole (DAPI) Staining

4',6-diamidino-2-phenylindole (DAPI) is a blue fluorescent nucleic acid stain that preferentially stains DNA [296]. DAPI stock solution was prepared at a concentration of 5 mg/mL in Ultra Pure H₂O, aliquoted in 50 µL, and stored at -20°C. Control and scaffold specimens were cultured until required at which time media removed and three washes in DPBS performed. Following this all samples were fixed in 3.7% formaldehyde at room temperature for 15 minutes followed by three DPBS washes,

lasting 5 minutes each, before DAPI staining unless otherwise specified.

Once cells were fixed and rinsed, 500 μ l of 5 μ g/mL diluted DAPI solution (1:1000 dilution) prepared in DPBS was added to each samples. Samples in DAPI solution were incubated at room temperature in the dark for 20 min. Three further washes of 5 minutes in DPBS were performed. Specimens were covered to protect them from light, and maintained in DPBS at room temperature for imaging within 4 hours, otherwise they were stored at 4°C. Images were captured at 10X and 20X magnifications using the Olympus BX51 Fluorescence Microscope with Cell^F Image software.

DAPI images Analysis

Samples were placed on the stage of the Olympus BX51 Fluorescence Microscope, the DAPI channel (excitation filter BP330-385) was selected, and five regions were captured per sample per objective (10X and 20X) using the Cell^F Image software as shown in Figure 6.2. DAPI stained cells (blue dots) were counted per region, and an average cell number obtained. Each sample average cell number was then calculated per regions of view, and scaled up to provide the average cell number per cm² using the known area per region of view. The average cell number per cm² of the samples were compared to each other in order to determine cell proliferation at different end points.

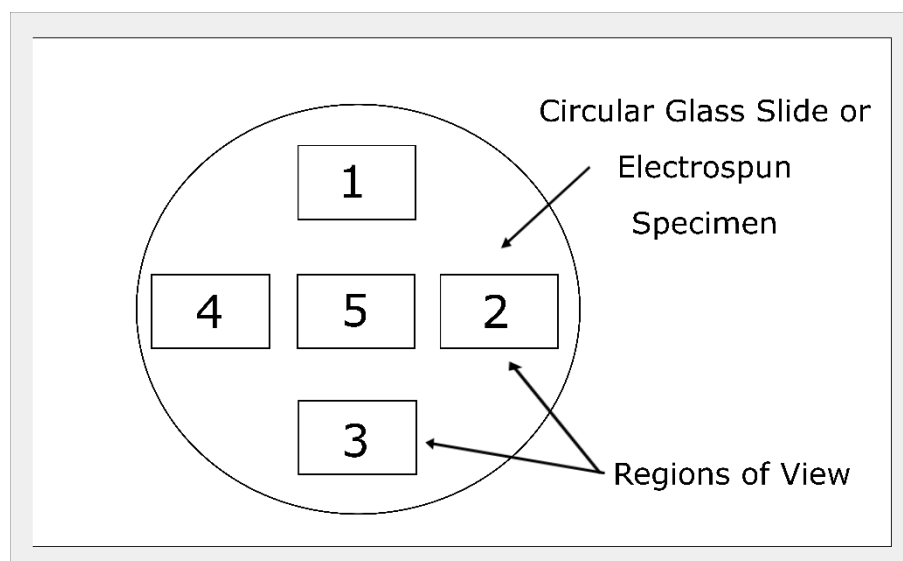


Figure 6.2: Schematic of cell counting method used on glass slides and scaffold constructs.

6.3.8 Cryofixation Fixation and Sample Sectioning

The infiltration rates of mMVSCs seeded on electrospun scaffolds was assessed according to the following cryofixation and sectioning protocol, as summarised in Figure 6.3. To begin a) the maintenance medium was discarded from each well and scaffolds were rinsed three times in DPBS to removed dead cells and any trace of medium, b) 1mL of 3.7% formaldehyde in DPBS was added to each well in a fume hood and left fixing at 4°C overnight, c) fixative solution was removed, and samples were washed three times in DPBS, d) scaffold constructs were lifted from the wells and carefully removed from the CELLCROWN system, e) Scaffolds were subsequently trimmed to remove the excess material and submerged in 15% sucrose-DPBS solution and incubated at 4°C for 24 hours followed by 30% sucrose for a further 24hrs, f) Samples were then directly transferred to a sterile non-coated 35 mm petri dish containing tissue freezing medium (TFM) (Leica Microsystems, Germany). TFM is a water-soluble solution consisting of glycols and resins that allows for the embedding of tissue samples during cryotomy. The cell seeded side of the scaffolds were placed facing downwards in the petri dishes, g) blank scaffolds of 10 mm diameter were pre-trimmed, and placed on top of the cell-containing scaffolds (one per sample) in order to prevent damage to the cell laden scaffold throughout the proceeding steps, h) a nylon rod was then used to gently press the scaffolds to ensure their flatness, and room temperature freezing medium was poured in to the petri dish to the height of vessel, i) the dish, rod and samples were incubated at -80°C till the medium was completely frozen, j) once the samples were frozen the rod was removed by gently twisting it in-situ, TFM medium was then added to fill the space preciously occupied by the rod. Samples were returned to -80°C for another freezing cycle until sectioning, k) Samples-TFM blocks were carefully lifted out of the petri dishes, and split in two halves with a cold scalpel in order to provide a sharp flat surface prior to the use of the cryotome.

At this point samples were either stored at -80°C till ready to use or sectioned using the CM3050s Research Cryostat (Leica, US), l) Samples were mounted on to a sectioning plate, and secured to the sectioning arm of the cryostat. The cryostat chamber was closed and allowed to reach the correct temperature before commencing sectioning, m) scaffolds were sliced at 20 µm sections using a new blade, n) sections

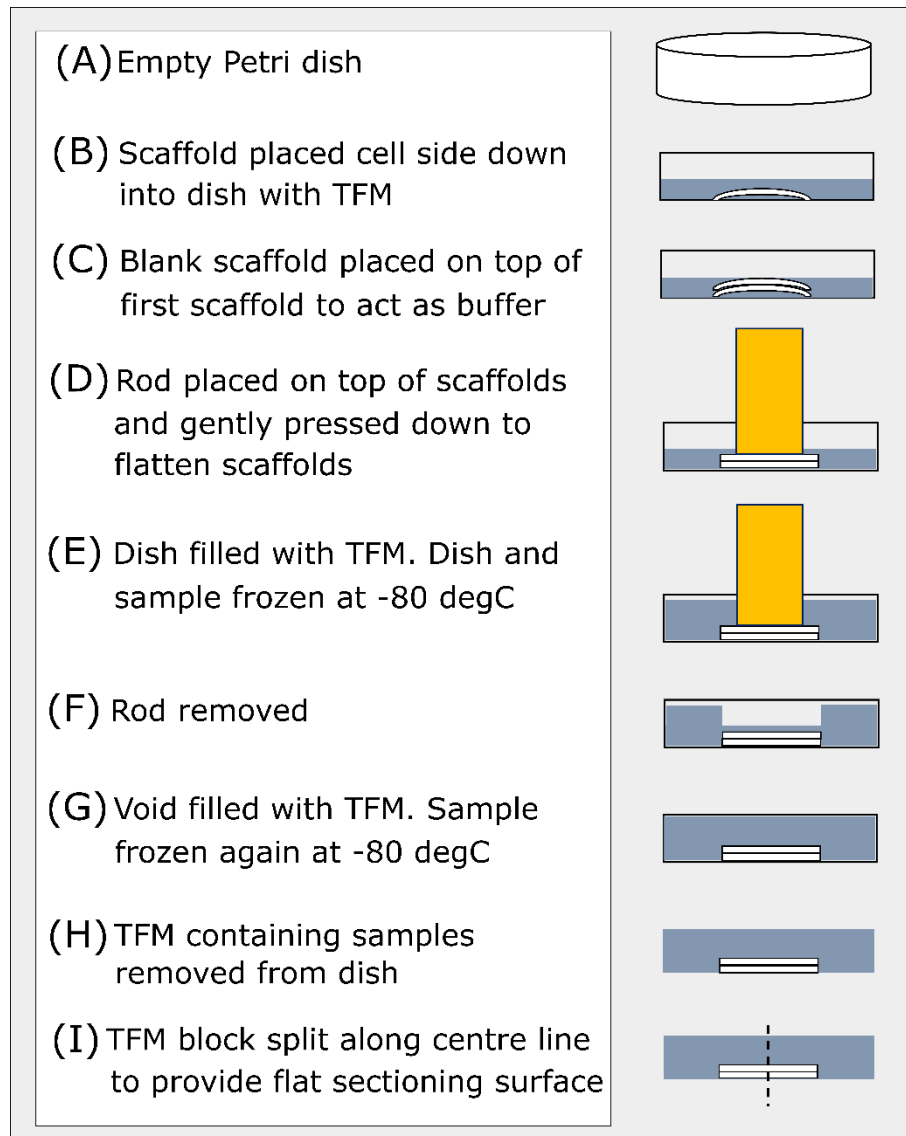


Figure 6.3: Schematic of protocol utilised for cryofixation and sectioning of electrospun specimens used to determine cell infiltration rates

were picked from the cryostat blade using cold tweezers, and placed on superfrost™ microscope slides (3-4 sections per slide), o) Samples on slides were carefully rinsed three times in room temperature DPBS in order to wash any trace of TFM medium as well as to rehydrate the samples before DAPI staining protocol.

Samples were stained and imaged according to the previously described protocol for DAPI staining, with 5 cross sections assessed at varying points throughout the thickness of the scaffold. A light microscope image of each scaffold was additionally taken to create an overlay image of cell infiltration and to calculate cell infiltration

depths. The average cell count and corresponding infiltration distance for each electrospun specimen was measured using the software program ImageJ.

6.3.9 SEM of Cell Scaffold Constructs

Scaffold constructs were washed in 1X Sterile DPBS to remove non-adherent cells and any other detritus materials. Samples were fixed in 2% Glutaraldehyde for 4 hours at room temperature. Following fixation scaffolds were washed three times with 1 ml of dH₂O at 5 min per wash. Scaffolds were then dehydrated by an ethanol gradient series. This series consisted of immersing scaffolds in 35% Ethanol for 15 min followed by 50% Ethanol (15 min), 70% Ethanol (15 min), 95% (15 min) and finally twice in 100% Ethanol (15 minutes each). The final Ethanol solution was removed, and 1ml of hexamethyldisilazane (HDMS) was added and removed after 1 min. The scaffolds were allowed to air dry in a fume hood overnight. Samples were then mounted on carbon tape and stored in a desiccator prior to imaging. Samples were sputter coated with gold prior to imaging, and viewed using an SEM.

6.4 Design of Cell Studies

6.4.1 alamarBlue® Analysis of mMVSCs Seeded on Electrospun Bi-layer Vessels

The metabolic activity of mMVSCs seeded on the bi-layer vessels was assessed by alamarBlue® assay. alamarBlue® was conducted according to previously described protocol for specimens at 1, 3 and 7 days post seeding. Each time point consisted of a glass slide acting as a control specimen, a random nanofibre membrane, aligned nanofibre membrane and finally a bi-layer vessel. In addition, a blank well, glass slide and electrospun scaffold were placed in culture medium to act as baseline measurements against which the corresponding average fluorescent intensity could be normalised. The experiment was repeated in triplicate for all time points.

6.4.2 PicoGreen® Analysis of mMVSCs Seeded on Electrospun Bi-layer Vessels

PicoGreen® measurements of specimens were similarly conducted according to the

previously described protocol. The same experimental design was employed as detailed above for the alamarBlue® analysis.

6.4.3 Cell Nuclei Staining of mMVSCs Seeded on Electrospun Bi-layer Vessels by DAPI

DAPI staining was conducted on the specimens utilised for the alamarBlue® analysis due to the non-toxic nature of the alamarBlue® assay. DAPI staining, imaging, and counting was conducted according to previously described protocol.

6.4.4 Assessment of mMVSC Infiltration of Electrospun Bi-Layer Vessels by Cryosectioning Techniques

The infiltration properties of mMVSCs on the bi-layer vessels was assessed by seeding them onto random and aligned nanofibre membranes along with the bi-layer vessels. 25,000 cells were seeded per sample, with one set of samples cultured for 7 days and the second set cultured for 14 days. No glass slide controls were employed due to the fact that cells could never penetrate the slide material making them irrelevant for this experiment. Cryosectioning was performed on the scaffolds according to previously described fixation and sectioning protocol.

6.4.5 SEM of Cell Scaffold Constructs

The morphology of mMVSCs seeded upon the bi-layer vessels was examined by SEM analysis. SEM was performed on both random and aligned nanofibre membranes, along with the bi-layer vessel under investigation in this work. The scaffolds were seeded with 25,000 cells and cultured for 1, 3 and 7 days after which they were fixed and mounted according to previously described SEM protocol.

6.5 Results

6.5.1 alamarBlue® Analysis of mMVSCs Seeded on Electrospun Bi-layer Vessels

The results of the alamarBlue® analysis performed for mMVSCs seeded upon the bi-layer electrospun vessels compared with control specimens and random and aligned nanofibre membranes can be seen in Figure 6.4. The results show the %Metabolic Activity for each of the specimen types examined after 1, 3 and 7 days of culturing (Figure 6.4 (A)). The values presented for each time point are expressed relative to the

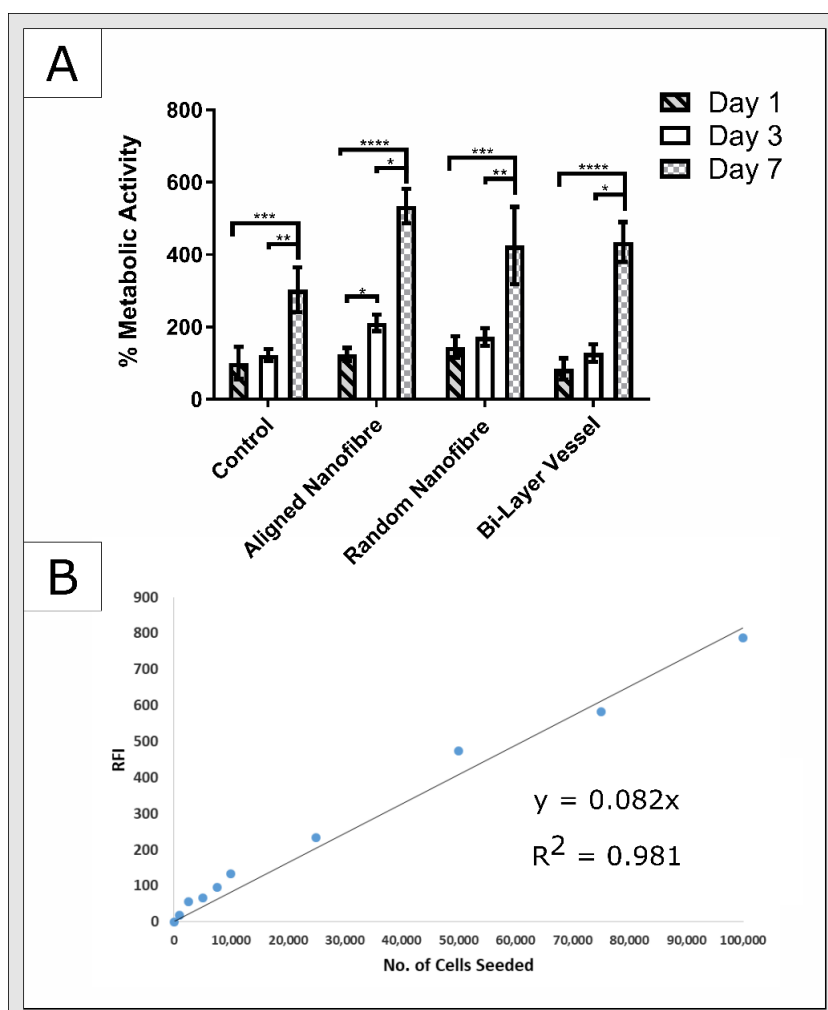


Figure 6.4: alamarBlue® of mMVSCs seeded upon control and electrospun specimens (A) %Metabolic activity of mMVSCs seeded on random, aligned and bi-layer electrospun structures with metabolic activity expressed relative to day 1 control specimens (B) Cell standard curve generated for alamarBlue® assay. (* $P \leq 0.05$)(** $P \leq 0.01$)(*** $P \leq 0.001$)(**** $P \leq 0.0001$). $N=3$ for each group (three replicates taken per sample).

metabolic activity of the control specimens at day 1. The results showed that there was a small but non-statistical increase in metabolic activity after 1 and 3 days post seeding for the control, random and bi-layer vessel specimens. The aligned nanofibre membranes did show a statistical increase in metabolic activity between day 1 and 3 ($p < 0.05$). At day 7 all specimens showed a statistical increase in metabolic activity compared to that of the control specimen at day 1 and their own corresponding metabolic activity at previous time points of days 1 and 3 (not annotated within the Figure). The aligned nanofibre membranes showed the highest metabolic activity at day 7 at $534.1 \pm 47.70\%$, with this being statistically higher than the metabolic activity for the controls, random nanofibre membranes and the bi-layer vessels for the same time point. The random ($424.8 \pm 106.7\%$) and bi-layer vessels ($434.7 \pm 55.12\%$) had statistically equivalent metabolic activities at day 7 ($p=0.0622$), while the bi-layer vessel showed an increased metabolic activity compared to that of the control specimen at day 7 ($302.9 \pm 62.10\%$) ($p < 0.0001$). The cell standard curve prepared (Figure 6.4 (B)), additionally demonstrated a linearly proportional trend between cell number and relative fluorescent intensity. This indicated the assay had not become saturated and had been performed efficiently.

6.5.2 PicoGreen® Analysis of mMVSCs Seeded on Electrospun Bi-layer Vessels

The results of the PicoGreen® experiments performed to assess the %DNA concentration found within the control and scaffold specimens at 1, 3 and 7 days post seeding can be seen in Figure 6.5 (A). No statistical difference in %DNA concentration was detected between day 1 and 3 for any of the specimens examined. At day 7 statistical increases were observed between all specimens compared to the control specimen for day 1 and equally to their corresponding day 1 samples. The aligned nanofibre membranes were again found to have the highest %DNA concentration for day 7 specimens at $404.7 \pm 78.44\%$. This was found to be statistically higher than that of the bi-layer vessels ($300.7 \pm 76.90\%$, $p=0.0034$), random nanofibres ($248.8 \pm 32.11\%$, $p < 0.001$) and control specimens ($241.7 \pm 26.69\%$, $p < 0.0001$) for the day 7 specimens (not annotated on the Figure). The bi-layer vessel was found to possess a statistically higher %DNA concentration to both the control specimens ($p=0.0199$),

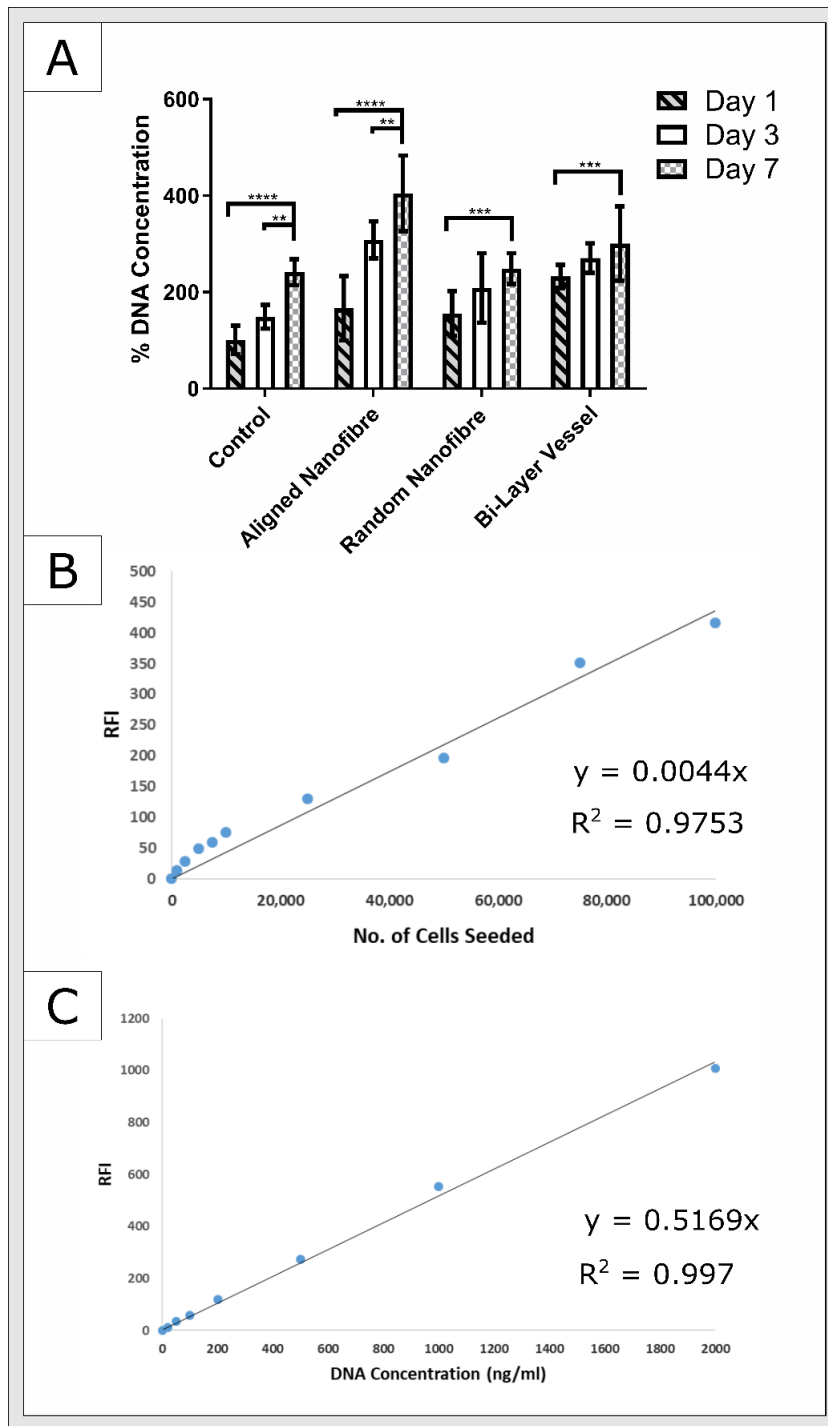


Figure 6.5: PicoGreen® of mMVSCs seeded upon control and electrospun specimens (A) %DNA concentration of mMVSCs seeded on random, aligned and bi-layer electrospun structures expressed relative to day 1 control specimens (B) Cell standard curve generated for PicoGreen® assay (C) DNA standard curve used to relate RFI to DNA concentration. N=3 for each group (three replicates taken per sample).

and random nanofibre membranes (p=0.0010) at day 7. Figure 6.5 (B) shows the cell standard curve prepared demonstrating a linearly proportional relationship between

the number of seeded cells and the RFI measured. This again provides confidence that the assay worked correctly as it did not show signs of saturation. Figure 6.5 (C) similarly shows the DNA standard curve prepared using the control standards. This again displayed a highly linearly proportional relationship with a strong regression at 99.7%, suggesting accuracy in the measurement process.

6.5.3 Cell Nuclei Staining of mMVSCs Seeded on Electrospun Bi-layer Vessels by DAPI

Figure 6.6 (A) displays the results obtained for the %Cell Count assessed through the measurement of DAPI stained cell nuclei, while Figure 6.6 (B) shows a typical image of the blue fluorescent staining of cell nuclei obtained using DAPI. Again the %Cell Count for each of the specimens studied for 1, 3 and 7 days posts seeding is presented. A statistical increase in cell numbers was observed between day 1 and 3 for the control and aligned nanofibre specimens. No increase between day 1 and 3 was observed for the random nanofibre and bi-layer vessels. All specimen groups showed a statistical increase in cell count at day 7 compared to the control specimens for day 1 and to their own corresponding day 1 samples. The control and aligned fibre membranes

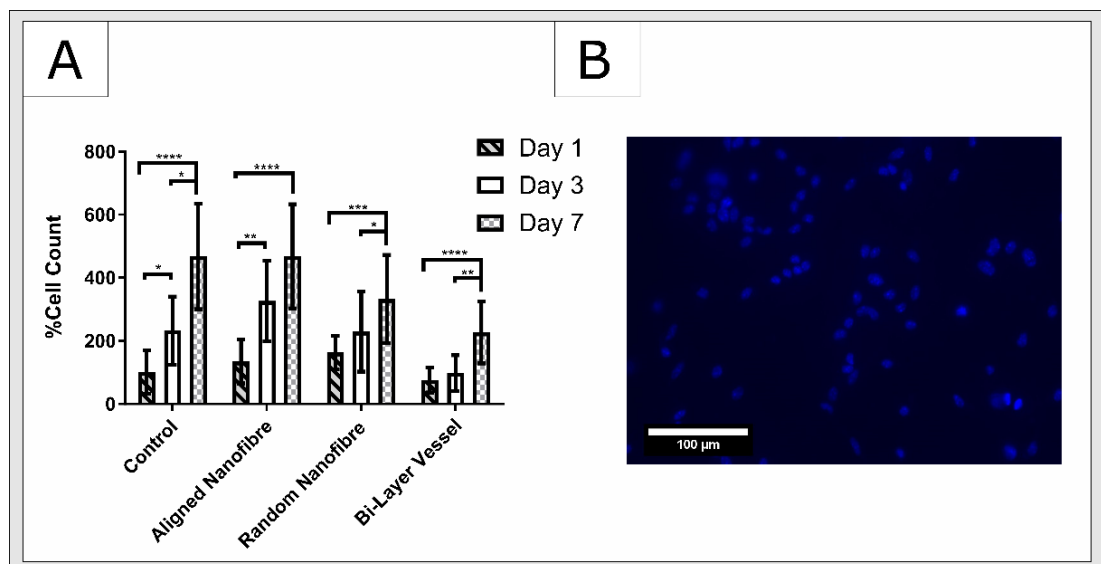


Figure 6.6: DAPI nuclei staining of mMVSCs seeded upon electrospun scaffolds and control specimens (A) Percentage cell count results showing count of aligned, nanofibre and bi-layer electrospun structures expressed with respect to day 1 control specimens. N=3 for each group (three replicates taken per sample). (B) Sample image of DAPI stained cells showing blue cell nuclei (taken at 20X magnification)

displayed no statistical difference ($p > 0.9999$) in their cell counts at $467.7 \pm 167.3\%$ and $467.7 \pm 165\%$ respectively (not annotated on the Figure). The bi-layer vessel ($226.4 \pm 97.95\%$) was found to have a statistically lower cell count than that of the day 7 control specimens ($p < 0.0001$) and the day 7 aligned nanofibre membranes ($p < 0.0001$). Additionally, the bi-layer vessel was found to have a statistically lower cell count to that of the random nanofibre membranes at day 7 ($332.3 \pm 139.8\%$ $p = 0.0232$).

6.5.4 Assessment of mMVSC Infiltration of Electrospun Bi-Layer Vessels by Cryosectioning Techniques

Figure 6.7 presents the quantitative results of the mMVSC infiltration studies performed for the electrospun scaffolds, while Figure 6.8 shows the corresponding cross sectional images of the electrospun scaffolds prepared by cryosectioning with DAPI stained nuclei indicated. The infiltration depths of cells, relative to the thickness of the electrospun construct they were seeded upon are shown in Figure 6.7 (A). This infiltration rate was termed ‘%Relative Cell Infiltration’. It can be seen that the aligned, random and bi-layer vessel displayed similar relative cell infiltration rates at day 7. On day 14, a significant increase was observed between the bi-layer vessels at $12.35 \pm 5.259\%$ and the corresponding day 14 specimens for the aligned ($4.484 \pm 2.945\%$, $p = 0.0079$) and random nanofibre membranes ($2.896 \pm 3.342\%$, $p = 0.0317$).

The analysis of the pure depth measurements of infiltrating cells is shown in Figure 6.7 (B). Here, a much more prominent difference can be seen between the infiltration levels of cells in the bi-layer vessels compared to those of the aligned and random nanofibre constructs. The infiltration at day 7 for the bi-layer vessels was found to be significantly higher at $30.14 \pm 16.04 \mu\text{m}$ to that of the aligned nanofibre ($1.459 \pm 0.4393 \mu\text{m}$, $p = 0.0079$), but not to that of the random nanofibre membranes ($4.956 \pm 2.446 \mu\text{m}$ $p = 0.0556$). The infiltration at day 14 for the bi-layer vessels was found to be equivalent to that of the day 7 bi-layer specimens, indicating no change in cell infiltration within the bi-layer vessels. The day 14 bi-layer specimens ($56.76 \pm 22.49 \mu\text{m}$) were however found to possess higher cell infiltration depths than both that

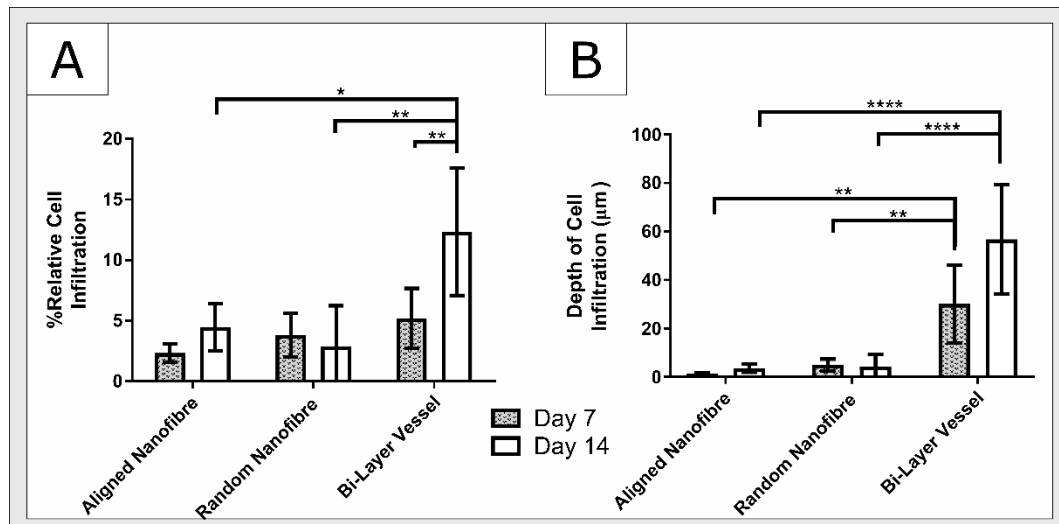


Figure 6.7: Assessment of mMVSC infiltration of electrospun specimens (A) ‘%Relative Cell Infiltration’ showing statistically higher infiltration of cells on bi-layer vessels at day 14 compared to both aligned and random fibre constructs (B) Actual depth measurements of infiltrating cells showing statistically higher infiltration on bi-layer vessels for both day 7 and 14 specimens compared to the random and aligned fibre constructs. $N=5$ per group.

of the aligned (3.638 ± 1.663 , $p=0.0079$) and random nanofibre (4.233 ± 5.156 μm , $p=0.0317$) constructs at day 14.

6.5.5 SEM of Cell Scaffold Constructs

The SEM images of mMVSCs seeded upon the bi-layer vessels along with the aligned and random nanofibre membranes can be seen in Figure 6.9 and Figure 6.10. Figure 6.9 shows a low magnification image of the three scaffold variants at day 1, 3 and 7 post seeding. Figure 6.10 similarly shows the three scaffold variants at day 1, 3 and 7 post seeding but at an increased magnification level.

Cells seeded upon the aligned nanofibre membranes exhibited an elongated phenotype with apparent alignment to the preferential axis of fibre orientation. An interesting note was that at day 7, cells appeared to form colonies that displayed a stacked like morphology often termed as a hill-and-valley pattern. On the other hand cells seeded upon the random nanofibre scaffolds exhibited a flat but dendritic/star phenotype, with protrusions seemingly following the randomly orientated fibres. The mMVSCs seeded upon the bi-layer vessel appeared to attach to the fibre bundles, aligning along the direction of the fibres. These cells did however appear to bridge the gaps between the

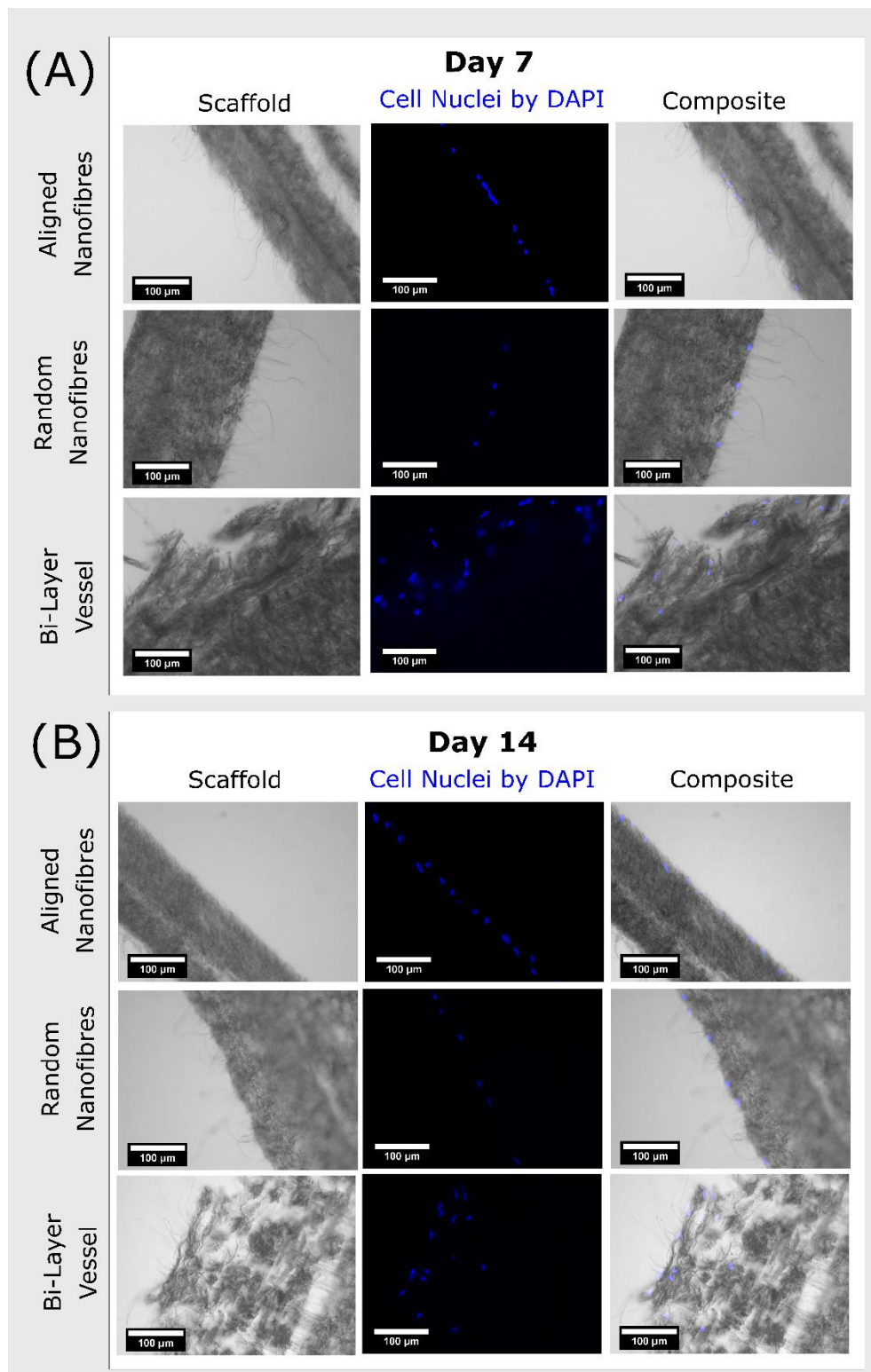


Figure 6.8: Cross sectional images of electrospun scaffolds seeded with mMVSCs after 7 and 14 days in culture (A) Cross sectional views of aligned, random and bi-layer electrospun structures showing DAPI stained cell nuclei and corresponding light microscope images of scaffold after 7 days in culture (B) Cross sectional views of aligned, random and bi-layer electrospun structures showing DAPI stained cell nuclei and corresponding light microscope images of scaffold after 14 days in culture.

fibre bundles, resulting in a three-dimensional dendritic phenotype. The cells also appeared to infiltrate into the gaps between fibre bundles, particularly visible at day 7. Extracellular matrix material (ECM) was observed across all the scaffold variants at the day 7, surrounding the cell colonies.

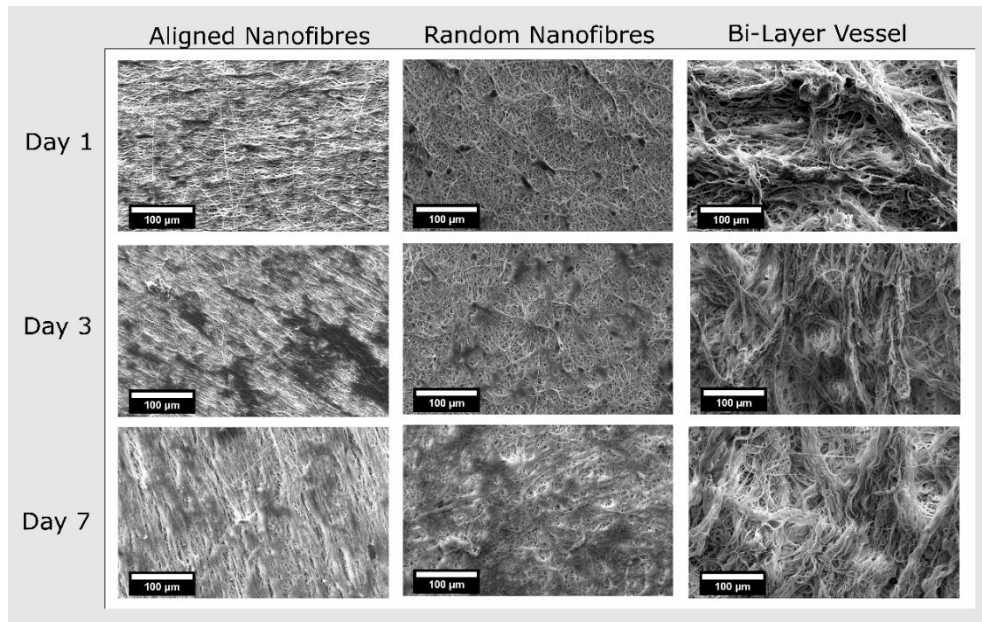


Figure 6.9: SEM images of cell laden electrospun scaffolds viewed at low level magnification.

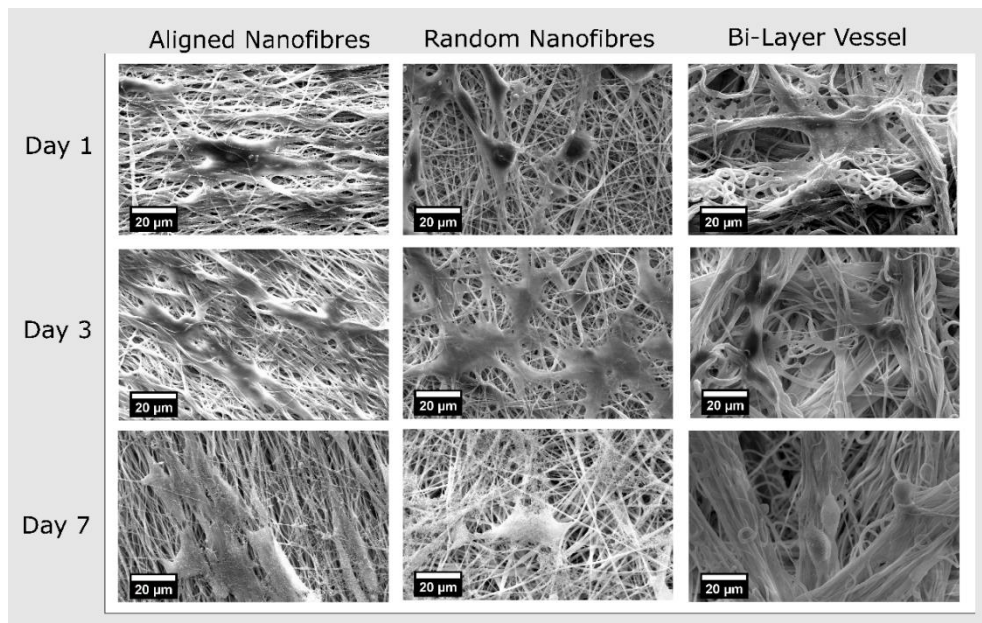


Figure 6.10: SEM images of cell laden electrospun scaffolds viewed at high level magnification.

6.6 Discussion

6.6.1 Viability of mMVSCs Seeded upon Electrospun Materials

In order to assess the viability of mMVSCs seeded upon the bi-layer vessel under investigation in this work, the results of alamarBlue®, PicoGreen® and DAPI staining were considered in unison. The results of the alamarBlue®, PicoGreen® and DAPI staining all indicated an increase in cell number between day 1 and 7 for the bi-layer vessel. Cell metabolic activity is considered to be an indirect indicator of cell proliferation and thus cell viability [297]. An increase in %Metabolic activity from $84.11 \pm 29.87\%$ to $434.7 \pm 55.12\%$ was seen between the day 1 and 7 specimens for the bi-layer vessel. This increase in cell metabolic activity paired with a higher content of dsDNA shown through the PicoGreen® assay at $232.8 \pm 23.84\%$ at day 1 to $300.7 \pm 76.90\%$ at day 7, further suggests an increase in overall cell numbers upon the bi-layer scaffold, representing an increase in cell proliferation and viability.

The results of the DAPI staining appeared to show slightly altered findings to that of the metabolic activity and DNA content findings. Control specimens were found to have higher cell counts than those of the electrospun constructs, despite having reduced metabolic activities and DNA content to the electrospun constructs. This discrepancy may result from two technical issues attributed to the staining process and the increased infiltration of cells on particular scaffold constructs. A loss of cells may have occurred within the electrospun scaffolds due to the numerous washing steps employed within the DAPI staining protocol. The hydrophobic nature of PCL may result in reduced cell adhesion properties compared to that of the glass slides [259]. This may ultimately result in cell removal from the scaffold and thus the underestimation of cell quantities.

In addition, the bi-layer vessel also appeared to show a reduced cell proliferation through DAPI staining in contrast to that indicated by the metabolic activity and dsDNA content. This may occur due to the highly three-dimensional nature of the bi-layer scaffolds allowing for the subsequent infiltration of cells into the inner volumes of the scaffold. This may prevent cells from being stained by DAPI or result in an inability to successfully image these cells due to the limitations of the fluorescent

microscopy.

These results none the less are highly promising indicators that the bi-layer vessel is capable of allowing for appropriate cell attachment and proliferation despite the complex architecture and the hydrophobic nature of the polymer PCL. Despite the discrepancies between the test methods in terms of the highest performing construct, it was clear that the bi-layer vessel was highly comparable to the control specimens and random nanofibre materials, both of which are commonly used in cell culture and tissue-engineering applications.

6.6.2 Comparison of Cell Infiltration Properties

The cross sectional samples of the electrospun specimens prepared by cryo-sectioning techniques displayed clear differences in the cell infiltration rates between the electrospun membranes studied. Both the ‘%Relative Cell Infiltration’ and ‘Depth of Cell Infiltration’ measurements confirmed that significantly higher infiltration of cells was observed at day 14 for mMVSCs seeded upon bi-layer vessels compared to that of the traditional electrospun membranes. Increased infiltration was also observed at day 7 between the scaffolds when the actual depth of cells was considered. This clearly indicates an increased ability for cells to infiltrate into the bi-layer constructs compared to the random and aligned nanofibre membranes. The sections taken show the formation of cell monolayers upon the surface of the aligned and random nanofibre membranes with little to no migration into the scaffold depths witnessed. On the other hand, cells were detected at significant depths within the bi-layer materials, most notably within the nanofibrous bundle layer of the vessels. It is noted that this cell infiltration witnessed for the bi-layer vessels may not be due to the migration of cells inwards over time but rather the ability of cells to penetrate further in the scaffold depths upon initial seeding. This is suspected due to the non-statistical increase in infiltration observed between the actual depth of cells seen on the bi-layer vessel between day 7 and 14.

6.6.3 Assessment of Cell morphology

It was clear that the architecture and fibre properties of the electrospun constructs highly influenced the morphology of the seeded mMVSCs. Aligned fibre constructs were found to induce elongated phenotypes compared to the dendritic morphologies witnessed on the random nanofibre and bi-layer constructs. The elongated cells visualised on day 7 aligned nanofibre scaffolds displayed a hill and valley or stacked cell morphology typically found within smooth muscle cell cultures (SMCs) [298].

In addition, cell colonies were clearly visible upon the surfaces of the aligned and random nanofibre constructs, however, those seeded on the bi-layer vessel were difficult to detect due to highly integrated nature of the cells amongst the scaffold fibres. This again is a promising finding as it was hoped to develop a scaffold that is accommodating to cell infiltration into the inner volumes of the scaffold body.

In all, the result of the cell culture studies performed indicated the ability of the bi-layer vessel under investigation to support cell proliferation while offering increased cell infiltration properties compared to the traditional nanofibre membranes prepared by electrospinning approaches.

Chapter 7 Conclusions & Recommendations

7.1 Main Findings

The aim of this project was to explore the fabrication of a suitable small diameter vascular graft (<6mm) created through the use of electrospinning techniques and tissue engineering approaches. A bi-layer vessel combining a hybrid fibre diameter PCL tubular core membrane, paired with highly porous and aligned nanofibre bundles was explored within this work to achieve the objective. The following goals met during this work are summarised below:

- Electrospun PCL tubular core scaffolds comprised of hybrid fibre diameter populations were created through the systematic design, screening and regression analysis of a single step multi-modal spinning process. The multi-modal PCL core layers fabricated, exhibited comparable mechanical properties including ultimate tensile strengths, Young's moduli and compliance characteristics to published values for common conduits currently used in arterial bypass applications.
- A custom designed and built dynamic liquid collection apparatus was successfully commissioned that allowed for the controlled electrospinning of highly porous nanofibre bundles. Extensive screening trials were conducted on solutions of PCL dissolved in Chloroform and DMF, studying the effects of solution and processing parameters on overall process stability, fibre bundle morphology and subsequent mechanical properties.
- A novel composite bi-layer vessel incorporating a multi-modal PCL core layer coated with aligned nanofibre bundles was successfully fabricated. These vessels were found to possess equivalent compliance characteristics to that of

native arterial tissue.

- The ability of the bi-layer vessel to support the adhesion and proliferation of seeded Multi Potent Vascular Stem Cells (MVSCs) was confirmed through metabolic activity, DNA content and cell nuclei quantification. The increased infiltration properties of the bi-layer vessels compared to traditional electrospun nanofibre membranes was additionally demonstrated.

7.2 Recommendations

Following on from the important findings outlined above, there is significant potential for the further development and analysis of the newly developed electrospun bi-layer vessel as a tissue engineered blood vessel. Possible future recommendations and works include:

- Further mechanical assessment of the bi-layer vessels is required in order to provide an increased understanding of the vessel performance when subjected to physiological loading scenarios. This should include the determination of pulsatile compliance properties along with the assessment of fatigue attributes.
- The development of twisted nanofibre PCL yarns through further refinement and adaptation of the dynamic liquid collection process is anticipated to provide electrospun structures that offer increased processing potential. The ability to manipulate a single strand nanofibre bundle or yarn offers increased manufacturing potential, allowing for the development of highly porous scaffolds through knitting and weaving principles.
- It is envisaged that the blending of the polymer PCL with suitable biomolecules such as RGD peptides, or biopolymers such as those of the Polyhydroxyalkanoate family, will improve the hydrophobic properties of the material, ultimately allowing for the development of a scaffold with increased cell adhesion and proliferation rates.

- The characterisation of stem cell differentiation upon the bi-layer vessel is of great interest due to the complex fibrous architecture of the scaffold. The ability to induce controlled cell differentiation throughout the thickness of the scaffold could allow for the development of a scaffold material that better mimics the natural cell populations of native arterial tissue.

Bibliography

- [1] World Health Organization, *World health statistics 2016 monitoring health for the sustainable development goals*. World Health Organization, 2016.
- [2] D. Mozaffarian *et al.*, “Heart disease and stroke statistics - 2016 Update: A report from the American Heart Association.,” *Circulation*, vol. 133, no. 4, pp. 38–360, Jan. 2016.
- [3] M. Nichols, N. Townsend, P. Scarborough, and M. Rayner, “Cardiovascular disease in Europe: epidemiological update.,” *Eur. Heart J.*, vol. 34, no. 39, pp. 3028–34, Oct. 2013.
- [4] I. F. Charo and R. Taub, “Anti-inflammatory therapeutics for the treatment of atherosclerosis,” *Nat. Rev. Drug Discov.*, vol. 10, no. 5, pp. 365–376, May 2011.
- [5] Heart, “What is a stent?,” *Am. Hear. Assoc.*, 2015.
- [6] K. A. Eagle, “ACC/AHA 2004 guideline update for coronary artery bypass graft surgery: Summary article: A report of the American college of cardiology/American Heart Association task force on practice guidelines,” *Circulation*, vol. 110, no. 9, pp. 1168–1176, Aug. 2004.
- [7] X. Wang, P. Lin, Q. Yao, and C. Chen, “Development of small-diameter vascular grafts.,” *World J. Surg.*, vol. 31, no. 4, pp. 682–9, Apr. 2007.
- [8] F. H. Silver, *Biomaterials, Medical Devices and Tissue Engineering: An Integrated Approach*. Dordrecht: Springer Netherlands, 1994.
- [9] B. H. Walpoth and G. L. Bowlin, “The daunting quest for a small diameter vascular graft,” *Expert Rev. Med. Devices*, vol. 2, no. 6, pp. 647–651, Nov. 2005.
- [10] S. Sarkar, H. J. Salacinski, G. Hamilton, and M. . Seifalian, “The mechanical properties of infrainguinal vascular bypass grafts: Their role in influencing patency,” *Eur. J. Vasc. Endovasc. Surg.*, vol. 31, no. 6, pp. 627–636, 2006.
- [11] H. J. Salacinski *et al.*, “The mechanical behavior of vascular grafts: a review.,” *J. Biomater. Appl.*, vol. 15, no. 3, pp. 241–278, 2001.
- [12] S. Hoerstrup, “Tissue engineering of small caliber vascular grafts,” *Eur. J. Cardio-Thoracic Surg.*, vol. 20, no. 1, pp. 164–169, Jul. 2001.
- [13] L. E. Niklason, J. Gao, W. M. Abbott, K. K. Hirschi, R. Marini, and R. Langer,

- “Functional arteries grown in vitro,” *Sci. AAAS*, vol. 284, no. 5413, pp. 489–493, 1999.
- [14] C. B. Weinberg and E. Bell, “A blood vessel model constructed from collagen and cultured vascular cells.,” *Science*, vol. 231, no. 4736, pp. 397–400, Jan. 1986.
- [15] R. Langer and J. Vacanti, “Tissue engineering,” *Science (80-.)*, vol. 260, no. 5110, pp. 920–926, May 1993.
- [16] C. Kasper, M. van Griensven, and R. Portner, *Bioreactor systems for tissue engineering- in Advance in Biochemical Engineering/Biotechnology*. Springer, 2009.
- [17] K. Lee, D. Kaplan, and K. Lee, *Tissue Engineering, I: Scaffold systems for tissue engineering*. Springer, 2006.
- [18] R. L. Mauck *et al.*, “Engineering on the straight and narrow: The mechanics of nanofibrous assemblies for fiber-reinforced tissue regeneration,” *Tissue Eng. Part B Rev.*, vol. 15, no. 2, pp. 171–193, Jun. 2009.
- [19] W. E. Teo and S. Ramakrishna, “A review on electrospinning design and nanofibre assemblies,” *Nanotechnology*, vol. 17, no. 14, pp. R89–R106, Jul. 2006.
- [20] S. Zhong, Y. Zhang, and C. T. Lim, “Fabrication of large pores in electrospun nanofibrous scaffolds for cellular infiltration: a review,” *Tissue Eng. Part B. Rev.*, vol. 18, no. 2, pp. 77–87, Apr. 2012.
- [21] P. T. J. Hwang *et al.*, “Poly(ϵ -caprolactone)/gelatin composite electrospun scaffolds with porous crater-like structures for tissue engineering.,” *J. Biomed. Mater. Res. A*, vol. 104, no. 4, pp. 1017–29, Apr. 2016.
- [22] M. F. Leong, M. Z. Rasheed, T. C. Lim, and K. S. Chian, “In vitro cell infiltration and in vivo cell infiltration and vascularization in a fibrous, highly porous poly(D,L-lactide) scaffold fabricated by cryogenic electrospinning technique.,” *J. Biomed. Mater. Res. A*, vol. 91, no. 1, pp. 231–40, Oct. 2009.
- [23] B. M. Baker, R. P. Shah, A. M. Silverstein, J. L. Esterhai, J. A. Burdick, and R. L. Mauck, “Sacrificial nanofibrous composites provide instruction without impediment and enable functional tissue formation.,” *Proc. Natl. Acad. Sci. U. S. A.*, vol. 109, no. 35, pp. 14176–81, 2012.
- [24] B. M. Baker *et al.*, “The potential to improve cell infiltration in composite fiber-

- aligned electrospun scaffolds by the selective removal of sacrificial fibers,” *Biomaterials*, vol. 29, no. 15, pp. 2348–2358, May 2008.
- [25] J. Wu *et al.*, “Electrospun nanoyarn scaffold and its application in tissue engineering,” *Mater. Lett.*, vol. 89, pp. 146–149, Dec. 2012.
- [26] Y. Xu *et al.*, “Fabrication of electrospun poly(L-lactide-co- ϵ -caprolactone)/collagen nanoyarn network as a novel, three-dimensional, macroporous, aligned scaffold for tendon tissue engineering,” *Tissue Eng. Part C. Methods*, vol. 19, no. 12, pp. 925–36, Dec. 2013.
- [27] G. J. Tortora and B. H. Derrickson, *Principles of Anatomy and Physiology*, 11th ed. Wiley, 2006.
- [28] B. F. Waller, C. M. Orr, J. D. Slack, C. a Pinkerton, J. Van Tassel, and T. Peters, “Anatomy, histology, and pathology of coronary arteries: a review relevant to new interventional and imaging techniques-Part I,” *Clin. Cardiol.*, vol. 15, no. 6, pp. 451–457, 1992.
- [29] J. D. Humphrey, *Cardiovascular solid mechanics: cells, tissues, and organs*. Springer, 2002.
- [30] “The cardiovascular system (blood vessels).” [Online]. Available: <http://www2.highlands.edu/academics/divisions/scipe/biology/faculty/harden/2122/notes/cvbw.htm>. [Accessed: 29-Apr-2017].
- [31] N. T. Wu, S.G., Lee, G. C., Tseng, “Nonlinear Elastic Analysis of Blood Vessels,” *J. Biomech. Eng.*, vol. 106, no. 4, p. 376, Jun. 2009.
- [32] C. Lally, A. J. Reid, and P. J. Prendergast, “Elastic behavior of porcine coronary artery tissue under uniaxial and equibiaxial tension,” *Ann. Biomed. Eng.*, vol. 32, no. 10, pp. 1355–1364, 2004.
- [33] G. A. Holzapfel, “Determination of layer-specific mechanical properties of human coronary arteries with nonatherosclerotic intimal thickening and related constitutive modeling,” *AJP Hear. Circ. Physiol.*, vol. 289, no. 5, pp. H2048–H2058, Nov. 2005.
- [34] G. A. Holzapfel, T. C. Gasser, and R. W. Ogden, “A new constitutive framework for arterial wall mechanics and a comparative study of material models,” *J. Elast.*, vol. 61, no. 1/3, pp. 1–48, 2000.
- [35] R. T. Venkatasubramanian, E. D. Grassl, V. H. Barocas, D. Lafontaine, and J. C. Bischof, “Effects of freezing and cryopreservation on the mechanical

- properties of arteries,” *Ann. Biomed. Eng.*, vol. 34, no. 5, pp. 823–832, 2006.
- [36] Y. C. Fung, *Biomechanics - Mechanical properties of living tissues*, Second. Springer, 2002.
- [37] S. L. Humphrey, Jay D., Delange, *An introduction to biomechanics: solids and fluids, analysis and design*, 1st ed. London: Springer, 2004.
- [38] S. Cheng, E. C. Clarke, and L. E. Bilston, “The effects of preconditioning strain on measured tissue properties,” *J. Biomech.*, vol. 42, no. 9, pp. 1360–1362, 2009.
- [39] M. Cecelja and P. Chowienczyk, “Role of arterial stiffness in cardiovascular disease.,” *JRSM Cardiovasc. Dis.*, vol. 1, no. 4, p. 11, 2012.
- [40] A. Seifalian, A. Giudiceandrea, T. Schmitz-Rixen, and G. Hamilton, “Non-compliance: The silent acceptance of a villain,” in *Tissue Engineering of Prosthetic Vascular Grafts*, R G Landes Company Publishers, 1998, pp. 43–56.
- [41] P. D. Ballyk, C. Walsh, J. Butany, and M. Ojha, “Compliance mismatch may promote graft-artery intimal hyperplasia by altering suture-line stresses,” *J. Biomech.*, vol. 31, no. 3, pp. 229–237, 1997.
- [42] N. R. Tai, H. J. Salacinski, A. Edwards, G. Hamilton, and A. M. Seifalian, “Compliance properties of conduits used in vascular reconstruction,” *Br. J. Surg.*, vol. 87, no. 11, pp. 1516–1524, 2000.
- [43] Who, “global_burden_disease_DTH6_2008.” p. 1, 2008.
- [44] R. Ross, “Atherosclerosis-an inflammatory disease.,” *N. Engl. J. Med.*, vol. 340, no. 2, pp. 115–26, Jan. 1999.
- [45] C. Yutani, M. Imakita, H. Ishibashi-Ueda, Y. Tsukamoto, N. Nishida, and Y. Ikeda, “Coronary atherosclerosis and interventions: pathological sequences and restenosis.,” *Pathol. Int.*, vol. 49, no. 4, pp. 273–90, Apr. 1999.
- [46] I. Sipahi *et al.*, “Beta-blockers and progression of coronary atherosclerosis: pooled analysis of 4 intravascular ultrasonography trials,” *Ann. Intern. Med.*, vol. 147, no. 1, pp. 10–18, 2007.
- [47] J. B. Elmore, E. Mehanna, S. A. Parikh, and D. A. Zidar, “Restenosis of the Coronary Arteries,” *Interv. Cardiol. Clin.*, vol. 5, no. 3, pp. 281–293, Jul. 2016.
- [48] K. Miura *et al.*, “Five-year outcomes after paclitaxel-coated balloon angioplasty for drug-eluting stent restenosis,” *Am. J. Cardiol.*, vol. 119, no. 3, pp. 365–371, Feb. 2017.

- [49] A. S. Go *et al.*, “Heart disease and stroke statistics - 2013 update: A report from the American Heart Association,” *Circulation*, vol. 127, no. 1, pp. e6–e245, Jan. 2013.
- [50] R. J. Shemin, “Coronary artery bypass grafting versus stenting for unprotected left main coronary artery disease: Where lies the body of proof?,” *Circulation*, vol. 118, no. 23, pp. 2326–2329, 2008.
- [51] P. Mølsted, “Survival difference between coronary bypass surgery and percutaneous coronary intervention,” *Scand. Cardiovasc. J.*, vol. 49, no. 4, pp. 177–182, Jul. 2015.
- [52] N. I. of Health, “Diagram of coronary angioplasty and stent placement,” 2006. [Online]. Available: http://www.nhlbi.nih.gov/health/dci/Diseases/Angioplasty/Angioplasty_WhatIs.html. [Accessed: 18-Jul-2015].
- [53] C. C. Canver, “Conduit options in coronary artery bypass surgery,” *CHEST J.*, vol. 108, no. 4, p. 1150, 1995.
- [54] B. W. Lytle, “Prolonging patency--choosing coronary bypass grafts.,” *N. Engl. J. Med.*, vol. 351, no. 22, pp. 2262–2264, 2004.
- [55] H. Staff, “Coronary artery bypass surgery for coronary artery disease,” *University of Michigan Health System*, 2014. [Online]. Available: <http://www.uofmhealth.org/health-library/zm2642>. [Accessed: 05-Aug-2015].
- [56] L. Provenzale, “Arterial homografts.,” *Minerva Chir.*, vol. 12, no. 10, pp. 517–542, 1957.
- [57] K. J. Pawlowski, S. E. Rittgers, S. P. Schmidt, and G. L. Bowlin, “Endothelial cell seeding of polymeric vascular grafts,” *Front. Biosci.* 9, no. 6, pp. 370–377, 2004.
- [58] S. Ravi, Z. Qu, and E. L. Chaikof, “Polymeric materials for tissue engineering of arterial substitutes.,” *Vascular*, vol. 17 Suppl 1, no. Suppl 1, pp. S45–S54, 2009.
- [59] J. G. Meinhart, “Clinical autologous in vitro endothelialization of 153 infrainguinal ePTFE grafts,” *Ann Thorac Surg*, vol. 71, no. 5 Suppl, pp. S327–S331, 2001.
- [60] H. Haruguchi and S. Teraoka, “Intimal hyperplasia and hemodynamic factors in arterial bypass and arteriovenous grafts: A review,” *J. Artif. Organs*, vol. 6,

no. 4, pp. 227–235, 2003.

- [61] A. J. White *et al.*, “Compliance mismatch between stenotic and distal reference segment is associated with coronary artery disease instability.,” *Atherosclerosis*, vol. 206, no. 1, pp. 179–85, Sep. 2009.
- [62] G. J. Hademenos and T. F. Massoud, “Biophysical mechanisms of stroke,” *Stroke*, vol. 28, no. 10, pp. 2067–2077, Oct. 1997.
- [63] G. M. Abouna, “Organ shortage crisis: Problems and possible solutions,” *Transplant. Proc.*, vol. 40, no. 1, pp. 34–38, 2008.
- [64] J. Kartus, L. Magnusson, S. Stener, S. Brandsson, B. I. Eriksson, and J. Karlsson, “Complications following arthroscopic anterior cruciate ligament reconstruction. A 2-5-year follow-up of 604 patients with special emphasis on anterior knee pain.,” *Knee Surg. Sports Traumatol. Arthrosc.*, vol. 7, no. 1, pp. 2–8, Jan. 1999.
- [65] F. Berthiaume and M. L. Yarmush, *Tissue engineering*. London: CRC PRESS, 2003.
- [66] T. Dvir, B. P. Timko, D. S. Kohane, and R. Langer, “Nanotechnological strategies for engineering complex tissues,” *Nat. Nanotechnol.*, vol. 6, no. 1, pp. 13–22, Jan. 2011.
- [67] S. Sarkar, T. Schmitz-Rixen, G. Hamilton, and A. M. Seifalian, “Achieving the ideal properties for vascular bypass grafts using a tissue engineered approach: A review,” *Med. Biol. Eng. Comput.*, vol. 45, no. 4, pp. 327–336, 2007.
- [68] P. Guha, J. W. Morgan, G. Mostoslavsky, N. P. Rodrigues, and A. S. Boyd, “Lack of immune response to differentiated cells derived from syngeneic induced pluripotent stem cells,” *Cell Stem Cell*, vol. 12, no. 4, pp. 407–412, 2013.
- [69] S. Michael *et al.*, “Tissue engineered skin substitutes created by laser- assisted bioprinting form skin-like structures in the dorsal skin fold chamber in mice,” 2013.
- [70] B. Weber *et al.*, “Off-the-shelf human decellularized tissue-engineered heart valves in a non-human primate model,” *Biomaterials*, vol. 34, no. 30, pp. 7269–7280, Oct. 2013.
- [71] Z. Zhou, F. Buchanan, C. Mitchell, and N. Dunne, “Printability of calcium phosphate: Calcium sulfate powders for the application of tissue engineered

- bone scaffolds using the 3D printing technique,” *Mater. Sci. Eng. C*, vol. 38, pp. 1–10, May 2014.
- [72] J. W. Reboredo, T. Weigel, A. Steinert, L. Rackwitz, M. Rudert, and H. Walles, “Investigation of migration and differentiation of human mesenchymal stem cells on five-layered collagenous electrospun scaffold mimicking native cartilage structure,” *Adv. Healthc. Mater.*, vol. 5, no. 17, pp. 2191–2198, Sep. 2016.
- [73] P. L. Lewis and R. N. Shah, “3D printing for liver tissue engineering: Current approaches and future challenges,” *Curr. Transplant. Reports*, vol. 3, no. 1, pp. 100–108, Mar. 2016.
- [74] R. Grant, D. C. Hay, and A. Callanan, “A drug-induced hybrid electrospun poly(caprolactone): Cell-derived extracellular matrix scaffold for liver tissue engineering,” *Tissue Eng. Part A*, p. ten.tea.2016.0419, May 2017.
- [75] M. Dvir-Ginzberg, I. Gamlieli-Bonshtein, R. Agbaria, and S. Cohen, “Liver tissue engineering within alginate scaffolds: effects of cell-seeding density on hepatocyte viability, morphology, and function,” *Tissue Eng.*, vol. 9, no. 4, pp. 757–766, 2003.
- [76] G. Konig *et al.*, “Mechanical properties of completely autologous human tissue engineered blood vessels compared to human saphenous vein and mammary artery,” *Biomaterials*, vol. 30, no. 8, pp. 1542–1550, Mar. 2009.
- [77] N. L’Heureux *et al.*, “Human tissue-engineered blood vessels for adult arterial revascularization,” *Nat. Med.*, vol. 12, no. 3, pp. 361–365, Mar. 2006.
- [78] S. Rayatpisheh, D. E. Heath, A. Shakouri, P.-O. Rujitanaroj, S. Y. Chew, and M. B. Chan-Park, “Combining cell sheet technology and electrospun scaffolding for engineered tubular, aligned, and contractile blood vessels,” *Biomaterials*, vol. 35, no. 9, pp. 2713–2719, Mar. 2014.
- [79] B. W. Tillman, S. K. Yazdani, S. J. Lee, R. L. Geary, A. Atala, and J. J. Yoo, “The in vivo stability of electrospun polycaprolactone-collagen scaffolds in vascular reconstruction,” *Biomaterials*, vol. 30, no. 4, pp. 583–588, Feb. 2009.
- [80] C. M. Vaz, S. van Tuijl, C. V. C. Bouten, and F. P. T. Baaijens, “Design of scaffolds for blood vessel tissue engineering using a multi-layering electrospinning technique,” *Acta Biomater.*, vol. 1, no. 5, pp. 575–582, Sep. 2005.

- [81] W. J. Zhang, W. Liu, L. Cui, and Y. Cao, "Tissue engineering of blood vessel.," *J. Cell. Mol. Med.*, vol. 11, no. 5, pp. 945–957, 2007.
- [82] U. Hersel, C. Dahmen, and H. Kessler, "RGD modified polymers: Biomaterials for stimulated cell adhesion and beyond," *Biomaterials*, vol. 24, no. 24, pp. 4385–4415, 2003.
- [83] T. P. Richardson, M. C. Peters, a B. Ennett, and D. J. Mooney, "Polymeric system for dual growth factor delivery.," *Nat. Biotechnol.*, vol. 19, no. 11, pp. 1029–1034, 2001.
- [84] B. P. Chan and K. W. Leong, "Scaffolding in tissue engineering: General approaches and tissue-specific considerations," *Eur. Spine J.*, vol. 17, no. SUPPL. 4, 2008.
- [85] N. L'Heureux, S. Pâquet, R. Labbé, L. Germain, and F. A. Auger, "A completely biological tissue-engineered human blood vessel," *FASEB J.*, vol. 12, no. 1, pp. 47–56, 1998.
- [86] E. Claes *et al.*, "Mechanical properties of human coronary arteries.," *Conf. Proc. IEEE Eng. Med. Biol. Soc.*, vol. 2010, pp. 3792–3795, 2010.
- [87] J. A. Matthews, G. E. Wnek, D. G. Simpson, and G. L. Bowlin, "Electrospinning of collagen nanofibers," *Biomacromolecules*, vol. 3, no. 2, pp. 232–238, 2002.
- [88] T. Huynh, G. Abraham, J. Murray, K. Brockbank, P. O. Hagen, and S. Sullivan, "Remodeling of an acellular collagen graft into a physiologically responsive neovessel.," *Nat. Biotechnol.*, vol. 17, no. 11, pp. 1083–1086, 1999.
- [89] W. F. Daamen, J. H. Veerkamp, J. C. M. van Hest, and T. H. van Kuppevelt, "Elastin as a biomaterial for tissue engineering," *Biomaterials*, vol. 28, no. 30, pp. 4378–4398, 2007.
- [90] G. Dubey and K. Mequanint, "Conjugation of fibronectin onto three-dimensional porous scaffolds for vascular tissue engineering applications," *Acta Biomater.*, vol. 7, no. 3, pp. 1114–1125, 2011.
- [91] J. D. Berglund, M. M. Mohseni, R. M. Nerem, and A. Sambanis, "A biological hybrid model for collagen-based tissue engineered vascular constructs," *Biomaterials*, vol. 24, no. 7, pp. 1241–1254, 2003.
- [92] E. D. Boland, J. a Matthews, K. J. Pawlowski, D. G. Simpson, G. E. Wnek, and G. L. Bowlin, "Electrospinning collagen and elastin: preliminary vascular tissue

- engineering.,” *Front. Biosci.*, vol. 9, no. July 2015, pp. 1422–1432, 2004.
- [93] F. M. Shaikh, A. Callanan, E. G. Kavanagh, P. E. Burke, P. a. Grace, and T. M. McGloughlin, “Fibrin: A natural biodegradable scaffold in vascular tissue engineering,” *Cells Tissues Organs*, vol. 188, no. 4, pp. 333–346, 2008.
- [94] Y. Li, H. Meng, Y. Liu, and B. P. Lee, “Fibrin gel as an injectable biodegradable scaffold and cell carrier for tissue engineering,” vol. 2015, 2015.
- [95] G. Q. Chen and Q. Wu, “The application of polyhydroxyalkanoates as tissue engineering materials,” *Biomaterials*, vol. 26, no. 33, pp. 6565–6578, 2005.
- [96] A. Patel, B. Fine, M. Sandig, and K. Mequanint, “Elastin biosynthesis: The missing link in tissue-engineered blood vessels,” *Cardiovasc. Res.*, vol. 71, no. 1, pp. 40–49, 2006.
- [97] H. Hajiali, S. Shahgasempour, M. R. Naimi-Jamal, and H. Peirovi, “Electrospun PGA/gelatin nanofibrous scaffolds and their potential application in vascular tissue engineering.,” *Int. J. Nanomedicine*, vol. 6, pp. 2133–2141, 2011.
- [98] S. In Jeong *et al.*, “Tissue-engineered vascular grafts composed of marine collagen and PLGA fibers using pulsatile perfusion bioreactors,” *Biomaterials*, vol. 28, no. 6, pp. 1115–1122, 2007.
- [99] D. C. Miller, A. Thapa, K. M. Haberstroh, and T. J. Webster, “Endothelial and vascular smooth muscle cell function on poly(lactic-co-glycolic acid) with nano-structured surface features,” *Biomaterials*, vol. 25, no. 1, pp. 53–61, 2004.
- [100] S. de Valence *et al.*, “Long term performance of polycaprolactone vascular grafts in a rat abdominal aorta replacement model,” *Biomaterials*, vol. 33, no. 1, pp. 38–47, Jan. 2012.
- [101] M. J. McClure, “Optimization of a tri-layered vascular graft: The influence of mechanical and cellular properties,” Virginia Commonwealth University, 2011.
- [102] S. de Valence *et al.*, “Advantages of bilayered vascular grafts for surgical applicability and tissue regeneration,” *Acta Biomater.*, vol. 8, no. 11, pp. 3914–3920, 2012.
- [103] T. H. Nguyen and B. T. Lee, “The effect of cross-linking on the microstructure, mechanical properties and biocompatibility of electrospun polycaprolactone–gelatin/PLGA–gelatin/PLGA–chitosan hybrid composite,” *Sci. Technol. Adv. Mater.*, vol. 13, no. 3, p. 035002, Jun. 2012.

- [104] M. R. Williamson, R. Black, and C. Kielty, "PCL-PU composite vascular scaffold production for vascular tissue engineering: Attachment, proliferation and bioactivity of human vascular endothelial cells," *Biomaterials*, vol. 27, no. 19, pp. 3608–3616, 2006.
- [105] W. J. van der Giessen *et al.*, "Marked inflammatory sequelae to implantation of biodegradable and nonbiodegradable polymers in porcine coronary arteries," *Circulation*, vol. 94, no. 7, pp. 1690–1697, Oct. 1996.
- [106] Y. Zhang, H. Ouyang, C. T. Lim, S. Ramakrishna, and Z.-M. Huang, "Electrospinning of gelatin fibers and gelatin/PCL composite fibrous scaffolds," *J. Biomed. Mater. Res.*, vol. 72B, no. 1, pp. 156–165, Jan. 2005.
- [107] J. S. Lim *et al.*, "Fabrication and evaluation of poly(epsilon-caprolactone)/silk fibroin blend nanofibrous scaffold," *Biopolymers*, vol. 97, no. 5, pp. 265–275, 2012.
- [108] Y. Lee, J. Kwon, G. Khang, and D. Lee, "Reduction of inflammatory response and enhancement of extracellular matrix formation by Vanillin-incorporated PLGA scaffolds," *Tissue Eng. Part A*, vol. 18, no. 19–20, pp. 1967–1978, 2012.
- [109] J. C. Middleton and A. J. Tipton, "Synthetic biodegradable polymers as orthopedic devices," *Biomaterials*, vol. 21, no. 23, pp. 2335–2346, Dec. 2000.
- [110] M. Abedalwafa, F. Wang, L. Wang, and C. Li, "Biodegradable poly(caprolactone) (PCL) for tissue engineering applications: A review," *Rev. Adv. Mater. Sci.*, vol. 34, pp. 123–140, 2013.
- [111] K. H. Lee, H. Y. Kim, M. S. Khil, Y. M. Ra, and D. R. Lee, "Characterization of nano-structured poly(ϵ -caprolactone) nonwoven mats via electrospinning," *Polymer (Guildf.)*, vol. 44, no. 4, pp. 1287–1294, Feb. 2003.
- [112] W. Li, J. A. Cooper, R. L. Mauck, and R. S. Tuan, "Fabrication and characterization of six electrospun poly(α -hydroxy ester)-based fibrous scaffolds for tissue engineering applications," *Acta Biomater.*, vol. 2, no. 4, pp. 377–385, Jul. 2006.
- [113] Z. G. Tang, R. A. Black, J. M. Curran, J. A. Hunt, N. P. Rhodes, and D. F. Williams, "Surface properties and biocompatibility of solvent-cast poly[ϵ -caprolactone] films," *Biomaterials*, vol. 25, no. 19, pp. 4741–4748, Aug. 2004.
- [114] A. G. A. Coombes, S. C. Rizzi, M. Williamson, J. E. Barralet, S. Downes, and W. A. Wallace, "Precipitation casting of polycaprolactone for applications in

- tissue engineering and drug delivery,” *Biomaterials*, vol. 25, no. 2, pp. 315–325, Jan. 2004.
- [115] A. P. Ebrahimi, “Mechanical properties of normal and diseased cerebrovascular system.,” *J. Vasc. Interv. Neurol.*, vol. 2, no. 2, pp. 155–62, 2009.
- [116] P. Xiang, M. Li, C. Zhang, D. Chen, and Z. Zhou, “Cytocompatibility of electrospun nanofiber tubular scaffolds for small diameter tissue engineering blood vessels.,” *Int. J. Biol. Macromol.*, vol. 49, no. 3, pp. 281–8, Oct. 2011.
- [117] H. Zhang, C. Y. Lin, and S. J. Hollister, “The interaction between bone marrow stromal cells and RGD-modified three-dimensional porous polycaprolactone scaffolds,” *Biomaterials*, vol. 30, no. 25, pp. 4063–4069, 2009.
- [118] L. Ghasemi-Mobarakeh, M. P. Prabhakaran, M. Morshed, M.-H. Nasr-Esfahani, and S. Ramakrishna, “Electrospun poly(epsilon-caprolactone)/gelatin nanofibrous scaffolds for nerve tissue engineering.,” *Biomaterials*, vol. 29, no. 34, pp. 4532–9, Dec. 2008.
- [119] Yale University, “Polycaprolactone as a hydrophobic membrane.” [Online]. Available:
<http://beng43427f2015.coursepress.yale.edu/2015/10/06/polycaprolactone-as-a-hydrophobic-membrane/>. [Accessed: 30-Apr-2017].
- [120] P. Bianco and P. G. Robey, “Stem cells in tissue engineering.,” *Nature*, vol. 414, no. 6859, pp. 118–121, 2001.
- [121] J. L. Olson, A. Atala, and J. J. Yoo, “Tissue engineering: Current strategies and future directions,” *Chonnam Med. J.*, vol. 47, no. 1, p. 1, 2011.
- [122] A. Wang *et al.*, “Induced pluripotent stem cells for neural tissue engineering,” *Biomaterials*, vol. 32, no. 22, pp. 5023–5032, 2011.
- [123] D. Howard, L. D. Buttery, K. M. Shakesheff, and S. J. Roberts, “Tissue engineering: Strategies, stem cells and scaffolds,” *J. Anat.*, vol. 213, no. 1, pp. 66–72, 2008.
- [124] J. W. Shin and D. E. Discher, “Blood and immune cell engineering: Cytoskeletal contractility and nuclear rheology impact cell lineage and localization: Biophysical regulation of hematopoietic differentiation and trafficking,” *BioEssays*, vol. 37, no. 6, pp. 633–642, 2015.
- [125] C. A. Heath, “Cells for tissue engineering.,” *Trends Biotechnol.*, vol. 18, no. 1, pp. 17–9, Jan. 2000.

- [126] M. F. Griffin, P. E. Butler, A. M. Seifalian, and D. M. Kalaskar, "Control of stem cell fate by engineering their micro and nanoenvironment.," *World J. Stem Cells*, vol. 7, no. 1, pp. 37–50, 2015.
- [127] M. P. Lutolf, P. M. Gilbert, and H. M. Blau, "Designing materials to direct stem-cell fate.," *Nature*, vol. 462, no. 7272, pp. 433–41, Nov. 2009.
- [128] P. K. Shah, "Inflammation, neointimal hyperplasia, and restenosis: as the leukocytes roll, the arteries thicken.," *Circulation*, vol. 107, no. 17, pp. 2175–7, May 2003.
- [129] Z. Tang *et al.*, "Differentiation of multipotent vascular stem cells contributes to vascular diseases.," *Nat. Commun.*, vol. 3, p. 875, Jun. 2012.
- [130] C. H. Lee *et al.*, "Nanofiber alignment and direction of mechanical strain affect the ECM production of human ACL fibroblast," *Biomaterials*, vol. 26, no. 11, pp. 1261–1270, 2005.
- [131] W. J. Li, C. T. Laurencin, E. J. Caterson, R. S. Tuan, and F. K. Ko, "Electrospun nanofibrous structure: A novel scaffold for tissue engineering," *J. Biomed. Mater. Res.*, vol. 60, no. 4, pp. 613–621, 2002.
- [132] D. H. Reneker and I. Chun, "Nanometre diameter fibres of polymer, produced by electrospinning," *Nanotechnology*, vol. 7, no. 3, pp. 216–223, 1999.
- [133] Z. M. Huang, Y. Z. Zhang, M. Kotaki, and S. Ramakrishna, "A review on polymer nanofibers by electrospinning and their applications in nanocomposites," *Compos. Sci. Technol.*, vol. 63, no. 15, pp. 2223–2253, Nov. 2003.
- [134] J. F. Cooley, "Apparatus for electrically dispersing fluids.," 1902.
- [135] A. Formhals, "Process and apparatus for preparing artificial threads," 1,975,504, 1934.
- [136] J. Doshi and D. H. Reneker, "Electrospinning process and applications of electrospun fibers," *J. Electrostat.*, vol. 35, pp. 151–160, 1993.
- [137] M. Ignatova, I. Rashkov, and N. Manolova, "Drug-loaded electrospun materials in wound-dressing applications and in local cancer treatment.," *Expert Opin. Drug Deliv.*, vol. 10, no. 4, pp. 469–83, 2013.
- [138] P. O. Rujitanaroj, N. Pimpha, and P. Supaphol, "Wound-dressing materials with antibacterial activity from electrospun gelatin fiber mats containing silver nanoparticles," *Polymer (Guildf.)*, vol. 49, no. 21, pp. 4723–4732, 2008.

- [139] S. Agarwal, J. H. Wendorff, and A. Greiner, "Use of electrospinning technique for biomedical applications," *Polymer (Guildf)*, vol. 49, no. 26, pp. 5603–5621, 2008.
- [140] H. Cho, S. Y. Min, and T. W. Lee, "Electrospun organic nanofiber electronics and photonics," *Macromol. Mater. Eng.*, vol. 298, no. 5, pp. 475–486, 2013.
- [141] J. A. Park, J. Moon, S. J. Lee, S. C. Lim, and T. Zyung, "Fabrication and characterization of ZnO nanofibers by electrospinning," *Curr. Appl. Phys.*, vol. 9, no. 3 SUPPL., pp. S210–S212, 2009.
- [142] R. Bagherzadeh, M. Latifi, S. S. Najar, M. A. Tehran, M. Gorji, and L. Kong, "Transport properties of multi-layer fabric based on electrospun nanofiber mats as a breathable barrier textile material," *Text. Res. J.*, vol. 82, no. 1, pp. 70–76, 2012.
- [143] Y. K. Kang, C. H. Park, J. Kim, and T. J. Kang, "Application of electrospun polyurethane web to breathable water-proof fabrics," *Fibers Polym.*, vol. 8, no. 5, pp. 564–570, 2007.
- [144] R. Gopal, S. Kaur, Z. Ma, C. Chan, S. Ramakrishna, and T. Matsuura, "Electrospun nanofibrous filtration membrane," *J. Memb. Sci.*, vol. 281, no. 1–2, pp. 581–586, 2006.
- [145] K. M. Yun, C. J. Hogan, Y. Matsubayashi, M. Kawabe, F. Iskandar, and K. Okuyama, "Nanoparticle filtration by electrospun polymer fibers," *Chem. Eng. Sci.*, vol. 62, no. 17, pp. 4751–4759, 2007.
- [146] K. J. Pawlowski and N. Langley, "Electrospun electroactive polymers for aerospace applications," *Am. Inst. Aeronaut. Astronaut.*, pp. 1–5, 2003.
- [147] D. Li and Y. Xia, "Electrospinning of nanofibers: Reinventing the wheel?," *Adv. Mater.*, vol. 16, no. 14, pp. 1151–1170, 2004.
- [148] D. H. Reneker, A. L. Yarin, H. Fong, and S. Koombhongse, "Bending instability of electrically charged liquid jets of polymer solutions in electrospinning," *J. Appl. Phys.*, vol. 87, no. 9, pp. 4531–4547, 2000.
- [149] G. Taylor, "Electrospray," *Proc. R. Soc. London*, vol. A280, pp. 383–387, 1964.
- [150] D. H. Reneker and A. L. Yarin, "Electrospinning jets and polymer nanofibers," *Polymer (Guildf)*, vol. 49, no. 10, pp. 2387–2425, 2008.
- [151] N. Bhardwaj and S. C. Kundu, "Electrospinning: A fascinating fiber fabrication technique," *Biotechnol. Adv.*, vol. 28, no. 3, pp. 325–347, 2010.

- [152] S. H. Tan, R. Inai, M. Kotaki, and S. Ramakrishna, "Systematic parameter study for ultra-fine fiber fabrication via electrospinning process," *Polymer (Guildf)*., vol. 46, no. 16, pp. 6128–6134, Jul. 2005.
- [153] J. H. Wendorff, S. Agarwal, and A. Greiner, *Electrospinning*. Weinheim, Germany: Wiley-VCH Verlag GmbH & Co. KGaA, 2012.
- [154] Z. Li and C. Wang, "Effects of working parameters on electrospinning," *One-Dimensional nanostructures*, pp. 15–29, 2013.
- [155] N. Bock, M. a. Woodruff, D. W. Hutmacher, and T. R. Dargaville, "Electrospraying, a reproducible method for production of polymeric microspheres for biomedical applications," *Polymers (Basel)*., vol. 3, no. 1, pp. 131–149, 2011.
- [156] W. K. Son, D. Cho, and W. H. Park, "Direct electrospinning of ultrafine titania fibres in the absence of polymer additives and formation of pure anatase titania fibres at low temperature," *Nanotechnology*, vol. 17, no. 2, pp. 439–443, 2005.
- [157] J. Zhang *et al.*, "Molecular weight-modulated electrospun poly(ϵ -caprolactone) membranes for postoperative adhesion prevention," *RSC Adv.*, vol. 4, no. 79, pp. 41696–41704, Aug. 2014.
- [158] C. T. Lim, E. P. S. Tan, and S. Y. Ng, "Effects of crystalline morphology on the tensile properties of electrospun polymer nanofibers," *Appl. Phys. Lett.*, vol. 92, no. 14, p. 141908, Apr. 2008.
- [159] Electrospin Tech, "Electrospinning Solution Properties," *Electrospin Tech*, 2015. [Online]. Available: <http://electrospintech.com/solution.html#.VbeHvflVhHx>. [Accessed: 28-Jul-2015].
- [160] H. Fong, I. Chun, and D. H. Reneker, "Beaded nanofibers formed during electrospinning," *Polymer (Guildf)*., vol. 40, no. 16, pp. 4585–4592, 1999.
- [161] S. Ramakrishna, *An Introduction to Electrospinning and Nanofibers*. World Scientific, 2005.
- [162] L. Jia and X.-H. Qin, "The effect of different surfactants on the electrospinning poly(vinyl alcohol) (PVA) nanofibers," *J. Therm. Anal. Calorim.*, vol. 112, no. 2, pp. 595–605, 2013.
- [163] T. Subbiah, G. S. Bhat, R. W. Tock, S. Parameswaran, and S. S. Ramkumar, "Electrospinning of nanofibers," *J. Appl. Polym. Sci.*, vol. 96, no. 2, pp. 557–

- 569, 2005.
- [164] X. Zong, K. Kim, D. Fang, S. Ran, B. S. Hsiao, and B. Chu, "Structure and process relationship of electrospun bioabsorbable nanofiber membranes," *Polymer (Guildf)*, vol. 43, no. 16, pp. 4403–4412, Jul. 2002.
- [165] J. S. Choi *et al.*, "Effect of organosoluble salts on the nanofibrous structure of electrospun poly(3-hydroxybutyrate-co-3-hydroxyvalerate)," *Int. J. Biol. Macromol.*, vol. 34, no. 4, pp. 249–256, 2004.
- [166] J. A. Knopf, "Investigation of linear electrospinning jets," University of Delaware, 2009.
- [167] J. M. Deitzel, J. Kleinmeyer, D. Harris, and N. C. Beck Tan, "The effect of processing variables on the morphology of electrospun nanofibers and textiles," *Polymer (Guildf)*, vol. 42, no. 1, pp. 261–272, 2001.
- [168] C. Zhang, X. Yuan, L. Wu, Y. Han, and J. Sheng, "Study on morphology of electrospun poly(vinyl alcohol) mats," *Eur. Polym. J.*, vol. 41, no. 3, pp. 423–432, 2005.
- [169] S. Megelski, J. S. Stephens, D. Bruce Chase, and J. F. Rabolt, "Micro- and nanostructured surface morphology on electrospun polymer fibers," *Macromolecules*, vol. 35, no. 22, pp. 8456–8466, 2002.
- [170] C. M. Wu, H. G. Chiou, S. L. Lin, and J. M. Lin, "Effects of electrostatic polarity and the types of electrical charging on electrospinning behavior," *J. Appl. Polym. Sci.*, vol. 126, no. S2, pp. E89–E97, Nov. 2012.
- [171] Electrospin Tech, "Solution Feed-rate," *Electrospin Tech*, 2015. [Online]. Available: http://electrospintech.com/feedrate.html#.Vbi4Y_IVhBc. [Accessed: 29-Jul-2015].
- [172] A. Greiner and J. H. Wendorff, "Electrospinning: A fascinating method for the preparation of ultrathin fibers," *Angew. Chemie - Int. Ed.*, vol. 46, no. 30, pp. 5670–5703, 2007.
- [173] C. Y. Xu, R. Inai, M. Kotaki, and S. Ramakrishna, "Aligned biodegradable nanofibrous structure: A potential scaffold for blood vessel engineering," *Biomaterials*, vol. 25, no. 5, pp. 877–886, Feb. 2004.
- [174] A. Karimi, M. Navidbakhsh, A. Shojaei, and S. Faghihi, "Measurement of the uniaxial mechanical properties of healthy and atherosclerotic human coronary arteries," *Mater. Sci. Eng. C*, vol. 33, no. 5, pp. 2550–2554, Jul. 2013.

- [175] M. J. McClure, S. a Sell, C. E. Ayres, D. G. Simpson, and G. L. Bowlin, “Electrospinning-aligned and random polydioxanone–polycaprolactone–silk fibroin-blended scaffolds: geometry for a vascular matrix,” *Biomed. Mater.*, vol. 4, no. 5, p. 055010, Oct. 2009.
- [176] M. J. McClure, D. G. Simpson, and G. L. Bowlin, “Tri-layered vascular grafts composed of polycaprolactone, elastin, collagen, and silk: Optimization of graft properties,” *J. Mech. Behav. Biomed. Mater.*, vol. 10, pp. 48–61, Jun. 2012.
- [177] S. Drilling, J. Gaumer, and J. Lannutti, “Fabrication of burst pressure competent vascular grafts via electrospinning: Effects of microstructure,” *J. Biomed. Mater. Res. Part A*, vol. 88A, no. 4, pp. 923–934, Mar. 2009.
- [178] E. Pektok *et al.*, “Degradation and healing characteristics of small-diameter poly(epsilon-caprolactone) vascular grafts in the rat systemic arterial circulation,” *Circulation*, vol. 118, no. 24, pp. 2563–70, Dec. 2008.
- [179] T. Fukunishi *et al.*, “Tissue-engineered small diameter arterial vascular grafts from cell-free nanofiber PCL/chitosan scaffolds in a sheep model,” *PLoS One*, vol. 11, no. 7, p. e0158555, Jul. 2016.
- [180] S. H. Javanmard, J. Anari, A. Z. Kharazi, and E. Vatankhah, “In vitro hemocompatibility and cytocompatibility of a three-layered vascular scaffold fabricated by sequential electrospinning of PCL, collagen, and PLLA nanofibers,” *J. Biomater. Appl.*, vol. 31, no. 3, pp. 438–449, Sep. 2016.
- [181] R. Zhou, L. Zhu, S. Fu, Y. Qian, D. Wang, and C. Wang, “Small Diameter Blood Vessels Bioengineered From Human Adipose-derived Stem Cells,” *Sci. Rep.*, vol. 6, no. 1, p. 35422, Dec. 2016.
- [182] A. Hasan *et al.*, “Electrospun scaffolds for tissue engineering of vascular grafts,” *Acta Biomater.*, vol. 10, no. 1, pp. 11–25, Jan. 2014.
- [183] Z. Tan, H. Wang, X. Gao, T. Liu, and Y. Tan, “Composite vascular grafts with high cell infiltration by co-electrospinning,” *Mater. Sci. Eng. C*, vol. 67, pp. 369–377, Oct. 2016.
- [184] S. Soliman *et al.*, “Multiscale three-dimensional scaffolds for soft tissue engineering via multimodal electrospinning,” *Acta Biomater.*, vol. 6, no. 4, pp. 1227–1237, Apr. 2010.
- [185] C. T. Laurencin, A. M. A. Ambrosio, M. D. Borden, and J. A. Cooper, “Tissue engineering: Orthopedic applications,” *Annu. Rev. Biomed. Eng.*, vol. 1, no. 1,

- pp. 19–46, Aug. 1999.
- [186] A. I. Teixeira, G. A. Abrams, P. J. Bertics, C. J. Murphy, and P. F. Nealey, “Epithelial contact guidance on well-defined micro- and nanostructured substrates.,” *J. Cell Sci.*, vol. 116, no. Pt 10, pp. 1881–92, May 2003.
- [187] A. Martins, R. L. Reis, and N. M. Neves, “Electrospinning: processing technique for tissue engineering scaffolding,” *Int. Mater. Rev.*, vol. 53, no. 5, pp. 257–274, Sep. 2008.
- [188] A. Martins, J. V Araújo, R. L. Reis, and N. M. Neves, “Electrospun nanostructured scaffolds for tissue engineering applications.,” *Nanomedicine (Lond)*, vol. 2, no. 6, pp. 929–42, Dec. 2007.
- [189] S. J. Eichhorn and W. W. Sampson, “Statistical geometry of pores and statistics of porous nanofibrous assemblies.,” *J. R. Soc. Interface*, vol. 2, no. 4, pp. 309–318, 2005.
- [190] S. E. Kim *et al.*, “Electrospun gelatin/polyurethane blended nanofibers for wound healing,” *Biomed. Mater.*, vol. 4, no. 4, p. 044106, Aug. 2009.
- [191] A. Guimarães, A. Martins, E. D. Pinho, S. Faria, R. L. Reis, and N. M. Neves, “Solving cell infiltration limitations of electrospun nanofiber meshes for tissue engineering applications.,” *Nanomedicine (Lond)*, vol. 5, no. 4, pp. 539–554, Jun. 2010.
- [192] B. M. Baker and R. L. Mauck, “The effect of nanofiber alignment on the maturation of engineered meniscus constructs,” *NIH Public Access- Biomater.*, vol. 28, no. 11, pp. 1967–1977, 2007.
- [193] J. F. Li and J. Lowengrub, “The effects of cell compressibility, motility and contact inhibition on the growth of tumor cell clusters using the Cellular Potts Model,” *J. Theor. Biol.*, vol. 343, no. 2, pp. 79–91, Feb. 2014.
- [194] L. Lao, Y. Wang, Y. Zhu, Y. Zhang, and C. Gao, “Poly(lactide-co-glycolide)/hydroxyapatite nanofibrous scaffolds fabricated by electrospinning for bone tissue engineering,” *J. Mater. Sci. Mater. Med.*, vol. 22, no. 8, pp. 1873–1884, Aug. 2011.
- [195] M. F. Leong, W. Y. Chan, K. S. Chian, M. Z. Rasheed, and J. M. Anderson, “Fabrication and in vitro and in vivo cell infiltration study of a bilayered cryogenic electrospun poly(D,L-lactide) scaffold,” *J. Biomed. Mater. Res. - Part A*, vol. 94, no. 4, pp. 1141–1149, 2010.

- [196] Q. P. Pham, U. Sharma, and A. G. Mikos, “Electrospun poly(epsilon-caprolactone) microfiber and multilayer nanofiber/microfiber scaffolds: characterization of scaffolds and measurement of cellular infiltration.,” *Biomacromolecules*, vol. 7, no. 10, pp. 2796–805, Oct. 2006.
- [197] M. I. Santos *et al.*, “Endothelial cell colonization and angiogenic potential of combined nano- and micro-fibrous scaffolds for bone tissue engineering,” *Biomaterials*, vol. 29, no. 32, pp. 4306–4313, 2008.
- [198] B. Nottelet *et al.*, “Factorial design optimization and in vivo feasibility of poly(epsilon-caprolactone)-micro- and nanofiber-based small diameter vascular grafts,” *J. Biomed. Mater. Res. - Part A*, vol. 89A, no. 4, pp. 865–875, Jun. 2009.
- [199] R. Gentsch, B. Boysen, A. Lankenau, and H. G. Börner, “Single-step electrospinning of bimodal fiber meshes for ease of cellular infiltration,” *Macromol. Rapid Commun.*, vol. 31, no. 1, pp. 59–64, 2010.
- [200] A. L. Yarin, W. Kataphinan, and D. H. Reneker, “Branching in electrospinning of nanofibers,” *J. Appl. Phys.*, vol. 98, no. 6, pp. 1–12, 2005.
- [201] M. I. van Lieshout *et al.*, “Electrospinning versus knitting: two scaffolds for tissue engineering of the aortic valve,” *J. Biomater. Sci. Polym. Ed.*, vol. 17, no. 1–2, pp. 77–89, 2006.
- [202] D. Li, Y. Wang, and Y. Xia, “Electrospinning of polymeric and ceramic nanofibers as uniaxially aligned arrays,” *Nano Lett.*, vol. 3, no. 8, pp. 1167–1171, 2003.
- [203] C. Luo, S. Stoyanov, E. Stride, E. Pelan, and M. Edirisinghe, “Electrospinning versus fibre production methods: from specifics to technological convergence.,” pp. 4708–4735, 2012.
- [204] F. Zhou and R. Gong, “Manufacturing technologies of polymeric nanofibres and nanofibre yarns,” vol. 845, no. August 2007, pp. 837–845, 2008.
- [205] P. J. Denton and Daniels, *Textile terms and definitions*. Manchester: Textile Institute, 2002.
- [206] A. Formhals, “Method and apparatus for the production of fibers,” 2,116,942, 1944.
- [207] A. Formhals, “Artificial fibre construction,” 2,109,333, 1938.
- [208] A. Formhals, “Method and apparatus for spinning,” 1944.

- [209] U. Ali, Y. Zhou, X. Wang, and T. Lin, “Electrospinning of continuous nanofiber bundles and twisted nanofiber yarns,” *Nanofibers - Prod. Prop. Funct. Appl.*, pp. 153–174, 2011.
- [210] M. Abbasipour and R. Khajavi, “Nanofiber bundles and yarns production by electrospinning: A review,” *Adv. Polym. Technol.*, vol. 32, no. 3, pp. 1–9, 2013.
- [211] L. Bosworth and S. Downes, “Biocompatible three-dimensional scaffolds for tendon tissue engineering using electrospinning,” in *Cellular Response to Biomaterials*, D. Silvio, Ed. 2008, pp. 3–27.
- [212] A. Theron, E. Zussman, and A. L. Yarin, “Electrostatic field-assisted alignment of electrospun nanofibres,” *Nanotechnology*, vol. 12, no. 3, pp. 384–390, 2001.
- [213] E. Zussman, D. Rittel, and a. L. Yarin, “Failure modes of electrospun nanofibers,” *Appl. Phys. Lett.*, vol. 82, no. 22, pp. 3958–3960, 2003.
- [214] H. Fong, W. Liu, C. Wang, and R. A. Vaia, “Generation of electrospun fibers of nylon 6 and nylon 6-montmorillonite nanocomposite,” *Polymer (Guildf.)*, vol. 43, pp. 775–780, 2002.
- [215] P. D. Dalton, D. Klee, and M. Möller, “Electrospinning with dual collection rings,” *Polymer (Guildf.)*, vol. 46, no. 3, pp. 611–614, 2005.
- [216] W. E. Teo and S. Ramakrishna, “Electrospun fibre bundle made of aligned nanofibres over two fixed points,” *Nanotechnology*, vol. 16, no. 9, pp. 1878–1884, 2005.
- [217] J. Deitzel, J. Kleinmeyer, and B. Tan, “Controlled deposition of electrospun poly(ethylene oxide) fibers,” *Polymer (Guildf.)*, vol. 42, no. 19, pp. 8163–8170, Sep. 2001.
- [218] S. F. Fennessey and R. J. Farris, “Fabrication of aligned and molecularly oriented electrospun polyacrylonitrile nanofibers and the mechanical behavior of their twisted yarns,” *Polymer (Guildf.)*, vol. 45, no. 12, pp. 4217–4225, 2004.
- [219] M. S. Khil, S. R. Bhattarai, H. Y. Kim, S. Z. Kim, and K. H. Lee, “Novel fabricated matrix via electrospinning for tissue engineering,” *J. Biomed. Mater. Res. B. Appl. Biomater.*, vol. 72, no. 1, pp. 117–24, Jan. 2005.
- [220] E. Smit, U. Buttner, and R. D. Sanderson, “Continuous yarns from electrospun fibers,” *Polymer (Guildf.)*, vol. 46, no. 8, pp. 2419–2423, 2005.
- [221] W. E. Teo, R. Gopal, R. Ramaseshan, K. Fujihara, and S. Ramakrishna, “A dynamic liquid support system for continuous electrospun yarn fabrication,”

- Polymer (Guildf.)*, vol. 48, no. 12, pp. 3400–3405, Jun. 2007.
- [222] M. Yousefzadeh, M. Latifi, W. E. Teo, M. Amani-Tehran, and S. Ramakrishna, “Producing continuous twisted yarn from well-aligned nanofibers by water vortex,” *Polym. Eng. Sci.*, vol. 51, no. 2, pp. 323–329, 2011.
- [223] W. E. Teo, S. Liao, C. K. Chan, and S. Ramakrishna, “Remodeling of three-dimensional hierarchically organized nanofibrous assemblies,” *Curr. Nanosci.*, vol. 4, no. 4, pp. 361–369, 2008.
- [224] M. Yousefzadeh, M. Latifi, M. Amani-tehran, W. Teo, and S. Ramakrishna, “A note on the 3D structural design of electrospun nanofibers,” *J. Eng. Fiber. Fabr.*, vol. 7, no. 2, pp. 17–23, 2012.
- [225] X. Wang *et al.*, “Continuous polymer nanofiber yarns prepared by self-bundling electrospinning method,” *Polymer (Guildf.)*, vol. 49, no. 11, pp. 2755–2761, May 2008.
- [226] H. Pan, L. Li, L. Hu, and X. Cui, “Continuous aligned polymer fibers produced by a modified electrospinning method,” *Polymer (Guildf.)*, vol. 47, no. 14, pp. 4901–4904, Jun. 2006.
- [227] U. Ali, Y. Zhou, X. Wang, and T. Lin, “Direct electrospinning of highly twisted, continuous nanofiber yarns,” *J. Text. Inst.*, vol. 103, no. 1, pp. 80–88, 2012.
- [228] J. He, Y. Zhou, K. Qi, L. Wang, P. Li, and S. Cui, “Continuous twisted nanofiber yarns fabricated by double conjugate electrospinning,” *Fibers Polym.*, vol. 14, no. 11, pp. 1857–1863, 2013.
- [229] F. Dabirian and S. A. Hosseini, “Novel method for nanofibre yarn production using two differently charged nozzles,” *Fibres Text. East. Eur.*, vol. 74, no. 3, pp. 45–47, 2009.
- [230] H. Maleki, a a Gharehaghaji, L. Moroni, and P. J. Dijkstra, “Influence of the solvent type on the morphology and mechanical properties of electrospun PLLA yarns,” *Biofabrication*, vol. 5, no. 3, p. 035014, 2013.
- [231] L. Yu. Yu, H. M. Shen, and Z. L. Xu, “PVDF–TiO₂ composite hollow fiber ultrafiltration membranes prepared by TiO₂ sol–gel method and blending method,” *J. Appl. Phys.*, vol. 113, pp. 1763–1772, 2009.
- [232] F. Dabirian, S. a H. Ravandi, R. H. Sanatgar, and J. P. Hinestroza, “Manufacturing of twisted continuous PAN nanofiber yarn by electrospinning process,” *Fibers Polym.*, vol. 12, no. 5, pp. 610–615, 2011.

- [233] A. A. Gharehaghaji, "Study on the effects of application of surface tension on the structure of electrospun nanofiber yarn," in *Evaluation*, 2010, pp. 10–13.
- [234] L. A. Bosworth, S. R. Rathbone, R. S. Bradley, and S. H. Cartmell, "Dynamic loading of electrospun yarns guides mesenchymal stem cells towards a tendon lineage," *J. Mech. Behav. Biomed. Mater.*, vol. 39, pp. 175–183, 2014.
- [235] J. Wu *et al.*, "Cell infiltration and vascularization in porous nanoyarn scaffolds prepared by dynamic liquid electrospinning," *J. Biomed. Nanotechnol.*, vol. 10, no. 4, pp. 603–614, 2014.
- [236] W. Liu *et al.*, "Injectable hydrogel incorporating with nanoyarn for bone regeneration.," *Journal of biomaterials science. Polymer edition*, vol. 25, no. 2, pp. 168–80, 2014.
- [237] R. Rezakhaniha *et al.*, "Experimental investigation of collagen waviness and orientation in the arterial adventitia using confocal laser scanning microscopy.," *Biomech. Model. Mechanobiol.*, vol. 11, no. 3–4, pp. 461–73, Mar. 2012.
- [238] J. Širc *et al.*, "Morphological characterization of nanofibers: Methods and application in practice," *J. Nanomater.*, vol. 2012, 2012.
- [239] X. Qin and D. Wu, "Effect of different solvents on poly(caprolactone)(PCL) electrospun nonwoven membranes," *J. Therm. Anal. Calorim.*, vol. 107, no. 3, pp. 1007–1013, 2012.
- [240] C. J. Luo, E. Stride, and M. Edirisinghe, "Mapping the influence of solubility and dielectric constant on electrospinning polycaprolactone solutions," *Macromolecules*, vol. 45, no. 11, pp. 4669–4680, 2012.
- [241] K. A. G. Katsogiannis, G. T. Vladisavljevic, and S. Georgiadou, "Porous electrospun polycaprolactone (PCL) fibres by phase separation," *Eur. Polym. J.*, vol. 69, pp. 284–295, 2015.
- [242] S. Soliman, S. Sant, J. W. Nichol, M. Khabiry, E. Traversa, and A. Khademhosseini, "Controlling the porosity of fibrous scaffolds by modulating the fiber diameter and packing density," *J. Biomed. Mater. Res. - Part A*, vol. 96 A, no. 3, pp. 566–574, 2011.
- [243] J. P. Jeun, Y. M. Lim, and Y. C. Nho, "Study on morphology of electrospun poly(caprolactone) nanofiber," *J. Ind. Eng. Chem.*, vol. 11, no. 4, pp. 573–578, 2005.
- [244] A. Martins, J. Cunha, F. Macedo, R. L. Reis, and N. M. Neves, "Improvement

- of polycaprolactone nanofibers topographies: Testing the influence in osteoblastic proliferation,” *2006 NSTI Nanotechnol. Conf. Trade Show - NSTI Nanotech 2006 Tech. Proc.*, vol. 2, no. January 2015, pp. 148–151, 2006.
- [245] C. Guo, L. Zhou, and J. Lv, “Effects of expandable graphite and modified ammonium polyphosphate on the flame-retardant and mechanical properties of wood flour-polypropylene composites,” *Polym. Polym. Compos.*, vol. 21, no. 7, pp. 449–456, 2013.
- [246] U. of Washington, “Properties of common solvents.” [Online]. Available: [http://depts.washington.edu/eo optic/linkfiles/dielectric_chart\[1\].pdf](http://depts.washington.edu/eo optic/linkfiles/dielectric_chart[1].pdf). [Accessed: 16-Aug-2015].
- [247] V. Pillay *et al.*, “A review of the effect of processing variables on the fabrication of electrospun nanofibers for drug delivery applications,” *J. Nanomater.*, vol. 2013, 2013.
- [248] S. Koombhongse, W. Liu, and D. H. Reneker, “Flat polymer ribbons and other shapes by electrospinning,” *J. Polym. Sci. Part B Polym. Phys.*, vol. 39, no. 21, pp. 2598–2606, Nov. 2001.
- [249] H. Yoshimoto, Y. M. M. Shin, H. Terai, and J. P. P. Vacanti, “A biodegradable nanofiber scaffold by electrospinning and its potential for bone tissue engineering,” *Biomaterials*, vol. 24, no. 12, pp. 2077–2082, May 2003.
- [250] M. Hasan, K. A. Nayem, M. B. Hossain, and S. Nahar, “Production of tissue engineering scaffolds from Poly(caprolactone) (PCL) and its microscopic analysis,” vol. 3, no. 3, pp. 39–43, 2014.
- [251] Q. Yang *et al.*, “Influence of solvents on the formation of ultrathin uniform poly(vinyl pyrrolidone) nanofibers with electrospinning,” *J. Polym. Sci. Part B Polym. Phys.*, vol. 42, no. 20, pp. 3721–3726, Oct. 2004.
- [252] L. Du, H. Xu, Y. Zhang, and F. Zou, “Electrospinning of polycaprolactone nanofibers with DMF additive: The effect of solution properties on jet perturbation and fiber morphologies,” *Fibers Polym.*, vol. 17, no. 5, pp. 751–759, 2016.
- [253] K. Garg and G. L. Bowlin, “Electrospinning jets and nanofibrous structures,” *Biomicrofluidics*, vol. 5, no. 1, p. 13403, Mar. 2011.
- [254] A. Haider, S. Haider, and I. K. Kang, “A comprehensive review summarizing the effect of electrospinning parameters and potential applications of nanofibers

- in biomedical and biotechnology,” *Arab. J. Chem.*, 2015.
- [255] N. S. Binulal *et al.*, “Role of nanofibrous poly(caprolactone) scaffolds in human mesenchymal stem cell attachment and spreading for in vitro bone tissue engineering—response to osteogenic regulators,” *Tissue Eng. Part A*, vol. 16, no. 2, pp. 393–404, Feb. 2010.
- [256] R. Safaeijavan, M. Soleimani, A. Divsalar, A. Eidi, and A. Ardeshirylajimi, “Comparison of random and aligned pcl nanofibrous electrospun scaffolds on cardiomyocyte differentiation of human adipose-derived stem cells,” *Iran. J. Basic Med. Sci.*, vol. 17, no. 11, pp. 903–911, 2014.
- [257] F. Chen, Y. Su, X. Mo, C. He, H. Wang, and Y. Ikada, “Biocompatibility, alignment degree and mechanical properties of an electrospun chitosan–P(LLA-CL) fibrous scaffold,” *J. Biomater. Sci. Polym. Ed.*, vol. 20, no. 14, pp. 2117–2128, 2009.
- [258] X. Wang, B. Ding, and B. Li, “Biomimetic electrospun nanofibrous structures for tissue engineering,” *Mater. Today*, vol. 16, no. 6, pp. 229–241, 2013.
- [259] D. Gupta *et al.*, “Aligned and random nanofibrous substrate for the in vitro culture of Schwann cells for neural tissue engineering,” *Acta Biomater.*, vol. 5, no. 7, pp. 2560–2569, 2009.
- [260] J. C. Uecker, G. C. Tepper, and J. Rosell-Llompart, “Ion-assisted collection of Nylon-4,6 electrospun nanofibers,” *Polymer (Guildf.)*, vol. 51, no. 22, pp. 5221–5228, 2010.
- [261] G. Collins, J. Federici, Y. Imura, and L. H. Catalani, “Charge generation, charge transport, and residual charge in the electrospinning of polymers: A review of issues and complications,” *J. Appl. Phys.*, vol. 111, no. 4, 2012.
- [262] L. Liu and Y. A. Dzenis, “Analysis of the effects of the residual charge and gap size on electrospun nanofiber alignment in a gap method,” *Nanotechnology*, vol. 19, no. 35, p. 355307, 2008.
- [263] K. Kim, K. Lee, M. Khil, Y. Ho, and H. Kim, “The effect of molecular weight and the linear velocity of drum surface on the properties of electrospun poly(ethylene terephthalate) nonwovens,” *Fibers Polym.*, vol. 5, no. 2, pp. 122–127, 2004.
- [264] A. M. El-hadi and F. Y. Al-Jabri, “Influence of electrospinning parameters on fiber diameter and mechanical properties of poly(3-Hydroxybutyrate) (PHB)

- and polyanilines (PANI) blends,” *Polymers (Basel)*, vol. 8, no. 3, 2016.
- [265] H. Jahani, S. Kaviani, M. Hassanpour-Ezatti, M. Soleimani, Z. Kaviani, and Z. Zonoubi, “The effect of aligned and random electrospun fibrous scaffolds on rat mesenchymal stem cell proliferation,” *Cell J.*, vol. 14, no. 1, pp. 31–38, 2012.
- [266] C. T. Koh, D. G. T. Strange, K. Tonsomboon, and M. L. Oyen, “Failure mechanisms in fibrous scaffolds,” *Acta Biomater.*, vol. 9, no. 7, pp. 7326–7334, 2013.
- [267] S. H. Kim, C. H. Mun, Y. Jung, S.-H. Kim, D.-I. Kim, and S. H. Kim, “Mechanical properties of compliant double layered poly(L-lactide-co- ϵ -caprolactone) vascular graft,” *Macromol. Res.*, vol. 21, no. 8, pp. 886–891, 2013.
- [268] A. N. Standard, “ISO 7198: Cardiovascular implants - Tubular vascular prostheses.” pp. 1–56, 2001.
- [269] A. Nieponice *et al.*, “Development of a tissue-engineered vascular graft combining a biodegradable scaffold, muscle-derived stem cells and a rotational vacuum seeding technique,” *Biomaterials*, vol. 29, no. 7, pp. 825–833, 2008.
- [270] C. M. Quick, J. K. Li, H. W. Weizsicker, and A. Noordergraaf, “Laplace’s law adapted to a blood vessel with two-phase wall structure,” *Proc. IEEE 21st Annu. Northeast Bioeng. Conf.*, 1995.
- [271] C. J. Van Andel, P. V. Pistecky, and C. Borst, “Mechanical properties of porcine and human arteries: Implications for coronary anastomotic connectors,” *Ann. Thorac. Surg.*, vol. 76, no. 1, pp. 58–64, 2003.
- [272] C. Del Gaudio, L. Fioravanzo, M. Folin, F. Marchi, E. Ercolani, and A. Bianco, “Electrospun tubular scaffolds: On the effectiveness of blending poly(ϵ -caprolactone) with poly(3-hydroxybutyrate-co-3-hydroxyvalerate),” *J. Biomed. Mater. Res. Part B Appl. Biomater.*, vol. 100B, no. 7, pp. 1883–1898, Oct. 2012.
- [273] L. Soffer *et al.*, “Silk-based electrospun tubular scaffolds for tissue-engineered vascular grafts,” *J. Biomater. Sci. Polym. Ed.*, vol. 19, no. 5, pp. 653–664, 2008.
- [274] R. Gauvin *et al.*, “Mechanical properties of tissue-engineered vascular constructs produced using arterial or venous cells,” *Tissue Eng. Part A*, vol.

- 17, no. 15–16, pp. 2049–2059, 2011.
- [275] D. Seliktar, R. A. Black, R. P. Vito, and R. M. Nerem, “Dynamic mechanical conditioning of collagen-gel blood vessel constructs induces remodeling in vitro,” *Ann. Biomed. Eng.*, vol. 28, no. 4, pp. 351–362, 2000.
- [276] R. Seyedmahmoud *et al.*, “A primer of statistical methods for correlating parameters and properties of electrospun poly(L-lactide) scaffolds for tissue engineering-Part 1: Design of experiments,” *J. Biomed. Mater. Res. A*, vol. 103, no. 1, pp. 91–102, Jan. 2015.
- [277] R. Seyedmahmoud *et al.*, “A primer of statistical methods for correlating parameters and properties of electrospun poly(L-lactide) scaffolds for tissue engineering-Part 2: Regression,” *J. Biomed. Mater. Res. A*, vol. 103, no. 1, pp. 103–114, Jan. 2015.
- [278] A. L. Sisson, D. Ekinici, and A. Lendlein, “The contemporary role of ϵ -caprolactone chemistry to create advanced polymer architectures,” *Polymer (Guildf.)*, vol. 54, no. 17, pp. 4333–4350, Aug. 2013.
- [279] D. T. Gentekos, L. N. Dupuis, and B. P. Fors, “Beyond dispersity: Deterministic control of polymer molecular weight distribution,” *J. Am. Chem. Soc.*, vol. 138, no. 6, pp. 1848–1851, 2016.
- [280] R. M. Nezarati, M. B. Eifert, and E. Cosgriff-Hernandez, “Effects of humidity and solution viscosity on electrospun fiber morphology,” *Tissue Eng. Part C Methods*, vol. 19, no. 10, pp. 810–819, 2013.
- [281] D. L. Donovan, S. P. Schmidt, S. P. Townshend, G. O. Njus, and W. V Sharp, “Material and structural characterization of human saphenous vein,” *J. Vasc. Surg. Off. Publ. Soc. Vasc. Surg. [and] Int. Soc. Cardiovasc. Surgery, North Am. Chapter*, vol. 12, no. 5, pp. 531–537, 1990.
- [282] M. A. Badawi and L. K. El-Khordagui, “A quality by design approach to optimization of emulsions for electrospinning using factorial and D-optimal designs,” *Eur. J. Pharm. Sci.*, vol. 58, no. 1, pp. 44–54, 2014.
- [283] I. Y. Enis, H. Sezgin, and T. G. Sadikoglu, “Full factorial experimental design for mechanical properties of electrospun vascular grafts,” *J. Ind. Text.*, no. 65, p. 152808371769061, 2017.
- [284] A. Jaworek, “Micro- and nanoparticle production by electrospraying,” *Powder Technol.*, vol. 176, no. 1, pp. 18–35, Jul. 2007.

- [285] S. S. Zargarian and V. Haddadi-Asl, “A nanofibrous composite scaffold of PCL/Hydroxyapatite-chitosan/PVA prepared by electrospinning,” *Iran. Polym. J.*, vol. 19, no. 6, pp. 457–468, 2010.
- [286] A. Gevorkyan, G. E. Shter, Y. Shmueli, A. Buk, R. Meir, and G. S. Grader, “Branching effect and morphology control in electrospun $\text{PbZr}_{0.52}\text{Ti}_{0.48}\text{O}_3$ nanofibers,” *J. Mater. Res.*, vol. 29, no. 16, pp. 1721–1729, Aug. 2014.
- [287] S. Shang, F. Yang, X. Cheng, X. Frank Walboomers, and J. A. Jansen, “The effect of electrospun fibre alignment on the behaviour of rat periodontal ligament cells,” *Eur. Cells Mater.*, vol. 19, pp. 180–192, 2010.
- [288] S. R. Bhattarai, N. Bhattarai, H. K. Yi, P. H. Hwang, D. Il Cha, and H. Y. Kim, “Novel biodegradable electrospun membrane: scaffold for tissue engineering,” *Biomaterials*, vol. 25, no. 13, pp. 2595–602, Jun. 2004.
- [289] R. Jalili, M. Morshed, and S. A. H. Ravandi, “Fundamental parameters affecting electrospinning of PAN nanofibers as uniaxially aligned fibers,” *J. Appl. Polym. Sci.*, vol. 101, no. 6, pp. 4350–4357, 2006.
- [290] T. Liang, S. Mahalingam, and M. Edirisinghe, “Creating ‘hotels’ for cells by electrospinning honeycomb-like polymeric structures,” *Mater. Sci. Eng. C*, vol. 33, no. 7, pp. 4384–4391, 2013.
- [291] S. Thandavamoorthy, N. Gopinath, and S. S. Ramkumar, “Self-assembled honeycomb polyurethane nanofibers,” *J. Appl. Polym. Sci.*, vol. 101, no. 5, pp. 3121–3124, 2006.
- [292] E. M. Campbell, “Investigation of small-diameter decellularised artery as a potential scaffold for vascular tissue engineering,” Dublin City University, 2013.
- [293] A. Baji, Y. W. Mai, S. C. Wong, M. Abtahi, and P. Chen, “Electrospinning of polymer nanofibers: Effects on oriented morphology, structures and tensile properties,” *Compos. Sci. Technol.*, vol. 70, no. 5, pp. 703–718, 2010.
- [294] D. Li *et al.*, “Nerve conduits constructed by electrospun P(LLA-CL) nanofibers and PLLA nanofiber yarns,” *J. Mater. Chem. B*, vol. 3, pp. 8823–8831, 2015.
- [295] C. Ellerström, R. Strehl, K. Noaksson, J. Hyllner, and H. Semb, “Facilitated expansion of human embryonic stem cells by single-cell enzymatic dissociation,” *Stem Cells*, vol. 25, no. 7, pp. 1690–1696, Jul. 2007.
- [296] “DAPI 4',6-Diamidine-2'-phenylindole dihydrochloride | Sigma-Aldrich.”

[Online].

Available:

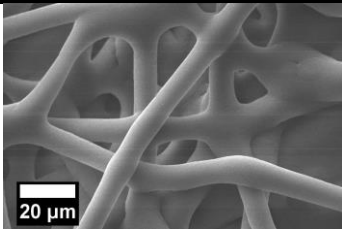
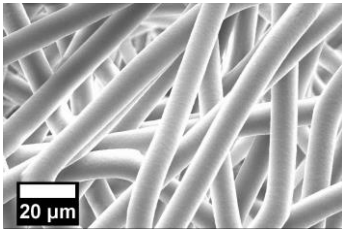
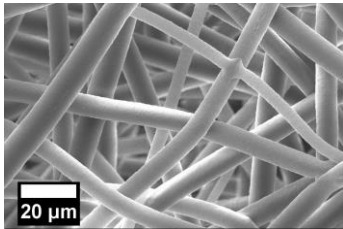
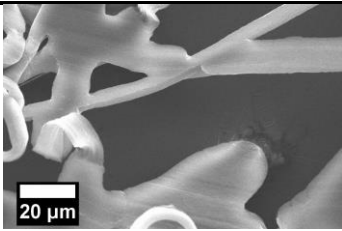
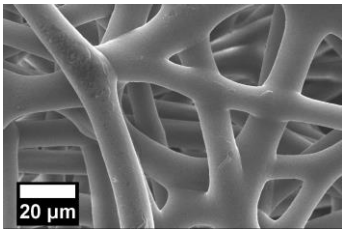
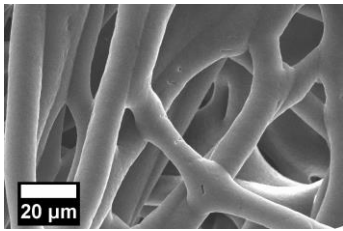
<https://www.sigmaaldrich.com/catalog/product/roche/10236276001?lang=en®ion=IE>. [Accessed: 22-Dec-2017].

- [297] S. N. Rampersad, “Multiple applications of alamar blue as an indicator of metabolic function and cellular health in cell viability bioassays,” *Sensors*, vol. 12, no. 12, pp. 12347–12360, Sep. 2012.
- [298] N. Endlich, K. Endlich, N. Taesch, and J.-J. Helwig, “Culture of vascular smooth muscle cells from small arteries of the rat kidney,” *Kidney Int.*, vol. 57, pp. 2468–2475, 2000.
- [299] F. Khoffi, F. Dieval, N. Chakfé, and B. Durand, “A development of a technique for measuring the compliance of the textile vascular prostheses,” *Phys. Procedia*, vol. 21, pp. 234–239, 2011.
- [300] S. G. Yates *et al.*, “The preclotting of porous arterial prostheses,” *Ann. Surg.*, vol. 188, no. 5, pp. 611–622, 1978.
- [301] S. Venkatraman, F. Boey, and L. L. Lao, “Implanted cardiovascular polymers: Natural, synthetic and bio-inspired,” *Prog. Polym. Sci.*, vol. 33, no. 9, pp. 853–874, 2008.
- [302] J. J. Stankus, L. Soletti, K. Fujimoto, Y. Hong, D. A. Vorp, and W. R. Wagner, “Fabrication of cell microintegrated blood vessel constructs through electrohydrodynamic atomization,” *Biomaterials*, vol. 28, no. 17, pp. 2738–2746, 2007.

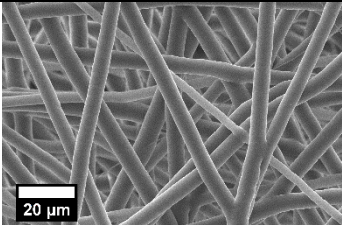
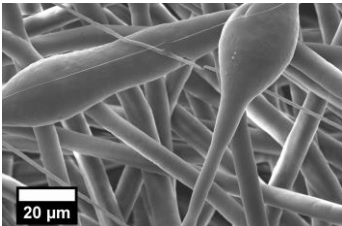
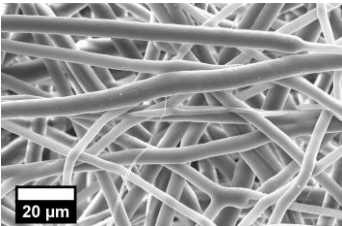
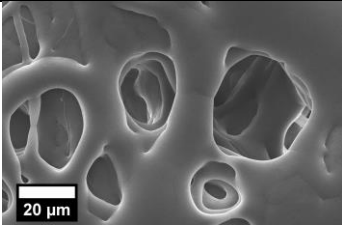
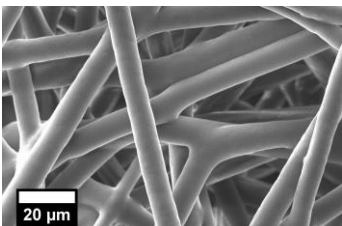
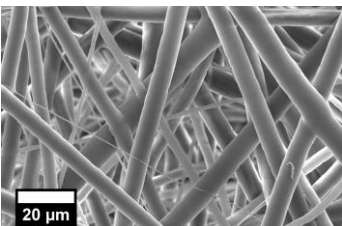
Appendices

Appendix A: Complete Results of Solution Screening Trial

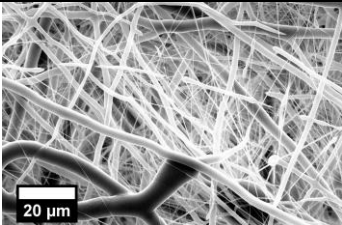
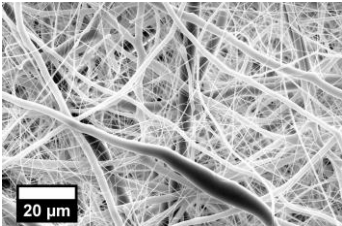
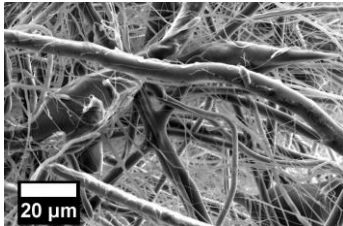
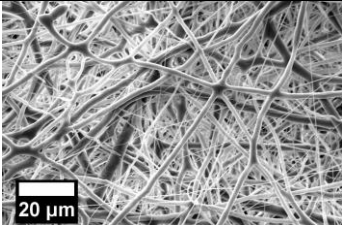
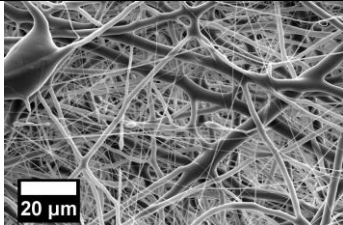
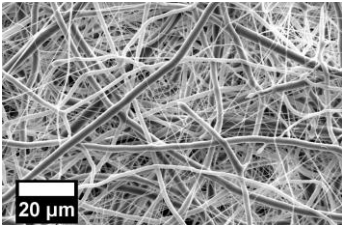
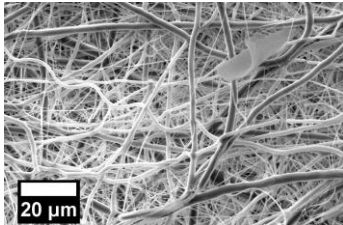
Table A.0.1: SEM results of micron and multimodal solution screening trial

14wt% Chloroform			
Applied Voltage (kV)	Collector Distance (cm)	Flow Rate (ml/hr)	
		6	12
15	15		Liquid Polymer
	20	 	
20	15		Liquid Polymer
	20	 	

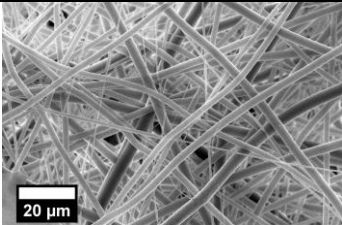
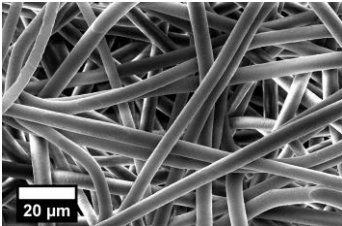
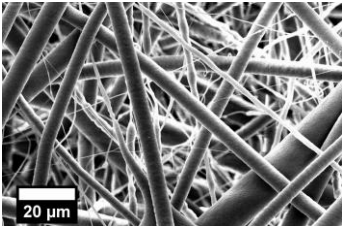
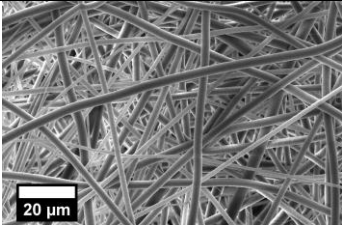
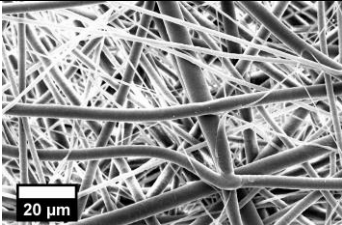
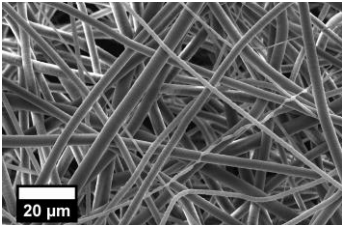
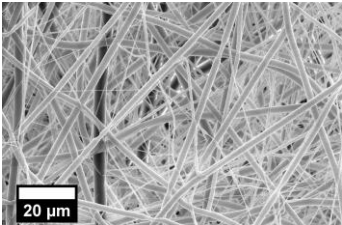
14wt% Chloroform/Ethanol (9:1)

Applied Voltage (kV)	Collector Distance (cm)	Flow Rate (ml/hr)	
		6	12
		15	
20			
20	15		Liquid Polymer
	20		

14wt% Chloroform/Ethanol (7:3)

Applied Voltage (kV)	Collector Distance (cm)	Flow Rate (ml/hr)	
		6	12
		15	
20			
20	15		
	20		

14wt% Chloroform/Methanol (9:1)

Applied Voltage (kV)	Collector Distance (cm)	Flow Rate (ml/hr)	
		6	12
		15	
20			
20	15		
	20		

14wt% Chloroform/Methanol (7:3)

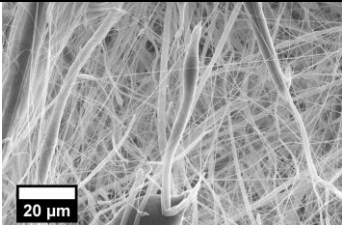
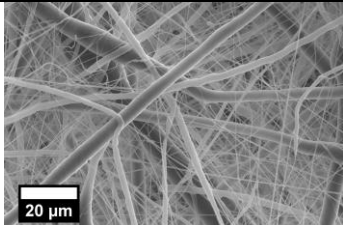
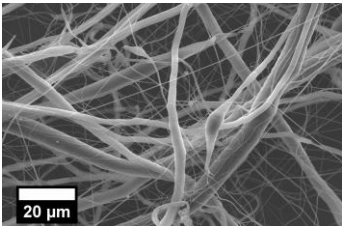
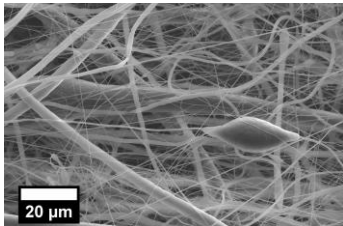
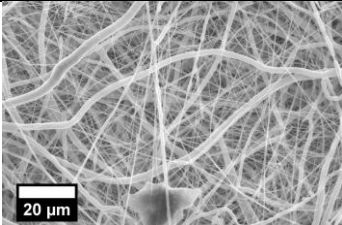
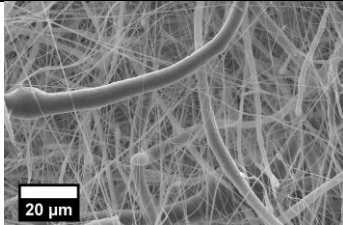
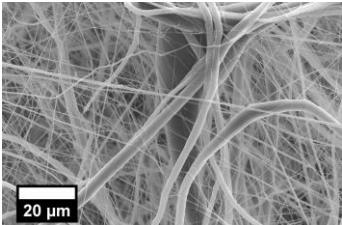
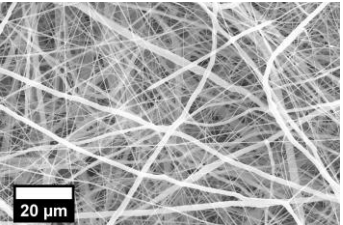
Applied Voltage (kV)	Collector Distance (cm)	Flow Rate (ml/hr)	
		6	12
		15	20
20	15		
			
	20		
			

Table A.0.2: Fibre diameter results for micron and multimodal solution screening trial. Results presented as average \pm standard deviation

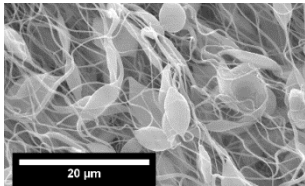
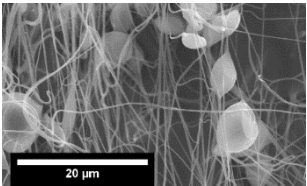
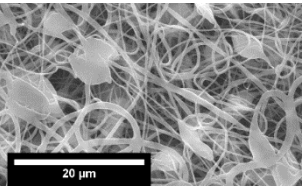
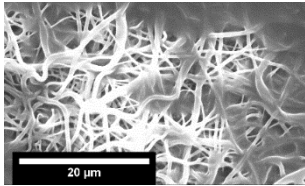
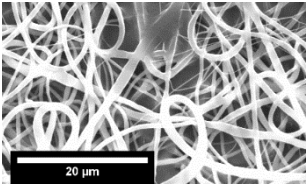
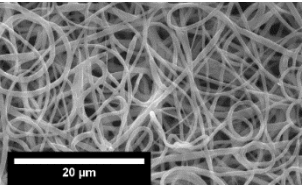
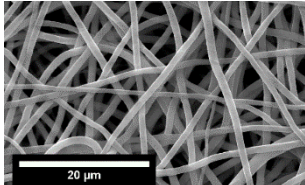
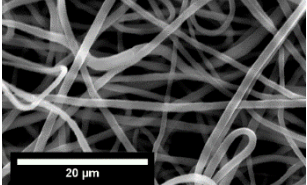
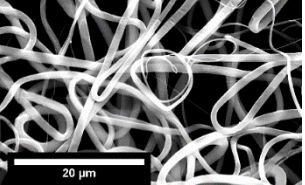
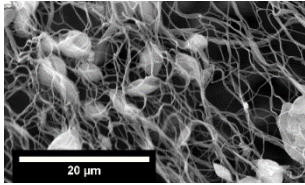
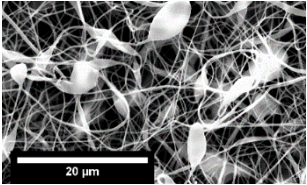
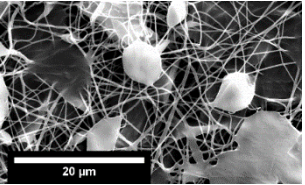
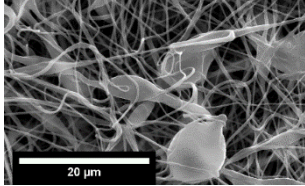
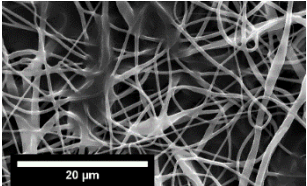
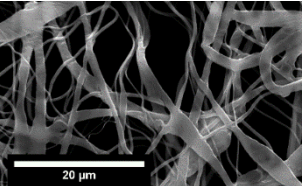
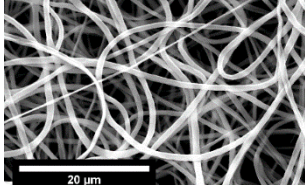
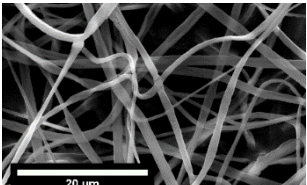
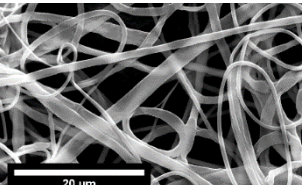
Applied Voltage (kV)	Collector Distance (cm)	Chloroform		Chloroform Ethanol (9:1)		Chloroform/Ethanol (7:3)		Chloroform/Methanol (9:1)		Chloroform/Methanol (7:3)	
		Flow Rate (ml/hr)									
		6	12	6	12	6	12	6	12	6	12
		Fibre Diameters (μm)									
15	15	-	-	5.22 \pm 1.57	-	2.24 \pm 1.56	1.9 \pm 1.55	2.10 \pm 1.17	1.97 \pm 1.09	0.76 \pm 0.9	2.74 \pm 2.33
	20	8.60 \pm 0.71	7.87 \pm 1.51	7.81 \pm 2.56	4.55 \pm 1.24	1.56 \pm 1.3	-	5.06 \pm 0.86	4.33 \pm 2.81	2.02 \pm 1.77	1.81 \pm 1.66
20	15	-	-	-	-	0.95 \pm 0.49	2.0 \pm 1.37	2.35 \pm 0.9	2.79 \pm 1.6	1.55 \pm 0.84	2.06 \pm 2.07
	20	9.01 \pm 1.3	9.51 \pm 1.3	8.3 \pm 1.4	5.24 \pm 2.58	1.54 \pm 0.88	1.9 \pm 1.0	2.94 \pm 0.99	2.15 \pm 0.73	1.73 \pm 1.16	1.26 \pm 0.755

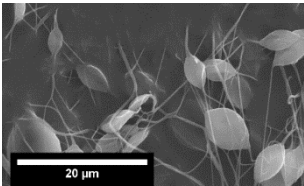
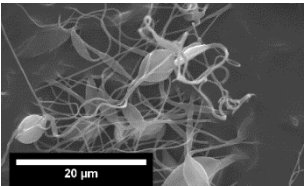
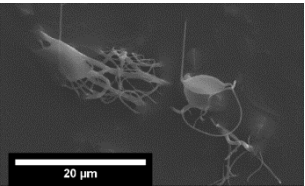
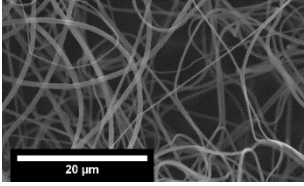
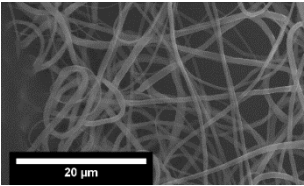
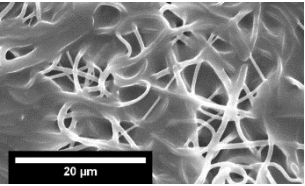
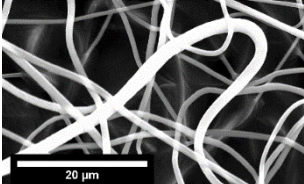
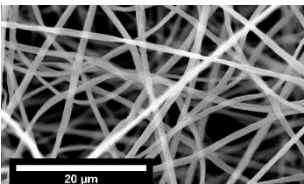
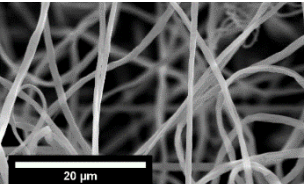
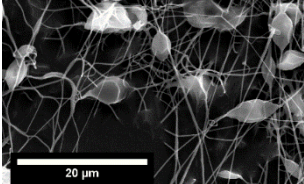
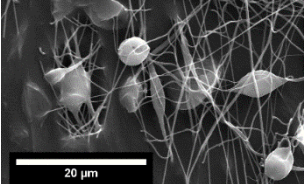
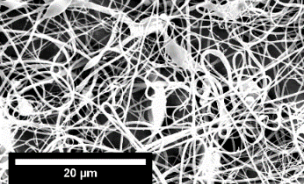
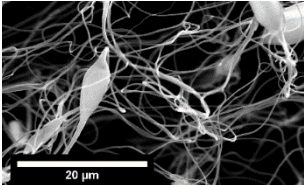
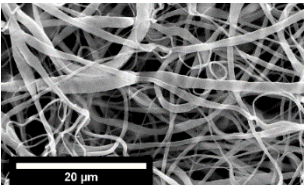
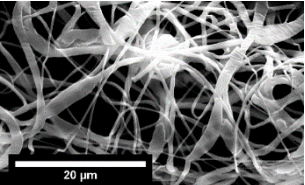
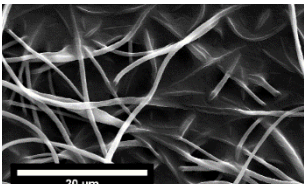
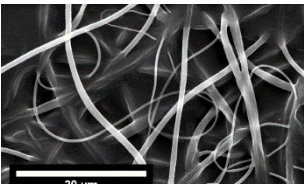
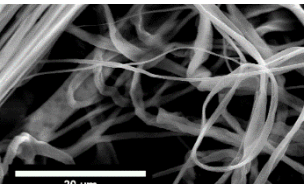
Table A.0.3: Ambient spinning conditions and airflow measurements recorded during solution screening trial

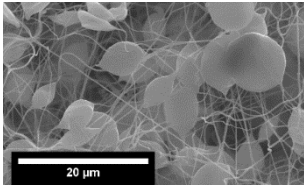
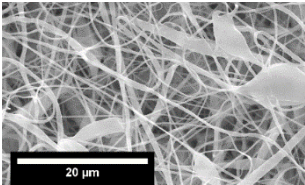
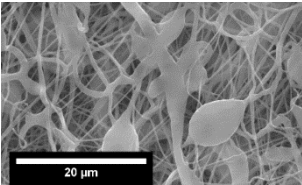
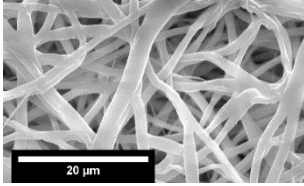
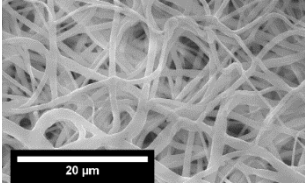
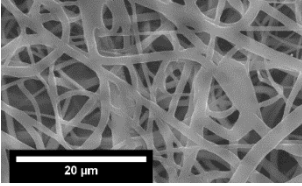
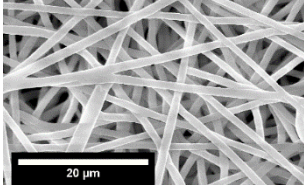
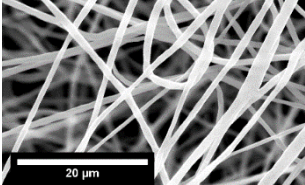
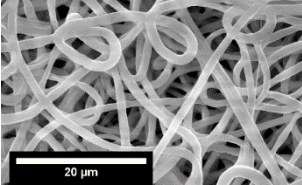
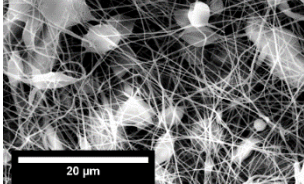
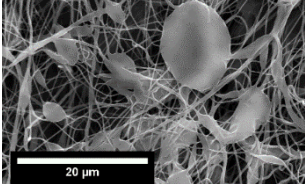
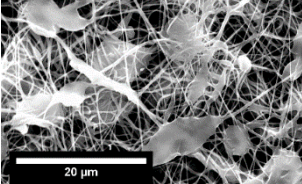
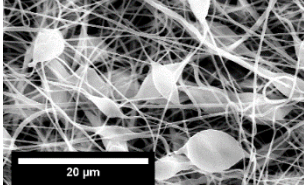
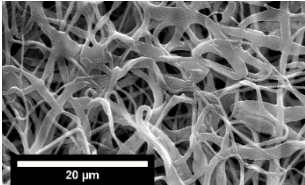
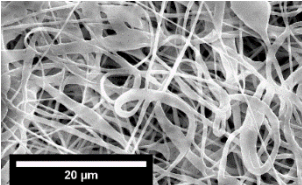
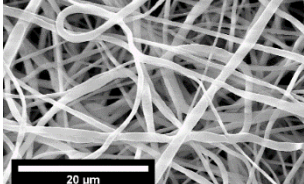
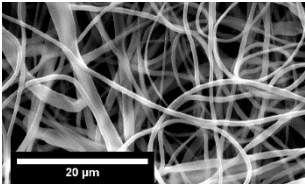
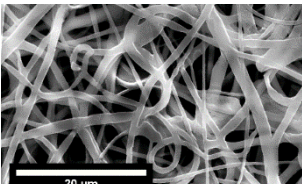
Measured Parameter	Maximum	Minimum	Avg. \pm S.D.
Relative Humidity (RH%)	59.7	43.8	44.6 \pm 9.2
Temperature ($^{\circ}\text{C}$)	22.6	19.1	20.8 \pm 0.8
Air Speed at Spinneret Tip (m/s)	0.67	0.31	0.53 \pm 0.12
Air Speed at Collector Surface at 15cm (m/s)	0.14	0.08	0.11 \pm 0.02
Air Speed at Collector Surface at 25cm (m/s)	0.13	0	0.12 \pm 0.6

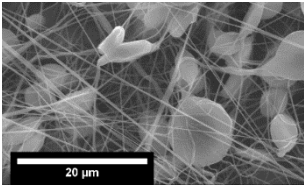
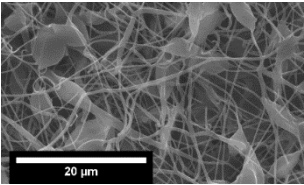
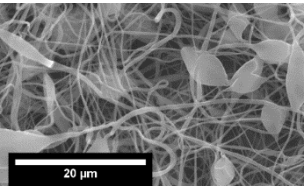
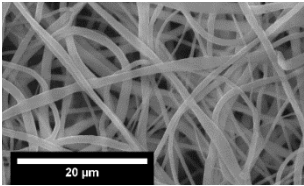
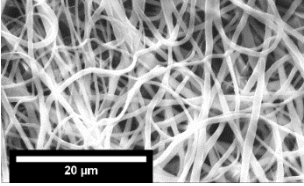
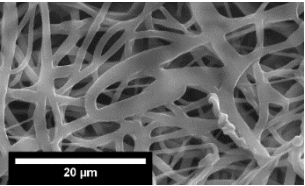
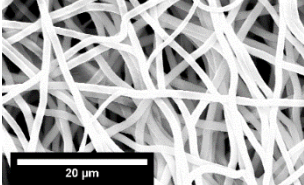
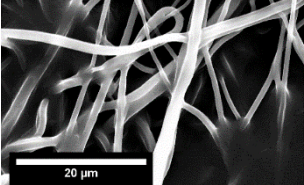
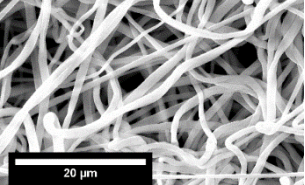
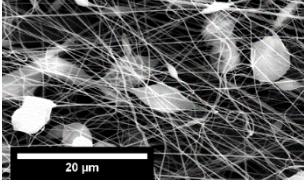
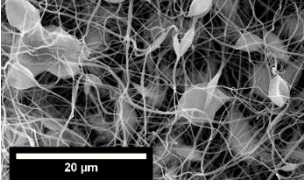
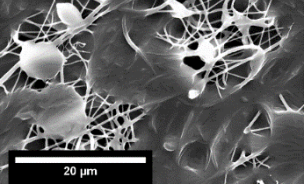
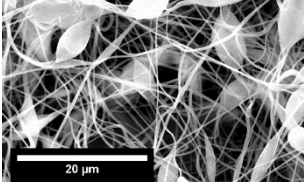
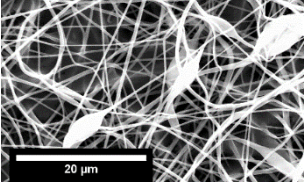
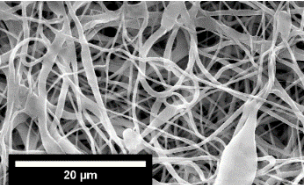
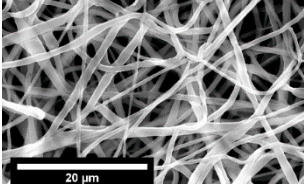
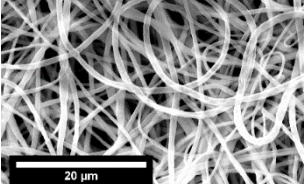
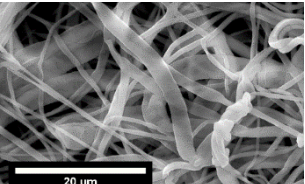
Table A.0.4: SEM results of solution screening trial for nanofibre solution screening

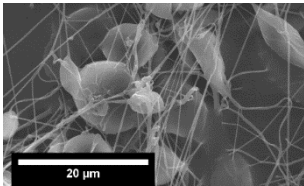
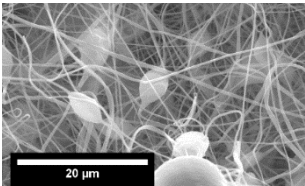
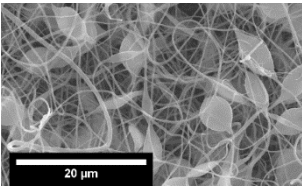
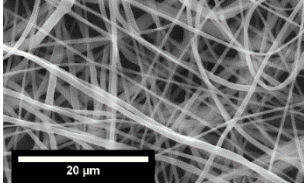
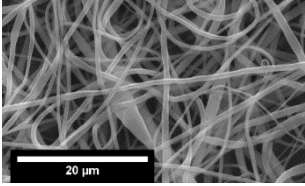
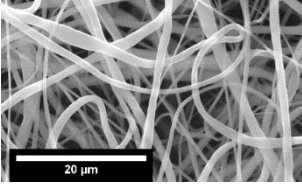
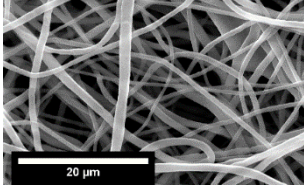
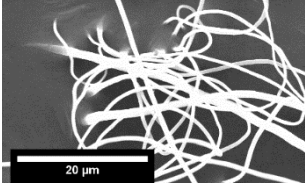
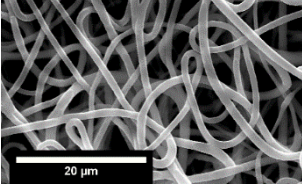
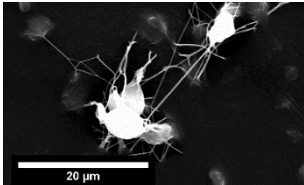
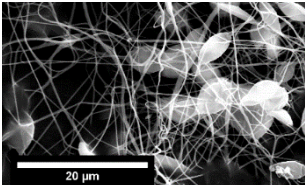
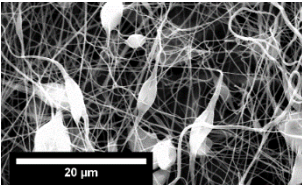
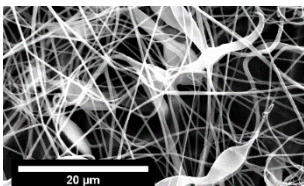
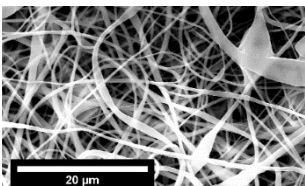
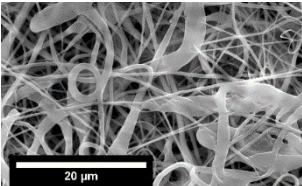
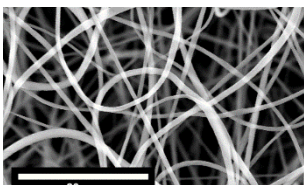
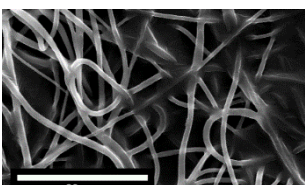
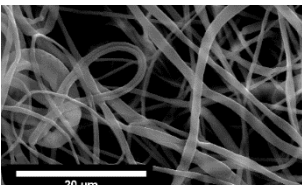
		0.25 ml/hr		
Dist. (cm)	10kV	15kV	20kV	
10	Chloroform/DMF (7:3)			
		<i>6wt%</i>	<i>6wt%</i>	<i>6wt%</i>
		<i>8wt%</i>	<i>8wt%</i>	<i>8wt%</i>
		<i>11wt%</i>	<i>11wt%</i>	<i>11wt%</i>
	Chloroform/DMF (1:1)			
		<i>6wt%</i>	<i>6wt%</i>	<i>6wt%</i>
		<i>8wt%</i>	<i>8wt%</i>	<i>8wt%</i>
	<i>11wt%</i>	<i>11wt%</i>	<i>11wt%</i>	

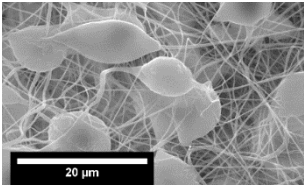
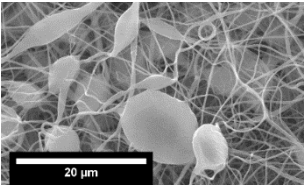
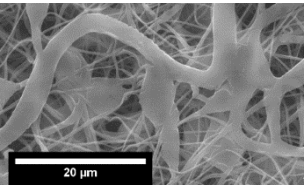
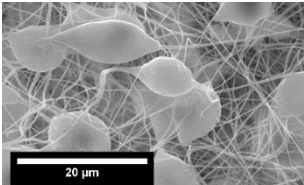
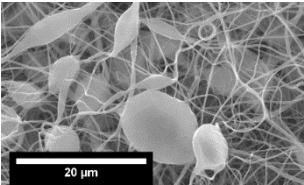
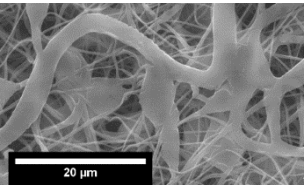
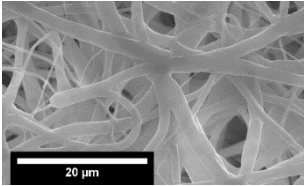
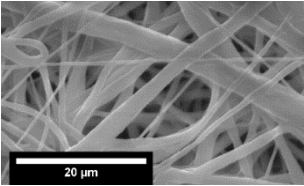
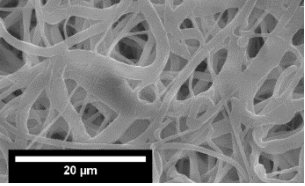
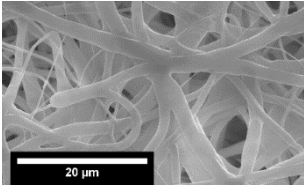
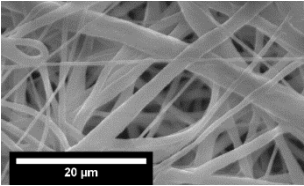
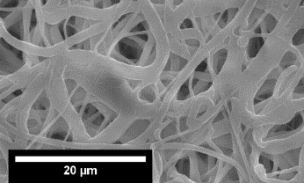
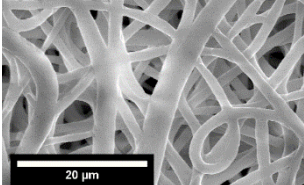
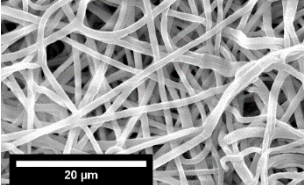
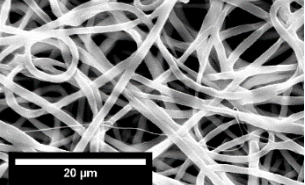
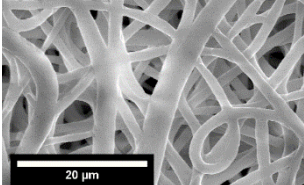
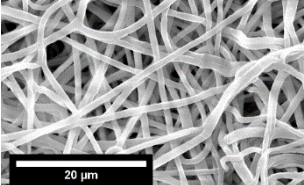
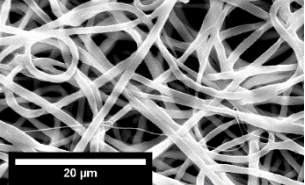
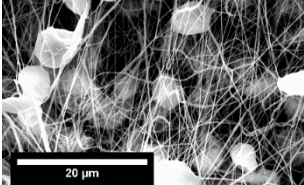
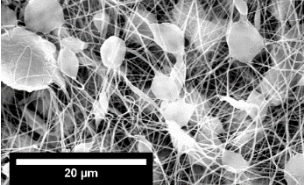
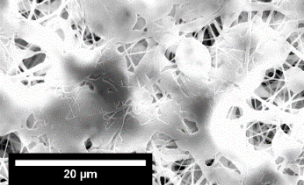
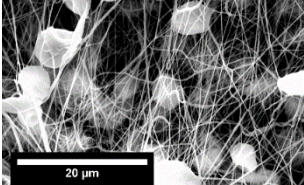
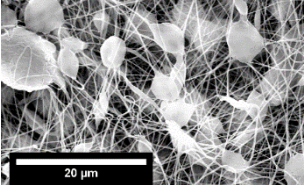
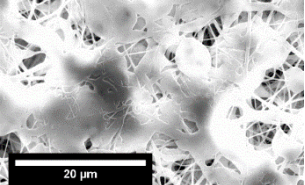
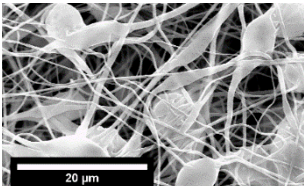
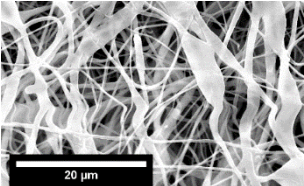
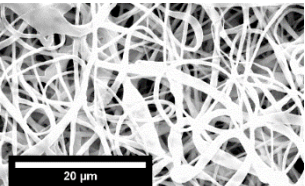
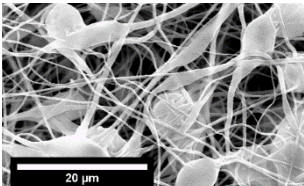
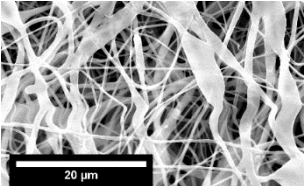
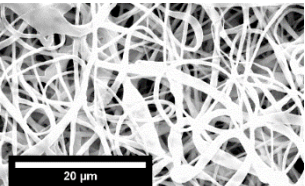
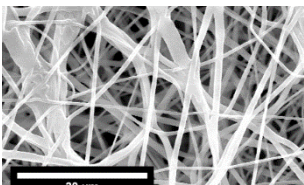
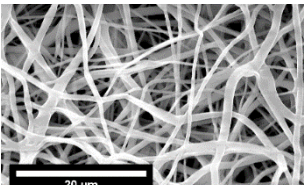
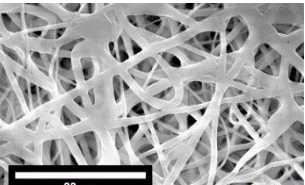
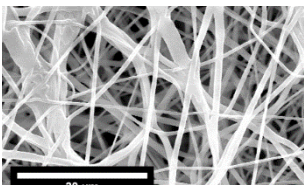
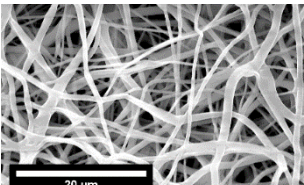
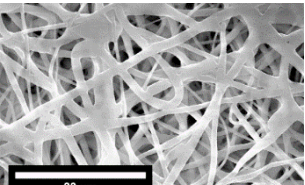
0.25 ml/hr			
Dist. (cm)	10kV	15kV	20kV
12.5	Chloroform/DMF (7:3)		
	<i>6wt%</i>	<i>6wt%</i>	<i>6wt%</i>
			
	<i>8wt%</i>	<i>8wt%</i>	<i>8wt%</i>
			
	<i>11wt%</i>	<i>11wt%</i>	<i>11wt%</i>
			
	Chloroform/DMF (1:1)		
	<i>6wt%</i>	<i>6wt%</i>	<i>6wt%</i>
			
	<i>8wt%</i>	<i>8wt%</i>	<i>8wt%</i>
			
<i>11wt%</i>	<i>11wt%</i>	<i>11wt%</i>	
			

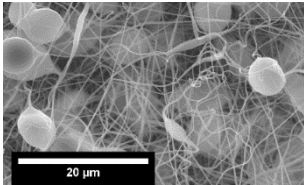
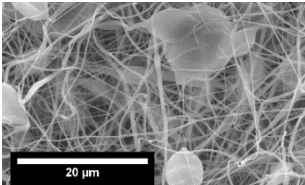
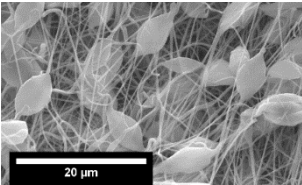
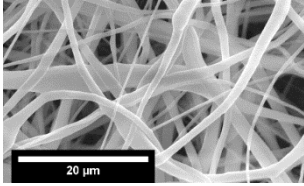
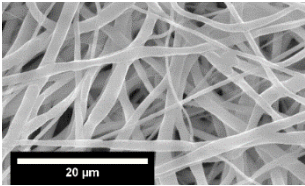
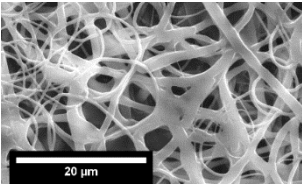
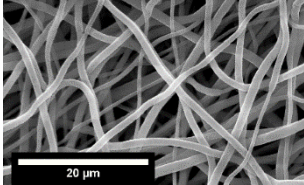
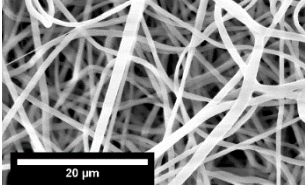
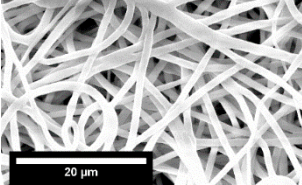
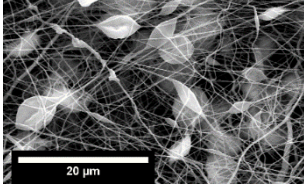
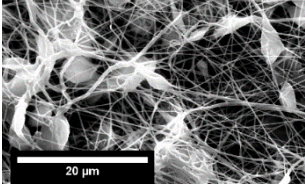
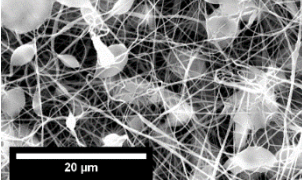
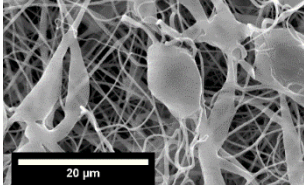
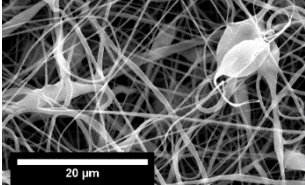
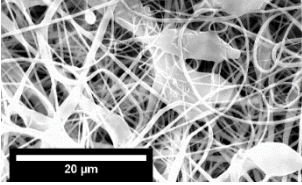
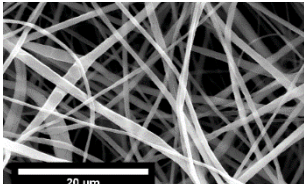
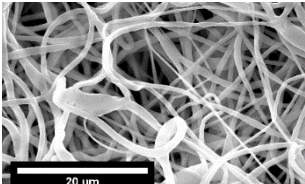
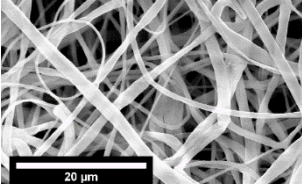
0.25 ml/hr			
Dist. (cm)	10kV	15kV	20kV
15	Chloroform/DMF (7:3)		
	<i>6wt%</i>	<i>6wt%</i>	<i>6wt%</i>
			
	<i>8wt%</i>	<i>8wt%</i>	<i>8wt%</i>
			
	<i>11wt%</i>	<i>11wt%</i>	<i>11wt%</i>
			
	Chloroform/DMF (1:1)		
	<i>6wt%</i>	<i>6wt%</i>	<i>6wt%</i>
			
	<i>8wt%</i>	<i>8wt%</i>	<i>8wt%</i>
			
	<i>11wt%</i>	<i>11wt%</i>	<i>11wt%</i>
			

0.5 ml/hr			
Dist. (cm)	10kV	15kV	20kV
10	Chloroform/DMF (7:3)		
	<i>6wt%</i>	<i>6wt%</i>	<i>6wt%</i>
			
	<i>8wt%</i>	<i>8wt%</i>	<i>8wt%</i>
			
	<i>11wt%</i>	<i>11wt%</i>	<i>11wt%</i>
			
	Chloroform/DMF (5:5)		
	<i>6wt%</i>	<i>6wt%</i>	<i>6wt%</i>
			
	<i>8wt%</i>	<i>8wt%</i>	<i>8wt%</i>
			
	<i>11wt%</i>	<i>11wt%</i>	<i>11wt%</i>
			

0.5 ml/hr				
Dist. (cm)	10kV	15kV	20kV	
12.5	Chloroform/DMF (7:3)			
	<i>6wt%</i>	<i>6wt%</i>	<i>6wt%</i>	
				
	<i>8wt%</i>	<i>8wt%</i>	<i>8wt%</i>	
				
	<i>11wt%</i>	<i>11wt%</i>	<i>11wt%</i>	
				
	Chloroform/DMF (5:5)			
	<i>6wt%</i>	<i>6wt%</i>	<i>6wt%</i>	
				
	<i>8wt%</i>	<i>8wt%</i>	<i>8wt%</i>	
				
	<i>11wt%</i>	<i>11wt%</i>	<i>11wt%</i>	
				

		0.5 ml/hr		
Dist. (cm)		10kV	15kV	20kV
15	Chloroform/DMF (7:3)			
		<i>6wt%</i>	<i>6wt%</i>	<i>6wt%</i>
				
		<i>8wt%</i>	<i>8wt%</i>	<i>8wt%</i>
				
		<i>11wt%</i>	<i>11wt%</i>	<i>11wt%</i>
				
	Chloroform/DMF (5:5)			
		<i>6wt%</i>	<i>6wt%</i>	<i>6wt%</i>
				
		<i>8wt%</i>	<i>8wt%</i>	<i>8wt%</i>
				
	<i>11wt%</i>	<i>11wt%</i>	<i>11wt%</i>	
				

				1 ml/hr		
Dist. (cm)	10kV	15kV	20kV			
10	Chloroform/DMF (7:3)					
	<i>6wt%</i>		<i>6wt%</i>		<i>6wt%</i>	
						
	<i>8wt%</i>		<i>8wt%</i>		<i>8wt%</i>	
						
	<i>11wt%</i>		<i>11wt%</i>		<i>11wt%</i>	
						
	Chloroform/DMF (5:5)					
	<i>6wt%</i>		<i>6wt%</i>		<i>6wt%</i>	
						
	<i>8wt%</i>		<i>8wt%</i>		<i>8wt%</i>	
						
	<i>11wt%</i>		<i>11wt%</i>		<i>11wt%</i>	
						

				1 ml/hr		
Dist. (cm)	10kV	15kV	20kV			
12.5	Chloroform/DMF (7:3)					
	<i>6wt%</i>	<i>6wt%</i>	<i>6wt%</i>			
	<i>8wt%</i>	<i>8wt%</i>	<i>8wt%</i>			
	<i>11wt%</i>	<i>11wt%</i>	<i>11wt%</i>			
	Chloroform/DMF (5:5)					
	<i>6wt%</i>	<i>6wt%</i>	<i>6wt%</i>			
	<i>8wt%</i>	<i>8wt%</i>	<i>8wt%</i>			
	<i>11wt%</i>	<i>11wt%</i>	<i>11wt%</i>			

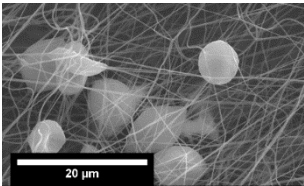
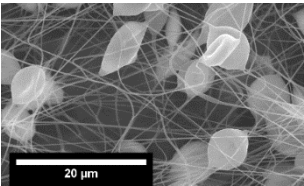
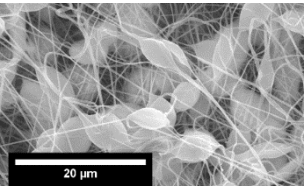
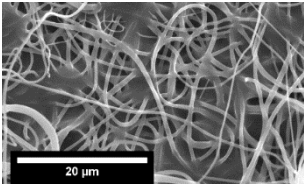
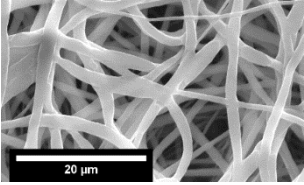
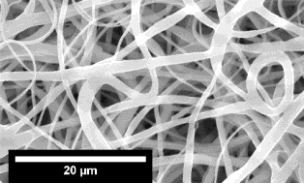
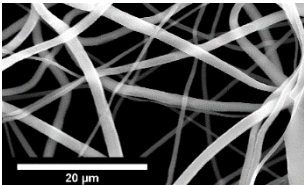
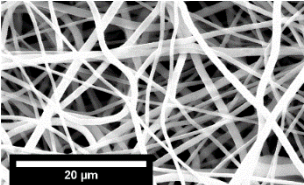
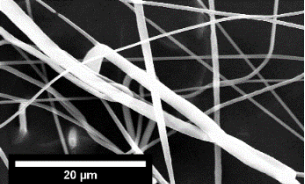
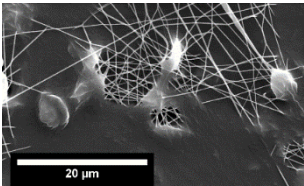
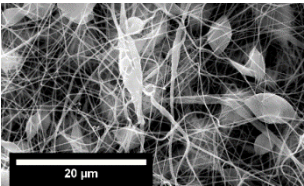
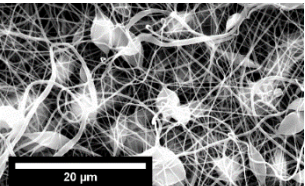
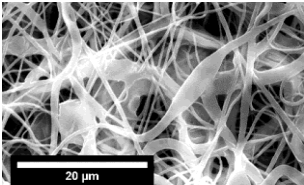
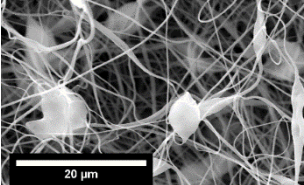
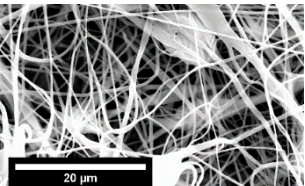
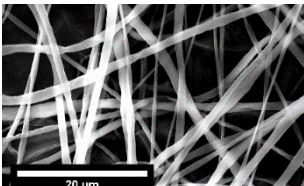
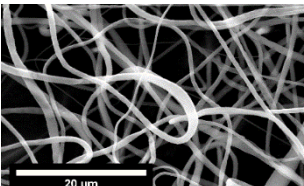
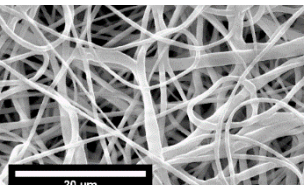
		1 ml/hr		
Dist. (cm)		10kV	15kV	20kV
15	Chloroform/DMF (7:3)			
		<i>6wt%</i>	<i>6wt%</i>	<i>6wt%</i>
				
		<i>8wt%</i>	<i>8wt%</i>	<i>8wt%</i>
				
		<i>11wt%</i>	<i>11wt%</i>	<i>11wt%</i>
				
	Chloroform/DMF (5:5)			
		<i>6wt%</i>	<i>6wt%</i>	<i>6wt%</i>
				
		<i>8wt%</i>	<i>8wt%</i>	<i>8wt%</i>
				
	<i>11wt%</i>	<i>11wt%</i>	<i>11wt%</i>	
				

Table A.0.5: Fibre diameter results for nanofibre spinning solution screening trial. Results presented as average \pm standard deviation

Polymer Concentration - 6wt%										
Applied Voltage	10kV			15kV			20kV			
Collector Distance	10cm	12.5cm	15cm	10cm	12.5cm	15cm	10cm	12.5cm	15cm	
Fibre Diameters (μm)	0.25ml/hr									
	Chloroform/DMF (7:3)									
	-	-	-	-	-	-	-	-	-	-
	Chloroform/DMF (1:1)									
	-	-	-	-	-	-	-	-	-	-
	0.5 ml/hr									
	Chloroform/DMF (7:3)									
	-	-	-	-	-	-	-	-	-	-
	Chloroform/DMF (1:1)									
	-	-	-	-	-	-	-	-	-	-
	1 ml/hr									
	Chloroform/DMF (7:3)									
-	-	-	-	-	-	-	-	-	-	
Chloroform/DMF (1:1)										
-	-	-	-	-	-	-	-	-	-	

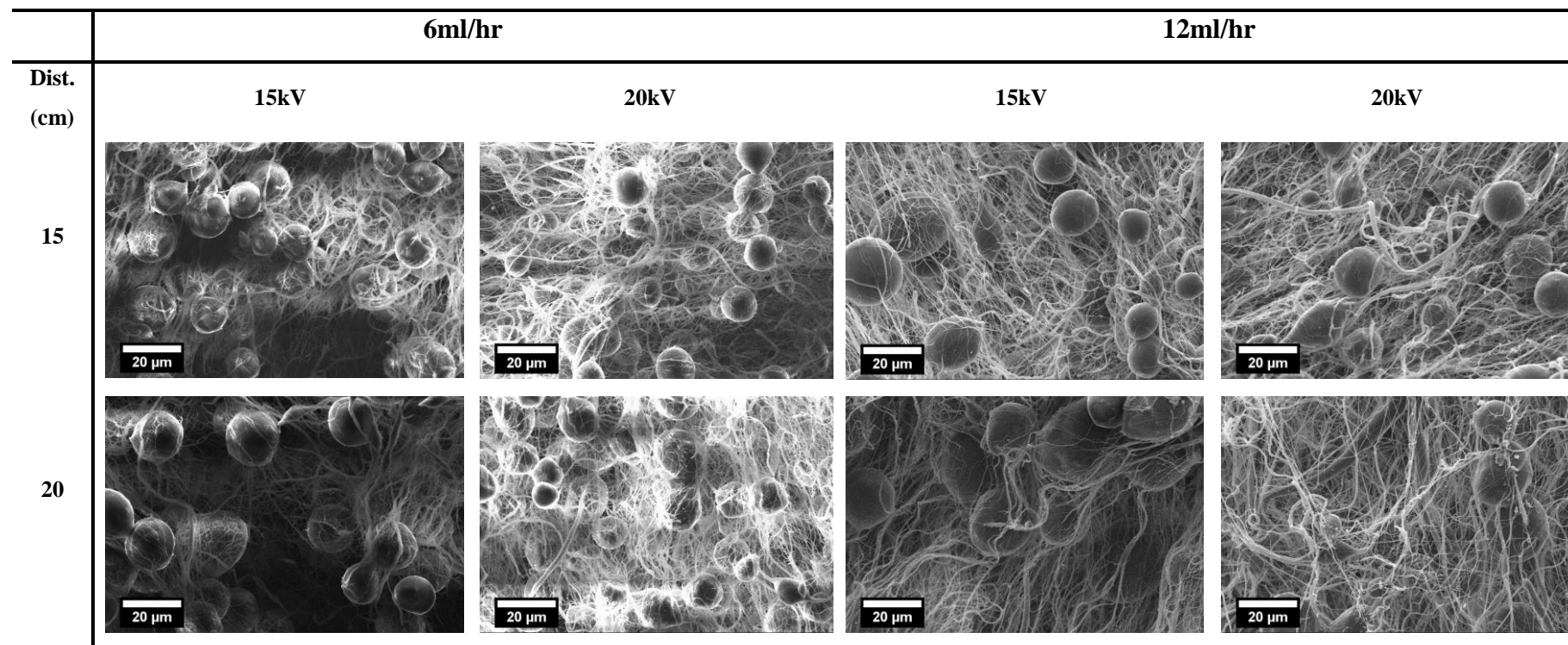
Polymer Concentration - 8wt%									
Applied Voltage	10kV			15kV			20kV		
Collector Distance	10cm	12.5cm	15cm	10cm	12.5cm	15cm	10cm	12.5cm	15cm
Fibre Diameters (μm)	0.25ml/hr								
	Chloroform/DMF (7:3)								
	1.21 \pm 0.58	0.68 \pm 0.34	0.50 \pm 0.18	0.74 \pm 0.45	0.83 \pm 0.43	0.78 \pm 0.31	0.89 \pm 0.38	0.62 \pm 0.20	0.60 \pm 0.22
	Chloroform/DMF (1:1)								
	-	-	-	-	-	-	-	-	-
	0.5 ml/hr								
	Chloroform/DMF (7:3)								
	1.34 \pm 0.63	0.88 \pm 0.41	0.69 \pm 0.36	0.95 \pm 0.61	0.65 \pm 0.29	0.86 \pm 0.66	1.30 \pm 0.84	1.21 \pm 0.63	1.04 \pm 0.58
	Chloroform/DMF (1:1)								
	-	-	-	-	-	-	-	-	-
	1 ml/hr								
	Chloroform/DMF (7:3)								
1.46 \pm 0.88	1.13 \pm 0.59	0.63 \pm 0.29	1.26 \pm 0.71	1.22 \pm 0.59	1.6 \pm 0.59	1.39 \pm 0.98	0.93 \pm 0.45	0.97 \pm 0.53	
-	-	-	-	-	-	-	-	-	

Polymer Concentration - 11wt%									
Applied Voltage	10kV			15kV			20kV		
Collector Distance	10cm	12.5cm	15cm	10cm	12.5cm	15cm	10cm	12.5cm	15cm
Fibre Diameters (μm)	0.25ml/hr								
	Chloroform/DMF (7:3)								
	0.93 \pm 0.26	0.99 \pm 0.22	1.01 \pm 0.31	0.81 \pm 0.45	1.07 \pm 0.3	0.85 \pm 0.17	1.14 \pm 0.43	1.12 \pm 0.29	1.17 \pm 0.31
	Chloroform/DMF (1:1)								
	0.80 \pm 0.31	0.80 \pm 0.16	0.77 \pm 0.35	1.15 \pm 0.56	0.99 \pm 0.37	0.68 \pm 0.36	1.23 \pm 0.73	1.22 \pm 0.67	2.04 \pm 2.03
	0.5 ml/hr								
	Chloroform/DMF (7:3)								
	1.16 \pm 0.14	1.08 \pm 0.17	0.87 \pm 0.3	0.96 \pm 0.31	1.25 \pm 0.48	0.65 \pm 0.2	1.18 \pm 0.38	1.04 \pm 0.39	1.01 \pm 0.24
	Chloroform/DMF (1:1)								
	0.93 \pm 0.47	0.87 \pm 0.28	0.81 \pm 0.29	0.79 \pm 0.44	0.86 \pm 0.3	0.76 \pm 0.28	0.95 \pm 0.47	1.35 \pm 0.58	1.06 \pm 0.60
1 ml/hr									
Chloroform/DMF (7:3)									
1.83 \pm 0.81	0.96 \pm 0.29	1.54 \pm 1.21	0.93 \pm 0.21	0.95 \pm 0.41	0.82 \pm 0.31	1.13 \pm 0.30	1.05 \pm 0.23	0.83 \pm 0.48	
Chloroform/DMF (1:1)									
0.97 \pm 0.78	0.94 \pm 0.48	0.94 \pm 0.45	0.85 \pm 0.33	1.30 \pm 0.70	0.82 \pm 0.49	1.49 \pm 0.51	1.14 \pm 0.55	0.97 \pm 0.47	

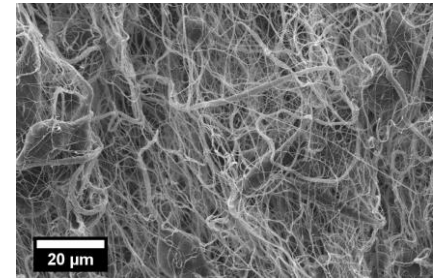
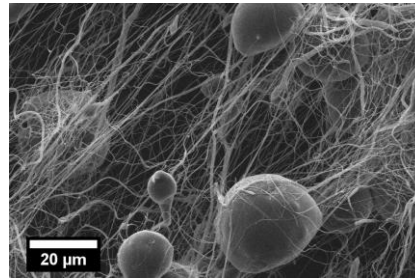
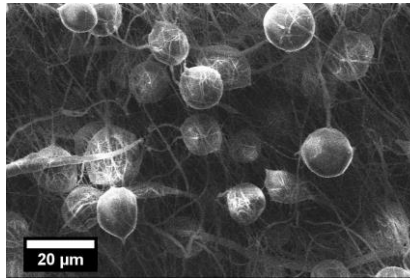
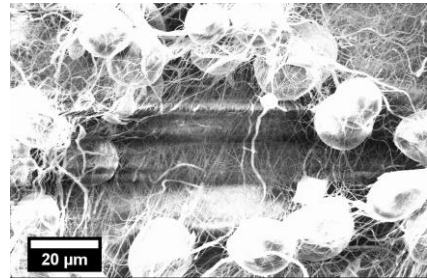
Appendix B: Complete Results of Multimodal Fibre Spinning - Solution Concentration Study

Table B.0.1: SEM results of multimodal polymer concentration trial showing sample created over a polymer concentration range of 10-18wt%, flow rate range of 6 and 12ml/hr, applied voltage of 15 and 20kV, and collector distance of 15 to 20cm

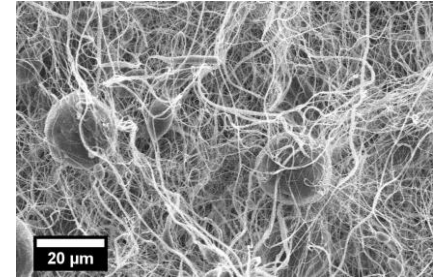
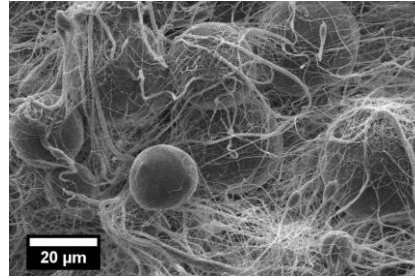
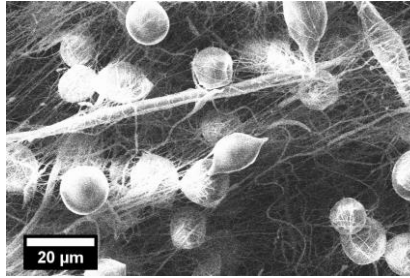
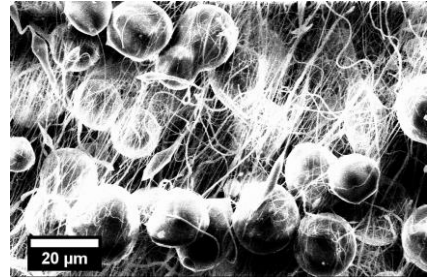
Solution – 10wt% Chloroform/Ethanol (7:3; v:v)



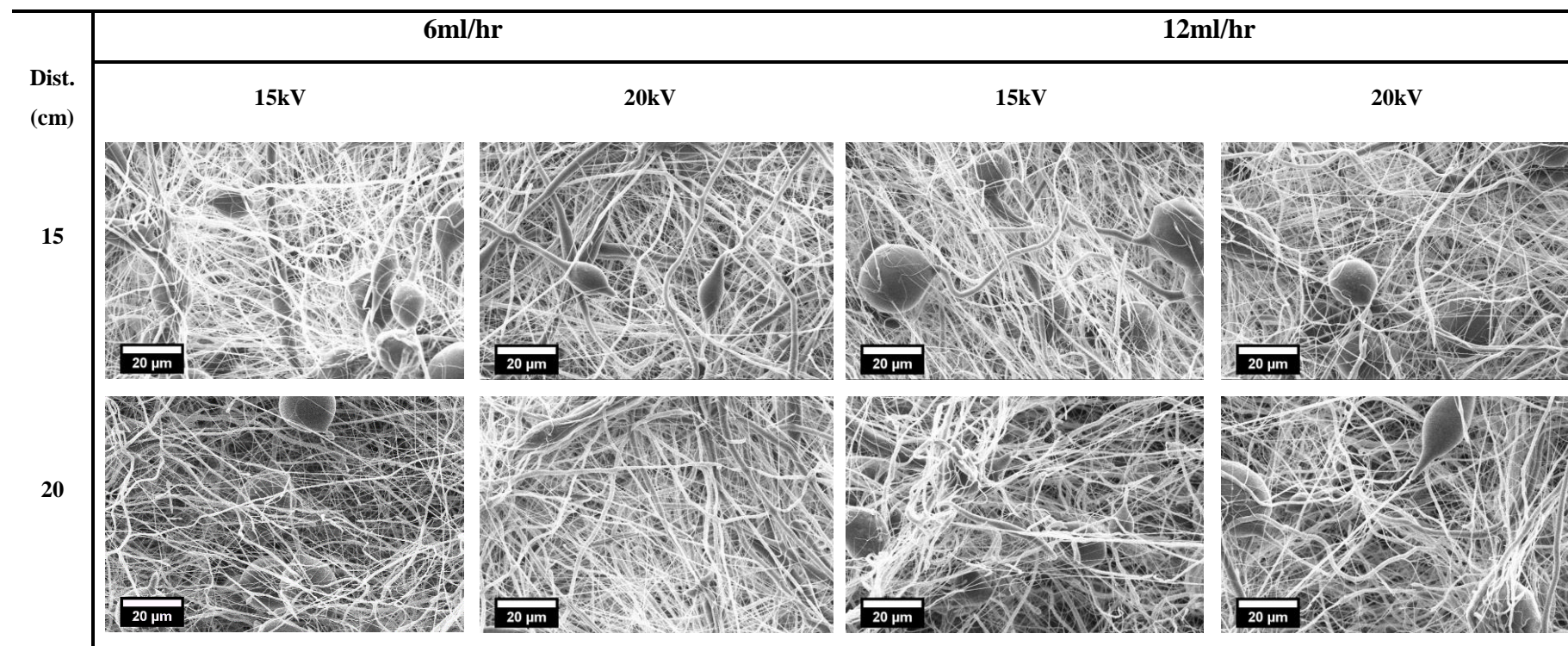
25



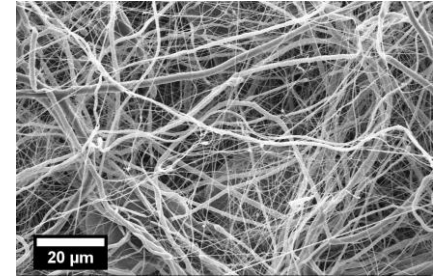
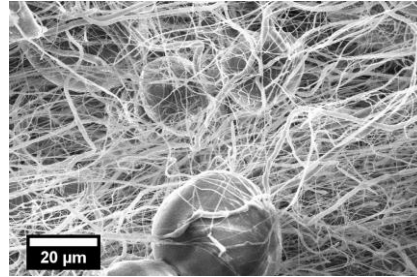
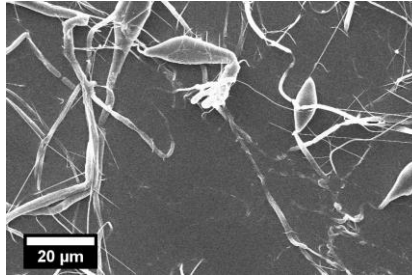
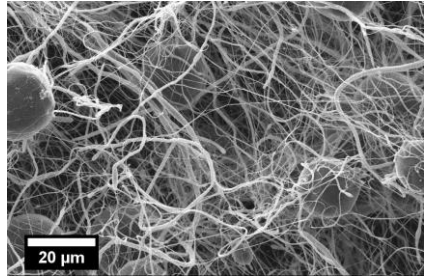
30



Solution – 12wt% Chloroform/Ethanol (7:3; v:v)



25



30

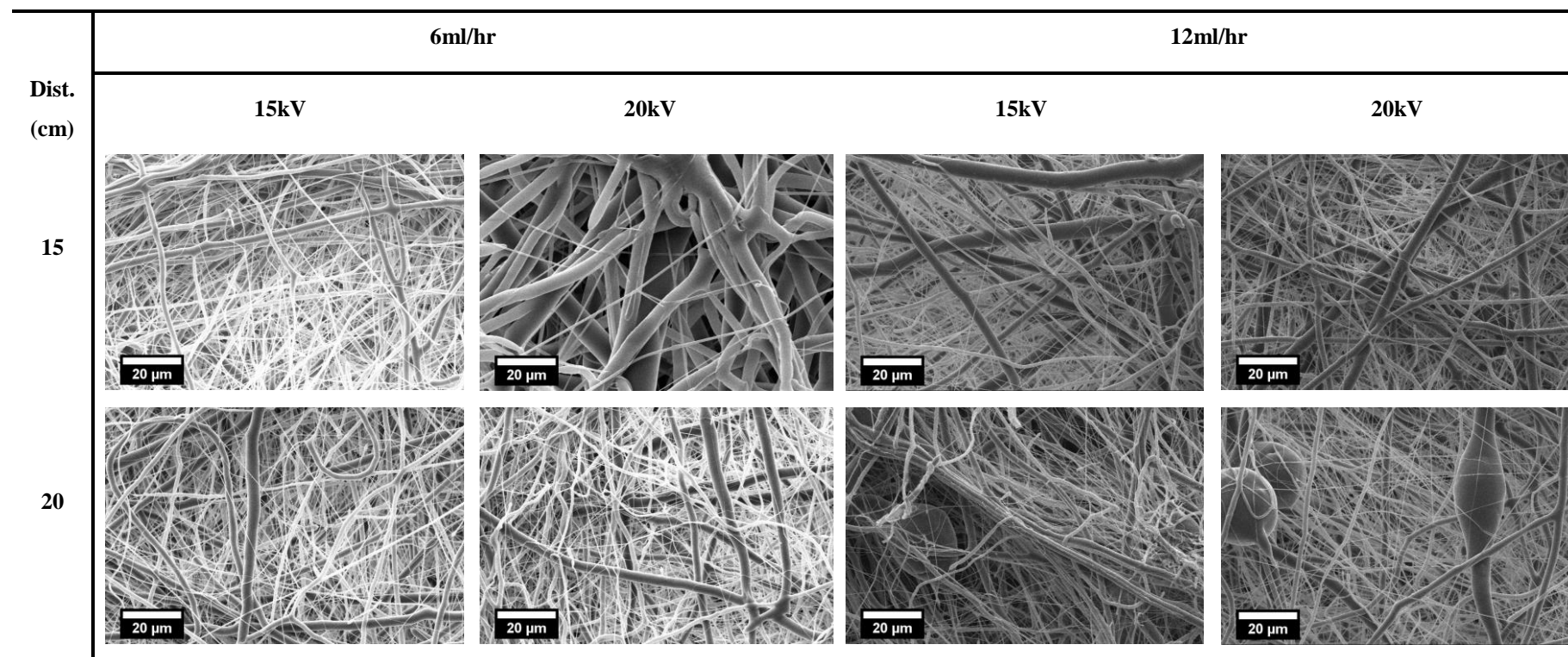
No sample collected

No sample collected

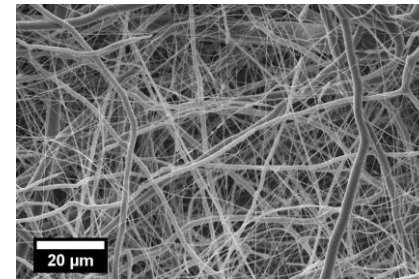
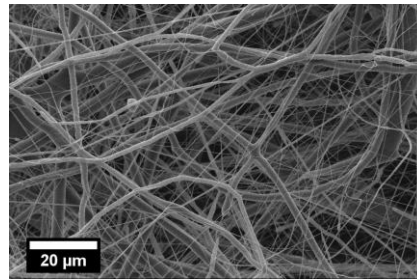
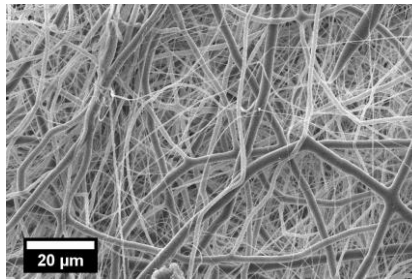
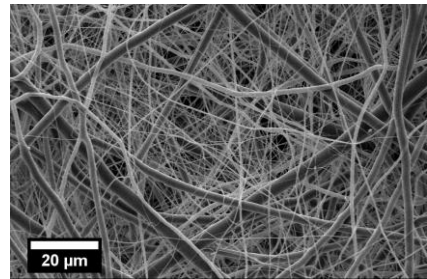
No sample collected

No sample collected

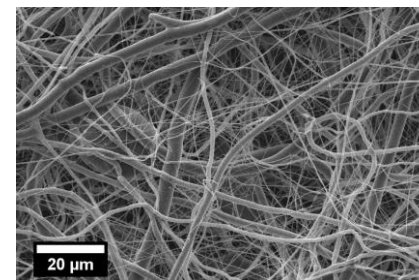
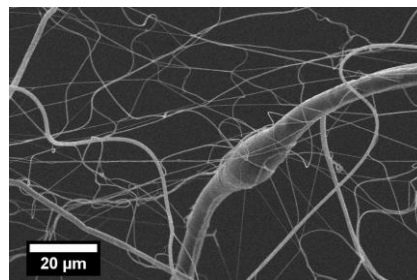
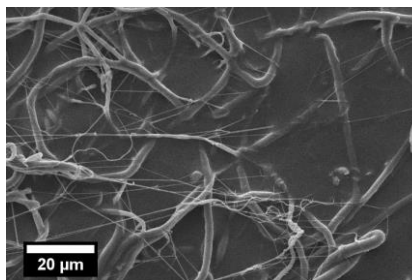
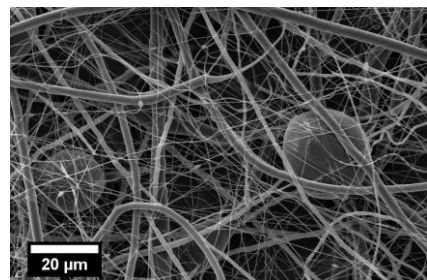
Solution – 14wt% Chloroform/Ethanol (7:3; v:v)



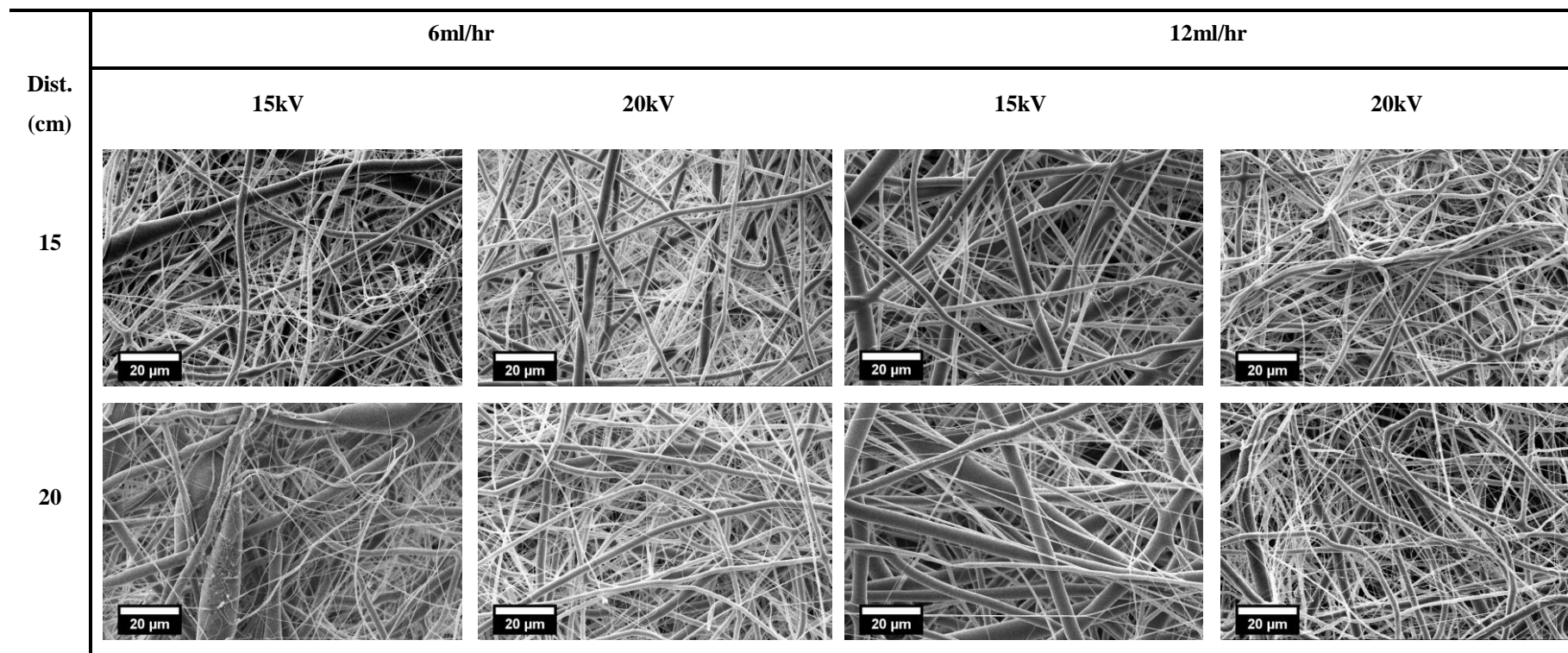
25

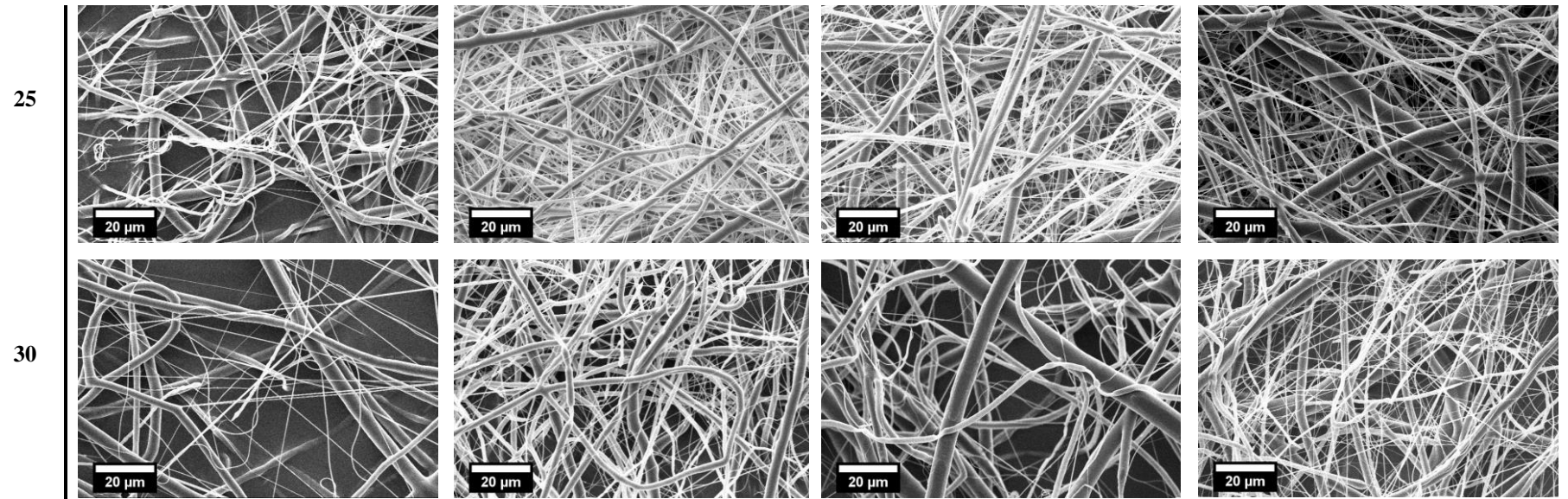


30

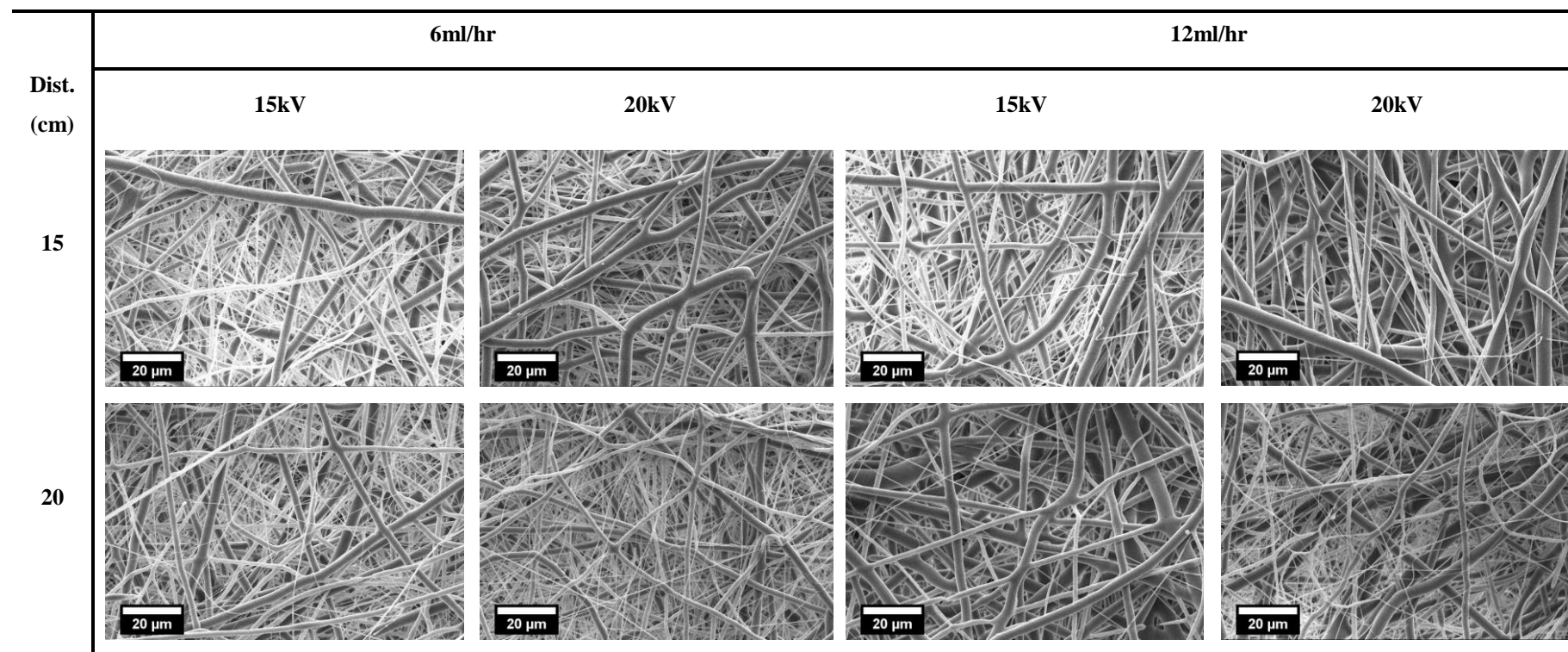


Solution – 16wt% Chloroform/Ethanol (7:3; v:v)

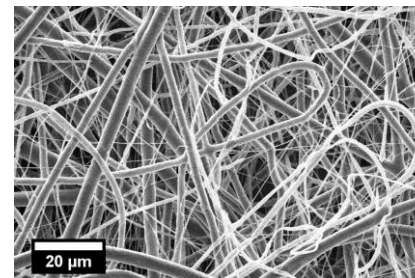
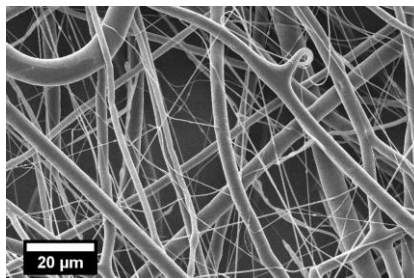
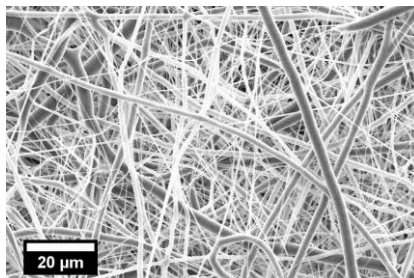
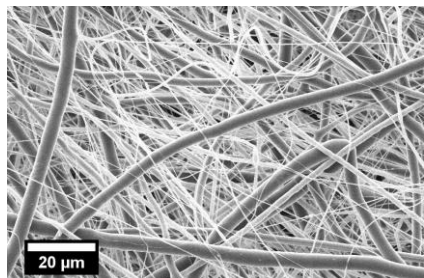




Solution – 18wt% Chloroform/Ethanol (7:3; v:v)



25



30

No sample collected

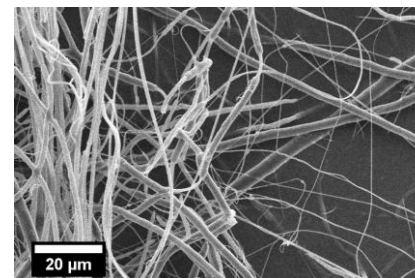
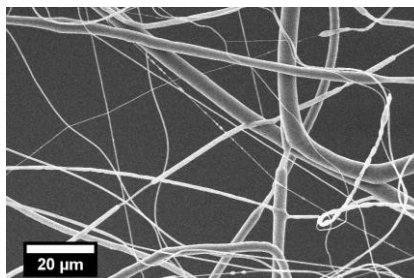
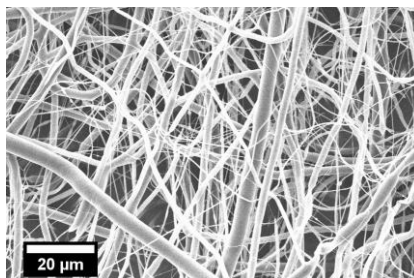


Table B.0.2: Fibre diameter results for multimodal fibre spinning – polymer concentration study. Results

		10wt% PCL Chloroform/Ethanol (7:3)		12wt% PCL Chloroform/Ethanol (7:3)		14wt% PCL Chloroform/Ethanol (7:3)		16wt% PCL Chloroform/Ethanol (7:3)		18wt% PCL Chloroform/Ethanol (7:3)	
		Flow Rate (ml/hr)									
Applied Voltage (kV)	Collector Distance (cm)	6	12	6	12	6	12	6	12	6	12
		Fibre Diameters (μm)									
15	15	-	-	-	-	0.86 \pm 0.65	1.38 \pm 1.28	1.28 \pm 1.01	1.30 \pm 0.97	1.48 \pm 1.02	1.57 \pm 1.23
	20	-	-	-	-	1.29 \pm 1.15	0.97 \pm 0.86	1.60 \pm 1.69	2.03 \pm 2.12	1.74 \pm 1.11	2.16 \pm 1.52
	25	-	-	-	-	0.92 \pm 1.10	0.97 \pm 1.00	0.97 \pm 1.01	1.32 \pm 1.21	1.48 \pm 1.09	1.40 \pm 1.76
	30	-	-	-	-	0.94 \pm 0.94	-	1.06 \pm 1.14	2.12 \pm 2.21	-	1.94 \pm 1.74
20	15	-	-	-	-	1.11 \pm 0.74	1.50 \pm 1.31	1.44 \pm 1.07	1.28 \pm 0.76	1.60 \pm 1.30	2.27 \pm 1.51
	20	-	-	-	-	0.91 \pm 1.54	1.41 \pm 1.07	1.41 \pm 0.96	1.45 \pm 1.23	1.33 \pm 1.03	1.84 \pm 1.81
	25	-	-	-	-	1.28 \pm 0.99	0.89 \pm 0.83	1.32 \pm 0.91	1.32 \pm 1.69	1.31 \pm 1.03	1.75 \pm 1.41
	30	-	-	-	-	1.31 \pm 0.89	1.10 \pm 1.11	1.38 \pm 1.00	1.43 \pm 2.19	1.33 \pm 1.23	1.29 \pm 1.146

Table B.0.3: Ambient spinning conditions and airflow measurements recorded during multimodal polymer concentration trial

<i>Measured Parameter</i>	<i>Maximum</i>	<i>Minimum</i>	<i>Avg. ± S.D.</i>
Relative Humidity (RH%)	48.4	40.4	42.3 ± 3.6
Temperature (°C)	21.3	19.6	20.2 ± 0.3
Air Speed at Spinneret Tip (m/s)	0.71	0.33	0.55 ± 0.4
Air Speed at Collector Surface at 15cm (m/s)	0.15	0.10	0.12 ± 0.1
Air Speed at Collector Surface at 25cm (m/s)	0.13	0.05	0.10 ± 0.2

Appendix C: Development of Uniaxial Ringlet Test Method

Introduction

ISO 7198 outlines a uniaxial tensile test method designed specifically for the testing of tubular cardiovascular prostheses. In this method tubular test specimens or ‘ringlets’, are placed on two small diameter pin grips. One pin grip is attached to a load cell and is capable of applying an extension load to the test specimen. A clear issue with this method is the inability to accurately determine the true start point of the test, from which the sample gauge length is determined and strain measurement commences. In principle, the true gauge length of the sample should occur when the walls of the tubular structure align parallel to the axis of loading and where no overall change in sample perimeter has occurred. This ensures that the subsequent strain measured translates to a direct deformation of the specimen, rather than a reconfiguration of its overall geometry. Traditional tensile test methods typically employ a preload in order to bring a test specimen into a desired configuration before measurements commence. This ensures that no slack is present within the sample allowing for an accurate assessment of strain to be achieved. Due to the varying wall thicknesses of specimens investigated within this study, no single pre-load value could be selected to ensure uniform and controlled reconfiguration of the vessel geometry. If the selected pre-load is too small, the vessel walls do not align with the axis of loading resulting in increased strain rates for small applied loads. This in turn results in increased strains observed before failure and an apparent reduction in Young’s modulus characteristics. If the applied pre-load is too large, the sample will begin to elongate before measurement commences, resulting in specimen failure at reduced strain levels.

In order to counteract the issue it was anticipated that by calculating the theoretical gauge length of the specimens based upon dimensions measured prior to testing, a retrospective corrective action could be made to account for this lack of wall alignment. By removing the observed strain up until the correct configuration point was achieved, a more accurate assessment of the specimen mechanics could be made.

The correct configuration point is determined to be the point at which the theoretical gauge length of the specimen was reached.

In order to verify this assessment, a video analysis was performed to correlate the stress vs strain profiles to the corresponding vessel geometry at key points within the loading cycle. Through this it could be determined if the concept of normalising strain to the theoretical gauge length provided an accurate starting point for future testing. To do this a video extensometer capable of capturing the extension profile of the samples was employed to provide a time course analysis of the testing cycle. This time course analysis allows for a direct link between the force and strain values observed to a corresponding still image showing vessel configuration.

Method

A mintron video extensometer capable of synchronisation to a Zwick tensile test machine was used to capture images of the specimens during testing (Figure C.0.1 (A)). In order to track specimen deformation during loading, small black marker beads were glue to the outer face of the ringlet specimens (Figure C.0.1 (B)). These marker beads allowed clear reference points to be observed during the testing cycle and allowed for the video extensometer to automatically track specimen deformation. This provided an alternative stress-strain response capture to that of the Zwick crosshead displacement system. It is however noted that the extensometer was only capable of distinguishing one axis of movement at a time i.e. it could only track the movement of a point in the x or y-axis during a test. Due to this, the extensometer was set to track the motion of the beads within the y-axis of testing (direction of grip separation). The specimens were then subjected to a pre-load of 0.1N, followed by testing to failure at a rate of 10 mm min⁻¹. Following this an excel file with corresponding data was generated and the time course video was separated into time stamped still images.

Analysis

Three stress-vs strain profiles were generated from the corresponding data measured. The first profile was based upon a gauge length value calculated at the point at which the pre-load was reached, labelled by the 'Gauge length at preload' within Figure C.0.2.

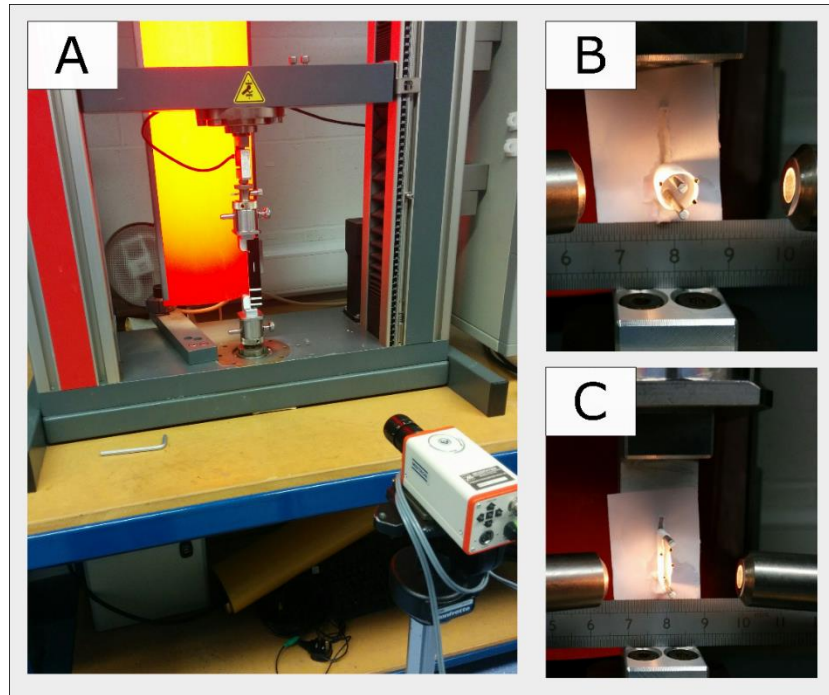


Figure C.0.1: Uniaxial ringlet testing of electrospun vessels using video extensometer tracking (A) Calibration of extensometer using tracking gauge (B) Ringlet specimen prior to loading with black tracking beads attached to surface of specimen (C) Ringlet specimen after testing with black track beads intact

The second method utilised the video extensometer results to determine when testing began. Testing was deemed to have begun when the black marker beads began to move along the y-axis of test measurement. The result is labelled as ‘Gauge length by extensometer’ within Figure C.0.2. The third method employed utilised the concept of normalising the resulting test data to the point at which the theoretical gauge length was achieved. This method is a pure mathematical correction of the test profiles obtained from the Zwick crosshead displacement. The corresponding response is labelled as ‘Theoretical gauge length’ within Figure C.0.2. Figure C.0.3 shows the corresponding response curve with key regions annotated, relating to specific points of interest during the uniaxial ringlet test cycle. Here it can be seen that at the pre-load the (Region 1) test specimen is not in the correct geometry for an accurate assessment of strain and gauge length to be made. Region 2 shows the response curve generated after the point at which the theoretical gauge length was deemed to have been reached. Region 3 represents the point of yielding determined to be the point at which a plastic deformation of the vessel walls occurred. Region 4 shows the corresponding response confirming the failure of the vessel.

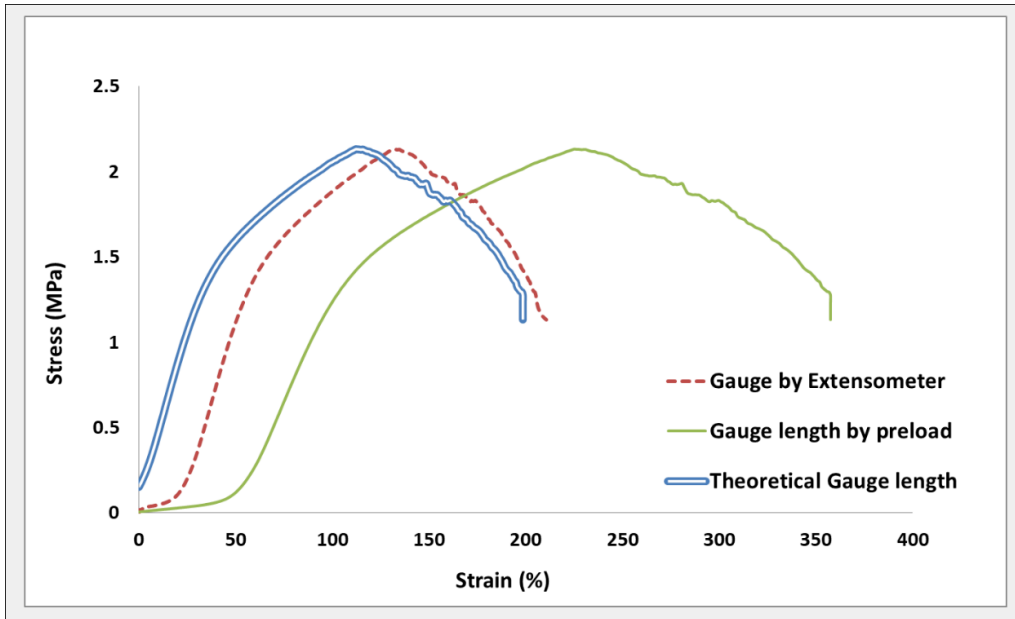


Figure C.0.2: Stress vs strain profiles obtained from one test specimen showing the three methods used to determine the point at which test commencement began

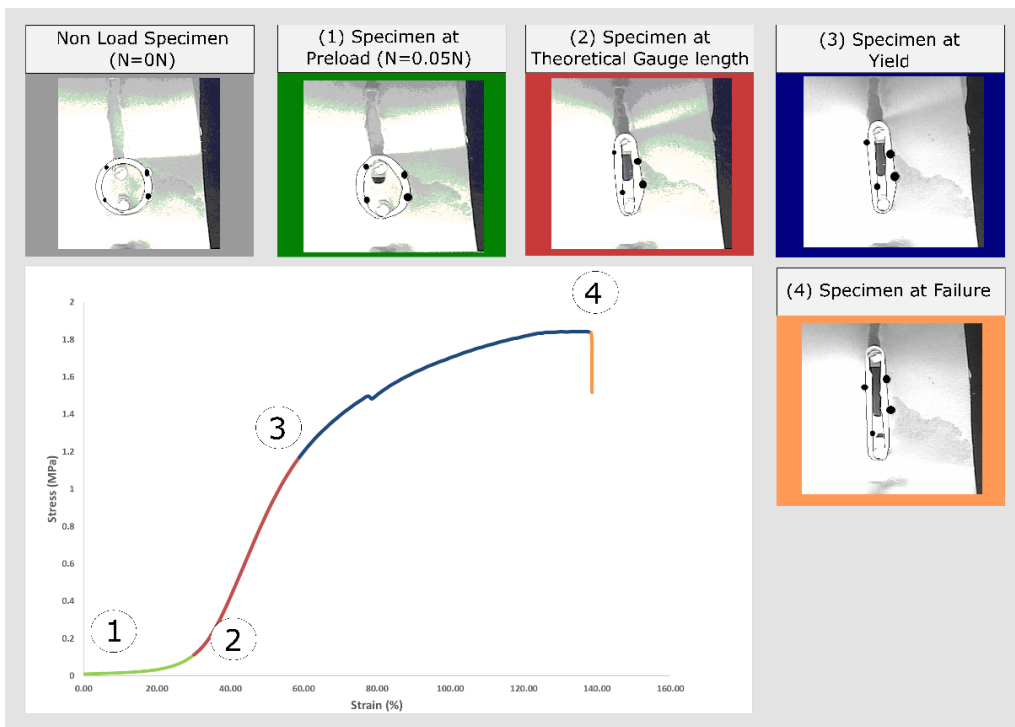


Figure C.0.3: Stress vs strain profile of electrospun ringlet specimen showing distinct loading stages with corresponding specimen configurations as verified by video extensometer. Region (1) shows sample after pre-load with walls of ringlet in a non-parallel configuration, resulting in a large strain for a small applied load. Region (2) shows an increased stress response with the video extensometer confirming the specimen has reached its theoretical gauge length point. Region (3) shows yielding of sample. Region (4) showing specimen failure. It is noted that enhanced outlines have been added to the samples to aid in image clarity

Discussion and Conclusion

Based on the response curves generated it is clear that the choice at which the true sample gauge length has occurred drastically alters the corresponding results obtained. By using the pre-load method, it was clear that the test specimen was in a non-aligned configuration as measurement commenced. A large toe region seen in the response profile reflects this false deformation of the test specimen. The reconfiguration of the specimen geometry upon loading results in a large straining effect for a small applied load resulting in considerably higher overall reported strain values. A stress stiffening effect was found to occur within the vessel with this being correlated to the point at which the theoretical gauge length was achieved, represented by the transition at Region 2. After this, the specimen was elongated until yielding (Region 3) and finally until failure of the specimen occurred (Region 4).

The video extensometer was also found to underestimate the point at which the gauge length occurred. This is suspected to have occurred as the camera was only capable of measuring movement in one axis of movement. As the specimen began to reconfigure its geometry under loading, the black marker bands were found to move slightly upwards along the y-direction of testing. This movement activated the measurement of strain again giving rise to a toe region. It is however noted the toe region was smaller than that observed in pure pre-load profile, suggesting that there was a movement of the tracker beads in the x-axis of movement before slowly moving along the y-axis, again reinforcing the concept of an incorrect vessel orientation at the start of testing.

The resulting time series analysis clearly demonstrates a link between the sample reaching its theoretical gauge length and the corresponding stress-stiffening effect observed within Region 2 of Figure C.0.3. This stress stiffening effect represents a true uptake of force by the walls of the ringlet specimen rather than a force to induce reconfiguration of the vessel geometry. For this reason, it is clear that the theoretical gauge length approach offers the most accurate assessment of vessel deformation. Although the method may not be completely flawless it provides a reasonable and accurate approach to determine sample gauge length for a wide array of vessels and hence the point at which test commencement begins.

Appendix D: Mechanical Assessment of Tubular Latex Membranes for Compliance Testing

Introduction

Cardiovascular tubular prostheses produced through synthetic approaches are inherently porous due to the fabrication techniques employed in their production including knitting and weaving [299]. In order to prevent blood loss through the pores within the vessel walls, the vessels typically undergo a technique known as pre-clotting before implantation. In this method, the surgeon soaks the tubular prostheses in a sample of the patients' blood prior to surgery [300]. This soaking step allows for the coagulation of blood within the pores of the graft, helping to seal them, and in turn minimising blood loss upon implantation. Other techniques employ fibrin glues to form a sealant along the outer surface of the tubular grafts, although it has been shown that these sealants can reduce the long term patency of the vascular grafts [301].

In order to assess the mechanical properties of the tubular prostheses *In vitro*, where vessel pressurisation is required, a number of methods have been devised within the literature to overcome fluid leakage. These include the use of thick viscous fluids including petroleum jell to minimise the rate of leakage upon pressurisation [102], the use of glues to seal the graft surface [302], and small membranes applied to the inner or outer surface to provide a barrier layer to the fluid [268]. ISO 7198 details techniques that may be employed in order to successfully pressurise a vessel using small compliant membranes. The general criteria set out for these membranes is that they should have a length five times that of the nominal relaxed internal diameter of the vascular prostheses along with a diameter at least 1.05 times the nominal pressurised diameter of the prosthesis.

The electrospun membranes under investigation in this work were similarly found to suffer from fluid leakage upon pressurisation. To overcome this issue for the required compliance testing, small diameter latex membranes were created using a simple dipping process. In order to verify that the produced latex membranes had the required properties for use within this test method, a verification study was performed to

determine their Young's modulus and compliance properties compared to that of a representative electrospun specimens under investigation.

Method

Small diameter latex membranes/balloons were created using a dipping process. In this method, a stainless steel mandrel with a diameter of 5mm was dipped into a reservoir of liquid latex (Kryolan, UK). The first layer of latex was allowed to air dry for up to 24hrs. Following this, the mandrel was inverted to the opposite orientation of the first dip and a second coating applied. To ensure no stress concentration effects were generated on the barbed luer connections upon mounting, a partial dip was performed on either end of the membranes provide reinforcement once the second coating layer had dried. The membranes were subsequently removed from the mandrel by applying a layer of talcum powder to the surface of the membranes and inverting the membrane back upon itself.

Uniaxial ringlet tensile testing was performed on 10mm long ringlets of the latex membranes (n=10). Representative electrospun tubular specimens (n=6) were also tested to provide a comparison between the membranes and electrospun specimen stiffness's. Compliance testing was also performed on the bare latex membranes (n=3) and electrospun specimens mounted upon a latex membrane (n=3).

Analysis

The resulting response curves obtained from the uniaxial ringlet tensile testing can be seen in Figure D.0.1. A clear and distinct difference in the specimen stiffness was observed, with the latex membranes possessing a modulus of 0.458 ± 0.089 MPa compared to the electrospun tubular scaffolds that possessed an average modulus of 3.861 ± 0.835 MPa. The latex membranes were also shown to possess a significantly higher strain at break of $1238.33 \pm 67.77\%$ compared to the electrospun specimens at $273.64 \pm 11.71\%$.

Compliance analysis also showed that the latex membranes were significantly more compliant compared to the electrospun specimen and latex membrane combination.

Latex membranes exhibited statically higher average compliances of 11.11 ± 0.661 %mmHg $\times 10^{-2}$ compared to the electrospun specimens which exhibited average compliances of 1.095 ± 0.605 %mmHg $\times 10^{-2}$ ($p=0.004$).

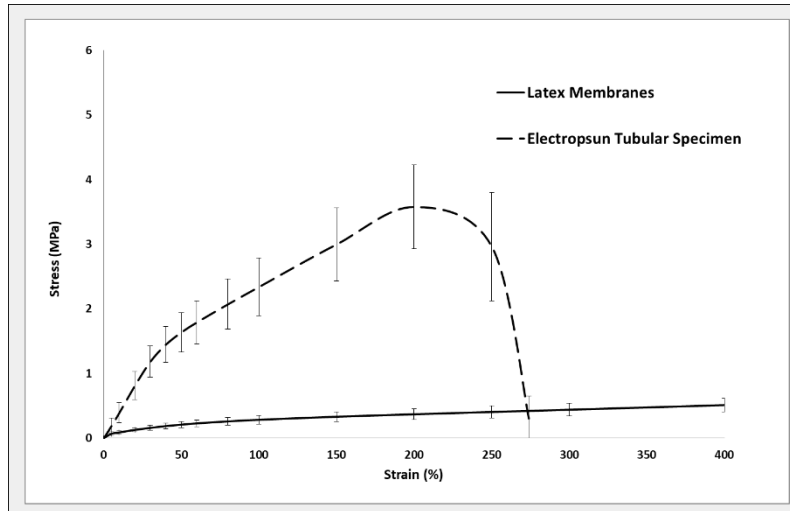


Figure D.0.1: Stress-Strain response of latex membranes ($n=3$) and electrospun tubular scaffolds ($n=6$) showing a distinct difference in sample stiffness. It is noted that the full profile of the latex balloon is not displayed due to excessively high strain at break witnessed.

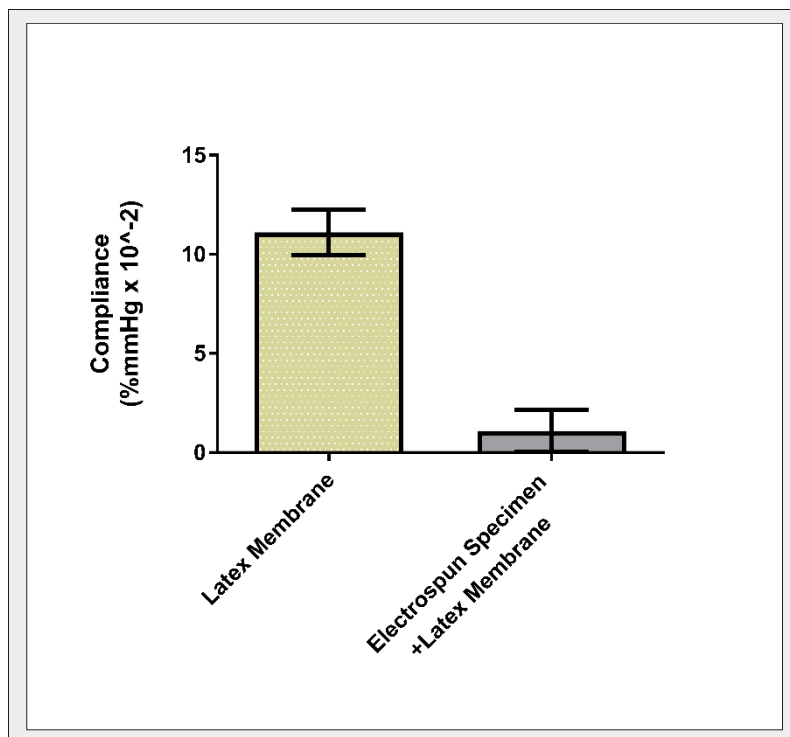


Figure D.0.2: Compliance comparison of pure latex membranes ($n=10$) compared to electrospun tubular specimens ($n=6$) mounted upon latex membranes. Latex membranes showed significantly higher compliance ($p=0.004$).

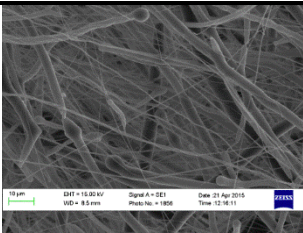
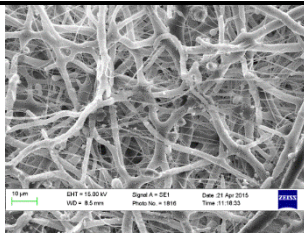
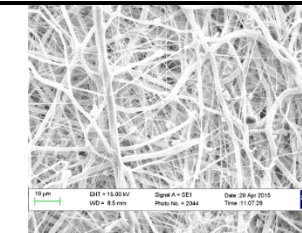
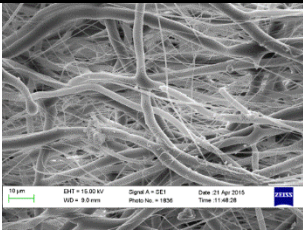
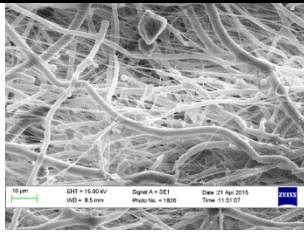
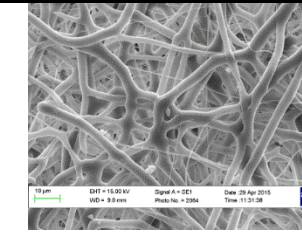
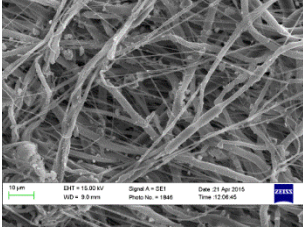
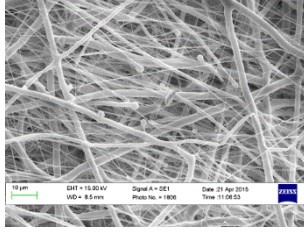
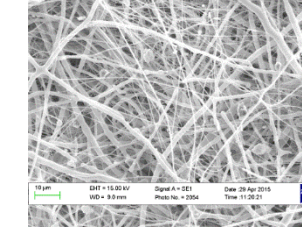
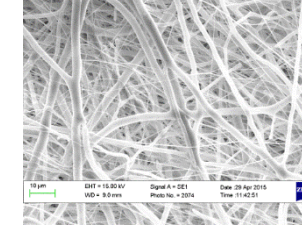
Discussion and Conclusion

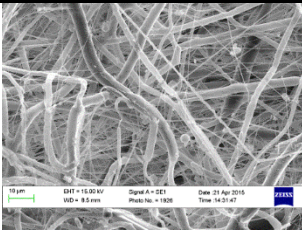
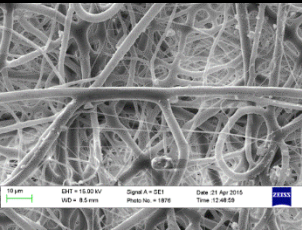
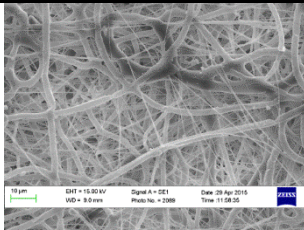
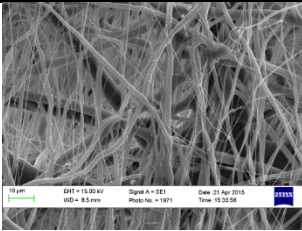
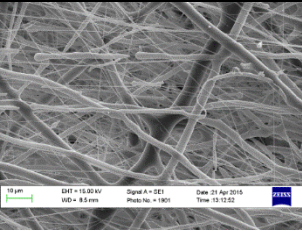
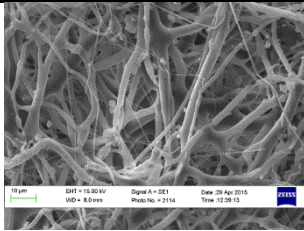
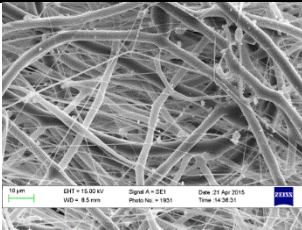
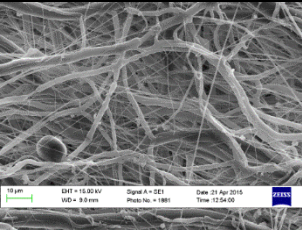
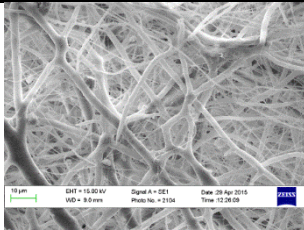
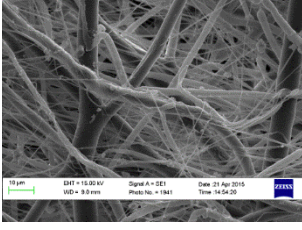
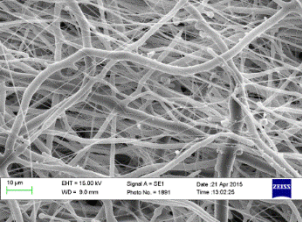
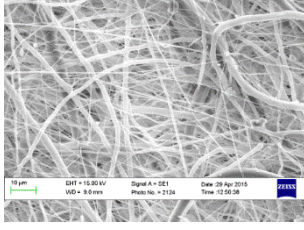
Based upon the results of the uniaxial ringlet testing and compliance testing performed on the latex membranes prepared, it is clear they demonstrate a significantly higher elasticity and therefore distensibility properties compared to the electrospun specimens. This allows for the appropriate transfer of pressure to the walls of the electrospun specimens during compliance testing without a shielding effect occurring due to the presence of the latex membrane. Due to this, it can be concluded that the produced latex membranes are suitable for use in the compliance testing of electrospun specimens without resulting in a biasing of the measured values. The consistency of the test results obtained for the latex membranes also demonstrates the repeatability of the preparation protocol ensuring reproducible test conditions amongst specimens.

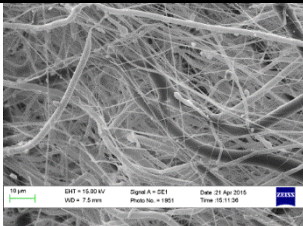
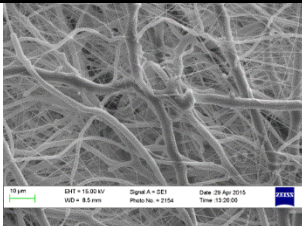
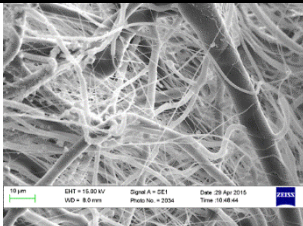
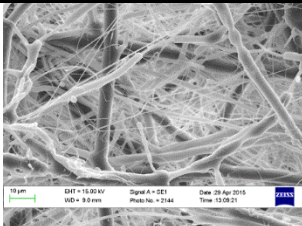
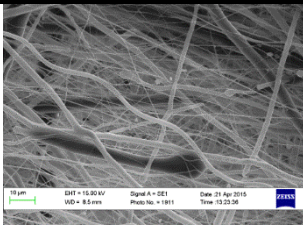
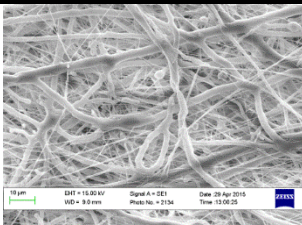
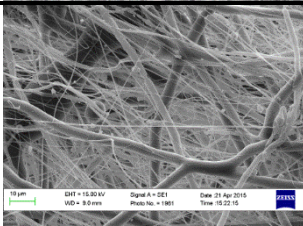
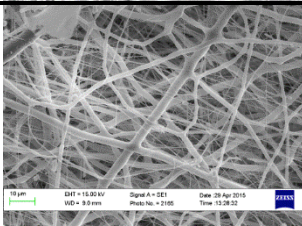
Appendix E: Regression Analysis of Multi-modal Electrospinning Process

16wt% Chloroform/Ethanol (7:3; v:v)- 1600 RPM

Table E.0.1: SEM images of samples prepared using 16wt% PCL dissolved in Chloroform/Ethanol (7:3; v:v) spun onto rotating mandrel spinning at 1600 RPM

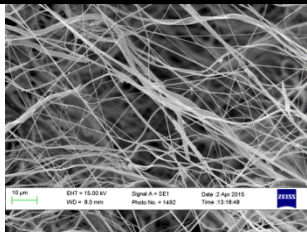
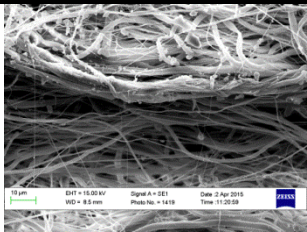
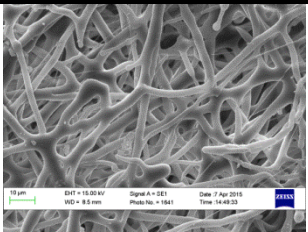
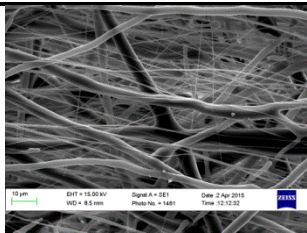
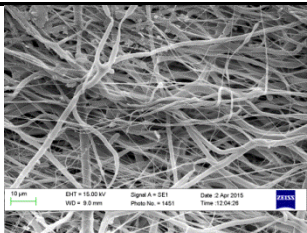
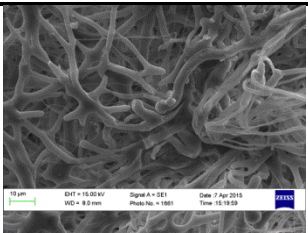
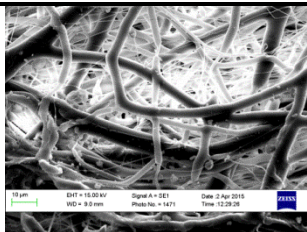
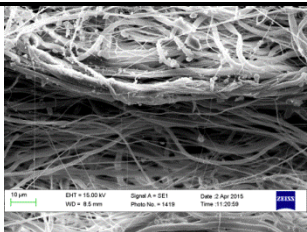
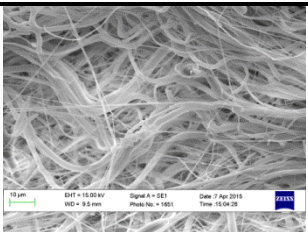
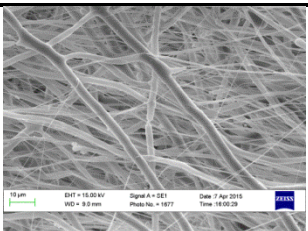
Dist. (cm)	4ml/hr		
	10KV	15kV	20kV
15			
17.5			
20			
22.5	No Specimen Collected	No Specimen Collected	

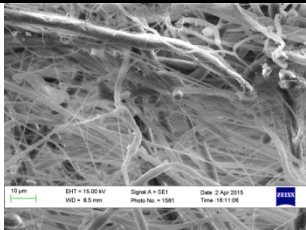
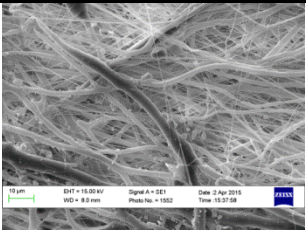
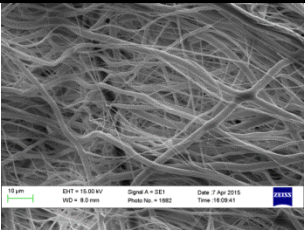
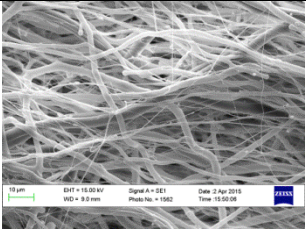
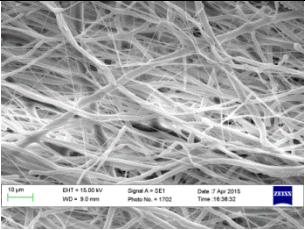
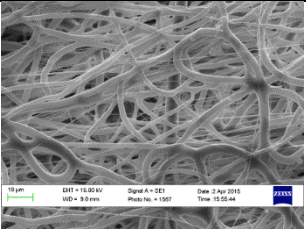
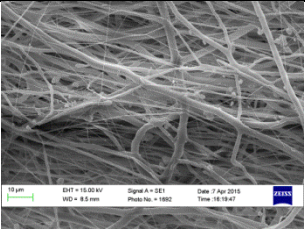
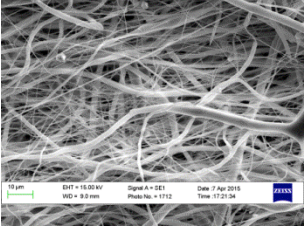
				8ml/hr		
Dist. (cm)	10KV	15kV	20kV			
15						
17.5						
20						
22.5						

		12ml/hr	
Dist. (cm)	10KV	15kV	20kV
15	No Specimen Collected		
17.5	No Specimen Collected		
20	No Specimen Collected		
22.5	No Specimen Collected		

16wt% Chloroform/Ethanol (7:3; v:v)- 3200 RPM

Table E.0.2: SEM images of samples prepared using 16wt% PCL dissolved in Chloroform/Ethanol (7:3; v:v) spun onto rotating mandrel spinning at 3200 RPM

		4ml/hr		
Dist. (cm)	10KV	15kV	20kV	
15				
17.5				
20				
22.5	No Specimen Collected	No Specimen Collected		

8ml/hr			
Dist. (cm)	10KV	15kV	20kV
15			
17.5	No Specimen Collected		
20	No Specimen Collected		
22.5	No Specimen Collected	No Specimen Collected	

12ml/hr

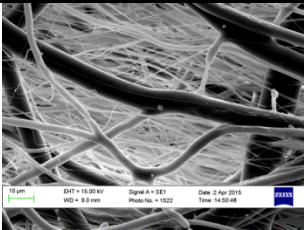
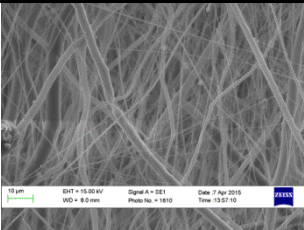
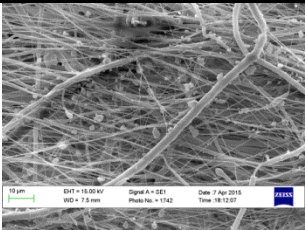
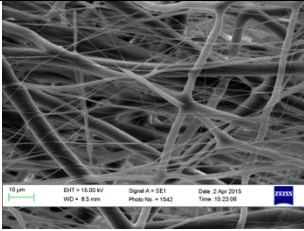
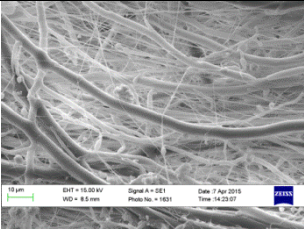
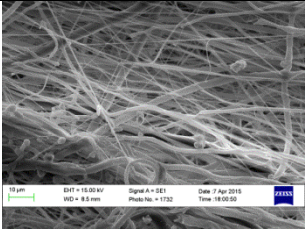
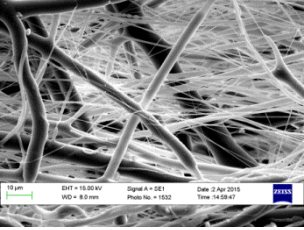
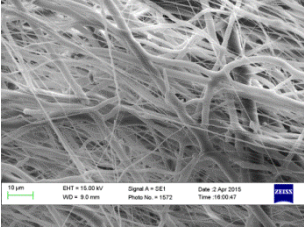
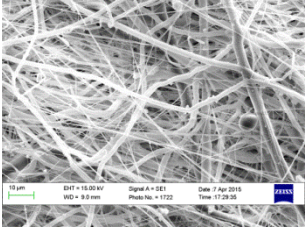
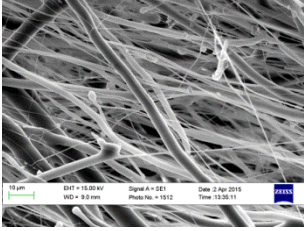
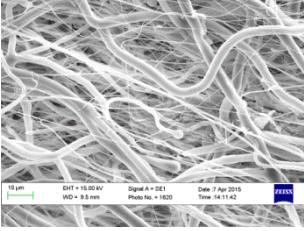
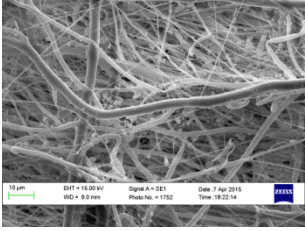
Dist. (cm)	10KV	15kV	20kV
15	 <p>10 μm DHT = 15.00 kV Signal A = SE1 Date: 2 Apr 2015 Time: 14:50:48 Photo No. = 1522</p>	 <p>10 μm DHT = 15.00 kV Signal A = SE1 Date: 7 Apr 2015 Time: 15:37:10 Photo No. = 1510</p>	 <p>10 μm DHT = 15.00 kV Signal A = SE1 Date: 7 Apr 2015 Time: 18:12:07 Photo No. = 1542</p>
17.5	 <p>10 μm DHT = 15.00 kV Signal A = SE1 Date: 2 Apr 2015 Time: 15:23:08 Photo No. = 1542</p>	 <p>10 μm DHT = 15.00 kV Signal A = SE1 Date: 7 Apr 2015 Time: 14:23:07 Photo No. = 1501</p>	 <p>10 μm DHT = 15.00 kV Signal A = SE1 Date: 7 Apr 2015 Time: 18:00:50 Photo No. = 1532</p>
20	 <p>10 μm DHT = 15.00 kV Signal A = SE1 Date: 2 Apr 2015 Time: 14:59:47 Photo No. = 1532</p>	 <p>10 μm DHT = 15.00 kV Signal A = SE1 Date: 2 Apr 2015 Time: 16:00:47 Photo No. = 1572</p>	 <p>10 μm DHT = 15.00 kV Signal A = SE1 Date: 7 Apr 2015 Time: 17:29:35 Photo No. = 1515</p>
22.5	 <p>10 μm DHT = 15.00 kV Signal A = SE1 Date: 2 Apr 2015 Time: 15:25:11 Photo No. = 1512</p>	 <p>10 μm DHT = 15.00 kV Signal A = SE1 Date: 7 Apr 2015 Time: 14:11:42 Photo No. = 1520</p>	 <p>10 μm DHT = 15.00 kV Signal A = SE1 Date: 7 Apr 2015 Time: 18:22:14 Photo No. = 1532</p>

Table E.0.3: Mechanical and Porosity Results for Regression Analysis Specimens created at 1600 RPM

Flow Rate (ml/hr)	Volatge (kV)	Collector Distance (cm)	Avg. UTS (MPa)	Total Avg. UTS±Dev	Young's Mod. (MPa)	Total Avg. Young Mod.±Dev	Max Force (N)	Total Avg. MF±Dev	Ring Modulus (N/%)	Total Avg. RM±Dev	Porosity (%)	Total Avg. PO±Dev
4	15	15	2.004	2.099±0.126	6.265	6.48±0.421	17.87	17.314±2.166	0.558	0.536±0.047	86.237	84.928±2.49
			2.145		6.954		14.977		0.485		86.744	
			3.149		6.22		19.094		0.566		81.804	
		1.681	1.862±0.215	17.5	6.475	6.74±0.447	8.605	10.753±2.475	0.331	0.386±0.063	82.857	84.581±1.882
		2.133			7.159		12.673		0.424		86.38	
		1.771			6.585		10.98		0.404		84.507	
		1.939	1.902±0.209	20	6.839	6.988±0.337	14.733	10.631±3.251	0.519	0.388±0.103	83.487	83.686±1.406
	3.099	7.363			8.713		0.305		83.787			
	1.667	6.762			8.447		0.341		83.783			
	1.609	1.864±0.222			15		6.274		5.853±0.435		9.113	
	1.945		5.687	14.466		0.475	82.661					
	2.037		5.598	13.88		0.438	83.04					
	2.261		2.043±0.214	17.5	6.613	6.586±0.47	16.129	12.185±2.809	0.418	0.389±0.075	84.329	83.128±2.05
	1.998				6.261		18.097		0.33		84.408	
1.87	6.884				14.651		0.421		80.646			
2.069	6.285				10.648		0.323		83.287			
2.136	2.000±0.178	20	7.027	6.791±0.425	18.447	5.528±3.865	0.099	0.179±0.109	85.29	83.938±1.687		
1.795			7.06		19.677		0.114		83.237			

Flow Rate (ml/hr)	Volatge (kV)	Collector Distance (cm)	Avg. UTS (MPa)	Total Avg. UTS±Dev	Young's Mod. (MPa)	Total Avg. Young Mod.±Dev	Max Force (N)	Total Avg. MF±Dev	Ring Modulus (N/%)	Total Avg. RM±Dev	Porosity (%)	Total Avg. PO±Dev
8	15	15	1.924	1.996±0.111	6.114	5.499±0.612	19.728	22.902±3.904	0.622	0.624±0.076	86.554	86.077±1.4
			2.048		4.901		24.023		0.574		86.802	
			2.015		5.483		24.936		0.676		84.873	
		17.5	1.567	1.978±0.341	6.074	6.37±0.417	9.914	16.502±6.111	0.373	0.516±0.136	86.053	85.27±0.86
			2.272		6.372		21.35		0.6		84.653	
			2.094		6.664		18.242		0.574		85.105	
			1.98		1.822±0.274		6.368		6.513±0.27		13.567	
	1.999	6.627	14.67	0.485		85.384						
	20	1.486		6.545		4.439		0.195		84.237		
		20	15	2.099	2.193±0.102	5.479	6.007±0.53	22.642	22.032±3.785	0.591	0.6±0.094	83.632
	2.262			6.554		23.274		0.667		86.202		
	2.218			5.988		20.179		0.544		83.457		
	17.5		2.363	2.154±0.2	5.774	6.228±0.511	11.861	17.68±5.874	0.683	0.652±0.073	83.325	83.689±1.355
			2.171		6.353		23.952		0.698		85.294	
1.929			6.556		17.228		0.576		82.447			
2.019			1.835±0.274		6.178		6.768±0.771		10.997		8.941±2.792	
1.692	7.618	6.421		0.288	83.66							
1.794		6.508		9.404		0.338		83.039				

Flow Rate (ml/hr)	Volatge (kV)	Collector Distance (cm)	Avg. UTS (MPa)	Total Avg. UTS±Dev	Young's Mod. (MPa)	Total Avg. Young Mod.±Dev	Max Force (N)	Total Avg. MF±Dev	Ring Modulus (N/%)	Total Avg. RM±Dev	Porosity (%)	Total Avg. PO±Dev
12	15	15	1.861	1.995±0.25	5.155	4.789±0.732	29.025	32.13±7.58	0.802	0.758±0.109	86.626	84.886±1.589
			2.296		5.33		28.399		0.652		84.387	
			1.828		3.88		38.966		0.82		83.645	
		17.5	1.765	1.861±0.15	5.505	5.166±0.517	27.966	26.614±4.555	0.682	0.671±0.056	85.335	85.387±0.761
			2.02		4.658		29.585		0.68		85.647	
			1.799		5.335		22.291		0.651		85.179	
			1.746		5.729		5.85±0.24		18.154		16.785±3.097	
	20	1.756	1.716±0.136	5.913	5.907	16.686	15.514	0.558	0.553	84.767	84.801	
		1.646		5.907		15.514		0.553		84.801		
		2.362		2.314±0.271		4.158		4.674±0.728		47.413		39.345±11.314
	2.575	4.277	44.951		0.878	86.267						
	2.004	5.586	25.671		0.705	83.173						
	20	17.5	1.952	1.963±0.44	4.88	5.72±0.684	23.77	19.123±7.194	0.547	0.524±0.085	84.981	83.801±1.156
			2.453		6.189		22.111		0.556		83.346	
1.485			6.091		11.489		0.469		83.075			
1.582		1.812±0.336	5.618	6.024±0.641	6.194	10.937±5.747	0.217	0.355±0.158	81.864	82.821±1.109		
1.842			6.205		9.41		0.317		83.56			
20	2.012	6.25	17.207	0.531	83.04							

Table E.0.4: Morphological Results for Regression Analysis Specimens created at 1600 RPM

Flow Rate (ml/hr)	Volatge (kV)	Collector Distance (cm)	Mean Outer Fib Dia.	Outer Fib Dev.	Total Avg. Outer Dia±Dev	Mean Inner Fib Dia.	Inner Fib Dev.	Total Avg. Inner Dia±Dev	Outer Fibre Coherency	Total Avg. Co.±Dev	Inner Fibre Coherency	Total Avg. Co.±Dev	
4	15	15	1.386	0.964	1.252±1.149	1.49	1.231	1.342±1.188	0.18891	0.178±0.069	0.14092	0.146±0.043	
			1.146	1.058		1.313	1.093		0.24023		0.19206		
			1.225	1.384		1.223	1.234		0.1038		0.10568		
		17.5	1.031	0.91	1.063±0.9	1.133	0.923	1.171±1.029	0.26244	0.313±0.059	0.25396	0.211±0.044	
		1.105	0.887	1.338		0.995	0.29781		0.16697				
		1.053	0.903	1.043		1.154	0.37823		0.21322				
		20	1.597	0.97	1.344±0.071	1.227	0.997	1.221±1.002	0.39948	0.325±0.072	0.24031	0.165±0.075	
		1.431	1.27	1.198		0.886	0.25592		0.09048				
	1.004	0.941	1.239	1.111		0.32054	0.16428						
	20	15	15	2.48	1.337	1.418±1.033	1.775	0.806	1.227±0.826	0.15235	0.175±0.116	0.10793	0.197±0.093
				1.012	1		1.018	0.849		0.29992		0.29032	
				0.763	0.646		0.887	0.822		0.0719		0.019132	
		17.5	0.661	0.676	1.346±1.158	1.085	0.891	1.133±0.938	0.29166	0.228±0.072	0.34569	0.29±0.057	
		0.933	1.056	1.014		1.003	0.14948		0.232				
		2.443	1.566	1.301		0.915	0.24301		0.29144				
		20	0.816	0.697	0.802±0.783	1.046	0.857	0.994±0.896	0.26155	0.249±0.086	0.22089	0.237±0.034	
0.858		0.936	1.054	0.974		0.32893	0.27701						
0.733	0.691	0.881	0.854	0.15748		0.21441							

Flow Rate (ml/hr)	Volatge (kV)	Collector Distance (cm)	Mean Outer Fib Dia.	Outer Fib Dev.	Total Avg. Outer Dia±Dev	Mean Inner Fib Dia.	Inner Fib Dev.	Total Avg. Inner Dia±Dev	Outer Fibre Coherency	Total Avg. Co.±Dev	Inner Fibre Coherency	Total Avg. Co.±Dev
8	15	15	1.149	1.168	1.299±1.252	1.547	1.478	1.434±1.346	0.25303	0.299±0.086	0.25748	0.217±0.084
			1.351	1.276		1.213	1.142		0.2493		0.27297	
			1.396	1.306		1.541	1.396		0.099		0.12078	
		17.5	1.385	1.566	1.281±1.412	1.512	1.385	1.4±1.284	0.33526	0.38±0.058	0.20122	0.197±0.084
		1.333	1.341		1.131	0.963		0.35965		0.27845		
		1.125	1.314		1.558	1.449		0.44645		0.11066		
		1.107	1.068	1.266±1.235	1.26	1.062	1.164±1.104	0.21586	0.276±0.086	0.20512	0.287±0.072	
	20	1.392	1.292		1.082	1.012		0.37524		0.31171		
	1.298	1.312		1.151	1.228		0.2376		0.34324			
	20	15	1.053	0.957	1.1±0.967	0.975	0.771	1.076±0.912	0.28944	0.225±0.123	0.13132	0.138±0.043
			1.237	1.078		1.167	1.087		0.3033		0.184	
			1.009	0.851		1.087	0.848		0.08373		0.09803	
		17.5	1.284	1.008	1.397±1.386	0.872	0.782	1.257±1.142	0.20796	0.219±0.077	0.14725	0.188±0.025
		1.34	1.514		1.522	1.394		0.30125		0.10146		
1.567		1.568		1.346	1.166		0.14866		0.10656			
1.205		1.153	1.19±1.14	1.261	1.102	1.394±1.306	0.36684	0.228±0.128	0.06319	0.061±0.002		
20	1.133	1.018		1.486	1.351		0.20384		0.05908			
1.231	1.239		1.434	1.44		0.11378		0.06052				

Flow Rate (ml/hr)	Volatge (kV)	Collector Distance (cm)	Mean Outer Fib Dia.	Outer Fib Dev.	Total Avg. Outer Dia±Dev	Mean Inner Fib Dia.	Inner Fib Dev.	Total Avg. Inner Dia±Dev	Outer Fibre Coherency	Total Avg. Co.±Dev	Inner Fibre Coherency	Total Avg. Co.±Dev		
12	15	15	1.425	1.33	1.32±1.472	1.381	1.011	1.567±1.474	0.51238	0.335±0.173	0.40452	0.251±0.164		
			1.45	1.743		1.615	1.402		0.16684		0.27091			
			1.084	1.301		1.704	1.88		0.32576		0.07758			
		17.5	17.5	1.112	1.187	1.162±1.24	1.189	1.329	1.171±1.218	0.35706	0.306±0.111	0.36765	0.256±0.098	
		1.157		1.347		1.293	1.29		0.38308		0.18411			
		1.217		1.177		1.031	1.009		0.1793		0.21702			
		1.287		1.21	1.19±1.281	1.107	0.939	1.145±1.183	0.39489	0.473±0.097	0.33456	0.308±0.029		
	20	20	1.348	1.526		1.133	1.353		0.58166		0.27643			
	0.936		1.063		1.194	1.218		0.44165		0.31183				
	20	20	15	0.898	0.697	1.133±1.111	1.356	1.02	1.356±1.166	0.28875	0.299±0.082	0.1042	0.198±0.092	
				1.199	1.173		1.081	1.014		0.3859		0.2889		
				1.301	1.356		1.631	1.417		0.22351		0.20016		
			17.5	17.5	1.008	1.002	1.241±1.463	0.917	0.902	1.066±1.061	0.26029	0.317±0.073	0.21125	0.196±0.071
			1.185		1.563		1.006	1.095		0.29068		0.11869		
1.531			1.726			1.276	1.168		0.39978		0.25837			
1.177			1.142		1.168±1.207	1.073	0.83	1.147±1.214	0.16512	0.227±0.056	0.21642	0.223±0.057		
20	20	1.268	1.371		1.202	1.605		0.24323		0.28303				
1.058		1.089		1.165	1.077		0.27357		0.17039					

Table E.0.5: Mechanical and Porosity Results for Regression Analysis Specimens created at 3200 RPM

Flow Rate (ml/hr)	Volatge (kV)	Collector Distance (cm)	Avg. UTS (MPa)	Total Avg. UTS±Dev	Young's Mod. (MPa)	Total Avg. Young Mod.±Dev	Max Force (N)	Total Avg. MF±Dev	Ring Modulus (N/%)	Total Avg. RM±Dev	Porosity (%)	Total Avg. PO±Dev					
4	15	15	1.865	2.282±0.5	4.471	5.34±1.284	28.892	26.187±4.649	0.692	0.656±0.031	85.065	85.158±0.647					
			2.045		4.519		29.401		0.627		85.694						
			2.935		7.03		20.267		0.649		84.714						
		17.5	2.899	2.695±0.362	9.347	8.518±1.513	12.505	16.821±6.131	0.389	0.532±0.17	79.896						
					2.484							7.578	23.082	0.702	82.403		
					2.704							8.63	14.876	0.505	78.903		
			20	3.291	3.061±0.322	9.88	10.481±1.277	8.892	6.919±2.29	0.264	0.213±0.052	83.952					
						2.817							11.538	7.271	0.193	84.954	
						3.076							10.026	4.593	0.181	84.318	
	20	15	2.933	2.887±0.336	7.279	7.07±0.504	23.082	25.415±3.407	0.57	0.623±0.065	80.949						
					2.553							6.533	25.981	0.664	84.559		
					3.173							7.4	27.182	0.633	84.516		
		17.5	2.194	2.429±0.288	7.78	7.542±0.697	21.217	21.959±3.38	0.749	0.72±0.071	77.774						
					2.394							6.761	22.683	0.64	82.034		
					3.173							8.085	21.976	0.77	82.304		
			20	2.194	2.115±0.36	8.124	8.069±0.495	18.974	15.085±4.902	0.639	0.568±0.15	81.589					
						1.693							8	7.719	12.304	0.435	84.907
						2.274							8.364	13.978	0.663	83.628	

Flow Rate (ml/hr)	Volatge (kV)	Collector Distance (cm)	Avg. UTS (MPa)	Total Avg. UTS±Dev	Young's Mod. (MPa)	Total Avg. Young Mod.±Dev	Max Force (N)	Total Avg. MF±Dev	Ring Modulus (N/%)	Total Avg. RM±Dev	Porosity (%)	Total Avg. PO±Dev						
8	15	15	2.558	2.696±0.166	5.788	6.073±0.472	43.626	37.242±5.936	0.986	0.831±0.126	93.903	90.78±5.277						
			2.732		6.544		32.851		0.786		87.684							
			2.797		5.793		35.25		0.72		90.754							
		17.5	2.641	2.37±0.243	6.899	6.608±0.45	8.568	14.359±5.936	0.357	0.448±0.117	58.245	74.362±12.977						
			2.283		6.657		19.92		0.569		86.661							
			2.185		6.269		14.588		0.417		78.181							
			2.818		2.466±0.379		6.922		6.883±0.632		7.69		5.985±2.096	0.265	0.194±0.063	96.648	80.228±15.61	
			2.395				6.945				5.418			0.169		74.968		
			2.185				6.783				4.848			0.148		69.068		
	20	17.5	15	2.254	2.357±0.304	6.396	5.889±0.962	27.403	28.429±5.472	0.777	0.7±0.093	83.061	84.347±1.428					
				2.205		5.098		28.703		0.647		84.126						
				2.613		6.172		29.182		0.674		85.855						
			17.5	2.035	2.138±0.385	8.257	7.695±0.534	12.633	12.769±4.407	0.511	0.528±0.105	82.082	82.505±1.709					
				1.774		7.508		8.511		0.497		82.387						
				2.603		7.321		17.164		0.575		83.046						
				1.914		1.949±0.135		9.481		8.335±1.002		6.606		10.032	0.325	0.339±0.095	81.68	82.738±1.583
				2.043				7.666				9.754			0.257		83.457	
				1.89				7.857				13.737			0.435		83.075	

Flow Rate (ml/hr)	Volatge (kV)	Collector Distance (cm)	Avg. UTS (MPa)	Total Avg. UTS±Dev	Young's Mod. (MPa)	Total Avg. Young Mod.±Dev	Max Force (N)	Total Avg. MF±Dev	Ring Modulus (N/%)	Total Avg. RM±Dev	Porosity (%)	Total Avg. PO±Dev	
12	15	15	2.692	2.711±0.177	5.658	5.434±0.556	56.701	43.693±13.855	1.187	0.869±0.266	85.931	84.67±1.06	
			2.824		4.802		47.499		0.806		84.067		
			2.617		5.844		27.688		0.614		84.013		
		17.5	2.451	2.241±0.317	7.251	6.287±0.844	34.233	24.99±10.779	1	0.688±0.28	85.04	83.092±1.564	
			2.268		5.682		28.172		0.698		82.089		
			2.003		5.928		12.574		0.365		82.147		
			1.8		1.793±0.198		7.626		7.104±0.947		8.758		10.709±3.58
	20	1.769	1.769	6.56	6.56	11.709	11.709	0.418	0.418	82.177	82.177		
		1.811		7.125		11.661		0.423		81.828			
	12	20	15	2.518	2.515±0.153	7.031	5.506±1.327	45.444	45.374±5.703	1.261	0.982±0.217	82.694	83.244±1.642
				2.366		4.068		49.386		0.843		83.458	
				2.661		5.419		41.291		0.841		83.579	
			17.5	2.632	2.575±0.23	7.929	7.031±1.113	18.55	30.641±11.15	0.557	0.711±0.148	80.933	81.974±1.129
				2.507		7.348		42.847		0.888		82.455	
2.585				5.818		30.527		0.688		82.534			
2.041				2.014±0.336		8.306		7.882±0.736		13.935		19.894±8.901	
20			2.311	2.311	7.393	7.393	27.937	27.937	0.67	0.67	83.154	83.154	
	1.69	7.947	17.81		0.689		81.511						

Table E.0.6: Morphological Results for Regression Analysis Specimens created at 3200 RPM

Flow Rate (ml/hr)	Volatge (kV)	Collector Distance (cm)	Mean Outer Fib Dia.	Outer Fib Dev.	Total Avg. Outer Dia±Dev	Mean Inner Fib Dia.	Inner Fib Dev.	Total Avg. Inner Dia±Dev	Outer Fibre Coherency	Total Avg. Co.±Dev	Inner Fibre Coherency	Total Avg. Co.±Dev
4	15	15	0.85	0.713	0.89±0.716	0.949	0.937	0.967±0.884	0.3484	0.383±0.09	0.21217	0.236±0.024
			0.831	0.657		1.169	1.012		0.31517		0.23658	
			0.989	0.774		0.783	0.664		0.4846		0.26048	
		1.023	0.893	0.94±0.874	0.926	0.877	1.157±0.964	0.35059	0.413±0.06	0.28506	0.295±0.021	
		0.883	0.9		1.431	0.98		0.41205		0.31954		
		0.915	0.826		1.113	1.029		0.47783		0.28083		
		0.911	0.776	0.882±0.643	0.926	0.756	0.95±0.682	0.34388	0.329±0.021	0.24158	0.286±0.041	
	0.762	0.609		1.104	0.614		0.30529		0.32151			
	0.972	0.517		0.82	0.668		0.33922		0.29446			
	20	15	0.937	0.813	0.912±0.843	1.083	0.893	1.1±0.797	0.36664	0.311±0.05	0.30605	0.242±0.075
			0.99	1.005		1.342	0.796		0.29924		0.26072	
			0.81	0.678		0.876	0.69		0.26853		0.16037	
		2.657	1.081	1.614±1.14	1.027	0.845	1.105±0.822	0.27885	0.214±0.071	0.32255	0.274±0.052	
		1.279	1.244		1.031	0.727		0.13733		0.21891		
0.906		1.088		1.256	0.885		0.22577		0.28132			
1.918		1.425	1.299±1.132	1.766	1.054	1.225±0.941	0.08209	0.141±0.052	0.10794	0.178±0.062		
1.103	0.863		0.987	0.845		0.17844		0.22602				
0.876	1.034		0.921	0.911		0.16211		0.19988				

Flow Rate (ml/hr)	Volatge (kV)	Collector Distance (cm)	Mean Outer Fib Dia.	Outer Fib Dev.	Total Avg. Outer Dia±Dev	Mean Inner Fib Dia.	Inner Fib Dev.	Total Avg. Inner Dia±Dev	Outer Fibre Coherency	Total Avg. Co.±Dev	Inner Fibre Coherency	Total Avg. Co.±Dev	
8	15	15	1.026	0.912	1.062±0.927	1.031	0.99	1.081±1.009	0.32645	0.419±0.107	0.15475	0.228±0.065	
			2.095	0.985		1.083	0.967		0.53543		0.27753		
			1.066	0.811		1.128	1.067		0.39492		0.25122		
		17.5	3	1.337	1.346	1.047±1.124	1.606	1.167	1.198±1.025	0.48299	0.365±0.136	0.33582	0.335±0.028
		5	0.88	0.949		1.029	0.997		0.39568		0.36295		
		7	0.923	1.037		0.959	0.892		0.21666		0.30756		
		9	1.148	1.254	1.11±1.05	1.366	0.656	1.242±0.92	0.31721	0.346±0.04	0.27929	0.308±0.048	
	20	1.083	0.963		1.294	0.897		0.32888		0.28191			
	1.1	0.899		1.065	1.142		0.39083		0.36368				
	20	15	0.947	0.948	1.015±1.131	1.442	0.935	1.303±0.962	0.25361	0.242±0.012	0.26689	0.223±0.038	
			1.079	1.436		1.519	1.098		0.22936		0.20321		
			1.019	0.936		0.949	0.834		0.24372		0.1997		
		17.5	3	1.069	0.943	0.978±0.819	0.972	0.875	0.981±1.008	0.43024	0.305±0.108	0.27968	0.272±0.007
		5	1.189	0.856		1.071	1.087		0.24074		0.26938		
7		0.676	0.626		0.901	1.051		0.2447		0.26664			
9		0.853	0.851	0.965±0.89	1.166	1.019	1.08±0.986	0.32906	0.348±0.034	0.18746	0.21±0.049		
20	1.092	0.936		1.274	1.144		0.32731		0.26639				
0.951	0.882		0.799	0.755		0.38762		0.17762					

Flow Rate (ml/hr)	Volatge (kV)	Collector Distance (cm)	Mean Outer Fib Dia.	Outer Fib Dev.	Total Avg. Outer Dia±Dev	Mean Inner Fib Dia.	Inner Fib Dev.	Total Avg. Inner Dia±Dev	Outer Fibre Coherency	Total Avg. Co.±Dev	Inner Fibre Coherency	Total Avg. Co.±Dev	
12	15	15	1.035	1.05	1.176±1.639	1.044	1.02	1.089±1.238	0.33442	0.298±0.093	0.24687	0.257±0.069	
			1.253	2.086		1.218	1.43		0.19245		0.33112		
			1.241	1.614		1.094	1.229		0.36714		0.19333		
		17.5	1.2	1.337	1.208±1.395	0.979	1.126	1.23±1.341	0.41668	0.324±0.092	0.10515	0.139±0.041	
			1.353	1.496		1.623	1.735		0.23022		0.18498		
			1.071	1.347		1.088	1.056		0.32587		0.1272		
			1.041	0.94		1.114±1.24	0.906		0.878		0.988±1.041		0.48003
	20	1.324	1.502	1.075	1.046		0.39385	0.34498					
				0.976	1.215		0.982	1.176		0.44083		0.30991	
	20	17.5	15	0.855	0.893	1.024±1.425	1.112	0.901	1.095±1.043	0.37809	0.383±0.01	0.29866	0.249±0.043
				1.205	1.832		1.196	1.141		0.39456		0.22084	
				1.011	1.391		0.979	1.073		0.37606		0.22886	
			20	1.036	1.128	1.04±1.218	0.949	0.973	0.956±0.949	0.27637	0.266±0.013	0.31688	0.311±0.064
				1	1.261		1.101	1.047		0.2714		0.24459	
1.085				1.259	0.818		0.811	0.25134		0.37222			
0.909				0.877	0.877±0.833		1.172	1.244		1.22±1.149		0.46985	
20	0.713	0.502	1.345	1.153		0.40646	0.22689						
			1.008	1.031		1.142	1.041		0.42881		0.21323		

Appendix F: Residual Plots for Regression Analysis of Multi-modal Electrospinning Process

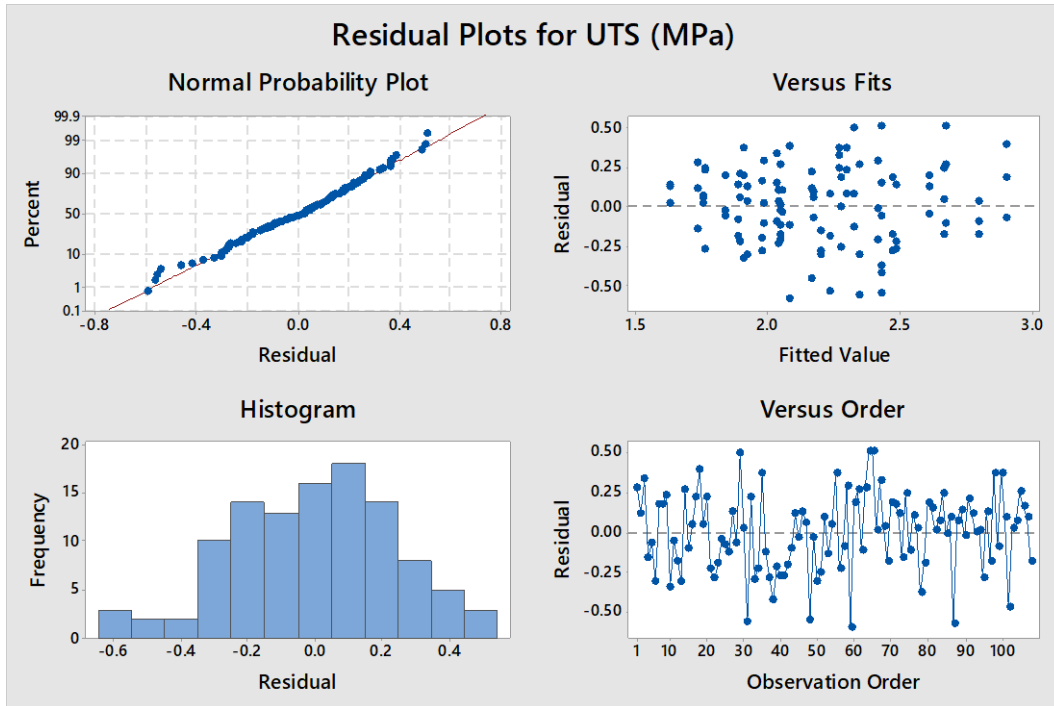


Figure F.0.1: Residual Plots for Response Variable UTS ‘ Y_1 ’

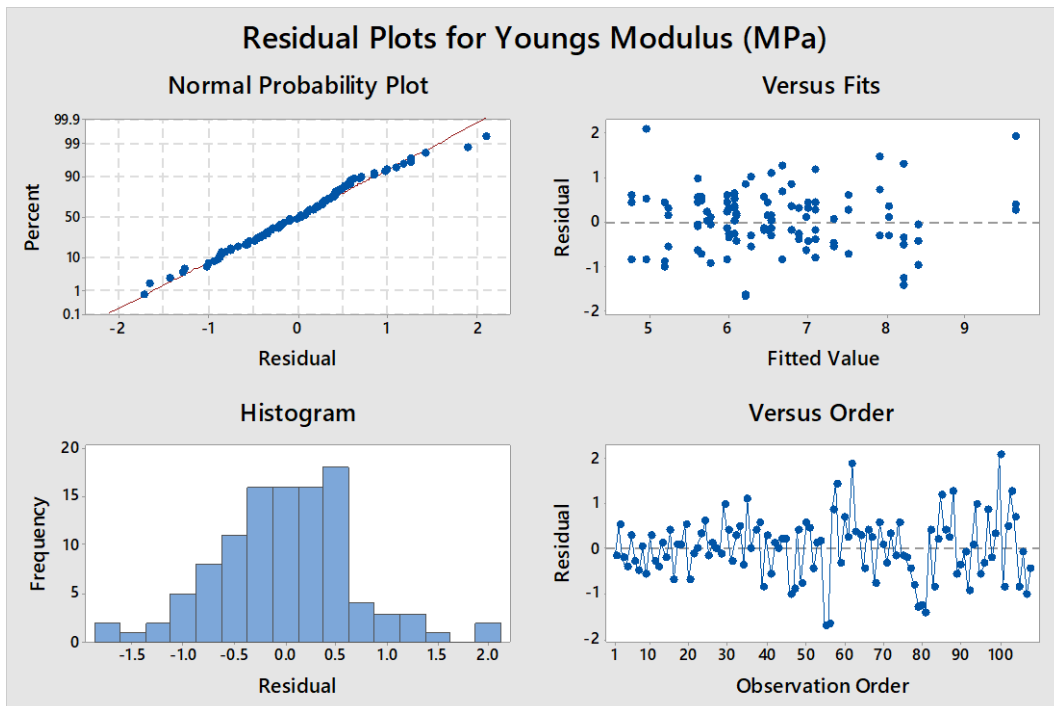


Figure F.0.2: Residual Plots for Response Variable Young's modulus ‘ Y_2 ’

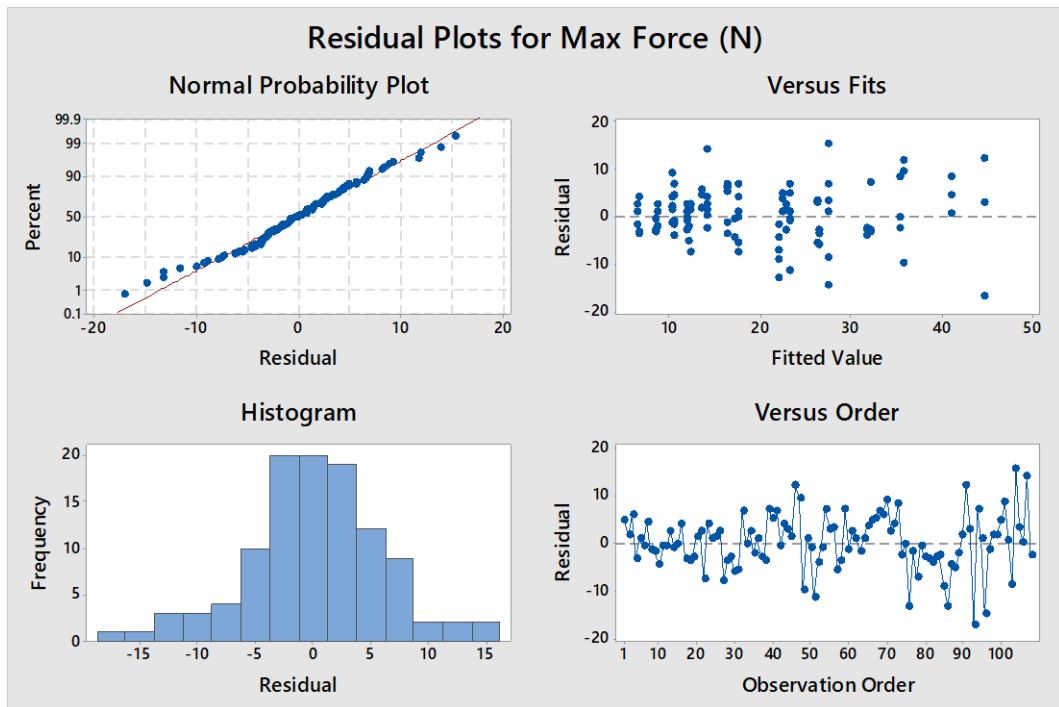


Figure F.0.3: Residual Plots for Response Variable Max Force 'Y₃'

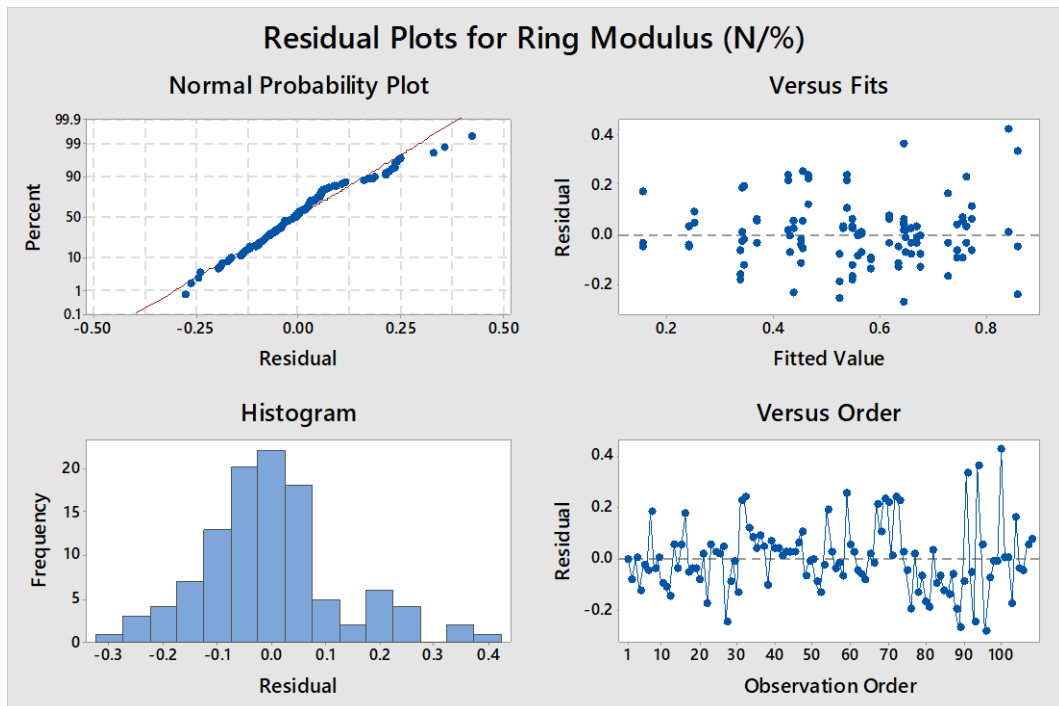


Figure F.0.4: Residual Plots for Response Variable Ring modulus 'Y₄'

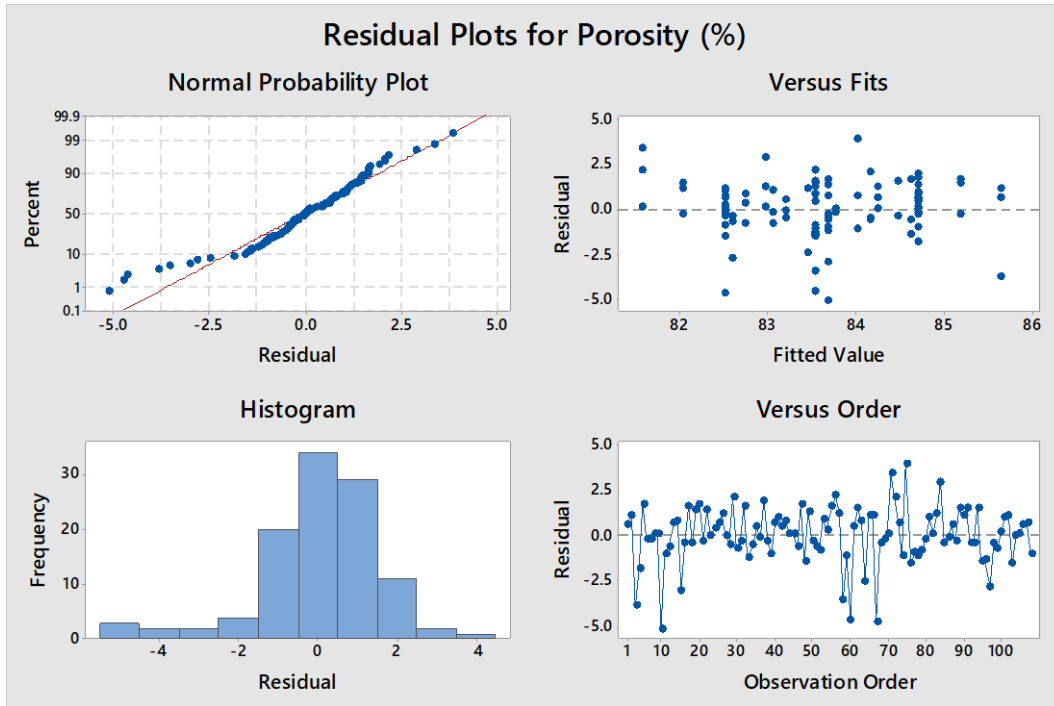


Figure F.0.5: Residual Plots for Response Variable Porosity 'Y₅'

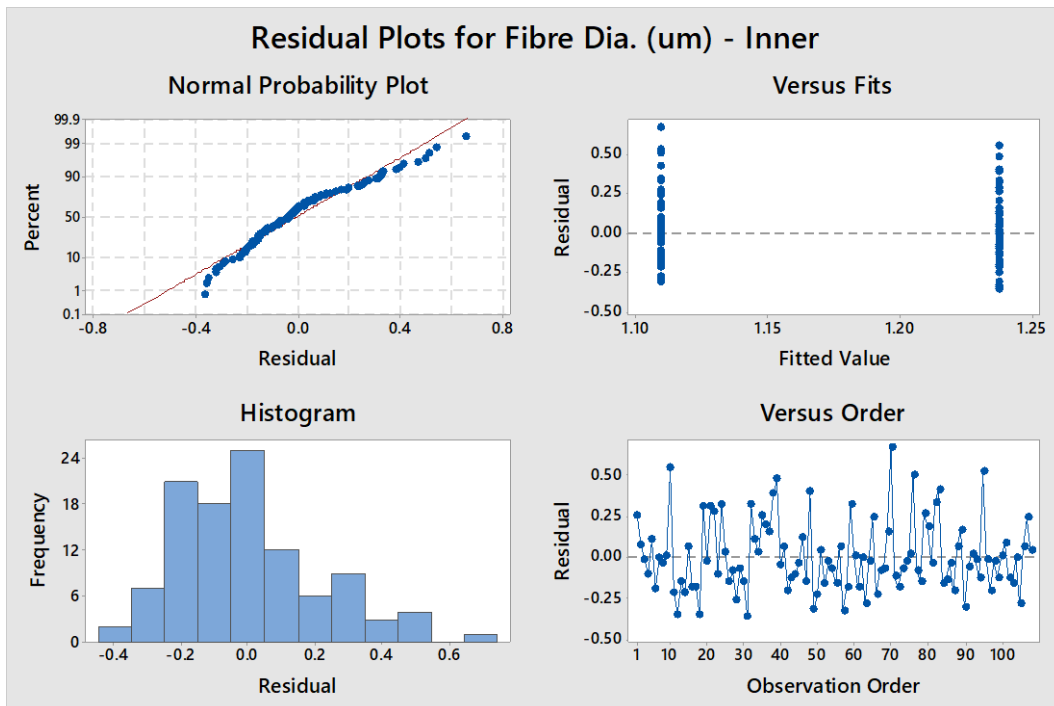


Figure F.0.6: Residual Plots for Response Variable Mean Inner Fibre Diameter 'Y₆'

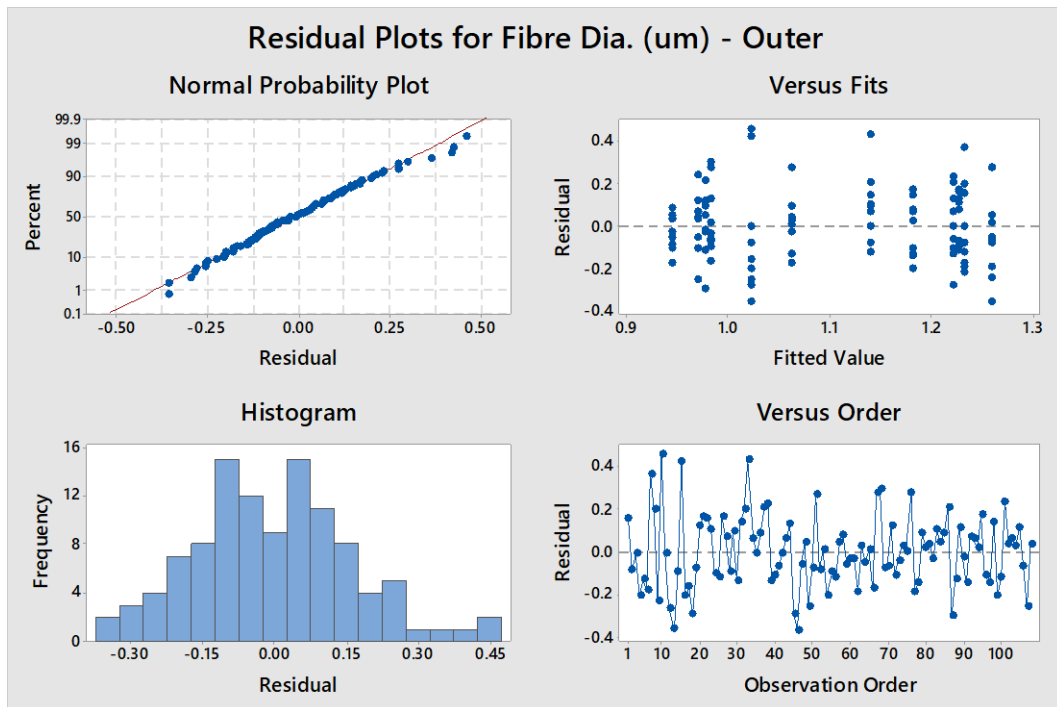


Figure F.0.7: Residual Plots for Response Variable Mean Outer Fibre Diameter 'Y₇'

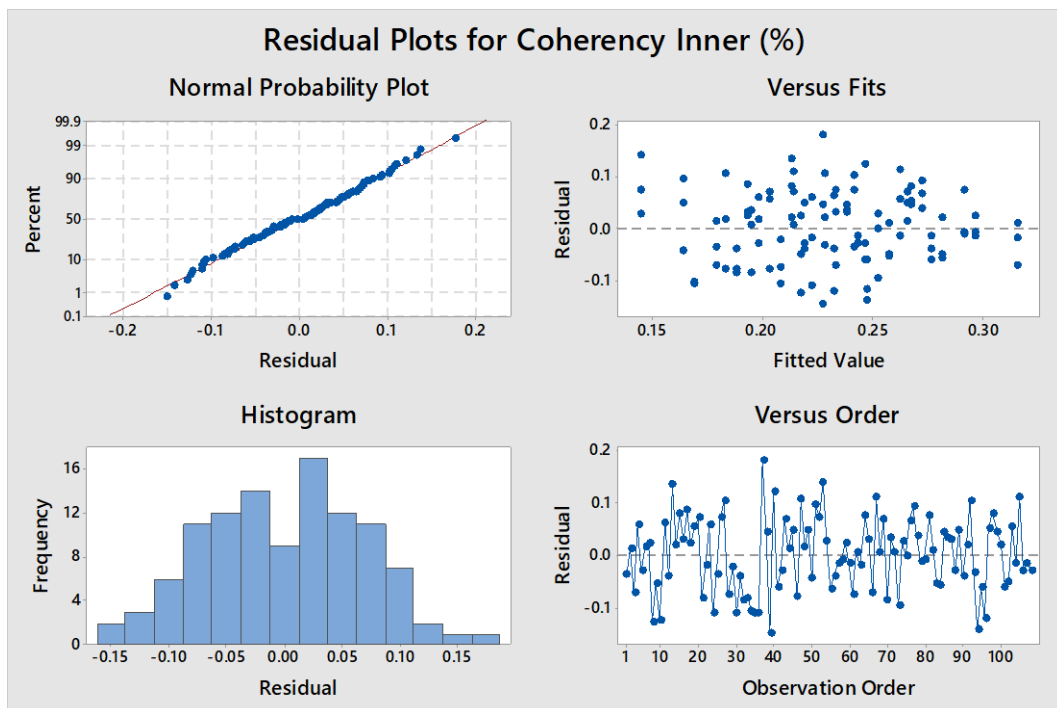


Figure F.0.8: Residual Plots for Response Variable Inner Fibre Coherency 'Y₈'

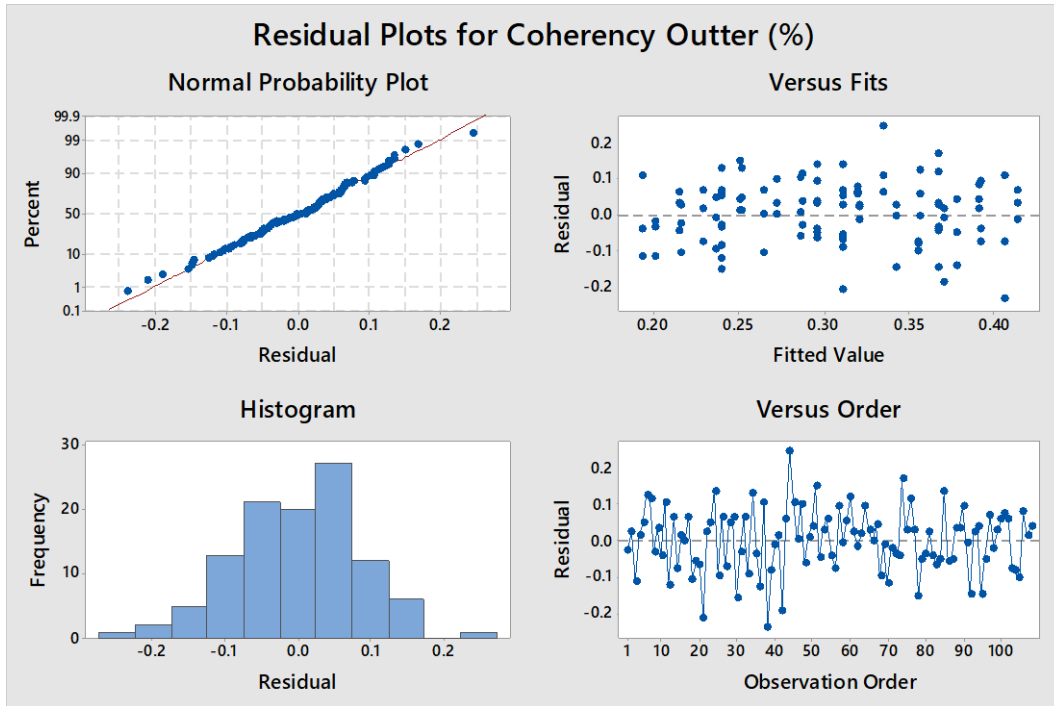


Figure F.0.9: Residual Plots for Response Variable Outer Fibre Coherency 'Y₉'

Appendix G: SEM Images of PCL Comparison Trial

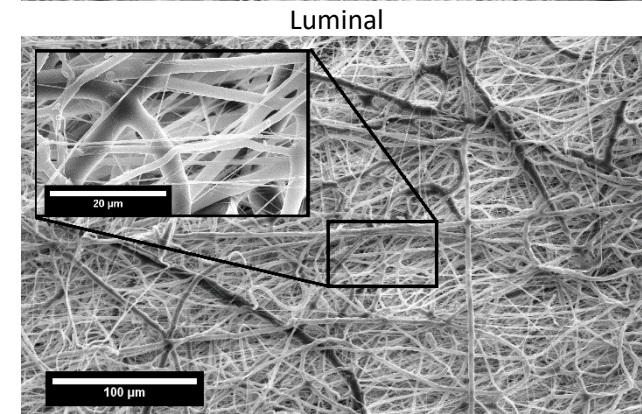
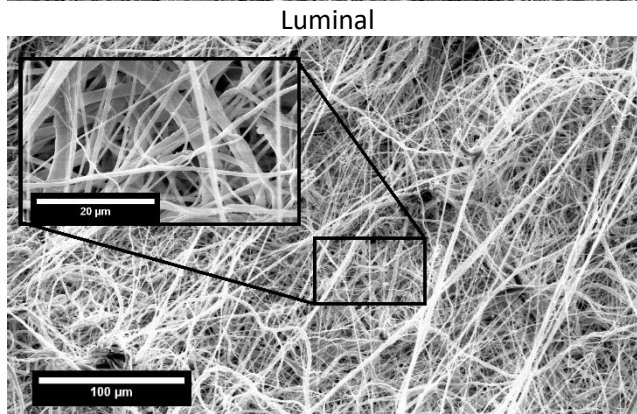
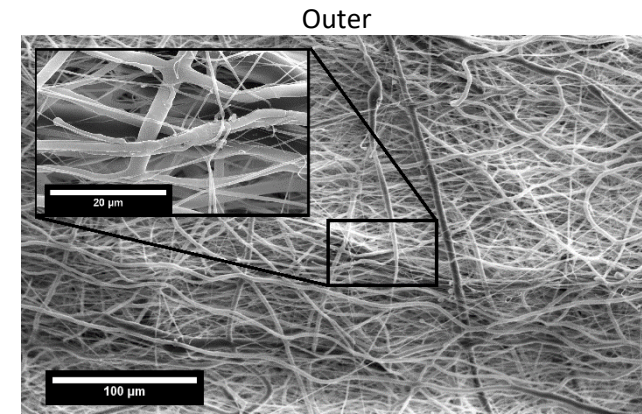
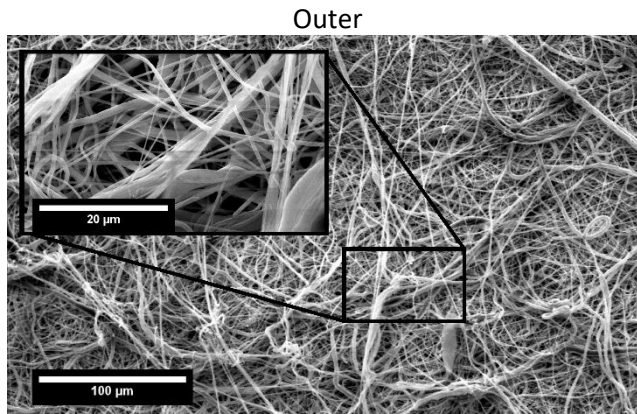
Table G.0.1: SEM images of PCL Comparison Trial

**Set 1 – PCL chloroform/Ethanol (7:3; v:v) on High RPM mandrel (3200 rpm)
(12ml/hr, 20kV, 17.5cm)**

New PCL Batch – 7.8wt%

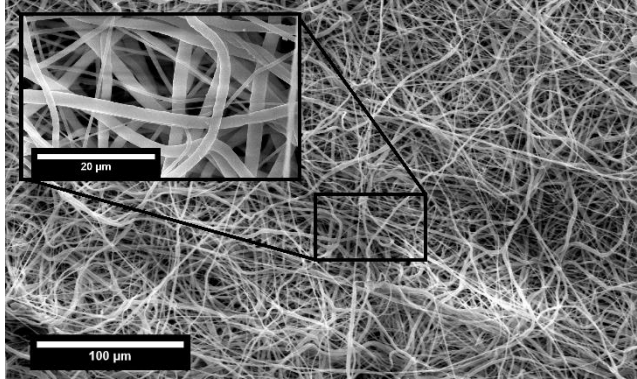
Old PCL Batch – 16wt%

10 min

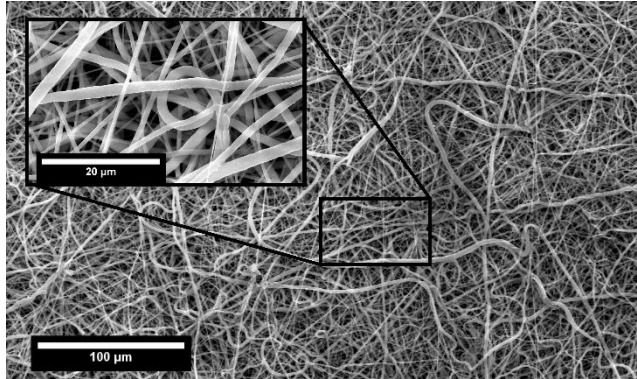


20 min

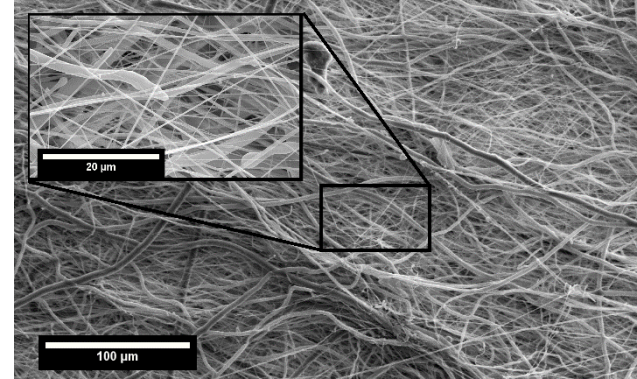
Outer



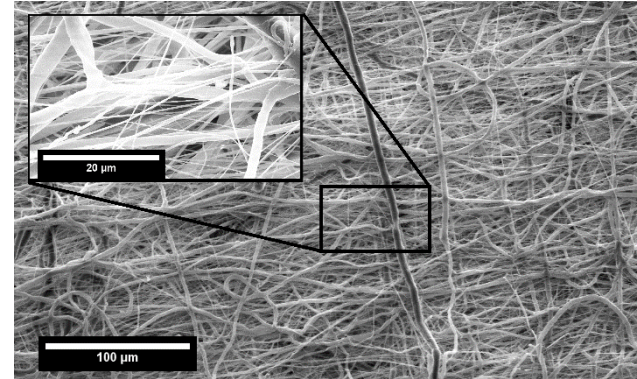
Luminal



Outer

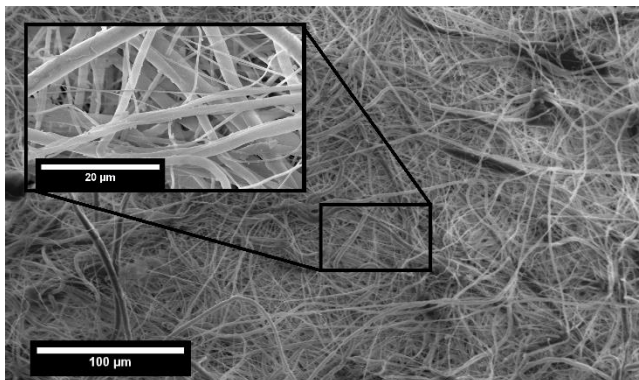


Luminal

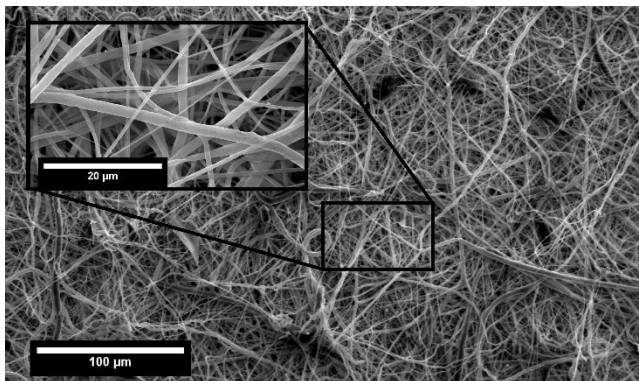


40 min

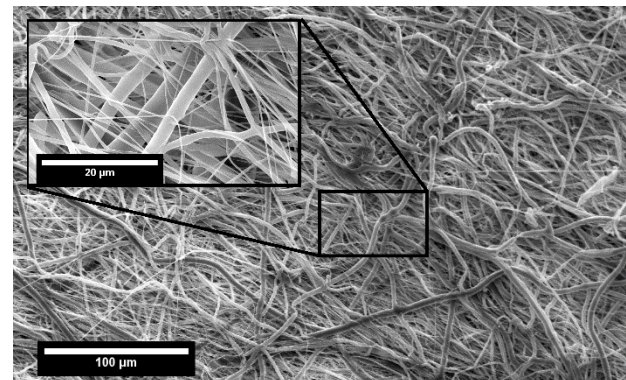
Outer



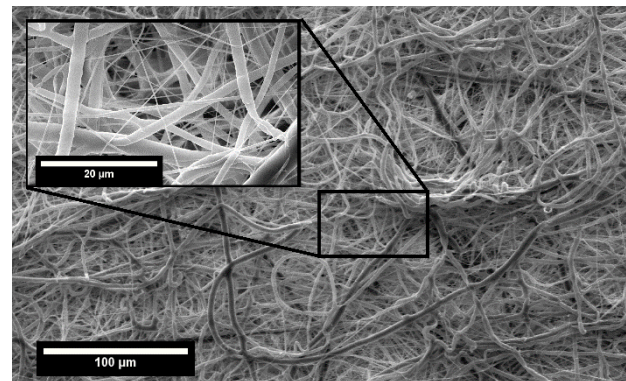
Luminal



Outer



Luminal



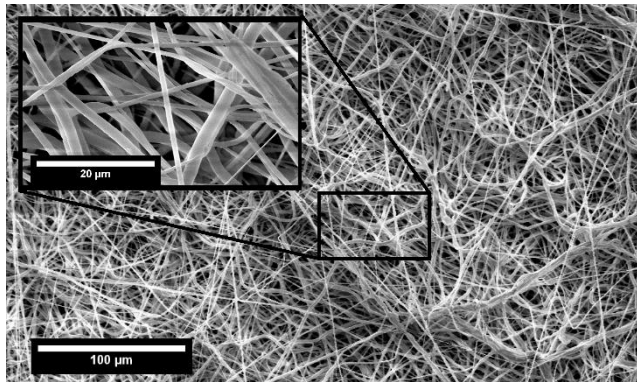
**Set 2 - PCL chloroform/Ethanol (7:3; v:v) on High RPM mandrel (3200 rpm)
(4ml/hr, 15kV, 17.5cm)**

New PCL Batch – 7.8wt%

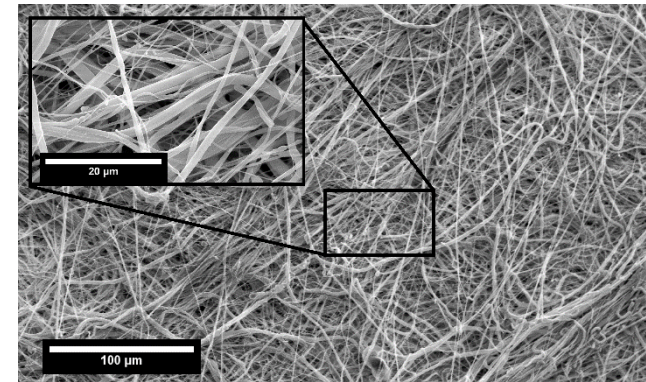
Old PCL Batch – 16wt%

20 min

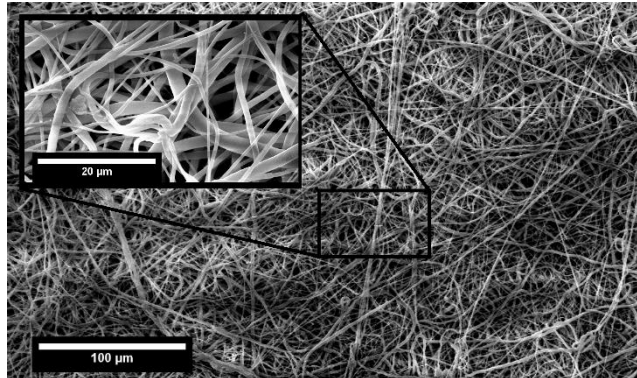
Outer



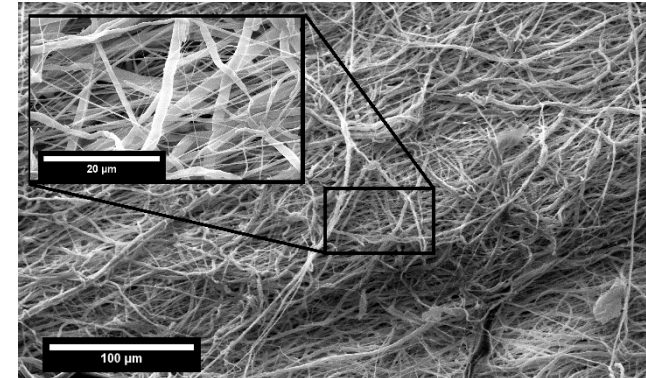
Outer



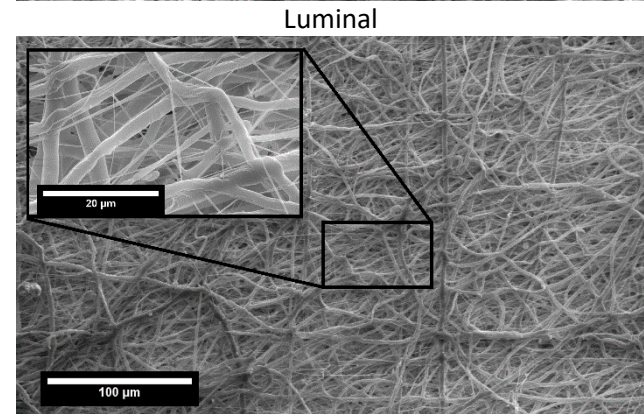
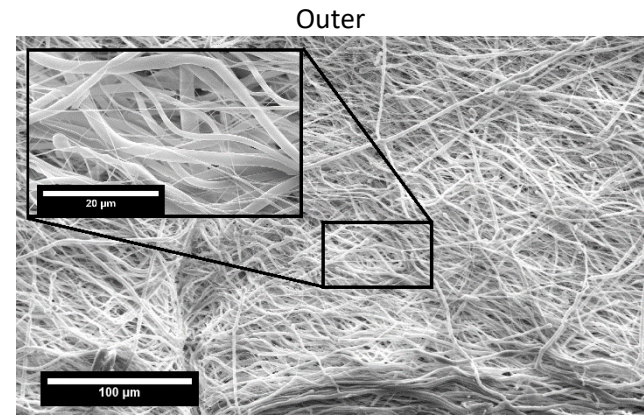
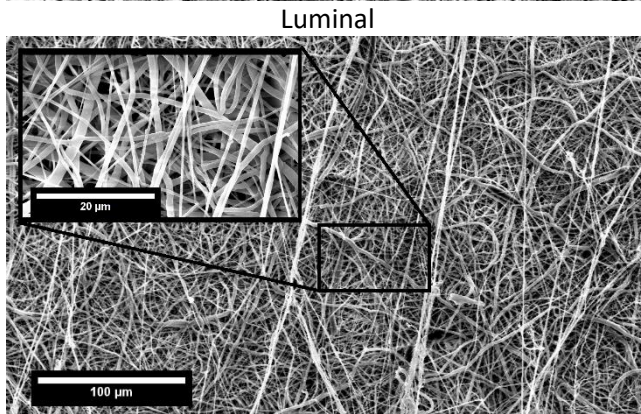
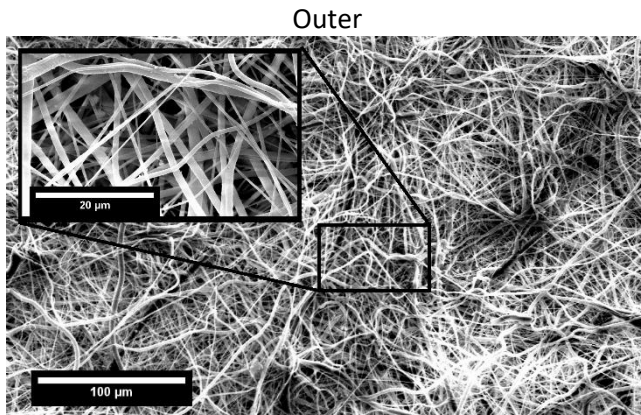
Luminal



Luminal

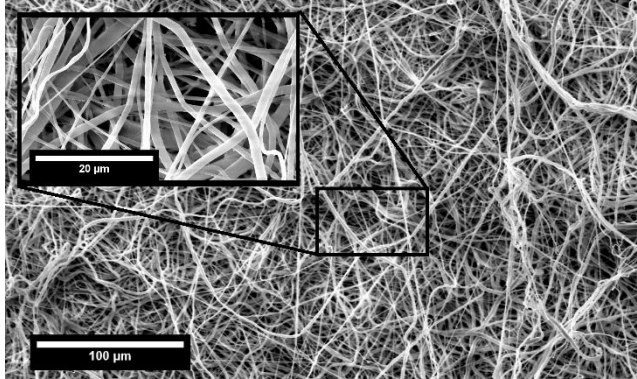


40 min

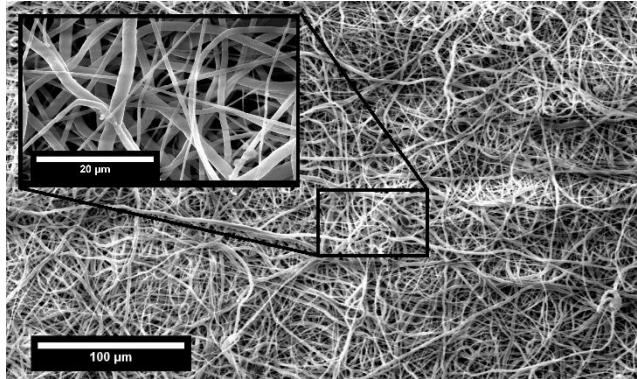


60 min

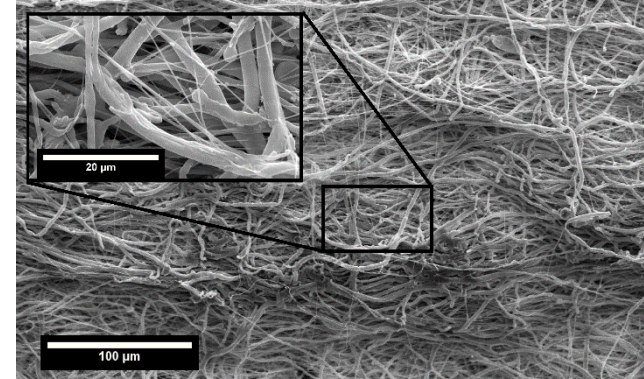
Outer



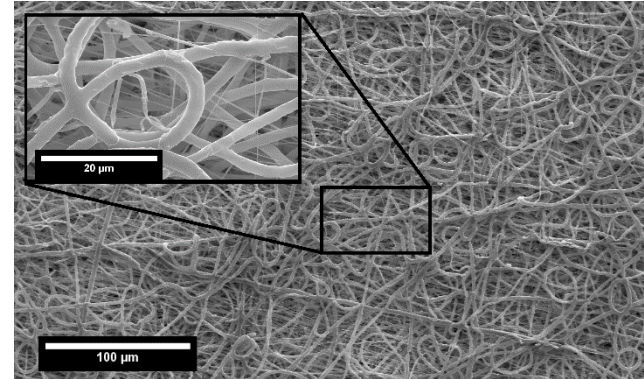
Luminal



Outer

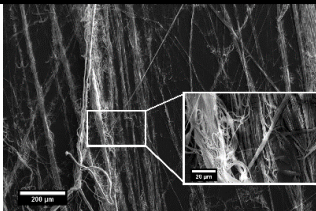
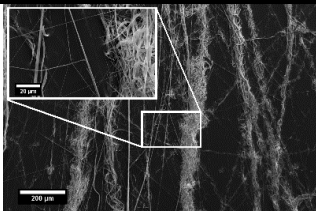
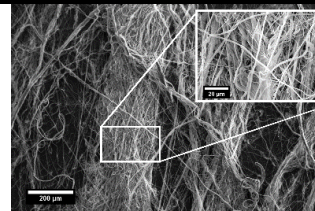
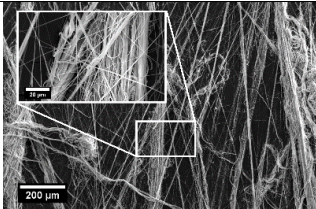
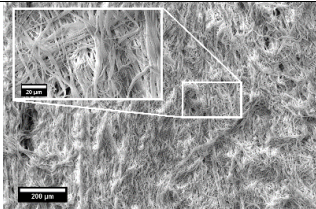
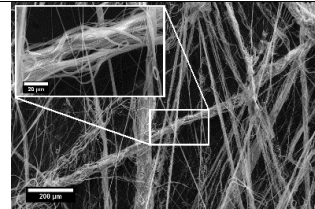
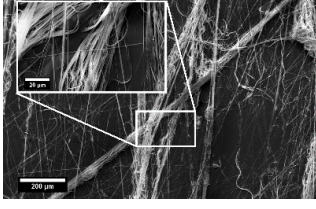
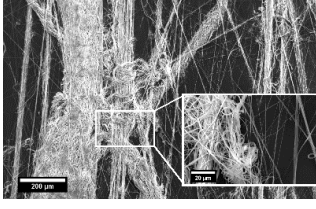
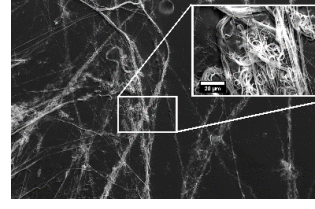
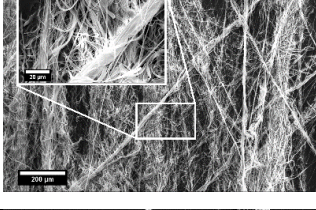
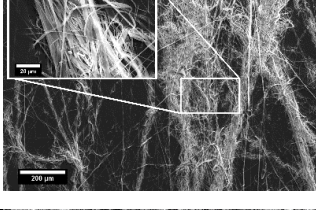
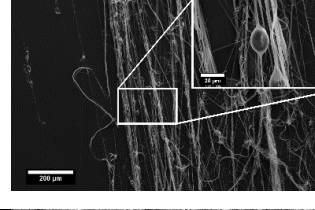

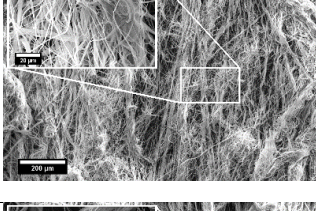
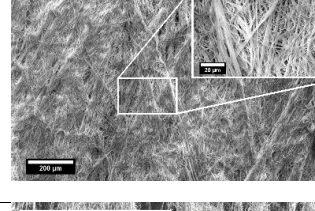
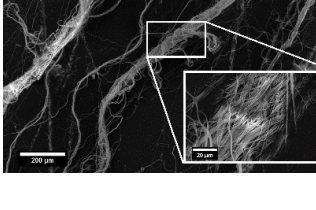
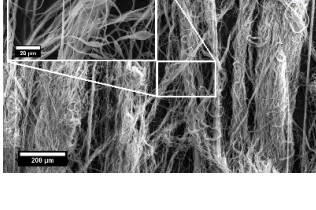
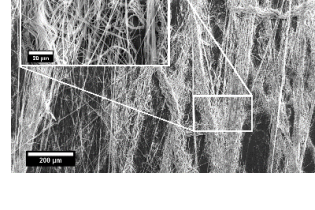


Luminal



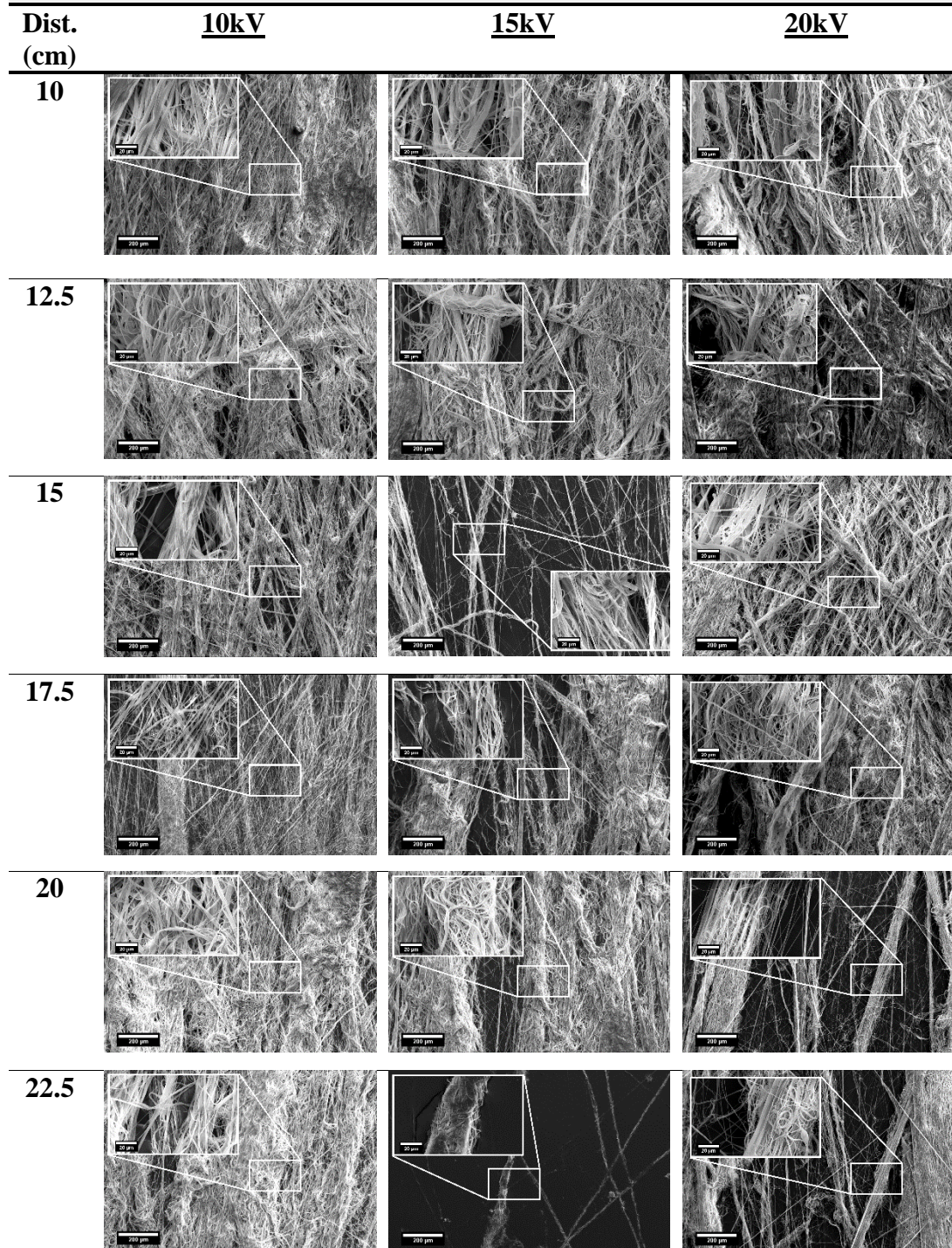
Appendix H: SEM Images of Dynamic Liquid Electrospinning Screening Trial

Table H.0.1: SEM images of PCL nanofibre bundles created through dynamic liquid electrospinning approaches

8wt% PCL chloroform/DMF (7:3; v:v)			
Spinning to Centre of Dynamic Liquid Collection Bath			
0.25 ml/hr			
Dist. (cm)	<u>10kV</u>	<u>15kV</u>	<u>20kV</u>
10			
12.5			
15			
17.5			
20			
22.5			

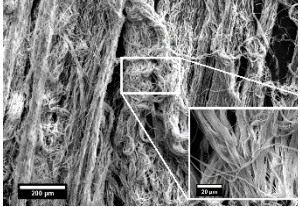
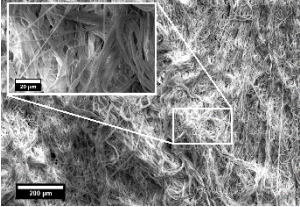
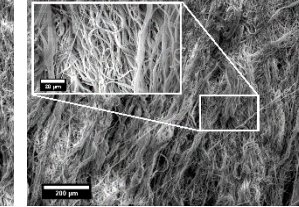
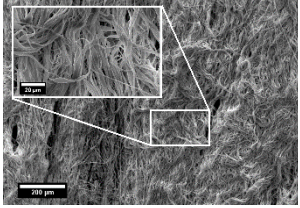
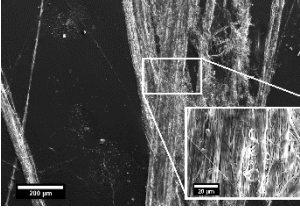
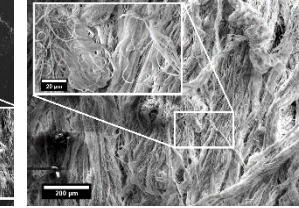
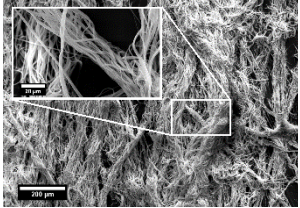
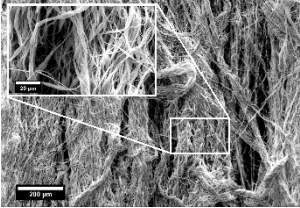
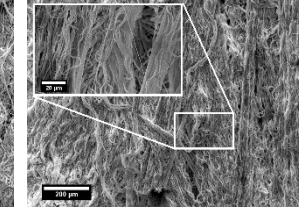
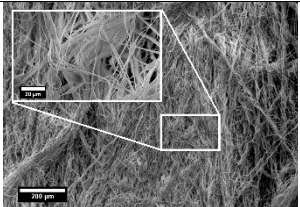
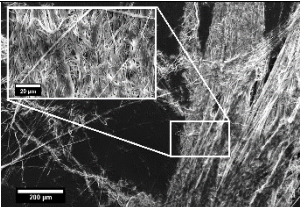
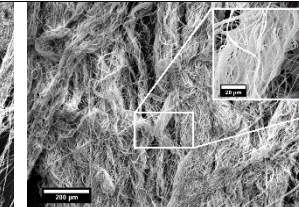
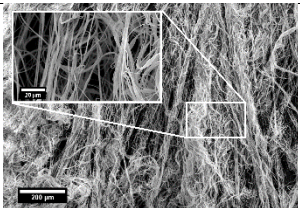
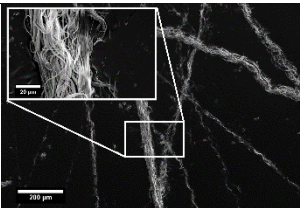
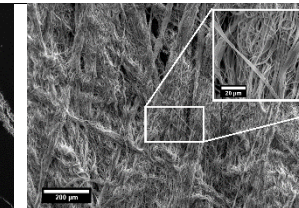
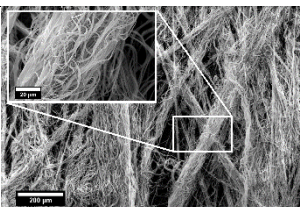
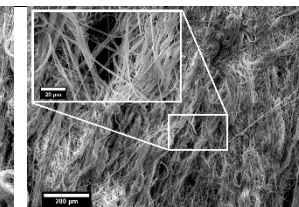
8wt% PCL chloroform/DMF (7:3; v:v)
Spinning to Centre of Dynamic Liquid Collection Bath

0.5 ml/hr



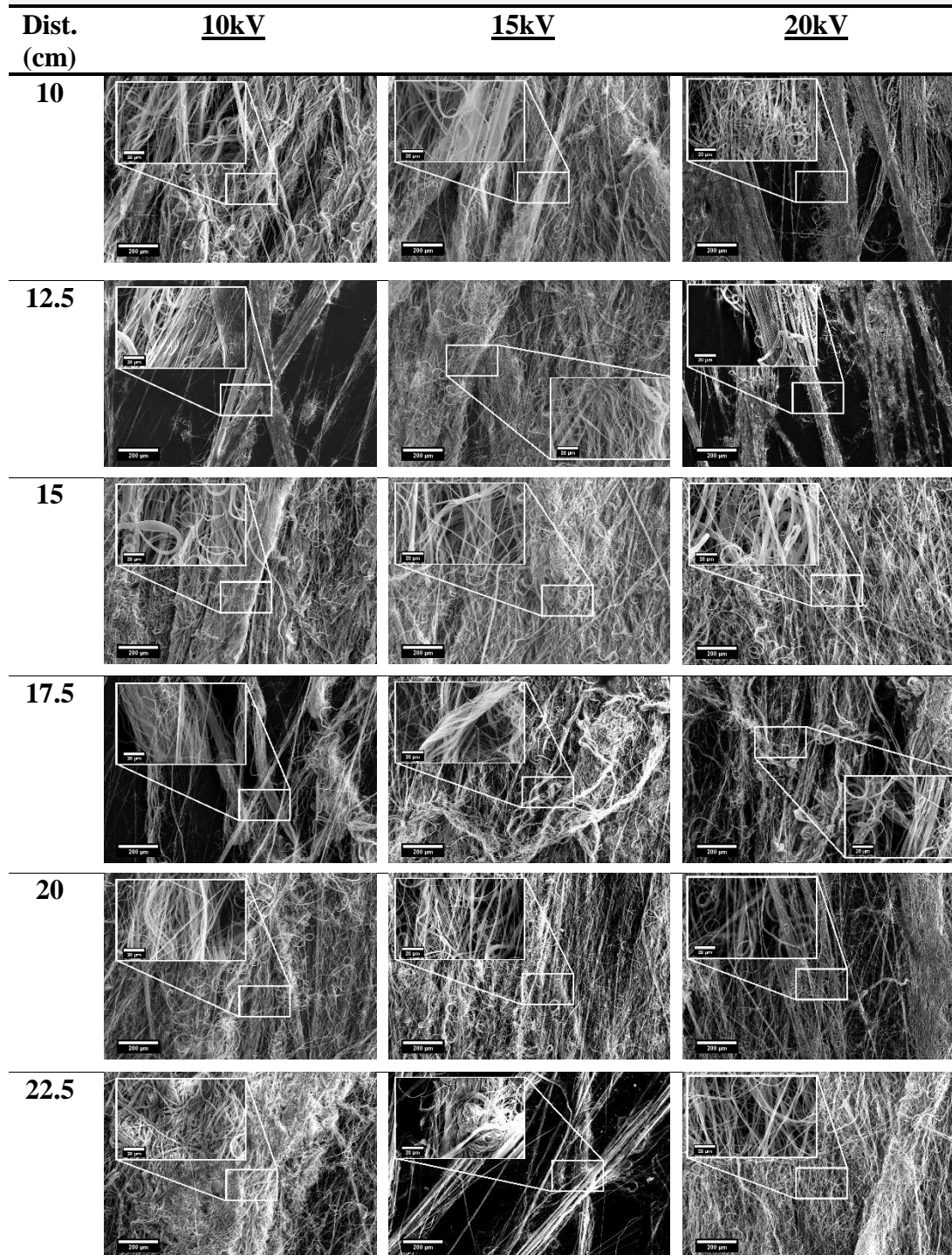
**8wt% PCL chloroform/DMF (7:3; v:v)
Spinning to Centre of Dynamic Liquid Collection Bath**

1 ml/hr

Dist. (cm)	<u>10kV</u>	<u>15kV</u>	<u>20kV</u>
10			
12.5			
15			
17.5			
20			
22.5	-		

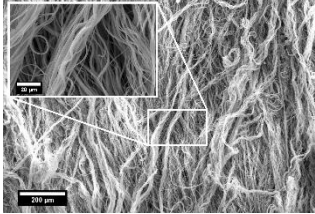
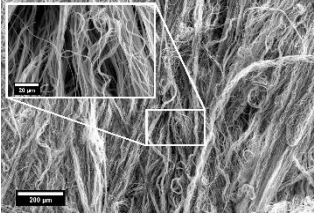
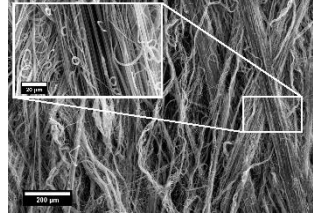
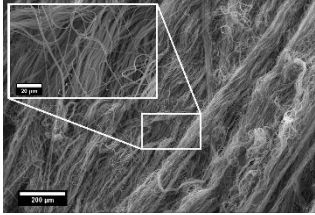
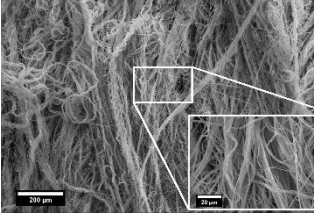
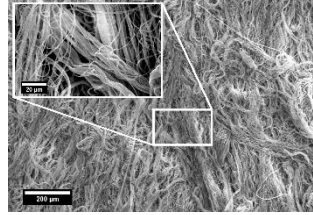
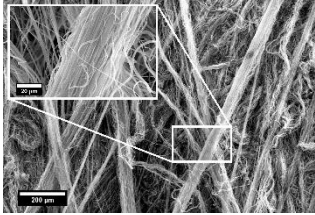
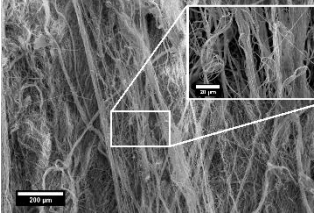
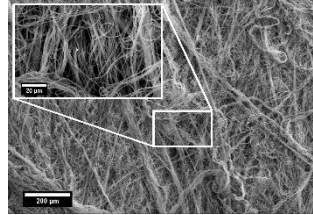
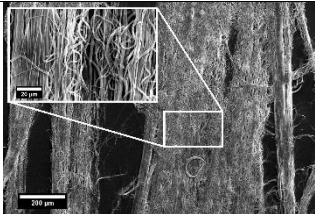
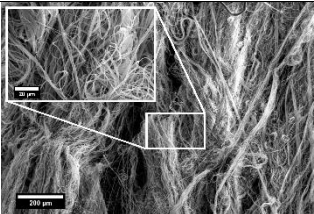
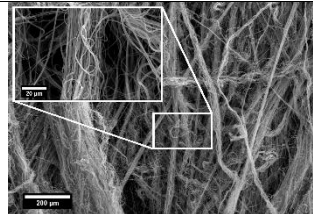
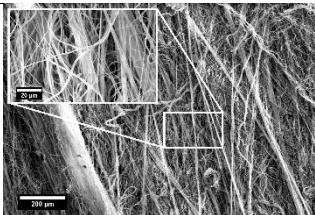
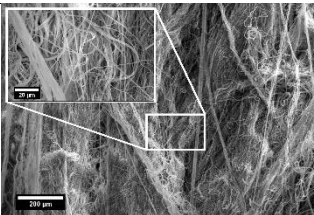
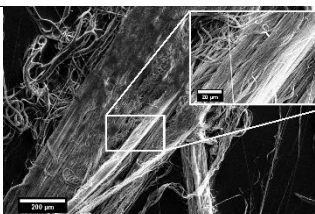
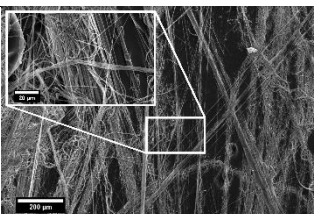
11wt% PCL chloroform/DMF (7:3; v:v)
Spinning to Centre of Dynamic Liquid Collection Bath

0.25 ml/hr



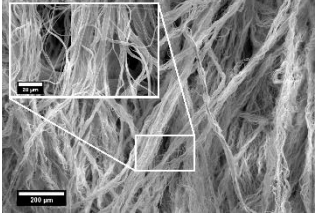
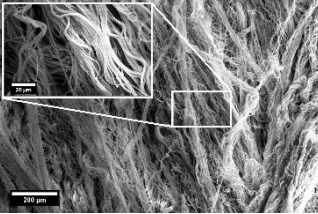
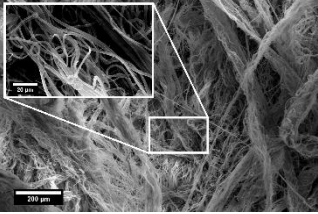
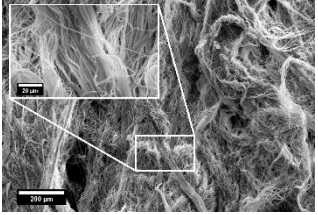
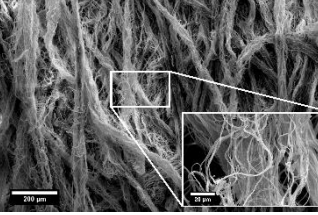
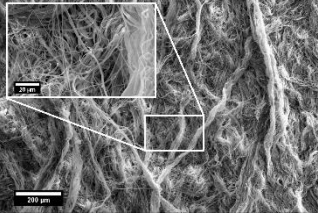
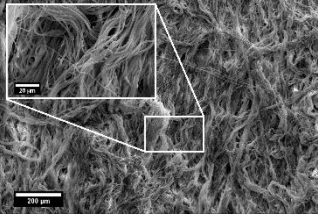
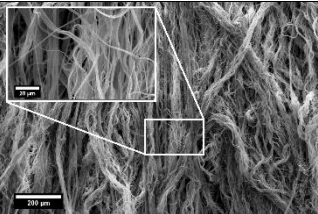
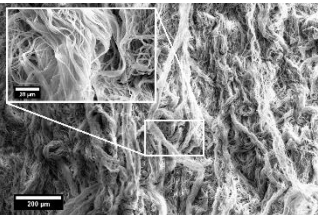
**11wt% PCL chloroform/DMF (7:3; v:v)
Spinning to Centre of Dynamic Liquid Collection Bath**

0.5 ml/hr

Dist. (cm)	<u>10kV</u>	<u>15kV</u>	<u>20kV</u>
10			
12.5			
15			
17.5			
20			-
22.5			-

**11wt% PCL chloroform/DMF (7:3; v:v)
Spinning to Centre of Dynamic Liquid Collection Bath**

1 ml/hr

Dist. (cm)	<u>10kV</u>	<u>15kV</u>	<u>20kV</u>
10			
12.5			
15	-	-	
17.5	-	-	
20	-	-	
22.5	-	-	